Taiyuan, China
July 21-24,2024

CFB 14

Proceedings of the 14th International Conference on Fluidized Bed Technology

CFB-14 ORGANIZING COMMITTEE

Taiyuan, China
July 21-24,2024

Proceedings of the

14th International Conference on Fluidized Bed Technology

Edited by

Guangxi Yue
Tsinghua University, Beijing, China

Hairui Yang
Tsinghua University, Beijing, China

Tuo Zhou
Tsinghua University, Beijing, China

Suxia Ma
Taiyuan University of Technology, Taiyuan, China

Host

Tsinghua University

Held by

Taiyuan University of Technology
Shanxi Key Laboratory of Efficient and Clean Combustion
and Utilization of Circulating Fluidized Bed

Chinese Society of Particuology

Sponsors

CFB-14 Organizing Committee

Chairman

Prof. Guangxi Yue   Tsinghua University, China

Vice Chairman

Prof. Fei Wei   Tsinghua University, China

Prof. Guangwen Xu   Shenyang University of Chemical Technology,China

Local Organizing Committee Members

Qingshan Zhu	Institute of Process Engineering, CAS, China
Wei Ge	Institute of Process Engineering, CAS, China
Qinggang Lyu	Institute of Engineering Thermophysics, CAS, China
Haigang Wang	Institute of Engineering Thermophysics, CAS, China
Yuhan Sun	Huairou Laboratory Shanxi Research Institute, China
Guogang Sun	China University of Petroleum, China
Lunbo Duan	Southeast University, China
Hui Wang	Harbin Institute of Technology, China
Yitian Fang	Institute of Coal Chemistry, CAS, China
Junfu Lyu	Tsinghua University, China
Zhenshan Li	Tsinghua University, China
Xiaogang Hao	Taiyuan University of Technology, China
Suxia Ma	Taiyuan University of Technology, China

International Advisory Board

PREFACE

The CFB-14 Conference continued the long-standing tradition of this conference series dating back to 1985, focusing on both fundamental research and practical applications in the field of circulating fluidized bed technology. Furthermore, it integrated innovative fluidized bed reactor technologies, particularly those pertaining to environmentally friendly processes, sustainable and clean energy generation, energy storage and conversion systems, and carbon capture and utilization methods such as chemical looping combustion/gasification. In addition to investigating the fundamental and applied aspects of fluidized beds and fluidization systems, CFB-14 also placed a strong emphasis on fluidized bed technologies aimed at addressing energy and environmental challenges.

CFB-14 is the 14th conference in a series following the 13 successful conferences over the past 38 years:

• CFB-1, Halifax, Canada, 1985

• CFB-2, Compiegne, France, 1988

• CFB-3, Nagoya, Japan, 1991

• CFB-4, Hidden Valley, USA, 1993

• CFB-5, Beijing, China, 1996

• CFB-6, Wurzburg, Germany, 1999

• CFB-7, Niagara Falls, Canada, 2002

• CFB-8, Hangzhou, China, 2005

• CFB-9, Hamburg, Germany, 2008

• CFB-10, Sunriver, USA, 2011

• CFB-11, Beijing, China, 2014

• CFB-12, Krakow, Poland, 2017

• CFB-13, Vancouver, Canada, 2021

Following the tradition of the conference series, CFB-14 covers broad topics ranging from eight colloquiums including Dynamics, heat and mass transfer of gas-solid flow, Modeling and simulation, Measurements and instrumentation, Catalytic reaction and novel reaction process, Combustion, pyrolysis and gasification, Looping and energy storage processes, Fine particle and nano-particle systems, Industrial experience and application.

Other activities have been planned to celebrate the accomplishment of the first 13 CFB conference series, which include a historical review given by the convenor of the CFB conference series (Prof. Xiaotao Bi), and the presentation of fluidization achievement awards to two fluidization researchers who have made outstanding contributions in advancing the fluidization science and CFB

technology.

We are proud to present them with this proceeding and wish to gratefully acknowledge the authors, sponsors, reviewers, organizing committee members and all the people who have volunteered generously with their time and efforts to make this conference a great success.

CFB-14 Organizing Committee

TABLE OF CONTENTS

Session A:

Dynamics, heat and mass transfer

of gas-solid flow

CALCULATION OF SHORT-CIRCUIT FLOW RATE IN A GAS CYCLONE

Shiwei Yuan, Guogang Sun*, Gang Cao, Yunpeng Yue, Yingyi Wu

College of Mechanical and Transportation Engineering, China University of Petroleum, Beijing 102249, PR China

18 Fuxue Road, Changping, Beijing 102249, P. R. China

*Email: sunguogang@cup.edu.cn

Abstract

Short-circuit flow is an important indicator for evaluating the performance of a cyclone separator. In this paper, a new short-circuit flow calculation method is proposed through numerical simulation. Based on the response surface method, the short-circuit flow rate in the cyclone separator was analyzed under different inlet velocity V_i, inlet cross-section coefficient KA, and vortex finder diameter Der, and the effects of the three parameters on the short-circuit flow rate and the interactions among the parameters were comprehensively investigated. The formula for short-circuit flow rate was also obtained according to the Design-Expert software, which was examined and shown to be accurate. It can provide a reference basis for the optimized design of cyclone separators.

Key words: Cyclone separator; Short-circuit flow rate; Numerical simulation

1. Introduction

Circulating fluidized beds (CFBs) are versatile in industrial use and favored for handling materials and waste due to their efficiency. Cyclone separators within CFB systems play a crucial role in particle-gas separation, impacting system stability and performance. Short-circuit flow is a common type of local secondary flow in cyclone separators, often carrying small particle sizes that escape, thereby reducing separation efficiency [1,2]. Therefore, the magnitude of the short-circuit flow rate also becomes an important indicator for evaluating separation performance [3].

Although the concept of short-circuit flow has a clear physical meaning, it lacks an accurate mathematical description. In existing literature, due to differences in understanding short-circuit flow, there are variations in the methods used to calculate it. For example, Qian [4] calculates the short-circuit flow of the separator by taking the difference between the downward flow at a position 0.002m below the inlet of the vortex finder and the total inlet flow. Fu [5] divides a circular ring based on the inflection points of the radial flow's centripetal and centrifugal trends, considering the downward flow within this ring as the short-circuit flow of the separator. Different calculation methods also lead to different results for short-circuit flow, even contradictory ones. Moreover, due to the complexity of the short-circuit flow concept and the difficulty in measurement and calculation, there is currently no quantitative expression for calculating short-circuit flow in research.

To this end, this study proposes a novel method for calculating short-circuit flow based on variations in the flow field. Furthermore, the impacts of the riser diameter ratio (*Der*), inlet area coefficient (*KA*), and inlet velocity (*V_i*) on the short-circuit flow inside cyclone separators were investigated using the response surface methodology. A regression analysis was conducted to derive a formula for calculating the short-circuit flow rate. The aim is to provide assistance for the development and structural optimization of cyclone separators in engineering applications.

2. Methodology of the study

2.1 Geometrical of cyclone separators

The cyclone separator used in this study is a typical Stairmand type and is represented in Figure 1. The primary dimensions of the model are listed in Table 1.
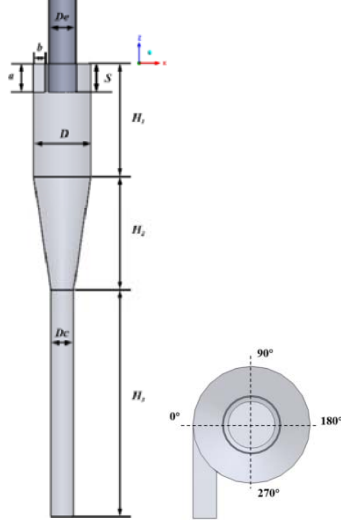
Fig. 1 Geometrical model of cyclone separator   Fig. 2 Vertical lines located on the CS surface
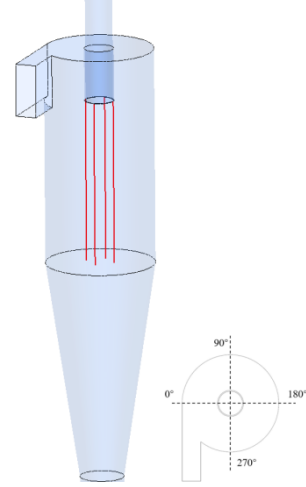
Table 1. Cyclone separator geometry (Unit：mm）

a	b	D	De	Dc	S	H_1	H_2	H_3
105/85/73	42/34/29	150	40/66/93	60	105/85/73	300	300	600

2.2 Numerical Simulation Settings

This study chooses to use LES for computing the flow field within the cyclone separator. The pressure-velocity coupling scheme used the PRESTO! method, and the turbulent diffusion scheme employed QUICK. The algorithm implemented was SIMPLEC. Unsteady-state simulations were performed with a time step of 0.0001 seconds [6,7]. In this computation, a velocity inlet boundary condition was applied. The outlet boundary condition was set as outflow. All walls were modeled as no-slip boundaries. The medium considered was air, characterized by a density of 1.225 kg/m^3 and a viscosity of 1.7894×10^{-5} Pa·S.

3. Results and discussion

3.1 Calculation of short-circuit flow rate

In this study, we propose a novel method for short-circuit flow calculation based on the radial velocity changes near the inlet of the vortex finder. To illustrate this method, we provide a brief introduction using the example of a separator with KA=8 and Der=0.25 at V_i=20 m/s.

The short-circuit flow refers to the escaping airflow near the inlet of the vortex finder. By identifying the short-circuit region on the interface and integrating the radial velocity, the radial inflow rate in the short-circuit region can be determined. In this study, the circumferential surface (CS surface) is used as the interface between the inner and outer swirling flows [8]. Four vertical lines located at 0°, 90°, 180°, and 270° on the underside of the separator's vortex finder are employed to determine the axial positions corresponding to the short-circuit region, as depicted in Fig. 2.

The radial velocity variations along four vertical lines are shown in Fig. 3. Fig. 3(a) provides a magnified view of the region enclosed by the red dashed box in Fig. 3(A). The separator is divided into centripetal and centrifugal flow regions based on the negative and positive radial velocities, respectively. A significant difference in radial velocity can be observed near the inlet of the vortex finder and the cylindrical section due to the occurrence of short-circuit flow. Initially, there is a large centripetal radial velocity at the inlet of the vortex finder, up to 30m/s. This indicates that the flow in this region is centripetal, and the short-circuit phenomenon is more pronounced here. Subsequently, the centripetal radial velocities along the four vertical lines gradually decrease. Some lines have transitioned from centripetal to

centrifugal flow, indicating a diminishing impact of short-circuit flow on the flow field. This trend continues until the centripetal radial velocities along all four lines reach turning points and cease to decrease, signifying that the radial velocities are no longer influenced by the short-circuit flow phenomenon. The axial interval from the turning point position to the inlet of the vortex finder is where the short-circuit flow occurs in the corresponding axial interval position, as shown by the black dashed line in Fig. 5(a).
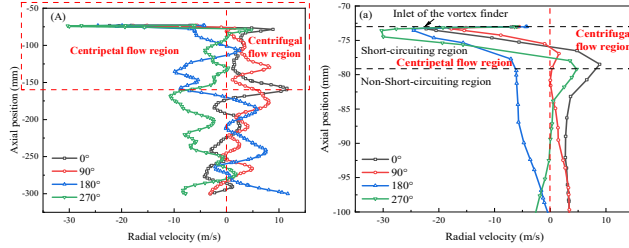
Fig. 3 Radial velocity distribution on the CS surface   Fig. 4 Short-circuit flow regions in cyclone
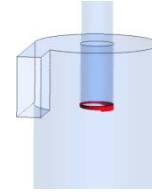
Using the Create/Iso-clip function in Fluent software, the region at the CS surface with negative radial velocity corresponding to the mentioned axial interval position was clipped. This region represents the occurrence of short-circuit flow, as shown by the red area in Fig.4. The short-circuit flow occurrence region is not a complete cylindrical surface, which differs significantly from the traditional radial velocity method (the traditional radial velocity method assumes that the short-circuit flow region is a complete cylindrical surface [9]). To determine the integration of the short-circuit flow region with respect to radial velocity, the Reports/Surface Integrals function in Fluent software can be utilized. Upon calculation, the radial inflow for this cyclone separator is determined to be 0.007369 m³/s.

The calculated radial inflow rate for the short-circuit region is the sum of the short-circuit flow rate and the radial seepage flow rate [10]. Therefore, to calculate the short-circuit flow rate, it is necessary to subtract the radial seepage flow rate from the total radial inflow rate. Fig. 5 illustrates the downward flow rate calculated averaged over the cross section at different axial positions (heights) of the cyclone separator. Using Origin software, a fitting was performed for the downward flow rate of the separator, as shown in Eq. (1). The fitted formula allows for the prediction of the radial seepage flow rate in the short-circuit region of the separator as 0.000549 m³/s. Consequently, by subtracting the predicted radial seepage flow rate from the total radial inflow rate in the short-circuit region, the short-circuit flow rate can be determined, accounting for 16.12% of the total inlet flow.
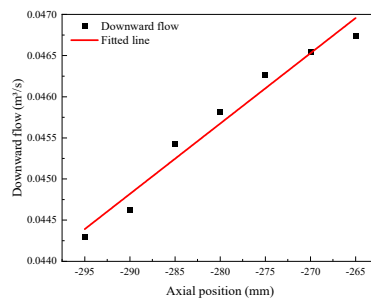
Fig.5 Downward flow of the cyclone

$$y = 0.06962 + \left(8.55176 \times 10^{-5}\right)x \tag{1}$$

where, x is the axial position, mm; y is the downward flow rate corresponding to the axial position, m³/s.

3.2 Design of the response surface methodology

In this paper, a three-factor, three-level simulation test was conducted using the principle of Box-Behnken experimental design, with the factors and levels outlined in Table 2.

Table 2. Box-Behnken Design Factors and Levels

Levels	Factors		
	Inlet area coefficient KA	dimensionless vortex finder diameter Der	inlet velocity V_i / （m/s）
-1	4	0.25	10
0	6	0.42	20
1	8	0.60	30

3.3 Regression modeling and accuracy validation

This study employed Design-Expert to obtain a multivariate quadratic regression equation for the short-circuit flow rate within the cyclone separator, as represented by Equation (2). To evaluate the accuracy of the regression model, simulations were conducted on a set of cyclone separators with structural parameters KA=5.5 and Der=0.4. These simulations were performed at two different inlet velocities, namely 15m/s and 25m/s. The simulated results were then compared with the predictions made by the model, as shown in Table 3. The results indicate that although the model predictions tend to be slightly higher, the absolute errors are all within 4%. Based on these findings, it can be concluded that the model demonstrates strong predictive capability.

$$Q_{Short-circuiting} = -40.57 + 3.34KA + 219.36D_{er} + 1.95V_i - 7.35KAD_{er}$$
$$-0.39V_iKA + 0.77V_iD_{er} + 0.25KA^2 - 169.99D_{er}^2 + 0.0068V_i^2$$

(2)

Table 3. Comparison of model prediction results with simulation results

V_i/(m/s)	KA	D_{er}	Model prediction results	Simulation results	absolute errors
15	5.5	0.4	32.93%	29.86%	3.07%
25	5.5	0.4	36.81%	33.85%	2.96%

3.4 Analysis of the impact of the main factors

Fig. 6 presents the results of the sensitivity analysis conducted on the main factors influencing the short-circuit flow rate. The horizontal axis represents the normalized level coding of each influencing parameter, while the vertical axis represents the average value of 'short-circuit flow rate ' corresponding to the coding. KA exhibits the most significant impact on the short-circuit flow rate, decreasing as KA increases, aligning with improved separation efficiency at higher KA values. Elsayed [11] found in their study that increasing KA reduces the velocity near the inlet of the vortex finder, decreasing the short-circuit flow rate, and thereby improving separation efficiency. Wu [12] obtained similar experimental results by measuring the separator flow field. There is a significant positive correlation between short-circuit flow rate and Der, consistent with previous research [13]. When Der decreases, the inlet area of the vortex finder shrinks, increasing the tangential velocity and impeding airflow escape near the inlet of the vortex finder, consequently reducing the short-circuit flow rate and improving separation efficiency. Additionally, there is a significant positive correlation between short-circuit flow rate and V_i. As the inlet velocity increases, the total inlet air volume increases, proportionally amplifying the tangential and radial velocities in the separator. However, the relative amount of gas escaping from the short-circuit flow also increases, consistent with the results of Dong [14] in their study. Thus, maintaining a moderate V_i and considering increasing KA or reducing Der are crucial in cyclone separator design to effectively diminish short-circuit flow and enhance separation performance.
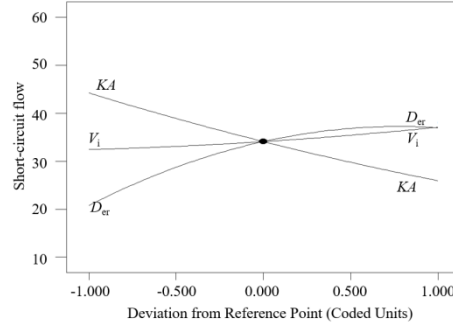
Fig. 6 Analysis of factors affecting short-circuit flow rate

3.5 Analysis of the interaction of factors

Using response surface methodology and the regression equation, contour plots and response surface plots were generated as shown in Fig. 7, providing a more intuitive representation of the interaction effects of the pairwise factors KA, V_i, and Der on short-circuit flow rate. From Figs. 7(a) and (b), it is observed that when KA is large, increasing Der leads to a rapid increase in short-circuit flow rate in the separator; conversely, when KA is small, the increase in Der results in a slower growth rate of short-circuit flow rate. Figs. 7(c) and (d) reveal that when KA is small, increasing V_i results in a gradual increase in short-circuit flow rate, while when KA is large, increasing V_i leads to a gradual decrease in short-circuit flow rate. Similarly, Figs. 7(e) and (f) demonstrate that when Der is small, increasing V_i results in a slow growth rate of short-circuit flow rate, whereas when Der is large, increasing V_i leads to a faster growth rate of short-circuit flow rate. These findings indicate that the pairwise interactions between KA, Der, and V_i in the cyclone separator have a relatively strong impact on short-circuit flow rate. Therefore, when considering the influence of one factor on short-circuit flow rate, it is essential to take into account the values of the other two parameters.
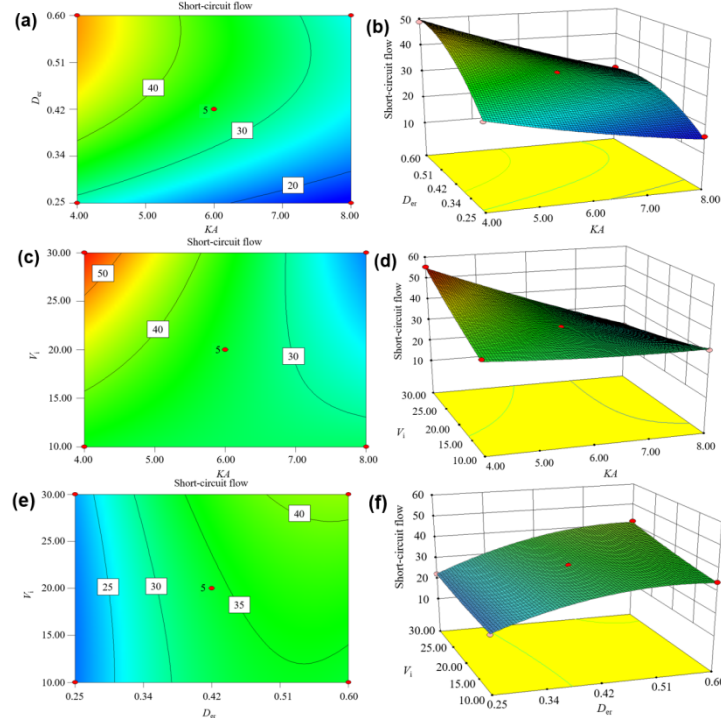
Fig. 7 Effect of factor interactions on short-circuit flow rate

4. Conclusion

In this study, a novel method for calculating short-circuit flow rate is proposed through numerical simulation. Utilizing response surface methodology, the comprehensive effects of

the inlet area coefficient (*KA*), dimensionless vortex finder diameter (*Der*), and inlet velocity (*V*$_i$) on short-circuit flow rate were investigated. The results obtained are as follows:

(1) A novel method for calculating short-circuit flow rate is introduced in this research. This method accurately delineates the short-circuit and non-short-circuit regions based on the variations in radial velocity at different orientations near the inlet of the vortex finder. Importantly, it eliminates the influence of radial seepage on the short-circuit flow rate.

(2) Regression equations for the short-circuit flow rate in relation to *KA*, *Der*, and *V*$_i$ were established using response surface methodology. The formula was verified to have a small error, providing a valuable reference for the optimized design of cyclone separators.

(3) Main factor analysis revealed a significant negative correlation between short-circuit flow in the cyclone separator and *KA*, while positive correlations were observed with *Der* and *V*$_i$. The interaction analysis showed a strong interaction between the effects on the short-circuit flow rate in *KA*, *Der*, and *V*$_i$.

Acknowledgment

References

[1]   Li, Z., Tong, Z., Zhang, H., Chu, K., et.al. CFD-DEM simulation of the supercritical water-solid flow in cyclone. Powder Technology.418(2023),118261.
[2]   Fatahian, H., Fatahian, E., Erfani. R., Square Cyclone Separator: Performance Analysis Optimization and Operating Condition Variations Using CFD-DPM and Taguchi Method. Powder Technology.428(2023),118789.
[3]   Misiulia, D., Lidén, G., & Antonyuk, S. (2023). Secondary Lip Flow in a Cyclone Separator. Flow, Turbulence and Combustion, 110, 581–600.
[4]   Qian, F., & Wu, Y. (2009). Effect of the inlet section angle on the separation performance of a cyclone. Chemical Engineering Research and Design, 87, 4567-1572.
[5]   Fu, X., Sun, G., Liu, J., et al. (2011). Discussion on the estimation of short-circuit flow in cyclone separator and its numerical calculation method. CIESC Journal, 62, 2535-2540.
[6]   Pandey, S., & Brar, L.S. (2023). Performance analysis of cyclone separators with bulged conical segment using large-eddy simulation. Powder Technology, 425, 118584.
[7]   Wang, Z., Sun, G., Yuan, S., Qian, Z., & Song, Z. (2022). Effect of number of inlets on performance and flow field of large-scale cyclone separators. Asia-Pacific Journal of Chemical Engineering, 6, 1-10.
[8]   Barth, W. (1956). Berechnung und Auslegung von Zyklonabscheidern auf Grund neuerer Untersuchungen. Brennstoff-Warme-Kraft, Bd8(1), Heft1-9.
[9]   Hoffmann, A.C., Stein, L.E., & Bradshaw, P. (2003). Gas cyclones and swirl tubes: Principles, design and operation. Applied Mechanics Reviews, 56(B28-B29).
[10] Muschelknautz, E., & Trefz, M. (1990). Design and calculation of higher and highest loaded gas cyclones. Proceedings of Second World Congress on Particle Technology, 52-71.
[11] Elsayed, K., Lacor, C. (2011). The effect of cyclone inlet dimensions on the flow pattern and performance. Applied Mathematical Modeling, 35, 1952-1968.
[12] Wu, X., & Huang, X. (1993). Experimental research on particle concentration distribution in cyclone. Journal of the University of Petroleum, China, 17(4), 54-59. (In Chinese).
[13] Elsayed, K., Lacor, C. (2013). The effect of cyclone vortex finder dimensions on the flow pattern and performance using LES. Computers and Fluids, 71, 224–239.
[14] Dong, S., Wang, C., Zhang, Z., Cai, Q., Dong, K., Cheng, T., & Wang, B. (2023). Numerical study of short-circuiting flow and particles in a gas cyclone. Particuology, 1, 81-93.

IMPROVING THE PERFORMANCE OF CYCLONE SEPARATOR WITH A SPIRAL GUIDE VANE

Gang Cao[1], Guogang Sun[2]*, Shiwei Yuan[3], Yingyi Wu[4]

College of Mechanical and Transportation Engineering, China University of Petroleum, Beijing 102249, PR China

*Email: sunguogang@cup.edu.cn

Abstract

Spiral guide vanes are often used to improve the collection efficiency of cyclones, but they are closely related to the parameter variables of the guide vanes. This study conducted multi-objective optimization of the guide vanes in the spiral-roof (SR) separator to obtain the most suitable geometric structure to improve performance. First, numerical experiments were designed using the Box-Behnken method in the response surface (RSM) for the pitch (L), number of turns (N), and side wall gap (*l*). Secondly, the significance regression model of efficiency and pressure drop was obtained through variance analysis. Finally, a multi-objective genetic algorithm was used to find the optimal performance solution based on a well-constructed fitness function. The results show that compared with the SR separator, the optimal structure finally selected reduces the cutting particle size of the separator by approximately 54.8%. The optimal geometry of the spiral guide vanes obtained can be used as an effective reference for the factory, providing a comprehensive and effective design strategy.

1. Introduction

Cyclone separator is a common gas-solid separation equipment in various industrial processes. It has the advantages of a simple structure, convenient maintenance, and high collection efficiency. In order to improve the efficiency or reduce the pressure drop of cyclone separators, a large amount of basic research and technological development work has been carried out, which has continuously improved the performance of cyclone separators [1-3]. Research has shown that correctly setting spiral guide vanes in a conventional cyclone separator can effectively improve flow field distribution, increase swirl stability, and pre-separate dust particles, thereby improving the separation performance of the cyclone separator [4, 5]. However, since the performance of the cyclone separator is closely related to the structural variations of the spiral guide vanes, the design of the dimensional parameters of the guide vanes is a key factor in the efficient operation of the equipment.

Previous researches have been conducted to explore the effect of guide vane structure on the performance of cyclone separators. Tsai et al. [6] and Gong et al. [7] conducted experimental and simulation analysis on the axial flow cyclone with guide vane, and the results showed that the efficiency decreases as the particle size decreases. When the particle size is about 1 μm, the separator is no longer suitable. Therefore, Li et al. [8] further studied the separator with a radial inlet. It is found that the pressure drop increases with the number of vane turns, and 1.5 turns is the optimal number of turns. For spiral guide vanes with different numbers of turns, Zhou et al. [9] found that there is a critical value for guide vane turns. When the number of guide vane turns is below or above this value, the collection efficiency, pressure drop, and tangential velocity increase significantly. However, the height of the separator is significantly increased compared to the baseline separator. Contrary to their work, Dehdarinejad et al. [4,5] further analyzed the impact of variable pitch guide vanes with different turns on the separator performance. It is found that when the number of spiral turns is constant, the collection efficiency increases with the decrease of pitch length. At the same time, after the separator is equipped with spiral guide vanes, the collection efficiency of particles with a particle size less than 2 μm is improved. However, its pressure drop has increased several times compared with the baseline structure. Taken together, a flat-roof separator equipped with spiral guide vanes cannot achieve a significant improvement in efficiency while ensuring

a certain pressure drop. Therefore, on the basis of ensuring its collection efficiency, reducing the pressure drop of the equipment is still an area that needs improvement urgently. Misiulia et al. [10, 11] conducted a comparative analysis on spiral-roof and flat-roof separators under the same gas volume, and the results showed that the pressure drop of the spiral-roof separator was lower. Karadeniz et al. [12] also conducted experimental studies on flat-roof and spiral-roof separators. It was found that the efficiency of the spiral-roof separator was reduced, but the pressure drop was reduced by more than 30%. Compared with flat-roof separators, spiral-roof separators have lower pressure drops. However, the spiral-roof separator has the performance disadvantage of reduced efficiency, so improving its collection efficiency is a more meaningful issue.

To this end, we combined a genetic algorithm (GA) with computational fluid dynamics (CFD) to conduct multi-objective optimization of the spiral guide vanes in the SR separator. In our study, we aimed to find the most suitable geometric dimensions of the spiral guide vanes to achieve minimum pressure and maximum collection efficiency of the cyclone separator. The optimal solution of the spiral guide vanes can be used as an effective reference for factory design. We only need to make minor changes to the structure of the spiral guide vanes to obtain considerable performance improvements.

2. Setting

a/D	0.587
b/D	0.243
De/D	0.5
Dc/D	0.4
Be/D	0.7
Dd/D	0.3
S/D	0.587
hb/D	1.4
hc/D	2
hd/d	1.67
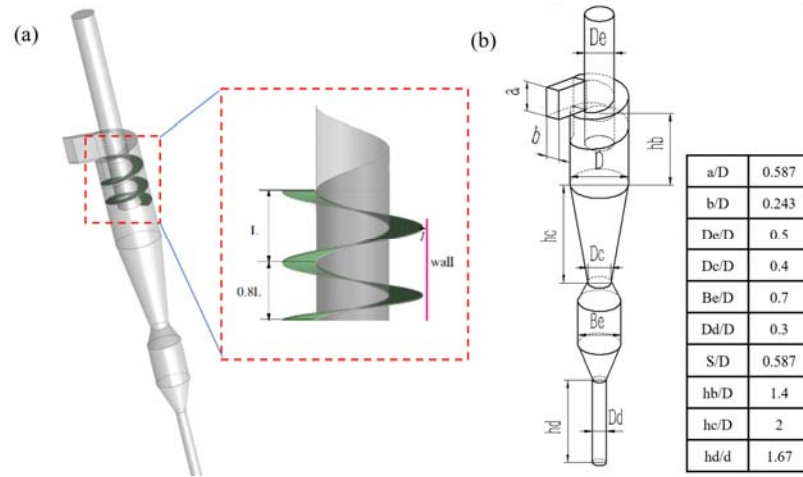
Fig. 1 (a) Three-dimensional model and (b) structural dimension diagram
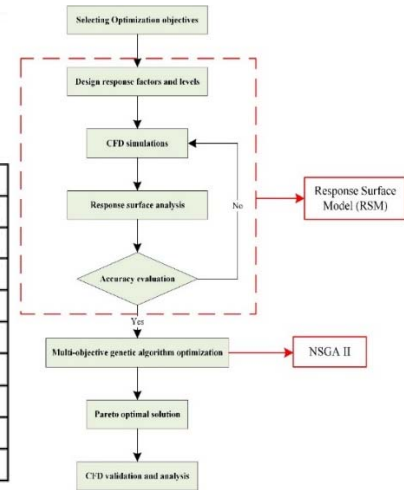
Fig. 2 Flow chart of multi-objective optimization

2.1 Geometric structure

The cyclone separator used in this study is based on the spiral-roof (SR) cyclone separator equipped with spiral guide vanes, with a main body diameter of 300 mm, as shown in Fig. 1. It shows the three-dimensional model and geometric dimensions of the separator used for the simulation. According to previous research [9], it has been concluded that when the number of spiral guide vane turns is greater than 2, it has better performance. At the same time, the pitch is an important factor that determines the performance of the separator. If the pitch is too small, the pressure drop will be several times higher than that of the baseline structure [4,5]. In order to further reduce the pressure drop and at the same time provide a downward path for the particles concentrated at the side wall, we introduce the parameter of the side wall clearance (l). The three design parameters of pitch (L), number of spiral turns (N), and side wall clearance (l) are considered together to achieve the most appropriate geometric configuration of the spiral guide vanes.

2.2 Numerical simulation

The flow field in the cyclone separator is a strong cyclone flow field. From the perspective of economy and accuracy, the Reynolds stress model is currently considered the most suitable

for the simulation of cyclone separators [13,14]. In this study, the inlet boundary condition is set to velocity inlet, the medium is air at normal temperature and pressure, the density is 1.225kg/m^3, and the viscosity is 1.79×10^{-5} Pa·s. The outlet boundary condition is the pressure outlet, there is no slip on the wall, and the standard wall function is used for the near-wall grid. The gas phase flow field is solved using QUICK differential format and the SIMPLEC algorithm.

2.3 Mesh division

Meshing software is used to establish the structural calculation grid of the cyclone separator. In order to ensure the accuracy of numerical simulation, four grid results were generated for the SR cyclone separator under the same operation. When the number of grids is greater than 414635, the performance is not affected by the number of grids. Therefore, the minimum size of the subsequently selected grid is 0.5mm, and the maximum size is 7mm.

2.4 Optimization method

In the Design-expert design platform, multi-objective optimization of the spiral guide vanes of the cyclone separator was carried out by combining RSM and NSGA II. The overall optimization process flow is shown in Fig. 2

The value range of the design variables is shown in Table 1.

Table 1 Design factors and levels in Box-Behnken

Level	Factor		
	A. Pitch L/mm	B. Number of turns N	C. side wall clearance l/mm
-1	110	2	2
0	130	2.5	4
1	150	3	6

3 Results and discussion

3.1 Establishment of response equation

The RSM was used to analyze the influence of the three parameters of the spiral guide vanes: pitch (L), number of turns (N), and side wall clearance (l) on the performance of the separator. Collection efficiency "η" and pressure drop "ΔP" are used to evaluate the separation performance of the cyclone separator. Therefore, collection efficiency and pressure drop were selected as optimization target variables.

$$\eta = \frac{G_c}{G_i} \times 100\% \tag{1}$$

$$\Delta P = P_{in} - P_{out} \tag{2}$$

Before applying the RSM, a Box-Behnken Design (BBD) matrix was carried to arrange the required simulation with several combinations of independent variables. The designed matrix consists of 14 factor points and 3 additional repeat points. The simulation results of pressure drop and efficiency were further analyzed.

The multiple regression model between fitting efficiency and independent variables is performed through the least square method (LSM). In order to discuss the interaction between various factors, the final fitting formula is as follows:

$$\eta = 92.242 - 0.087L + 8.625N - 0.886l + 0.048LN + 2.5E - 003Ll + 0.155Nl - 2.063E - 004L^2 - 2.87N^2 - 0.0156l^2 \tag{3}$$

Similarly, a multiple regression model was fitted between pressure drop and independent variables to discuss the relationship between interactions, as shown in the following equation:

$$\Delta P = 5661.821 - 84.316L + 4477.033N - 903.013l - 7.074LN$$
$$+ 6.216Ll - 191.758Nl + 0.206L^2 - 383.415N^2 + 32.267l^2$$

(4)

3.2 Response surface analysis

Fig. 3 shows the contours and plots of the interaction factors for η. It can be seen from the figure that the color bands in the projection images of Fig. 3(a) and Fig. 3(b) are almost parallel. This indicates that there are no interaction effects between L and N, and L and l. The interaction between N and l is a little more complicated. When 2＜N＜2.5, the efficiency increases with the increase of l; when 2.5＜N＜3, the separation efficiency decreases as the value of l further increases. Therefore, the efficiency change trend based on N and l has an interactive effect. The gradient of the color band can also reflect the significance of the factor. The larger the gradient, the higher the significance of the factor. Fig. 3 shows that N has the most significant effect on η, followed by L and l.

Fig. 4 shows the contours and plots of the interaction factors for ΔP. The results showed that all plots showed flat slopes at different angles, which was different from the trend of η. This phenomenon illustrates the lack of interaction between ΔP and parameters. In addition, the pressure drop ΔP increases with the decrease of L and l, and increases with the increase of N. Therefore, in order to reduce energy consumption, the pitch and side wall clearance should be appropriately increased.
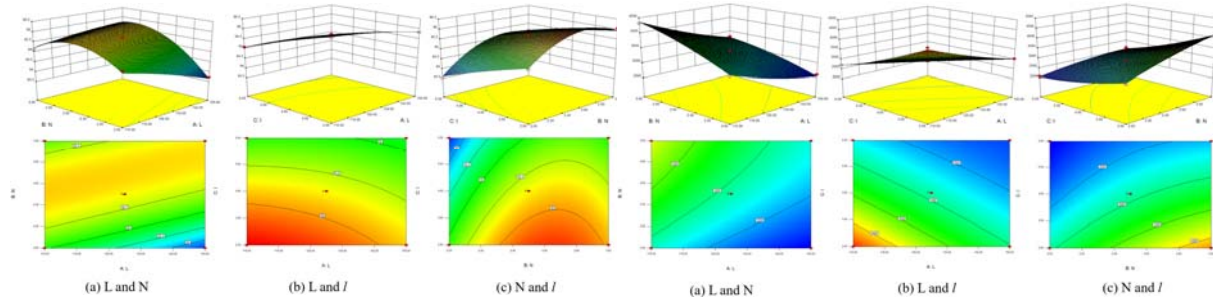
| Fig. 3 Response surface contours of the interaction factors for η | Fig. 4 Response surface contours of the interaction factors for ΔP |

3.3 Optimization results of genetic algorithm

The genetic algorithm NSGA II is used to perform multi-objective optimization of spiral guide vanes, and the efficiency and pressure drop regression models obtained by RSM are used as fitness functions. The mathematical description of multi-objective optimization is:

$$\begin{cases} Minimize: -\eta(L, N, l) \\ Minimize: \Delta P(L, N, l) \\ 110 \le L \le 150, L \in N^+ \\ 2 \le N \le 3, N \in 0.1 \times N^+ \\ 2 \le l \le 6, l \in 0.1 \times N^+ \end{cases}$$

(5)

According to the pitch, number of turns, and side wall clearance, the two conflicting objective functions (η and ΔP) were optimized, as shown in Fig. 5. At the same time, designers can choose from Pareto points according to specific requirements (the fitting function is: $\eta = -0.58\Delta P^4 + 8.22\Delta P^3 - 43.22\Delta P^2 + 100.41\Delta P + 8.84$)
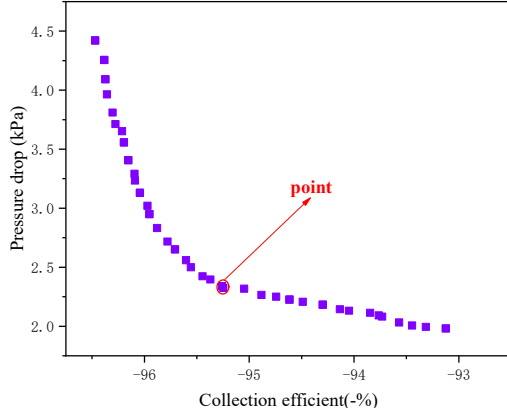
Fig. 5 Pareto optimal solution of guide vanes
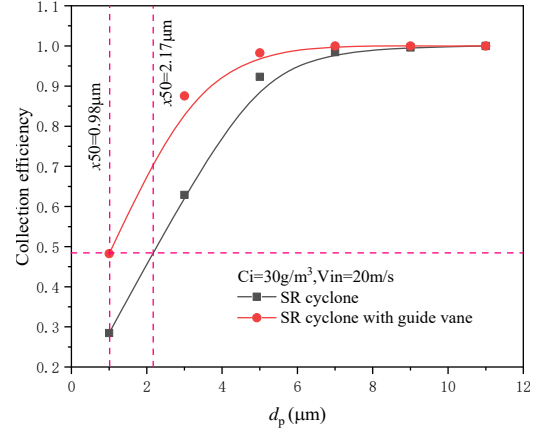
Fig. 6 Collection efficiency under different particle sizes

According to the purpose of low pressure drop and high collection efficiency, the appropriate optimized structure is selected. Table 2 shows the comparison between multi-objective optimization results and simulation calculation results. It can be seen that the difference is small, indicating that the multi-objective optimization results of this article have high accuracy.

Table 2 Comparison between multi-objective optimization and simulation calculations

Point A	Collection efficiency (%)	Pressure drop (Pa)
Multi-objective optimization (L=147mm, N=2.7, *l*=5.5mm)	95.37	2396.1
Simulation	95.17	2400.61
Difference (%)	0.21	0.19

For the SR separator and the SR separator configured with the optimal spiral guide vane, the grain efficiency and cut-off size predictions are shown in Fig. 6. Compared with the SR separator, the cut-off size is reduced by approximately 54.8% after configuring the optimal guide vane structure.

4 Conclusions

By using CFD, RSM, and GA technologies, this paper conducts multi-objective optimization of the spiral guide vanes configured in the SR separator. The optimized structure further enhances the overall performance of the cyclone separator and obtains a Pareto solution, which can provide a comprehensive design strategy for the guide vane. The conclusions of this study are as follows:

(1) After configuring spiral guide vanes in the SR cyclone separator, the gas flow rate can be increased to achieve the purpose of improving efficiency. The pitch (L), number of turns (N), and side wall clearance (l) have a significant impact on the collection efficiency and pressure drop of the cyclone separator. At the same time, a scheme for synergistic operation of L, N and l was proposed.

(2) RSM is used to construct the fitness function between the sampling point and the design target (pressure drop and collection efficiency). The obtained model can accurately predict collection efficiency and pressure drop, while efficiency and pressure drop are most affected by L and N.

(3) The Pareto point is obtained through multi-objective optimization, and the relationship between collection efficiency and pressure drop is nonlinear. Design parameters close to L = 147 mm, N = 2.7, and l = 5.5 mm are more conducive to obtaining the best performance. Compared with SR separators, the optimal structure reduces the cutting particle size by 54.8%.

The Pareto optimal solution obtained can provide a comprehensive and effective design strategy for spiral guide vanes.

Acknowledgment

References

[1] M. Wasilewski, L.S. Brar, Effect of the inlet duct angle on the performance of cyclone separators, Separation and Purification Technology, 213(2019) 19-33.

[2] Y.G. Yao, W.S. Huang, Y.X. Wu, et al, Effects of the inlet duct length on the flow field and performance of a cyclone separator with a contracted inlet duct, Powder Technology, 393(2021) 12-22.

[3] H. Fatahian, E. Fatahian, M.E. Nimvari, Novel designs for square cyclone using rounded corner and double-inverted cones shapes, Powder Technology, 380(2021) 67-79.

[4] E. Dehdarinejad, M. Bayareh, Performance improvement of a cyclone separator using spiral guide vanes with variable pitch length, Journal of the Brazilian Society of Mechanical Sciences and Engineering, 44(2022).

[5] E. Dehdarinejad, M. Bayareh, Experimental and numerical investigation on the performance of a gas-solid cyclone with twisted baffles and roughened cone surface, Powder Technology, 420(2023) 118401.

[6] C.J. Tsai, D.R. Chen, H.M. Chein, et al. Theoretical and experimental study of an axial flow cyclone for fine particle removal in vacuum conditions, Journal of Aerosol Science, 35(2004) 1105-1118.

[7] G.C. Gong, Z.Z. Yang, S.L. Zhu, Numerical investigation of the effect of helix angle and leaf margin on the flow pattern and the performance of the axial flow cyclone separator, Applied Mathematical Modelling, 36(2012) 3916-3930.

[8] Q.P. Li, Y.J. Xu, L.H. Du, e, Numerical simulation of JLX cyclone separator with guiding vane, Chemical Engineering, 43(2015) 37-41.

[9] F.Q. Zhou, G.G. Sun, X.P. Han, Y. Zhang, W.Q. Bi, Experimental and CFD study on effects of spiral guide vanes on cyclone performance, Advanced Powder Technology, 29(2018) 3394-3403.

[10] D. Misiulia, A.G. Andersson, T.S. Lundström, Effects of the inlet angle on the flow pattern and pressure drop of a cyclone with helical-roof inlet, Chemical Engineering Research and Design, 102(2015) 307-321.

[11] D. Misiulia, A.G. Andersson, T.S. Lundström, Effects of the inlet angle on the collection efficiency of a cyclone with helical-roof inlet, Powder Technology, 305(2017) 48-55.

[12] A. Karadeniz, S. Demir, Experimental Investigation of the Effects of Helical Roof on the Performance of Stairmand High Efficiency Cyclone, International Journal of Chemical Engineering, (2021).

[13] H. Safikhani, M. Shams, S. Dashti, Numerical simulation of square cyclones in small sizes, Advanced Powder Technology, 22(2011) 359-365.

[14] S.K. Shukla, P. Shukla, P. Ghosh, Evaluation of numerical schemes using different simulation methods for the continuous phase modeling of cyclone separators, Advanced Powder Technology, 22(2011) 209-219.

EFFECT OF GAS-INLET GEOMETRY ON HYDRODYNAMICS IN A SMALL-DIAMETER RISER OF CIRCULATING FLUIDIZED BED

Suyoung Kim[1], Chae Eun Yeo[2], Geunhye Won[2], Sung Won Kim[1,2*]

[1]*Department of IT·Energy Convergence,* [2]*Department of Chemical and Biological Engineering, Korea National University of Transportation, 50 Daehak-ro, Chungju, Chungbuk 27469, Republic of Korea*

*Email: kswcfb@ut.ac.kr

Abstract

Effect of gas-inlet geometry on hydrodynamics in a small-diameter riser (0.01 m-i.d. × 3.07 m-high) of circulating fluidized bed with FCC catalysts (d_p=77μm, ρ_s=1813kg/m³) has been determined based on experimental and simulation results. A particle-fluid dynamics model was established and verified by comparing with experimental results on hydrodynamics such as axial solids holdup distribution in the riser. At a constant gas velocity and solid circulation rate, the solid holdup in the bottom region of riser increased with increases of the area ratio of gas-nozzle orifice to riser due to decreasing the jet momentum. The solid holdup increased with increasing the distance between the nozzle orifice and the solid re-entry (H_N/H_r) by increased down-flow flux of particles to riser bottom. Particle behavior in bottom region near gas-inlet of nozzle which was difficult to determine from the experimental result, was investigated through simulation. It was observed that an increase of H_N/H_r resulted in decrease of stagnant zone formed near the nozzle. The model showed that local particle behavior in bottom region of riser was affected by the different nozzle geometry. An optimum geometry of gas-inlet in small-diameter riser was proposed for high solid holdup without stagnant bed.

1. Introduction

Circulating fluidized beds (CFBs) have been employed in numerous gas-solid contacting processes for continuous catalytic reaction and regeneration such as the fluid catalytic cracking (FCC) reactors. In the CFB reactors, product selectivity and yield are strongly dependent upon average solids holdup and their distribution in the riser. The solid holdup distribution at a given condition is very important for the design of commercial circulating fluidized bed reactors as well as lab and pilot scale reactors, which are a starting point of the design for determination of further scale up [1]. The solid holdup distribution of catalyst in the riser is influenced by particle properties, operating condition and riser geometry [2]. It has been known that the configuration of gas-injection to the riser significantly affects the hydrodynamics within the riser, but the results in small-diameter risers with gas nozzle at lab and pilot scale are comparatively sparse despite their wide application such as catalysts evaluation [3]. Therefore, it is necessary to study the effect of the gas-nozzle geometry on the solid holdup distribution in the small-diameter riser for the design and the prediction of the gas-solid flow in the lab scale reactor [4].

Modeling and simulation have become an important tool in the fluidization system design, optimization, and scale up in the past decades [5]. Approach on computational simulation has been used as an auxiliary method for the analysis of complex particle behavior, which is hard to access experimentally in gas-solid fluidized beds. Multi-phase particle in cell (MP-PIC) method specifically designed for CPFD (computational particle fluid dynamics) simulation has been applied as an efficient method of simulating large-scale particle system, with a considerable saving of time and technical and economic resources [6]. In the present study, the effect of the gas-nozzle geometry on hydrodynamics such as solid holdup distribution and local solids behavior in the small-diameter riser has been determined based on experimental and simulation results. Experiments were carried out in a lab-scale CFB cold model, and a particle-fluid dynamics model was established and applied to investigate particle behavior.

2. Mathematical Models

2.1 Governing Equations

Barracuda Virtual Reactor 22.0.0 software based on MP-PIC method was used for analysis of particle behavior on geometry of gas nozzle in the CFB riser. The MP-PIC model uses the Lagrangian approach to particle phase, while the Eulerian approach or Eulerian-Lagrangian method applied continuity equations to gas phase. The model is advantageous to reduce the calculation time for fluidized bed process analysis with complex particle behavior by using the particle distribution function to track the movement of particle groups [7]. The drag force between the gas and solid was calculated by EMMS-Yang mod el, which is suitable to reproduce the multiphase flow interactions in system such as CFB [8]. An overview of the main governing equation in this study is shown in Table 1.

Table 1. Governing equations for MP-PIC model.

Equation	Equation expression
Continuity equation	$\frac{\partial(\alpha_g\rho_g)}{\partial t} + \nabla \cdot (\alpha_g\rho_g u_g) = \delta m_p$
Momentum conservation equation	$\frac{\partial(\alpha_g\rho_g u_g)}{\partial t} + \nabla \cdot (\alpha_g\rho_g u_g u_g) = -\nabla p + F + \alpha_g\rho_g g + \nabla \cdot \tau_g$ $\tau_g = \mu_{eff}\left(\frac{\partial u_{g,i}}{\partial x_j} + \frac{\partial u_{g,j}}{\partial x_i}\right) - \frac{2}{3}\mu_{eff}\delta_{ij}\frac{\partial u_k}{\partial x_k}$
Particle equation of motion	$\frac{du_p}{dt} = D_p(u_g - u_p) - \frac{\nabla p}{\rho_p} + X + g + \frac{\overline{u_p} - u_p}{2\tau_D}$ $X = -\frac{1}{\overline{\rho_p}\alpha_s}\frac{\partial \tau_p}{\partial \chi_i} + g_1(\alpha_s)\left[\overline{D}(u_g - \widetilde{u_p}) - D(u_g - \widetilde{u_p}) - \left(\frac{1}{\overline{\rho_p}} - \frac{1}{\rho_p}\right)\frac{\partial p}{\partial \chi_i}\right]$
Particle collision model Acceleration and contact stress	$\tau_p = \frac{10 P_s \alpha_p^\beta}{\max[(\alpha_{cp}-\alpha_p), \epsilon(1-\alpha_p)]}$ $\qquad$ $\overline{D} = \frac{\iiint fm D dm_p du_p dT_p}{\overline{\rho_p}\alpha_s}$ $g_1(\alpha_s) = \begin{cases} 0 & \text{if}\alpha_s = 0 \\ 1 & \text{if}\alpha_s = \alpha_{s,cp} \end{cases}$ $\qquad$ $\widetilde{u_p} = \frac{\iiint fm D u_p dm_p du_p dT_p}{\overline{\rho_p}\alpha_s \overline{D}}$
Energy transfer between gas and solid model (drag models)	$F = \iiint f\left\{m_p\left[D_p(u_g - u_p) - \frac{\nabla p}{\rho_p}\right] + u_p\frac{dm_p}{dt}\right\} dm_p du_p dT_p$ $D_P = \frac{9}{2}\frac{\mu_g}{\rho_p(d_p/2)^2}f_e$ $f_e = \begin{cases} \frac{1}{180\varepsilon_s}(150\frac{\varepsilon_s}{\varepsilon_g} - 1.75Re) & \varepsilon_g < 0.74 \\ (1 + 0.15Re^{0.687})\omega & \varepsilon_g \geq 0.74 \text{ and } Re < 1000 \\ 0.44\frac{Re}{24}\omega & \varepsilon_g \geq 0.74 \text{ and } Re \geq 1000 \end{cases}$ $\omega = \begin{cases} -0.5760 + \frac{0.0214}{4(\varepsilon_g - 0.7463)^2 + 0.0044} & 0.74 \leq \varepsilon_g \leq 0.82 \\ -0.0101 + \frac{0.0038}{4(\varepsilon_g - 0.7789)^2 + 0.0040} & 0.82 < \varepsilon_g \leq 0.97 \\ -31.8295 + 32.895\varepsilon_g & 0.97 < \varepsilon_g \leq 1 \end{cases}$

2. 2 Geometry and operating conditions for CPFD simulation

Experiments were carried out in a lab-scale CFB cold model as shown in Fig.1(a). The experimental apparatus is consisted of a riser, regenerator, cyclone, slid valve and solid recycle line. Details for the experiments can be found elsewhere [4]. The CPFD model simulated entire riser first for validation of solid holdup distribution in the riser, and bottom part of riser (0.01 m i.d. by 3.0 m height) as in Fig.1(b) was simulated to investigate local particle behavior around solid re-entry and gas-nozzle. Particle re-injection line from regenerator of the CFB were simulated; the setting conditions of the solid transfer line were U_g=0.48m/s, $\dot{m}$=0.0095kg/s based on commercial FCC unit condition. Fig.1(c) shows the shapes of gas nozzle. The area ratio of nozzle orifice to riser (A_{Nh}/A_R) was changed from 0.04 to 056. The distance between the nozzle orifice and the solid re-entry (H_N/H_r) was changed from 0 to 1.

Total number of cells of the cold model was 1,758,315, and the grids was enough for application of CPFD model used the MP-PIC. The simulated results were calculated in a time period of 30s. The simulated results of a time period between 20s and 30s were post-processed for analysis of particle behavior, because steady state of fluidized operation reaches after 20s [9]. The solid particles of this study were FCC catalyst. The input parameters and particle properties are report in Table 2.
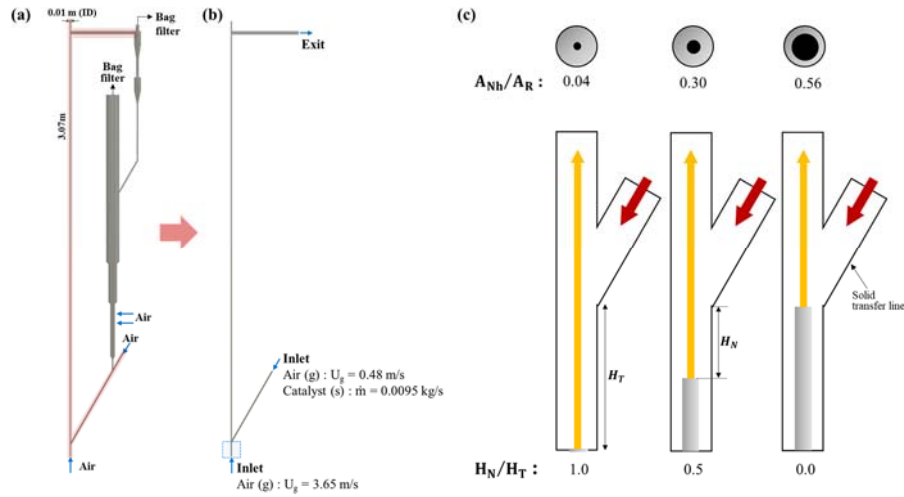
Fig. 1. The geometry of (a) CFB cold model, (b) riser and (c) gas-nozzle.

Table 2. Input parameters used in CPFD simulation.

Parameters	Numerical Value
Catalyst bulk density	1813 kg/m^3
Catalyst particle density	1027 kg/m^3
Mean particle diameter	77 μm
Gas velocity	4.13 m/s
Gas composition	Air
Solid circulation rate	121 kg/m^{2}s
Total number of all cells	1,758,315
Total number of real cells	112,403
Time step	0.001s
Simulation time	30s

3. Result and Discussion

3.1 Axial solid holdup distribution in riser

In this study, CPFD simulations were conducted to investigate the hydrodynamic characteristics on effect of the geometry of the gas-injection nozzle in a CFB riser, and the results were compared with experimental data to validate the model. Fig.2 presents the time-averaged axial solid holdup(ε_s) distribution of the riser by gas-nozzle geometry in the simulation and experiment at given condition of U_g=4.13m/s and G_s=121kg/m^{2}s. The experimental values of solid holdups in the riser were obtained from pressure drops along the height, and calculated from Eq.(1) using gas density (ρ_g) and particle density (ρ_s) values, assuming that the gas acceleration and the wall fraction were ignored [4].

$$\varepsilon_s = \frac{\Delta P}{\Delta L}/\left[(\rho_s - \rho_g)g\right] \qquad (1)$$

The solid holdup distribution in the Riser is a typical C-shape that appears in the fast fluidization regime [10], where solids holdup is high around riser bottom region and remains low in the middle region. The holdups of particles are high around the riser exit due to the geometry of abrupt exit with the diameter (D_e=0.0089 m) smaller than the riser diameter (D_r=0.010 m).

As A_{Nh}/A_R increased, the solid holdup in bottom region is increased (Fig. 2(a)). At the same gas volumetric flow rate, an increase in the orifice area of nozzle results in a decrease in jet velocity, which reduces the jet-momentum per riser area and jet penetration length from the nozzle [11]. Consequently, the solid holdup increased with increased residence time in bottom region of particles injected from the solid re-entry due to decreased entrainment by inlet gas.

The solid holdup increased with increasing the distance between the nozzle orifice and the solid re-entry (H_N/H_r). When particles are injected into the riser along an inclined solid transport line with aeration, some particles immediately ascend with the upward gas/solid flow depending on the momentum of the gas injected from the nozzle. However, most particles move downward below the re-entry due to gravity and the momentum of the gas injected from the transport line, then ascending by the jet gas from nozzle. As the H_N/H_r increases, the downward mass flux from the riser re-entry increases. At 0.125 m in the riser bottom region, the higher the H_N/H_r, the lower the jet momentum affecting bed at the location, resulting in a higher solid holdup. However, the solid holdup keeps almost constant value above 0.45 m (0.55 m in riser height) from the riser re-entry position.
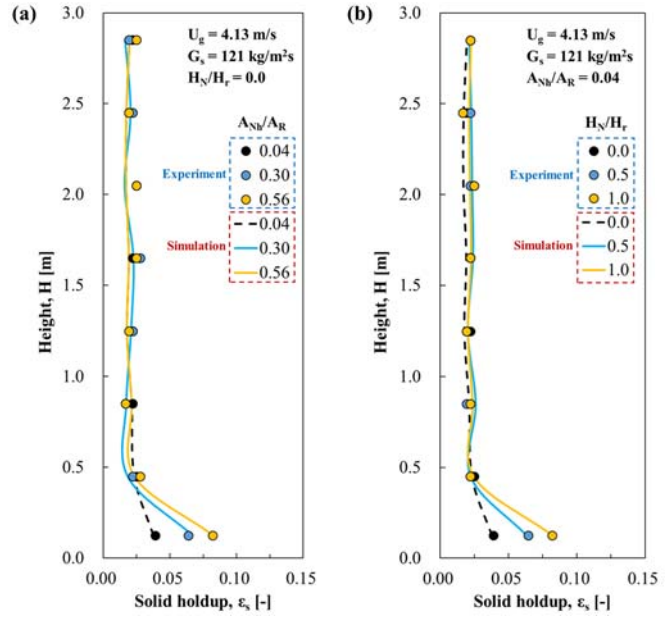
Fig. 2. The effect of (a) A_{Nh}/A_R and (b)H_N/H_r on axial solid holdup

The experimental results were compared with simulated results from the MP-PIC model, incorporating the governing equations from Table 1. The model successfully simulated the C-shape of the axial solid holdup distribution under given conditions, as shown in Fig. 2. It also accurately predicted the axial solid holdups in the lower region with variations in the gas-nozzle diameter and position.

3.2 Effect of gas-nozzle geometry on local solid behavior

3.2.1 Effect on area ratio of nozzle orifice to riser

Fig.3 shows simulated results on average solid holdup in the riser bottom and local solid holdup at various heights with A_{Nh}/A_R at H_N/H_r = 0. A stagnant bed formed near the nozzle as shown in Fig.3(a), which is not detected through pressure drop measurements, but observed near the nozzle through a transparent column in experiment. The formation of stagnant zone is because the bed near nozzle was not affected by jet momentum from the nozzle. As an A_{Nh}/A_R increases from 0.04 to 0.56, the solid holdup in the bottom region of riser increases due to a reduction in jet momentum from the nozzle by decreased jet velocity from 101 to 6 m/s, which supports the results of Fig. 2(a).

In Fig. 3(b), the stagnant zone is clearly observed at 0.005m near nozzle with A_{Nh}/A_R = 0.04 due to narrow jet width, indicating that jet momentum does not affect the stagnant bed around the nozzle. However, the high gas-jet velocity and long jet penetration length from the nozzle resulted in low local solid holdup in the center above 0.05 m. The stagnant zone gradually disappeared with increasing the A_{Nh}/A_R, because the jet momentum expanded near the riser bottom. Interestingly, there is an uneven distribution of solid holdup in the height range of 0.05 – 0.20 m at A_{Nh}/A_R = 0.30 and 0.56, where higher solid holdups were shown at the direction of solid re-entry. Jets from nozzles at A_{Nh}/A_R= 0.30 and 0.56 have relatively low jet velocity and gas momentum, which are influenced strongly by the momentum of descending gas-particles from solid re-entry line, leading to skewed the jet flow from nozzle to the left of the riser. The effect by solid re-entry was diminished above 0.5m, but core-annulus structure with lower solid holdup in the center and higher solid holdup near the wall was observed [12]. The core-annulus structure is due to lower particle velocity near the wall than center by the wall effect, which appeared stronger in this small-diameter riser as shown in Fig.3(b) [4,13].

The simulation results for the gas velocity profile in the riser bottom region with A_{Nh}/A_R are shown in Fig. 4. It was observed that the higher the A_{Nh}/A_R, the lower the jet velocity and jet

penetration length, and the wider the jet width. With an increase in A_{Nh}/A_R, the influence of momentum by gas-entrained particles from solid re-entry on the nozzle jet increases, causing skewed jet and ascending gas profile, which explains well the characteristics of the radial solid holdup distribution at each height in Fig. 3(b).
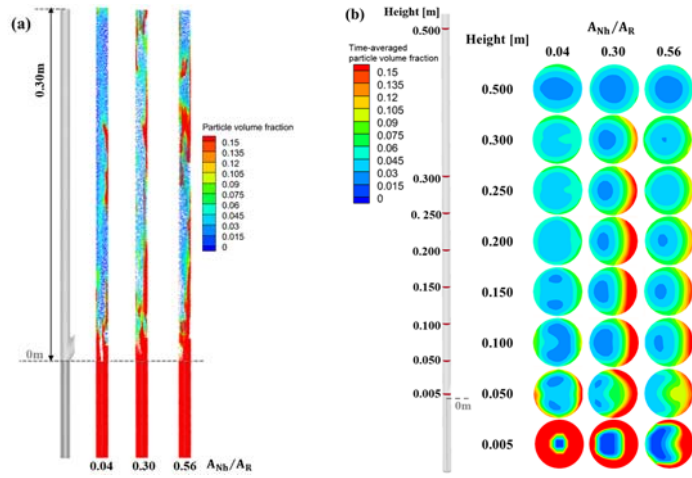
Fig. 3. Particle volume fraction (a) of riser bottom (time = 20s), (b) at different height in riser with A_{Nh}/A_R.
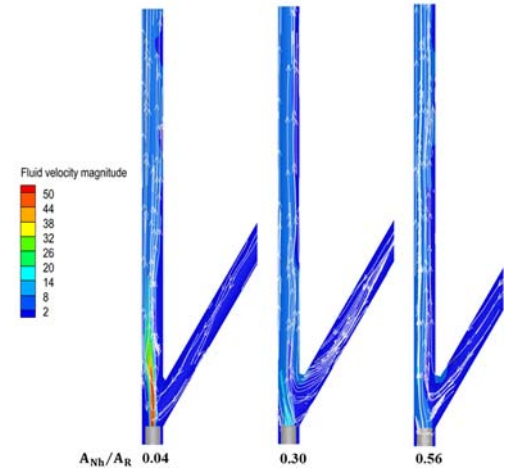
Fig. 4. Effect A_{Nh}/A_R of on local gas velocity in a riser bottom.

3.2.2 Effect of distance between the nozzle orifice and the solid re-entry

Fig.5 shows simulation results on average solid holdup in the riser bottom and local solid holdup at various heights with H_N/H_r at A_{Nh}/A_R =0.04. The stagnant zone formed near the nozzle below the solids re-entry disappeared with increasing the H_N/H_r due to expansion of the area affected by jet momentum with decreased nozzle-length and widen jet width within riser (Fig.5(a)). The solids downward flux increased by the weakened jet momentum near solid re-entry as the gas-injection position was lowered, leading to high solid holdup in the riser bottom which support the results in Fig. 2(b). The solid behavior in the riser bottom with H_N/H_r could be described well in Fig. 6 on particle velocity vector around gas inlet region. The stagnant zone disappeared gradually, and particle movement near gas-nozzle became vigorous with increase of H_N/H_r. In the case of H_N/H_r =0 where gas-nozzle orifice is located at the same height of the solid re-entry, the jet from the nozzle did not affect the stagnant zone around nozzle. Jet at H_N/H_r =0.5 and 1.0 diminished the stagnant zone due to shortened nozzle length within riser, whereas jet momentum reaches weakly at the height of 0.005m, resulting in high and uneven local solid holdups near the solid re-entry.
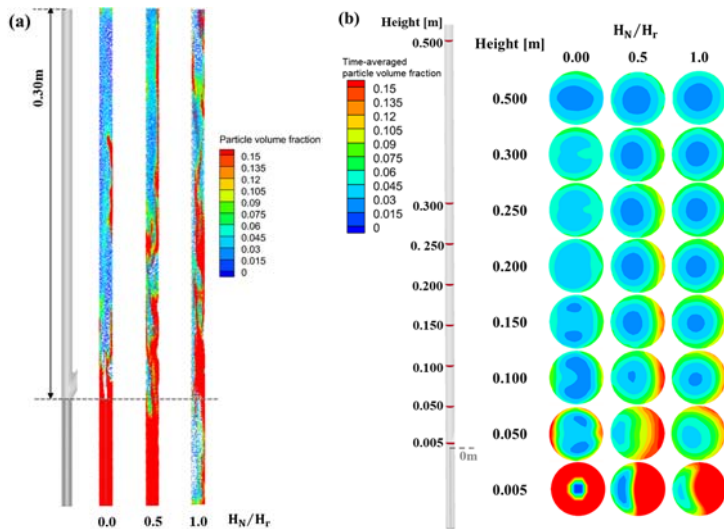
Fig. 5. Particle volume fraction (a) of riser bottom (time = 20s), (b) at different height in riser with H_N/H_r.
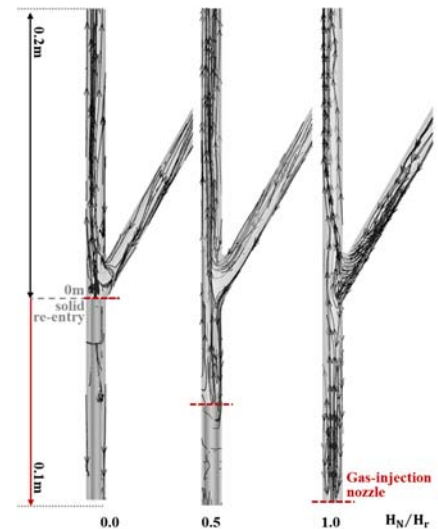
Fig. 6. Particles velocity vectors on H_N/H_r in the inlet region.

Finally, the high A_{Nh}/A_R and H_N/H_r lead to relatively high and uniform solid holdups of the riser bottom, and could be beneficial for increased catalyst residence time and improved contact efficiency.

4. Conclusion

Effect of gas-inlet geometry on hydrodynamics in a small-diameter riser of CFB with FCC catalysts has been determined based on experimental and simulation results. The MP-PIC model was used in CPFD simulations to analyze solids behavior in the riser bottom region. Axial solids holdup distributions predicted by the CPFD model were matched well with experimental results. The local solids behavior in the riser bottom was dominated by the geometry of the gas-nozzle. The solids holdup increased as A_{Nh}/A_R and H_N/H_r increased. The decrease of A_{Nh}/A_R and H_N/H_r led to the formation of a stagnant bed near the nozzle. The injection of recycled solids skewed the path of the rising jet stream and caused uneven local solid holdups near the solids re-entry. Finally, it was concluded that the condition of A_{Nh}/A_R=0.56 and H_N/H_r=1.0 is advantageous for high solid holdup without stagnant bed in the bottom region of the small-diameter riser.

Acknowledgment

References

[1] I.A. Vasalos, A.A. Lappas, D.K. Iatridis, S.S. Voutetakis, V.M. Kwauk, J. Li, Eds., in: Proceedings of Circulating Fluidized Bed Technology V. Proc. Science Press, Beijing, China. 1996, 408413.

[2] R.W. Breault, E.R. Monazam, L.J. Shadle, S. Rowan, L.H. Macfarlan, The effect of riser end geometry on gas-solid hydrodynamics in a CFB riser operating in the core annular and dilute homogeneous flow regimes. Powder technology. 2017. 316, 181-189.

[3] A. Angelos, A.A. Lappas, D.K. et. al., Ind. Eng. Chem. Res. 2017. 56, 12927.

[4] C.E. Yeo, C.E., S.W. Kim, S.W., Adv. Powder Technol. 2020. 31, 1946.

[5] J. Xie, W. Zhong, A. Yu, MP-PIC modeling of CFB risers with homogeneous and heterogeneous drag models. Advanced Powder Technology. 2018. 29, 2859-2871.

[6] J.C. Bandara , C. Jayarathna, R. Thapa, H.K. Nielsen, B.M. Moldestad, M.S. Eikeland, Loop seals in circulating fluidized beds–Review and parametric studies using CPFD simulation. Chem. Eng. Sci. 2020. 227, 115917.

[7] J.H. Lim, D.H. Lee, Two-and Three-dimensional Analysis on the Bubble Flow Characteristics Using CPFD Simulation. Korean Chem. Eng. Res. 2017. 55, 698-703.

[8] Savuto, E., Stendardo, S., & Di Carlo, A. Modelling and design of a novel calcination reactor integrated with a CO_2 capture process for intensified hydrogen production. Fuel Processing Technology. 2022. 231, 107253.

[9] J.H. Lim, K. Bae, J.H. Shin, J.H. Kim, D.H. Lee, J.H. Han, D.H. Lee, D.H. Effect of particle–particle interaction on the bed pressure drop and bubble flow by computational particle-fluid dynamics simulation of bubbling fluidized beds with shroud nozzle. Powder Technol. 2016. 288, 315-323.

[10] T. Li, J.F. Dietiker, M. Shahnam, MFIX simulation of NETL/PSRI challenge problem of cir1ulating fluidized bed. Chemical engineering science. 2012. 84, 746-760.

[10] R.Y. Hong, Q.J. Guo, G.H. Luo, J.Y. Zhang, J. Ding, On the jet penetration height in fluidized beds with two vertical jets. Powder Technol. 2003. 133, 216-227.

[12] S.W. Kim, G. Kirbas, H. Bi, C.J. Lim, J.R. Grace, Flow behavior and regime transition in a high-density circulating fluidized bed riser. Chemical Engineering Science. 2004. 59, 3955-3963.

[13] J. Zhou, J. R. Grace, C. J. Lim, C. M. H. Brereton, Particle velocity profiles in a circulating fluidized bed riser of square cross-section. Chem. Eng., Vol. 50, No. 2, 1995, pp. 237–244.

The Cold Model Experimental Study on the Effect of Rapid Changes in Fluidization Air Velocity on Gas-Solid Concentration in the Riser of Circulating Fluidized Bed

Rongdi Zhang[1], Zhicun Liu[1], Zhonghao Dong[1], Jianbo Li[1], Xiaofeng Lu [1*]

1.Key laboratory of Low-grade Energy Utilization Technologies & Systems, Ministry of Education, Chongqing 400044, China

Abstract

In this paper, the gas-solid flow characteristics in a riser under the condition of rapid change of fluidizing air volume were studied on a self-designed CFB cold model test bench. The test results show that when the air volume changes continuously, the change of particle concentration in the riser is consistent with the change trend of the fluidizing air volume, but there is a time delay. There is a positive correlation between the delay time and the axial height, and the weighted average degree of delay is positively correlated with the changing rate of the air volume. The results can provide theoretical basis and engineering application data for CFB boiler to participate in rapid peak regulation.

Key words: CFB boiler; Rapid peaking; Gas-solid flow; Flow inertia

1. Introduction

Circulating fluidized bed (CFB) combustion technology has developed rapidly in recent years[1, 2] because of its advantages of wide fuel adaptability[3], large peak load balancing range[4] and low cost of pollutant control[5]. The policy of carbon reduction, "carbon peaking and carbon neutrality" has a great impact on the energy production process in China. The new policy requires the thermal power industry to be able to peak load more broadly and quickly[6, 7] to ensure the balance and stability of the power grid after the increasing number of renewable energy is connected to the grid[8]. Among them, the *National Key Research and Development Program* require the changing rate of load of CFB boiler units to reach 3%Pe/min.

In the process of rapid peaking of CFB boiler, theoretically, the ash concentration and flue gas temperature in the upper part of the furnace can be rapidly adjusted by the change of the total air volume or the ratio of primary and secondary air, so as to realize the rapid change of load[9]. In the regulation process, the uniformity of air and coal should also be ensured to maintain a low amount of pollutant generation[10, 11] and to enable the normal operation of the pollutant control mechanism in the furnace. However, when air volume and coal feed volume are adjusted in the process of rapid peaking, because the movement inertia of bed particles is usually larger than that of gas, the change of particle concentration lags behind the change of air volume. For the gas-solid flow state in the furnace, this results in a large difference between the rapid peaking and the steady state. The problems of increasing pollutant discharge, fluctuating furnace temperature and fluctuating water parameters in the process of rapid peaking are brought about. At present, domestic and foreign scholars have fully studied the CFB boiler's peaking operation in the field of slow peaking[12-14], while the research and exploration in the field of rapid peaking are relatively shallow. The gas-solid concentration distribution and flow pattern in CFB boiler are fully studied in the field of steady state operation[15-17], but further exploration is needed in the field of unsteady state (rapid peaking). To improve the peaking speed of CFB boiler, first of all, it is necessary to clarify the evolution mechanism of gas solid concentration and flow state in the furnace during the rapid peaking process, and take this as the core to adjust the amount of air and coal in the furnace to ensure the uniformity and stability

of combustion during the peaking process, so as to achieve a load changing rate of 3%Pe/min or higher. Therefore, in this paper, the gas-solid flow variation characteristics in CFB riser with rapid changing rate of the fluidizing air volume were experimentally studied on a cold model test bench.

2. Experimental facilities

The full-loop visual CFB test device used in this research is shown in Fig.1. The furnace, separator, riser, loop seal and suspended heating surfaces (SHSs) are all made of plexiglass. The size of the furnace and SHSs should be proportional to that of a 350 MW supercritical CFB boiler as far as possible, and the specific height and depth should be reduced by a geometric ratio of about 1:15. At the same time, the actual arrangement of the SHSs in the furnace should be considered to have better symmetry. In order to simplify the structure of the test bed, the number of SHSs is taken as one third of the actual furnace, that is, 6 SHSs.
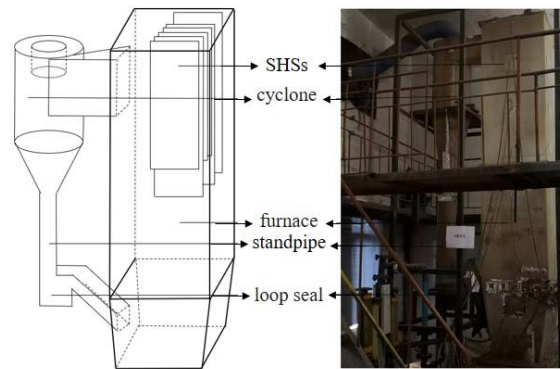
Fig.1 Schematic diagram of the small experimental CFB apparatus.

The fluidizing air required during the test is provided by a high-pressure centrifugal fan, and the loose air and return air required by the return valve are provided by an air compressor.

In order to realize the continuous change of the fluidizing air volume at a certain rate (1%-6%/min), the automatic air volume control system as shown in Fig.2a and the automatic air volume control strategy as shown in Fig.2b were developed by ourselves, so as to realize the real-time detection and continuous change of the fluidizing air volume in the riser and meet the requirements of the variable air volume test.

(a) System scheme   (b) Control strategy
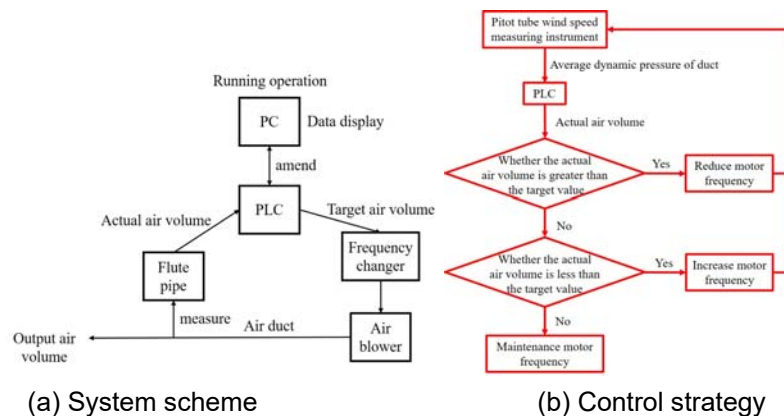
Fig.2 Air volume automatic control system

The circulating ash of a 600MW supercritical CFB boiler was used as the bed material, the apparent density was 1306.06 Kg/m^3, and the true density was 2047.64 Kg/m^3. The maximum particle size and median particle size of the tested bed were 2mm and 125.3 μm. The minimum fluidizing velocity (U_{mf}=0.38 m/s) of the test bed material was

obtained from the relationship between the bed pressure drop and the fluidizing wind speed.

The initial bed material height of this test is 150 mm. The steady-state operation test under different fluidizing air volume is first conducted, and then the air volume reduction test under different variable air rate (1, 2, 3, 4, 5, 6% Pe/min) is conducted. At this time, the air volume is reduced from 100% Pe/min to 40% Pe/min at the selected rate of change. In the test, the average particle concentration of the riser section was measured indirectly by the pressure drop method[18, 19]. The time delay data of average particle concentration data and fluidizing air volume data were calculated by cross-correlation analysis[20].

3. Experimental results and analysis

3.1 Typical variation characteristics of bed pressure drop in dense phase region during rapid air volume reduction

As shown in Fig.3, when the fluidizing air volume is reduced at the rate of 3% Pe/min, the target air volume, the actual air volume and the bed pressure drop in the middle and upper part of the dense phase region of the riser change with time.

In Fig.3, when the target air volume is reduced at a rate of 3% Pe/min, the actual fluidizing air volume measured by the flute is obtained, and its value fluctuates around the target air volume, indicating that the drop rate of the fluidizing wind speed is in line with the expectation.

The bed pressure drop in the middle and upper part of the dense phase region is measured by a differential pressure transmitter, which presents the characteristics of uniform overall decrease and local fluctuation. This shows that when the fluidizing air volume of the riser is reduced, the number of particles that are effectively fluidized and thrown to the middle and upper part of the dense phase region is reduced. In addition, the change trend of particles in the middle and upper part of the dense phase region is similar to that of the fluidizing air volume, indicating that the change of the fluidizing air volume will directly affect the particle concentration in the area above the air distributor in the riser, and the movement of particles is directly related to the fluidizing air.
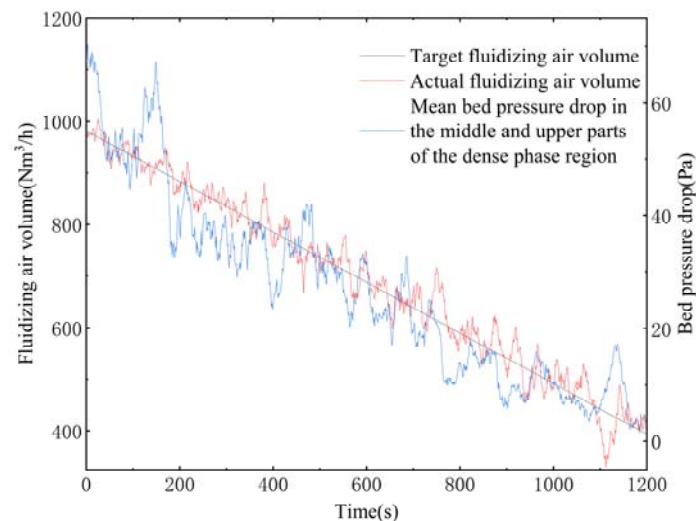
Fig.3 Relationship of bed pressure drop with time and air volume in dense phase area

3.2 Time delay characteristics of particle concentration change in the riser when the fluidizing air volume changes rapidly

3.2.1 Effect of axial height on delay characteristics

The relationship between the delay time(between the change of average particle concentration in the section of the riser and the change of air volume) and the axial height is shown in Fig.4. Fig.4 shows the relationship between the delay time and the axial height when the change rate of air volume is 5% Pe/min. As can be seen from Figure 5, the delay time basically increases with the increase of the axial height, but there is a decreasing area of the delay time at the distance of 2500-3000mm from the air distributor.
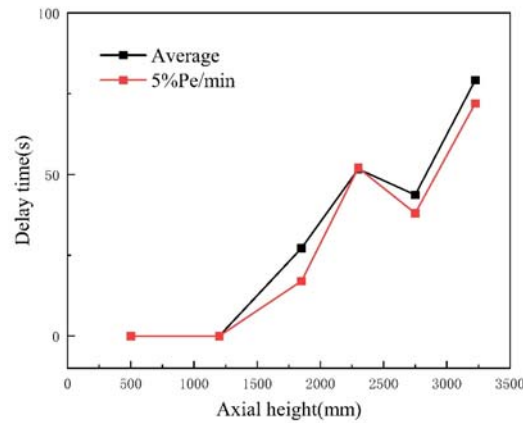
Fig.4 The relationship between delay time and axial height

3.2.2 Effect of change rate of air volume on delay characteristics

The relationship between the delay time(between the change of average particle concentration and the change of air volume) and the change rate of air volume is shown in Fig.5. As can be seen from Fig.5, at the axial height 2750 mm, the maximum delay time is 67 s, and the change rate of air volume is 3% Pe/min. The minimum delay time is 20s, when the change rate of air volume is 1% Pe/min.
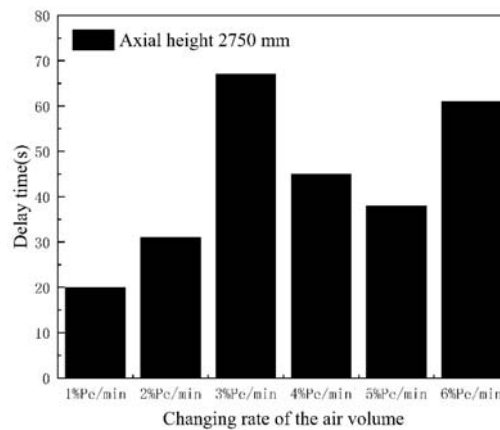
Fig.5 The relationship of delay time with the change rate of air volume

3.2.3 Effect of change rate of air volume on delay characteristics

In order to further analyze the effect of the change rate of air volume on the delay characteristics, the degree of time delay and the axial height are dimensionless. Aiming at the degree of time delay under a certain change rate of air volume, the weighted average value was calculated with the axial height as the weight, and the calculation results were shown in Fig.6. When the fluidizing air volume changes at a lower rate, the weighted average degree of delay in the riser is low. For example, when the air volume is reduced at a rate of 1% Pe/min, the average degree of delay is only 0.47%. When the change rate of air volume is high, such as 6% Pe/min, the average degree of delay reaches 2.91%.
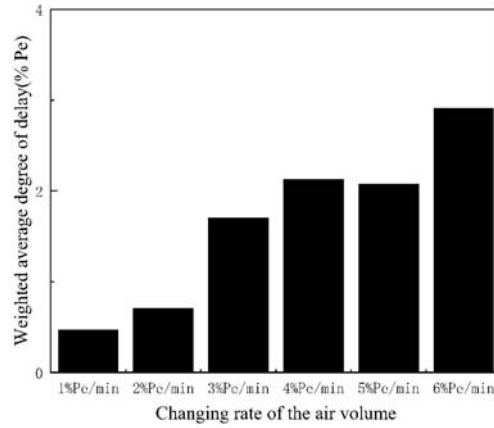
Fig.6 The relationship of the degree of time delay with the change rate of air volume

3.4 Research on the mechanism of time delay when the fluidizing air volume changes rapidly

By analyzing the above test results, the delay time(between the change of average particle concentration and the change of air volume) can be decomposed into: (1) The time difference between the change of the average solid bed particle concentration at the section and the change of the fluidized air flow due to the difference in movement inertia; (2) The difference between the time of the change in the number of particles that really participate in the whole circulation process and the time of the fluidizing air moving from the air distributor to the section.

3.4.1 Mechanism of axial height on time delay

According to the theory and practical engineering experience, some fine particles mainly exist in the middle and upper part of the CFB riser, and these particles can be returned to the riser through the recovery of the external loop. The change of fluidization state in the riser will lead to the change of recovery efficiency of the external loop, and thus the change of particle circulation amount. The change of the total particle circulation amount needs to pass through the external loop and then gradually transfer upward from the dense phase region.

According to the test results, the second type of time delay is related to axial height. The time for the movement of fluidizing air from the air distributor to the section can be simply obtained by dividing the axial height by the apparent fluidizing wind speed. Under the working conditions in this study, the maximum value of the time is 8.75s, which has less effect than the delay time in Fig.4. This suggests that the transport time of the change in particle number plays a major role. The parameters affecting the transfer time of particle number change can be simply expressed as the transfer distance and transfer rate. When the axial height increases, the transfer distance increases, the transfer time increases, and the corresponding delay time also increases.

The reason for the change of dynamic equilibrium state of particle movement is the change of fluidizing air volume, and the reason for the first type of time delay is that the movement inertia of solid bed particles is greater than that of fluidizing air, and its value is mainly determined by the difference of movement inertia between the fluidizing air and solid bed particles (assuming that the bed particles are "gaseous" and the movement inertia of the fluidizing air is the same, obviously there will be no time delay). The finer the particle size, the smaller the inertia difference between the particle and the fluidizing air, the smaller the delay time, and vice versa. Xu[21] et al. showed that the higher the axial height, the finer the particle size of the bed material. Therefore, when the axial height increases, the first type of time delay has a certain trend of decreasing, which is opposite to the change trend of the second type of time delay.

24

When the two are added together, it is possible to reduce the local delay time in the axial direction of the riser. As shown in Fig.4, there is a local decrease in the delay time in the area from 2300 mm to 2750 mm of the axial height.

Overall, the second type of time delay plays a major role.

3.4.2 Mechanism of change rate of air volume on time delay

According to the test results, the change rate of air volume does not directly affect the delay time, but from the perspective of CFB boiler operation. As shown in Fig.6, the time delay can measure the degree of separation between air volume and particle concentration in the process of variable air volume. When the air volume decreases continuously from 100% Pe at a rate of 6% Pe/min, the average particle concentration at the section of the riser at 0.92 relative axial height is the same as when the air volume level drops to 74.3%Pe without delay. The degree of time delay is 4.3 %Pe.

Further, based on the experimental results, the empirical formula obtained is as follows:

$$T=-0.0504+1.9883\left[1+erf\left\{\frac{H-0.6780}{0.3410}\right\}\right]\left[1+erf\left\{\frac{R-2.5592}{1.7822}\right\}\right]$$

Where, T is the degree of time delay; H is the relative axial height; R refers to the change rate of air volume, %Pe/min.

The weighted average degree of time delay is to explore the influence of the rate of air volume change from the perspective of the whole riser. As shown in Figure 8, there is a positive correlation between the weighted average degree of time delay and the change rate of the air volume, which indicates that when the change rate of the fluidized air volume is accelerated, the time delay in the riser will increase. For the actual boiler, there will be uneven gas-solid flow, combustion deterioration and other phenomena, which is consistent with the engineering experience.

4. Conclusion

By conducting steady-state test and variable air volume test with different air volume change rates on the full-loop visual CFB test device, this study explored the distribution and change in space and time of gas-solid concentration under variable air volume operation. The differences of gas-solid concentrations in steady-state and non-steady-state conditions are compared, and the main conclusions are as follows:

① When the air volume changes continuously, the change trend of particle concentration in the riser is consistent with that of the fluidizing air volume, but there is a time delay, which can be summarized as the inertia difference between gas and solid and the change of the number of particles participating in the circulation.

②The delay time is positively correlated with the axial height of the riser.

③There is a positive correlation between the weighted average time delay and the rate of air volume change Based on the test results, the empirical formula is summarized as follows:

$$T=-0.0504+1.9883\left[1+erf\left\{\frac{H-0.6780}{0.3410}\right\}\right]\left[1+erf\left\{\frac{R-2.5592}{1.7822}\right\}\right]$$

In this study, the influence of the rapid change of fluidizing air volume on the gas-solid concentration and flow pattern in the CFB riser was summarized, which can provide theoretical basis and basic engineering application data for CFB boiler to participate in rapid peaking.

References

[1] Cheng, L., Zhou, X., Zheng, C., et al. Development of Large-scale Circulating Fluidized Bed Boiler. Journal of Power Engineering. 2008, 28(06): 817-826.

[2] Song, C., Lv, J., Yang, H., et al. Research and Application of Supercritical and Ultra-supercritical Circulating Fluidized Bed Boiler Technology. Proceedings of the CSEE. 2018, 38(02): 338-347+663.

[3] Cheng, L., Xu, L., Xia, Y., et al. Key Issues and Solutions in Development of the 600 MW CFB Boiler. Proceedings of the CSEE. 2015, 35(21): 5520-5532.

[4] Huang, Z., Yang, J., Che, D. Application and development status of large-scale CFB boilers. THERMAL POWER GENERATION. 2019, 48(06): 1-8.

[5] Jiang, M., Huang, B. Prospects on Coal-fired Power Generation Technology Development. Proceedings of the CSEE. 2012, 32(29): 1-8+19.

[6] Lu, Y., Kevin, T. Wide Area Hierarchical Voltage Control to Improve Security Margin for Systems With High Wind Penetration. IEEE Transactions on Power Systems. 2018, 33(6): 6218-6228.

[7] Liu, J. Basic Issues of the Utilization of Large-scale Renewable Power With High Security and Efficiency. Proceedings of the CSEE. 2013, 33(16): 1-8+25.

[8] Liu, J., Hong, F., Gao, M., et al. Research on the Control Strategy for Quick Load Change of Circulating Fluidized Bed Boiler Units. Proceedings of the CSEE. 2017, 37(14): 4130-4137+4292.

[9] Gao, M., Yue, G., Lie X., et al. Research on Control System of 600 MW Supercritical Circulating Fluidized Bed Boiler. Proceedings of the CSEE. 2014, 34(35): 6319-6328.

[10] Zhang, C., Ma, S., Zhang, J., et al. Pollutant emission from 350 MW CFB boiler under varying load condition. THERMAL POWER GENERATION. 2020, 49(01): 41-47.

[11] Li, Y., Xin, S., Wang, F. Study on ultra-low NO_x emission technology of 660 MW ultra-supercritical circulating fluidized bed boiler. Clean Coal Technology. 2019, 25(05): 86-92.

[12] Tang, Z., Song G., Jiang, Y., et al. Experimental Study on the Effect of Bed Material Amount and Fuel Particle Size on Load Change of Circulating Fluidized Bed. Journal of Thermal Science. 2023, 32(5): 1758-1770.

[13] Yang, C., Hao, X., Zhang, Q., et al. Performance Analysis of a 300 MW Coal-Fired Power Unit during the Transient Processes for Peak Shaving. Energies. 2023, 16(9).

[14] Xin, S., Wang, H., Li, J., et al. Discussion on the Feasibility of Deep Peak Regulation for Ultra-Supercritical Circulating Fluidized Bed Boiler. Energies. 2022, 15(20): 7720-7720.

[15] Li, J., Shen, X., Zhao, Q., et al. Numerical simulation of particle flow characteristics of a 350 MW CFB boiler. THERMAL POWER GENERATION. 2022, 51(04): 62-69.

[16] Yan, J., Lu, X., Xue, R., et al. Validation and application of CPFD model in simulating gas-solid flow and combustion of a supercritical CFB boiler with improved inlet boundary conditions. Fuel Processing Technology. 2020, 208.

[17] Han, C., Hu, L., Song, T., et al. Effect of bed material size on gas-solid flow characteristics in a CFB at low solid recirculation rates. Fuel. 2023, 333: 126354.

[18] Hu, N., Wang, W., Yao, X., et al. Study on Gas-solids Flow Properties in the 38m/54m Riser of Circulating Fluidized Bed. Proceedings of the CSEE. 2009, 29(26): 7-12.

[19] Luo, Z., Ni, M., Chen, K. Experimental study on hydrodynamic characteristics of circulating fluidized bed. Journal of Zhejiang University. 1987, (06): 89-97.

[20] Li, S., Guo, H., Li, D. Review of vibration signal processing methods. Chinese Journal of Scientific Instrument. 2013, 34(08): 1907-1915.

[21] Xu, J., Lu, X., Zhang, W., et al. Effects of superficial gas velocity and static bed height on gas-solid flow characteristics in a 60-meter-high transparent CFB riser. Chemical Engineering Journal. 2018, 334: 545-557.

IMPACT OF AN EXTERNAL HORIZONTAL SOUND FIELD ON A PARTICLE IN FLUIDIZATION

Yanqin Li*, Fidel C. X. Mário, Borui Zhou

School of Mechanical & Power Engineering, Zhengzhou University, China 450001

*Email: yqli1@hotmail.com

Abstract

Particle motion characteristics in a horizontal sound wave are novelly studied, related to fluidization etc. It indicates that the acoustic velocity amplitude of a particle decays in a quasi exponential manner with increase of sound frequency, and particle size as well. In contrast, the particle Reynolds number increases with the frequency in a manner of quasi power function. And it is intriguing that the horizontal sound field shows not only to cause the corresponding horizontal harmonic vibration of the particle, but to generate a certain periodic motion along the vertical direction. Nevertheless, the horizontal sound waves appear to hinder the vertical movement of the particle as well, and exhibiting certain nonlinearity. The mechanism of such a phenomenon is studied and uncovered by means of the Newton's law, which turns out to originate from the drag force by a combined oscillation movement between the horizontal sound wave and the vertical gravity settlement, and the virtual mass force, respectively.

1. Introduction

Typical two phase flow exists in fluidization, industrial flue gas, etc.[1,2] Acoustic measurement of two-phase flow[3], and particle acoustic agglomeration[4-6] are important and typical applications, related to interaction between the added sound field and a two-phase flow. It is crucial to effectively reveal the relevant motion mechanism of particles in a two-phase flow with a sound field added. Refs.[2,5] analyzed the particle dynamics in Stokes region, ignoring the influence of gravity on the acoustic vibration of the particles. Yang et al[7] analyzed the drag, gravity, buoyancy and Brownian forces on particles in acoustic field. Yuan et al[8] analyzed PM2.5 particles suspended in the air under the action of a sound. Li et al[9] simulated coalescence of cloud and fog droplets impacted by traveling acoustic waves. Stanly et al[10] studied the gas-solid two-phase flow characteristics in a fluidized bed under the action of a longitudinal sound field.

Comparatively, much fewer works have been focused on particle dynamics in a horizontal sound field. Refs. [6,8,11] discussed the aggregation behavior of particles in a horizontal sound field, but their works did not involve the effects of the horizontal sound on the vertical settling motion of particles. We found that the horizontal sound field complicatedly affects the vertical movement of particles, and studied related mechanisms based on numerical models validated by literature experimental results.

2. Principle

The gas medium sound field model is obtained based on N-S equations[12]. And a linear acoustic model relates to a small disturbance problem. In order to study the movement of particles in a sound field, a background sound wave is set up:

$$\qquad (1)$$

is the sound pressure amplitude, is the angular frequency, and *k* is the wave number. The gas phase acoustic particle velocity in gas-solid two-phase flow can be defined as:

$$. \qquad (2)$$

is the Laplacian sound speed, and is is the density of the medium. The forces on a particle in a sparse gas-solid two-phase flow field can be defined based on the Newton's law:

$$m_p \frac{d\vec{v}_p}{dt} = \vec{F}_d + \vec{F}_b + \vec{F}_p + \vec{F}_{vm} + \sum_i \vec{F}_i \qquad (3)$$

where $\vec{v}_p$ is the acoustic vibration velocity of particles in the gas-solid two-phase flow field, which is produced by the gas movement velocity $\vec{v}_g$ as defined previously. $\vec{F}_d$, $\vec{F}_b$, $\vec{F}_p$, $\vec{F}_{vm}$, and $\sum_i \vec{F}_i$ are respectively the drag force, Basset force, pressure gradient force, virtual mass force, and other small forces that the particle experience in the gas-solid two-phase flow field. In the formula (3), the influence of Basset force on the movement of a solid particle in gas can be ignored[13], while other forces, $\vec{F}_d$, $\vec{F}_p$, $\vec{F}_{vm}$, and $\vec{G}$ are involved in the model established in this paper.

Drag force:

$$\vec{F}_d = \frac{1}{2} C_D \rho_f A_f (\vec{v}_g - \vec{v}_p) \left| \vec{v}_g - \vec{v}_p \right| \qquad (4)$$

where C_D is the drag coefficient, ρ_f is the fluid density, and A_f is the projected area of the particle in the direction of movement. The drag coefficient is related to the particle Reynolds number (Re_p). In the gas-solid two-phase flow, different forms of drag force formulas are applicable in different ranges[14], as displayed in Table 1.

Table 1 Drag force at different regions on Re_p

Stokes region: $Re_p \leq 1$	$C_{Ds} = \dfrac{24}{Re_p}$, $\vec{F}_{ds} = 6\pi\mu R(\vec{v}_g - \vec{v}_p)$
Transition region: $1 \leq Re_p \leq 1000$	$C_{Dg} = \dfrac{18.5}{Re_p^{0.6}}$, $\vec{F}_{dg} = \dfrac{37}{16}\pi\rho_f^{0.4}D^{1.4}(\vec{v}_g - \vec{v}_p)^{1.4}\mu^{0.6}$
Turbulent region: $Re_p \geq 1000$	$C_{Dt} = 0.44$, $\vec{F}_{dt} = 0.22\rho_f A_f(\vec{v}_g - \vec{v}_p)^2$

Pressure gradient force:

$$\left| \vec{F}_p \right| = -\frac{4}{3}\pi R^3 \left| \frac{\partial p}{\partial x} \right| = p_A \frac{4}{3}\pi R^3 k \sin(\omega t - kx) \qquad (5)$$

Virtual mass force:

$$\vec{F}_{vm} = \frac{1}{12}\pi D^3 \rho_g \left(\frac{d\vec{v}_g}{dt} - \frac{d\vec{v}_p}{dt} \right) \qquad (6)$$
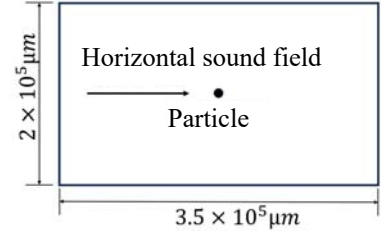
Fig.1 Geometric of particle motion in a sound field

3. Numerical model

The motion of a single particle in 2-D horizontal traveling sound waves is modeled, as configured in Fig.1. The upper and lower boundaries are set as slip for flow, and plane wave radiation for the sound, to simulate related application in a large space, and the left and right ones are set open.

The model was validated based on literature experimental results[15], where a sound pressure level is 152.55dB, ~1200Pa of amplitude. Figure 2 gives their comparison, to show a good reliability of the numerical model built in this paper.

4. Results and analysis
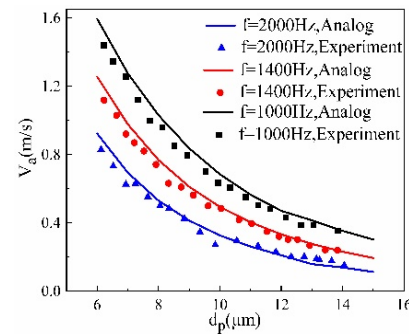
Fig.2 Comparison of particle velocity amplitude between literature experiment and the simulation in this paper

Based on the above verification to the established single particle motion model in the horizontal sound field, this paper further studies the motion characteristics of a particle in a horizontal sound field, combining with the gravity settlement, and focus on the acoustic velocity amplitude, the sedimentation, as well as the particle Reynolds number, Re_p, to effectively reveal the influence of different parameters of both the external sound field and the particle on the motion of the particle.

4.1 Boundary conditions

As a further, pulverized coal particle is selected for study, one of which typical applications is the acoustic measurement in a power plant furnace and its primary air ducts. Parameters of the particle, with the density 1800kg/m^3, and the sound field, for the numerical modeling, are shown in Table 2. The temperature is 293.15K.

Table 2 Model parameters

	Parameters
Particle diameter (μm)	0.2, 0.5, 1, 2, 5, 10, 15, 20
Sound pressure (Pa)	400, 600, 800, 1200, 1600, 2000, 2600, 3000
Sound frequency (Hz)	200, 400, 600, 800, 1000, 1200, 1400, 1600, 1800, 2000

4.2 Particle acoustic velocity

Figure 3 shows the characteristics of the acoustic velocity magnitude of the particle in a horizontal sound field. The total velocity of the particle shows regular sinusoidal oscillation, as shown in Fig.3(a). It reveals that the smaller the particle is, the closer it's acoustic velocity is to that of the gas medium. On the other hand, a vertical velocity component turns out to be generated by the horizontal sound wave, and by the gravity in couple, as shown in Fig.3(b), although such an induced vertical vibration appears quite weak. It's magnitude and amplitude reveal to relate to the particle size and sound frequency, etc. Fig.3(c) shows the change of the acoustic velocity amplitude of the particle with sound frequency in a certain exponential descending trend, for different particle sizes. Correspondingly, Fig.3(d) demonstrates the variation of the acoustic amplitude decreasing with the particle size in an exponential law as well, except for the region with minor particle sizes. And the local characteristics at that region is amplified in the sub-figure. It shows that a larger sound frequency corresponds to a larger velocity amplitude when the particle size is small enough, which is converse to the law demonstrated while the particle size exceeds a critical value.
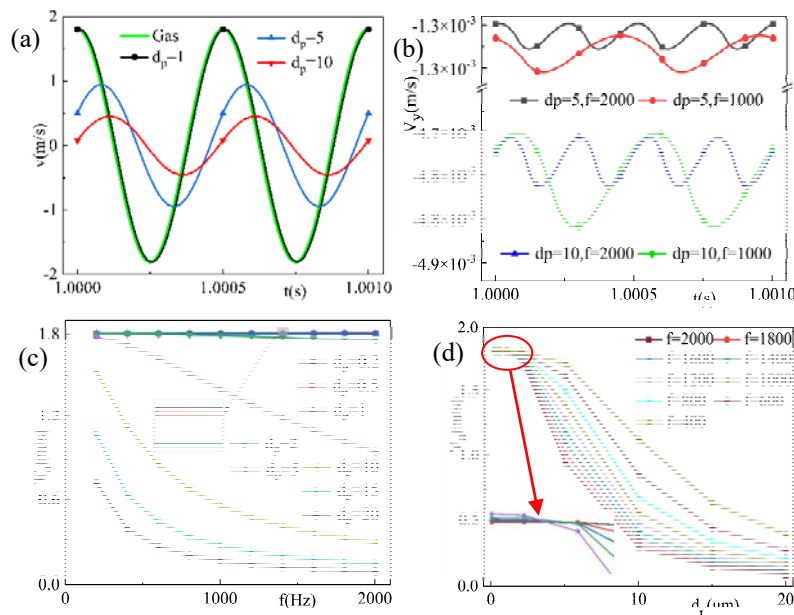
Fig.3 Particle acoustic velocities under the sound pressure of 1200Pa. (a) variation with time at illustrated particle sizes, and (b) the induced vertical vibrations. The particle velocity amplitude varying with (c) sound frequency, and (d) particle size

4.3 Particle Reynolds number

The particle Reynolds number in a two-phase flow is an important indicator to describe its motion dynamics. It is related to the slip velocity of the particle to the continuous phase, and the particle size, etc. The larger the Re_p is, the weaker the carrying capacity of the continuous medium is to a particle. The characteristics of Re_p changing with different parameters of the sound and the particle, respectively, are dealt with. Figure 4 show the relationship of Re_p with related sound and particle parameters in the horizontal sound field.
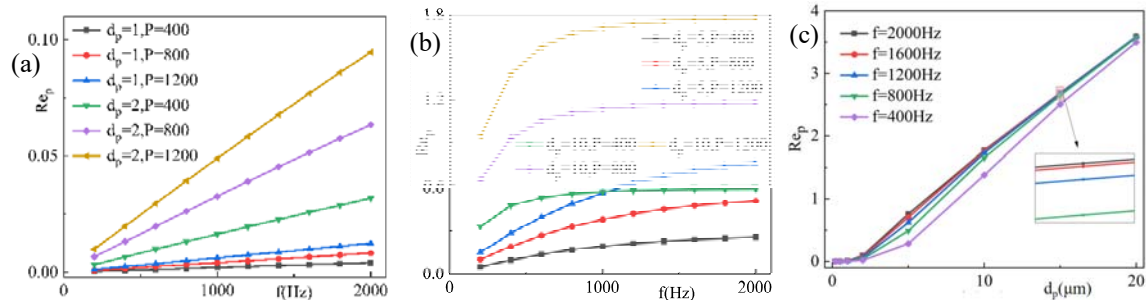
Fig.4 Re_p amplitude changing with sound frequency and sound pressure, with particle sizes (a)1 and 2 µm, (b)5 and 10 µm. The sound pressure in (c) is 1200Pa

Figures 4(a)(b) show that, in general, Re_p increases with frequency in a certain sound field, and the greater the sound pressure is, the greater the Re_p is. When the particles are small, as in Fig.4(a), it increases linearly with the frequency within a certain sound pressure and frequency range, and the particle vibration falls in the Stokes zone; and when the particle size increases to a certain extent, as in Fig.4(b), it shows a growth in a law like a power function, f^n, $0 < n < 1$. And in the latter situation, the particle motion characteristics are corresponding to around the upper limit of the Stokes region. It shows that after a critical frequency value, Re_p basically no longer increases with the sound frequency. And comparing to Fig.3(b), even for the Stokes region ($Re_p<1$), the derived acoustic vibrations in the gravity direction appear nonlinear wave forms to a certain extent, but it appears some different from those when Re_p is larger.

Figure 4(c) shows that the Re_p demonstrates a monotonic increase with the particle size under a certain sound pressure, in a global nonlinearity and local linear trend. This trend spans over the Stokes zone and the non-Stokes zone. Moreover, the larger the particle size is, the less obvious the impact of the sound frequency is.

4.4 Sedimentation of particles in the sound field

In the horizontal sound field, in addition to the corresponding longitudinal vibration, the particle also moves in the vertical direction due to the action of gravity. The sedimentation distance of the particle within 1s is studied, to depict it's settling speed in the horizontal sound field. The results are compared with that without sound field added. Figure 5 displays the changing of the sedimentation distance of the particle, within 1s, with sound frequency and particle size, respectively.

The results show that the settlement of a particle is affected by the added horizontal sound field. In general, the greater the sound pressure is, the more the horizontal sound hinders the settlement of the particle. In addition, the trend in the figures shows that the greater the sound frequency is, the most hindering to the particle is. Typically, for particle size under ~0.5µm, the sedimentation speed appears weak and almost linear with the frequency, as shown in Fig.5(a); when the particle size is over ~5µm, the settling distance shows an obvious exponential decrease with the increase of sound frequency, as shown in Fig.5(c); while at the intermediate particle sizes, it shows characteristics of a transitional change

between the former two trends, as shown in Fig.5(b), for which when the frequency exceeds a certain critical value, it suddenly changes into an obvious hindering to the particle. At the same time, the transition zone shows that the larger the sound pressure is, the smaller the critical sound frequency value for mutation occurs. Additionally, Fig.5(d) shows the sedimentation changing with particle size in a law of exponential increase, which, however, demonstrates certain exponential increase of hindering from the horizontal sound, comparing to to the that without horizontal sound action.
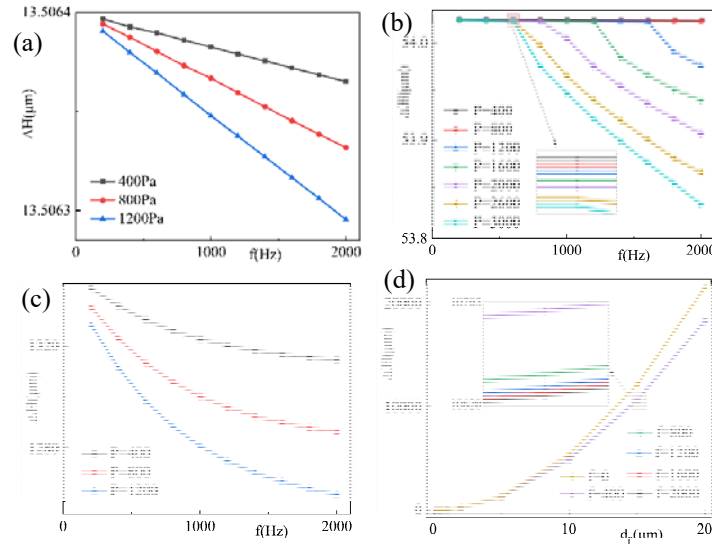
Fig.5 The particle sedimentation distance changing with sound frequency within 1s under different sound pressures, with the particle sizes are: (a) 0.5μm, (b) 1μm, and (c) 5μm, and (d) changing with particle size at the sound pressure 800Pa

5. Discussion

In this section a principle in line with Newton's law was proposed to uncover the complex dynamics of a certain particle under a horizontal sound field, by which the particle also shows to vibrate in a vertical direction due unlike forces. Therefore, we tried to find the certain forces acting on the particle, which causes the related particle mechanics. In this instance, for the one-dimensional horizontal planar wave, the force expression as Eq.(3) can be met with. For the instance of a solid particle in air, with a certain horizontal sound field added, the working forces are demonstrated in Fig.6. The trajectory of the particle, with a 5μm diameter, generated in the horizontal sound field is shown, and it is prolonged by 15 times in the y- direction for a clearer demonstration.
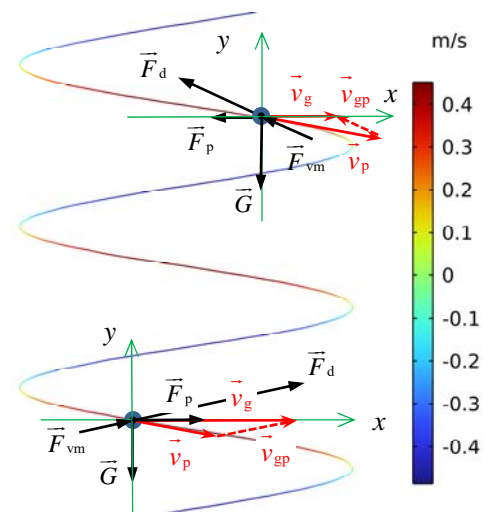
In the particle sedimentation as shown in Fig.6, the actual drag force, $\vec{F}_{\mathrm{d}}$, is generated by the relative

Fig.6 Forces to the particle settling in a horizontal sound field in air

motion velocity of the gas to the particle, $\vec{v}_{\mathrm{gp}} = \vec{v}_{\mathrm{g}} - \vec{v}_{\mathrm{p}}$. Here the particle velocity, $\vec{v}_{\mathrm{p}}$, originates from the coupling between the horizontal gas sound oscillation and the gravity settlement of the particle. The drag force correspondingly produces an oscillation force component in the vertical direction, as well as the horizontal one. And then, an oscillation movement in the vertical direction can be generated by such a force component, i.e. the velocity component as shown in Fig.3(b). In theory, the drag force to a particle in a laminar flow is approximated as directly proportional to the slip velocity between the particle and the continuous medium; while in a turbulent flow, it is proportional to the squared slip velocity, with detailed formulations presented in Table 1.

On the other hand, the virtual mass force, $\vec{F}_{\mathrm{vm}}$, as shown in Fig.6 and defined in Eq.(5), appears always directing upward during oscillation of the particle sedimentation. It is presumably the cause of the hindering to the particle sedimentation, as displayed in Fig.5.

4. Conclusion

Fundamentally, this paper conducts a numerical simulation study on the motion characteristics of a single particle in a horizontal sound field based on experimental verification from literature. The main conclusions are as follows:

(1) The Reynolds number increases with the sound frequency in a power law, and totally in a nonlinear law of monotonic increasing with the particle size.

(2) By contrast, the acoustic velocity amplitude of a particle varies in a certain approximate exponential law with increase of the sound frequency and particle size, respectively. On the other hand, changes in sound pressure cause significant variations in the motion of a particle.

(3) The existence of a horizontal sound field turns out to hinder the movement of particles in the direction of gravity and shows intriguing nonlinear law with sound frequency and particle size, respectively; at the same time, it shows to generate a corresponding harmonic vibration of the particle in the vertical direction, whereas with certain another nonlinear characteristics whether in the Stokes region or not. Related mechanisms are discussed.

References

[1] Zhou, Y., Wang, T., Zhu, J. Development of gas-solid fluidization: particulate and aggregative. Powder Technology. 2023. 421, 118420.
[2] Lu, M., Fang, M., He, M., et al. Insights into agglomeration and separation of fly-ash particles in a sound wave field. RSC Advances. 2019. 9, 5224-5233.
[3] Wang, D., Sun, J., Wang, Y., et al. Eliminating the influence of moisture on solid concentration measurement in gas-solid flows using combined sensors. IEEE Trans Instrum Meas. 2023. 72, 7500310.
[4] Yao, G., Zhao B., Shen X. Experimental study and numerical analysis of the acoustic agglomeration effectiveness of inhalable particles of burned coal. Journal of Engineering for Thermal Energy and Power. 2006. 21(2), 175-178.
[5] Liu, J., Zhang, G., Zhou, J., et al. Experimental study of acoustic agglomeration of coal-fired fly ash particles at low frequencies. Powder Technology. 2009. **193**(1), 20-25.
[6] Kacianauskas, R., Maknickas, A., Vainorius, D. DEM analysis of acoustic wake agglomeration for mono-sized microparticles in the presence of gravitational effects. Granular Matter. 2017. 19, 48.
[7] Yang, N., Fan, F., Hu, X., et al. Influence of large seed particle on acoustic particle interaction dynamics: A numerical study. J Aerosol Sci. 2022. 165, 106018.
[8] Yuan, L., Fan, X., Yao, G., et al. Study of sound wave effect on the $PM_{2.5}$ suspended in the air by numerical simulation and experiments. J Combust Sci Technol. 2005. 11(4), 298-302.
[9] Li, F., Jia, H., Wang, Q., et al. Mechanism of Cloud Droplet Motion under Sound Wave Actions. J Atmos Ocean Technol. 2020. 37(9), 1539-1550.

[10] Stanly, R., Shoev, G., Kokhanchik, A. A. Numerical Simulation of Gas-Solid Flows in Fluidized Bed with TFM Model. AIP Conference Proceedings. 2017. 1893, 1030040.

[11] Valverde, M. Acoustic streaming in gas-fluidized beds of small particles. Soft Matter. 2013. 9, 8792-8814.

[12] Zhao, D., Ji, C., Wang, B. Geometric shapes effect of in-duct perforated orifices on aeroacoustics damping performances at low Helmholtz and Strouhal number. J Acoust Soc Am. 2019. 145(4), 2126-2137.

[13] Ju, H., Bian, F., Wei, M. Modeling of soot particle collision and growth paths in gas-solid two-phase flow. Therm Sci. 2021. 25(5 Part B), 3741-3752.

[14] Pramod, K., Baron, P. A., Willeke, K. Aerosol measurement: principles, techniques, and applications, 3rd Edition. New York: Wiley. 2011.

[15] Lu, M. Visualization research and numerical simulation on movement and agglomeration characteristic of particles. Hangzhou: Zhejiang University. 2019. (in Chinese)

Study on Gas-Solid Flow Characteristics in a CFB with Internal Circulating Ash Bin

Zhonghao Dong[1], Zhaoliang Wu[1], Rongdi Zhang[1], Jianbo Li[1], Xiaofeng Lu[1,*]

1. Key Laboratory of Low-grade Energy Utilization Technologies and Systems of Ministry of Education, Chongqing University, Chongqing 400044, China

Email: xfluke@cqu.edu.cn

Abstract

The adjustable characteristics of internal circulating ash play a crucial role in the rapid load adjustment of large Circulating Fluidized Bed (CFB) boilers. This study investigates the influence of varying internal circulating ash quantity on the gas-solid concentration distribution within the CFB by constructing a cold-state experimental platform with internal circulating ash bins. Experimental results demonstrate that releasing internal circulating ash from internal circulating ash bins significantly alters the gas-solid concentration in the upper part of the riser. Moreover, the operating airflow velocity of the CFB bed and the fluidizing airflow velocity of the internal circulating ash bin also exhibit notable effects on its operation. Under the condition of a fluidizing airflow velocity of 1.5 times the minimum fluidization velocity (U_{mf}), increasing the ash discharge rate from the internal circulating ash bin leads to higher bed material concentration in the dilute phase region of the CFB bed. The bed material mass increment in the middle section of the riser corresponds to approximately 90% of the ash discharge rate, while in the upper section, it corresponds to approximately 60% of the ash discharge rate. These findings confirm that internal circulating ash adjustment serves as an effective means to adjust the ash concentration in the upper section of the riser in CFB boilers.

Keywords: Circulating Fluidized Bed (CFB); Internal circulating; Ash quantity regulation; Load variation

1. Introduction

As is well recognized, the heat transfer coefficient on the furnace side of CFB boilers is influenced by the concentration of solid particles [1]. During load variation, it is essential to maintain appropriate gas-solid concentrations and flue gas temperatures in the upper part of the furnace to meet the heat transfer requirements corresponding to load changes. Hence, it is necessary to rapidly increase or decrease the concentration of dilute-phase bed material particles during load variation processes [2-4]. During load reduction, the internal circulating ash concentration can be rapidly decreased through methods such as slag discharge and ash removal. However, a significant challenge arises in rapidly increasing the circulating ash concentration during load ramping processes.

To address this issue, practical engineering approaches involve the use of auxiliary ash bins outside the furnace. This method employs the addition of bottom ash, circulating ash, limestone powder, or similar substances to alter the gas-solid concentration in the upper part of the furnace. Several scholars have conducted similar studies in this regard [5-7].

To overcome the limitations of the aforementioned techniques, this study proposes a CFB boiler system with internal circulating ash bins to achieve rapid adjustment of gas-solid concentrations within the furnace during load ramping processes. Based on this concept, a CFB cold-state experimental platform with internal circulating ash bins was constructed and the experimental researches on the ash storage capacity of the internal circulating ash bin and its ability to regulate circulating ash quantities within the furnace were conducted.

2. Experiment Overview

2.1 Introduction to cold-state experimental system of CFB with internal circulation

2.1.1 Introduction to the experimental platform body

To construct the cold-state experimental platform with internal circulating ash bins, one-third of the furnace of a 350 MW supercritical CFB boiler in a 15:1 ratio was downscaled, as depicted in Fig.1. Internal circulating ash bins were positioned in the upper part of the dense-phase zone of the riser. During the experiment, solid particles entered the circulating ash bin through the opening of the internal circulating ash bin. Regulating baffles were installed at the outlet of each internal circulating ash bin to control the ash storage capacity and inlet area of the internal circulating ash bin.

The bed material in the internal circulating ash bin remains in a fluidized state resembling a bubbling bed. A ash discharge pipe was installed at the bottom of each internal circulating ash bin, connected to the return pipe of the external circulating loop. During ash storage, each ash discharge pipe is sealed with a plug valve. When discharging ash, the plug valve is opened, allowing the bed material to enter the riser through the return pipe, thereby facilitating rapid adjustment of ash concentration within the riser. The primary dimensions of the cold-state experimental platform are outlined in Table 1.

Table 1 Main structural dimensions of the experimental platform for fluidized bed with internal circulation

Project		Unit	Length
Furnace	Height	mm	3250
	Width	mm	640
	Depth	mm	710
	Dense phase region height	mm	550
Air distributor	Width	mm	292
	Depth	mm	710
Internal circulating ash bin	Height	mm	250
	Width	mm	120
	Depth	mm	200
	Adjustable baffle height	mm	50/100/150/200
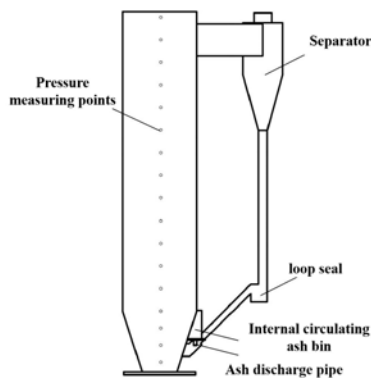
(a) Schematic diagram of the structure   (b) Cold-state experimental platform main body

Fig. 1. Cold-state experimental platform for CFB system with internal circulating ash bin.

2.1.2 Measurement points

During the experimental process, bed pressure measurements are conducted using 16 pressure measurement points arranged on the left wall of the riser. The suspension concentration of solid particles within the riser is obtained by calculating the pressure difference between adjacent points. The numbering and distances of pressure measurement

points from the distributor plate are provided in Table 2. Additionally, PV6D instruments are used to measure local particle concentration and velocity.

Table 2 The numbering and distances of pressure measurement points from the distributor

Position	Measurement Point Number	Distance from Distribution Plate to Riser / mm
Lower part of riser	1、2、3	250、400、550
Middle part of riser	4、5、6、7、8、9、10	750、950、1150、1350、1550、1750、1950
Upper part of riser	11、12、13、14、15、16	2150、2350、2550、2750、2950、3150

2.1.3 Particle characteristics

During the experiment, the bed material used consists of bottom ash from the Baima 600 MW supercritical CFB boiler, with 20% mass fraction of entrained fines. The median particle size of the experimental bed material is 134.4 μm, and the particle size distribution is depicted in Fig. 2. The bulk density of the experimental bed material is 1076 kg/m^3, and the true density is 1778 kg/m^3. The critical fluidization velocity of the experimental bed material is determined to be approximately 0.38 m/s through critical fluidization velocity tests.

2.2 Experimental conditions

2.2.1 The tests of ash storage performance of internal circulating ash bin

To investigate the effect of the primary fluidizing air velocity and the outlet fluidizing air velocity of the internal circulating ash bin on the ash storage rate and to assess the ash storage capacity of the internal circulating ash bin, ash storage performance tests were conducted.

During the experiment, ash storage tests were conducted under different primary fluidizing air velocities and outlet fluidizing air velocities of the internal circulating ash bin. The entrance area of the internal circulating ash bin was varied by adjusting the height of the inlet baffle, and the outlet fluidizing air velocity of the internal circulating ash bin was controlled by adjusting the fluidizing air volume. The experimental conditions are presented in Table 3.

During the experiment, the mass of circulating ash entering the internal circulating ash bin within a designated time period was measured by sampling and weighing. This data was then used to calculate the solid mass flux at the inlet of the internal circulating ash bin. The initial bed height during the experiment was set to 100mm. Where, $U_{abair,out}$ means fluidizing air velocity at the outlet of the internal circulating ash bin; U_{abair} means internal circulating ash bin fluidization velocity.

Table 3 Operating conditions for ash storage characteristics test of internal circulating ash bin

Number	U_g	U_{abair}	Adjustable baffle height /mm	$U_{abair,out}$
S1	$1.5U_{mf}$	$0.3U_{mf}$	50/100/150/200	$0\sim1U_{mf}$
S2	$2U_{mf}$	$0.3\sim0.4U_{mf}$	50/100/150/200	$0\sim2U_{mf}$
S3	$2.5U_{mf}$	$0.3\sim0.5U_{mf}$	50/100/150/200	$0\sim2.5U_{mf}$
S4	$3U_{mf}$	$0.3\sim1U_{mf}$	50/100/150/200	$0\sim3.5U_{mf}$
S5	$3.5U_{mf}$	$0.3\sim1U_{mf}$	50/100/150/200	$0\sim3.5U_{mf}$

2.2.2 The experiment on the regulatory performance of ash storage in the internal circulating ash bin on solid particle concentration control in the riser

To investigate the ability of ash storage in the internal circulating ash bin to regulate the solid concentration within the riser under low-load conditions, solid particle concentration control experiments were conducted.

Initially, under the condition of a primary fluidizing air velocity of $3U_{mf}$, the system was operated stably for a period to allow the internal circulating ash bin to collect circulating ash. Then, the primary fluidizing air velocity was reduced to $1.5U_{mf}$ to simulate the rapid load reduction process during low-load conditions. At this point, the outlet fluidizing air velocity of the internal

circulating ash bin was adjusted to $1.5U_{mf}$, ensuring no solid particles could enter the internal circulating ash bin under this condition.

Subsequently, the regulating baffles of each ash discharge pipe were opened to allow the ash stored in the internal circulating ash bin to enter the riser. The mass of bed material entering the riser was controlled by adjusting the ash height within the circulating ash bins.

During the experiment, the variation in solid particle concentration within the riser at different heights was obtained by measuring the pressure difference at various height points in the riser under different ash storage rates. The specific experimental conditions are outlined in Table 4.

For ease of description, the following definitions are provided:

Ash discharge rate: It is the ratio of the mass of solid bed material entering the riser from the internal circulating ash bin to the original mass of bed material in the riser.

Bed material mass change rate: After ash storage from the internal circulating ash bin enters the riser, it refers to the ratio of the increment in bed material mass within a certain height segment to the original bed material mass within that segment of the riser.

Table 4 Operating conditions for adjustment characteristics test of internal circulating ash bin

Number	U_g	Primary fluidizing air velocity during ash Storage	Ash storage height /mm	U_{abair}	Adjustable baffle height /mm
A1	$1.5U_{mf}$	$3U_{mf}$	200	$0.32U_{mf}$	200
A2	$1.5U_{mf}$	$3U_{mf}$	150	$0.32U_{mf}$	200
A3	$1.5U_{mf}$	$3U_{mf}$	100	$0.32U_{mf}$	200
A4	$1.5U_{mf}$	$3U_{mf}$	50	$0.32U_{mf}$	200
A5	$1.5U_{mf}$	$3U_{mf}$	0	$0.32U_{mf}$	200

3. Experimental Research Results and Discussion

3.1 Ash storage performance of internal circulating ash bin

3.1.1 The influence of primary fluidizing air velocity on ash storage performance

The relationship between the mass flux at the inlet of the internal circulating ash bin and the primary fluidization number is depicted in Fig. 2, showing that the ash storage flux increases with the increase in the primary fluidization number.

From Fig. 5, it can be observed that as the primary fluidization number increases, the mass flux of circulating ash at the inlet of the internal circulating ash bin gradually increases. Particularly, after $U_g \geqslant 2.5U_{mf}$, the mass flux of solid particles at the inlet of the internal circulating ash bin sharply increases. This is because, when U_g is less than $2.5U_{mf}$, the circulating ash entering the internal circulating ash bin mainly consists of ash flowing downward along the wall of the riser. The flow rate of circulating ash is relatively small, resulting in limited circulating ash entering the internal circulating ash bin. However, when U_g is greater than $2.5U_{mf}$, the fluidization of the bed becomes more intense, leading to a large amount of circulating ash being ejected into the internal circulating ash bin due to bubble elutriation. Consequently, the mass flux of solid particles at the inlet of the internal circulating ash bin increases.

3.1.2 The influence of fluidizing air velocity in the internal circulating ash bin on ash storage characteristics

The relationship between the ash storage mass flux and the outlet fluidization number of the internal circulating ash bin is illustrated in Fig. 3.

From Fig. 6, it can be observed that as the outlet fluidization number of the internal circulating ash bin increases, the mass flux of bed material at the inlet of the internal circulating ash bin gradually decreases, exhibiting an exponential trend. Particularly, when U_g is less than $2.5U_{mf}$,

even under the condition of $U_{abair,out} = 0.38U_{mf}$, the mass flux of bed material at the inlet of the internal circulating ash bin tends to approach zero.

This phenomenon is attributed to the influence of the wide sieve distribution of bed material in the CFB boiler. The particle size of the circulating ash particles flowing downward along the wall is generally smaller compared to the particles undergoing bubble elutriation. Under the action of the fluidizing air in the internal circulating ash bin, the circulating ash particles moving to the region above the inlet of the internal circulating ash bin will be re-entrained by the fluidizing air of the internal circulating ash bin and carried back into the dilute phase zone of the riser. As a result, the mass flux of circulating ash at the inlet of the internal circulating ash bin decreases

Based on experimental results, the empirical formula for obtaining the mass flux of bed material at the entrance of the CFB is shown in Equation 1.

$$\frac{G_{ab,i}}{\rho_p U_{mf}} = 2.3902 \times 10^{-5} EXP(1.8764 \frac{U_g}{U_{mf}} - 1.2919 \frac{U_{abair,out}}{U_{mf}}) - 4.6970 \times 10^{-4}$$

(1)

This empirical formula fits the experimental results well under the condition of $U_{abair,out} < U_{mf}$, $R^2 = 0.9306$. Where, $G_{ab,i}$ means mass flux of solid at the inlet of the ash bin.
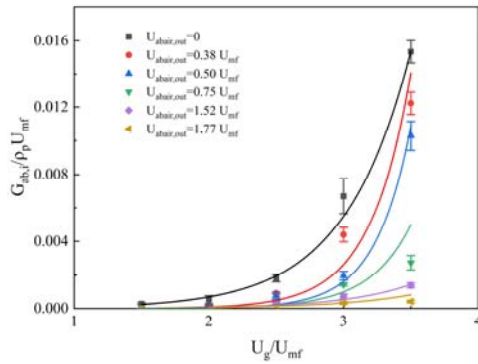
Fig. 2. Relationship between ash storage mass flux and primary fluidization number.
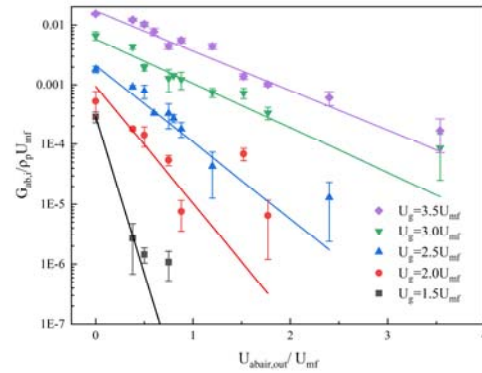
Fig. 3. Relationship between ash storage mass flux and fluidization number at the outlet of the internal circulating ash bin.

3.2 Regulatory performance of ash storage in the internal circulating ash bin on solid particle concentration control in the riser

The experiment obtained the variation trend of solid particle suspension concentration along the height of the riser at different ash discharge rates under a primary fluidizing air velocity of $1.5U_{mf}$, as shown in Fig. 4.

During the experiment, the fluidizing air velocity was maintained at $1.5U_{mf}$ to simulate rapid load increase conditions. At this velocity, the gas-solid two-phase flow in the lower part of the riser is in a bubbling bed state, resulting in generally low solid particle suspension concentrations (<0.001) in the upper part of the riser. Additionally, it can be observed that with increasing ash discharge rate, there is a slight increase in the solid particle suspension concentration throughout the height range of the riser.

The relationship between the bed material mass change rate at different heights of the riser and the ash discharge rate from the ash bin is shown in Fig. 5.

From Figure 8, it can be observed that under different operating conditions, the bed material mass change rate at the lower part of the riser is approximately equal to the ash discharge rate from the ash bin. However, as the height increases, the bed material mass change rate gradually becomes lower than the ash discharge rate. This is because the ash storage in the internal circulating ash bin occurs under high fluidizing air velocity, during which a large

amount of relatively coarse bed material is ejected into the internal circulating ash bin through the bubbling process. The particle size of the bed material in the circulating ash bin is relatively coarse. Additionally, during the adjustment of the riser ash concentration in the experiment, the fluidizing air velocity is relatively low, resulting in a lower saturation carrying rate of the fluidizing air. This leads to a slowdown in the increase of the solid particle suspension density inside the riser as the height of the riser increases.

The experimental results indicate that the use of the internal circulating ash bin provides good control over the solid particle concentration inside the riser. In the middle part of the riser, the bed material mass change rate is approximately 90% of the ash discharge rate from the ash bin, while in the upper part of the riser, the bed material mass change rate is approximately 60% of the ash discharge rate.
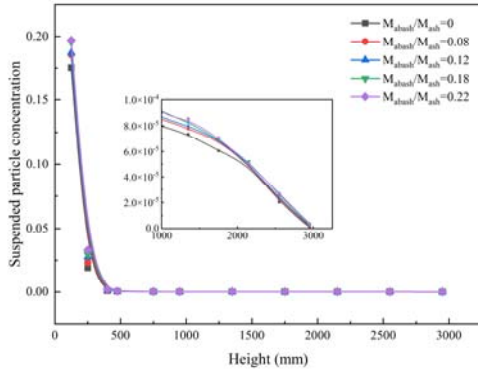
Fig. 4. Relationship between suspended particle concentration at different heights and ash discharge rate.
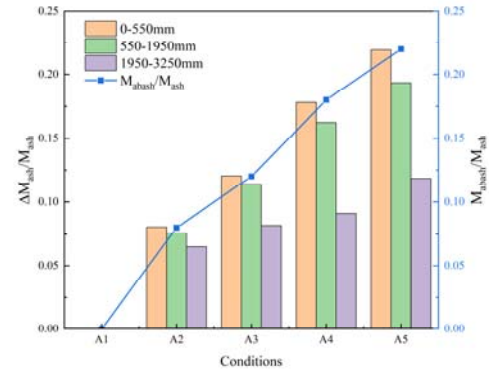
Fig. 5. Relationship between bed material mass change rate and ash discharge rate.

4. Conclusion

This study designed and constructed a cold-state experimental platform for the internal circulating ash bin and conducted cold-state experiments. The main research conclusions are as follows:

1. A method was proposed to rapidly adjust the gas-solid concentration in the upper part of the furnace of a CFB boiler by setting up an internal circulating ash bin.

2. The results of the cold-state experiments show that the Primary fluidizing air velocity and ash bin fluidizing air velocity have a significant impact on the ash storage performance. Through systematic experiments on ash storage in the internal circulating ash bin, it was found that the ash storage rate is jointly influenced by the Primary fluidizing air velocity and the internal circulating ash bin fluidizing air velocity. An empirical formula for the mass flux at the inlet of the ash bin was obtained, which demonstrated good fitting capability within the range of $U_{abair,out} < U_{mf}$.

3. Experiments were conducted to adjust the ash concentration in the CFB using the internal circulating ash bin. It was found that at a Primary fluidizing air velocity of $1.5U_{mf}$, the internal circulating ash bin exhibited good control over the solid particle concentration in the riser. In the middle section of the riser, the rate of change in bed material mass was approximately 90% of the ash discharge rate, while in the upper section of the riser, it was approximately 60% of the ash discharge rate.

The experimental results demonstrate that the internal circulating ash bin possesses good ash storage performance and the ability to regulate the ash concentration in the dilute phase zone.

Acknowledgment

References

[1] Song, C., Lyu, J., Yang, H., Wang, S., Ling, W., Yue, G. Research and application of supercritical and ultra-supercritical CFB boiler technology. Proceedings of the CSEE, 2018, 38, 338-347+663.

[2] Cai, J., Shan, L., Wang, Z., Zhang, M., Jin, Y., Cai, X., Wang, P., Yang, H. Variable load characteristics of a supercritical 350 MW CFB boiler. Thermal Power Generation, 2020, 49, 98-103+108.

[3] Zhang, X., Yang, X., Xin, G., Liu, K., Cui, F., Zhang, Z. Experimental study on deep peak regulation operation of coal-fired thermal power unit. Clean Coal Technology, 2022, 28, 144-150.

[4] Yang, Z., Lu, X., Jiao, J., Meng, B., Wang, P. Study on temperature stability characteristics of low load reheat steam in large CFB boiler. Clean Coal Technology.2022, 1-10.

[5] Stefanitsis, D., Nesiadis, A., Nikolopoulos, A., Nikolopoulos, N. Simulation of a CFB power plant integrated with a thermal energy storage system during transient operation. Journal of Energy Storage, 2021, 43.

[6] Lyu, J., Shang, M., Ke, X., Zhou, T., Huang, Z., Zhang, H., Zhang, M., Zhang, Y., Wu, Y., Yue, G. Powdered coal CFB combustion technology. Journal of China Coal Society, 2023, 48, 430-437.

[7] Li, D., Ahn, S., Kim, R., Li, J., Jung, S., Jeon, C. Formation of agglomerates with core–shell structure in a large-scale CFB boiler. Fuel, 2023, 332, 126197.

NUMERICAL SIMULATION STUDY ON COAL-FIRED FLUE GAS HCL REMOVAL BY ADSORBENT INJECTION IN A 300MW CIRCULATING FLUIDIZED BED BOILER

Yanjun Zuo[1], Xiaoshuo Liu[2], Haiyang Li[2], Yuqing Wang[3], Yufeng Duan*

(Key Laboratory of Energy Thermal Conversion and Control of Ministry of Education, School of Energy and Environment, Southeast University, Nanjing, 210096, China)

Corresponding Author: Y. Duan yfduan@seu.edu.cn

Abstract

In this work, based on high-performance ethanol-hydrated CaO adsorbent, optimization of adsorbent injection parameters for the removal of HCl in a 300MW circulating fluidized bed boiler was conducted using finite element simulations. Specifically, critical parameters such as injection velocity, injection height, and Ca/Cl molar ratio were meticulously examined to elucidate their influence on HCl removal efficiency. Ultimately, the optimal injection dechlorination approach for the 300MW boiler was proposed. The results suggest that Ca/Cl molar ratio is the most fundamental influencing factor, injection velocity can alter the uniformity and spatial coverage of the chlorination agent, and injection height changes residence time, thus significantly affecting dechlorination efficiency. The optimization strategy based on the CFD simulation can provide a solid foundation and guidance for the industry application of coal-fired flue gas HCl removal technology.

1. Introduction

Chlorine is an environmentally hazardous trace element in coal ranging from 0.01% to 0.2% with an average of 0.02% in most Chinese coal. It mainly consists of two different forms: inorganic chlorine and organic chlorine [1]. Most chlorine (more than 90%) would be released to flue gas as gaseous HCl after combustion owing to the strong volatility [2], and is eventually enriched into the wet flue gas desulfurization (WFGD) in the form of chlorine ions, which brings about the undesirable WFGD device corrosion, wastewater discharge and gypsum quality degradation [3].

Recently, flue gas dechlorination technologies have attracted considerable attention due to their effective contributions to ultra-low emission and zero discharge of wastewater policies in coal-fired power plants [4]. The vast majority of coal-fired power plants including CFB plants use WFGD dechlorination technology in China, adsorbing HCl by desulfurization slurry, which will generate desulfurization wastewater with a very high concentration of chloride ions, seriously affecting the normal operation of desulfurization equipment and the water recycling and reuse of coal-fired power stations [5]. The burning of high-chlorine fuels such as coal slime, coal gangue, and garbage aggravates these hazards [13]. In comparison, alkaline adsorbent injection into flue gas is considered a cost-effective method to capture HCl [6,7], and it can be divided into three categories according to the product form: wet, semi-dry, and dry method dechlorination technology. Although the wet method dechlorination technology has a high removal efficiency and can synergistically capture multiple polluants[8], the substantial capital investment required for equipment and the intricate nature of wastewater treatment techniques present great challenges in its adoption[9]. The process of semi-dry removal exhibits analogous drawbacks[10]. The dry dechlorination technology is poised for promising application prospects due to its uncomplicated equipment structure, cost-effectiveness, and robust stability[11]. Nevertheless, its efficiency is influenced by both the adsorbent performance and the injection approach. Enhancing the dechlorination efficiency of dry injection hinges on the superior HCl

adsorbents and the strategic design of the injection device arrangement. Based on the high-performance ethanol-hydrated CaO adsorbent produced by our previous experimental result [12], a finite element simulation was conducted to obtain the optimal arrangement of the injection device, which promotes an effective HCl removal technology for coal-fired flue gas.

2. Physical model and evaluation indexes

This study focuses on simulating the entire process of adsorbent injection into the flue gas for HCl removal and the full size for a 300MW CFB boiler. The physical model starts downstream of the economizer and ends before the ESP. To verify the accuracy of the adsorption model, field tests and equal-size simulations were first performed on a 75t/h CFB boiler. Both of the physical models are shown in Fig. 1 respectively. The structure of the injection device of the two CFB units is similar, which divides the injection section into numbers of equal-area zones. Each zone is placed by a spray pipe gun, on which a plurality of nozzles is installed, and a plurality of orifices are opened circumferentially and evenly around each nozzle so that the adsorbent injected from each orifice can diffuse and cover the entire cross-sectional area of the duct.

| (a) The duct of a 75t/h CFB | (b) The duct of a 300 WM CFB |
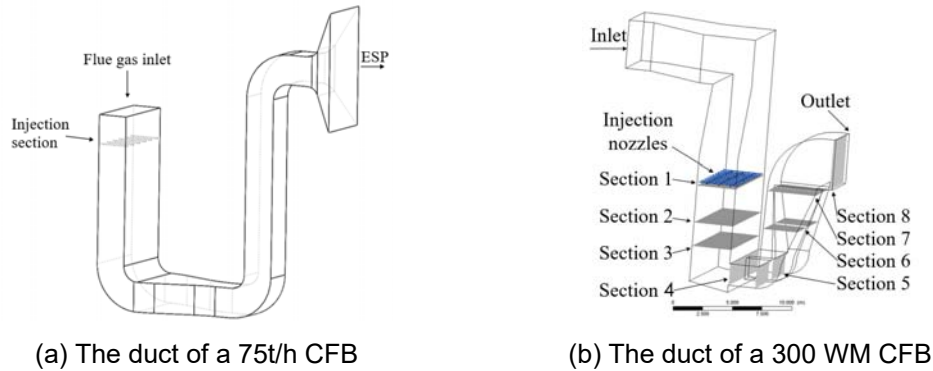
Fig. 1. The sketch diagram of duct physical models

Geometric meshes are generated as mixed elements, with hexahedral meshes dominating. To eliminate the influence of the number of grids on the calculation accuracy, the grid independence verification was carried out, and according to the independence verification results, the final grid number of the 75t/h boiler duct model is about 1.25 million, while the final optimized grid number of the 300MW CFB boiler duct is about 2 million. To guide future industrial practice accurately, boundary conditions are set regarding the actual flue gas parameters. The specific calculation conditions are shown in Table 1. To discuss the efficacy of adsorbent injection, several evaluation indexes are set up, which are defined in Table 2. In order to study local homogeneity, local flow field, and HCl removal efficiency in the duct, the cross-sections of the central axis of the vertical duct are selected as the control sections, the coordinate positions of the control section are shown in Fig. 1(b)

3. Results and discussion

The calcium-chlorine ratio, which is commonly defined as the ratio of sorbent to gaseous HCl in mass, is used to character the sorbent consumption quantity. Three field tests of calcium chlorine molar ratio of 3, 6, and 9 were carried out within the test of adsorbent injection in the 75t/h CFB boiler. The result can be seen in Fig. 2. With the increase of the calcium-chlorine molar ratio, the dechlorination efficiency will show a significant upward trend, up to 74.92% maximum When the calcium-chlorine ratio reaches 9. The predicted HCl removal efficiencies by the simulation at different Ca/Cl molar ratios were compared with the field test results under the same conditions. The relative error between the predicted value and the test value is 1.71%~11.47, which is a permissible range for engineering applications. Subsequently, the model was used in the flue of the 300WM CFB boiler to explore the influence of critical parameters on the HCl removal efficiency.

3.1 Impact of Injection Velocity

Injection velocity directly affects the uniformity of the adsorbent distribution. The parameters are taken as: injection velocity ranges from 10 to 40 m/s, Ca/Cl molar ratio 6, injection height 9 m, and HCl concentration 65 mg/m^3. The impact of the injection velocity on the standard deviation coefficient (C_v), the residence time (T), the sorbent coverage (δ), and chlorine removal efficiency (η), is shown in Fig. 3.

Table 1. The specific boundary conditions

Numbers	Variable	Unit	75t/h boiler parameters setting	300MW boiler parameters setting
Multiphase models	Turbulent model	\	Standard k-ε	Standard k-ε
	Particulate model	\	Discrete phase model	Discrete phase model
	Wall function	\	Standard wall functions	Standard wall functions
Sorbent parameters	Injection velocity	m/s	20-40	10-40
	Ca/Cl rate	\	3-9	3-9
	Density	kg/m^3	3350	3350
Flue gas parameters	Flue gas amount	Nm^3/h	103500	12157797
	Temperature	K	423.15	393.15
	Flue gas density	kg/m^3	0.748	0.852
	Dynamic velocity	kg/(m·s)	2.4×10-5	2.4×10-5
	HCl concentration	mg/m^3	50	65

Table 2. The definition of evaluation indexes

Name	Symbol	Expression	Definition
HCl removal efficiency	η	$\eta = \dfrac{HCl_{in} - HCl_{out}}{HCl_{in}} \times 100\%$	Calculated by the average HCl concentration of the inlet and outlet;
Standard deviation coefficient	C_v	$C_v = \dfrac{1}{\overline{x}}\sqrt{\dfrac{1}{n-1}\sum_{i=1}^{n}\left(x_i - \overline{x}\right)^2}$	The uniformity of the distribution of a single substance in a certain plane;
Sorbent spatial coverage	δ	\	The volume ratio of the space covered by the adsorbent to the overall flue;
Sorbent residence time	T	\	The residence time of the sorbent particles in the flue space.
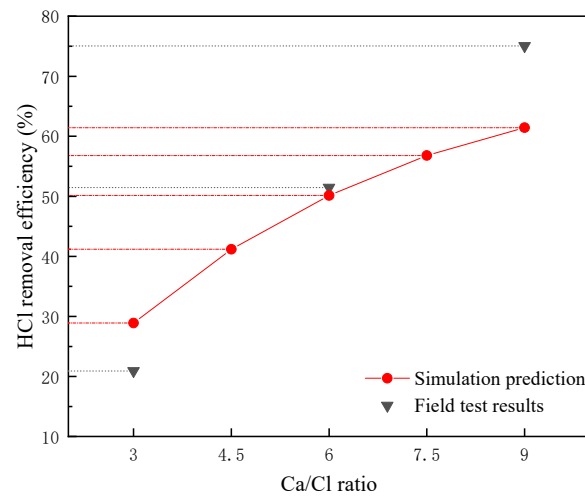
Fig. 2. Comparison of HCl removal efficiency between simulation and field test results
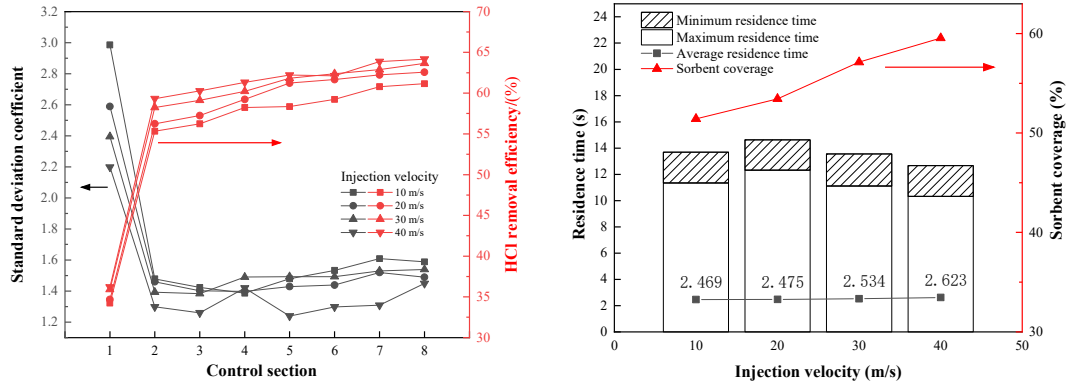
Fig. 3. The standard deviation coefficient, HCl removal efficiency, residence time, and sorbent coverage affected by injection velocity

It can be inferred that the injection velocity has an apparent effect on C_v, especially in the control section 1, where the injection velocity increases from 10 m/s to 40 m/s, and C_v decreases from 2.99 to 2.20. There is an obvious drop in C_v from control sections 1 to 3, and it can be inferred that the adsorbent is sufficiently diffused in the vertical flue, especially along the control section 1~2. However, C_v increases from section 3 to 7 under all injection velocities, which is because of the change of the structure around the duct such as the appearance of bypasses and the elbows of ascending pipes, causing the change of the flow field and affecting the distribution of the adsorbent. Along the flue gas flow, the HCl removal efficiency of each section gradually increases irrespective of injection velocity because of further contact and interaction between adsorbent and HCl in flue gas. A larger initial injection velocity increased the spray range of the adsorbent, resulting in an increase in the sorbent coverage from 51.42% at 10m/s to 59.54% at 40 m/s, with a relative increase of 6.24% of the average residence time. The maximum residence time shows irregular changes because the collision of a single particle in the flue is random. In the contrary, the minimum residence time is greatly affected by the flow field, in the range of 2.31~2.43 s on the conditions of different injection speeds，which contributes to the relatively small total amount of adsorbent particles in the coal-fired flue gas.

3.2 Impact of Ca/Cl molar ratio

The Ca/Cl molar ratio is a significant parameter for HCl removal efficiency. This parameter was taken as 3, 4.5, 6, 7.5, and 9, with injection velocity 20 m/s, injection height 9 m, and HCl concentration 65 mg/m^3. The impact of the Ca/Cl molar ratio which represents the injection amount on the HCl removal efficiency is shown in Fig. 4.
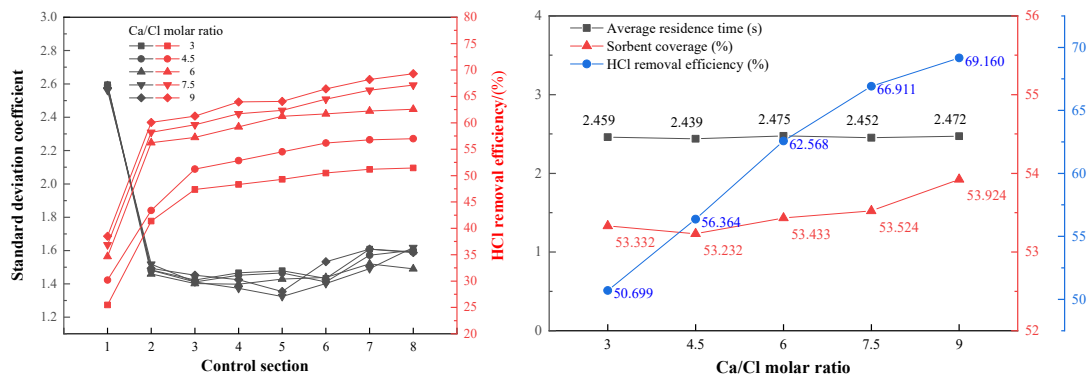
Fig. 4. The standard deviation coefficient, residence time, sorbent coverage, and HCl removal efficiency affected by Ca/Cl molar ratio

The result shows an obvious positive correlation trend between Ca/Cl molar ratio and HCl removal efficiency, for the chlorine removal efficiency increases from 51.43% to 69.29% while the Ca/Cl molar ratio increases from 3 to 9. According to the mass transfer theory, the mass transfer rate is affected by the surface area of the adsorbent

particles per unit volume of flue gas. Therefore, the improvement of HCl removal efficiency is closely related to the increase of the concentration of adsorbent particles per unit volume of flue gas. However, as the Ca/Cl ratio continues to increase, the growth rate of HCl removal efficiency decreases. In addition, there is little difference in Cv between the sections under different Ca/Cl ratios since the volume fraction of the adsorbent particle accounts for less than 10% of the total flue gas. The average residence time is not found to increase significantly. The coverage rate has ascended, but compared with the increase in injection velocity, the gain of injection amount on the coverage is negligible.

3.3 Impact of injection height

The HCl concentration gradually decreases along the flue gas flow, and the adsorption efficiency enhances obviously between the control section 1 and 2 (shown in Fig. 3 and Fig. 4). Increasing the vertical distance from the injection inlet to the section 1 and extending the contact time of the adsorbent particles with by increasing injection height is considered as a possible approach to improve the de-chlorination efficiency. The parameters are taken as: injection height from 8 to 12 m, Ca/Cl molar ratio 6, injection velocity 20 m/s, and HCl concentration 65 mg/m^3. The impact of injection height on the evaluation indexes is shown in Fig. 6.
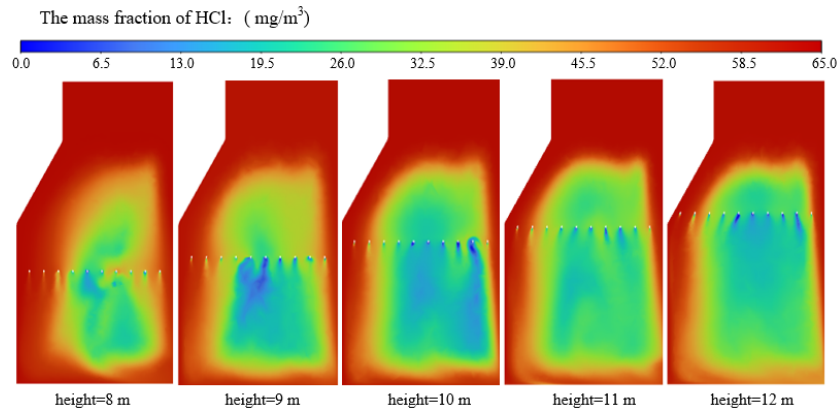
Fig. 5. The HCl mass fraction contour of adsorbent injection at different heights
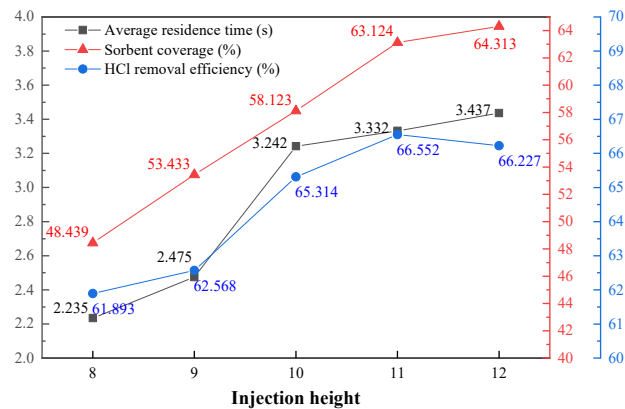
Fig. 6. The residence time, sorbent coverage, and HCl removal efficiency affected by injection height

Fig. 5 shows that the distribution of adsorbents is greatly affected by injection height, with the increase of nozzle height, the sorbent spatial coverage increases obviously, and the average residence time of particles also increases from the lowest 2.24 s to 3.44s. However, there is a reverse point when the jet height is 11m, which is because the injection gun was in the expansion duct at the height of 12m, where the flue gas velocity is larger, causing a worse radial diffusion effect. In addition, the adsorbent concentration per unit volume in the flue gas near the wall behind the expansion duct

is higher when the injection height is below 11m, which is determined by the flue flow field. For this reason, it suggests that the injection height should be 11 m.

4. Conclusion

The numerical simulation of the adsorbent injection device was carried out on the flue gas duct of a 300MW coal-fired unit, and the effects of injection and operational parameters on the HCl removal efficiency were explored. The results show that: (1) The injection velocity increases from 10 m/s to 40 m/s and the dechlorinated adsorption rate increases by 3.02%. Injection speed will affect the spatial coverage of the adsorbent particles at the initial stage of injection, and the appropriate increase of the injection speed will improve the HCl removal adsorption rate at the dust outlet; (2) The Ca/Cl molar ratio will significantly improve the HCl removal efficiency. When the Ca/Cl ratio increases from 3 to 9, the HCl removal efficiency increases from 50.70% to 69.16%. Therefore, it is advantageous to maintain a higher Ca/Cl molar ratio on the premise of economy and no clogging of the pipeline; (3) The nozzle height can significantly improve the HCl removal efficiency by increasing residence time. When injection height reaches 11m, residence time increases by 34.97%, and HCl removal efficiency increases by 7.52%. Combined with the result of the simulation and other factors, the optimal adsorbent injection device parameters recommended are injection height of 11m, Ca/Cl molar ratio of 9, and injection speed of 30 m/s.

References

[1] Zhang, L., Wang, S., Meng, Y., et al. Influence of Mercury and Chlorine Content of Coal on Mercury Emissions from Coal-Fired Power Plants in China. Environmental Science & Technology. 2012. 46(11), 6385-6392

[2] Tsubouchi, N., Mochizuki, Y., Wang, Y., et al. Fate of the Chlorine in Coal in the Heating Process. ISIJ International. 2018. 58(2), 227-235

[3] Liu, X., Wang, R., Geng, X., et al. Intrinsic reaction selectivity between gaseous HCl and SO2 over ethanol-hydrated CaO adsorbent in coal-fired flue gas dechlorination. Chemical Engineering Journal. 2023. 473, 145019

[4] Liu, X., Wang, R., Huang, T., et al. Insights into the HCl formation and volatilization mechanism from organochlorine in coal: A DFT study. Fuel. 2023. 338, 127271

[5] Guo, S., Yang, J., Liu, Z. The Fate of Fluorine and Chlorine during Thermal Treatment of Coals. Environmental Science & Technology. 2006. 40(24), 7886-7889

[6] Liu, X., Wang, R., Wang, Y., et al. Effect of SO_2 on HCl removal over ethanol-hydrated CaO adsorbent: Mechanism of competitive adsorption and product layer shielding. Chemical Engineering Journal. 2023. 464, 142516

[7] Cai Z, Du B, Dai X, et al. Coupling of alkaline and mechanical modified fly ash for HCl and SO2 removal in the municipal solid waste incineration plant[J]. Fuel, 2023, 346: 128354.

[8] Tsiliyannis, C. Control of dioxin emissions from alternative fuels via regulated activated carbon injection and fluegas recirculation. Journal of Hazardous Materials. 2018. 358, 405-415

[9] Li, C., Jia, Z., Ye, X., et al. Simulation on deacidification performance of waste incinerator flue gas by rotating spray drying. Energy. 2018. 152, 652-665

[10] Geysen, D., Vandecasteele, C., Jaspers, M., et al. Effect of improving flue gas cleaning on characteristics and immobilisation of APC residues from MSW incineration. Journal of Hazardous Materials. 2006. 128(1), 27-38

[11] Yang, J., Geng, Z., Yuan, W Z., et al. The technology of coal-fired flue gas dechlorination for realizing zero-discharge of desulfurization wastewater and its influences on boiler. Proc CSEE. 2018. 38(09), 2657-2664

[12] Wang, R., Liu, X., Chen, C., et al. CaO hydrated with ethanol solution for flue gas HCl immobilization. Part I: Modification & dechlorination. Fuel. 2023. 348, 128589

[13] Luts, D., Devoldere, K., Laethem, B., et al. Co-incineration of dried sewage sludge in coal-fired power plants: a case study. Water science and technology. 2000. 42(9), 259-268

VERTICAL MIXING OF SOLIDS IN BINARY BEDS – ANALYSIS BY MAGNETIC SOLIDS TRACING

Azka Rizwana Siddiqui[1]*, Anna Köhler[2],

Diana Carolina Guío-Pérez[1], David Pallarès[1]

[1] *Division of Energy Technology, Department of Space, Earth and Environment,*

Chalmers University of Technology, SE-412 96 Gothenburg, Sweden

[2] *BioShare AB, Karlstad (Sweden)*

* azkar@chalmers.se

Abstract

Understanding the dynamics of solids mixing and segregation in fluidized beds is fundamental for the design and improvement of industrial processes that involve several solid phases. In this study, we introduce a novel measurement method for the assessment of solid phases distribution in the vertical direction and their segregation time under bubbling fluidization conditions. This method utilizes the magnetic solid tracing (MST) technique by using small coils mounted along a thin pin to capture the local concentration of one of the solid phases (in this case, the lean solids phase) with a time resolution of 20 Hz. The experimental procedure validates the reliability and efficacy of the MST pin method, highlighting its potential as a useful technique for studying complex solids systems. The measurements are carried out under fluid-dynamically downscaled conditions to resemble the mixing of biomass (lean phase) in a hot large-scale reactor (700ºC) for thermochemical conversion.

The vertical concentration profiles of the lean phase and the transition times between mixed and segregated states are reported, for different fluidization velocities. The results show a consistent stronger penetration of the lean solids phase (consisting of particles lighter and larger than the bulk solids) into the dense bed as the fluidization velocity is increased. Further, it is shown that at very low fluidization velocity (fluidization number 1.5) segregation occurs much more rapidly than the mixing, while an increase in the fluidization velocity inverses this relation by continuously accelerating the mixing process and slowing down the transition to a segregate state.

Keywords: Magnetic Solids Tracing, Binary Fluidized Beds, Solids Mixing, Solids Segregation

1. Introduction

For decades, the study of solids mixing and segregation has been a focus within the fluidized bed research community. Often, parameters such as efficiency and production yield crucially depend upon the ability to steer and understand the complex dynamics of solids mixing and segregation. Beyond the expected influence of buoyancy, these phenomena have been found to be principally governed by the bubble flow behavior and drag forces. Over the years, a number of measurement techniques, both invasive and non-invasive, have been used to investigate the solids flow in dense beds, and more specifically mixing and segregation patterns. Most of the experimental research concerns the study of binary beds based on measurements either of surface concentration by means of imaging techniques (Chen & Fan, 1992; Emiola-Sadiq et al., 2021; X. Zhu et al., 2024), or of local in-bed concentration using different solids sampling methods (Cluet et al., 2015; Emiola-Sadiq et al., 2021; Q. Zhu et al., 2023). The investigation of the solid phases distribution on a space- and time-resolved basis

has been limited by the lack of suitable experimental techniques, leaving gaps in understanding the underlying phenomena of solids mixing and segregation in binary beds.

Magnetic solids tracing (MST) is an experimental technique that enables the measurement of the local and time-resolved concentration of a ferromagnetic solid tracer. This technique has previously been used to determine the residence time distributions and circulation rates of solids in circulating fluidized beds (Eder et al., 2020; Guío-Pérez et al., 2017; Guío-Pérez, Pröll, & Hofbauer, 2013; Guío-Pérez, Pröll, Wassermann, et al., 2013) and to measure mean solids velocities in a cross-flow fluidized bed (Farha et al., 2023).

This work aims to propose a method based on the MST technique through the development of pin configuration, for the measurements of local tracer concentration and evaluate its ability to provide valuable insights into solids mixing and segregation in binary beds. More specifically, MST is used for the obtention of space- and time-resolved concentration profiles of one of the two solid phases in a binary bed, to study both, steady-state conditions and transition times between the segregated and mixed states. The experiments are conducted at cold lab-scale conditions, applying fluid-dynamic scaling to replicate the flow in a large-scale hot bed of sand-like bulk solids and biomass as a lean phase.

2. Method

2.1 Experimental setup

The experiments are conducted in a fluid-dynamically downscaled unit with a cross-sectional area of 0.3×0.3 m^2 and a settled bed height of 0.08 m. The bed material, a bronze powder (described in Table. 1), is fluidized with air at room conditions. By applying (Glicksman, 1984), this setup resembles the fluid-dynamics of an upscaled hot pyrolysis unit of 1.25×1.25 m^2 in cross-section and a 0.33 m settled bed height operating at 700°C and consisting of a sand bed fluidized by flue gas. Table. 1 provides further details of the characteristics and operation of the down-scaled cold model and the resembled hot reactor. The bed material (here dense phase) belongs to the Geldart B type particles and has a minimum fluidization velocity of 0.082 m/s in ambient air. Regarding the lean phase (here tracer solids), biomass particles are resembled by cuboid-shaped particles made of a synthetic expanded foam doped with magnetic powder yielding a density of approximately 1600 kg/m^3 and representing 5 % of the total solids volume.

Table. 1: Fluid-dynamical scaling of the operating parameters and physical properties of the gas and solids phases.

	Parameters	Hot reactor		Cold model	
Operating conditions	Temperature [°C]	700		20	
	Pressure [atm]	1		1	
	Minimum Fluidization Velocity [m/s]	0.16		0.082	
Fluidizing gas	Density [kg/m^3]	Flue gas	0.36	Air	1.20
	Viscosity [N/m.s]		4.07e-5		1.83e-5
Bed material bulk solids	Particle density [kg/m^3]	Sand	2600	Bronze	8492
	Mean particle size [mm]		0.789		0.189
Lean solid phase	Particle density [kg/m^3]	Biomass	300 – 700	Synthetic tracer	990 – 2300
	Mean particle Size [mm]		1 – 90		0.26 – 23.76
Scaling factors (cold/hot)	Length	0.26			
	Time	0.509			
	Mass	0.06			

Fig. 1 illustrates the experimental setup. The local transient concentrations of tracer solids are measured simultaneously at different vertical locations by means of a pin of 10 mm in

diameter (here referred to as MST pin) equipped with three coils positioned at 0.065, 0.08, and 0.101 m above the distributor plate. The sampling frequency is set to 20 Hz. The local concentration of the lean phase is calculated based on the impedance of each coil, using the following equation:

$$X_t = k \frac{L - L_0}{L_0}$$

Where, X_t is the volume fraction of the tracer solids, L is the sampled impedance signal, and k is a calibration factor assessed beforehand for the given tracer material.

Further, pressure is also recorded using two immersed probes (placed at 0.045 and 0.06 m above the gas distributor, respectively) coupled to pressure transducers.
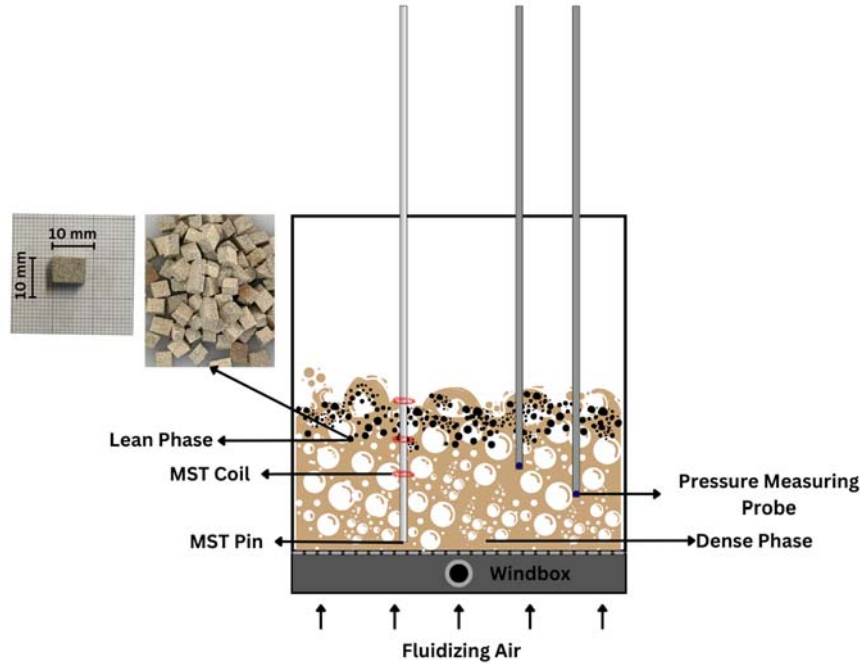
Fig. 1: Schematic of the experimental setup (0.3 x 0.3 m in cross-section) indicating the position of the MST pin and the pressure measurement probes.

2.2 Experimental procedure and data processing

The measurement data in Fig. 2 exemplifies the course of one experiment. In the figure, the local concentration measured by the three coils throughout the different stages of the experiment is presented. The binary bed is fluidized at a fluidization number FN=u/u$_{mf}$=3 before the start of each experiment to establish homogenous conditions before returning to minimum fluidization conditions. Following this, the lean phase solids are then evenly spread across the bed and the MST sampling system is started. After approximately 70 s of sampling at minimum fluidization conditions, the fluidization velocity is increased to the desired test conditions. The bed transits from the segregated state (at minimum fluidization) to a mixed state (mixing quality depending on fluidization conditions). After approximately 180 s, the bed is brought back to minimum fluidization (t ≈ 250 s in Fig. 2). The sampling is stopped roughly 60 s afterward. Four fluidization numbers have been tested for the mixed state: 1.5, 2, 2.5, and 3. Each experimental case is repeated 3 times to ensure the robustness of the results.

The original time series sampled at 20 Hz, undergoes a moving average filtering process with a window of 100 sample points (i.e. 5 s) to make it more suitable for the identification of the transition and equilibrium states, as shown in Fig. 2. The five distinct states can be identified in every experiment. These are (see Fig. 2): 1) an initial segregated equilibrium at minimum fluidization conditions, 2) a transition from the segregated to the mixed state, 3) a mixing

equilibrium at bubbling conditions, 4) a transition from mixed to segregated bed, and, lastly, 5) a segregated equilibrium at minimum fluidization.
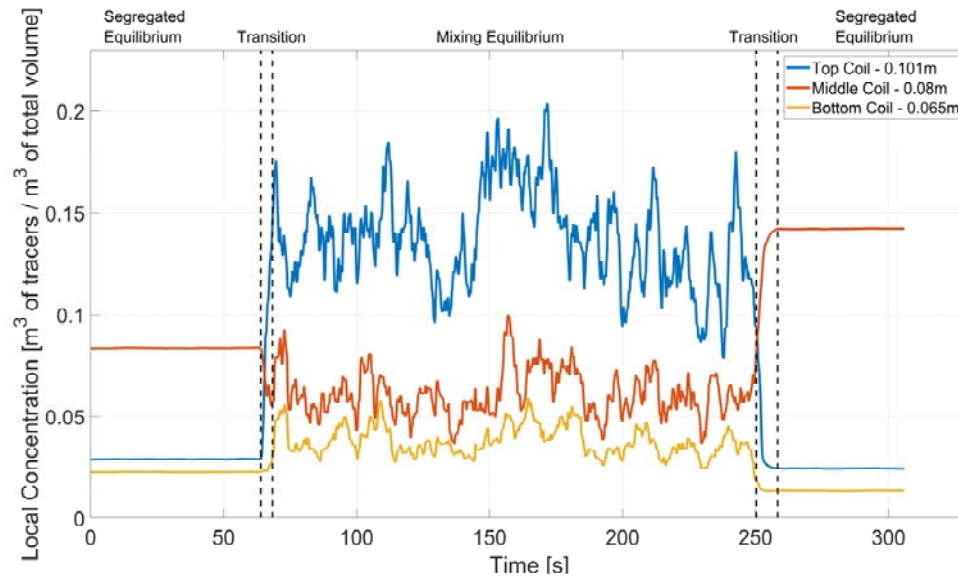
Fig. 2: Example of the measured transient local concentrations of lean solids phase for each of the coils (FN=3). Dashed lines indicate transitions between mixed and segregated states.

Note from Fig. 2 that since the coils measure a local concentration, the measured tracer concentration values at minimum fluidization at the start and the end of a given experimental run may differ from one another, as the horizontal mixing is not perfect. The repetitions (three) of each given operational case are used to account for this variability.

3. Results and Discussion

The bed expansion, calculated based on the bed voidage resulting from pressure difference measurements, is shown in Fig. 3. for each fluidization velocity. The fluidized bed height is of importance later on when analyzing the lean solids concentration profiles.
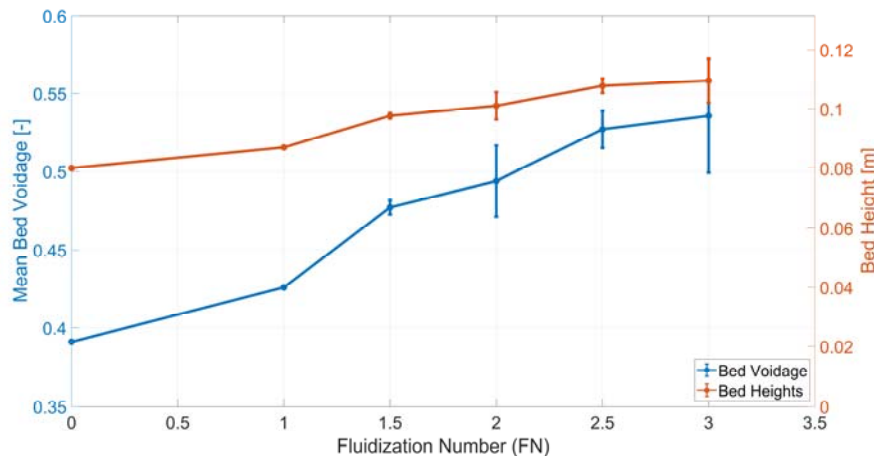
Fig. 3: Mean bed voidage and fluidized bed height at different fluidization numbers.

Fig. 4 illustrates the vertical profile of tracer concentration around the location of the MST pin for the mixed stage and the different fluidization velocities tested. Note that under bubbling conditions, due to bed expansion, the top coil is the closest to the bed surface. In view of the foregoing, observations reveal distinct yet consistent patterns: at FN=1.5 much of the lean phase accumulates near the surface of the bed, predominantly detected by the middle coil. As the fluidization velocity increases and bed expansion occurs, the vertical solids mixing improves gradually and leads to an increased immersion of the tracer in the bed, which can be seen from the continuous increase of the tracer concentration measured by the lowest coil.

From FN=2.5 to FN=3, a notable increase in the tracer concentration in the bottom coil is observed, which coincides with a decrease of the concentration at the top coil, this is, a tendency towards a more homogeneous vertical profile and thus a strongly promoted vertical solids mixing. Note that, for FN=3, the decreased tracer concentration sampled by the top coil is probably due to the significant amounts of tracer being immersed into the bed at heights below than that of the bottom coil, hence a decrease in the averaged concentration measured is also observed.
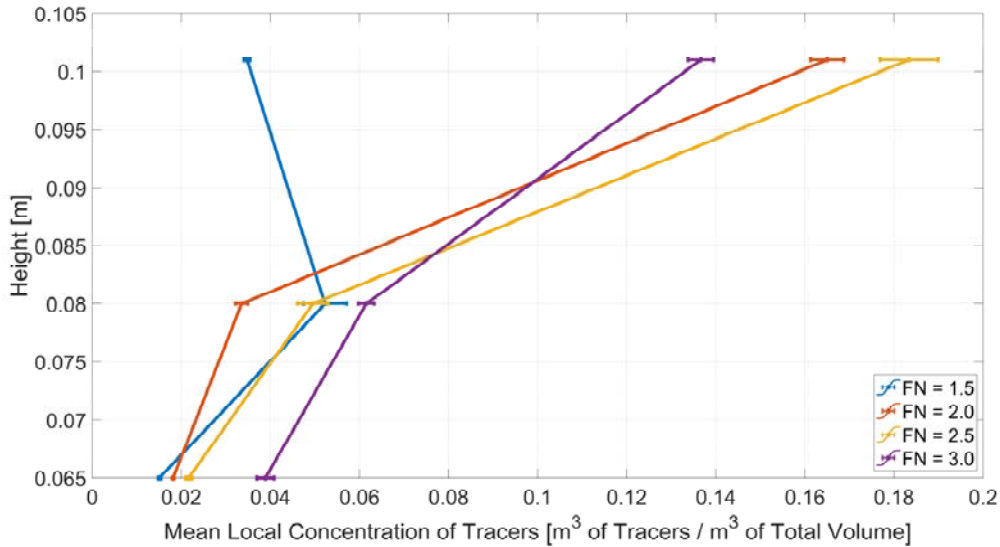
Fig. 4: Vertical profiles of tracer concentration under bubbling conditions at different fluidization numbers.

The transition times from the segregated equilibrium (at minimum fluidization) to the mixing equilibrium (at bubbling conditions) and vice versa are depicted in Fig. 5. The transition times from the segregated to the mixed state are longer for lower fluidization numbers, and are reduced drastically as fluidization velocity is increased, possibly due to the enhanced bubble flow and consequent promotion of the solids mixing. On the contrary, the time required to yield segregation starting from a mixing equilibrium is shorter when departing from bubbling conditions at lower fluidization velocities, since the mixing equilibrium established is already close to segregation. As expected, departing from higher fluidization velocities (and thus a higher degree of mixing) requires a longer time to yield segregation equilibrium, although the effect of fluidization velocity on such segregation times is not as strong as on the mixing times. By considering the reference time scaling factor of 0.509 (see Table. 1), the transition times are extrapolated to those at hot conditions and presented in Fig. 5.
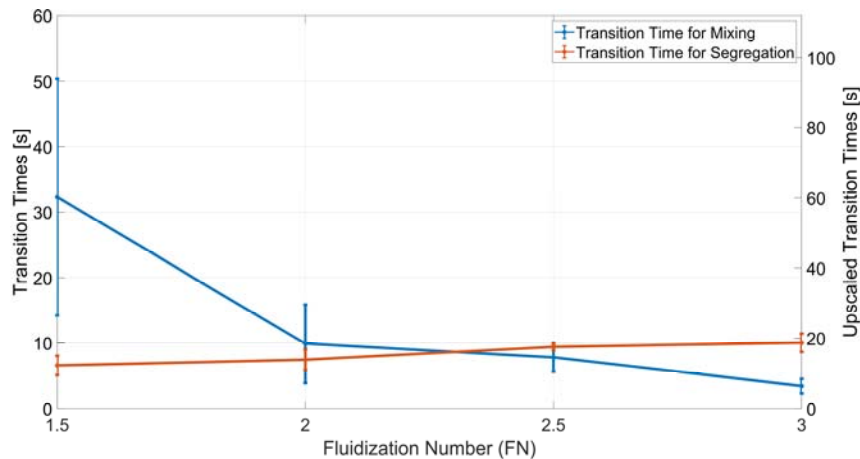
Fig. 5: Transition times for mixing/segregation of lean phase for different fluidization conditions.

4. Conclusion

A new measurement device based on the magnetic solids tracing technique is used in this study to measure the local concentrations of the lean solids phase at different heights in a binary bed. The experimental vertical profiles of tracer concentration show a consistent trend towards homogeneity (increased mixing) with the increase of fluidization velocity. Furthermore, the transient concentrations are used to extract the transition times from mixing to segregation and vice versa, concluding that with an increase of the fluidization velocity the time for achieving mixing decreases, while increases for reaching segregation equilibrium. The results obtained highlight the suitability of the designed method for the study of mixing and segregation in binary beds, as well as its potential for use in a detailed description of transient phenomena related to these processes.

Acknowledgment

References

Chen, R. C., & Fan, L. S. (1992). Particle image velocimetry for characterizing the flow structure in three-dimensional gas-liquid-solid fluidized beds. *Chemical Engineering Science*, *47*(13–14), 3615–3622. https://doi.org/10.1016/0009-2509(92)85077-O

Cluet, B., Mauviel, G., Rogaume, Y., Authier, O., & Delebarre, A. (2015). Segregation of wood particles in a bubbling fluidized bed. *Fuel Processing Technology*, *133*, 80–88. https://doi.org/10.1016/j.fuproc.2014.12.045

Eder, C., Hofer, G., Beer, J., & Pröll, T. (2020). Particle mixing in bubbling fluidized bed reactors with immersed heat exchangers and continuous particle exchange. *Industrial and Engineering Chemistry Research*, *59*(44), 19736–19750. https://doi.org/10.1021/acs.iecr.0c03568

Emiola-Sadiq, T., Wang, J., Zhang, L., & Dalai, A. (2021). Mixing and segregation of binary mixtures of biomass and silica sand in a fluidized bed. *Particuology*, *58*, 58–73. https://doi.org/10.1016/j.partic.2021.01.010

Farha, M., Guío-Pérez, D. C., Aronsson, J., Johnsson, F., & Pallarès, D. (2023). Assessment of experimental methods for measurements of the horizontal flow of fluidized solids under bubbling conditions. *Fuel*, *348*(April). https://doi.org/10.1016/j.fuel.2023.128515

Glicksman, L. R. (1984). Scaling relationships for fluidized beds. *Chemical Engineering Science*, *39*(9), 1373–1379. https://doi.org/10.1016/0009-2509(84)80070-6

Guío-Pérez, D. C., Dietrich, F., Ferreira Cala, J. N., Pröll, T., & Hofbauer, H. (2017). Estimation of solids circulation rate through magnetic tracer tests. *Powder Technology*, *316*, 650–657. https://doi.org/10.1016/j.powtec.2017.04.062

Guío-Pérez, D. C., Pröll, T., & Hofbauer, H. (2013). Measurement of ferromagnetic particle concentration for characterization of fluidized bed fluid-dynamics. *Powder Technology*, *239*, 147–154. https://doi.org/10.1016/j.powtec.2013.01.040

Guío-Pérez, D. C., Pröll, T., Wassermann, J., & Hofbauer, H. (2013). Design of an inductance measurement system for determination of particle residence time in a dual circulating fluidized bed cold flow model. *Industrial and Engineering Chemistry Research*, *52*(31), 10732–10740. https://doi.org/10.1021/ie400211h

Zhu, Q., Zhang, Q., Yang, P., Gai, H., Lin, M., Song, H., Xiao, M., & Huang, T. (2023). Measuring segregation in fluidized bed with magnetizable and nonmagnetizable particles based on magnetic permeability. *Fuel*, *340*(September 2022), 127554. https://doi.org/10.1016/j.fuel.2023.127554

Zhu, X., Jiang, X., Liu, Y., Wang, Z., Wang, H., & Ocone, R. (2024). Mixing/segregation characteristics and bubble behaviors of density-segregated binary particles in a pressurized fluidized bed. *Powder Technology*, *434*(December 2023), 119367. https://doi.org/10.1016/j.powtec.2024.119367

Measurements of the solids lateral flow in the transport region of a fluid-dynamically down-scaled circulating fluidized bed

Philip Kjaer Jepsen[*1,2], Diana Carolina Guío-Pérez[1], Marlene Bonmann[3], Henrik Ström[2], David Pallarès[1]

Chalmers University of Technology, Gothenburg, SE-412 96, Sweden

[1]Division of Energy Technology, Department of Space, Earth, and Environment
[2]Division of Fluid Dynamics, Department of Mechanics, and Maritime Sciences
[3]Terahertz and Millimetre Wave Laboratory, Department of Microtechnology and Nanoscience
[*]jepsen@chalmers.se

Abstract:

In this work, we tested the novel high Frequency-Modulated Continuous Wave (FMCW)-Doppler THz-radar technique as a tool to characterize and quantify lateral flows of solids in the transport region of a fluid-dynamically down-scaled circulating fluidized bed (CFB). The radar technique offers the possibility to simultaneously measure concentration and velocity of the solid particles, with a spatial resolution of 5 mm (in the direction of the radar beam) and a temporal resolution of 5 Hz. Experiments performed in the downs-scaled model (cross-sectional area of 0.45 m² and height 3.1 m) of an existing 200-MW boiler, was operated with copper particles (mean size of 35 µm and density 8920 kg/m³) using air at ambient temperature as the fluidization agent. Measurements were done in a horizontal plane in the riser, with superficial velocities ranging from 0.4 to 0.8 m/s. Based on the resolved data for solids velocity distribution and concentration, these measurements demonstrate the capabilities of the high-frequency radar technique in analyzing lateral movement of fine solids. The instrument showed good performance in detecting small metallic particles and provided reasonable lateral velocity and concentration profiles, which can be correlated through scaling laws to the reference boiler. Given the observed fluctuations in the mean velocity profiles, extending integration times may prove advantageous, whereas the concentration profiles appear more stable. Further investigation into high-frequency radar readings near the walls is warranted, as the spatial resolution exceeds the particle size. In practice, this technique, when combined with established scaling laws, offers a practical strategy for broadening our understanding of the complex motion behaviors that solids can exhibit in highly dynamic, industrial-scale fluidized bed boilers.

1. Introduction

Fluidized bed boilers are characterized using Geldart-B group solids and large cross-section areas [1, 2]. While providing good mixing conditions and enough time for the conversion of both the solid fuel particles and the evolving combustible gases, such a configuration aims at achieving the highest possible heat transfer rates to the walls in the so-called transport zone. Therefore, the dynamics of bed solids at smaller length scales have been a recurrent topic of research.

Today's commonly accepted flow description in the transport zone indicates that solids, entrained from the splashing zone (in the form of dispersed solids), form an ascending stream of solids in the core region of the furnace. While ascending, these solids may be transferred to the wall, where they form a down-flowing layer [3], or they can also back mix inside the core region by clustering and falling. Still today, there is only limited information about the horizontal (also called lateral) transfer of solids between the core region and the annular boundary layer.

Most descriptions regarding solids flow in large-scale fluidized beds are based on pressure measurements. Pressure transducers offer the most wide-spread method for assessment of the vertical profile of solids concentrations [4]. While present in virtually every fluidized bed unit, from the laboratory to the industrial scale, this method is very limited in terms of accuracy, stability, and spatial resolution, particularly for very low concentrations. In the horizontal direction, the solids flow characterization requires methods more sophisticated than the pressure drop, and so, data are rather scarce [5]. Semi-empirical models combined with Direct Numerical Simulations (DNS) have, to some extent, established mathematical descriptions of the solids lateral flow in fluidized bed boilers [6]. Moreover, Computational Fluid Dynamics (CFD) is frequently used and compared to experimental data, a fundamental step in developing and validating these models [7]. However, the

scarcity of reliable experimental data, particularly for large-scale CFBs—and even more so in the horizontal direction—significantly impedes the validation of these simulations.

One commonly used method for experimentally evaluating specific parameters in industrial fluidized-bed boilers is through fluid-dynamical scaling. In this approach, the dimensionless forms of the continuity and momentum equations are employed to achieve full similarity between a reference unit and its downscaled laboratory model [8, 9]. These can often be operated at room temperature, reducing construction costs, and enabling the use of advanced measurement techniques [10].

The Frequency-Modulated Continuous Wave (FMCW)-pulse Doppler THz-radar (high-frequency radar for short) technique can capture solids velocities and concentration with sub-millimeter spatial resolution along the radar beam's propagation [11, 12]. Moreover, unlike pressure transducers, the radar-based technique is effective in capturing transients and distributions of solids velocities while detecting solids volume concentrations between 10^{-6} and 10^{-1} m³/m³. This non-intrusive technique was demonstrated in [11] for a CFB using glass beads, and further substantiated in recent developments [5], where the velocity distributions and solids concentrations with radar-based measurements were used in conjunction to obtain the flux of solids in the vertical direction.

In this study, we aim to evaluate the high-frequency radar technique in its ability to directly assess horizontal solids flows under fluid-dynamically down-scaled conditions of an existing 200-MW CFB boiler. To do so, measurements are performed in the transport region of the fluid-dynamically down-scaled unit.

2. Methodology

2.1 Experimental setting and conditions

In this work, a fluid-dynamically down-scaled cold-flow model of a CFB boiler was employed, using copper powder as the bed material, characterized by a mean particle size of 35 µm and a density of 8920 kg/m³. The minimum fluidization and terminal velocities for these particles are 0.0045 m/s and 0.28 m/s, respectively. The measurements reported in this paper were conducted with superficial gas velocities ranging from 0.40 to 0.77 m/s and inventories in the main chamber corresponding to a total pressure drop between 0.38 and 0.84 kPa. The down-scaled unit was designed and built according to Glicksman's simplified set of scaling parameters [8, 9]. The scaling relations applied in this paper are outlined in Table 1. For a detailed analysis and comparison between the reference boiler and cold-flow model, readers are directed to [13].

Table 1. Scaling parameters employed in the fluid-dynamically down-scaled CFB model, as described in [13].

Parameter	Reference boiler	Down-scaled model	Unit
Length	L	0.077L	m
Time	t	0.277t	s
Velocity	u	0.277u	m/s
Mass	m	0.00165m	kg
Pressure	p	0.278p	Pa
Gas density	ρ_g	3.546ρ_g	kg/m³
Solids density	ρ_s	3.431ρ_s	kg/m³
Mean particle size	d_s	5.429d_s	µm
Mass flux	G_s	1.052G_s	kg/m²·s

The dimensions of the down-scaled unit, built in acrylic glass, are illustrated in Fig. 1, and preserves a 13:1 length ratio with the actual boiler and is fluidized with air at ambient conditions. Primary air is injected through a perforated plate with a pressure drop equivalent to that of the real unit and exits the chamber (furnace) through a single aperture located at the center top of the rear wall. The experimental setup also includes a cyclone and a loop seal, necessary for the external recirculation of bed solids. Although available, secondary air injection was not utilized in this study. The model includes 27 pressure transducers arranged vertically (not shown in Fig. 1). Additionally, Fig. 1 displays the relative positioning of the radar setup, with the radar beam directed horizontally toward the core of the unit. To minimize reflections and attenuation caused by the front wall, the middle section of the unit was replaced by a high-density polyethylene (HDPE) plate. The radar beam

penetrates this material and traverses the main chamber (furnace), reaching the rear wall. The radar antenna was positioned to ensure that its beam penetrated the HDPE plate 1.17 m above the distributor plate. Measurements were taken from two horizontal positions approximately 0.2 m apart, as depicted in Fig. 1.
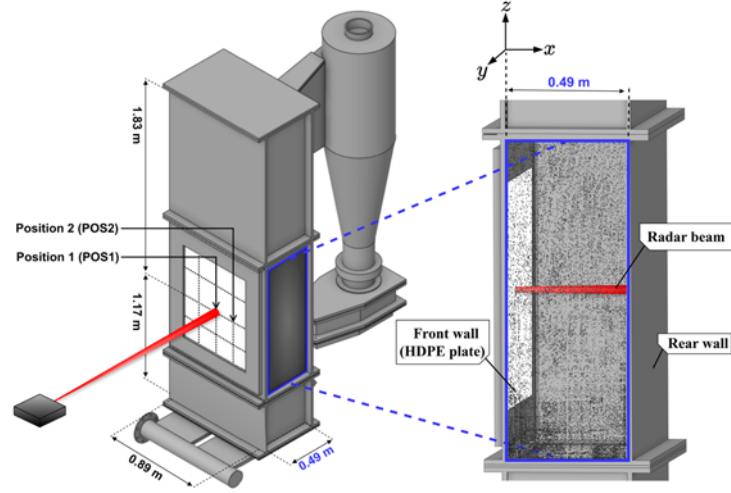
Fig. 1. Experimental setup, including the orientation of the radar beam relative to the unit, which maintains a 1:13 length relationship to the 200-MW reference boiler. The figure also indicates the general dimensions of the main chamber (corresponding to the furnace of the boiler) and positions where radar measurements were conducted: POS1 at the center, and POS2 situated 0.2 m to the right at the same height as POS1.

The time-averaged pressure measurements along the height of the furnace, Δp, under the assumption of negligible acceleration effects, allows for the solids volume concentration, α_s, to be determined, as follows:

$$\Delta p = \big(\rho_g(1 - \alpha_s) + \rho_s \alpha_s\big)g\Delta h, \tag{1}$$

where g is the acceleration constant due to gravity, and Δh denotes the height difference between the two selected pressure measurements.

2.2 High frequency radar

The type of radar used in the present work functions at a frequency high enough to detect solid particles in sizes below 1 mm. Due to the frequency-modulated continuous-wave mode it uses, this radar employs a single antenna for emitting and receiving the signal. Additionally, it incorporates a Doppler, to quantify particles velocities in the direction of propagation of the radar beam [12]. The space resolution is the product of the range resolution (the range, R or distance from the antenna has a resolution ΔR of 5 mm), and the beam cross-section (about 40 mm cross-range resolution d_R), delineating volumes $V_R = \pi \Delta R (0.5 d_R)^2$, for which the particle number concentration n_s and velocity distributions are assessed. The radar power equation, adjusted for the back-scattering efficiency of homogeneous spheres based on Mie theory and assuming single scattering, is presented as follows:

$$P_R = n_s \frac{K V_R}{R_R^4} \int_{r_{min}}^{r_{max}} f_s(r)\sigma_b(r)dr \cdot \exp\left[-2\int_0^R \left(f_e n_s(R') \int_{r_{min}}^{r_{max}} f_s(r)\sigma_e(r)dr\right)dR\right]. \tag{2}$$

As shown in Eq. (2), the reflected signal P_R is proportional to the cross-section covered by solids at the given range. The power equation also incorporates the solids size distribution f_s, and the factor K, which contains the calibration information for the specific setup as well as the natural signal processing gains and losses [12, 11]. The solids number concentration is evaluated as $\alpha_s = n_s V_s$ by solving this equation for n_s. For a given bulk material, experiments under controlled conditions are used to calibrate the radar signal to the solids number concentration, as detailed in [12]. The radar settings used were consistent with those specified in [11].

In this paper, average volume concentrations, acquired based on vertical pressure differences, are used as reference for the calibration of the radar measurement data. This alternative method, proposed in this paper by the first time, capitalizes on the equivalence between the integrated signal

power (integrated in time for 15 s, and in space, wall to wall) and the average concentration at an specific height (derived from pressure differences). This methodology assumes that the horizontal concentration profile measured by the radar beam is representative for that specific height, and that the mean concentration assessed based on pressure differences considers any possible lateral concentration variations.

3. Results & discussion

In this section, we present results from experiments conducted in the fluid-dynamically down-scaled cold model, alongside the equivalent up-scaled values, representative of an existing 200 MW (reference) boiler as defined by the scaling relations provided in Table 1. Section 3.1 focuses on the results concerning lateral solids velocity, while Section 3.2 examines the horizontal concentration profiles. Subsequently, these findings are integrated in Section 3.3 to demonstrate the net horizontal mass fluxes of solids across the horizontal segment.

3.1 Solids horizontal velocities

The upper part of Fig. 2 shows the solids mean horizontal velocity profiles measured in the down-scaled system, alongside the scaled values for the reference boiler, presented on a secondary axis. The lower part of Fig. 2 details the signal-to-velocity distributions from which the mean velocity profiles have been computed along the radar's trajectory, with each point-value separated by the range resolution of 5 mm. The mean velocity profiles, shown in the upper part of Fig. 2, are generally close to zero and display slight asymmetry at low superficial gas velocities. As the superficial velocity increases, these profiles tend to become more symmetric, indicating possible recirculation toward the wall layer.
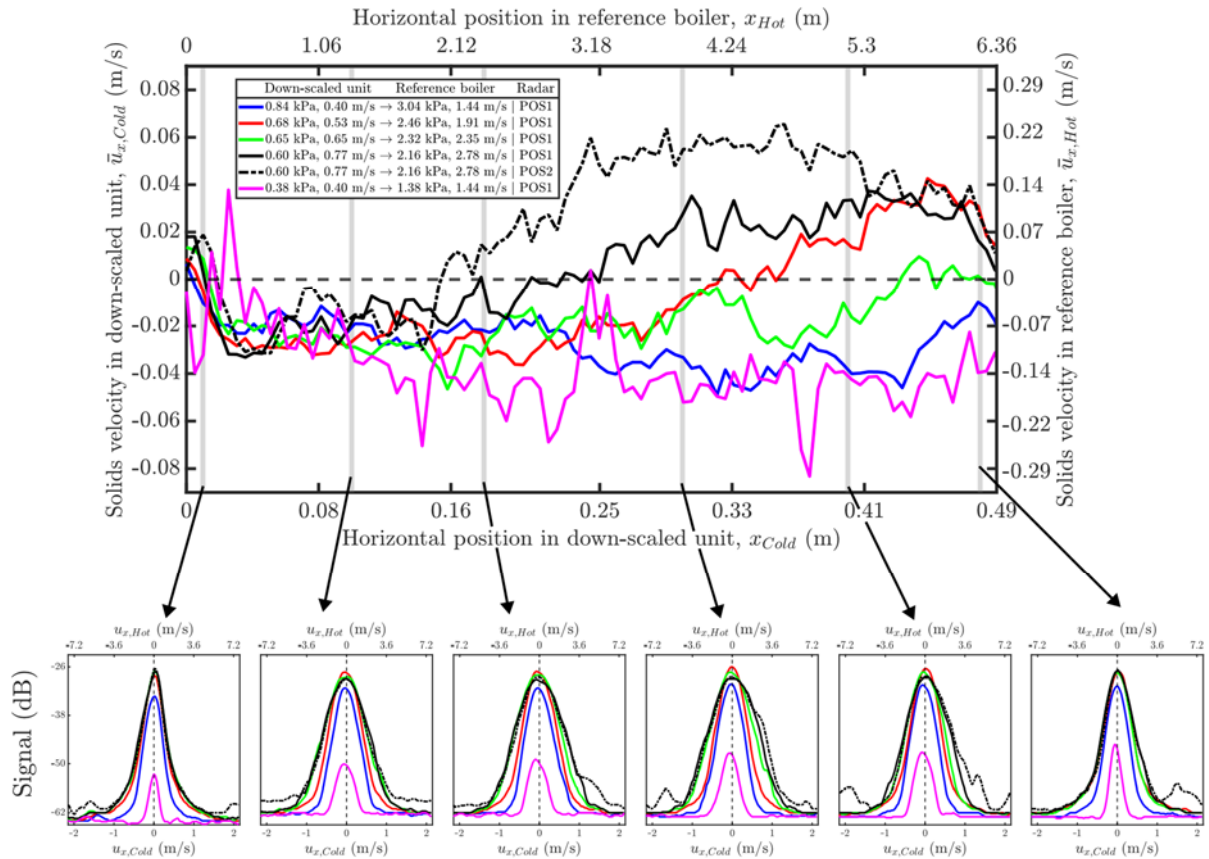
Fig. 2. Upper part of figure: Mean horizontal solids velocities within the radar beam, 1.17 m above the distributor plate in the downscaled CFB, corresponding to 15.2 m above the primary air nozzles in the reference boiler. Lower part of figure: signal-to-velocity distributions from which the mean velocities are calculated.

In the lower part of Fig. 2, the velocity distributions of the solids widen with higher superficial velocities, while near the walls, these distributions consistently narrow, regardless of the superficial gas velocity. Symmetry at the same gas velocities is more pronounced at position POS2 than at POS1, a distinction made clear by the high spatial and temporal resolution of the measurement technique, which enables detection of these localized differences. For more comprehensive analysis, further measurements at various locations at the same height could shed some light about the homogeneity of the solid horizontal velocities. It should also be noted that non-zero mean velocities measured near the walls may be caused by the fact that the range resolution is much larger than the size of the particles $\Delta R \gg d_s$.

Because of the strong fluctuations observed in the mean velocities, the apparent skewness towards the front wall at lower gas velocities cannot be fully confirmed. This could be due to the integration period not coinciding with the natural periods of the velocity profiles, suggesting the need for longer measurement durations. Despite these fluctuations, the overall observations conform to theoretical expectations, thus confirming the suitability of the technique in assessing lateral movements of solids in the system.

3.2 Solids horizontal volume concentrations

The vertical profiles of solids volume concentrations, obtained from pressure differences using Eq. (1), are given in Fig. 3a, with the highlighted area indicating the location of the horizontal radar-based measurement, culminating in the profiles presented in Fig. 3b.

(a) Vertical solids concentration profiles based on measurements with pressure transducers.

(b) Horizontal solids concentration profiles based on radar-based measurements.
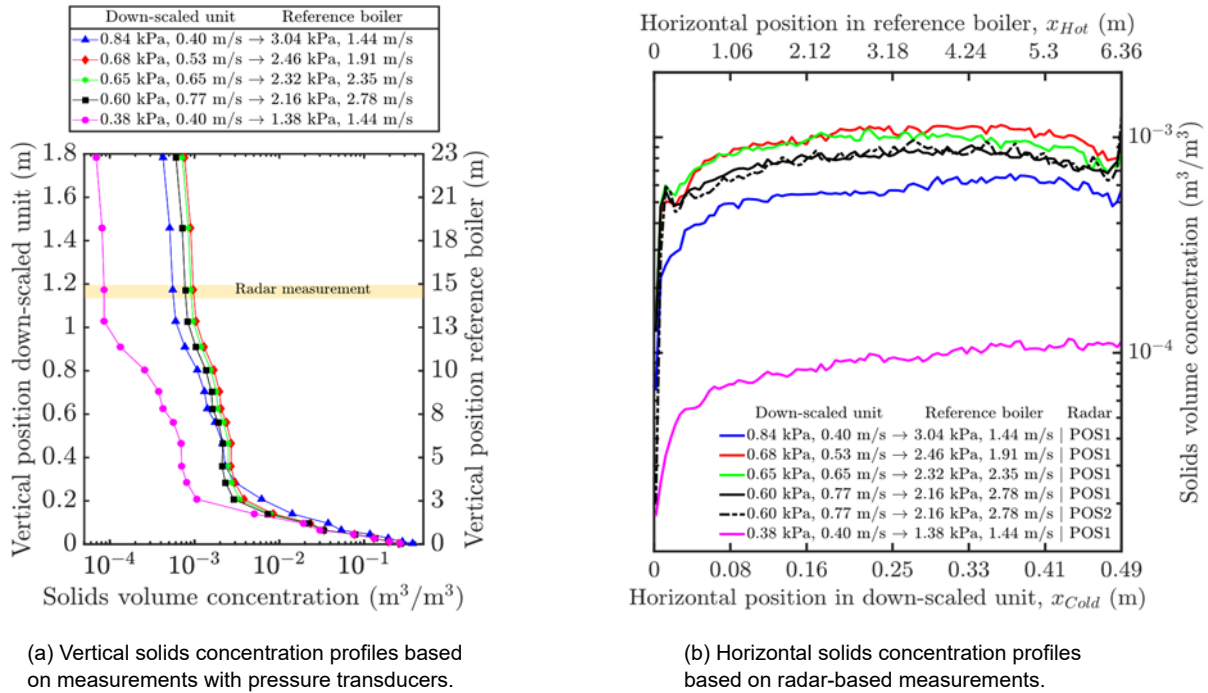
Fig. 3. Profiles of the volumetric concentration of solids in the furnace, with distances provided for both the cold model and the reference boiler. (a) Vertical profiles from pressure taps using Eq. (1), with the highlighted region indicating the height of radar-based measurements. These values represent time-volume averages over 3-5 minutes, covering the entire cross-section between consecutive pressure taps. (b) Horizontal profiles from radar measurements at a vertical height of 1.17 m, time-averaged over 15 s, as detailed in Section 2.

All the conditions used in this work yielded a nearly flat solids concentration profile in the core region and comparatively lower concentrations near the walls. The apparent asymmetry of the profiles, where the rear wall shows higher concentrations, is probably due to the solids back-flow at the exit duct but deserves further investigation. Since the range resolution is in the order of millimeter and some abrupt concentrations changes are observed in the few millimeters near the walls, it is not possible to rule out the possibility of shift in the observation window. It is worth mentioning that there are no considerable differences between the concentration profiles at POS1 and POS2, suggesting homogeneity in the flow and supporting the assumption that the average concentration

at a specific coordinate is representative of the whole cross section. In contrast to the velocity measurements, the concentration profiles exhibit milder fluctuations, suggesting that an integration time of 15 s might be sufficient for acquisition of representative concentration measurements.

3.3 Solids horizontal mass fluxes

Combining the horizontally measured profiles of concentration and velocity from Figs. 2 and 3b allows for the corresponding solids net flux to be computed as functions of these, as we present in Fig. 4. For the examined experimental conditions in this study, the mass flux profiles closely align with the velocity profiles, due to the even concentration profiles, markedly accentuating differences between various inventories and gas velocities, especially when compared to conditions with the lowest inventory and superficial velocity.
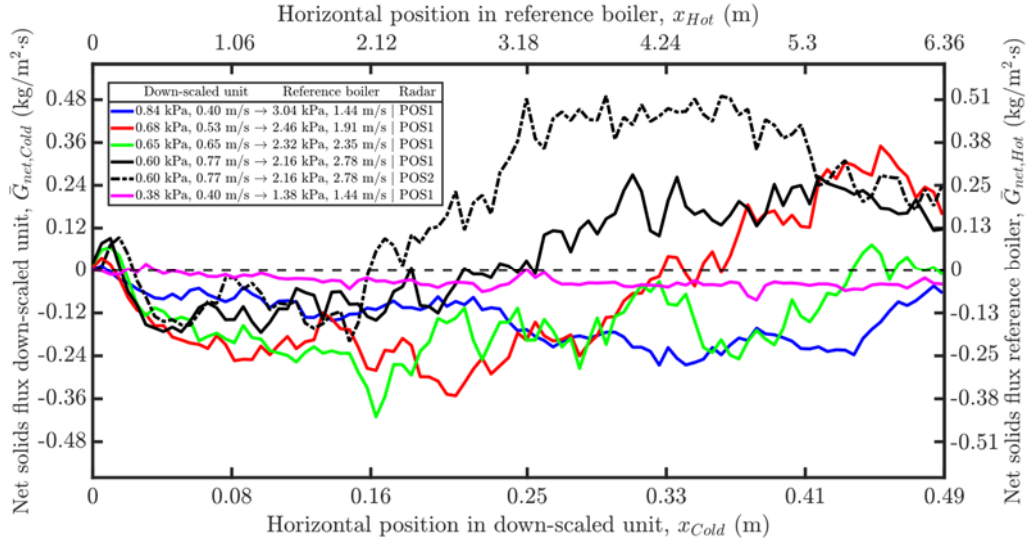
Fig. 4. Net horizontal mass flux of solids, derived from integrated radar-based measurement of concentration and velocity profiles, with up-scaled horizontal positions in the reference boiler shown on the secondary axis.

4. Conclusions

This paper demonstrates the capabilities of the FMCW-pulse Doppler THz-radar technique in analyzing solids flow under fluid-dynamically down-scaled conditions using copper powder with a mean particle size of 35 µm. While this work is limited to presenting initial measurements that include data for a flow region with low concentration levels, the high-frequency radar measurements provide detailed descriptions of the solids' horizontal concentrations and velocities. We demonstrate the technique's ability to simultaneously capture these profiles with high spatial resolution along the radar beam's propagation path, with a range resolution set to $\Delta R = 5$ mm in this study. Consequently, signal-to-velocity distributions are obtained at every distance ΔR, wall-to-wall, which can be readily converted into probability density functions (PDFs). Moreover, through calibration using pressure transducers concurrently during these experiments, at the given conditions, we derive the solids concentration profiles horizontally that are combined with the velocities of the solids to calculate their mass fluxes. In the continuation of this work, we will elaborate on how the local PDFs, captured along the trajectory of the beam, and highlighted herein, enable the elucidation of more intricate details. This objective will be achieved by presenting the flux of solids separated into their constituent components: the lateral flux in the direction of either the front or rear wall. Moreover, based on the well-established scaling relations, these findings directly relate to the reference boiler, thereby offering a viable method for improving our understanding and characterization of the lateral movement of solids in a full-scale CFB boilers.

5. Acknowledgement

References

[1] D. Geldart. Types of Gas Fluidization. *Powder Technology*, 7(5):285–292, 1973.

[2] Daizo Kunii and Octave Levenspiel. Chapter 3 - Fluidization and Mapping of Regimes. In Daizo Kunii and Octave Levenspiel, editors, *Fluidization Engineering (Second Edition)*, pages 61–94. Butterworth-Heinemann, Boston, second edition, 1991.

[3] Wennan Zhang, Filip Johnsson, and Bo Leckner. Fluid-dynamic boundary layers in CFB boilers. *Chemical Engineering Science*, 50(2):201–210, 1995.

[4] Srdjan Sasic, Bo Leckner, and Filip Johnsson. Characterization of fluid dynamics of fluidized beds by analysis of pressure fluctuations. *Progress in Energy and Combustion Science*, 33(5):453–496, 2007.

[5] Wanqiang Wu, Diana Carolina Guío-Pérez, Marlene Bonmann, Filip Johnsson, Lunbo Duan, and David Pallarès. Radar-based measurement of solids back-mixing in the freeboard of a circulating fluidized bed. *Chemical Engineering Journal*, 488:151150, 2024.

[6] Tove Djerf, David Pallarès, Filip Johnsson, Gaetano Sardina, and Henrik Ström. Solids backmixing in the transport zone of circulating fluidized bed boilers. *Chemical Engineering Journal*, 428:130976, 2022.

[7] Qiuya Tu, Haigang Wang, and Raffaella Ocone. Application of three-dimensional full-loop cfd simulation in circulating fluidized bed combustion reactors – a review. *Powder Technology*, 399:117181, 2022.

[8] Leon R. Glicksman. Scaling relationships for fluidized beds. *Chemical Engineering Science*, 43(6):1419–1421, 1988.

[9] L.R. Glicksman, M. Hyre, and K. Woloshun. Simplified scaling relationships for fluidized beds. *Powder Technology*, 77(2):177–199, 1993.

[10] Munavara Farha, Diana Carolina Guío-Pérez, Jesper Aronsson, Filip Johnsson, and David Pallarès. Assessment of experimental methods for measurements of the horizontal flow of fluidized solids under bubbling conditions. *Fuel*, 348:128515, 2023.

[11] Diana Carolina Guío-Pérez, Marlene Bonmann, Tomas Bryllert, Martin Seemann, Jan Stake, Filip Johnsson, and David Pallarès. Radar-based measurements of the solids flow in a circulating fluidized bed. *Fuel*, 345:128232, 2023.

[12] Marlene Bonmann, Diana Carolina Guío-Pérez, Tomas Bryllert, David Pallarès, Martin Seemann, Filip Johnsson, and Jan Stake. Sub-millimetre wave range-doppler radar as a diagnostic tool for gas-solids systems - solids concentration measurements. *Advanced Powder Technology*, 34(1):103894, 2023.

[13] Tove Djerf, David Pallarès, and Filip Johnsson. Solids flow patterns in large-scale circulating fluidised bed boilers: Experimental evaluation under fluid-dynamically down-scaled conditions. *Chemical Engineering Science*, 231:116309, 2021.

COMPARISON OF DIFFERENT SIMPLIFIED RISER STRUCTURES IN THE HIGH DENSITY CIRCULATING FLUIDIZED BED

Mingzhu Lv, Min Wang, Yunpeng Zhao, Xingying Lan, Jinsen Gao, Xiaogang Shi*

State Key Laboratory of Heavy Oil Processing, China University of Petroleum, Beijing 102249, China

*Email: *shixiaogang68@126.com*

Abstract

In the simulation of Circulating Fluidized Bed (CFB), the riser, as the main part of the CFB, needs to be built reasonably and accurately in the model. Reasonable structural simplification of riser can considerably reduce the computational cost. However, there are very few studies describing the effect of different simplified structures on the flow field of the riser. In this paper, Two-Fluid Model combined with Energy Minimization Multi-Scale (EMMS) model and modified solid pressure model are used to compare the hydrodynamic characteristics in four different simplified structures of the riser reactor. The gas-solid flow and pressure distribution are compared, and the effects of the feed pipe at the inlet and the elbow at the outlet on the gas-solid flow field are summarized. The comparison of the different simplified risers and the full-loop CFB shows that the gas-solid flow field in the riser can be greatly influenced by the inlet and outlet structure. When the feed pipe is neglected, a stable core-annulus distribution is formed at the lower part of the riser. The solids holdup will be overestimated at the bottom and the velocity of particles will be underestimated. The upper and middle of the riser is mainly affected by the outlet structure. The gas-solid flow in the simplified riser ignoring the outlet elbow is unstable. At the upper and middle part of riser, the solids holdup decreases along the axial height, which differs greatly from the real gas-solid flow field. The pressure drop is underestimated and the particle velocity in the upper part of riser is overestimated. Therefore, the real gas-solid flow distribution in the riser can be more accurately described by the riser structure that retains the feed pipe and the top elbow in the model.

1. Introduction

Gas-solid CFBs, with good gas-solid mixing, fast reaction and high mass and heat transfer efficiency, are widely used in industrial processes, such as CFB boiler and fluidized catalytic cracking (FCC) [1,2]. A full-loop gas-solid CFB generally consists of a riser, cyclone separator, downcomer, storage tank and feed pipe. Hydrodynamics in the riser are usually studied by Computational Fluid Dynamics (CFD) simulation for providing important information for the design and operation of the riser reactor. Due to the computational complexity and cost, a single riser is usually simulated with certain simplifications for representing the full-loop CFB riser. But some flow details may be missing in the simplified riser.

There are many scholars simulating a single riser of CFB. Wang et al [3] simulated the CFB riser using the Computational Particle Fluid Dynamics (CPFD) method to obtain the gas-solid flow and particle distribution. The segregation of larger particles at the bottom of the riser and the near-wall effects at different heights were correctly predicted. The abrupt T and smooth semi-bend exit of single risers were compared by Wang [4]. Larger and denser clusters were found to be formed near the abrupt T and smooth semi-bend exits and the solids holdup increased significantly. Meanwhile, in order to get more comprehensive information inside the CFB, many full-loop CFBs have been simulated. Yao et al [5] found that the solids holdup in the riser is affected by the structure and the aeration air at the bottom of the CFB. The pressure

drop distribution, which is larger at the bottom of the riser and smaller at the top of the riser, has been obtained by Huo et al [6]. Many flow field details were obtained, which are ignored in the simplified model.

It can be found that the gas-solid flow field in the riser will be significantly affected by the inlet and outlet structures. When the riser structure is over simplified, important flow information may be lost. The difference in gas-solid distribution between the simplified riser and the riser in full-loop CFB maybe large. Simplified structures of risers at low density have been explored [7]. However, the mechanism of influencing factors on the gas-solid flow field may be changed greatly as increasing solids concentration. It is necessary to compare the different simplified structures of the risers at high density CFB in more detail. In this paper, four different simplified structures of the riser are simulated and compared with the riser of a full-loop CFB. The mechanisms of the inlet structure and outlet structure of the riser on the gas-solid flow are explored, which can provide guidance for the simulation of the riser at high solids circulation rate.

2. Methods

2.1 Mathematic Model

In this work, the Euler-Euler model is used to simulate the gas-solid flow in riser and full-loop CFB. Both gas and solid phases in the Euler-Euler model are considered as interpenetrating continua. The Energy Minimization Multi-Scale (EMMS) model is used to describe the interaction between gas phase and solid phases [8,9].

The traditional solid pressure model needs to be modified by considering the effect of clusters at conditions of high solids circulation rate. Therefore, the solid pressure modification coefficient proposed in our laboratory is used to describe different contributions of clusters to solid pressure in the dilute region and dense region [10].

$$p_s = p_{s,0} \times B$$

Where, $B = 0.3, p_{s,0} = \varepsilon_s \rho_s \Theta_s \left[1 + 2 \left(1 + e_{ss} \right) \varepsilon_s g_0 \right]$

2.2 Simulation Objects and Boundary Conditions

The simulation objects are shown in Fig. 1, where (a) is the full-loop CFB geometry and (b), (c), (d), (e) are the geometries of different simplified riser. Both the feed pipe at the bottom of the riser and the elbow at the outlet of the riser are ignored in riser I. The feed pipe at the bottom of the riser is ignored in riser II. The elbow at the outlet of the riser is ignored in riser III. Both the feed pipe at the bottom and the elbow at the outlet of the riser are retained in riser IV. The height and diameter of the four simplified risers are the same as for that in the full-loop CFB.

In the simulation, air is used as the gas phase and the FCC catalyst is used as the solid phase. The solid phase circulating in the CFB was set with an initial patching height. No-slip wall boundary condition is used for all structures. The solids holdup of 630 kg/(m^{2}s), which belongs to operation at high density, was used for CFB. The material properties and boundary conditions in detail are shown in Table 1.

(a) Full-loop   (b) Riser I   (c) Riser II   (d) Riser III   (e) Riser IV
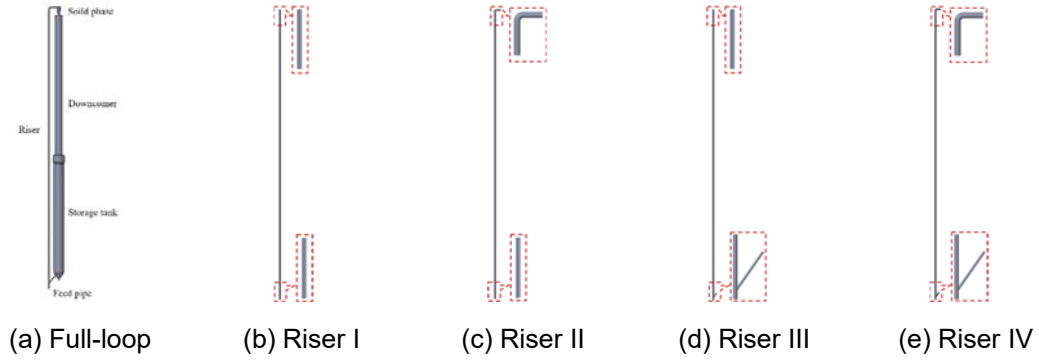
Fig. 1. Geometry of the simulated object.

Table 1. Material properties and operating conditions.

Items	Values
Air density [kg/m^3]	1.225
Air viscosity [Pa·s]	1.7894×10^{-5}
Particle density [kg/m^3]	1500
Particle diameter [m]	8.5×10^{-5}
Superficial gas velocity [m/s]	7
Fluidized air volume flow rate [m^3/s]	12
Solids circulating rate [kg/(m^{2}s)]	630

3. Results and discussion

3.1 Model Validation

The simulation data are compared with the experimental data from the CFB build in our laboratory, as shown in Fig. 2. The solid holdup of the full-loop CFB is higher near the wall and lower in the center, which is in good agreement with the experiment. The gas-solid distribution within the high density CFB can be predicted accurately by the present model.
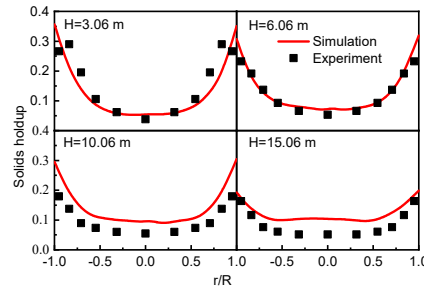
Fig. 2. Comparison of solids holdup in the CFB riser in simulation and experiment.

3.2 Comparison of Different Simplified Riser Models

3.2.1 Comparison of Solids Holdup

The axial distributions of solids holdup in the full-loop CFB riser and the four simplified risers are shown in Fig. 3. For the full-loop CFB riser, the solids holdup at the bottom of the riser increases and then decreases due to the influence of inlet structure. The solids holdup in the middle of the riser is basically constant. At the top of the riser, the solids holdup increased due to the influence of elbow. It can be found that riser I and riser II, ignoring the inlet structure, show rapid increase in solids holdup at the bottom. In the middle and top of the riser, the solids holdup of the riser III constantly decreases due to lacking of elbow structure. The fluctuation of the solids holdup of the riser I is wide, which indicates that it cannot realize stable gas-solid flow when simplifying the inlet and outlet of the riser. The axial distribution of solids holdup within the Riser IV, is essentially the same as in the full-loop CFB riser. In summary, the inlet structure and outlet structure will not only affect the feeding method of the gas phase and solid

phase, but also have significant impacts on the solids distribution and gas-solid flow hydrodynamic. The particle concentration in the lower part of the riser increases greatly when the feed pipe is ignored, and the particle concentration in the upper part of the riser decreases greatly when the elbow is ignored. It is crucial to retain inlet structure and outlet structure that are similar to full-loop CFB, to realize uniform distribution of solids holdup in the riser.

| (a) Riser I | (b) Riser II | (c) Riser III | (d) Riser IV |
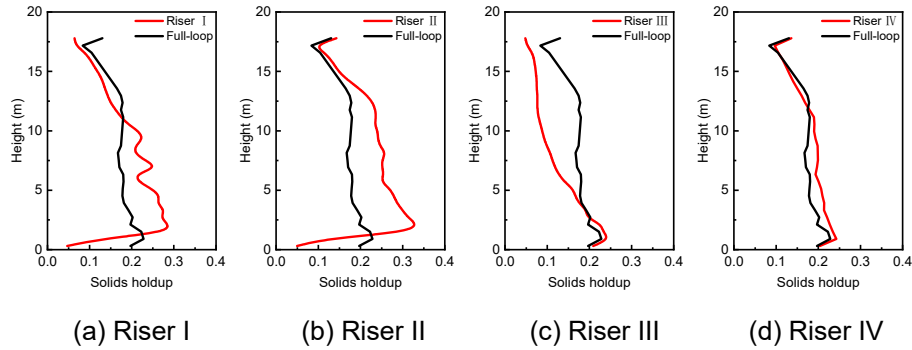
Fig. 3. Comparison of axial distribution of solids holdup in full-loop CFB and different simplified risers.

The solids holdup at the bottom of the riser with different structures are compared in detail in Fig. 4. The distribution of solids and clusters at the bottom of the riser is strongly influenced by the inlet structure. In the full-loop CFB, the low-velocity particles from the feed pipe mix with the high-velocity gas at the bottom of the riser, and some of the particles collide and aggregate on the opposite side wall. There are more clusters at the bottom of the riser comparing to that at the upper part of the riser. In the simplified riser I and riser II, the gas phase and solid phase are fed uniformly at the bottom of the riser and reach steady flow quickly, which is quite different from the actual gas-solid flow field. Ununiform distribution of solids at the radial direction and some clusters are found at the bottom of the riser III and riser IV, which is similar to that of the full-loop CFB riser. However, there is slight difference in the particle distribution at the inlet between riser III, riser IV and the full-loop riser. This phenomenon is due to the fact that the difference in particle distribution in the feed pipe results in the scouring of the wall by particles at the bottom of the riser being weakened in riser III and riser IV.

| (a) Full-loop | (b) Riser I | (c) Riser II | (d) Riser III | (e) Riser IV |
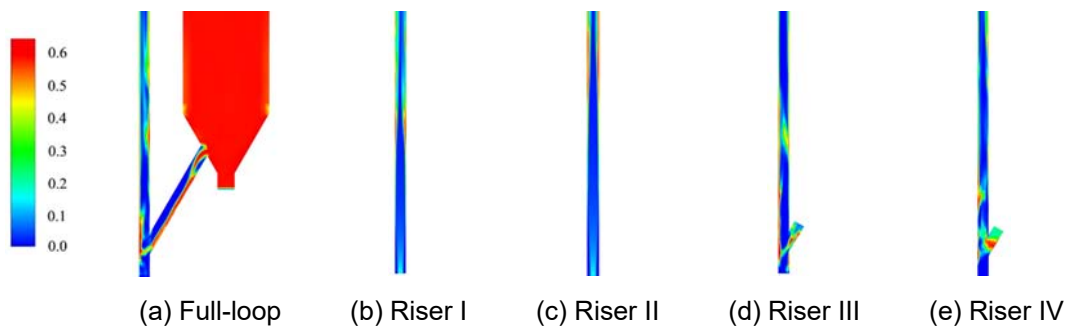
Fig.4. Distribution of solids holdup in full-loop CFB and different simplified risers.

3.2.2 Comparison of Particle Velocity

The axial distributions of particle velocity in the full-loop CFB riser and the four simplified risers are shown in Fig. 5. At the bottom of the riser, the particle velocity is low while the gas velocity is high, and the particle velocity is increasing under the effect of the drag force. Therefore, the bottom of the riser can be regarded as the acceleration zone. As the particle velocity increases, the drag force decreases and is balanced by particle gravity, which can be regarded as the fully developed zone. At the top of the riser, the particle velocity increases again due to the outlet effect. The particle velocity is affected with different degrees by the simplification method comparing to the full-loop riser. Along the height of the riser, the particle velocities in riser I and riser II decrease and then remain constant. The mixture of particles and gas entering the

riser with the same velocity due to the simplified inlet structure. As the drag force increases, the acceleration of particle settlement decreases until the gravity is equal to the drag force and the particle velocity remains constant. The particle velocity of riser III in the lower part of the riser is similar to that of the full-loop CFB. However, in the upper part of the riser, the particle velocity is slightly larger than that of the full-loop CFB, which may be due to the fact that the outlet elbow is replaced by the straight pipe and the particle flow is not prevented by the elbow. The axial distribution of particle velocity in riser IV is most similar to that of the full-loop CFB. In summary, the particle velocity is most influenced by the inlet structure, which is concentrated at the bottom of the riser. The whole particle velocity in the riser is reduced by simplifying the inlet structure, and the particle velocity in the upper part of the riser slightly increases due to simplifying the outlet structure.

| (a) Riser I | (b) Riser II | (c) Riser III | (d) Riser IV |
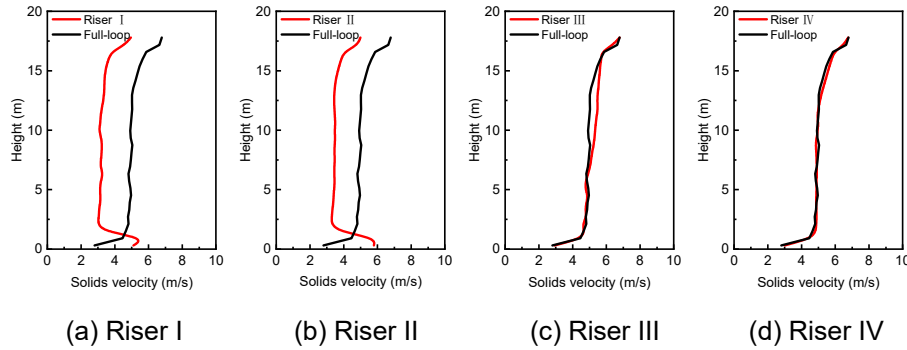
Fig. 5. Comparison of axial particle velocity in full-loop CFB and different simplified risers.

3.2.3 Comparison of Pressure Drop

The pressure distribution inside the riser is critical for pressure balance of the CFB and plays an important role to maintain stable gas-solid hydrodynamic. Fig. 6 shows the comparison of the pressure in the different simplified risers and the full-loop riser. Since the pressure drop inside the riser is mainly composed of the particle static pressure, the pressure drop is mainly affected by the change of solids holdup. In the full-loop CFB, the pressure drop at the inlet of the riser is higher because of the higher solids holdup, and the pressure drop at the outlet of the riser is lower because of the lower solids holdup. The overall pressure drop in the riser is about 45 kPa. The pressure drop in riser I is higher in the lower part of the riser and lower in the upper part of the riser, which is mainly due to the non-uniform distribution of solids holdup. The value of the overall pressure drop in the riser I is almost the same as the riser in full-loop CFB. The solids holdup in riser II, where the inlet structure is neglected, is smaller, which leads to the increase of pressure drop. The pressure drop of riser II is about 10 kPa larger than that of full-loop CFB due to higher solids holdup. The outlet of the riser III is simplified resulting in a smaller solids holdup in the upper part of the riser than the full-loop CFB riser, and the pressure drop is also 15 kPa lower than the full-loop CFB riser. It can be found that the simplification of the outlet structure of the riser has greater impacts on the overall pressure drop in the riser. The pressure drop distribution in the riser can be reasonably predicted by retaining both the inlet structure and the outlet structure, as shown in Fig.6 (d).

| (a) Riser I | (b) Riser II | (c) Riser III | (d) Riser IV |
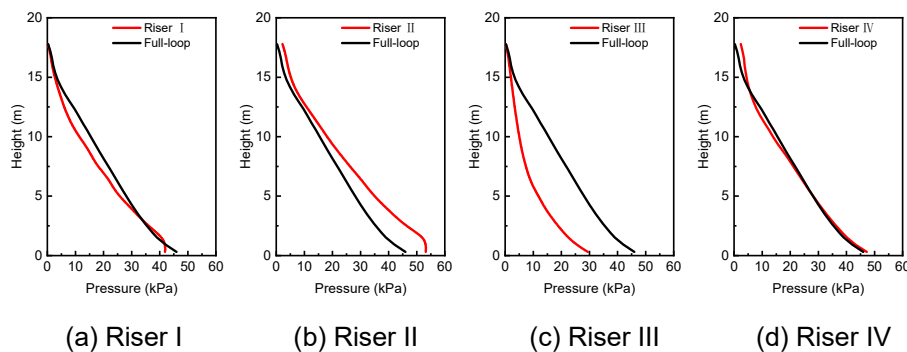
Fig. 6. Comparison of pressure drop in full-loop CFB and different simplified risers.

4. Conclusion

In this paper, the gas-solid flow of different simplified risers and the riser in a full-loop CFB are compared under high density operation, and the influence mechanisms of the inlet and outlet structures on the gas-solid flow characteristics in the riser are revealed.

The inlet structure in the riser mainly affects the gas-solid flow in the lower part of the riser. When the feed pipe is ignored, the solids holdup at the bottom of the riser is predicted to increase rapidly, which lead to higher solids holdup in whole riser. More clusters with larger size are formed near the wall, and clearly core-annulus distribution can be predicted. The pressure drop at the bottom of the riser also increases with increasing solids holdup. However, the particle velocity decreases at the bottom of the riser, and particle velocity is smaller than that of the riser in full-loop CFB after reaching stabilization.

The outlet structure of the riser mainly affects the gas-solid flow in the upper and middle parts of the riser. It is difficult to achieve stable gas-solid flow in the simplified riser without the outlet elbow in the model. The solids holdup decreases with increasing axial height, and the radial inhomogeneity at the outlet decreases, which differs greatly from actual flow field. The pressure drop inside the riser without the elbow structure greatly decreases, and the particle velocity slightly increases in the middle of the riser. In contrast, the gas-solid distribution obtained from the riser with feed pipe and elbow can be in good agreement with that of the riser in the full-loop CFB. Therefore, the simplification of riser with feed pipe and elbow can be used to represent the CFB riser during CFD simulations.

Acknowledgment

References

[1] Cruz, E., Steward, F R., Pugsley, T. New closure models for CFD modeling of high-density circulating fluidized beds. Powder Technology. 2006. 169, 115-122

[2] Yue, G., Cai, R., Lu, J., et al. From a CFB reactor to a CFB boiler - The review of R&D progress of CFB coal combustion technology in China. Powder Technology. 2017. 316, 18-28

[3] Wang, Q., Niemi, T., Peltola, J., et al. Particle size distribution in CPFD modeling of gas–solid flows in a CFB riser. Particuology. 2015. 21, 107-117

[4] Wang, X., Jiang, F., Xu, X., et al. Numerical simulation and experimental validation of gas-solid flow in the riser of a dense fluidized bed reactor. Particuology. 2009. 7, 278-282

[5] Yao, X., Yang, H., Zhang, H., et al. Gas Solid Flow Behavior in the Standpipe of a Circulating Fluidized Bed with a Loop Seal. Energy & Fuels. 2011. 25, 246-250

[6] Huo, P., Li, X., Liu, Y., et al. Investigation on influences of loose gas on gas-solid flows in a circulating fluidized bed (CFB) reactor using full-loop numerical simulation. International Journal of Chemical Reactor Engineering. 2021. 19, 53-62

[7] Wang, M., Wu, Y., Shi, X., et al. Comparison of Riser-Simplified, Riser-Only, and Full-Loop Simulations for a Circulating Fluidized Bed. Processes. 2019. 7, 306

[8] Zhang, N., Lu, B., Wang, W., et al. Virtual experimentation through 3D full-loop simulation of a circulating fluidized bed. Particuology. 2008. 6, 11

[9] Zhang, N., Lu, B., Wang, W., et al. 3D CFD simulation of hydrodynamics of a 150 MWe circulating fluidized bed boiler. Chemical Engineering Journal. 2010. 162, 821-828

[10] Wang, M., Lan, X., Wang, C., et al. Numerical Simulation of the Pilot-Scale High-Density Circulating Fluidized Bed Riser. Industrial & Engineering Chemistry Research. 2021. 60, 3184-3197

Study on drying characteristics and reduction kinetics of laterite nickel ore

Si-qi ZHENG[1,2], Xiao-fang WANG[1,2], Guo-tao QIN[1,2], Zhi-ping ZHU[1,2*]

1. State Key Laboratory of Coal Conversion, Institute of Engineering Thermophysics, Chinese Academy of Sciences, Beijing 100190, China

2. University of Chinese Academy of Sciences, Beijing 100049, China

Email: zhuzhiping@iet.cn

Abstract

The drying characteristics and solid-phase reduction kinetics of nickel laterite were investigated at both low and high temperatures. The results demonstrate a strong correlation between the drying efficiency of nickel laterite ore and temperature, with higher temperatures leading to faster drying rates. At 700 °C, the required drying requirements can be met, and the maximum drying rate during different temperature stages follows an approximately linear trend with temperature. A kinetic study was conducted on the reduction of nickel laterite ore using semi-coke as a reducing agent. Based on calculations of kinetic parameters, the weight loss rate was modeled as a function of heating temperature, which was then validated against experimental data. The results reveal that the reduction process consists of three stages: the first stage (30 ~ 400 °C), the second stage (400 ~ 800 °C) follows a nucleation and growth mechanism with activation energies of 38.59 kJ/mol and 89.11 kJ/mol respectively, while in the third stage (800 ~ 1000 °C), diffusion control dominates with an activation energy for nickel laterite in this stage being 109.97 kJ/mol.

Key words: laterite nickel ore, dehydration mechanism, kinetics, activation energy

1. Introduction

The exceptional properties of nickel, including its magnetism and ductility, make it extensively utilized in various sectors such as stainless steel production, aerospace engineering, and fuel cell technology within the military, industrial, and civil domains[1]. Nickel in nature primarily exists in the forms of laterite nickel ore and nickel sulfide ore. Although laterite70% of the total amount that can be mined, it only contributes to 40% of the available nickel resources[2]. In recent years, due to the gradual depletion sulfide reserves, low-grade laterite nickel ore has emerged as the primary source for ferro-nickel production.

Fluidized reduction roasting of nickel laterite ore is a highly efficient method for smelting. The water content of nickel laterite ore is very high, such that the free water and water of crystallization can reach more than 25% (mass fraction). The high-water content will lead to increased energy consumption in the high-temperature smelting process, and too much water can prevent the production process from running smoothly. The study of the characteristics and kinetics of the nickel laterite ore drying and reduction process is of great significance for improving and innovating the nickel laterite ore smelting process. Many scholars have carried out in-depth studies on the dehydration mechanism and solid carbon reduction kinetics of laterite nickel ore. For example, PICKLES[3] used the thermogravimetric method to study the drying kinetics of nickel-containing limonite ore in the range of 44 ~ 228 °C and determined the drying characteristic curve of the limonite dewatering process. Abdel-Halim et al.[4] elucidated the kinetics and mechanism of solid carbon reduction by analyzing the tail gas's CO and CO2 fraction changes. The reduction process is dominated by gas reactions, especially at low temperatures, and the Boudouard response is the key to controlling the reaction rate. LIU et al.[5] investigated the effect of sodium sulfate on the non-isothermal reduction kinetics of nickel laterite ores containing solid C. They determined the three-

dimensional diffusion equation as a function of the mechanism in the early and intermediate stages.

In recent years, different nickel laterite smelting processes, such as RK-EF and direct reduction roasting[6], have been developed rapidly at home and abroad. Still, the systematic study of the drying characteristics and reduction kinetics of nickel laterite is less, so it is significant to study the drying mechanism of nickel laterite and its phase transition characteristics. In this paper, the drying characteristics of nickel laterite ore are experimentally investigated by high-temperature thermal balance, and the kinetics of the reduction process of nickel laterite ore and semi-coke under non-isothermal conditions is also analyzed by thermogravimetric analysis, which provides theoretical references for the optimization of the pyrometallurgical smelting process of nickel laterite ore.

2. Materials and methods

2.1 Materials

The nickel laterite ore used in this paper has a chemical composition as shown in Table 1, with Ni content of 1.45% and Fe content of 24.30%, which belongs to the transitional nickel laterite ore.

Table1 Chemical composition analysis of nickel laterite ore (wt %)

Composition	Ni	TFe	Co	SiO_2	MnO	Al_2O_3	CaO	MgO	Cr_2O_3
Content	1.45	24.30	0.08	28.08	0.60	4.62	0.98	18.29	1.36

XRD and the results characterized the laterite nickel ore are shown in Fig. 1. The main mineral compositions of this lateritic nickel ore are kaolinite, acicular iron ore, hematite, quartz, and (nickel-bearing) serpentine. Serpentine and kaolinite are water-bearing silicate minerals, and acicular iron ore contains water for crystallization. Therefore, the crystalline and structural water content in this nickel laterite ore is high.
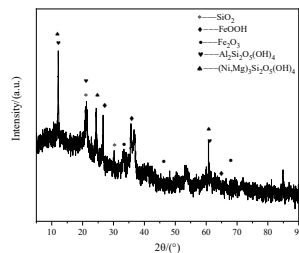
Fig. 1. XRD analysis of nickel laterite ore   Fig. 2. TG-DSC analysis of nickel laterite ore
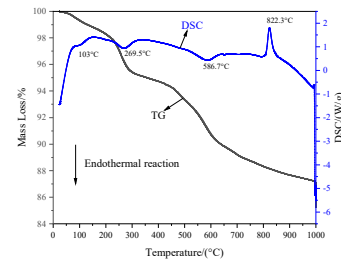
The TG-DSC analysis of nickel laterite ore is shown in Fig. 2. It can be seen in the figure that there is an apparent mass loss of nickel laterite ore with the increase in temperature, which is caused by the removal of water. The DSC curve has three heat-absorbing peaks and one exothermic peak. The removal of adsorbed water, water of crystallization, and structural water requires heat absorption, so the heat absorption peaks appeared at 103°C, 269.5°C, and 586.7°C. The exothermic peak occurred at 822.3°C because the serpentine in the laterite nickel ore was transformed into magnesium peridotite by a phase change, which released a large amount of heat.

2.2 Methods

The flow of the high-temperature tube furnace thermal balance experiment system is shown in Fig. 3, which consists of the furnace body, control system, measurement system, gas distribution system, and record storage system. Before the experiment, the reaction temperature was set to the desired temperature, and the furnace was turned on. After reaching the temperature, the furnace chamber was purged with N_2 at a flow rate of 4 SLM to displace the residual air. After that, the crucible containing a certain amount of nickel laterite (about 2.5 g) was quickly pushed into the constant temperature zone of the furnace chamber. During the experiment, an electronic balance was used to record the data in real time, and the experiment was stopped when the electronic balance showed that the mass no longer changed and stabilized for a while.
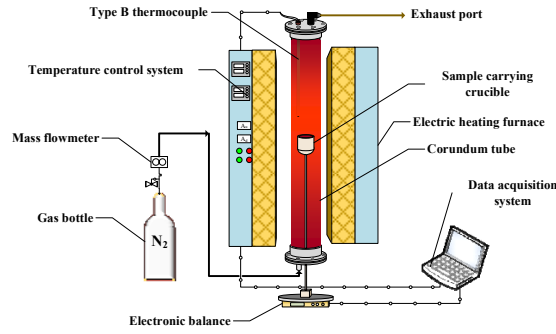
Fig. 3. Schematic diagram of high-temperature tube furnace thermal balance experiment system

In this paper, thermogravimetric experiments were carried out to perform reduction kinetic analysis. The specific experimental steps are as follows: firstly, the nickel laterite was placed in a blast drying oven, and dried at 105 °C for four hours to altogether remove its adsorbed water. To eliminate the influence of crystallization and structural water on the reduction process, the dried nickel laterite ore was roasted in a muffle furnace at a constant temperature (900 °C) for two hours. Finally, the roasted ore and semi-coke were thoroughly mixed with a semi-coke content of 4%. About 5 mg of the sample was weighed into a crucible, and the crucible was placed in a microcomputer differential thermal balance and heated up to 1000 °C under the conditions of the N_2 flow rate of 30 ml/min, and heating rates of 5 °C/min, 10 °C/min, 15 °C/min, and 20 °C/min, respectively.

3. Results and discussion

3.1 Low-temperature drying characteristic

Under the condition of N_2 flow rate of 4 SLM, 120 °C, 150 °C, 180 °C and 210 °C were selected as the drying temperatures to study the low-temperature drying characteristics of nickel laterite ore. Fig. 4(a) shows the weight loss curve of nickel laterite ore in the drying process. It can be seen from Fig. 4(a), with the increase in drying time, the wet base water content of nickel laterite ore decreases and finally tends to be constant; with the decrease of wet base water content, the drying rate of nickel laterite ore first increases and then decreases. Low-temperature drying removes the adsorbed water, the process does not cause phase change, and the drying curve is smooth and stable. With the increase in temperature, its maximum drying rate also increases.

3.2 High-temperature drying characteristic

Under the condition of N_2 flow rate of 4 SLM, 700 ~ 850 °C were selected as the drying temperatures to carry out high-temperature drying experiments on nickel laterite ore. It can be seen from Fig. 4(b) that, with the increase in drying time, the moisture content of the wet base decreases. Before 300 s, the moisture content of the wet base changes faster, and the drying rate is more significant; after 300 s, the moisture content of the wet base changes slower, and the drying rate becomes smaller and finally tends to be constant. Under the same drying time condition, the higher the temperature, the faster the water removal rate. When exceeding the phase change temperature (822.3 °C), the moisture removal rate will significantly improve and meet the drying requirements earlier.
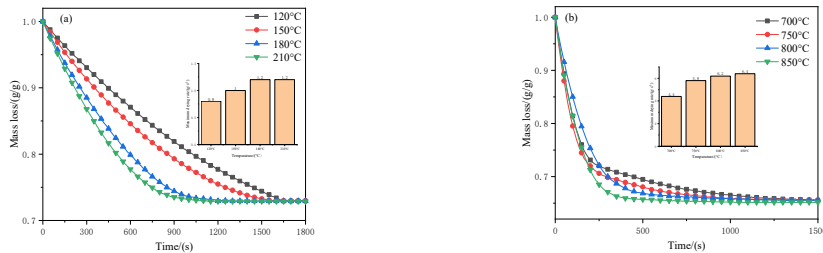
Fig. 4. Drying characteristic curve (a) Low-temperature (b) High-temperature

3.3 Drying kinetics analysis

The drying process of nickel laterite ore was analyzed kinetically. Fig. 5 shows lnk versus 1/T for the nickel laterite ore drying process, where k takes the maximum drying rate constant. It can be seen in Fig. 4 that the maximum drying rate increases with increasing temperature, but the drying rate is not constant, so k is taken as the maximum value of the drying rate. The results show that the maximum drying rate at different temperatures for both high and low-temperature drying stages is approximately linear with temperature. The Arrhenius empirical formula[7] is commonly used to describe the relationship between chemical reaction rate constants and temperature:

$$k = A\exp(-E_a / RT) \tag{1}$$

Taking logarithms on both sides of equation (1), we get:

$$Ink = InA - \frac{E_a}{RT} \tag{2}$$

where k is the reaction rate constant, A is the pre-exponential factor, E_a is the activation energy, R is the gas constant (8.314 J/(K·mol)), and T is the temperature.

According to Equation (2), the slope of the straight line in Fig. 5 is derived as E_a/R, and the activation energy of the low-temperature drying process can be found to be 7.5 kJ/mol, and that of the high-temperature drying process is 10.53 kJ/mol.
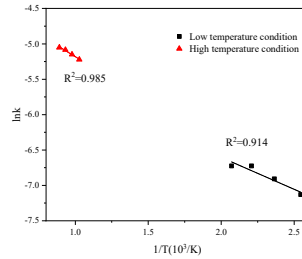
Fig. 5. Relationship between lnk and 1/T during drying

3.4 Reduction kinetics analysis

Throughout the reaction, the change in mass of the sample was recorded as a function of time, and the conversion of semi-coke with nickel laterite reduction was expressed as follows[8]:

$$\alpha = \frac{m_0 - m_t}{m_0 - m_\infty} \times 100\% \tag{3}$$

where m_0 is the initial mass of the sample, m_t is the mass of the sample at time t, and

m_∞ is the final mass of the sample.

Fig. 6 shows the relationship between conversion rate and temperature at different heating rates, from which it can be seen that the conversion rate is unaffected by the heating rate, and the whole reduction process can be divided into three stages according to the temperature intervals, which are the first stage (30~400°C), the second stage (400~800°C), and the third stage (800°C~1000°C), in which the reaction rate is the fastest in the third stage.
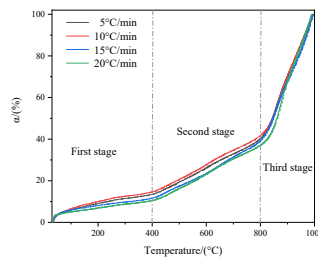
Fig. 6. The relationship between conversion and temperature at different heating rates

The following formula is derived by using the dynamic fitting method proposed by COATS and REDFERN[9]. The differential kinetic equation can be expressed as:

$$\frac{d\alpha}{dt} = k(T)f(\alpha)$$
(4)

Bringing Eq. (1) into Eq. (4) gives:

$$\frac{d\alpha}{dt} = A\exp(-E_a / RT)f(\alpha)$$
(5)

The heating rate is β is a constant:

$$\beta = \frac{dT}{dt}$$
(6)

Combining Eq. (5) and Eq. (6) and integrating over f(α) gives:

$$g(\alpha) = \frac{ART^2}{\beta E}(1 - \frac{2RT}{E})\exp(-\frac{E_a}{RT})$$
(7)

where g(α) is an integral function of f(α). Taking the logarithm of both sides of Eq. (7), which gives:

$$\ln\left[\frac{g(\alpha)}{T^2}\right] = \ln\left[\frac{AR}{\beta E_a}(1 - \frac{2RT}{E_a})\right] - \frac{E_a}{RT}$$
(8)

Eq. (8) shows that $\ln[g(\alpha)/T^2]$ is approximately linear with 1/T.

Common solid-phase reaction models include chemical reaction, diffusion, interface reaction, and nucleation and growth models[10]. The fifteen kinetic mechanism functions were used to validate and analyze the different stages. The relationship between $\ln[g(\alpha)/T^2]$ and 1/T can be obtained by combining with Eq. (8). The results are shown in Fig. 7. The validation indicates that the first stage (30~400 °C) and the second stage (400~800 °C) have the most significant correlation with the mechanism function A4, which is in line with the nucleation and growth model, and its differential expression with is:

$$f(\alpha) = 1 / (2\alpha)$$
(9)

The third stage (800~1000 °C) has the most considerable correlation with the mechanism function D1, which is determined to be a one-dimensional diffusion reaction, in which the diffusion is a velocity-controlled link, and its differential expression is:

$$f(\alpha) = 1 / 4(1-\alpha)[-\ln(1-\alpha)]^{-3}$$
(10)
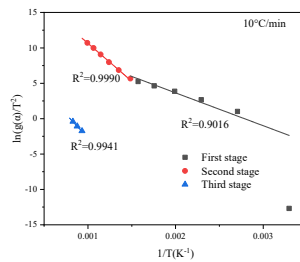
Fig. 7. Kinetic model in reduction process

After determining f(α) for each stage, the activation energy E_a for different stages can be easily calculated from the slope of the fitted straight line. The results are shown in Table 2.

Table 2 Activation energy at different stages of the reduction process

Reaction stage	First stage	Second stage	Third stage
$E_a/(kJ \cdot mol^{-1})$	38.59	89.11	109.97

As the reaction proceeds, the activation energy of each reaction stage increases sequentially, and the reaction rates of different stages are significantly different. For the first stage of the reduction reaction, this stage of the reaction temperature is low. The temperature limits the reaction of nickel-iron oxides and reductants. This stage of the reaction rate is low, and the principal reduction of easily reducible oxides Fe_2O_3 and NiO reduction; the second stage of the temperature is gradually increased, and the reaction rate is accelerated, but due to the reduction of iron oxides is step-by-step, the stage of the reduction of FeO will be FeO reduction, relative to the Fe_2O_3 and NiO. Fe_2O_3 and NiO, FeO is more difficult to reduce. Therefore, the activation energy of this stage is higher than that of the first stage; when the reaction enters the third stage, the activity of FeO will be reduced, FeO will react with SiO_2 to form silicate minerals, and serpentine phase change in this temperature range, decomposition to form amorphous magnesium-iron peridotite, and at the same time, the surface of the mineral will produce a layer of metallic iron, which will hinder the reduction reaction.

4. Conclusion

1) The water in laterite nickel ore mainly exists in adsorbed, crystal, and structural water. The water content in laterite nickel ore is 35%, of which crystal and structural water are 7%.

2) High-temperature and low-temperature drying experiments show that the maximum drying rate at different temperatures is approximately linear with temperature. 700 °C can meet the drying requirements required by the experiment.

3) The reduction process of the laterite nickel ore can be divided into three stages: the first and the second stage conform to the nucleation growth model, the kinetic equation of which is $(1−α) −1−1 = kt$, and the chemical reaction is the speed control link of the process; In the third stage, the kinetic equation is $α^2 = kt$, diffusion is the speed control link.

Acknowledgment

References

Sarbishei S, Tafaghodi L. A comprehensive kinetic investigation on sulfur deportment during nickel laterite calcination using model-free, model-fitting, and master plot approaches. Minerals Engineering, 2023, 192: 108001.

Xue Y, Zhu D, Pan J, et al. An investigation into the co-sintering process of limonitic nickel laterite and low-grade chromite via multi-force fields. Journal of Materials Research and Technology, 2021, 12: 1816–1831.

Pickles C A. Drying kinetics of nickeliferous limonitic laterite ores. Minerals Engineering, 2003, 16(12): 1327–1338.

Abdel-Halim K S, Khedr M H, Nasr M I, et al. Carbothermic reduction kinetics of nanocrystallite Fe_2O_3/NiO composites for the production of Fe/Ni alloy. Journal of Alloys and Compounds, 2008, 463(1): 585–590.

Liu Y, Lv X, You Z, et al. Kinetics study on non-isothermal carbothermic reduction of nickel laterite ore in presence of Na_2SO_4 [J]. Powder Technology, 2020, 362: 486–492.

Ochieng R, Cerón A L, Konist A, et al. A combined analysis of the drying and decomposition kinetics of wood pyrolysis using non-isothermal thermogravimetric methods. Energy Conversion and Management: X, 2023, 20: 100424.

Janković B, Adnađević B, Mentus S. The kinetic analysis of non-isothermal nickel oxide reduction in hydrogen atmosphere using the invariant kinetic parameters method. Thermochimica Acta, 2007, 456(1): 48–55.

Khawam A, Flanagan D R. Solid-state kinetic models: basics and mathematical fundamentals. The Journal of Physical Chemistry B, 2006, 110(35): 17315–17328.

A.W. Coats, J.P. Redfern. Kinetic parameters from thermogravimetric data. Nature,1964,201(68).

Ortega A. Some successes and failures of the methods based on several experiments. Thermochimica Acta, 1996, 284(2): 379–387.

NUMERICAL INVESTIGATION OF FLOW AND REACTION BEHAVIORS IN THE OXIDATIVE COUPLING OF METHANE BASED ON PARTICLE CLUSTER EFFECT

Sen Wang[1,2], Zhenhua Hao[1]*, Yitian Fang[1]*

1. Institute of Coal Chemistry, State Key Laboratory of Coal Conversion, Chinese Academy of Sciences, Taiyuan, 030001, Shanxi Province, China;

2. University of Chinese Academy of Sciences, Beijing, 100049, China

*Email: hzh@sxicc.ac.cn (Zhenhua Hao), fyt@sxicc.ac.cn (Yitian Fang)

Abstract

Fluidized bed reactor has been considered as one of the viable devices for the oxidative coupling of methane (OCM) compared to traditional fixed bed. However, particle clusters in fluidized bed affect flow behaviors of fluids, which is not conductive to OCM reaction. In this study, the flow and reaction behaviors of isolated particle and cluster model were studied by computational fluid dynamics (CFD) method. The results showed that the obstruction caused by outer particles resulted in a large volume of fluids flowing along cluster surface than through inner pores, leading to the poor gas-solid contact and heat transfer efficiency and the uneven distribution of products. The ethylene distributed continuously in isolated particle model with a yield of 23.31%, while it mainly concentrated on the upwind side in cluster model with a yield of 12.66%. This study provides some guidance for revealing the inhomogeneous characteristics caused by particle cluster on OCM reaction.

Keywords: particle cluster, oxidative coupling of methane, fluidized bed, gas-solid two-phase flow, numerical simulation.

1. Introduction

As one of the fundamental raw materials in the chemical industry, ethylene is widely utilized for large-scale production of various chemicals, including synthetic fibers, synthetic rubbers, synthetic plastics, synthetic ethanol. Among the ethylene production of oil-based, coal-based, and light olefins-based routes, the oxidative coupling of methane (OCM) technology stands out by utilizing abundant and cost-effective methane as raw materials, which contributes to the efficient utilization of natural gas resources like coal bed methane and shale gas [1-4]. However, the excessive oxidation of methane, ethane and ethylene on catalyst surfaces or in the gaseous phase produced the undesirable products, such as CO_x and H_2O [5]. These side reactions significantly limited the yield of desired products.

Traditionally, the OCM reactions were mainly conducted in a fixed bed reactor due to its simplicity of operation and lower limitation on catalyst particles. However, this approach was prone to local hot spots during such a highly exothermic reaction, leading to catalyst deactivation and excessive oxidation [6]. Therefore, the fluidized bed with high fluidization velocity and uniform temperature distribution was also employed for performing the OCM reaction [7]. Worthily, the particles were readily gathered to clusters during gas-solid fluidization processes, reducing the flow stability of particles and impacting the catalytic efficiency of catalysts in reactions [8]. However, there are few studies on particle cluster effect for OCM reactions. It is imperative to investigate the cluster effect of catalyst particles on the OCM reaction in fluidized bed reactors.

In this study, computational fluid dynamics (CFD) were employed to investigate the particle cluster effect on the OCM reaction. A local model of two-dimensional gas-solid fluidized bed was established to analyze flow and reaction characteristics under isolated particle model and particle cluster model with an aim to elucidate their influence on the OCM reaction.

2. Model description

2.1 Governing equations

The continuity equation, momentum equation and energy equation of continuous phase motion are shown as Eq. (1) to Eq. (3). To solve the turbulence of continuous species in fluidized bed, the realizable k-ε model is applied in this study.

$$\frac{\partial \rho}{\partial t} + \nabla \cdot \left(\rho \vec{u} \right) = 0 \tag{1}$$

$$\frac{\partial}{\partial t} \left(\rho \vec{u} \right) + \nabla \cdot \left(\rho \vec{u} \vec{u} \right) = -\nabla p + \nabla \cdot \left(\vec{\tau} \right) + \rho \vec{g} + \vec{S}_{mom} \tag{2}$$

$$\frac{\partial}{\partial t} \left(\rho (e + \frac{u^2}{2}) \right) + \nabla \cdot \left(\rho V (h + \frac{u^2}{2}) \right) = \nabla \cdot \left(k_{eff} \nabla T - \sum_j h_j \overline{J_j} + \tau_{eff} \cdot \vec{u} \right) + S_h \tag{3}$$

The mass conservation equation for gaseous space k (k = N_2, CH_4, O_2, C_2H_6, C_2H_4, CO, CO_2 and H_2O) are calculated as:

$$\frac{\partial}{\partial x_j} \left(\rho_g u_j Y_k \right) = \frac{\partial}{\partial x_j} \left(D_k + \frac{\mu_g}{\sigma} \frac{\partial Y_k}{\partial x_j} \right) + \sum_{k=1}^{8} S_k \tag{4}$$

2.2 OCM reaction mechanism

The mechanism of OCM reaction presented by Nastaran was employed in this study, which were characterized by the set of stoichiometric equations shown in Table 1 [9].

Table 1. The Nastaran kinetic models and parameters of OCM reaction [9].

No.	Reaction	$k_{0i}/$ kmol·m^{-2}·s^{-1}	$E_{ai}/$ kJ·mol^{-1}	m_i	n_i
1	$CH_4 + 0.25O_2 \rightarrow 0.5C_2H_6 + 0.5H_2O$	4.04×10^8	33.22	0.83	0.46
2	$CH_4 + 1.5O_2 \rightarrow CO + 2H_2O$	6.01×10^6	34.99	0.0072	0.7
3	$CH_4 + 2O_2 \rightarrow CO_2 + 2H_2O$	1.11×10^9	42.47	1.12	0.7
4	$C_2H_6 + 0.5O_2 \rightarrow C_2H_4 + H_2O$	6.32×10^9	68.00	0.00028	1.49
5	$C_2H_4 + 2O_2 \rightarrow 2CO + 2H_2O$	3.25×10^9	103.60	0.0000729	1.1
6	$CO + 0.5O_2 \rightarrow CO_2$	4.50×10^{13}	66.00	0.37	0.78

2.3 Geometrical modeling

(a) Particle cluster model   (b) Isolated particle model
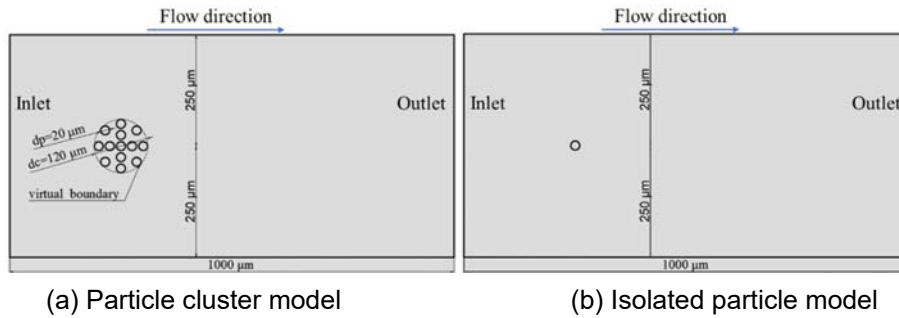
Fig. 1. The geometrical model of local fluidized bed.

(a) Global mesh   (b) Local mesh
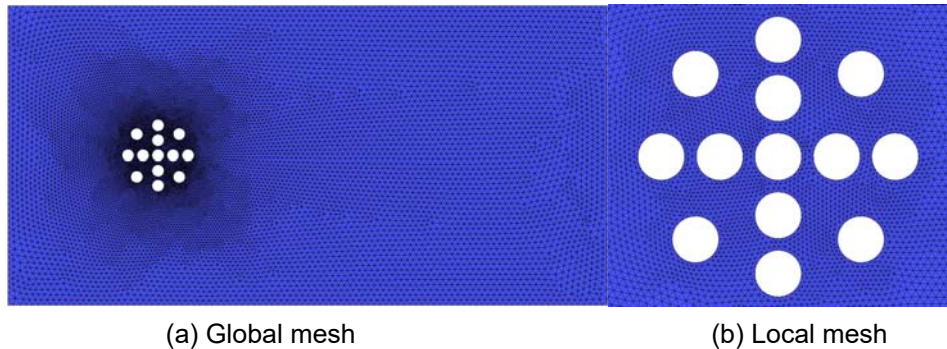
Fig. 2. The meshing of geometrical models.

As shown in Fig.1, the local 2D model of fluidized bed was established with a particle cluster (or an isolated particle). Cluster was consisted of multiple layers of particles (13 particles in total) to approximate the actual clustering behavior of particles. In this study, it was assumed that the physical structure of cluster was unchanged and the location of cluster in fluidized bed was time-invariant to simplify the analysis. The unstructured triangular grid was applied to meshing the geometrical models shown in Fig.2 and the grid refinement treatment near cluster and isolated particle was considered.

2.4 Simulation and operating parameters

The SIMPLE algorithm was chosen for the pressure-velocity coupling scheme. For the spatial discretization, the Least Squares Cell Based format, PRESTO format and second order upwind format were selected for gradient, pressure and other terms, respectively. The velocity-inlet, pressure-outlet, and no-slip walls were used for the boundary conditions. The wall surface reaction model was enabled and the surfaces of each particle in cluster were considered as the reaction surface. The detailed operating parameters were listed in the Table 2.

Table 2. The detailed parameters of simulation.

Parameters	Values	Parameters	Values
Feedstock	N_2, CH_4, O_2	Catalyst	$SnBaTiO_3$
Mixed gas density	Impressible ideal gas	Catalyst bulk density	1000 $kg \cdot m^{-3}$
Particle diameter	20 µm	Cluster diameter	120 µm
Inlet velocity	1~5 $m \cdot s^{-1}$	Total pressure	1 atm
Inlet CH_4/O_2	2~5	Surface temperature	700~800℃

3. Results and discussion

3.1 Model validation

As shown in Table 3, three different numbers of meshes were compared to keep the balance between computation accuracy and efficiency. The net mass flow rate and C_2H_4 yield (the ratio of the molar concentration of product C_2H_4 to consumed reactant CH_4) were both used to check the accuracy of grid. The results showed that the net mass flow rate of all three different number of grids were lower, which satisfied the mass conservation of fluids. However, the C_2H_4 yield obtained from medium and fine mesh was accurate and similar than coarse mesh model. Therefore, the medium mesh number (26,950) was employed for subsequent studies to reduce the calculation time and computer memories.

Table 3. Grid independence verification.

Mesh quality	Mesh number	Net mass flow rate	C_2H_4 yield
Coarse	16,363	2.73×10^{-9} $kg \cdot s^{-1}$	2.72%
Medium	26,950	8.82×10^{-10} $kg \cdot s^{-1}$	12.70%
Fine	69,123	3.05×10^{-11} $kg \cdot s^{-1}$	12.74%
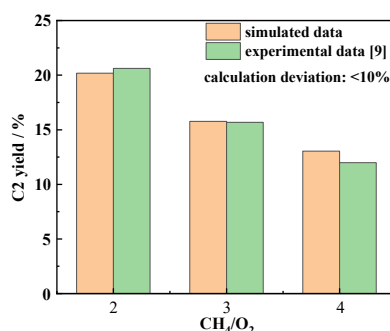
Fig.3. Model validation (Running conditions: flow rate: 160 ml/min, temperature: 725℃, CH_4/O_2: 2~4).

The accuracy of simulation results and experimental results was verified [39]. The physical properties and flow conditions of gas-solid phase were set in accordance with the experimental environment. The C2 yield obtained from the simulations and the experiments was compared. As shown in Fig.3, there was a good agreement of simulated and experimental data. The similar trend of C2 yield and the calculation deviation less than 10% under different feed CH_4/O_2 ratio were obtained, which demonstrated the accuracy of the simulation results.

3.2 Flow field characteristics in two models

In this section, the flow characteristics in isolated particle and cluster model were studied. As shown in Fig.4, the pressure distribution in two models was compared. A negative pressure region near the tail of catalyst was both observed in two models due to the obstruction of catalyst particles to gaseous phase flow. Compared to smaller diameter of isolated particle (d_p=20 μm), cluster occupied the larger area (d_c=120 μm) of flow field space to enforce more fluid to flow around it, leading to the wider area of negative pressure region.

| (a) Isolated particle model | (b) Cluster model |
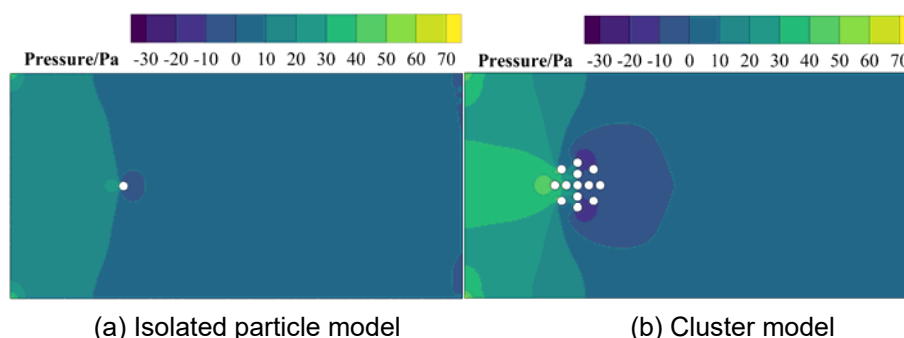
Fig.4. Pressure distribution of isolated particle and cluster model.

As shown in Fig.5, the streamlines were parallel to the horizontal axis approximately near the inlet, outlet and the wall in two models. However, most fluids near the center axis flowed nonhorizontally to cross over the obstacle (isolated particle or cluster) due to the disturbing effect of obstacle. In cluster model, moreover, the distribution of streamline was more uneven than isolated particle model and a significant pair of vortexes near the cluster tail were generated. Due to the higher pressure drag and body drag caused by particle cluster, partial fluids flowed along the surface firstly and then attracted to the negative pressure region located directly behind the cluster, eventually resulting the uneven streamline distribution and the generation of tail vortex (called as Karman vortex). The presence of vortexes consumed the kinetic energy of partial fluids, which led to the increase of residence time of gaseous species.

| (a) Isolated particle model | (b) Cluster model |
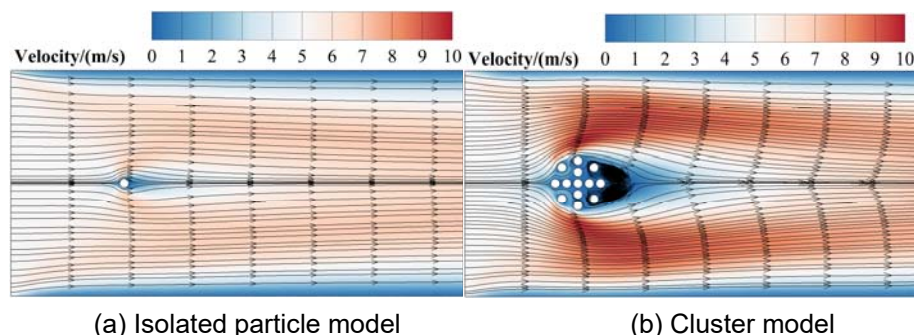
Fig.5. Streamline distribution of isolated particle and cluster model (inlet velocity: 5 m/s).

The temperature distribution of two models was shown in Fig.6. A higher temperature region was generated at the surface of isolated particle and particle cluster due to the exothermic character of OCM reaction. And there was a temperature band extended to the downstream of particle in which temperature gradually decreased along the axis due to the turbulence of fluids. In cluster model, the diameter of catalyst was larger, which led to the increase of the range of high temperature band. In the interior of particle cluster, a local

higher temperature region was appeared on the surface of No.10, indicating that the reaction heat of OCM reaction was not completely removed. As mentioned above, the gaseous phase mainly flowed through the surface of cluster instead of the interior, which led to the poor effect of heat transfer, resulting in the appearance of local hot spots inside the cluster [10].

(a) Isolated particle model (b) Cluster model
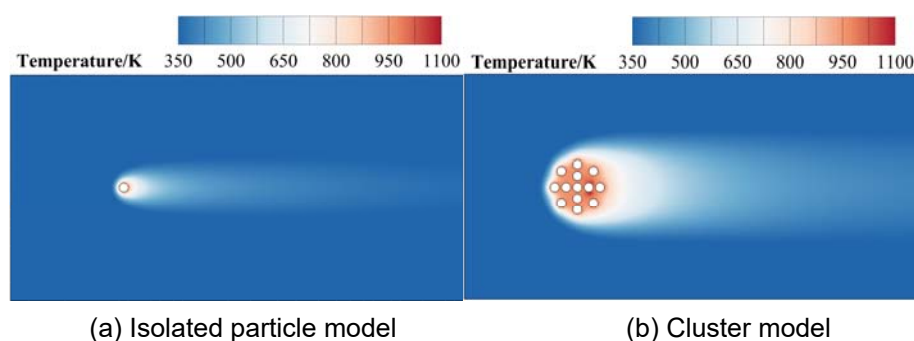
Fig.6. Temperature distribution of isolated particle and cluster model.

3.3 Reaction characteristics in two models

(a) Isolated particle model (b) Cluster model
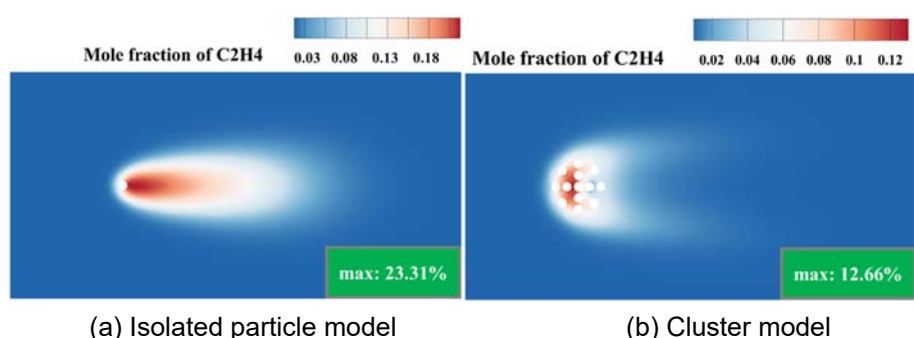
Fig.7. Mole fraction of isolated particle and cluster model (working condition: inlet velocity: 5 m/s, temperature: 700℃, CH_4/O_2: 2).

(a) Inlet velocity (b) Surface temperature (c) Feed CH_4/O_2 ratio
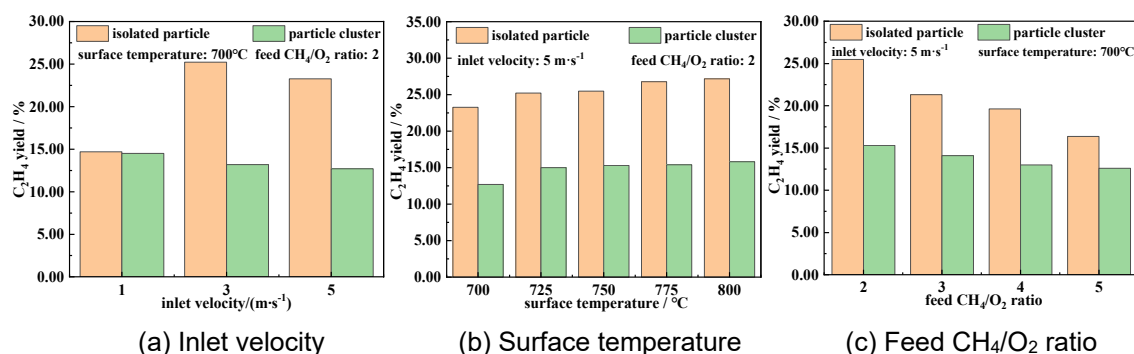
Fig.8. C_2H_4 yield of isolated particle and particle cluster under different working conditions.

In this section, the OCM reaction characteristics in isolated particle and cluster model were researched. The mole fraction of C_2H_4 in two models under the working condition with an inlet velocity of 5 m/s, a surface temperature of 700℃, and a feed CH_4/O_2 ratio of 2 (the mole fraction of N_2 was set as 0.4) were compared shown in Fig.7. For isolated particle model, there was no obstacle for the contact of gaseous phase and catalyst particle, resulting in the continuous generation and widely distributed range of C_2H_4 (shown in Fig.7(a)). However, there was a visibly discontinuous and sudden change of C_2H_4 distribution in cluster model due to the cluster effect of catalyst particles (shown in Fig.7(b)). A large amount of C_2H_4 was produced on the left side of cluster, which was ted to flow and separate from the surface of cluster than the inner pores of cluster affected by the flow around particle cluster. The C_2H_4 yield of 23.31% and 12.66% in isolated particle and cluster

model were correspondingly calculated, which demonstrated the inhibition effects of particle cluster on OCM reaction.

The C_2H_4 yield under different working conditions in isolated particle and cluster model was compared in Fig.8. It was found that C_2H_4 yield in isolated model was significantly higher than cluster model under different conditions. As mentioned above, the cluster of particles was not conductive to the good contact of particles with fluids as well as heat transfer. More gaseous species flowed along the surface of cluster, which were unable to escape from the inner pores before the occurrence of excessive oxidation [10], eventually leading to the uneven distribution of C_2H_4 and the decrease of yield.

4. Conclusion

The flow, heat transfer and reaction characteristics of isolated particle and particle cluster models on OCM reaction were investigated by utilizing CFD methods. The main conclusions are as follows:

(1) Particle clusters exhibited higher pressure drag and body drag in flow field, leading to the formation of large-scale tail vortex consuming kinetic energy of fluids.

(2) A large volume of fluids flowed along cluster surface than through inner pores, resulting in the untimely removal of reaction heat and the formation of local hot spots.

(3) The ethylene distributed continuously in isolated particle model, while it mainly concentrated on the upwind side in cluster model. Under different working conditions, cluster model exhibited lower C_2H_4 yield than isolated particle model.

Acknowledgment

References

Al-Shafei, E.N., Albahar, M.Z., Aljishi, M.F., et al. Catalytic cracking of heavy atmospheric gas oil to light olefins over ZSM-5 zeolite: Effect of crystal size in the absence/presence of steam. Journal of Analytical and Applied Pyrolysis. 2023. 172, 106003.

Li, J.J., Peng, L., Yan, Y.L., et al. Technological progress and coupling renewables enable substantial environmental and economic benefits from coal-to-olefins. Journal of Environmental Management. 2024. 353, 120225.

Chen, Y.Q., Kuo, M.J., Lobo, R., et al. Ethylene production: process design, techno-economic and life-cycle assessments. Green Chemistry. 2024.

Lunsford, J.H. The Catalytic Oxidative Coupling of Methane. Angewandte Chemie-International Edition in English. 1995. 34, 970-980.

Karakaya, C., Kee, R.J. Progress in the direct catalytic conversion of methane to fuels and chemicals. Progress in Energy and Combustion Science. 2016. 55, 60-97.

Kim, M., Arndt, S., Yildiz, M., et al. Reaction engineering of oxidative coupling of methane: Experimental observations and analysis of the impacts of operating parameters. Chemical Engineering Research and Design. 2021. 172, 84-98.

Ni, J.Y., Si, J.Q., Lan, T., et al. Mn_2O_3-Na_3PO_4/TiO_2 catalyst with high anti-agglomeration and attrition resistance for fluidized-bed oxidative coupling of methane. Fuel. 2024. 356, 129613.

Sadjadi, S., Jaso, S., Godini, H.R., et al. Feasibility study of the Mn-Na_2WO_4/SiO_2 catalytic system for the oxidative coupling of methane in a fluidized-bed reactor. Catalysis Science & Technology. 2015. 5, 942-952.

Farooji, N.R., Vatani, A., Mokhtari, S. Kinetic simulation of oxidative coupling of methane over perovskite catalyst by genetic algorithm: Mechanistic aspects. Journal of Natural Gas Chemistry. 2010. 19, 385-392.

Laurien, A.V., Kevin, M.V.G., Guy, B.M., et al. A Boudart number for the assessment of irreducible pellet-scale mass transfer limitation: application to oxidative coupling of methane. Industrial & Engineering Chemistry Research. 2021. 60, 6538-6553.

Influence of Heterogeneity of Dense-Phase Zone on Ultra-Low NOx Emission in CFB Boilers

Hongliang Xiao[2,3]，Hairui Yang[1]，Haiying Qi[1, 2,3*]

1. Department. of Energy & Power Engineering, Tsinghua University, Beijing 100084, China

2. Shanxi Research Institute of Huairou Laboratory, Taiyuan 030032, China

3. Beijing Huairou Laboratory, Beijing 101499, China

Email: hyqi@ mail.tsinghau.edu.cn (Haiying Qi)

Abstract

NOx emission is one of the key factors restricting the development of coal-fired circulating fluidized bed (CFB) boilers in China. It is found that the NOx emission of CFB boiler body can reach the ultra-low emission limit, i.e. 50 mg/Nm3, when the re-specification technology of the fluidization state technology is adopted and the particle size of bed material is reduced to below 100 μm. Further numerical simulation revealed that the main mechanism was that the small bed particles formed a large specific surface area, which enhanced the catalytic reduction effects against to NOx in the dilute phase zone at the upper part of the furnace. However, the same results were not observed in field tests of large CFB boilers over 300 MW. In order to reveal the reason why the catalytic reduction mechanism created by reducing the bed material size mentioned above fails in large boilers, the dense phase zone structure of a CFB boiler of 300 MW with three circulation loops was simulated numerically by using Euler-Euler approach based on the QC-EMMS drag model and the method which divides the wide-size-distribution particles into two solid phases.

Keywords: heterogeneity of dense-phase zone, ultra-low NOx emission, CFB boilers, Eulerian-Eulerian simulation, QC-EMMS drag model

1. Introduction

China is aiming to decrease pollution from coal-fired thermal power plants by stipulating that the NOx emissions concentration of coal-fired generating units must adhere to the ultra-low emissions standard of below 50 mg/Nm^3. Coal-fired circulating fluidized bed (CFB) boilers, extensively utilized in the thermal power generation industry, provide benefits including outstanding fuel flexibility, efficient load regulation capabilities, and reduced pollutant emissions. Nevertheless, achieving ultra-low emission standards continues to be a substantial challenge [1-3]. Tests on third-generation, energy-saving, coal-fired CFB boilers in China have demonstrated that ultra-low emission limits can be achieved by reducing the bed material particle sizes to below 100 µm (fine particle). This approach eliminates the need for an additional denitrification device, allowing NOx emissions concentrations in the boiler to remain under 50 mg/m3 across various loads and coal types [4, 5].

A preliminary theoretical analysis of the ultra-low emission mechanism has been conducted in existing literature [6, 7]. (1) In the dense phase region at the bottom of the furnace, reducing the bed material size diminishes mass transfer and enhances heat transfer within the bubbling fluidization area. This reduction in bed material size decreases the contact area between coke particles and oxygen, leading to reduced local overheating and, consequently, lower NOx production. (2) The dilute phase region at the top of the furnace contains numerous particle clusters. In these clusters, coke particles are enveloped, limiting their exposure to oxygen, while the ash particles within the clusters act as a catalytic medium for NOx reduction. Decreasing the material particle size promotes particle clustering, further reducing NOx generation. However, the limited field test data available do not conclusively validate these

mechanisms through measured data. Therefore, these proposed mechanisms require further investigation through high-fidelity numerical studies in full-size devices under operating conditions.

With the rapid development of computer technology and numerical algorithms, the use of experimental methods to study ultra-low emissions incurs a very high cost, leading to the widespread adoption of numerical simulations in this research area [8-10]. Classical homogeneous drag models do not adequately address heterogeneous flows, leading to the development of models grounded in the Energy Minimization Multi-Scale (EMMS) theory for predicting drag reduction. Utilizing EMMS theory, Chen developed sub-models for particle cluster density and size within the QC-EMMS model [11], resulting in accurate local drag predictions that aligned well with the traditional O-S model [12]. Given that variations in particle size influence the particle clustering effect, the relevance of the gas–solid drag model under specific working conditions needs to be evaluated. Previous research has successfully integrated the QC-EMMS model into the Eulerian-Eulerian framework, achieving favorable simulation results [7, 11, 13-15].

Numerical simulations revealed that the fine bed material technology proved successful in industrial boilers with capacities below 182 MW [7]. However, it was ineffective in boilers exceeding 300 MW, where NOx emissions continued to surpass the standard. This study found that the reintroduction of fine particles from the return point led to fluidization deterioration, which caused an oxidative atmosphere to dominate in the upper dilute phase region and diminished the reducing atmosphere.

2. Models and conditions

2.1 Model setting

The governing equations, gas-solid drag model, chemical reaction model, and heat transfer model are detailed in Reference 7.

2.2 Geometric model

Fig.1 illustrates the design of large and small capacity CFB boilers. Table 1 provides a detailed comparison of their key operational parameters.
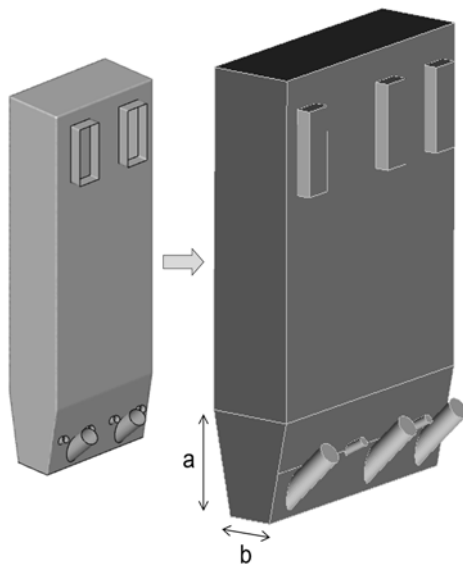
Fig.1. Small and large capacity CFB boilers

Table 1. Geometry and material settings

Parameter	Unit	Bed1	Bed2
Capacity	MW	182	300
Cross-sectional dimensions (width × depth)	(m)	10×5.2	31×9.8
Height, H		32	40.2
Lower conical section ($a×b$)		6×3.2	9.3×4.9
Coal feed height, H_{coal}		1.8	2.26
Return material height, H_{cir}		1.6	2.01
Airflow rate, G_a	(m³/h)	206706	485000
Primary rate, G_{a1}		103353	242500
Coal feed rate, G_{coal}	(t/h)	20.27	165.1
Fine/Coarse particle size	(μm)	73, 572	
Fine/Coarse particle volume	(%)	45, 55	
Excess air ratio	(-)	1.2	
Fluidization velocity, U_g	(m/s)	5	
Average particle concentration,$\varepsilon_{s,bed}$	(-)	0.0076	0.0082

3. Results and discussion

3.1 Axial concentration distribution of gas components
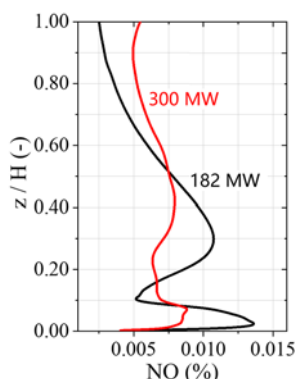
Fig.2. NOx distribution   Fig.3. CO distribution (Right is dilute phase)
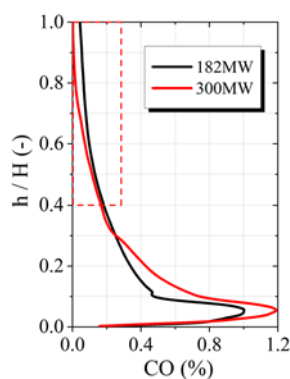
As depicted in Fig.2, the NOx emissions from a 300MW unit significantly surpass the established limits. The CO concentration and O2 concentration, illustrated in Fig.3 and 4, respectively, exhibit an inverse relationship with the small bed curve. The pivotal point at h/H=0.3 indicates a breakthrough in the dense phase area, resulting in lower oxygen consumption and allowing more residual oxygen to enter the dilute phase region.

The distribution pattern of NOx, as shown in Fig. 2, reveals a decrease in peak height within the dense phase region due to a dual effect. This includes reduced NOx formation because of diminished oxygen consumption and enhanced reduction, as evidenced by higher CO levels. Conversely, the dilute phase zone, characterized by an oxidizing atmosphere, shows an uptick in NOx levels.
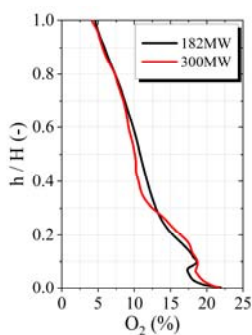
Fig.4. O$_2$ distribution (Right is dense zone)   Fig.5. CO$_2$ distribution
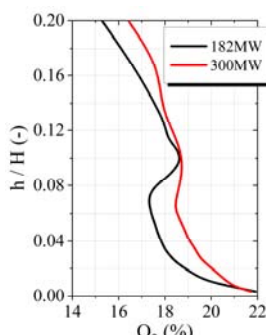
The CO$_2$ concentration, as illustrated in Fig. 5, directly correlates with the O$_2$ concentration, exhibiting a one-to-one relationship. A notable turning point occurs at h/H=0.1 for both curves, attributed to the introduction of secondary air.

3.2 Reaction rate

Table 2. NOx generation and reduction reactions

Generation	Reduction
R1:NH_3 + 1.25O_2 → NO + 1.5H_2O	R5:NO + CO → 0.5N_2 + CO_2 (fine particle)
R2:HCN + 1.25O_2 → NO + CO + 0.5H_2O	R6:NO + CO → 0.5N_2 + CO_2 (coarse particle)

Fig. 6 displays the NOx generation rate, revealing that the rates in the 300MW bed (R1 and R2 reactions) within the dense phase area are lower than those in the 182MW bed, a phenomenon resulting from uneven particle distribution. Conversely, the dilute phase area exhibits higher rates, indicative of an "oxidizing atmosphere." These findings corroborate the conclusions drawn from the analysis of Fig. 2.

Fig. 7 illustrates that the NOx reduction rate is inversely related to the generation rate, further validating the conclusions derived from examining Fig. 2.
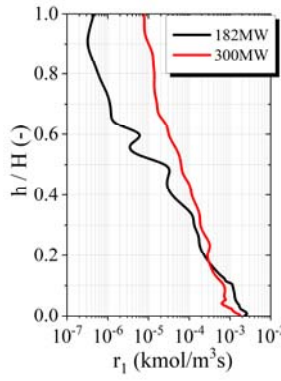
Fig.6. NOx generation reaction rates R1 and R2
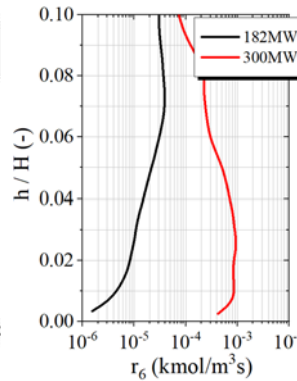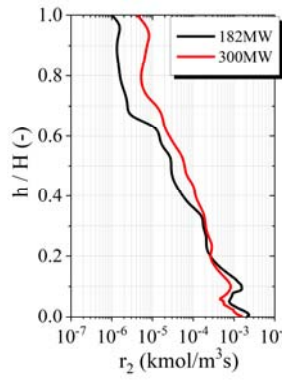
Fig.7. Catalytic reduction reaction rates of coarse ash (R6, left) and fine ash (R5, right)

3.3 Bubbling behavior

Fig. 8 clearly illustrates the presence of bubbles at various cross-sectional heights within the dense phase zone, where the bubble locations correspond closely with the return pipe's position. This phenomenon is observed in both the 182MW and 300MW beds.
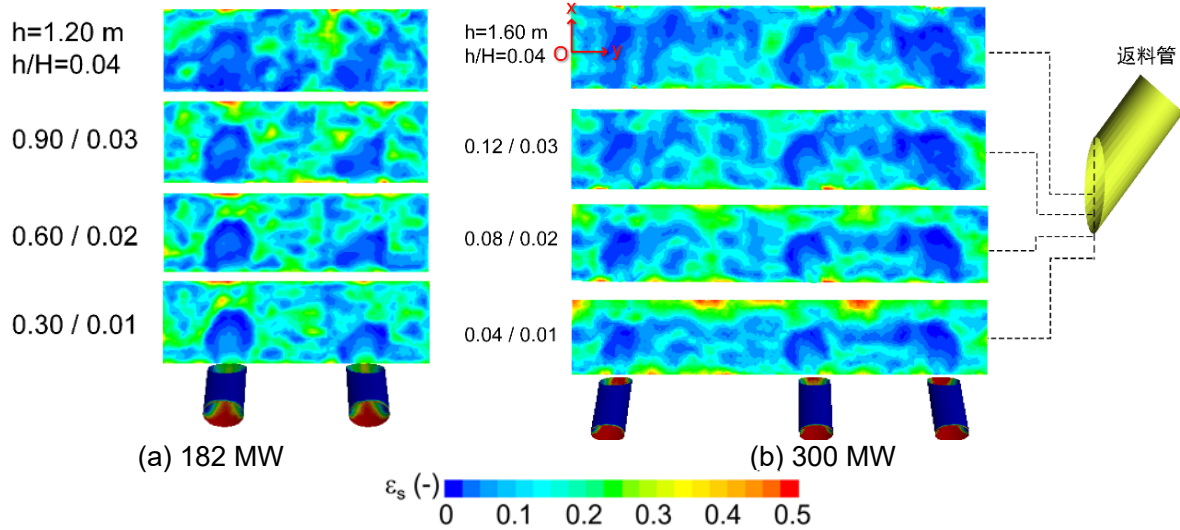
Fig.8. Correspondence between cross-sectional particle concentration distribution and return pipe

The formation of bubbles arises from several factors: (1) The bubbles' presence aligns with the zone where circulating ash from the return pipe accumulates, converting the initially homogenous bed of coarse particles into a layered configuration of coarse and fine particles across the width; (2) The smaller dimensions of the circulating ash lead to a terminal velocity below the fluidization velocity, coupled with reduced resistance at this point, resulting in penetration; (3) The stability of bubble locations, as depicted in particle concentration animations across various sections; (4) As bed pressure decreases with height, bubbles enlarge and claim a greater proportion of the cross-sectional area, intensifying cross-sectional non-uniformity with elevation.

The bubble boundary is determined at a particle concentration threshold of $\varepsilon_{b,cr}=0.18$, employing image processing techniques to delineate the bubble structure, as demonstrated in Fig.9.
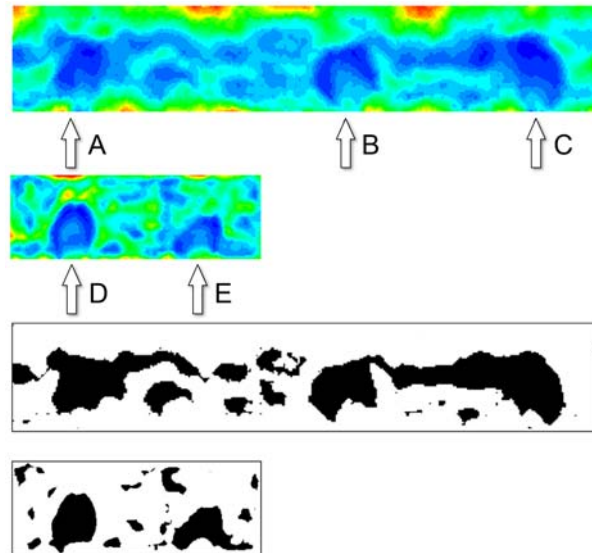
Fig.9. Instantaneous bubbles and their threshold boundaries

The primary cause of elevated NOx levels in the large bed (300MW) stems from the uneven distribution of particles within the dense phase zone, or even breakthrough events, leading to the creation of an oxidizing atmosphere in the dilute phase area. This significantly lowers the concentration of CO, the principal reactant for NOx reduction, despite the small size of circulating ash particles. The catalytic effectiveness remains consistent with that observed in smaller beds, preventing the achievement of ultra-low NOx emissions. Ultimately, the degree of NOx emissions is contingent upon the non-uniformity of particle distribution in the dense phase zone.

4. Conclusion

The study concludes that the heterogeneity of the dense-phase zone significantly influences ultra-low NOx emissions in large CFB boilers. Specifically, it identifies the uneven particle concentration distribution in the dense phase zone as the major contributor to excessive NOx emissions in larger boilers. This uneven distribution facilitates the entry of more O_2 into the dilute phase zone, creating an oxidizing atmosphere and substantially reducing the CO concentration, which is crucial for NOx reduction. The study underscores the role of circulating ash from return ports in creating large bubbles and altering the bed's homogeneity, which in turn affects NOx emissions. These findings offer a crucial basis for addressing NOx emission challenges in large-scale CFB boilers.

Acknowledgment

References

[1] L. Junfu, Z. Jiansheng, Z. Hai, L. Qing, Y. Guangxi, Performance evaluation of a 220t/h CFB boiler with water-cooled square cyclones, Fuel Process. Technol., 88 (2007) 129-135.
[2] Z. Gong, Z. Liu, T. Zhou, Q. Lu, Y. Sun, Combustion and NO emission of Shenmu char in a 2 MW circulating fluidized bed, Energy & Fuels, 29 (2015) 1219-1226.
[3] P. Basu, Combustion of coal in circulating fluidized-bed boilers: a review, Chem. Eng. Sci., 54 (1999) 5547-5557.
[4] X. Ke, R. Cai, M. Zhang, M. Miao, J. Lyu, H. Yang, Application of ultra-low NOx emission control for CFB boilers based on theoretical analysis and industrial practices, Fuel Process. Technol., 181 (2018) 252-258.
[5] R. Cai, H. Zhang, M. Zhang, H. Yang, J. Lyu, G. Yue, Development and application of the design principle of fluidization state specification in CFB coal combustion, Fuel Process. Technol., 174 (2018) 41-52.

[6] J.-J. Li, M. Zhang, H.-R. Yang, J.-F. Lu, X.-X. Zhao, J.-C. Zhang, The theory and practice of NO emission control for circulating fluidized bed boilers based on the re-specification of the fluidization state, Fuel Process. Technol., 150 (2016) 88-93.

[7] J. Zhao, Y. Liu, H. Yang, H. Qi, Eulerian investigation of the mechanism of Ultra-low NOx emissions from CFB boilers with finer bed material, Fuel, 359 (2024).

[8] A. Oloruntoba, Y. Zhang, H. Xiao, Hydrodynamics-reaction-coupled simulations in a low-scale batch FCC regenerator: Comparison between an annular and a free-bubbling fluidized beds, Powder Technol., 407 (2022) 117608

[9] H. Xiao, A. Oloruntoba, X. Ke, K. Gao, L. Duan, C. Liu, Y. Zhang, J. Wang, Improving the precision of solids velocity measurement in gas-solid fluidized beds with a hybrid machine learning model, Chem. Eng. Sci., 285 (2024) 119579

[10] H. Xiao, Y. Zhang, J. Wang, Correlating measurement qualities of cross-correlation based solids velocimetry with solids convection-mixing competing mechanism in different gas fluidization regimes, Chem. Eng. Sci., 253 (2022) 117602.

[11] Y. Liu, P. Huo, X. Li, H. Qi, Numerical study of coal gasification in a dual-CFB Plant based on the generalized drag model QC-EMMS, Fuel Process. Technol., 203 (2020).

[12] T.J. O'Brien, M. Syamlal, Particle cluster effects in the numerical simulation of a circulating fluidized bed, Circulating fluidized bed technology IV, (1993) 367-372.

[13] P. Huo, X. Li, Y. Liu, H. Qi, Investigation on influences of loose gas on gas-solid flows in a circulating fluidized bed (CFB) reactor using full-loop numerical simulation, Int. J. Chem. React. Eng., 19 (2021) 53-62.

[14] Y. Liu, P. Huo, X. Li, H. Qi, Numerical analysis of the operating characteristics of a large‐scale CFB coal‐gasification reactor with the QC‐EMMS drag model, Can. J. Chem. Eng., 99 (2020) 1390-1403.

[15] Y. Liu, Q. Dai, H. Qi, Cluster identification criterion with experimental validation for the cluster solid holdup model during fluidization, Powder Technol., 373 (2020) 459-467.

Experimental investigation of bed-to-wall heat transfer characteristics of a solid amine sorbent in a dense bed

Chenhuan Xu, Liang Wang, Yiming Zhang, Yongmin Zhang*

State Key Laboratory of Heavy Oil Processing, China University of Petroleum, Beijing 102249, PR China

18 Fuxue Road, Changping, Beijing 102249, P. R. China

*Email: zhym@cup.edu.cn

Abstract

Circulating fluidized bed temperature swing adsorption (CFB-TSA) carbon capture process using solid amine sorbents has become a widely recognized solution to reduce stationary sources CO_2 emissions. The successful design and optimize of the heat exchanger in the adsorber, desorber and cooler requires much information of the bed-to-wall heat transfer characteristics of the solid amine sorbent. However, the existing bed-to-wall heat transfer studies do not address this type of novel particle. More so, guidelines for industrial heat exchanger design based on solid amine sorbents is still lacking. Therefore, heat transfer characterization of a novel solid amine sorbent in bubbling and turbulent flow regimes is conducted in a large-scale CFB cold model unit, some guidance for the design and optimize of the heat exchanger in the adsorbers, desorbers and coolers are also given.

Key words: bed-to-wall heat transfer; solid amine sorbent; dense bed

1. Introduction

Circulating fluidized bed temperature swing adsorption (CFB-TSA) carbon capture process using solid amine sorbents has become a widely recognized solution to reduce stationary sources CO_2 emissions [1-3]. During the process, the sorbents selectively adsorb CO_2 from the flue gas at in the adsorber at 30~70°C. Then, the CO_2-loaded sorbents are continuously transferred to a desorber and heated to 80~120°C for CO_2 desorption. Finally, the desorbed sorbents are sent to the cooler for and cooled to the desired for adsorption. The above cyclic TSA process requires the study of bed-to-wall heat transfer characteristics of the sorbent in a fluidized bed unit.

To date, there have been numerous efforts paid to investigate bed-to-wall heat transfer in gas-solids fluidized beds. However, most of these studies associated with dense fluidized beds (especially experimental studies) were conducted in fluidized beds with Geldart A or C particles [4-6]. Only a few published studies on bed-to-wall heat transfer in fluidized beds of Geldart B particles can be found in literature. The only existing studies do not involve a systematic study of the solid amine sorbents used for the CFB-TSA carbon capture process [7]. This has resulted in a lack of fundamental data for industrial design and optimize of heat exchangers in adsorbers, desorbers, and coolers. In addition, as a new novel particle, solid amine sorbents have different physical property parameters from those of the common particles such as FCC catalyst, silica and so on. Therefore, there is still lacking knowledge of the flow and heat transfer characteristics of this kind of particle.

In this study, heat transfer characteristics of a novel solid amine sorbent in the bubbling and turbulent flow regimes has been carried out systematically. Based on the experimental results, guidelines for industrial heat exchanger design based on solid amine sorbents are given.

2. Experimental Sections

2.1 Materials

The solid amine sorbent used in this study is a high spherical particle synthesized by an in-situ polymerization method. Its average particle size is 572 μm, the bulk density and particle density of the sorbent are measured to be 480 kg/m³ and 716 kg/m³ respectively, so the sorbent particle is categorized in Geldart's group B. For more details about this sorbent, please refer to our previous study [8-10].

2.2 CFB cold model unit

The heat transfer as well as hydrodynamic characteristics of this sorbent particle were obtained in a large-scale circulating fluidized bed (CFB) cold model unit as shown in Fig. 1. The air for fluidization was supplied by a Roots blower (1) and controlled by the globe valves (3) and rotameters (4). The air passing through the riser (11) was distributed by a pre-lifter (12) with a ring distributor (6) inside, and the air passing through the dense bed (7) was also distributed by a ring distributor (6). Serval holes with a diameter of 3 mm were evenly opened on the ring distributor (6) to realize the hole friction of 0.4 %. Solid circulating rate of the sorbent was controlled by a rotary feed (5), which has been calibrated before the experiment. Particles entrained from the column are collected by a cyclone (10) and returned to the dense bed (7). The unit can realize the continuous operation of the sorbent particle under whole flow regimes such as bubbling, turbulent and fast fluidized regimes.

Besides, some measuring points are set up on the unit to facilitate the measuring of heat transfer and hydrodynamic parameters. Among them, h_1-h_4 represent the axial installing locations of the heat transfer probe (introduced in Section 2.3) and T_1-T_4 are the corresponding bed temperature measuring points at axial center of the heat transfer probe. O_1-O_4 represent the axial installing locations of the optical fiber probes (introduced in Section 2.4).
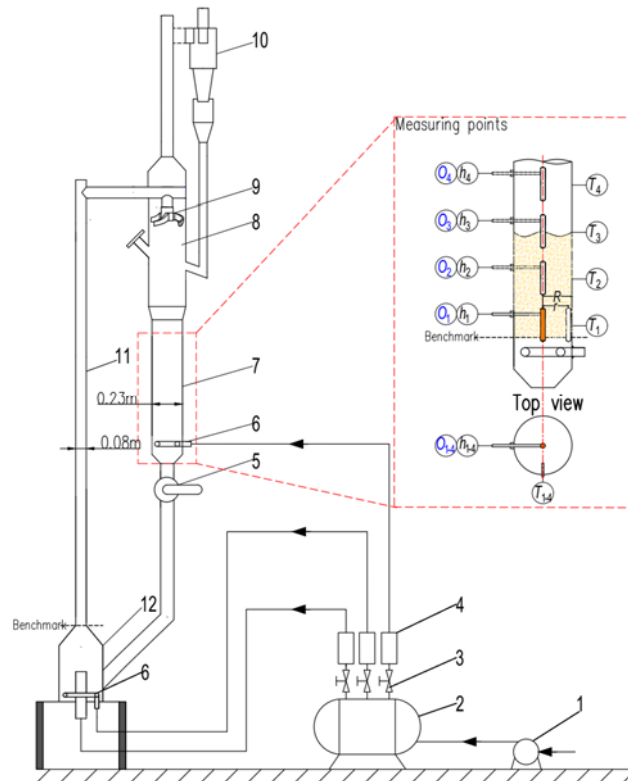
1 Roots blower; 2 surge tank; 3. globe values; 4 rotameters; 5 rotary feed; 6 ring distributor; 7 dense bed; 8 disengage; 9 vortex quick separator;10 cyclone; 11 riser; 12 pre-lifter;
(h_1-h_4: axial installing locations of the heat transfer probe; O_1-O_4: axial installing locations of optimal fiber probers; T_1-T_4: bed temperature measuring points)
Fig. 1 Schematic diagram of the large-scale CFB cold model unit.

2.3 Measurement of heat transfer coefficient

The bed-to-wall heat transfer coefficients were measured by a heat transfer probe, whose detailed structure is illustrated in Fig. 2. Ni-Cr heating wire was wound around a hollow cylindrical ceramic core, and this assembly was inserted in a copper shell (outer diameter 0.02 m, length 0.12 m). Copper was selected here to guarantee an even wall temperature. The annular space between the ceramic core and copper shell was filled with thermal grease to increase heat conduction. The heating wire was connected to an adjustable voltage AC power supply (STG-500 W). A T-type chip thermocouple was glued inside the copper shell. The heater was supported and positioned at different axial and radial locations by a Teflon supporting tube, and the supporting tube was connected to the copper shell wall by a threaded flange and gasket which were used to avoid gas or particles leakage. All the wires connecting heating wires and thermocouple wires were led through the ceramic core and then through the support tube to outside. For each measurement, there is a corresponding T-type rod thermocouple used to measure the bed temperature. The bed-to-wall heat-transfer coefficient was calculated by

$$h = \frac{Q_{in}}{A_w(T_w - T_b)} = \frac{UI}{A_w(T_w - T_b)} \qquad (1)$$

Here, Q_{in} (W) is the input flux of the heating wire, which is calculated by multiplying the voltage U (V) and current I (A) obtained from the AC power supply. A_w (m^2) is the contacting area between the copper shell and the sorbent bed, i.e. the external areas of a cylinder two cones of the copper tube. T_w (℃) and T_b (℃) is the temperature of the copper shell wall and bed respectively, where T_w is obtained by the T-type chip thermocouple glued inside the copper shell wall, and Tb is the temperature of the T-type rod thermocouple inside the bed. In order to ensure the representativeness of the data, a data acquisition program was used to record the values of T_w and T_b for one minute at one second intervals when they reached stability, and the average value of T_w and T_b are finally used to calculate the bed-to-wall heat transfer coefficient.
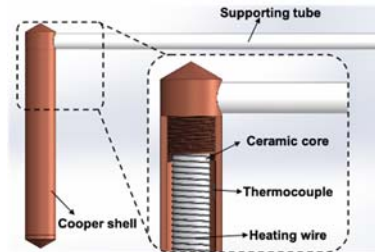
Fig. 2. Schematic of the internal structure of the heat transfer probe.

The heat transfer characteristics in bubbling and turbulent fluidized regimes were performed in the dense bed (7), where h was measured at four axial locations (h_1-h_4) and three radial locations (r/R=0, 0.5, 0.9) in the Ug range from 0.07-1.05 m/s. All the above measuring points are marked in Fig. 1.

2.4 Measurement of hydrodynamics

To explain the heat transfer phenomenon, local particle concentration ε (%) at the corresponding measuring position of h was measured by optical fiber probes (Institute of Processing Engineering, Chinese Academy of Science) at a sampling frequency of 5000 Hz. This type of probe has been widely introduced by others. Prior to measuring, each optical fiber probe was calibrated with the sorbent particles in the dense bed (7).

3. Results and discussion

3.1 Effect of superficial gas velocity

The effect of U_g on h at different radial locations were plotted in Fig. 3. It can be seen that in the central region (i.e. r/R=0-0.5), h first increases, then reaches a maximum value, and finally decreases with the increasing U_g. Similar trends have been widely reported by others [5,6,11,12],

which can be explained by the packet renewal theory [13]. As expressed in Equation (2), the packet renewal frequency f_{pa} (the reciprocal of mean packet residence time τ_{pa}) and the time fraction of packet δ_{pa} on the probe surface are the two main hydrodynamic parameters influencing h in our experiment. Qualitatively, f_{pa} is positively related to the number of bubbles on the probe surface, which increases as U_{g} increases. While δ_{pa} is positively related to the ε on the probe surface, which decreases as U_{g} increases due to the increase in the proportion of bubble phase. Under their counterbalanced effect on h, there exists an U_{opt}, before U_{opt}, ε in the central region is relatively high, so the variation of h with the increasing U_{g} is mainly controlled by the increase of f_{pa} on the probe surface, which facilities increasing h. After U_{opt}, however, ε in the central region has decreased to a relatively low level, so the variation of h with the increasing U_{g} is mainly controlled by the decrease of δ_{pa} on the probe surface, which results in the decrease of h.

$$h = 2\delta_{\text{pa}} \left[\frac{k_{\text{pa}} \rho_{\text{pa}} c_{\text{pa}}}{\pi \tau_{\text{pa}}} \right]^{1/2} \propto f_{\text{pa}} \delta_{\text{pa}} \tag{2}$$

In addition, for typical Geldart A particles (e.g. FCC catalyst), the U_{opt} for the optimal h is located near the onset of the turbulent fluidization regime [5,6]. For the coarser Geldart B particle (e.g. the DRC-I used in this study), however, U_{opt} was found to appear within the bubbling fluidized regime, which is consistent with previous publications on Geldart B particle [13-15].

In the wall-side region (i.e. r/R=0.98), however, h monotonically increases with the increasing U_{g} [6], which is different with that in the central region. Because unlike in the central region, ε in the wall-side region is always at a relatively high level in the tested U_{g} range of this study because particles in this region mostly move downward in a dense form, indicating that the variation of h is dominated by f_{pa}. As U_{g} increases, the faster downward speed of particles as well as more bubbles in the wall-side region increase the f_{pa} on the probe, thus increases the h monotonically. However, there should also be a critical value of U_{g}, after which h in the wall-side region begins to decrease. But due to different flow structures in the two regions, the optimal h value in the wall-side region reaches later than that in the central region.
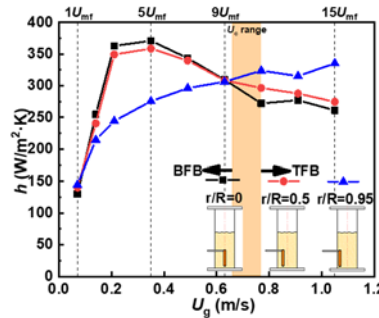
Fig. 3. Effect of U_{g} on h at different radial locations at axial location of h_1.

3.3 Effect of radial locations

The results in Fig. 3 also reveal another interesting phenomenon, that is, before the U_{c} range, the h value in the central region is higher than that in the wall-side region, while the above phenomenon is opposite after the U_{c} range. Therefore, three typical U_{g}s, namely U_{g} in fully bubbling fluidized regime, at the onset of turbulent fluidized regime and in fully turbulent fluidized regime are chosen to explore the radial profiles of h in Fig. 4, and the phenomenon are further explained by the packet renewal theory [13].

In fully bubbling fluidized regime (U_{g}=5U_{mf}) in Fig. 4(a), h is higher in the central region and decreases as the location approaches the wall-side region. This is commonly found in previous studies using Geldart A and B particles in the bubbling fluidized regime [4,5,15,16]. As mentioned in Section 3.1, both δ_{pa} and f_{pa} determine the value of h based on the packet renewal theory [13]. Among them, the varying trend of δ_{pa} can be qualitatively determined by the ε in Fig 5(b) because δ_{pa} is positively related to ε. And the varying trend of f_{pa} can be qualitatively

determined by the instantaneous ε signals in Fig 5(a), where the bubbles are comprised with many steep troughs. In Fig. 5(a), there are more bubbles in the central region than those in the wall-side region when $U_g=5U_{mf}$, indicating more packet renewal frequency f_{pa} on probe surface in the central region of the bed. Due to wall effect, it is difficult to form bubbles in the wall-side region, which enables packets to stay on tube surface longer and become a resistance of heat transfer. Therefore, h is higher in the central region and lower in the wall-side region. In addition, h is distributed more evenly along the radial direction in the dilute phase region such as locations h_3 and h_4, because there are fewer particles in the dilute phase region so that the wall effect is smaller.

At the onset of turbulent fluidized regime ($U_g=9U_{mf}$) in Fig. 4(b), h in the central and wall-side regions are numerically close, which means that the heat transfer in the same cross-section of the bed is more uniform under this operation condition. By further increasing U_g to the level that the bed reaches fully turbulent fluidized regimes ($U_g=15U_{mf}$) in Fig. 4(c), h in the wall-side region is even higher than that in the central region, which has never been reported before. The above radial profiles of h in turbulent fluidized regime can also be explained by the packet renewal theory [13]. As shown in Fig. 5(a), although there are obviously more bubbles in the central region at $9U_{mf}$ and $15U_{mf}$, which indicates higher f_{pa} on the probe surface. However, this also results in a lower ε in the central region. Specifically, at the onset of turbulent fluidized regime, ε in the central region is 30.2% lower than that in the wall-side region, and in the fully turbulent regime, this difference of ε between central and wall-side region even increases to 61.8%. At this time, the variation of h in different radial locations is mainly controlled by δ_{pa} rather than f_{pa} on the probe surface. Therefore, the interesting phenomenon that h in the central region is lower than that in the wall-side region appears in this study.
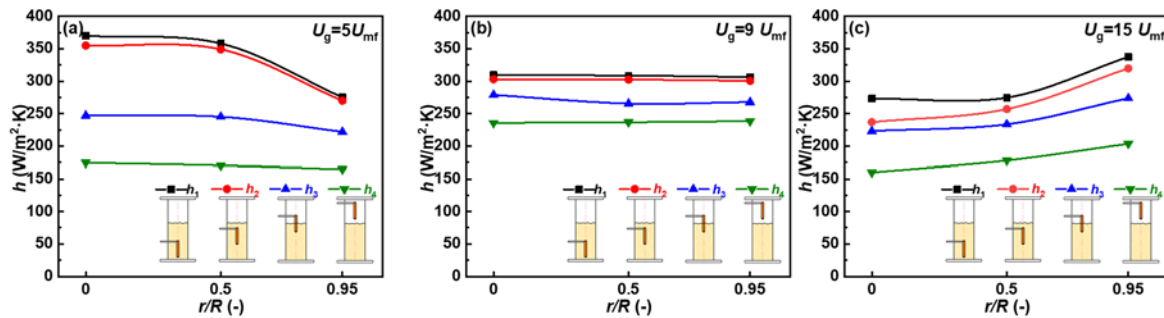
Fig. 4. Radial profiles of heat transfer coefficient at different heights at different fluidized regimes: (a) fully bubbling fluidized regime at $5U_{mf}$; (b) onset of turbulent fluidized regime at $9U_{mf}$; (c) fully turbulent fluidized regime at $15U_{mf}$.
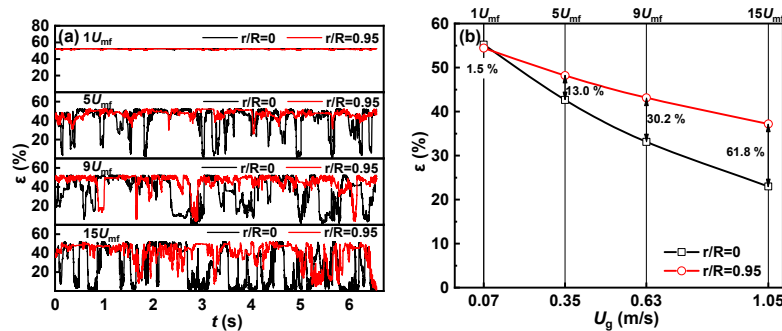
Fig. 5. Instantaneous (a) and average (b) particle concentration measured at the axial location h_2 at different radial positions and superficial gas velocities

4. Conclusion

This study systematically investigated the bed-to-wall heat transfer characteristics of a solid amine sorbent under bubbling and turbulent flow regimes. The following major conclusions can be drawn:

1. In the central region, the optimal h of the Geldart B sorbent particle used in this study lies within the bubbling fluidized regime, unlike typical Geldart A particle (e.g. FCC catalyst) whose optimal h is located near the onset of turbulent fluidized regime. Due to the different flow structures, the optimal h value in the wall-side region reaches later than that in the central region.

2. Due to the counterbalanced effect of δ_{pa} and f_{pa}, h is higher in the central region and lower in the wall-side region in bubbling fluidized regime. While the above phenomenon is opposite in turbulent fluidized regime.

3. Industrially, high and uniform heat transfer coefficients can be obtained by controlling the operating gas velocity near the onset of turbulent fluidized regime.

Acknowledgment

References

[1] Van Paasen S, Infantino M, Yao J, et al. Development of the solid sorbent technology for post combustion CO_2 capture towards commercial prototype[J]. International Journal of Greenhouse Gas Control, 2021, 109: 103368.

[2] Bao X, Ma J, Wu Y, et al. Gas-particle flows in a two-stage integrated bubbling-transport fluidized bed for CO_2 capture[J]. Industrial and Engineering Chemistry Research, 2022, 61(25): 8973-8981.

[3] Raganati F, Chirone R, Ammendola P. CO_2 capture by temperature swing adsorption: working capacity as affected by temperature and CO_2 partial pressure[J]. Industrial and Engineering Chemistry Research, 2020, 59(8): 3593-3650.

[4] Yao X, Zhang Y, Lu C, et al. Systematic study on heat transfer and surface hydrodynamics of a vertical heat tube in a fluidized bed of FCC particles[J]. AIChE Journal, 2015, 61(1): 68-83.

[5] Stefanova A, Bi H T, Lim J C, et al. Local hydrodynamics and heat transfer in fluidized beds of different diameter[J]. Powder Technology, 2011, 212(1): 57-63.

[6] Stefanova A, Bi H T, Lim C J, et al. Heat transfer from immersed vertical tube in a fluidized bed of group A particles near the transition to the turbulent fluidization flow regime[J]. International Journal of Heat and Mass Transfer, 2008, 51(7): 2020-2028.

[7] Blaszczuk A, Jagodzik S. Heat transfer characteristic in an external heat exchanger with horizontal tube bundle[J]. International Journal of Heat and Mass Transfer, 2020, 149: 119253.

[8] Xu C, Zhang Y, Peng Y-L, et al. Degradation characteristics and utilization strategies of a covalent bonded resin-based solid amine during capturing CO_2 from flue gas[J]. Separation and Purification Technology, 2024, 331: 125621.

[9] Xu C, Zhang Y, Yang T, et al. Adsorption mechanisms and regeneration heat analysis of a solid amine sorbent during CO_2 capture in wet flue gas[J]. Energy, 2023, 284: 129379.

[10] Xu C, Zhang Y, Peng Y-L, et al. Probing the differences in CO2 adsorption/desorption behaviors of solid amine sorbents in fixed and fluidized beds[J]. Separation and Purification Technology, 2024, 343: 127171.

[11] Hofer G, Schöny G, Fuchs J, et al. Investigating wall-to-bed heat transfer in view of a continuous temperature swing adsorption process[J]. Fuel Processing Technology, 2018, 169: 157-169.

[12] Martin H. Heat transfer between gas fluidized beds of solid particles and the surfaces of immersed heat exchanger elements, part I[J]. Chemical Engineering and Processing: Process Intensification, 1984, 18(3): 157-169.

[13] Mickley H, Fairbanks D F. Mechanism of heat transfer to fluidized beds[J]. AIChE Journal, 1955, 1(3): 374-384.

[14] Melerus O, Mattmann W. Heat transfer mechanisms in gas fluidized beds. part 1: Maximum heat transfer coefficients[J]. Chemical Engineering & Technology: Industrial Chemistry‐Plant Equipment‐Process Engineering‐Biotechnology, 1992, 15(3): 139-150.

[15] Pisters K, Prakash A. Investigations of axial and radial variations of heat transfer coefficient in bubbling fluidized bed with fast response probe[J]. Powder Technology, 2011, 207(1): 224-231.

[16] Hofer G, Schöny G, Pröll T. Acting on hydrodynamics to improve the local bed-to-wall heat transfer in bubbling fluidized beds[J]. Chemical Engineering Research and Design, 2018, 134: 309-318.

STUDY ON MOVING BED HEAT EXCHANGERS WITH GRADUALLY SHRINKING AND EXPANDING TUBE

Li zhihan[1], Lu Weiqin[2], Zhou Tuo[2]*, Liu Yongqi[1]

[1] School of Transportation and Vehicle Engineering, Shandong University of Technology, 255049 Shandong, China

[2.] Key Laboratory for Thermal Science and Power Engineering of Ministry of Education, Department of Energy and Power Engineering, Tsinghua University, Haidian District, 100084 Beijing, China

Email: zhoutuo@mail.tsinghua.edu.cn

Abstract

This paper analysis the effect of gradually shrinking and expanding tube as heat exchange tube in moving bed heat exchanger using discrete element method and compare with same volume cylindrical tube heat exchange tube. Through the analysis of contact force and granular flow condition, we find that this kind of tube may not have better granular flow conditions than cylindrical one under this condition. We shall do some further analysis under different conditions in the future to verify whether GSE tube is suitable for MBHE.

1. Introduction

High temperature solid slag, which mostly in micron-level, millimeter-level and centimeter-level, is widely produced as a by-product in many kinds of industry such as iron and steel making, coke industry, chemical industry and so on. Because of that, if we use a method to recover these waste heat and put them into good use, it can not only save considerable amount of energy, but also avoid environmental pollution caused by waste heat emissions [1~3].

Based on above reason, many kinds of waste heat recover methods are opened up and further developed in recent years, these methods can roughly be divided into two parts: wet methods and dry methods. Wet methods, mostly use water to quenched slag, are developed and used much earlier than dry ones because of its lower cost, simpler device (mostly only need a container and some tubes as the inlet and outlet of material) and developed technology so far. But compare with dry methods, water quenched method also have lots of water needed and smaller applicability (we may need an extra purifier system if we use water to cool down some nitrogen-containing slag or sulfur-containing slag in order to eradicate toxic and corrosive by-product produced during water quenched process). Because of that, dry methods gain more and more concerned in recently years with the development of technology [4].

Dry methods to recover waste heat from high temperature slag, for example, atomization by rotary cup, rotary disc or rotary drum [5~9], circulating fluidized bed [10~12], often have higher established cost and more complex system, however, the technology development already make some dry methods have even higher efficiency. Other methods, which may too fuzzy to be divided into these two parts, are also developed to recover the waste heat such as chemical methods [13].

Moving bed with heat exchanger system, (i.e. MBHE) one kind of dry method, is widely used to recover waste heat from high temperature solid slag as its simple structure, satisfactory efficiency, easily controlled system, sustainable working and other characteristics [14]. Many researchers put their effort to work on different aspects, like heat exchange efficiency, slag shape and size, tube ratio, flow speed, friction constant, tube arrangement method [15] and so on, and achieve some improvements.

There are several experiments and simulation around the shape of tube and angle of horizonal tubes MBHE. Tian et.al [16] research the influence of hexagonal tube on the granular flow and heat exchange efficiency, the result show that the hexagonal tube indeed has influence to both compare with circulate tube or ellipse tube but depends on the angle of above and bottom of

the tube, bigger angle lead to better upper flow and heat exchange condition, smaller angle lead to better lower condition. The same research team also design an elliptical-like heat exchange tube [17], the result shows that the elliptical-like tube has better granular flow condition and heat exchange efficiency than circular tube and has better flexural capacity than both circular tube and ellipse tube. Some more active methods are also researched like import oscillation or rotary rod to try to improve the efficiency of MBHE [18,19], but these methods face a same problem: part of recover energy is used to drive these devices work.

Guo et.al [20] research the influence of oblique single tube on the distribution of motion and temperature decline, the result shows that the higher region at upper of oblique single tube has better granular flow condition, meanwhile, slag at the lower region are squeezed or even stun in the acute angle between tube and wall. Based on above and our preliminary study about hopper shape which will be mentioned below [21], a gradually shrinking and expanding (GSE) tube is designed and analyzed using discrete element method.

2. Tube design and simulation setting

2.1 Tube design

The traditional tube can treat as a rotating body of rectangle, The gradually shrinking and expanding shape of tube is also can treat as a rotating body by a 2D face, but one of long edge is replaced by an arc of an ellipse, the process is as Fig.1 shows:

Use this type of tube, right angles between tube and wall are replaced by obtuse angles, especially top area of the tube, which matters the granular stagnation. In our inference, this shape can make the flow channel much like cylindrical instead of rectangular hopper and orifice, the vertical view of tube distribution inside is shown in Fig.2. Worth to be noticed, GSE tube is quite different from converging-diverging tube because GSE tube's target is not to change the flow condition of the inside fluid, but to change the shape of outside granular flow channel.

In detail, compare with the cylindrical tube, GSE tube cannot provide a radical force except center of tube, besides, but also only obtuse are exist angles at the connection area between tube and wall, which may means less quantity sum of force provided by tube and wall. in another word, stable structure will have less possibility to form in the granular flow.
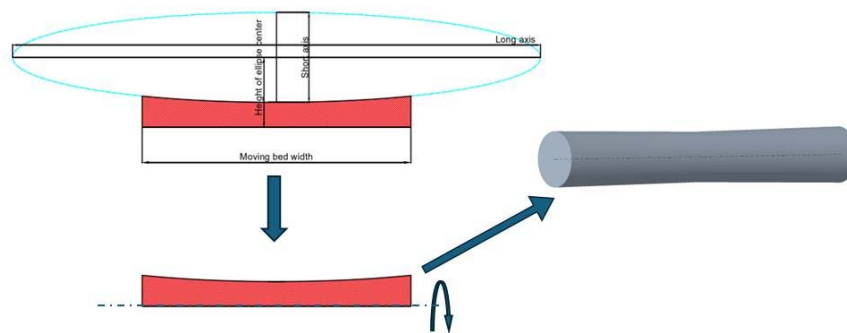
Fig.1 Gradually shrinking and expanding tube construct process

(a)   (b)
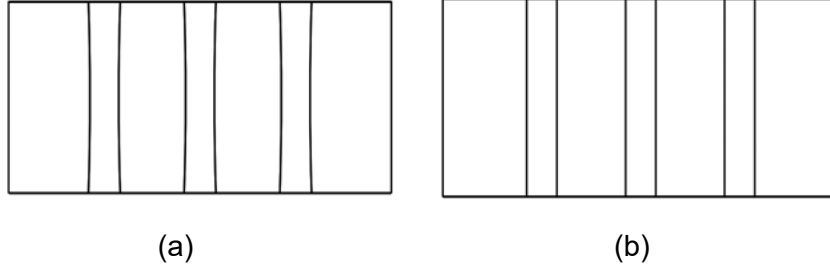
Fig.2 vertical view of two kind of moving bed((a): GSE tube (b): cylindrical tube)
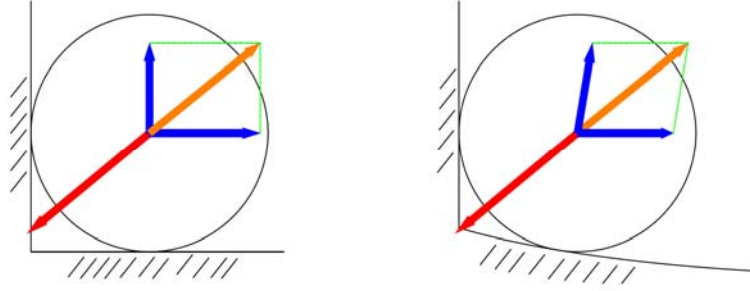
Fig.3 connection area of two kind of moving bed (red arrow: total force provided by other slag, blue arrow: force provided by wall and tube, orange arrow: total force provided by wall and tube, equal value to the red one but in opposite direction)

We also set a control group which use cylindrical tube with the same volume as GSE tube. The details of these tubes are listed in Table.1:

Table.1 parameters of two kind of tube and distribution method

Parameter name	Gradually shrinking and expanding tube	Cylindrical tube
Width of moving bed(m)	0.200	
Length of ellipse long axis(m)	0.400	
Length of ellipse short axis(m)	0.012	
Height of ellipse center(m)	0.027	
Diameter of tube(m)		0.035*
Volume of tube(m^3)	1.457*10^{-4} *	

(*: approximately value)

2.2 Simulation by discrete element method (DEM)

We use EDEM simulator to verify the actual influence of GSE tube, which is widely used in many researches [16,18,22] . Use Newton's second law to solve the particle motion in each time step, which consider the gravity and the interaction force between contacting force. The basic equation of each particle's translational and rotational motion are shown in eq.(1) and eq.(2) [22,23] :

$$m_i \frac{dv_i}{dt} = \boldsymbol{F_g} + \sum_{j=1}^{n} \boldsymbol{F}_{nij} \qquad (1)$$

$$I_i \frac{d\omega_i}{dt} = +\sum_{j=1}^{n} \boldsymbol{T}_{ij} \qquad (2)$$

Where m_i, v_i, I_i, ω_i are respectively the mass, velocity, rotational inertia and angular velocity of particle i, F_g is the gravity force, F_{nij} and T_{ij} are the radical force and moment of force from particle j to particle i, where T_{ij} can be calculated by the following method:

$$T_{ij} = r_i n_i \times F_{tij} \tag{2.1}$$

Where F_{tij} is the tangential force from particle j to particle i, r_i is the distance between contact point and particle center, n_i is the unit directional vector. The calculation method of F_n and F_t can be find in reference [22~24].

2.3 MBHE parameters setting

In order to imitate the gravity-driving moving package bed, we use a plane under the tube distribution area to brace pellets and keep them moving downward in a constant velocity, the velocity of plane is 2mm/s [16], tubes are staggered arranged in five horizontal layers, which is shown in Fig.4. Based on above setting, moving bed can be divided into two areas: tube arranged area and side area(two area are distinguished by vertical. Simulation pellets' parameters are same as Table.2, which is similar to alumina pellets' parameters, tubes' parameters are set as Table.1. Other parameters are listed in Table.3.

To verify the impact on the uniformity of granular flow in GSE tubes, besides common analysis, we also mark a thin layer of particles to help us confirm the disturbance in the process, and a parameter φ is defined by the following equation:

$$\varphi = \frac{\sum_{i=1}^{n} \Delta y_i}{n}$$

Δy_i is the vertical distance between the bottom marked particle and marked particle i in tubes arranged area. Because the particles in side area have similar vertical velocity in GSE tube MBHE and traditional cylindrical tube MBHE, parameter φ can describe the uniformity very well of granular flow, so that lower φ means better flow condition.

Table.2 simulation parameter setting in MBHE:

Parameter name	value
Pellets quantity	30000
Initial package height(m)	0.65
Pellets density(kg/m^3)	3600
Pellets diameter(m)	0.01
Poisson's ratio	0.22
Young's modulus	1.64*10^{10}
Wall friction angle(°)	5.2
Internal friction angle(°)	1.6

Table.3 Other parameters setting in MBHE

Parameter name	Value
Width of moving bed(m)	0.200
Length of moving bed(m)	0.400
Distance between two tube centers in same layer(m)	0.100
Distance between two tube layers(m)	0.100
Total number of particles	50000
Number of marked particles	500

3. Result and discussion

First of all, considered the particle exchange between tubes arranged area and side area, we count the change rate of total marked particle quantity in tubes arranged area by time advancing, this value is within the range of 940 to 1120, which means that the error caused by particles exchanging is acceptable. And we choose the central tube in the third layer as the count tube, which is at the central of tube displacement area.
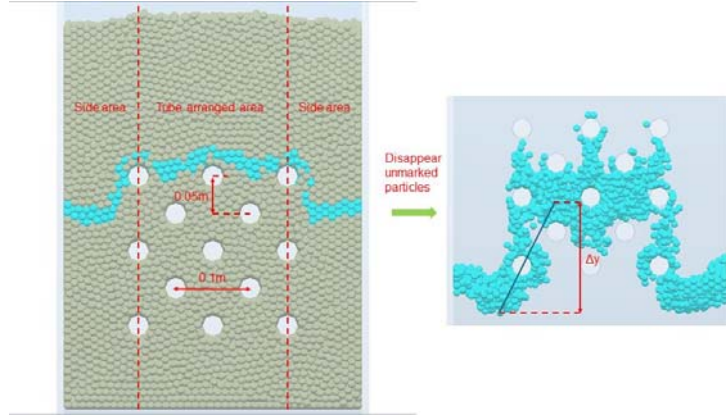
Fig.4 Geometry of MBHEs in this simulation
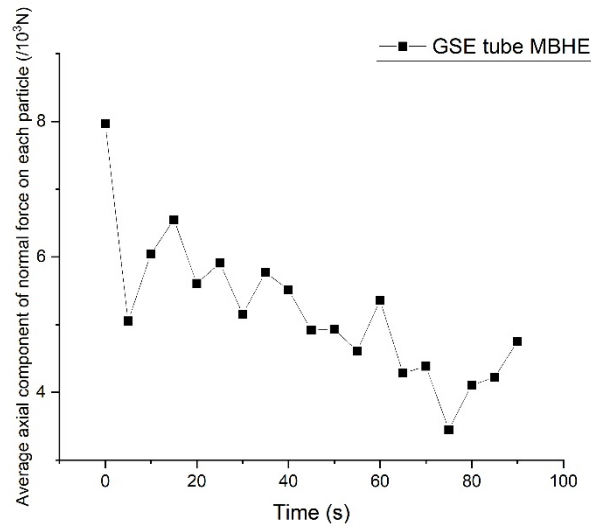
Fig.5 The vary of average axial component of total tube force along the time in GSE tube MBHE

3.1 Contact force between pellets and tubes or walls

To verify the propose our make above, the average axial component of normal force between each particle and two kinds of tubes are counted and summed, without doubt, the vary of force along the time in GSE tube MBHE are shown in Fig.5:

It can be clearly seen that an axial force appears and slowly decreases with the granular flow progress (because the total number of particles is a constant value), besides, without doubt, the number in cylindrical tube MBHE is nearly zero(the biggest value is less than 10-14N, because normal kind of tube can only provide radical force. From Fig.5, we can realize a small angle can obviously change the force distribution.

The total force at same time in two kinds of MBHE are counted, but because of the outer surface area difference between GSE tube and cylindrical tube, the numbers of contact

particles in each time is different, for this reason, we count the average force on each particle, which is calculated by the normal force divided by the number of contacting particles. The result is shown in Fig.6.

We can see from Fig.6 that most of times, each particle in GSE tube MBHE stand more normal force from tubes than normal cylindrical one as we proposed.
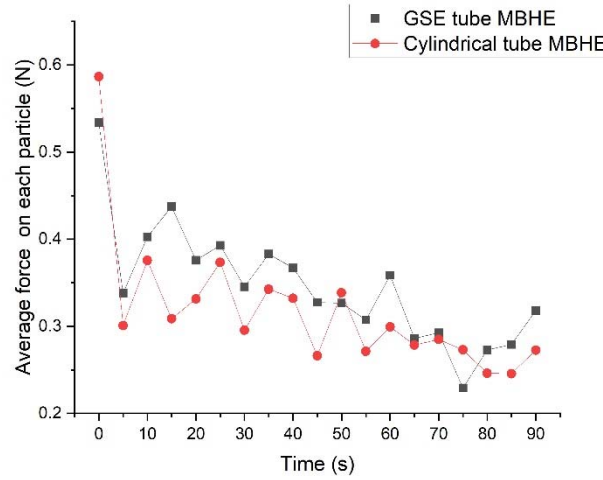
Fig.6 The average force between the tube and each particle in two kinds of MBHEs at certain time

However, bigger normal force may also become a reason lead to poor flow condition, which means more static and sliding friction forces between particles and tubes. The average normal force between wall and each particle around the tube are shown in Fig.7:

Unfortunately, it is hard to say GSE tube can really decrease the normal force between the wall around the tube and each particle from Fig.7, which means GSE tube MBHE don't have less quantity sum of force.
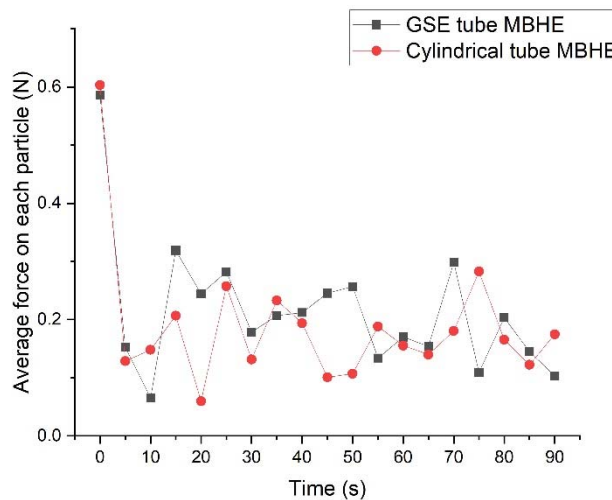
Fig.7 The average force between the wall around the tube and each particle in two kinds of MBHEs at certain time

3.2 Granular flow analysis

We compare parameter φ changes over time in GSE tube MBHE and normal cylindrical tube MBHE to judge whether GSE tube MBHE has more uniform flow conditions. The result is shown in Fig.8.
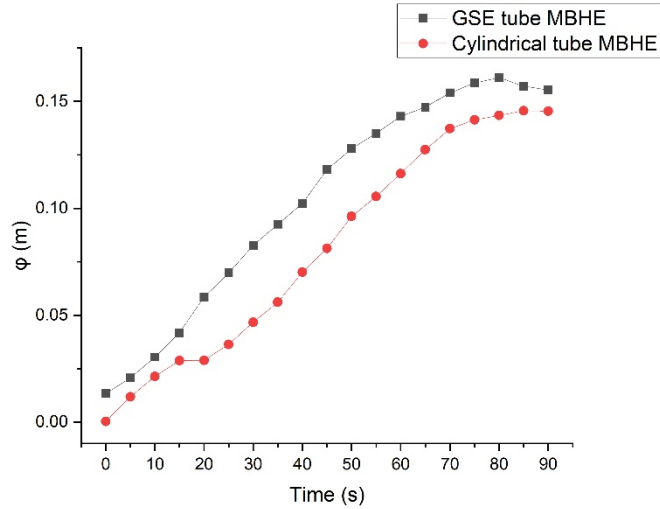
Fig.10 φ changes over time in two kinds of MBHEs

Fig.10 shows that the φ in GSE tube MBHE is bigger than the cylindrical one, which explains that GSE tube MBHE has even more ununiform flow conditions than the cylindrical one from the beginning to the end.

4. Conclusion

In this research, we design a gradually shrinking and expanding tube moving bed heat exchanger, analysis particle contact force and granular flow conditions in this MBHE by comparing with traditional cylindrical tube MBHE, the conclusion are as follows:

1. The GSE tube can provide a component of normal force along the axial of tube, based on this the average total normal force is bigger than cylindrical one, but the normal contact force between the wall around the tube and each particle don't decrease obviously.

2. The flow condition in GSE tube MBHE is worse than cylindrical one, we think the reason led to this result is bigger normal force cause bigger friction force between tubes and pellets.

Acknowledgment

References

[1] Lu, W., Ma, C., Liu, D., Zhao, Y., Ke, X., & Zhou, T. A comprehensive heat transfer prediction model for tubular moving bed heat exchangers using CFD-DEM: Validation and sensitivity analysis. Applied Thermal Engineering, 2024.247, 123072.
[2] Prause, M., Schulz, H. ‐ J, & Wagler, D. Rechnergestützte Führung von Fermentationsprozessen, Teil 2. Acta Biotechnologica, 1984.4(2), 143‒151.
[3] Cheng, Z., Guo, Z., Tan, Z., Yang, J., & Wang, Q.. Waste heat recovery from high-temperature solid granular materials: Energy challenges and opportunities. Renewable and Sustainable Energy Reviews,2019. 116, 109428.
[4] Wang, H., Wu, J.-J., Zhu, X., Liao, Q., & Zhao, L.. Energy–environment–economy evaluations of commercial scale systems for blast furnace slag treatment: Dry slag granulation vs. water quenching. Applied Energy, 2016.171, 314–324.
[5] He, W., Lv, X., Pan, F., Gao, L., Li, X., & Qiu, J.. Granulation of ferrosilicon alloy by rotary multi-nozzles cup atomizer: Granulation behavior and model formation. Advanced Powder Technology, 2019.30(5), 895–902.

[6] Wu, J., Tan, Y., Li, P., Wang, H., Zhu, X., & Liao, Q. Centrifugal-Granulation-Assisted thermal energy recovery towards low-carbon blast furnace slag treatment: State of the art and future challenges. Applied Energy, 2022.325, 119835.

[7] Sunkara, K. R., Herz, F., Specht, E., Mellmann, J., & Erpelding, R.. Modeling the discharge characteristics of rectangular flights in a flighted rotary drum. Powder Technology, 2013.234, 107–116.

[8] Ardalani, E., Yohannes, B., Borghard, W. G., Glasser, B. J., & Cuitiño, A. M. DEM analysis of the thermal treatment of granular materials in a rotary drum equipped with baffles. Chemical Engineering Science,2022. 251, 117476.

[9] Ma, H., Liu, Z., Zhou, L., Du, J., & Zhao, Y. Numerical investigation of the particle flow behaviors in a fluidized-bed drum by CFD-DEM. Powder Technology, 2023.429, 118891.

[10] Esmaeili Rad, F., Abbasian, J., & Arastoopour, H. CFD simulation of a circulating fluidized bed carbon capture system using a solid-supported amine sorbent. Powder Technology, 2024.434, 119358.

[11] Pitié, F., Zhao, C. Y., Baeyens, J., Degrève, J., & Zhang, H. L. Circulating fluidized bed heat recovery/storage and its potential to use coated phase-change-material (PCM) particles. Applied Energy, 2013.109, 505–513.

[12] Zeng, B., Lu, X., & Liu, H. Influence of CFB (circulating fluidized bed) boiler bottom ash heat recovery mode on thermal economy of units. Energy, 2010,35(9), 3863–3869.

[13] Akiyama, T., Oikawa, K., Shimada, T., Kasai, E., & Yagi, J. Thermodynamic Analysis of Thermochemical Recovery of High Temperature Wastes. ISIJ International, 2000.40(3), 286–291.

[14] Soria‐Verdugo, A., Almendros‐Ibáñez, J. A., Ruiz‐Rivas, U., & Santana, D. Exergy Optimization in a Steady Moving Bed Heat Exchanger. Annals of the New York Academy of Sciences, 2009.1161(1), 584‐600.

[15] Qi, C., Zhang, Z., Wang, M., Li, Y., Gong, X., Sun, P., & Zheng, B. Effects of the structure parameters of horizontal tube bundles on particle flow performance in the heat exchanger. Case Studies in Thermal Engineering,2023. 47, 103053.

[16] Tian, X., Yang, J., Guo, Z., Wang, Q., & Sunden, B. Numerical study of heat transfer in gravity-driven dense particle flow around a hexagonal tube. Powder Technology, 2020.367, 285–295.

[17] Tian, X., Guo, Z., Jia, H., Yang, J., & Wang, Q. Numerical investigation of a new type tube for shell-and-tube moving packed bed heat exchanger. Powder Technology, 2021.394, 584–596.

[18] Guo, Z., Zhang, S., Tian, X., Yang, J., & Wang, Q. (2020). Numerical investigation of tube oscillation in gravity-driven granular flow with heat transfer by discrete element method. Energy, 207, 118203. https://doi.org/10.1016/j.energy.2020.118203

[19] Jiang, B., Xia, D., Zhang, H., Pei, H., & Liu, X. Effective waste heat recovery from industrial high-temperature granules: A Moving Bed Indirect Heat Exchanger with embedded agitation. Energy, 2020.208, 118346.

[20] Guo, Z., Yang, J., Tan, Z., Tian, X., & Wang, Q. Numerical study on gravity-driven granular flow around tube out-wall: Effect of tube inclination on the heat transfer. International Journal of Heat and Mass Transfer, 2021.174, 121296.

[21] Beverloo, W. A., Leniger, H. A., & van de Velde, J. The flow of granular solids through orifices. Chemical Engineering Science, 1961.15(3–4), 260–269.

[22] Cundall, P. A., & Strack, O. D. L. A discrete numerical model for granular assemblies. Géotechnique, 1979.29(1), 47–65.

[23] Cleary, P. W., & Sawley, M. L. DEM modelling of industrial granular flows: 3D case studies and the effect of particle shape on hopper discharge. Applied Mathematical Modelling,2002. 26(2), 89–111.

[24] Guo, Y., Chen, Q., Xia, Y., Klinger, J., & Thompson, V. (2021). A nonlinear elasto-plastic bond model for the discrete element modeling of woody biomass particles. Powder Technology, 385, 557–571.

EXPERIMENTAL STUDY OF PARTICLE MOTION AND COLLISION WITHIN ASH BANDS IN CYCLONE SEPARATORS

He Meng[1,2], Jian-Yi Chen[1,2]*, Ming-Qian Cao[1,2], Yao-Dong Wei[2]

1 State Key Laboratory of Heavy Oil Processing, China University of Petroleum, Beijing 102249, P.R. China.

2 Beijing Key Laboratory of Process Fluid Filtration and Separation, 102249, P.R. China.

*Email: jychen@cup.edu.cn

Abstract

In cyclone separators, the ash bands were frequently observed on the wall surface, which were formed by the separated particles and rotated down. The particles move downward along the wall, interacting strongly with each other and the wall. Hitherto, movement parameters have been indirectly obtained, making it difficult to clearly describe the microscopic behavior of particle movement near the wall. In this paper, the collision and motion of particles within the ash band of a cyclone separator are studied experimentally. The experiments were conducted on a ϕ160 mm cyclone at inlet velocity of 12, 16, 20 m/s and inlet concentration of 30, 50, 70 g/m^3, with catalyst serving as experimental particles. The particle velocities were measured using the High-speed Particle Image Velocimetry (HPIV) method. The experimental results indicate that the particle velocity inside the ash band exhibit a significant reduction than the particle velocity outside the ash band, due to the aggregation of particles obstructed the airflow. As the ash band moves downward, its thickness increases due to the decrease in flow velocity and the accumulation of particles. Additionally, this study pioneers the establishment of a particle collision model within the ash band. Intriguingly, the results uncover a relationship between particle velocity pulsation and ash band concentration. Notably, smaller particle pulsation velocities corresponded to higher concentrations. The reliable data on particle movement and collision are essential to understand the gas- solid two-phase flow behavior inside the cyclone and improve its separation performance.

Key words: Cyclone separator, Ash band, Particle dynamic, Particle collision

1. Introduction

Cyclone separators utilize centrifugal force to separate gas and solid particles, providing advantages such as low operating costs, ease of maintenance, and high separation performance[1, 2]. In industrial settings, cyclone separators employed in fluidized bed reactors frequently generate ash bands as a result of particle aggregation, which can negatively impact separation efficiency and equipment lifespan[3, 4]. Studying the motion and collision of particles within the ash band is crucial for enhancing the performance of the cyclone separator. However, the complex flow field inside the cyclone separator restricts the availability of methods and studies for measuring particle motion and collisions within the ash band.

Computational Fluid Dynamics (CFD) offers an effective alternative method for studying the gas-solid two-phase flow field in cyclone separators. Numerous researchers have utilized different models to compute and analyze the characteristics of the flow field [5, 6]. However, in the near-wall region of a cyclone separator, the kinematic characteristics of the ash band deviate from those of the conventional advection and cyclonic fields. This is attributed to the effects of airflow trailing forces and mutual collisions between particles and the wall, as well as between particles themselves. Currently, there remains a dearth of studies on modeling the motion and collision of particles within the ash band on the wall.

To effectively observe and measure the motion and collision of particles within the ash band, a method is required that can accurately visualize it. High-speed cameras have the capability to measure instantaneous displacement changes over very short time periods. Hence, measurement points were experimentally arranged at various locations inside the cyclone separator in this study. This paper analyzes the change in thickness of the ash band and its mechanism by measuring the velocity change of particles both inside and outside the ash band, as well as the movement of the ash band. Additionally, a collision model for particles within the ash band is established to correlate particle velocity pulsation with the concentration of the ash band. Ultimately, this study proposes a model for characterizing the motion and collision of particles within a cyclone separator.

2. Experiment

2.1 Experimental setup

Fig. 1. presents the structure and geometrical parameters of the cyclone separator used for the experiments.

Parameter	Value
D (mm)	160
$a \times b$ (mm)	100×50
D_x/D	0.5
D_c/D	0.44
S/D	0.75
H/D	1.63
H_c/D	2
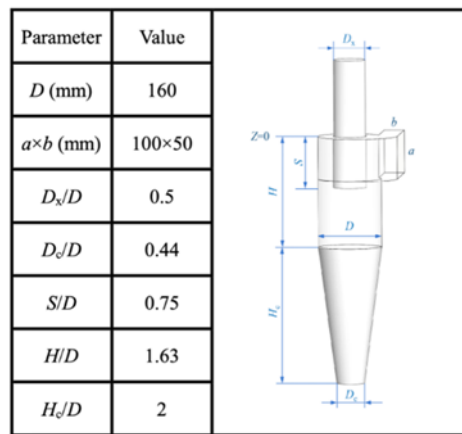
Fig. 1. Cyclone separator structure and dimensions schematic diagram

The high-speed camera system comprises a high-speed camera (Photron FA-X2) and three DSLRs (Canon EOS 60D). Illumination is provided by a 144w LED lamp, with a soft board featuring a white background positioned between the light source and the subject to minimize shadows and reflections while ensuring uniform lighting. Figure 2 illustrates the setup of the experiment, showing the arrangement of the high-speed camera unit and the pressure monitoring device.

Fig. 2. Experimental high-speed camera distribution

2.2 Experimental method

The High-speed Particle Image Velocimetry (HPIV) method[7] employs a high-speed camera to capture consecutive frames of images. A correlation algorithm is then utilized to identify the displacement of particles in the image. Subsequently, the velocity of the particles is calculated based on the displacement and the time interval between the two neighboring frames, as depicted in equation (1):

$$v_p = \frac{l_p}{\Delta t} \tag{1}$$

In the equation, v_p represents the particle velocity, l_p denotes the particle displacement, which is derived by converting the particle displacement and pixel scale between two frames in the viewport, and Δt signifies the time between two frames. Fig. 3. illustrates the positions of the particles in two consecutive frames (at times t_1 and t_2) in the recorded image. When employing the HPIV measurement technique, the projected velocity of the particles is determined based on the particle displacements within the viewport.
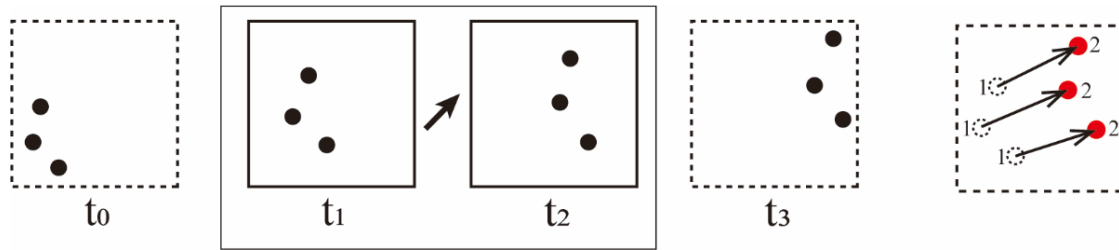
Fig. 3. HPIV velocity measurement schematic

3. Results and discussion

3.1 Particle motion in the ash band

Fig. 4. illustrates the tangential particle velocity and axial particle velocity distributions on the wall. The plots were obtained by the HPIV method using a catalyst at the inlet gas velocity V_{in}=16 m/s and particle concentration C_{in}=30 g/m³. The data in Fig. 4(c) were extracted from the corresponding positions of each pixel in the velocity distribution plots shown in Fig. 4(a) and Fig. 4(b). The particle velocity distribution shows that the tangential velocity is lowest in the center region of the ash band and significantly higher in the edge region of the ash band, showing a significant non-uniform distribution. In addition, there is a large difference in particle velocities within and outside the ash band, with relatively small variations in axial velocities.
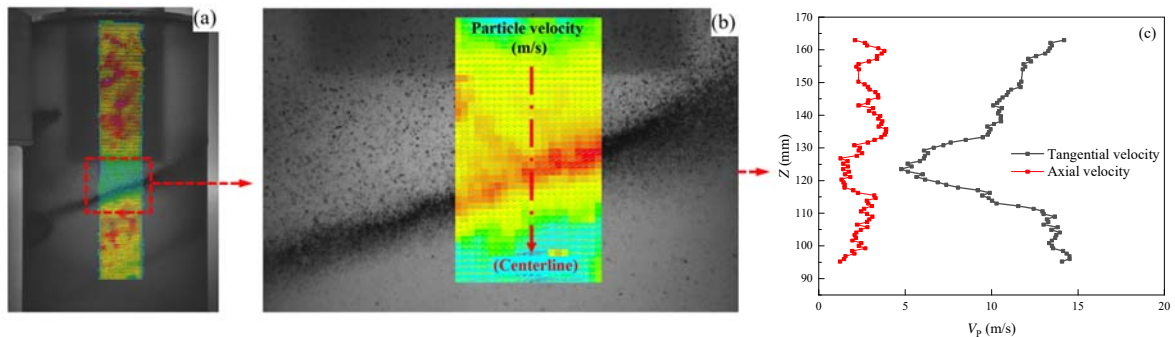
Fig. 4. Particle tangential and axial velocity along axial height

In the ash band, particles densely accumulate near the wall, restricting their movement and reducing velocity. Once away from the wall, gas no longer rubs against it, allowing particle

spacing to increase and gas velocity to rise until it surpasses particle velocity within the ash band. While directly measuring band thickness is infeasible, observing its gradual narrowing along motion and the decrease in flow velocity suggests a necessary increase in thickness to maintain mass flow stability. Additionally, particles surrounding the band are drawn into it during downward movement, increasing particle count and band thickness, as demonstrated in Fig. 5.
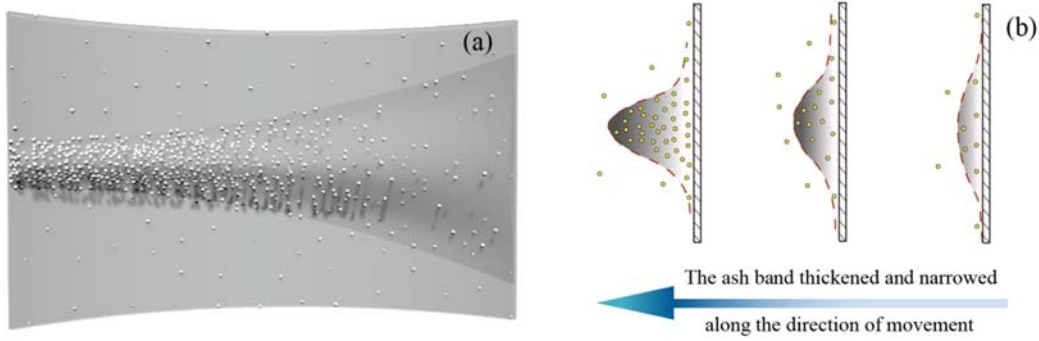
Fig. 5. Variation of the thickness of the ash band along the direction of movement

3.2 Particle collision model

In the ash band, particles can collide due to velocity pulsations, forming a potential collision area. These particles occupy a specific region, and the presence of a second particle can alter their positions upon collision. The maximum space occupied by a particle during a period in an ideal flow is termed the potential collision region. Fig. 6. demonstrates that by determining the size of the potential collision region, the local concentration of particles within this area can be estimated.
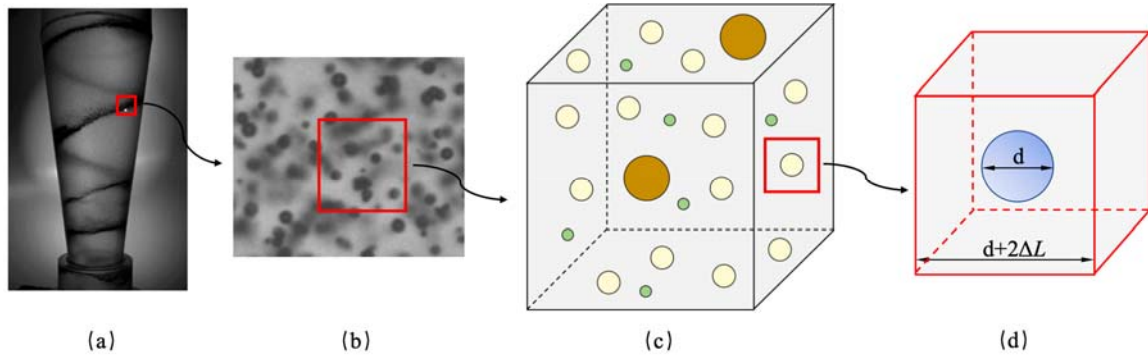
Fig. 6. Model of particle collisions

The following equation is proposed to calculate the change in interparticle distance ΔL due to velocity pulsation during particle advection motion.

$$\Delta L = 2 \times \Delta V_p \times \Delta t \tag{2}$$

where ΔV_p is the amplitude of the main frequency of the velocity pulsation and Δt is the particle collision interval time. The volume occupied by the particles can be calculated using this equation, considering them as an equivalent cube.

$$V^{'} = \left(d + 2\Delta L \right)^3 \tag{3}$$

According to Eq. (4), the local solidity of the particles due to velocity pulsations can be calculated.

$$C_v{}' = \frac{\pi d^3}{6V'} = \frac{d^3}{6(d+2\Delta L)^3}$$

(4)
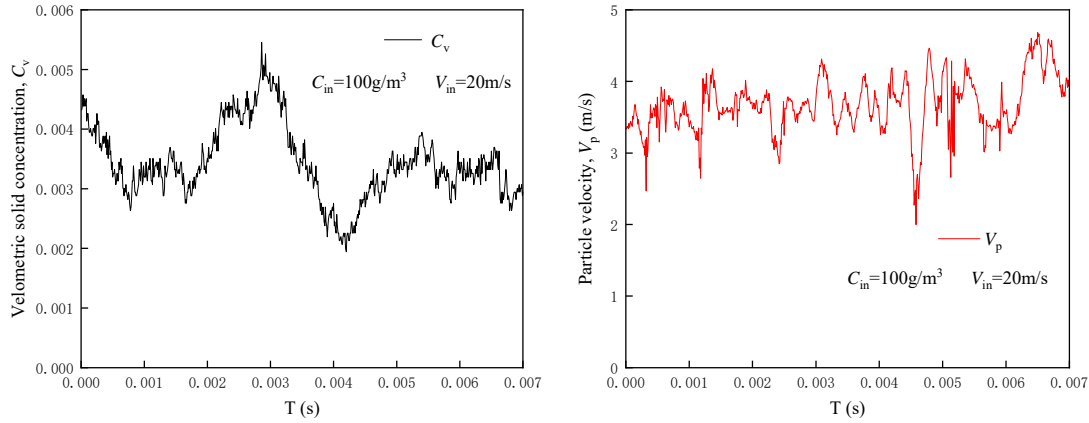
Fig. 7. Time-series signals of C_v and V_p: (a) Instantaneous concentration, (b) Instantaneous velocity.

Fig. 7. illustrates the instantaneous values of particle concentration and velocity, with the measurement point situated at Z = 430 mm, and inlet concentration C_{in}=100g/m^3 along with inlet gas velocity V_{in}=20m/s. Spectral analysis of the particle velocity data from Fig. 7(b). yields the particle velocity main frequency f=1389 Hz, corresponding to an amplitude of 0.213m/s, as shown in Fig. 8. By substituting these parameters into Eq. (4), the calculated solids content is 0.0028, which deviates by 12.5% compared with the mean value of particle concentration C_v=0.0034 obtained from the actual measurement in Fig. 7(a). Despite some error in this calculation model, it still reveals a trend: the concentration of the ash band is correlated with the particle pulsation velocity, suggesting that the smaller the particle pulsation velocity, the higher the concentration.
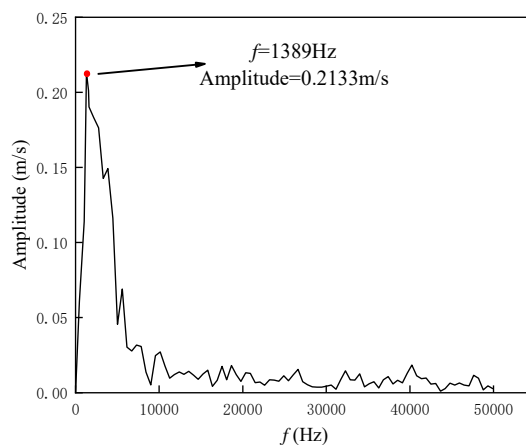
Fig. 8. Amplitude of instantaneous velocity of particles

4. Conclusion

The focus of this paper is on investigating the motion and collision model of particles within the ash band of a cyclone separator, encapsulated in the following three elements:

(1) The distribution of particle velocities within the ash band of the cyclone separator demonstrates significant non-uniformity, with tangential velocities lowest at the band's center and highest at its edges. Additionally, particles densely accumulate near the sidewalls, constraining their movement and reducing velocity, while gas velocity increases away from the wall until surpassing particle velocity within the band.

(2) The observed dynamics suggest that to maintain mass flow stability in the cyclone separator, there is a need for an increase in the thickness of the ash band. This increase is facilitated by the inward movement of particles during descent, reinforcing the band's structure.

(3) Data analysis was employed to model particle collisions within the ash band. Spectral analysis of particle velocity data shows a relationship between particle pulsation velocity and the concentration of the ash band. This suggests that lower pulsation velocities are associated with higher concentrations.

Acknowledgment

References

[1] A.C.Hoffmann, L.E.Stein, Gas Cyclones and Swirl Tubes: Principles, Design and Operation (2008) 1-422. https://doi.org/https://doi.org/10.1007/978-3-540-74696-6.

[2] C. Cortés, A. Gil, Modeling the gas and particle flow inside cyclone separators, Progress in Energy and Combustion Science 33(5) (2007) 409-452. https://doi.org/https://doi.org/10.1016/j.pecs.2007.02.001.

[3] E. Hugi, L. Reh, Focus on solids strand formation improves separation performance of highly loaded circulating fluidized bed recycle cyclones, Chemical Engineering and Processing: Process Intensification 39(3) (2000) 263-273. https://doi.org/https://doi.org/10.1016/S0255-2701(99)00072-0.

[4] M.-Q. Cao, J.-Y. Chen, B. Hu, X.-Q. Fan, H. Cui, Y. Wei, Measurements of particle velocity and solid concentration near the wall of a cyclone using high-speed particle shadow velocimetry, Powder Technology 426 (2023) 118662. https://doi.org/https://doi.org/10.1016/j.powtec.2023.118662.

[5] G. Li, Y. Lu, Cyclone separation in a supercritical water circulating fluidized bed reactor for coal/biomass gasification: Structural design and numerical analysis, Particuology 39 (2018) 55-67. https://doi.org/https://doi.org/10.1016/j.partic.2017.08.005.

[6] K. Jang, G.G. Lee, K.Y. Huh, Evaluation of the turbulence models for gas flow and particle transport in URANS and LES of a cyclone separator, Computers & Fluids 172 (2018) 274-283. https://doi.org/https://doi.org/10.1016/j.compfluid.2018.04.032.

[7] M.-Q. Cao, J.-Y. Chen, B. Hu, H. Meng, S.-Y. Li, Y.-d. Wei, Experimental study on flow characteristics of ash band in a cyclone separator using HPIV techniques, Separation and Purification Technology 337 (2024) 126437. https://doi.org/https://doi.org/10.1016/j.seppur.2024.126437.

Session B:

Modeling and simulation

DENSITY FUNCTIONAL THEORY STUDY ON THE INFLUENCE MECHANISM OF HYDROXYL GROUP ON NO REDUCTION OVER CHAR DURING OXY-FUEL CIRCULATING FLUIDIZED BED COMBUSTION

Wang Chuanhao, Ge Chen, Li Shiyuan*

School of Energy and Environmental Engineering, University of Science & Technology Beijing, Beijing, 100083, China

*Email: lishiyuan@ustb.edu.cn

Abstract

The circulating fluidized bed oxy-fuel combustion has been extensively studied as a highly promising means to reduce CO_2 emissions. Compared to conventional air combustion, oxy-fuel combustion atmosphere contains more hydroxyl group which is mainly from H_2O contained in recycled flue gas. The significant difference in atmosphere necessitates a reconsideration of various chemical reactions during the oxy-fuel combustion process. To further clarify the influence of the hydroxyl group on NO heterogeneous reduction over char, the pathway mechanism was studied using density functional theory (DFT). The results show that the hydroxyl group affects the NO reduction over char through two different pathways. For the first pathway, termed "Adsorption-only," the hydroxyl group merely adsorbs onto the char surface as a surface functional group. Contrastingly, for the second pathway, named "Modification", the hydroxyl group engages in reactions with the char, inducing a redistribution of active sites on the char surface. Kinetics calculations and pathway analysis reveal that the "Adsorption-only" pathway not only fails to facilitate NO heterogeneous reduction over char but also imposes an inhibitory effect on the process. Conversely, the "Modification" pathway substantially enhances the reduction process.

Keywords: Circulating fluidized bed, oxy-fuel combustion, Heterogeneous reduction of NO, Density functional theory, hydroxyl group, char

1. Introduction

Circulating fluidized bed oxy-fuel combustion, as a highly promising method for clean, efficient, and low carbon emission, has been extensively studied. Due to the presence of flue gas recirculation, the levels of H_2O and CO_2 in the oxy-fuel combustion atmosphere are higher, which represents a significant difference from traditional combustion methods. Therefore, a reevaluation of the various chemical reactions during the combustion process is necessary [1-3]. NO is one of the major pollutants from fossil fuel combustion, and controlling NO emissions is key to achieving clean and efficient combustion of fossil energy. During combustion, the NO heterogeneous reduction by char accounts for a significant portion of total NO reduction [4, 5].

The influence of the reaction atmosphere on the concentration of oxygen-containing functional groups on the carbon surface cannot be neglected during oxy-fuel combustion [6, 7]. Previous research has demonstrated that water molecules can decompose into hydrogen atoms and hydroxyl radicals at high temperatures, and the resulting free hydroxyls adsorb onto the char surface to form oxygen-containing functional groups [8]. Yue et al. [9, 10] further demonstrated by Fourier transform infrared spectroscopy (FTIR) that the concentration of hydroxyl groups on the pyrolyzed char surface increased significantly in the presence of H2O in the atmosphere. In their kinetic simulation calculations, Hong [11] revealed that the presence of both H_2O and O_2 in the atmosphere promotes reaction (1), resulting in a drastic increase in the concentration of hydroxyl radicals in the atmosphere.

$$H_2O + \text{-}O \rightarrow 2 \cdot OH \quad (1)$$
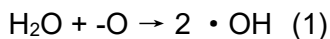
Before the gas-solid reaction can occur, hydroxyl groups in the reaction atmosphere must first be adsorbed onto the char surface. A critical aspect of understanding how hydroxyl groups affect the NO heterogeneous reduction on char is clarifying the adsorption process of these groups and their subsequent behavior on the char surface. Unfortunately, existing research has not focused specifically on this subject. Therefore, this paper analyzes the hydroxyl group adsorption process on char using quantum chemical calculations, kinetic analysis, pathways analysis and discusses the impact of its different subsequent behaviors on the NO heterogeneous reduction over char.

2. Computation and methods

This paper employs the zigzag char model with seven aromatic rings (Fig. 1) for research, whose practicality and scientific validity have been widely verified by scholars [12-13]. In terms of computational level, the combination of B3LYP-D3/6-31G(d) is chosen, which offers advantages such as low spin contamination, robustness, and broad applicability, effectively balancing accuracy and computational expense in calculations [14]. On the other hand, the def2-TZVP basis set is selected for single-point energy calculations, as these calculations are more sensitive to the choice of basis set. The thermodynamic parameters of each structure at different temperatures were calculated using the Shermo program [15].
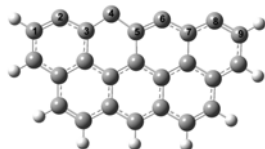
Fig. 1. Possible reaction pathways after IM1 structure

The transition state theory (TST) was used in the reaction kinetics analysis, with the formula for calculating the reaction rate constant of elementary reactions as：

$$k(T) = \sigma \frac{k_B T}{h} (\frac{RT}{P_0})^{\Delta n} \exp(-\frac{\Delta G^{0,\neq}}{k_B T})$$

In where, $\Delta G^{0,\neq}$ is standard-state activation free energy. k_B is the Boltzmann constant. h is the Planck constant. T is the thermodynamic temperature. R is the universal gas constant. σ is the reaction pathway degeneracy, which is generally 1 for large molecular systems.

3. Results and Discussions

3.1 The NO heterogeneous reduction over char surface

During the theoretical analysis, an interesting phenomenon was observed that the hydroxyl group adsorbed on the char surface may behave differently, implying that the chemical reactions could proceed via different mechanisms once the hydroxyl group is adsorbed on the char surface. Fig. 3 illustrates two different reaction pathways after hydroxyl group adsorption on the char surface, denoted as pathway 1 and pathway 2, respectively. In this paper, the notation used to represent various species in the chemical reactions is as follows: "R" denotes the reactants, "P" represents the products, "IM" is used for intermediates, and "TS" indicates the transition states. This notation will be consistently employed throughout the document to maintain clarity and consistency in describing the chemical processes under discussion.

In pathway 1, the hydroxyl group is adsorbed on the char surface only as a surface oxygen-containing functional group and does not participate in the generation of products. After the reaction product N_2 is desorbed from the char surface while the hydroxyl group remains intact, this mechanism is referred to as the "Adsorption-only" mechanism for ease of description in subsequent discussions. The chemical equation for the "Adsorption-only"

mechanism is R + 2NO + ·OH → N2 + I-P. The rate-determining step of the total response is the elementary reaction I-IM4 → I-TS2 → I-IM5, corresponding to the process of formation of the N-N structure on the char surface. The energy barrier for this process is 330.00 kJ/mol.
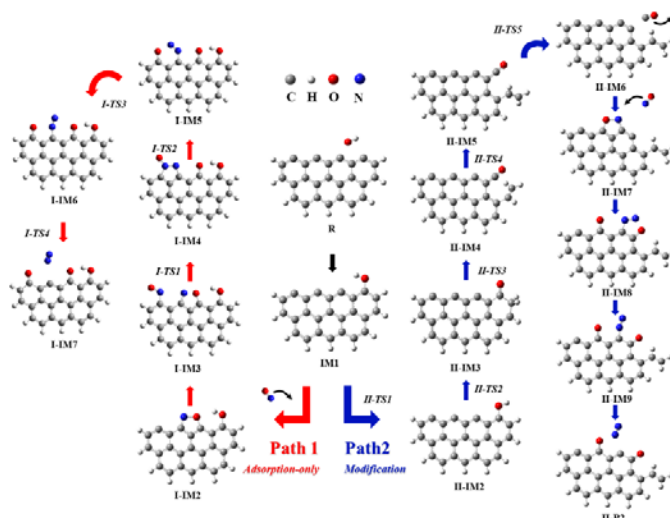
Fig. 2. Possible reaction pathways after IM1 structure

In pathway 2, the hydroxyl group reacts with char following adsorption. This reaction destroys the surface structure of the char and alters the subsequent processes of adsorption and reduction of NO molecules. This mechanism, hereafter termed the "Modification" mechanism for simplicity, is discussed in more detail in the following sections. The chemical equation for the "Modification" mechanism is R + ·OH + 2NO → CO + II-P2 + N$_2$. The rate-determining step of the chemical reaction is II-IM9 → II-TS8 → II-P2, with the highest energy barrier of 100.59 kJ/mol, corresponding to the desorption of N$_2$ from the char surface. In addition, the energy barrier for the adsorption of the second NO molecule onto the char surface is 91.77 kJ/mol, which is close to the energy barrier of the rate-determining step. Therefore, this aspect is further analyzed in the subsequent kinetic analysis.

In addition, chemical reactions in an atmosphere devoid of hydroxyl groups were also calculated, referred to as pathway 3. In an environment devoid of hydroxyl groups, the chemical equation representing the heterogeneous reduction of NO on the char surface can be expressed as R + 2NO → N$_2$ + III-P. The rate-determining step of the total response is III-IM3 → III-TS2 → III-IM4, corresponding to the formation process of N-N structure on the char surface, with an energy barrier of 195.36 kJ/mol.

3.2 Kinetic analysis for different reaction mechanisms

Reaction kinetics analysis, which quantitatively calculates rate constants indicative of the rates at which chemical reactions occur, is a crucial method in analyzing chemical reactions. In this section, the rate constants for several key elementary reactions and rate-determining steps in Pathways 1, 2, and 3 are calculated to elucidate the role of the hydroxyl group in the heterogeneous reduction of NO on the char surface. The formula for calculating the chemical reaction rate constants of elementary reactions is given in equation in Section 2.

As outlined in Sections 3.1, the energy barriers for the rate-determining steps in the "Adsorption-only" mechanism, the "Modification" mechanism, and the absence of hydroxyl groups in the atmosphere are respectively identified as 330 kJ/mol, 100.59 kJ/mol, and 195.36 kJ/mol. From an energy barrier perspective, the presence of hydroxyl groups in the reaction atmosphere leads to divergent outcomes. Specifically, the "Adsorption-only" mechanism increases the reaction energy barrier, thereby inhibiting the reduction reaction, while the "Modification" mechanism reduces the energy barrier, thus promoting NO heterogeneous reduction on char.

To more clearly compare the effects of different mechanisms on chemical reaction rates, Fig. 3 illustrates the variation of the rate constants for the rate-determining steps of pathways

1, 2, and 3 with temperature in the range of 600-1800 K. As observed in Fig. 3, the rate constants k for all three chemical reactions increase with temperature, suggesting that higher temperatures enhance these reactions. Notably, at approximately 1200℃, the rate constant curves of two elementary reactions with higher energy barriers in the "Modification" mechanism intersect. This indicates a potential shift in the rate-determining step at this temperature. Below 1200℃, the reaction rate of the elementary reaction II-IM9 → II-TS8 → II-P2 is lower, making it the rate-determining step of the chemical reaction, which corresponds to the desorption of the product N_2 from the char surface. Above 1200℃, the elementary reaction II-IM7 → II-TS6 → II-IM8 becomes slower, indicating that this process is now the rate-determining step, corresponding to the adsorption of the second NO molecule on the char surface.

Analysis of kinetic curves reveals that within the studied temperature range, the order of reaction rates for the three chemical pathways is as follows: "Modification" mechanism > chemical reactions in the absence of hydroxyl groups in the reaction atmosphere > "Adsorption-only" mechanism. This indicates that how hydroxyl groups in the reaction atmosphere affect the heterogeneous reduction of NO on the char surface is determined by their behavior on the char surface. The "Modification" mechanism enhances the reaction, while the "Adsorption-only" mechanism inhibits the chemical reaction.
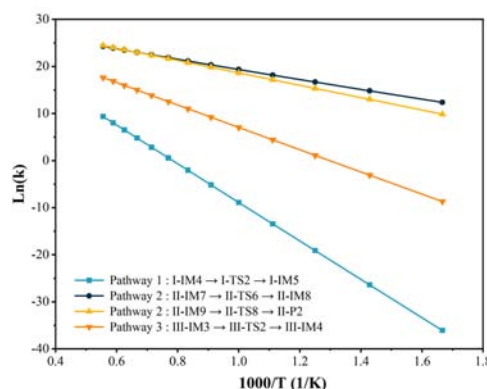
Fig. 3. Reaction rate constants for rate-determining steps

3.3 Chemical reaction pathway analysis for different mechanisms

In this section, the formation process of the N-N structure on the char surface, which is a crucial precursor to the reduction product N_2, is analyzed in three pathways. This analysis is essential for understanding why the "Modification" mechanism effectively facilitates chemical reactions. As illustrated in Fig. 4, for the process transitioning from NO adsorption on the char surface to the formation of the N-N structure, both the "Adsorption-only" mechanism (pathway 1) and the reaction in the absence of hydroxyl groups (pathway 3) involve three similar elementary reactions. Specifically, pathway 1 proceeds through Ⅰ-IM2 → Ⅰ-IM3 → Ⅰ-IM4 → Ⅰ-IM5, while pathway three follows Ⅲ-IM1 → Ⅲ-IM2 → Ⅲ-IM3 → Ⅲ-IM4. Firstly, two NO molecules are adsorbed on the char surface in turn, then the N atoms of the two NO molecules approach each other to form covalent bonds, and finally, the N-O bond of the second NO molecule is broken and the N-N structure is formed on the char surface. However, in the "Modification" mechanism (pathway 2), the above three steps can be completed by only one elementary reaction (pathway 2: II-IM7 → II-TS6 → II-IM8). In terms of reaction pathways, the "turn three to one" phenomenon in the "Modification" mechanism greatly shortens the pathway of N_2 production.
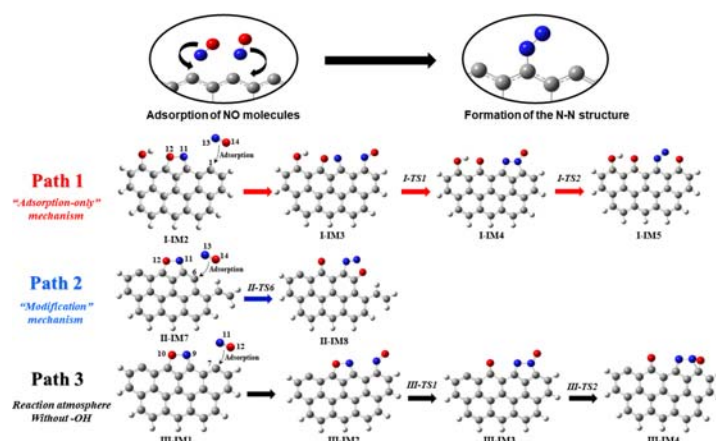
Fig. 4. The three reaction pathways from NO adsorption to N-O bond breakage

To clarify the "Turn three to one" phenomenon in the "Modification" mechanism, spin density contour maps for relevant structures in the three pathways were calculated and drawn, with a contour value of 0.1, as shown in Fig. 9. The spin density is the difference between the densities of α and β electrons in the molecular system, which can reveal the distribution of unpaired electrons in the molecular system and help us better understand molecular properties. The green region in the figure represents a positive spin density, while the blue region represents a negative spin density. As shown in Fig. 5, unlike the other two mechanisms, in the "Modification" mechanism, there are unpaired β electrons on the N atoms on the char surface, which are distributed on p orbitals perpendicular to the molecular axis. Therefore, during the adsorption process, the N13 atom in NO can combine with the N11 atom on the char surface to form an N11-N13 covalent bond. This is key to the above "Turn three to one" phenomenon and crucial for the "Modification" mechanism to shorten the chemical reaction pathway.

(a) II-TS6
"Modification" mechanism

(b) I-IM2
"Adsorption-only" mechanism

(c) III-IM1
without hydroxyl groups
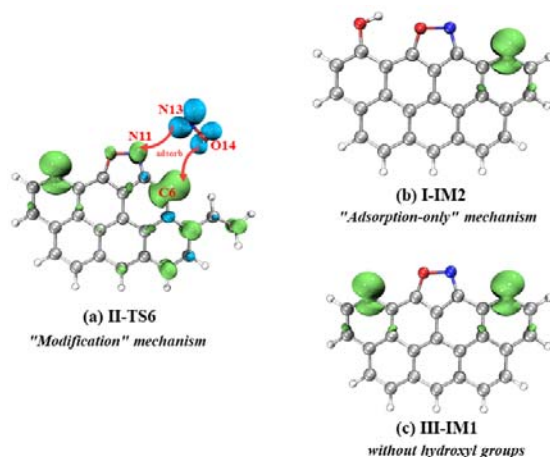
Fig. 5. Iso-surface maps of spin density for three structures

4. Conclusion

In this study, DFT was employed to investigate how hydroxyl groups in the reaction atmosphere can influence the reduction reaction through various mechanisms. Notably, these mechanisms have been found to have contrasting effects on the chemical reaction. The detailed conclusions of this research are summarized as follows:

1. Hydroxyl groups in the reaction atmosphere can affect the NO heterogeneous reduction by two different mechanisms. The first mechanism is named the "Adsorption-only" mechanism, in which the hydroxyl groups are adsorbed on the char surface only as surface functional groups. The second mechanism is called the "Modification" mechanism, in which the hydroxyl group reacts with the char, and new active sites are released on the char surface.

2. Kinetics analysis shows that the "Adsorption-only" mechanism not only fails to promote the NO heterogeneous reduction on char but also has an inhibitory effect, while the "Modification" mechanism significantly promotes the heterogeneous reduction of NO by char.

3. The "Modification" mechanism significantly shortens the chemical reaction pathway. From the adsorption of NO to the formation of the N-N structure is the critical process in the NO heterogeneous reduction on the char surface, and three elementary reactions are required to complete this process in other mechanisms. In the "Modification" mechanism, however, the electron distribution is changed, and only one elementary reaction is required to complete the above process.

Acknowledgment

References

[1] Yadav S, Mondal SS. A review on the progress and prospects of oxy-fuel carbon capture and sequestration (CCS) technology. Fuel. 2022;308.

[2] Deng L, Zhao Y, Sun S, Feng D, Zhang W. Review on thermal conversion characteristics of coal in O2/H2O atmosphere. Fuel Processing Technology. 2022;232.

[3] Ling JLJ, Yang W, Park HS, Lee HE, Lee SH. A comparative review on advanced biomass oxygen fuel combustion technologies for carbon capture and storage. Energy. 2023;284.

[4] Shu Y, Wang HC, Zhu JW, Tian G, Huang JY, Zhang F. An experimental study of heterogeneous NO reduction by biomass reburning. Fuel Processing Technology. 2015;132:111-7.

[8] Xu Z, Wang C, Yue S. A theoretical insight into the mechanism of NO heterogeneous reduction on char surface: The catalytic effect of potassium. Fuel. 2023;340.

[6] Luo Q, Bai Y, Wei J, Song X, Lv P, Wang J, et al. Insights into the oxygen-containing groups transformation during coal char gasification in H2O/CO2 atmosphere by using ReaxFF reactive force field. Journal of the Energy Institute. 2023;109.

[7] Qing M, Su S, Chi H, Xu J, Sun Z, Gao J, et al. Relationships between structural features and reactivities of coal-chars prepared in CO2 and H2O atmospheres. Fuel. 2019;258.

[8] Wang ZZ, Zhao YY, Sun R, Li YP, Ren XH, Xu J. Effects of reaction condition on NO emission characteristic, surface behavior and microstructure of demineralized char during O-2/H2O combustion process. Fuel. 2019;253:1424-35.

[9] Yue S, Wang C, Huang Y, Xu Z, Xing J, Anthony EJ. The role of H2O in structural nitrogen migration during coal devolatilization under oxy-steam combustion conditions. Fuel Processing Technology. 2022;225.

[10] Yue S, Wang C, Xu Z, Wang D, Zheng F, Anthony EJ. The role of H2O in NO formation and reduction during oxy-steam combustion of bituminous coal char. Combustion and Flame. 2022;237.

[11] Hong DK, Li ZH, Si T, Guo X. A study of the effect of H2O on char oxidation during O-2/H2O combustion using reactive dynamic simulation. Fuel. 2020;280.

[12] Chen N, Yang RT. Ab initio molecular orbital calculation on graphite: Selection of molecular system and model chemistry. Carbon. 1998;36(7):1061-70.

[13] Yang FH, Yang RT. Ab initio molecular orbital study of adsorption of atomic hydrogen on graphite:: Insight into hydrogen storage in carbon nanotubes. Carbon. 2002;40(3):437-44.

[14] Stephens PJ, Devlin FJ, Chabalowski CF, Frisch MJ. Ab Initio Calculation of Vibrational Absorption and Circular Dichroism Spectra Using Density Functional Force Fields. The Journal of Physical Chemistry. 1994;98(45):11623-7.

[15] Lu T, Chen QX. Shermo: A general code for calculating molecular thermochemistry properties. Comput Theor Chem. 2021;1200:8.`

AN INNOVATIVE APPROACH FOR ELECTROMAGNETIC INDUCTION HEAT STORAGE COUPLED WITH MOVING BED HEAT RELEASE: A CFD-DEM EXPLORATION

Weiqin Lu[a], Xueyu Tang[a], Changhao Ma[a], Junfu Lyu[a,b], Xiwei Ke*[a,b], Tuo Zhou*[a]
[a] *Key Laboratory for Thermal Science and Power Engineering of Ministry of Education, Department of Energy and Power Engineering, Tsinghua University, Beijing 100084, China*
[b] *Beijing Huairou Laboratory, Beijing 101499, China*
*E-mail: kexiwei@sxri.hrl.ac.cn zhoutuo@mail.tsinghua.edu.cn

Abstract

Given the disparity between the demand for development in electromagnetic induction heating and the current inadequacies in heat storage/release media, a novel electrothermal energy storage technology (ENST) is proposed. This technology integrates electromagnetic induction heat storage with moving bed heat release (EIHS-MBHR), featuring an electromagnetic induction coil for heating, millimeter-grade steel pellets for heat storage and release, and a particle moving bed for cooling. To further explore the performance and characteristics of the system operating in a continuous mode, a simulation approach base on CFD-DEM is established. A simplified quasi-2D geometry model with a thickness of 15 mm, a width of 84 mm, and a height of 522 mm, is constructed. Under the conditions of an initial particle temperature of 300 K, heating frequency of 50 kHz, magnetic field strength of 0.1 mT, and a controlled particle descent velocity of 2 mm/s, the stability of heat and mass transfer is analyzed in detail. The results suggest that the system requires a buffer period to achieve a steady state for heat and mass transfer. Following this, a quasi-stable state can be attained, with persistent minor fluctuations observed in the heat transfer results. According to the simulation, the system exhibits significant advantages, particularly in terms of its rapid heating capability (about 6 K/s) and competitive heat and mass transfer performance (91.3 W/m^2/K). Additionally, the characteristics of the main physical field distributions in the system are elucidated. This study provides an initial demonstration of the effectiveness of the proposed approach and offers valuable insights into the advanced improvement and development of the ENST system.
Key words: Electrothermal energy storage technology, electromagnetic induction, tubular moving bed heat exchanger, CFD-DEM, exploratory investigation

1. Introduction

Power-to-heat technology combined with thermal energy storage (P2H-TES), also known as electrothermal energy storage technology (ENST), represents a newly emerging innovation that facilitates the transformation of surplus electricity into storable and usable thermal energy (Meha et al., 2020). Herein, to our knowledge, the excess electric power primarily arises from sources such as unused renewable energy (Yang et al., 2018), needless electricity generated to meet the heating demand (Hu et al., 2023), and surplus electricity beyond the power demand (Yong et al., 2022). Through the implementation of ENST, it is indeed possible to effectively manage this surplus electricity and further prevent any adverse impact on the power grid or potential damage. Meanwhile, in China, coal-fired power plants are considered a vital component of the electrical power systems. Considering ENST's additional role in peak shaving, frequency regulation, enhancing the operational flexibility of coal-fired power plants, etc. (Miao et al., 2023), this technology has garnered significant attention.

Generally, a ENST can be characterized by its three key elements, which are the PtH equipment, the medium used in the heat storage and release cycle, and the heat-to-x (HtX) equipment. For instance, in the field of built environment, a heat pump or an electric boiler, as a PtH equipment, is commonly employed to convert electricity into heat. The medium can be water or air, and an indoor heat exchanger can be considered as a HtX equipment (Maruf et al., 2022). However, in the industry, the term HtX equipment usually refers to heat-to-power (HtP) equipment or heat-to-product (HtPro) equipment (converts thermal energy into chemical energy), aimed at maximizing economic benefits, rather than only supplying heat demands (Erro et al., 2024). An illustrative example involves the application of steam

turbines, utilizing steam Rankine cycles, to facilitate the conversion of heat into electricity through connection with an electric generator.

When it comes to industrial PtH equipment, the main heating forms include resistance heating, inductive heating, high-frequency heating, magnetic direct current heating, and electrical infrared heating (Maruf et al., 2022). Among these forms, the inductive heating type has attracted much attention due to its unique advantages, such as relatively uniform heating, rapid heating response, free of impurities introduced (Bio Gassi et al., 2022). Regarding the media used, they can store and subsequently release heat in various forms such as sensible heat, latent heat, or thermochemical heat. Although the amount of sensible heat storage is limited, it is still a preferred choice in industrial applications due to its mature technology and safe operation. Common heat storage/release media include solid particles, such as desert sand, rocks, gravel, and firebrick, as well as liquid materials, such as molten salts and conduction oil. Nevertheless, these media cannot be directly heated through the electromagnetic induction effect due to their material properties, leading to an unresolved mismatch. Based on these, there is great promise in developing a novel ENST by integrating an inductive heating approach, an electrically conductive material, and a suitable heat release method.

In this work, an innovative ENST design, which combines electromagnetic induction heat storage with moving bed heat release (EIHS-MBHR), is proposed firstly and features an electromagnetic induction coil for heating, millimeter-grade steel pellets for heat storage and release, and a particle moving bed for cooling. Given this, a numerical simulation method based on combined approach of computational fluid dynamics and discrete element method (CFD-DEM) is established to study the operation mode of simultaneous heat storage/release and further explore the feasibility of this conceptual ENST. This study aims to provide some meaningful insights into advanced improvement and development of the ENST system.

2. EIHS-MBHR system

Firstly, as shown in Fig. 1a, the system primarily comprises an electromagnetic induction heater, a hot bulk storage unit, a tubular MB heat exchanger (MBHE), a cold bulk storage unit, a material carrier, an AC power supply, an inverter, and a temperature controller. The bed materials, such as millimeter-grade steel pellets, are lifted by the carrier and then fed into the heater through its top inlet. Subsequently, the converter transforms the excess electricity into a higher frequency form before connecting it to a multiturn coil wrapped around the heater. As a result of the electromagnetic induction effect, the particles are heated by eddy currents, and their temperature is consistently maintained at a high level (>600 ℃) through the PID control mechanism of the temperature controller. After the heating process, the high temperature particles are transferred to the hot bulk storage unit for a long time with little heat loss. If required, the hot particles can be directed into the tubular MBHE for heat release, immediately transferring their sensible heat to the working medium (water or steam) flowing in tube banks. In the tubular MBHE, the particles are driven by their gravity and move slowly at a set descent velocity (mm/s), which can be controlled by a discharging device such as a screw discharging machine. The heated medium can be utilized for further electricity generation or other purposes. Afterward, the colder particles descend into the cold bulk storage unit to await being lifted back into the heater, thus completing the material cycle.

In more detail, as illustrated in Fig. 1b, an implementation example is provided. The rectangular cross-section design is adopted for both the EI heater and the tubular MBHE for easily feeding and discharging of granular materials. This also aids in simplifying the geometry model utilized in simulation to a quasi-2D form. Furthermore, the operation modes of this system include continuous mode and semi-continuous mode. The specific operation mode is determined by the particular application scenario. The continuous mode refers to an operation approach of continuously supplying surplus electricity with a stable heat output. This mode is suitable for the cases where there is a high heat demand, such as during cold winters. The cogeneration units generate electricity at the expense of negative returns to meet heating needs. Therefore, it is feasible to establish an ENST system working in continuous mode, which contributes to the heat-electricity decoupling of generator units. As for the semi-continuous mode, it is a relatively common method to solve the time-space mismatch between the electricity power and its demand. For instance, it is appropriate to store a certain amount of solar energy in the form of thermal energy during the day. This

helps mitigate the inherent volatility and instability of solar energy and prevents power shortfalls at night by releasing the absorbed thermal energy as electricity.
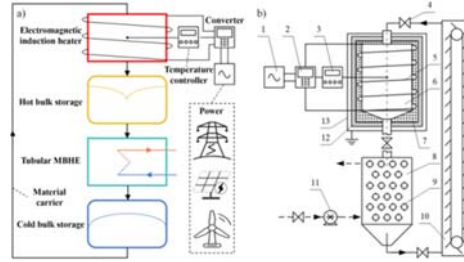
Fig. 1 The diagram of a) the EIHS-MBHR system and b) an implementation example of it.

1-AC power supply; 2-Frequency converter; 3-Temperature controller; 4-stop valve; 5-EI coil; 6-insulating barrel; 7-Inner insulation layer; 8-MBHE; 9-Heat exchange tube; 10-Particle lifting device; 11-Feed water pump; 12-Outer insulation layer; and 13-Electromagnetic shield.

3. Methods

3.1 Numerical method

In this section, the employed CFD-DEM as well as its heat transfer sub-models, including contact heat conduction (Chaudhuri et al., 2006), gas film heat conduction (Musser, 2011), heat radiation (Van Antwerpen et al., 2012), heat convection (Gunn, 1978), EI heating (Tanabe, 2021), and artificial softening correction (Zhou et al., 2010), are introduced. CFD-DEM combines the Eulerian and Lagrangian frameworks to respectively describe the behaviors of fluid and particle phases, and therefore, it consists of continuous phase model and discrete phase model. The conservation equations of mass, momentum, and energy in continuous phase model are detailed in ANSYS Fluent Theory Guide Release 2022 R1, while the motion model, contact model (no-slip Hertz-Mindlin model), and temperature update model can refer to EDEM 2020.2 Documentation. The Gidaspow drag model is used to characterize the gas-solid interaction. The sub-models are derived from existing literature and their applicability has been demonstrated by the researchers. The detailed equations for these sub-models can be found in the original research papers.

3.2 Simulation settings

As shown in Fig. 2, a simplified quasi-2D model with a thickness of 15 mm, a width of 84 mm, and a height of 522 mm, is constructed, including a prefeed zone, an EI heater (200 mm), two velocity control zones (10 mm), and a tubular MBHE with 6 aligned tubes (outer diameter: 34 mm, tubes 1-6, 252 mm). The CFD grids are provided with no grid independence test performed, due to the adoption of the unresolved form of CFD-DEM (Qiu et al., 2020). However, a mesh partitioning strategy that refining the grids as much as possible is used to ensure the proper resolution of the flow field. Besides, the main simulation parameters and operation conditions are listed in Table. 1.
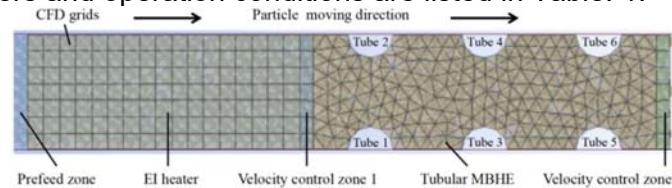
Fig. 2 The diagram of the geometry model of the EIHS-MBHR system, with CFD grids presented.

Table. 1 The main simulation parameters and operation conditions.

Name	Value	Name	Value
Particle material	304 stainless steel	Particle diameter mm	9.0
Wall material	20# steel	Heating frequency Hz	5.0×10^4
Environmental permeability H/m	$4\pi \times 10^{-7}$	Contact pair	Steel to steel
Material heat conductivity coefficient W/m/K	16.27	Effective magnetic induction intensity	1.3×10^{-4}
Particle specific heat capacity J/kg/K	500.0	Gas film thickness mm	0.9

Particle emissivity	0.8	Wall emissivity	0.5
Particle roughness m	2.5×10^{-6}	Wall roughness m	2.5×10^{-6}
Particle initial temperature K	300.0	Descent velocity of particles in zones 1 and 2 mm/s	NaN/2.0
CFD time step	5.0×10^{-4}	DEM time step	5.0×10^{-5}

4. Preliminary results and discussion

4.1 Stability of heat and mass transfer

In our simulation, the initial temperatures of both the particles and air are set to 300 K. Therefore, there is a necessary buffer time for the EIHS-MBHR system to reach a steady state for heat and mass transfer. Fig. 3 presents the over-time evolutions of average particle temperatures in velocity control zones 1 and 2 (ATP-o1 and ATP-o2), along with the average temperatures of particles and air across the entire simulation domain (ATP-all and ATA-all). The results illustrate that, when considering the stability of the parameters related to temperature, the system reaches a quasi-stable state, with consistent minor fluctuations observed, after approximately 240 s, which can be referred to as the so-called buffer time. The buffer time is basically consistent with the required time for the movement of particles at the inlet of the EI heater to the outlet of the tubular MBHE, which can be calculated by the equation $t = l_{EI-MB}/v_{descent} = (200 + 10 + 252 + 10)\text{mm}/2\text{mm/s} = 236s$. This also suggests that the startup time for continuous operation of the EIHS-MBHR system can be estimated approximately using the aforementioned method.

After the buffer time, the system experiences fluctuations, as evidenced by the temperatures in Fig. 3 and the total heat fluxes of tube walls in Fig. 4. Additionally, as shown in Fig. 4, fluctuations in heat flux results are much more dramatic than the temperatures. The phenomenon of system fluctuations may be attributed to several aspects: 1) the randomness of particle motion in particle-fluid-wall heat transfer system; 2) the volatility of particle-wall contact in particle-fluid-wall heat transfer system; 3) the random particle feeding mode; and 4) the quasi 2D bed setup. Meanwhile, the presence of fluctuations implies that achieving complete stability in the heat and mass transfer of particles and air in the EIHS-MBHR system is challenging compared to that of pure air. This usually requires a large amount of computational resource and is also time-consuming. It is imperative to establish stability criteria to determine whether the system has attained the so-called quasi-stable state. This study mainly adopted the heat transfer results, such as the parameters shown in Figs. 3 and 4, as the bases of stability criteria. In other words, the system can be deemed stable if all parameters remain relatively constant. Data obtained after system stabilization can then be utilized for stable-state analysis, whereas data collected before stabilization can be employed for dynamic analysis. As for the heat and mass transfer capacity of the proposed system running in continuous mode, it can be also inferred according to the results presented in Figs. 3 and 4. Under the studied operation conditions, the particles can be heated to 648.4 ℃ with a temperature rise of about 600 K, which demonstrates the rapid heating ability of the EI heater (about 6 K/s). Besides, once the particles release their sensible heat to the tubes, the average temperature of the particles decreases to 582.8 ℃, marking a temperature decrease of 65.6 K. According to the equation $heff = \sum_{i=1}^{6} HF_i /(6 \times 3\pi d_{tube}l_{tube} \times \Delta t) \approx 91.3 \text{ W/m}^2/\text{K}$, the average effective heat transfer coefficient of the system can be obtained. Given this, it can concluded that the heat transfer capacity of this system is also competitive compared to that of current technologies.

4.2 Characteristics of physical field distributions

Fig. 5 illustrates the distributions of particle temperature and velocity vector in the XY cross section, and the data of simulation time 256.6 s is adopted to ensure a certain representativeness. It can be found in Fig. 5a that in the zone of the EI heater, the particle temperature is continuous increasing, with a max value of 993.16 K. Particles at the same height exhibit similar temperature levels, due to the uniform EI heating and the high thermal conductivity of particles. Meanwhile, the particles in the zone of the tubular MBHE presents an obvious heat release mode, and their temperature decreases as they descend, reaching a minimum value of about 619.3 K. However, evident temperature boundary layers are observed near the tubes, indicating a higher heat transfer intensity in these regions. This

leads to a non-uniform distribution of particle temperature in the tubular MBHE. Fig. 5b reveals that particles exhibit integral flow in the EI heater, while they demonstrate a semi-integral flow, characterized by relatively significant differences in particle velocity at the same height, in the tubular MBHE, particularly near its outlet.
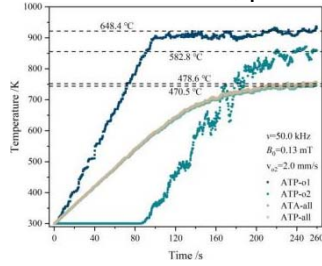
Fig. 3 Evolutions of the average temperatures over time.
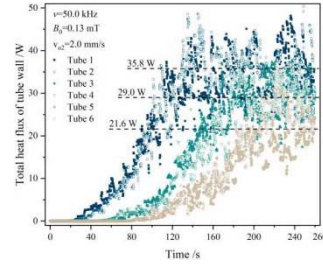
Fig. 4 Evolutions of the total heat fluxes of tube walls over time.

Regarding to air, Fig. 6a shows that a state of tightly packed particles can be found in the EI heater, while a relatively looser state is observed in the tubular MBHE. In the MBHE, there are several areas below the tubes characterized by large air volume fractions, which refer to the so-called void zones. The presence of the void zone results in weakened heat transfer. However, a reasonable distance between two vertically adjacent tubes can alleviate this issue, as evidenced by the phenomenon that the void zones below tubes 5 and 6 are significantly larger than those above. As depicted in Fig. 6b, the air exhibits limited mobility with velocities ranging from 0 to 0.03 m/s, primarily due to the absence of driving forces other than natural convection. Furthermore, the result in Fig. 6c suggests the existence of the fluid temperature boundary layers around the tube, similar to the findings in Fig. 5a.
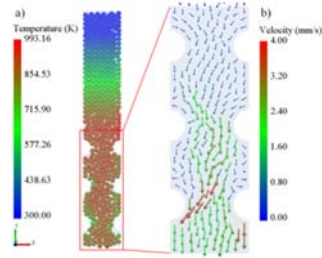
Fig. 5 The diagrams of a) particle temperature distribution and b) particle velocity vector.
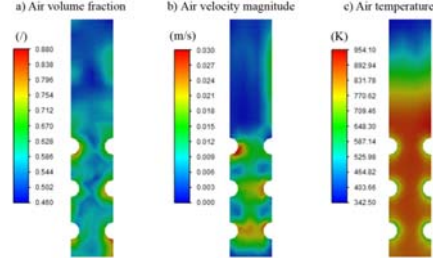
Fig. 6 The contour plots of a) air volume fraction, b) air velocity magnitude, and c) air temperature.

5. Conclusions and perspective

To address the mismatch between the application of electromagnetic induction heating and the unsatisfactory properties of current media used in the heat storage and release cycle, this work proposes a novel ENST. The ENST is characterized by an electromagnetic induction coil for heating, millimeter-grade steel pellets for heat storage and release, and a particle moving bed for cooling. Subsequently, an exploratory investigation is conducted using the established simulation approach base on CFD-DEM, with the purpose of clarifying the performance and characteristics of the EIHS-MBHR system operating in a continuous mode. The main conclusions are as follows:

1) The system requires a buffer period to reach a steady state for heat and mass transfer. After the buffer time, a quasi-stable state is obtained, with persistent minor fluctuations observed in heat transfer results. According to the simulation, the system exhibits significant advantages, particularly in terms of its rapid heating capability and competitive heat and mass transfer performance.

2) The subsequent analyses illustrate the characteristics of physical field distributions. The particle semi-integral flow and the temperature boundary layers around the tubes for both particles and air are found in the tubular MBHE. Additionally, the observed void zone below the tubes leads to weakened heat transfer and can be influenced by the distance between two vertically adjacent tubes.

This study offers valuable insights into the advanced improvement and development of the ENST system. However, the work presented in this paper is still limited and requires further improvement in certain areas. In our future work, conducting proper experimental verification is necessary to ensure the reliability of the simulation results. Besides, more and

wider operation conditions, as well as the operation mode, need to be further explored to match the practical applications.

Acknowledgment

References

ANSYS Fluent Theory Guide Release 2022 R1. *Southpointe. 2600 Ansys Drive Canonsburg, PA 15317, USA.*

Bio Gassi, K., Guene Lougou, B., & Baysal, M. (2022). Performance analysis of induction heated-porous thermochemical energy storage for heat applications in power systems. *Applied Thermal Engineering, 217*(August), 119226.

Chaudhuri, B., Muzzio, F. J., & Tomassone, M. S. (2006). Modeling of heat transfer in granular flow in rotating vessels. *Chemical Engineering Science, 61*(19), 6348–6360.

EDEM 2020.2 Documentation. *Edinburgh, UK.*

Erro, I., Aranguren, P., Sorbet, F. J., Bonilla-Campos, I., & Astrain, D. (2024). Enhancement of the Power-to-Heat Energy Conversion Process of a Thermal Energy Storage Cycle through the use of a Thermoelectric Heat Pump. *Applied Thermal Engineering, 246*(March), 122923.

Gunn, D. J. (1978). Transfer of heat or mass to particles in fixed and fluidised beds. *International Journal of Heat and Mass Transfer, 21*(4), 467–476.

Hu, W., Sun, R., Zhang, K., Liu, M., & Yan, J. (2023). Thermoeconomic analysis and multiple parameter optimization of a combined heat and power plant based on molten salt heat storage. *Journal of Energy Storage, 72*(PD), 108698.

Maruf, M. N. I., Morales-España, G., Sijm, J., Helistö, N., & Kiviluoma, J. (2022). Classification, potential role, and modeling of power-to-heat and thermal energy storage in energy systems: A review. *Sustainable Energy Technologies and Assessments, 53*(February).

Meha, D., Pfeifer, A., Duić, N., & Lund, H. (2020). Increasing the integration of variable renewable energy in coal-based energy system using power to heat technologies: The case of Kosovo. *Energy, 212*.

Miao, L., Liu, M., Zhang, K., Zhao, Y., & Yan, J. (2023). Energy, exergy, and economic analyses on coal-fired power plants integrated with the power-to-heat thermal energy storage system. *Energy, 284*(October), 129236.

Musser, J. M. H. (2011). Modeling of heat transfer and reactive chemistry for particles in gas-solid flow utilizing continuum-discrete methodology (CDM). *West Virginia University Doctoral Dissertation*.

Qiu, L., Sang, D., Li, Y., Feng, Y., & Zhang, X. (2020). Numerical simulation of gas–solid heat transfer characteristics of porous structure composed of high-temperature particles in moving bed. *Applied Thermal Engineering, 181*(March), 115925.

Tanabe, K. (2021). Selective electromagnetic induction heating of metal particles in molten salt for tritium extraction: A systematic numerical investigation. *Fusion Engineering and Design, 163*(December 2020), 112177.

Van Antwerpen, W., Rousseau, P. G., & Du Toit, C. G. (2012). Multi-sphere Unit Cell model to calculate the effective thermal conductivity in packed pebble beds of mono-sized spheres. *Nuclear Engineering and Design, 247*, 183–201.

Yang, Y., Guo, S., Liu, D., Li, R., & Chu, Y. (2018). Operation optimization strategy for wind-concentrated solar power hybrid power generation system. *Energy Conversion and Management, 160*(January), 243–250.

Yong, Q., Tian, Y., Qian, X., & Li, X. (2022). Retrofitting coal-fired power plants for grid energy storage by coupling with thermal energy storage. *Applied Thermal Engineering, 215*(February), 119048.

Zhou, Z. Y., Yu, A. B., & Zulli, P. (2010). A new computational method for studying heat transfer in fluid bed reactors. *Powder Technology, 197*(1–2), 102–110.

IMPROVING THE MANAGEMENT OF COMBUSTION BALANCE IN A CFB BY ADVANCED ANALYTICS

Mika Liukkonen[1]*, Swetha Authilingam[2], Ari Kettunen[1]

[1]*Sumitomo SHI FW Energia Oy (SFW), Relanderinkatu 2, 78200 Varkaus, Finland*

[2]*Sumitomo SHI FW Energia Oy (SFW), Metsänneidonkuja 10, 02130 Espoo, Finland*

*Email: *mika.liukkonen@shi-g.com*

Abstract

The identification of combustion imbalances during operation of any boiler is not only crucial, but also beneficial, because unbalanced combustion may have negative effects on boiler efficiency and emissions, and even increase corrosion-erosion of boiler parts. In this paper, we use machine learning -based classification methods to create models representing different conditions in the fuel feed of a Circulating Fluidized Bed (CFB) boiler firing clean and contaminated biomass. We then use these models to demonstrate the combustion balance in the process using a separate data set. The methods based on data and machine learning that are demonstrated in this paper can be applied to on-line type of diagnostics tools and can thereby assist in achieving the targets of minimized operating costs, maximized availability, and minimized emissions.

1. Introduction

Today, biogenic residues, such as forestry or agricultural waste, can provide a carbon-neutral and secure energy supply [Karras et al., 2022]. Unfortunately, these fuels often cause some variability in combustion due to their non-homogeneous characteristics. Fuel moisture, elemental composition and particle size distribution tend to fluctuate, and therefore operating a stable and undisturbed combustion process using biomass or waste as fuel requires special attention [Ikonen et al., 2023]. In addition, the varying quality of fuel, possibly added to unbalanced fuel feeding, may induce unbalance in the combustion process, which may lead to inefficient combustion, increased emissions, and unnecessary wear of critical parts in the boiler.

The identification of combustion imbalances in a CFB is theoretically feasible through various approaches under ideal conditions [Jiang et al., 2023]. For instance; 1) employing sensors to measure temperature fluctuations or differential temperatures within the fluidized bed allows the identification of combustion irregularities; 2) irregularities in gas composition may provide indication of non-uniform combustion, for example monitoring the changes in emissions, such as NOx and CO, can assist in detecting anomalies in combustion balance; 3) utilizing pressure sensors aids in identifying irregular variations and fluctuations that are indicative of combustion imbalances; 4) certain chemical compounds in the bed material composition may unveil signs of agglomeration or sintering, thus providing indirect evidence of combustion irregularities; 5) variation of O2 levels within the different parts of combustion chamber can reveal areas of incomplete combustion; and 6) elevated carbon levels in collected ash may be a sign of incomplete combustion. However, it is often so that the measuring abilities in a commercial boiler are limited, which prevents at least some of the mentioned ways of monitoring.

Sumitomo SHI FW (SFW) has developed advanced process diagnostics tools for fluidized bed combustion processes for over 20 years. Recently, the focus has been in finding online diagnostics methods to ensure high availability and efficiency even with ever worsening fuel quality [Ikonen et al., 2023]. When burning low quality solid fuels, management of bed material quality (particle size distribution and chemical composition) is critical to ensure a stable process without disruptions like blockages in the hotloop of a Circulating Fluidized Bed (CFB).

The measurable quantities that could be used, in combination with some advanced analytics, to detect signs of an evolving blockage in the hotloop include pressure and temperature in the wall seal and external heat exchanger parts. These analytics can trigger remedial actions before the problem evolves to a point of no return, where an unplanned shutdown cannot be prevented anymore.

In addition, it is important to maintain the balance in combustion to maximize the efficiency and reduce the risk for the material loss of structures like furnace walls, heating surfaces etc. The purpose of balance management is to diagnose potential lateral unbalance of combustion inside the furnace, and propose operating instructions to correct this unbalance, for example by adjusting fuel feeding between single feeding points. The unbalance can be detected by analyzing relevant data collected from the process, for example the temperature of flue gas and steam, and oxygen content of flue gas.

In this paper we show that methods based on data and machine learning can be very helpful to improve the balance and availability of the CFB process. The benefits include, for example, savings in operation cost and reduction of maintenance costs.

2. Materials and methods

2.1 CFB boiler and fuel balancing tests

The methodology presented in this paper is tested by real operational data from a CFB boiler designed for combined heat and power production. The boiler unit is a CFB boiler designed by Sumitomo SHI FW for wood-based fuels such as clean wood, recovered wood, and demolition wood collected from both households and industry (See Fig. 1).
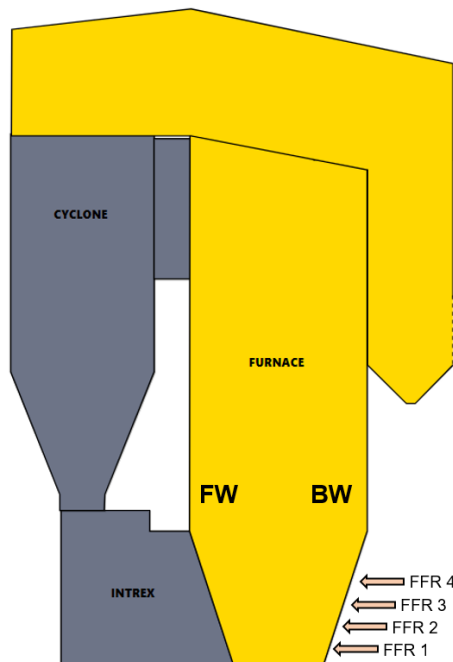
Fig. 1. Simplified presentation of the CFB boiler. FW = Front Wall, BW = Back Wall. Labels FFR 1, 2, 3, and 4 represent the fuel feeding points of the boiler.

Fuel tests were conducted onsite to simulate combustion imbalances. Other variables were set to normal operating conditions. Boiler load was also kept at a relatively constant level, avoiding any drastic changes. The fuel test was organized so that the Fuel Feeding Rates (FFR) in the fuel feeding lines were changed manually in the boiler and data was collected.

A baseline measurement (i.e., boiler running on maximum load with uniform fuel feeding) was conducted first for reference. During the tests, baseline test and four variations of fuel feeding settings were measured as follows (Fig. 1):

− Baseline, uniform feeding with all feeding points #1- #4
− Fuel feeding cut off to feeding point #1
− Fuel feeding cut off to feeding point #2
− Minimum fuel feeding to feeding point #3
− Minimum fuel feeding to feeding point #4

2.2 Data

The core process data used here comprised 344 measurement points over a span of approximately 4 months, including data from the fuel test. As training data for the classification models, the data collected from the fuel test period was utilized as labelled data with the label being combustion balanced at the reference scenario and imbalanced towards left and right as described above.

2.3 KPI selection methods

Manual analysis of a dataset consisting of hundreds of signal sensors may be extremely laborious. Therefore, it is useful to reduce the dimensionality of the dataset first using automated statistical methods. Principal component analysis (PCA) is a widely used statistical method for reducing the dimensionality of data. It aims to simplify complex datasets by identifying the most significant directions of variation and transforming the data onto a new coordinate system aligned with these directions [Labrín & Urdinez, 2020; Maćkiewicz & W. Ratajczak, 1993]. This process efficiently decreases the number of variables while preserving the most important information.

2.4 Classification models for combustion balance

Support Vector Machines (SVM) are supervised learning models used for classification and regression tasks. In this paper, SVM was used to classify the data points into their respective cases based on the values of the selected KPIs. The objective of SVM is to find the optimal hyperplane that splits the data points into separate classes, meanwhile maximizing the boundary between the classes. Various kernel functions can be used to achieve this objective, such as polynomial, Radial Basis Function (RBF), linear, and sigmoid.

The basic SVM classification does not allow interpretation of clusters as a probability distribution. However, the result of SVM's hard classification can be transformed to soft classification consisting of class probabilities using Platt scaling, which is a way of transforming the outputs of a classification model into a probability distribution over classes [Platt, 1999].

3. Results and discussion

3.1 Selected KPIs

Data from the fuel test period were fed into the Principal Component Analysis (PCA) to derive various metrics aimed at identifying the most varying tags. The evaluation included standard visualizations of PCA such as scree plots, cumulative variance plots, component loadings plots, and data such as the eigen values for all principal components. PCA returned 191 principal components with varying weights of component loadings. These graphs and data were examined to recognize the tags that PCA deemed most significant. Eventually, 24 unique tags were selected finalized based on this analysis. In practice, this is the set of tags that the PCA indicates to contain maximum information and variation in the whole data set.

The set of tags preselected by PCA were finally screened by process experts for additional interactions that could not be identified by basic machine learning method. Experts screening require an understanding of the boiler process and studying the data behavior over the entire test period to distinguish between tags with an insignificant effect from the fuel test and potential KPIs. Finally, based on the manual screening, seven KPIs were chosen for the actual classification task. The seven KPIs selected represent key indicators of combustion imbalance and therefore are used with ML models for class prediction.

The effect of combustion imbalance on the NOx emission is one interesting point to raise up. An example of this can be seen in Fig. 2. The values in the figure have been normalized. It is remarkable that the NOx emission, in this case, can be as much as 30% higher when imbalanced, compared to balanced combustion.
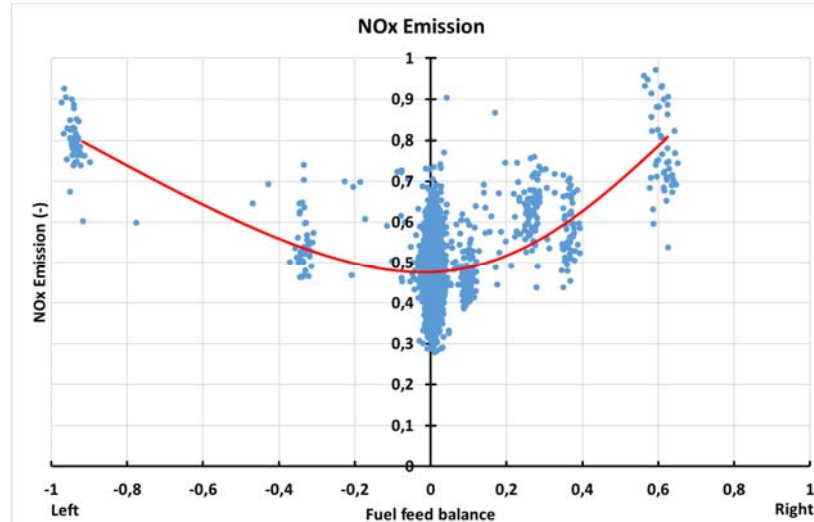
Fig. 2. Example of an emission KPI which changes with the balance in fuel feed during the fuel test.

3.2 Constructing the classification model

Separate training and testing data sets were created from the collected dataset, with 80% of the data going to the training set and the remaining 20% going to the testing set.

SVM classification of the fuel test data was tested with three kernel types. The SVM method based on RBF kernel emerged as the best choice for KPI-based classification analysis of CFB boiler data, using the selected KPIs. The summary of classification results using different kernel types can be seen in Table 1. The reported accuracy, precision, recall, and F1-score metrics for classification (See [Hossin & Sulaiman, 2015] for details) were used for discriminating the results and obtaining the optimal classifier.

Table 1. Summary of classification results.

Case	Precision	Recall	F1-score
Kernel: Polynomial			
Accuracy		1	
Macro Avg.[1]	1	1	1
Kernel: Gaussian RBF			
Accuracy		1	
Macro Avg.[1]	1	1	1
Kernel: Sigmoid			
Accuracy		0.97	
Macro Avg.[1]	0.97	0.98	0.97
[1]The metric is calculated independently for each class, and then the average is calculated across all classes.			

Based on the results we can see that all the developed SVM classification models have been successfully validated using new data. The ability of these models to successfully and correctly predict classes using new data suggests they are applicable for combustion balance detection.

In this study, we utilized a training dataset consisting of five cases in our Machine Learning models. The output of these models was transformed into soft classification using the Platt's scaling method, which provided prediction probabilities for every test data point across all cases to improve the prediction accuracy. RBF was eventually chosen as the kernel function.

The created classification model was then used to classify another, independent dataset that was totally outside the span of training data. An example of this can be seen in Fig. 3. The results show that, even if the ratio of measured fuel flows remains approximately the same, some fuel imbalance is detected by the classification model indicating that there is occasional unbalance in the combustion process.
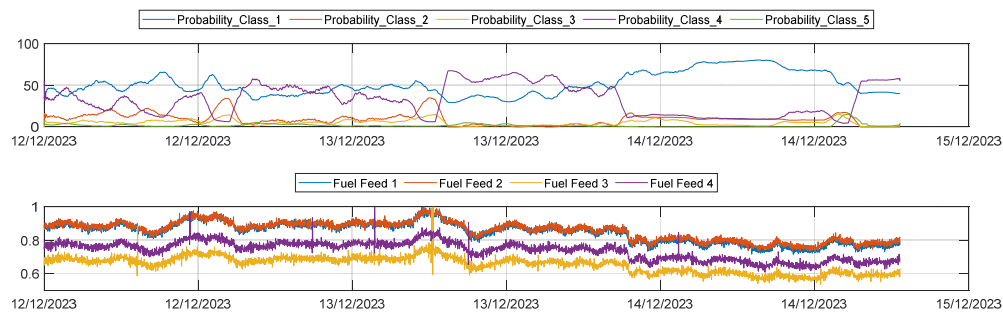
Fig. 3. Example period in which the classification model is used to estimate the combustion balance: soft classification showing the class probabilities above, and the fuel feed into the boiler below (the values are normalized).

4. Conclusion

In conclusion, we have studied the use of ML techniques to analyze CFB boiler data using KPIs describing the combustion balance in the boiler. By the study, some useful and important insights into the operational dynamics and combustion balance in CFB boilers have been gained. The SVM classification method, particularly with the RBF kernel, emerged as the preferred choice due to its robustness, generalizability, and ability to identify complex patterns in high-dimensional data.

Despite the promising results, the study has some limitations to be considered. One of the most crucial ones is the reliance of the classification model on a specific dataset with potential gaps in capturing all operational scenarios. Furthermore, the training dataset for the SVM model was quite small in this case, which highlights the importance of ongoing development in this area. Therefore, future development will concentrate especially on expanding the fuel test and thereby the training dataset, and on fine-tuning the parameters of the machine learning algorithm.

By correct remedy actions, like balancing the fuel feed or adjusting the combustion air flow, it would be possible to correct a detected combustion imbalance. It is easy to see some benefits achieved by this kind of improved balance control. During boiler imbalance, the emission levels can easily rise (See Fig. 2) and peak up due to inefficient combustion. In addition, boiler efficiency can decrease, which increases fuel costs. Boiler imbalance may also lead to material loss of critical boiler parts, which may cause unplanned shutdowns. That can be extremely costly, possibly 100k€ per day for a typical mid-size boiler.

In a summary, this study has offered valuable insights into the use of ML techniques for analyzing the imbalance in a CFB process and has proven it's applicability for on-line process performance diagnostics tools, setting the basis for future development in the field and

contributing to continuing efforts to optimize energy production, and in the meantime reducing its environmental impact.

References

Karras, T., Brosowski, A., Thrän, D. A Review on Supply Costs and Prices of Residual Biomass in Techno-Economic Models for Europe. Sustainability, 2022, 14, 7473.

Ikonen, E., Liukkonen, M., Hansen, A.H., Edelborg, M., Kjos, O., Selek, I., Kettunen, A. Fouling monitoring in a circulating fluidized bed boiler using direct and indirect model-based analytics. Fuel, 2023, 346, 128341.

Jiang, Y., Tang, Z., Zhang, X., Wang, C., Song, G., Lyu, Q. Comparative Analysis of Combustion Characteristics of a CFB Boiler during the Changes Process between High-Rated Loads and Low-Rated Loads. Energies, 2023, 16, 6190.

Labrín, C., Urdinez, F. Principal component analysis. In: R for Political Data Science, Chapman and Hall/CRC, 2020, pp. 375–393.

Maćkiewicz A., Ratajczak, W. Principal components analysis (PCA). Computers & Geosciences, 1993, 19, 303–342.

Platt, J. Probabilistic outputs for support vector machines and comparisons to regularized likelihood methods. Advances in Large Margin Classifiers. 1999, 10, 61–74.

Hossin, M., Sulaiman, M.N. A Review on Evaluation Metrics for Data Classification Evaluations. International Journal of Data Mining & Knowledge Management Process (IJDKP), 2015, 5, 1-11.

USING DEM TO EVALUATE TRIBOCHARGING AND ELECTROSTATIC FORCES OF POLARIZABLE PARTICLES IN FLUIDIZED BED

Maria Giordano[1], Francesca Orsola Alfano[1], Francesco Paolo Di Maio[1], Alberto Di Renzo[1,*]

[1]University of Calabria, DIMES Department, Via P. Bucci, Cubo 42C, 87036 Rende (CS), Italy

Email: alberto.direnzo@unical.it

Abstract

During fluidization of dielectric particles, particle-particle and particle-wall collisions tend to generate electric charge transfer (tribocharging) and electrostatic interactions. The accumulation of electrostatic charges can cause particles agglomeration and the formation of particle layers stuck on the walls (sheeting), leading to severe and costly issues. The underlying processes are not fully understood, as various aspects appear counterintuitive and are debated. One of these is the role of polarisation, whose attractive contribution to the electrostatic force can, under certain conditions, lead to particles charged with the same polarity attracting instead of repelling one another. Current implementations of tribocharging and electrostatic interactions in DEM fail to account for the effect of polarization and are unable to capture the broad variety of behaviours that charged particles can exhibit. In this contribution, a new model of tribocharging and electrostatic interactions for DEM is presented, in which interactions including both net and polarization-induced charges are accounted for. The required formalism is introduced, and the assumptions discussed. Model verification is carried out against theoretical trends for individual charged particles with the same polarity and for charged-neutral inter-particle interactions. Then, results of extended CFD-DEM simulations implementing the above model are illustrated and discussed for fluidized systems.

1. Introduction

Gas-solid fluidization technology is widely used in various applications such as heterogeneous gas-solid reactions, drying, mixing and coating. Without specific measures, the frequent contacts between fluidized particles and between the particles and the column inner walls yield the transfer of small electrostatic charges, which in time can lead to charge build-up. High charges on particles or walls give rise to a variety of electrostatic issues, like particle agglomeration, segregation, wall adhesion or, in extreme cases, significant electrostatic discharges, spark formation and even explosions. As an example, in reactors where gas-solid polymerization takes place, agglomeration of particles is known to be the main cause of the "sheeting" phenomenon [1-4]. As charge builds up, particles accumulate on the walls and, because of the exothermal nature of the reaction, melt in growing layers. At some size, these then dislodge from the column wall and fall on the distributor plate, resulting in prolonged shut down periods, production losses and high maintenance costs [5].

According to the classical "condenser model" [6], charges are exchanged between different materials in contact, with the direction of the charge transfer being dictated by the materials' work functions, i.e. by their relative position in the tribological series. Theoretically, this means that when a given particulate solids is fluidized in a column of a given material, all the particles charge with one polarity and all the walls with the opposite polarity. Consequently, following Coulomb's law, the particles should repel each other and do not form agglomerates. This results from considering each particle with their associated net charge. Several experimental observations contrast with the above theoretical result. Some researchers related the attractive nature of some contacts to the "bipolar charging" phenomenon [7], i.e. the largely

unexplained fact that a fraction of the smallest particles tend to charge with different polarity than the rest of the solid particles.

Particles of insulating or dielectric materials are characterized by another phenomenon with potentially relevant implications, named polarization of their surfaces. It can arise as a result of microscopic interaction between close charged particles or from an electric field acting on a larger scale. As will be shown below, accurate theories of finite-size particle surface charging (opposed to point charge equivalent to the particle) predict that interparticle attractions can be observed also between particles charged with the same polarity or between a charged particle and a neutral one.

In recent times, CFD-DEM simulations have been extended to include tribocharging and electrostatic interactions, with various applications, like fluidized beds [5,8-9], aerodisperion devices [10], pneumatic conveying lines [11], dry powder inhalers [12]. In all the above cases, polarization effects have not been included in the model. In the present work, a new model for DEM taking charged surface polarization into account is presented and discussed. Single particle-particle interactions are investigated first, followed by simulated fluidized bed charging tests.

2. Computational model

The computational model for hydrodynamics is based on the conventional approach integrating a local-average CFD for the fluid phase and DEM for the solid. The most important equations, including the point-charge approximation for the tribocharging and electrostatic interactions, are listed in Table 1. Each particle is assigned a charge which evolves according to the particle-particle and the particle-wall contacts experienced during its motion.

According to Eqs. 3a-b, contacts involving different materials yield charge transfer even when the two materials have the same surface charge density, e.g. they are both neutral, like at the beginning of the typical simulation. When particles of the same materials get in contact, they exchange charge only if they have different surface charge density, in the direction of equalizing the charge density. For the motion (Eqs. 2a-b), attractive-repulsive forces are determined simply by Coulomb's law, with intensity depending proportionally by both charges and inversely proportional to the interparticle distance squared.

Table 1. Main equations composing the conventional CFD-DEM model and the point-charge approximation of the electrostatic interactions.

Eulerian local-average continuity and momentum (Navier-Stokes) partial differential equations (CFD)	$\dfrac{\partial \varepsilon \rho_f}{\partial t} + \boldsymbol{\nabla} \cdot \left(\varepsilon \rho_f \boldsymbol{u} \right) = 0$	1a)
	$\dfrac{D \varepsilon \rho_f u}{Dt} = -\nabla p + \nabla \cdot \tau + F_{fp} + \varepsilon \rho_f g$	1b)
Lagrangean particle translation and rotational motion ordinary differential equations (DEM), including electrostatic force interactions	$m_i \dfrac{d\mathbf{v}_i}{dt} = \displaystyle\sum_{j=1}^{Nc} \mathbf{f}_{c,ij} + \mathbf{f}_{d,i} + \mathbf{f}_{b,i} + \mathbf{f}_{L,i} + \mathbf{f}_{g,i} + \mathbf{f}_{k,i} + \displaystyle\sum_{j=1}^{Mc} \mathbf{f}_{e,ij}$	2a)
	$I_i \dfrac{d\boldsymbol{\omega}_i}{dt} = \displaystyle\sum_{j=1}^{Nc} \mathbf{T}_{c,ij} + \mathbf{T}_{r,i} + \mathbf{T}_{f,i}$	2b)
Condenser model for tribocharging: charge transfer during particle-particle (P-P) and particle-wall (P-W) collision	$\Delta q_{p-p} = kS_m \left(\dfrac{\Phi_i - \Phi_s}{e} + \xi \dfrac{z_s}{4\pi\varepsilon_0} \left(\dfrac{q_i}{R_i^2} - \dfrac{q_j}{R_j^2} \right) \right)$	3a)
	$\Delta q_{p-w} = kS_m \left(\dfrac{\Phi_i - \Phi_s}{e} + \xi \dfrac{z_s}{4\pi\varepsilon_0} \dfrac{q_i}{R_i^2} \right)$	3b)
Electrostatic force formulas for long-range particle-particle (P-P) and particle-wall (P-W) interactions	$\mathbf{f}_{e,PP} = -\dfrac{1}{4\pi\varepsilon_0} \dfrac{q_i q_j}{R_{i,j}^2} \hat{n}_{i,j}$	4a)
	$\mathbf{f}_{e,PW} = \dfrac{1}{4\pi\varepsilon_0} \dfrac{q_i^2}{\left(2R_{i,w}\right)^2} \hat{n}_{i,w}$	4b)

2.1 Alternative models for electrostatic interactions

As anticipated, the main limitation of the point-charge approximation lies in its inability to capture the attraction between like-charged particles and between a charged particle and a neutral one. More rigorous treatments of the charge distributions on the surfaces of interacting particles require detailed consideration of the local inhomogeneities, together with more sophisticated mathematical methods. A method based on multipole expansion in Legendre polynomials was proposed and successfully employed by Bitchoutskaia et al [13] and Lindgren et al [14] to describe the interaction between polarizable dielectric spheres. The approach allows calculating the actual charge distribution on the interacting surfaces, deriving the net force by summing all the microscopic contributions. The key formula is summarized in Eq. 5.

$$F_{12} = K \frac{q_1 q_2}{h^2} - q_1 \sum_{m=1}^{\infty} \sum_{l=0}^{\infty} A_{1,l} \frac{(k_2 - 1)m(m+1)}{(k_2 - 1)m + 1} \frac{(l+m)!}{l!\,m!} \frac{r_2^{2m+1}}{h^{2m+l+3}} - \frac{1}{K} \sum_{l=1}^{\infty} A_{1,l} A_{1,l+1} \frac{(k_1 + 1)(l+1) + 1}{(k_1 - 1)r_1^{2l+3}} \qquad 5$$

where q_1 and q_2 are the net charges, r_1, r_2, k_1 and k_2 are the radii and dielectric constants, respectively, of the two particles and h is the distance between the particles' centers.

The first term in Eq. 5 is the Coulomb force, the second and the third include the polarization contributions. The formula requires infinite summations, which can be truncated to a finite number of terms to get reasonable estimates of the actual force. Unfortunately, the number of terms required to satisfy a prescribed precision depends on the level of charge and on the particle separating distance. In the authors experience, it is generally possible to achieve good convergence within minutes of computing time. However, if this can be acceptable for one particle pair, it is easily out of scale for DEM simulations involving thousands of particles, if not less.

An alternative approach is based on the effective dipole approximation, which is added to the point-charge approximation, in an attempt to expand the modelling capabilities. One such model was proposed for interacting polarizable ions by Chan [15], who introduced the effective dipole moment concept. We propose a slight modification which allows the model and its results to be applicable to solid particles, by using the particle dielectric constant to describe the ion volume polarizability. The resulting effective dipole moment is defined as:

$$p_i = 4\pi\varepsilon_0 \frac{k_i - 1}{3} r_i^3 E_i \qquad 6$$

where E_i is the electric field. These effective dipoles, one for each particle, aim to represent the non-uniform charge distributions on the particle surfaces by a simple method. There is one temporary dipole for each particle-particle or particle-wall interaction, which eventually affects the electrostatic force calculation. By combining the mutual polarization induced by two interacting spheres, it is possible to express the total electrostatic force between the two, in a compact form, by:

$$F_{12} = K \frac{q_1 q_2}{h^2} \frac{1 - 2(f_{12} + f_{21})(1 + 2y) + 2y(3 + 4y)}{(1 - 4y)^2} \qquad 7$$

with $f_{12} = \frac{k_1 - 1}{3}\left(\frac{R_1}{h}\right)^3 \frac{q_2}{q_1}$ and $y = f_{12}f_{21} = \frac{(k_1 - 1)(k_2 - 1)}{9}\left(\frac{R_1 R_2}{h^2}\right)^3$

Compared to the multipole expansion method of Eq. 5, the effective dipole approach is much more manageable and compact. It does not require iterations or summations of many terms. On the other hand, its accuracy is expected to be also more limited.

3. Results

3.1 Model comparison: particle pair

A two-sphere system is considered and the results of the electrostatic force versus the separation distance, that is the gap between the particles, using the different models are reported in Fig. 1. The line denoted by "Coulomb" denotes results with the point-charge approximation, "Exact" denotes the multipole expansion method results and "Dipole" denotes the values obtained with the effective dipole approximation.
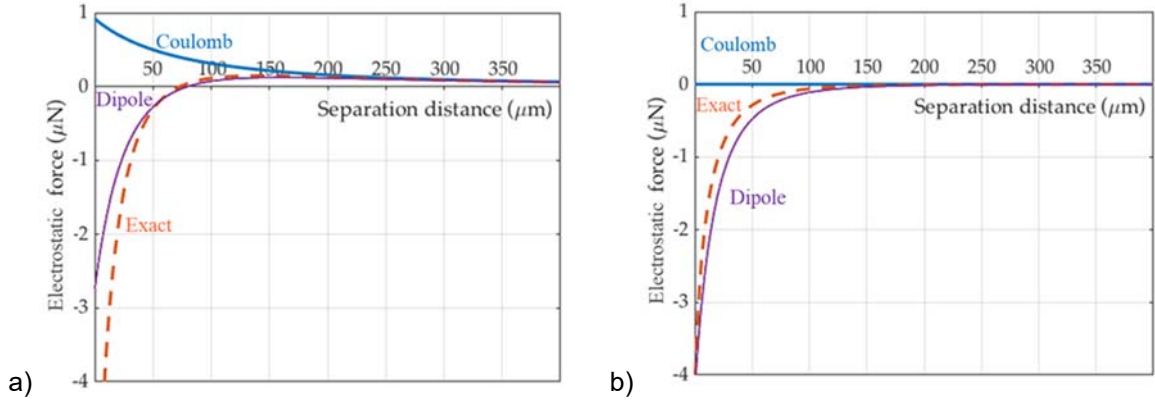
Figure 1: Absolute electrostatic force (positive is repulsive) as a function of the surface-to-surface separating distance calculated using different models ("Coulomb": point-charge approximation; "Dipole": effective dipole approximation; "Exact": multipole expansion method). a) Different-size particle pair: $r_1 = 100\ \mu m$; $r_2 = 40\ \mu m$; $q_1 = +0.5\ pC$; $q_2 = +4\ pC$; $k_1 = k_2 = 3$. b) Same-size, charged-neutral particle pair: $r_1 = 50\ \mu m$; $r_2 = 50\ \mu m$; $q_1 = 0\ pC$; $q_2 = +4\ pC$; $k_1 = k_2 = 4$.

In Fig. 1a, like-charged particles with different sizes are considered. Electrostatic interactions, modelled with Coulomb's law, appear to be always repulsive: as the separation distance decreases and particles approach each other, the repulsive force increases. The "Dipole" and "Exact" models follows the same trend at long distances, indicating that the effect of the surface polarization is negligible. However, they exhibit a different profile for values of the separation distance below 75 μm. The electrostatic force becomes negative, indicating an attractive force between the particles. Overall, the results obtained with the simple effective dipole follow reasonably well the "exact" values. Interestingly, at very short distances, the magnitude of the attractive force becomes significantly higher than the Coulombic repulsive force. As a reference, the gravitational force of a glass particle 1 would be 0.1 μN. In Fig. 1b, the plot shows analogous results for a neutral and a positive charged particle with the same size. According to Coulomb model, no interaction is obtained, as expected. With the other two models, when the distance between particles is less than about 100 μm, an attractive force is again observed. The agreement between the effective dipole approximation and the exact solution is also satisfactory.

For the investigated cases, the effective dipole and exact models, which consider induced polarization, prove to be reliable methods to simulate electrostatic interactions. To investigate the capability of the effective dipole model under more general conditions, broad differences in the sizes and charges of the two particles have been explored. Fig. 2 shows the variation of the dimensionless electrostatic force (with respect to Coulomb formula) with the charge and size ratios.
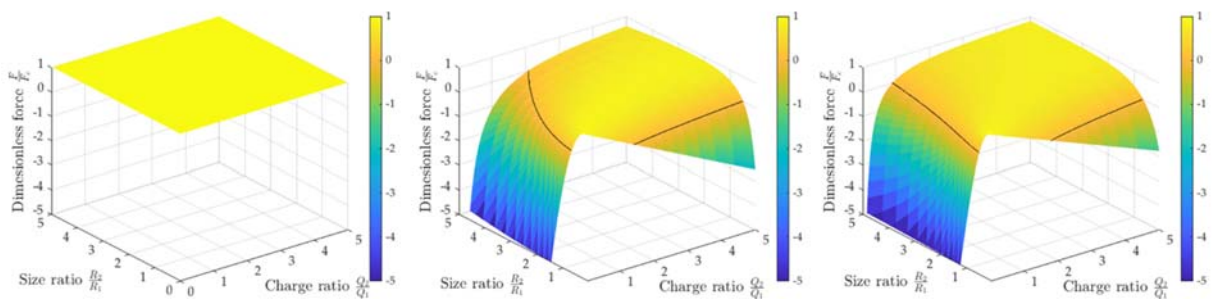
Figure 2: Colored elevation map of the dimensionless electrostatic force (with respect to Coulomb's formula) versus the two particles' size ratio and charge ratio. (left) results of the point-charge approximation; (middle) results of the multipole expansion ("exact") model; (right) results of the effective dipole model. Black lines denote zero force.

In Fig. 2, the point-charge approximation dimensionless force is systematically equal to 1, simply because the electrostatic force is calculated by the Coulomb's law. Both the multipole expansion method and the effective dipole approximation model yields a force sign inversion for some combination of size ratio and charge ratio (see the black lines, denoting zero force on the colored map). It is worth noting that the predicted force resembles Coulomb's value when the size ratio and the charge ratio assume similar values, e.g. the bigger particle is also more charged, with similar ratios. On the other hand, strongly attractive forces are obtained when the reverse occurs, e.g. when the smaller particle is more charged.

Overall, the dipole approximation yields a reasonable estimate of the electrostatic force, capturing the attractive-repulsive change and the absolute value satisfactorily compared with the exact method. For a global assessment, it should be recalled that the multipole expansion solution is not practicable from DEM simulations of many interacting particles and is, therefore, not a viable option. On the other hand, the improvement of the effective dipole model over the point-charge approximation is rather significant.

3.2 Simulation of fluidized bed of polymeric particles

The charge evolution of a small-scale fluidized bed of polyethylene particles is simulated using the open-source CFD-DEM code MFIX (https://mfix.netl.doe.gov), developed by NETL, USA, in which specific modules implementing the point-charge and effective dipole approximations have been integrated. The geometry is analogous to the lab-scale system investigated experimentally and by simulation by Sippola et al. [16]. Relevant data are listed in Table 2.

Table 2. Simulated system parameters.

Particle diameter	276 μm
Particle density (polyethylene)	960 kg/m^3
Number of particles	140400
Young's modulus	0.063 MPa
Restitution coefficient	0.9
Dielectric constant	2.25
Work function difference	1.43 eV
Grid size	1 x 1 x 1 mm^3
Inlet air velocity	1.50 m/s
Bulk superficial air velocity	0.54 m/s
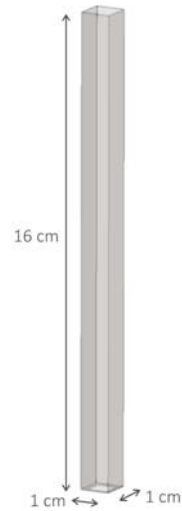
Figure 3. Simulated geometry
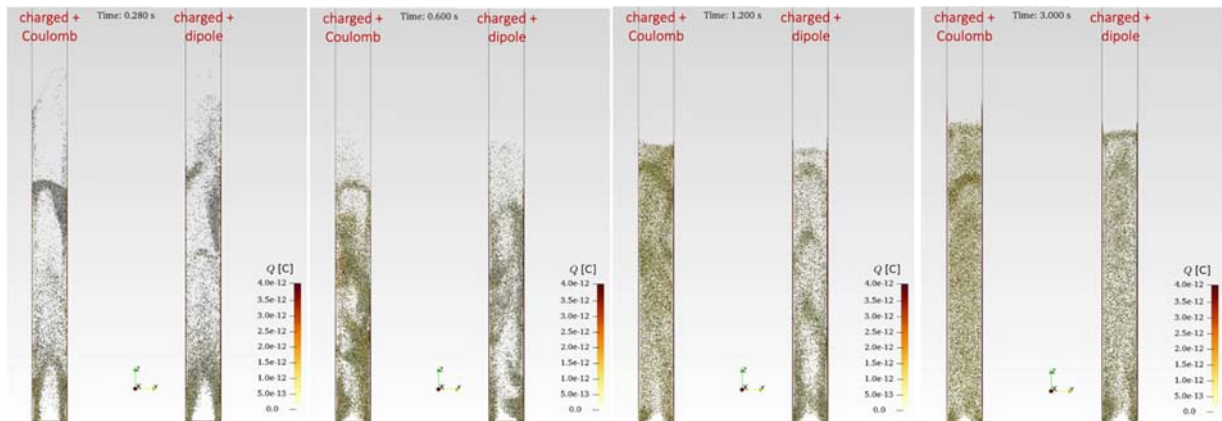
Figure 4. Snapshots of an internal slice of the fluidized bed after (from left to right) 0.28, 0.60, 1.20 and 3.00 s. in each figure, the left column shows results with Coulomb's law and the right one with the dipole.

Figure 3 shows the square cross-section geometry and the system height. Figure 4 shows four snapshots of the simulated particle dynamics, comparing the point-charge (Coulomb's law) with the effective dipole approximation. The typical evolution starts from neutral particles, then the initial charging due to particle wall collisions can be observed. A particle layer formed along the wall is clearly visible. Overall, the bubbling regime switches slowly to the slugging regime (see also Figure 5), until after tens of seconds, the bed becomes fully charged. At this stage, except for the layer stuck on the walls, the other particles fluctuate inside the column, kept levitating by the action of the electrostatic forces and the upflowing air.

Figure 5. Average particle charge vs. time. Coulomb model (blu) vs. dipole model (red)

4. Conclusion

A new model based on the concept of effective dipole, accounting for the charge polarization on the particle surface, is described and implemented into a CFD-DEM code, for the analysis of fluidized bed behavior. The proposed model is compared against the point-charge approximation (Coulomb's law) and a more demanding, rigorous mathematical method, used as a reference. Compared to the current implementations (e.g. the point-charge approximation) the effective dipole model allows capturing the sign reversal for given combinations of size and charge ratios in two-particle interactions. Then, a fluidized bed in considered, where the dynamic results obtained with Coulomb's law are compared with those of the effective dipole. Qualitatively, there is no striking difference in the charge dynamics. On the other hand, the dipole model, under comparable conditions, yields a lower charging characteristic time. Overall, the proposed model proves capable of capturing interactions at the particle level well. In real multiparticle systems, control on the exact conditions many not be easy, so additional testing on larger units are necessary.

Acknowledgment

References

[1] P. Mehrani, et al. (2010) *Journal of Electrostatics*, 68, 492-502.

[2] P. Mehrani, et al. (2017), *Journal of Electrostatics*, 87, 64-78.

[3] Sowinski, A. et al. (2010). *Chemical Engineering Science*, 65(9), 2771–2781.

[4] Lacks, D.J., & Shinbrot, T. (2019). *Nature Reviews Chemistry,* 3 (8), 465–476.

[5] Kazemi, S. et al. (2021). *Canadian Journal of Chemical Engineering*, 99(7), 1582–1594.

[6] Matsusaka, S. et al. (2010). *Chemical Engineering Science*, *65*(22), 5781–5807.

[7] Konopka, L. et al. (2020). *Powder Technology*, *367*, 713–723.

[8] Pei, C. et al. (2013). *Powder Technology*, *248*, 34–43.

[9] Pei, C. et al. (2016). *Powder Technology*, *304*, 208–217.

[10] Alfano, F. O. (2021). *Powder Technology*, 382, 491–504.

[11] Grosshans, H. et al. (2022). *Chemical Engineering Science*, 254, 117623.

[12] Alfano, F. O. (2022). *Powder Technology*, 408, 117800.

[13] Bichoutskaia, E. et al. (2010). *Journal of Chemical Physics*, 133(2).

[14] Lindgren, E. B. et al. (2016). *Physical Chemistry Chemical Physics*, 18(8), 5883–5895.

[15] Chan, H. K. (2020). *Journal of Electrostatics*, 103435, 105.

[16] Sippola, P. (2018). *Journal of Fluid Mechanics*, 849, 860–884.
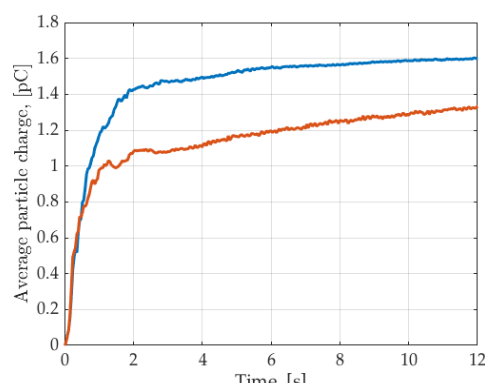
A SELF-ADAPTIVE FITTING ALGORITHM FOR EMMS DRAG USING ARTIFICIAL NEURAL NETWORK

Bingzhen Zhang, Feifei Song*

School of Chemistry and Chemical Engineering, Tianjin University of Technology, Tianjin 300384, China

*Email: *songfeifei@email.tjut.edu.cn*

Abstract

The previous fitting algorithms for energy-minimization multi-scale (EMMS) drag all required human involvement, such as determining the formula in advance or choosing the network structure from several grid search results. In this study, we proposed a self-adaptive fitting algorithm for EMMS drag (SA-EMMS algorithm) by using the Artificial Neural Network (ANN). The SA-EMMS algorithm can automatically optimize its network structure according to the network complexity and specified error requirement. It was found that the SA-EMMS algorithm can automatically obtain the optimal network structure under specified error requirements, which shows good applicability for different fluidization systems.

1. Introduction

The drag force plays a crucial role in gas-solid fluidization simulations, which has received growing attention from researchers in the past decades (Lu et al.,2019). However, except for particle-resolved direct numerical simulation (Deen et al.,2014), where the flow fields of both the gas and solid phases are fully resolved and no drag closure is required, most multiphase flow models require a sub-grid drag model to account for effects of the unresolved, meso-scale structures on drag force (Liu et al., 2020; Wang et al., 2020).

One sub-grid drag model which has been successfully used in fluidized bed simulations is the energy minimization multiscale (EMMS) model (Li et al., 1994). In this model, the fluidization system is characterized by a dense phase and a dilute phase, which are controlled by conservation equations for mass and momentum, as well as a stability condition. These equations are typically solved to generate the heterogeneity index for drag in conjunction with the corresponding structural parameters in EMMS model (Yang et al., 2003).

To integrate EMMS model into computational fluid dynamics (CFD) simulations, such drag index needs to be fitted as a function of the voidage, slip velocity and so on (Lu et al., 2009). However, fitting the drag index non-linearly could be quite difficult, especially when the number of degrees of freedom exceeds two. Additionally, such fitting also requires specifying an appropriate fitting formula in advance and manual segmentation based on the data, which can be time-consuming and inconvenient to use.

Thanks to the rapid development of deep learning, artificial neural network (ANN) has become a powerful tool for solving the nonlinear fitting problem in sub-grid drag models. Nikolopoulos et al. (2021) applied ANN to fitting problem of EMMS drag model for the first time, solving the need for specifying formulas and data segmentation in traditional fitting methods. However, because ANN is trained under certain operating conditions and material properties, the applicable scope of their scheme is limited. Using it in a quiet different operating condition and material property always means the requirement of retraining and choosing the network structure from grid search results. To solve this problem, researchers (Stamatopoulos et al.,2023; Yang et al.,2021) developed the generic EMMS-ANN drag model, where ANN is trained under a wide range of operating conditions and material properties, so it can be integrated into different CFD simulations without the need of retraining. But compared to fitting for a specified condition, generic EMMS-ANN drag model need to be applicable to a wide range of conditions, and hence requires a more complex network structure, which means more computation time. As drag will be calculated at every iteration and for each grid, it may be called millions or billions of times during one CFD simulation, so even a slight increase in drag

calculation time can lead to a significant increase in simulation time, which means that the generic EMMS-ANN has a higher computational burden.

This work aims to develop a self-adaptive fitting algorithm for EMMS drag (SA-EMMS algorithm) using ANN. The algorithm can automatically optimize its network structure according to the network complexity and specified error requirement, making it both user-friendly and computationally efficient. To achieve this, the training and testing datasets are generated by solving the EMMS equations under the specified operating conditions and material properties. The ANN is trained with the training dataset, and the optimal structure is obtained through a binary search based on its network complexity. Then, the algorithm is tested against the original EMMS model for different cases, and the conclusion and future work are summarized at last.

2. Methodology

2.1 Procedure description
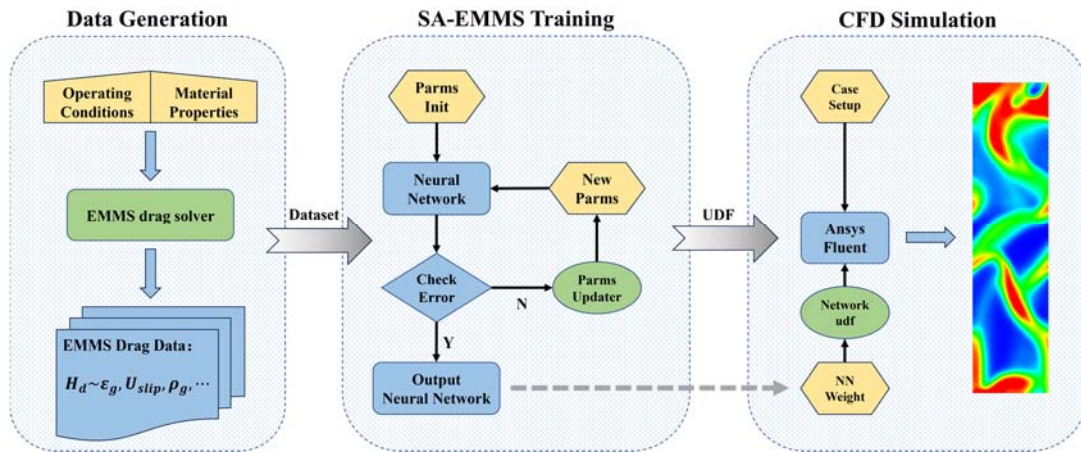
Fig. 1. Schematic diagram of the SA-EMMS algorithm.

Compared to previous methods, the SA-EMMS algorithm requires no human intervention at all. To implement a CFD simulation with SA-EMMS algorithm, in addition to inputting the operating conditions and material properties, the only thing that users need to do is specifying the error requirement, and the following processes will be automatically completed by the SA-EMMS algorithm. As shown in Fig. 1, a custom-build code is used to generate the training dataset by solving the EMMS equations under specified conditions. Afterwards, the SA-EMMS algorithm will automatically search for the optimal network structure that meets the specified error requirement, and output the optimal structural parameters to a weight file. Finally, a pre-build UDF is used to load the weight file and couple the EMMS model into the CFD simulation.

2.2 Binary search for the optimal structure

Fig. 2 shows the pseudo-code of SA-EMMS algorithm, which details the process of using binary search to find the optimal structure of ANN. During this search process, ANNs with different structures are sorted by the network complexity (which is defined as the parameter quantity in this work), then a binary search algorithm is used to find the optimal ANN, which has the least number of parameters while meeting the specified error requirement.

3. Results and discussion

3.1 Model validation in bubbling fluidized bed

The SA-EMMS algorithm was first implemented using the same conditions as presented in Luo et al. (2017). Here, the SA-EMMS algorithm takes voidage and particle Reynolds number as inputs, which is consistent with the independent variables of EMMS/Matrix used in the literature.

Algorithm 1: SA-EMMS algorithm

Input: operating conditions X_{op}, material properties X_{mp}, specified error requirement ε,

       search upper bound for layer number $N_{l,ub}$ and neurons per layer $N_{n,ub}$.

Procedure:

  # Phase 1: Generate the training dataset

  EMMS/Matrix algorithm is solved under the specified X_{op} and X_{mp}, the generated EMMS drag dataset will be used to train ANN

  # Phase 2: Binary search for the optimal structure

  1:   List = []

  2:   **for** $i \leftarrow 1$ to $N_{l,ub}$ **do**

  3:      **for** $j \leftarrow 1$ to $N_{n,ub}$ **do**

  4:         $PN_{i,j} \leftarrow$ number of parameters in ANN with i hidden layers and j neurons per layer

  5:         List.append([$i, j, PN_{i,j}$])

  6:      **end for**

  7:   **end for**

  8:   List $\leftarrow$ sorted(List, key=lambda t: t[2])

  9:   left $\leftarrow$ 0

  10: right $\leftarrow$ len(List) - 1

  11: **while** left<right **do**

  12:     mid $\leftarrow$ left + (right − left)//2

  13:     Build ANN$_{mid}$ with List[mid][0] hidden layers and List[mid][1] neurons per layer

  14:     Train ANN$_{mid}$ on EMMS drag dataset, whose training error is ε_{mid}

  15:     **if** $\varepsilon_{mid} > \varepsilon$ **then**

  16:        left $\leftarrow$ mid+1

  17:     **else**

  18:        right $\leftarrow$ mid

  19:     **end if**

  20: **end while**

Output: Save trained ANN$_{left}$ to a disk file

Fig. 2. Pseudo-code of SA-EMMS algorithm.

In this case, the error requirement is specified as 10^{-4}, and the optimal structure found by the SA-EMMS algorithm is 7 layers * 8 neurons/layer. The heterogeneity indexes calculated by SA-EMMS and EMMS/Matrix are shown in Fig. 3. It can be seen that results of the two models are almost identical, with only some slight deviation under low Reynolds number conditions, which may be due to the small values of the corresponding heterogeneity indexes. Meanwhile, to better validate the SA-EMMS algorithm, we also calculated the relative error and determination coefficient between SA-EMMS and EMMS/Matrix, and the results were 0.006569 and 0.998668, respectively, indicating that the accuracy of SA-EMMS algorithm is very good.
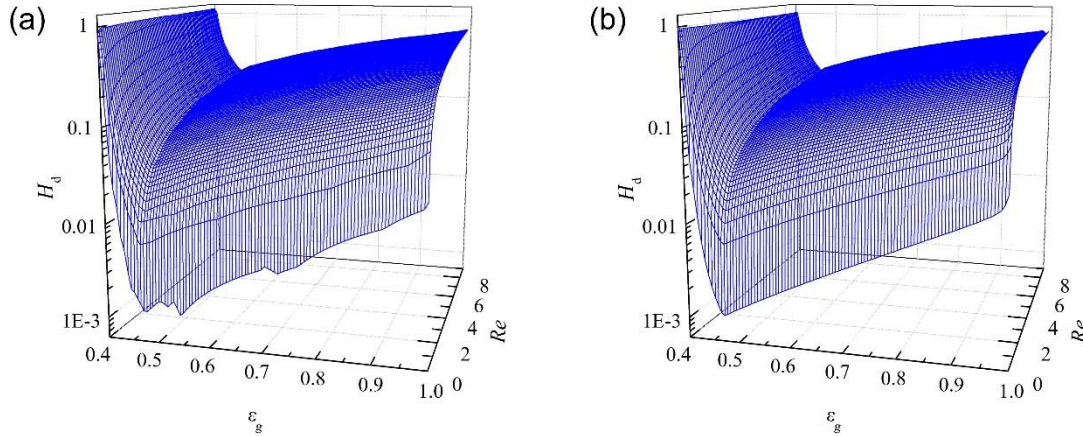
Fig. 3. Comparison of the heterogeneity index between (a) SA-EMMS and (b) EMMS/Matrix.

3.2 Model validation in tapered-in riser

To further evaluate the SA-EMMS algorithm, we performed it in a tapered-in riser as presented by Liu et al. (2019). Unlike the literature that only uses voidage as the independent variable, considering the axial variation of the EMMS drag in the tapered-in riser, we use both voidage and the superficial gas velocity as inputs.
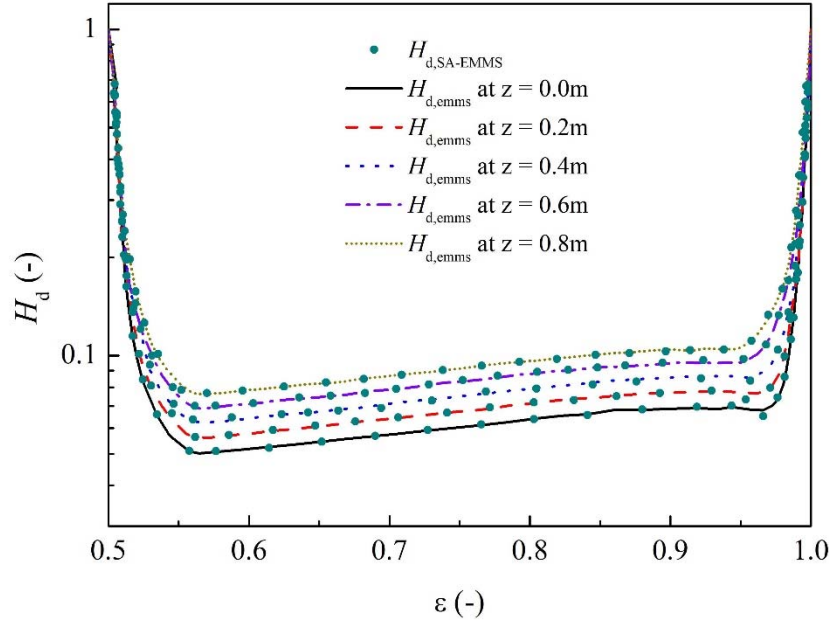
Fig. 4. Comparison of the heterogeneity index between EMMS model and this work at different height.

In this case, the error requirement is also specified as 10^{-4}, and the optimal structure found by the SA-EMMS algorithm is 9 layers * 10 neurons/layer. In Fig. 4, the heterogeneity indexes calculated by the traditional EMMS model at different heights (corresponding to different superficial gas velocities) and the SA-EMMS algorithm are compared, showing a perfect agreement.
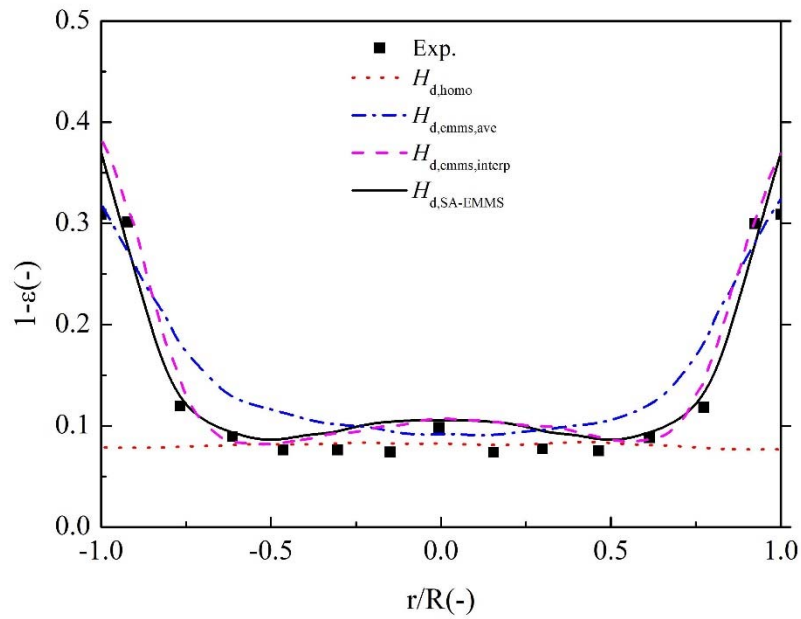
Fig. 5. Comparison of the radial solid concentration distributions at z = 0.2 m by using different drag models.

To further validate the performance of the SA-EMMS algorithm in CFD, simulations were implemented for the tapered-in riser using 4 different drag models: the homogeneous drag ($H_{d,homo}$), the average EMMS drag ($H_{d,emms,ave}$), the interpolated EMMS drag ($H_{d,emms,interp}$) and the SA-EMMS drag ($H_{d,SA-EMMS}$). Please refer to the work of Liu et al. (2019) for the specific model meanings and detailed simulation setups.

The simulated radial solid concentration distributions are depicted in Fig. 5. It can be found that results using the SA-EMMS drag and the interpolated EMMS drag are generally the same, which are both closer to the experimental data than results using the average EMMS drag. Meanwhile, the simulation using the homogeneous drag predicts a nearly uniform distribution, which is consistent with results of Liu et al. (2019).
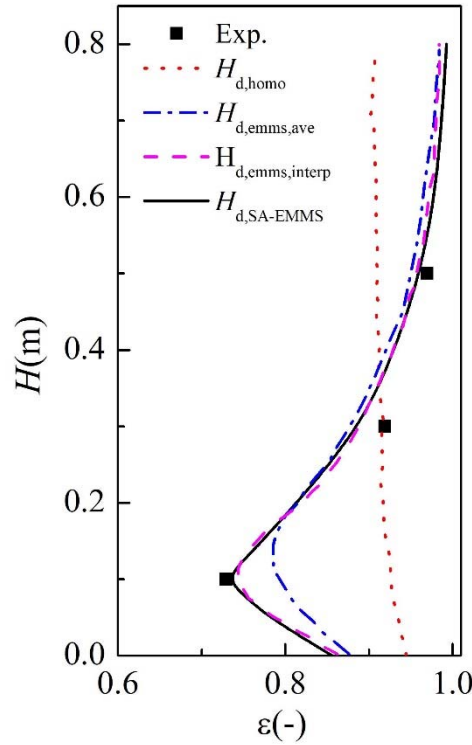
Fig. 6. Comparison of the time-averaged voidage profiles by using different drag models.

Fig. 6 compares the time-averaged voidage profiles obtained from experiments and simulations using the 4 different drag models. Similarly, the SA-EMMS and the interpolated EMMS drag make much better predictions than the other 2 models. Results using SA-EMMS drag are very close to the interpolated EMMS drag, and even show a slightly better agreement with experimental data at the lower part of the riser, which may be due to interpolation errors in the interpolated EMMS drag.

Comparisons above indicate that the SA-EMMS algorithm can automatically achieve comparable results to the EMMS model specially calculated for a specific condition, which enables it to provide a simple, accurate and efficient fitting for the EMMS model.

4. Conclusion

A SA-EMMS algorithm was developed using ANN for the fitting problem of the EMMS drag. By setting the error requirement, the algorithm can automatically implement the binary search algorithm to find the optimal network structure, which is quantified by the network complexity. Then the SA-EMMS algorithm was tested for different cases, and its results were highly consistent with the original EMMS model, indicating that our new algorithm has a good applicability in different fluidization systems. As our algorithm requires no human involvement,

and can get the optimal structure, compared to previous methods, it is more user-friendly and computationally efficient.

Although the SA-EMMS algorithm is designed for fitting the EMMS drag model, it is also applicable to any problem that requires a fitting algorithm, such as usage in fitting other drag model, the granular pressure and viscosity can be expected in future.

Acknowledgment

References

Deen, N.G., Peters, E.A.J.F., Padding, J.T., et al. Review of direct numerical simulation of fluid–particle mass, momentum and heat transfer in dense gas–solid flows. Chemical Engineering Science. 2014. 116, 710-724

Liu, X., Ge, W., Wang, L. Scale and structure dependent drag in gas–solid flows. AIChE Journal. 2020. 66(4), 16883

Li, J., Kwauk, M. Particle-fluid two-phase flow energy-minimization multi-scale method. Beijing: Metallurgical Industry Press. 1994

Luo, H., Lu, B., Zhang, J., et al. A grid-independent EMMS/bubbling drag model for bubbling and turbulent fluidization. Chemical Engineering Journal. 2017. 326, 47-57

Lu, B., Niu, Y., Chen, F., et al. Energy-minimization multiscale based mesoscale modeling and applications in gas-fluidized catalytic reactors. Reviews in Chemical Engineering. 2019. 35(8), 879-915

Lu, B., Wang, W., Li, J. Searching for a mesh-independent sub-grid model for CFD simulation of gas–solid riser flows. Chemical Engineering Science. 2009. 64(15), 3437-47

Liu, X., Zhao, M., Hu, S., et al. Three-dimensional CFD simulation of tapered gas-solid risers by coupling the improved EMMS drag. Powder technology. 2019. 352, 305-313

Nikolopoulos, A., Samlis, C., Zeneli, M., et al. Introducing an artificial neural network energy minimization multi-scale drag scheme for fluidized particles. Chemical Engineering Science. 2021. 229, 116013

Stamatopoulos, P., Stefanitsis, D., Zeneli, M., et al. Development of an artificial neural network EMMS drag model for the simulation of fluidized beds in chemical looping combustion. Chemical Engineering Science. 2023. 282, 119286

Wang, W., Lu, B., Geng, J., et al. Mesoscale drag modeling: a critical review. Current Opinion in Chemical Engineering. 2020. 29, 96-103

Yang, Z., Lu, B., Wang, W. Coupling Artificial Neural Network with EMMS drag for simulation of dense fluidized beds. Chemical Engineering Science. 2021. 246, 117003

Yang, N., Wang, W., Ge, W., et al. CFD simulation of concurrent-up gas-solid flow in circulating fluidized beds with structure-dependent drag coefficient. Chemical Engineering Journal. 2003. 96(1-3), 71-80

Coarse grained CFD-DEM simulation of industrial scale CFB

Zhengquan Li*, Boqun Zhang, Huimin Chen, Yide Wang, Kaixuan Li

International Institute for Innovation, Jiangxi University of Science & Technology, Ganzhou 341000, China
*Email: zhengquan.li@jxust.edu.cn

Abstract

The combined model of computational fluid dynamics and discrete element method (CFD-DEM) is becoming one of the indispensable tools to study particle-fluid flows in particle scale. But the number of calculated particles is restricted because of the excessive calculation cost and/or limited memory address space, and thus it is hardly used in investigating design and operational conditions relevant to industries. In this paper, a coarse-grained CG CFD-DEM model is developed and used to model the gas-solid two-phase flow in an industrial scale CFB riser. The simulation results are analyzed in terms of axial pressure gradient, differences of gas and solids velocities and solid concentration, solids back-mixing, and particle clusters in the riser reactor. It is shown that the typical flow structures in the large-scale CFB riser can be captured well by the CG CFD-DEM approach. Good agreement between the simulation results and experiment ones is observed. Further, the effects of different model particle sizes and solid mass flow rate on the on the gas-solid flow pattern are studied too. The results show that this model is generally valid and reasonably accurate when the flow is dilute. Some uncertainties or errors may appear if the solid mass flow rate is too big.

1. Introduction

Circulating Fluidized Bed (CFB) technology, an advanced fluidization technique facilitating the suspension of solid particles in rapid fluid states, has been broadly applied in industries such as petrochemicals (Huang et al., 2024). This technology allows for fluid-like dynamic behavior of suspended solid particles, thereby optimizing gas-solid contact efficiency, heat transfer performance, and selectivity in chemical reactions under rapid fluidization conditions. The primary components of a CFB system include a riser reactor, a cyclone separator, and a recycling mechanism, where the characteristics of gas-solid flow within the riser directly influence the efficiency of chemical reactions and the overall system performance. Despite over half a century of application history and research foundation, the design and construction of CFB technology at an industrial scale still confront challenges related to inadequate understanding of complex flow structures and uncertainties in performance prediction during scaling processes.

In terms of gas-solid flow simulation, the widely adopted Two-Fluid Model (TFM) and the Computational Fluid Dynamics-Discrete Element Method (CFD-DEM) models serve as potent tools for understanding and optimizing CFB technology (Li et al., 2024; Tang et al., 2024). While TFM is capable of simulating flows independent of particle numbers, it fails to accurately capture particle-level gas-solid flow details within CFB risers. On the other hand, CFD-DEM models, despite significant achievements in revealing the fundamental mechanisms of gas-solid flow, are limited in their widespread industrial application due to high computational costs.

Given these considerations, the current study employs a Coarse-Grained CFD-DEM (CG CFD-DEM) model aimed at optimizing the use of computational resources by reducing the required computational load without compromising simulation accuracy (Che et al., 2023). This paper will delve into the applicability of the CG CFD-DEM model in simulating real-world

industrial-scale CFB risers, analyze the impact of different operational variables on gas-solid flow patterns, and further evaluate the model's limitations and potential in elucidating flow mechanisms within CFB risers. This exploration seeks to advance the application and development of CFB technology across various industrial domains.

2. Coarse-grained (CG) concept and Simulation conditions

The CFD-DEM model has been extensively studied and will not be elaborated upon in detail in this document (Li et al., 2024; Wang et al., 2024). Instead, the primary focus will be on elucidating the principles and concepts of the CG (Coarse-Grained) CFD-DEM model.

In the CG concept, the system is described by focusing on larger subcomponents (coarse-grained description) and the smaller components that make up these larger components (fine-grained description). The central premise is that particles with similar attributes can be aggregated into a larger CG particle, which represents a group of real particles with the same properties, exhibiting identical translational and rotational behaviors. Compared to the standard CFD-DEM model, the CG approach assumes that (i) like particles can be aggregated into a larger CG particle, (ii) collisions between particles are represented by collisions between CG particles, and (iii) particle-fluid interactions are substituted by CG particle-fluid interactions. The motion of CG particles is assumed to be consistent with the movement of the original particle group it represents, with rotation assumed to occur around their own centers of mass, not considering the rotation of original particles around the center of the CG particle. The CG particle model attempts to emulate the behavior of real particles in calculations of particle-fluid interaction forces and CG particle interaction forces, yet the precise simulation of particle-particle interaction forces remains a challenge. The modeling of drag forces is achieved by balancing the CG particles with the real particles (Chu et al., 2016; Li, 2016).

Table 1. Parameters used in this work

Phases	Parameters	Symbol	Units	Value
Solid	Solids density	ρ	Kg/s	863
	Solids particle radius	R_i	µm	802
	Size distribution			Mono-size
	Solids mass flow rate	M_s	Kg/s	5.54
	Time step for solids	Δt	s	1×10^{-6}
Gas	Gas velocity	v_g	m/s	5.71
	Gas flow rate	M_g	Kg/m^3/s	0.476
	Gas density	ρ	Kg/m^3	1.225
	Gas viscosity	µm	Pa s	1.79e-5
	Time step for gas	Δt	s	1×10^{-4}

The side inlet is engineered with an inclination angle to facilitate a smoother entry of solids. The experimental data employed in this study are derived from the "Third Challenge Problem," as indicated in Table 1, (Breault et al., 2010) aligning with the parameters of NETL experiments. The CG CFD-DEM model, developed by the "SIMPAS" group at Monash University, was integrated into Fluent 12.1 via User-Defined Functions (UDF), enabling bidirectional coupling. To mimic real-life conditions, the simulation utilized non-periodic boundary conditions and included 100,000 particles.

3. Results and discussion

This paper analyzes the axial pressure gradient of gas-solid velocities, solid concentration, solid backmixing, and particle agglomeration in riser reactors, drawing upon the classical characteristics of gas-solid flow within CFB (Circulating Fluidized Bed) risers reactor.

3.1 Solids distribution, velocity and concentration analysis

The axial pressure gradient curve is a commonly utilized methodology for analyzing the distribution of solids within the riser of a Circulating Fluidized Bed (CFB). Fig. 1. (a) illustrates the variation of pressure gradients at different heights, juxtaposed with experimental data for comparison. These curves exhibit a U-shape, reflecting the distribution characteristics of solids—concentrated at the bottom, sparse in the middle, and increasing again at the top—corresponding to the loading, acceleration, and exit processes of solids within the riser. Overall, the simulation results show a basic consistency with experimental outcomes, with most simulation data falling within the 95% confidence interval of the experiments (Breault et al., 2010; Li, 2016).
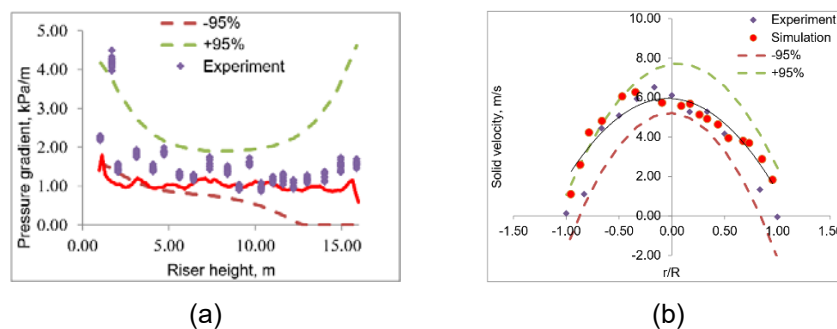
Fig. 1. (a) Profiles of pressure gradient and (b) radial profiles of solid velocity at 8.88m.

One of the quintessential characteristics of CFB risers is the core-annular flow, where solid particles move more rapidly in the core area and decrease towards the wall area; conversely, the solid concentration is higher in the wall area and lower in the core area. By repeatedly reading and averaging the solid velocity data from relevant data files, Fig. 1. (b) presents the radial distribution of solid velocity at 8.88m, compared with the 95% confidence level of experimental data, demonstrating a reasonable consistency between simulation results and experiments. Although the simulation slightly overestimates solid velocity at certain heights, this may be related to the arrangement of gas inlets and outlets on the side of the riser. Figure 3 further validates the uneven distribution, with lower solid concentration in the center region and higher concentration in the wall region, showcasing the characteristics of core-annular flow.

3.2 Particle cluster and interaction force analysis

As noted in the introduction, a key characteristic of the fluid dynamics within Circulating Fluidized Bed (CFB) riser reactors is the presence of solid agglomeration, which significantly influences the macroscopic gas-solid flow behaviors within the reactor. Fig. 2 demonstrates the overall pattern of solid particle flow within the CFB riser, confirming the non-uniform distribution of particles with agglomerations predominantly formed in the wall region, consistent with prior experimental outcomes. Fig. 2. (b) distinctly illustrates the upward gas-solid flow in the central region and the downward flow near the walls, effectively capturing the

solid recirculation phenomenon, primarily induced by the opposing airflow direction near the non-slip walls, which is one of the critical factors for the formation of agglomerations in the wall area. As depicted in Fig. 2. (c), most particles within agglomerates have very low velocities and move in the opposite direction to the main flow, indicating the presence of solid recirculation, aligning with well-known experimental results and the qualitative conclusions of some researchers regarding riser reactor simulations (Zhang et al., 2008).
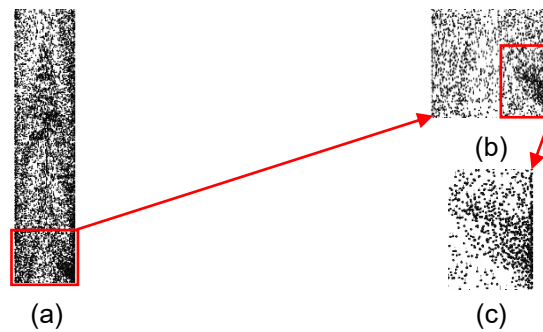
Fig. 2. (a) Solid particle flow pattern; (b) partially enlarged view of (a); (c) partially enlarged view of (b).

The key factors controlling the characteristics of gas-solid two-phase flow within risers include the forces between gas and particles, among particles themselves, and between particles and walls. Measuring these forces poses technical challenges, yet they can be readily acquired through CG CFD-DEM methods. Fig. 3. (a) and (b) display an uneven distribution of the Z-direction gas-solid interaction forces within the CFB riser, with smaller forces in the central region and greater forces on the sides. In conjunction with the solid concentration distribution shown in Fig. 3. (c), it is evident that the particle layer is denser in the wall region, offering greater resistance to the airflow and thereby increasing the gas-solid forces. Fig. 3. (d) and (e) reveal that the distribution of gas and solid velocities is inversely related to the distribution of interaction forces, indicating that intense solid-phase action redirects the airflow towards areas of lower resistance.
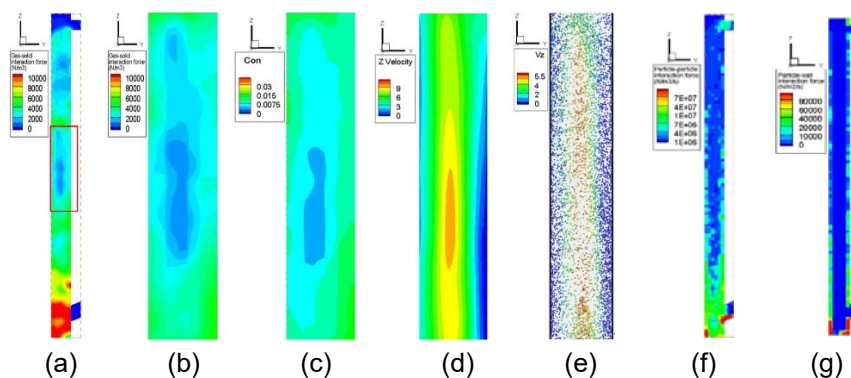
Fig. 3. Distribution of (a) gas-solid interaction force in Z direction in the CFB riser; (b) partially enlarged view of (a); (c) solid particle concentration; (d) gas velocity in Z direction; and (e) solid particle velocity in Z direction; (f) solid-solid and (g) solid-wall interaction forces in the CFB riser.

The forces of solid-solid and solid-wall interactions directly affect the fracturing, degradation, or wear of solids, as well as the wear of riser walls, but experimental data on these interactions are scarce. This study has surmounted this challenge through CG CFD-DEM simulations, with Fig. 3. (f) and (g) showing the distribution of these interaction forces. The distribution reveals that both solid-solid and solid-wall interaction forces are greater in the bottom region, decrease

in the middle region, and then increase near the outlet, corresponding to the changes in solid concentration within the riser and the core-annular flow structure.

3.3 Effects of different model particle sizes

In this study, the variables under investigation within the coarse-grained (CG) model are the sizes of particles used and different solid mass flow rates. As depicted in Fig. 4. (a), at a height of 8.88 meters, the radial solid velocity profiles for different model particle diameters (20, 25, 30 mm) are generally similar, capturing the characteristic features of radial solid velocity. Fig. 4. (b) illustrates the radial solid velocity profiles at the same height under three different mass flow rates. Each profile displays a core-annular flow structure with particle velocity decreasing from the central to the wall region. The highest particle velocities in the center increase with the mass flow rate, likely due to more solids accumulating in the wall region and thereby constraining the airflow. To maintain a constant superficial gas velocity, the gas velocity in the riser's center must increase accordingly, resulting in an elevation of central particle velocities, aligning with findings from other researchers (Wang et al., 2013).
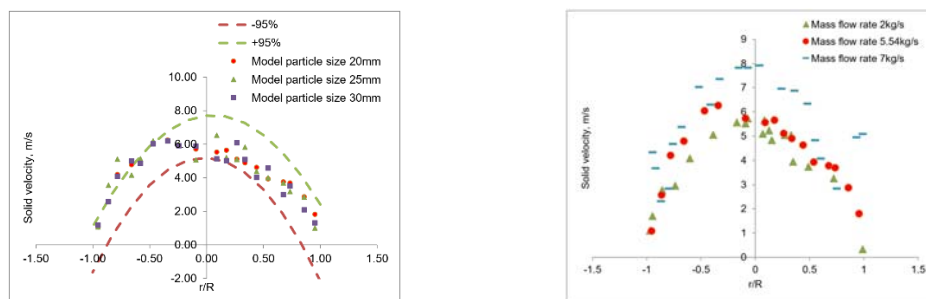
  (a) Particle sizes are 20, 25, 30 mm   (b) Solid mass flow rates are 2, 5.54, 7.0 Kg/s
  Fig. 4. Radial distribution of solid velocity under different particle sizes and solid mass flow rates.

Fig. 5. (a) to (c) show the solid particle flow patterns in the CFB riser for different particle diameters, including magnified views. With the increase in model particle diameter, the number of particles decreases since a 30 mm diameter model particle represents more actual-sized particles, given the fixed number of real-size particles in the CFB riser. Additionally, the gas-solid flow patterns are similar across these scenarios, with solid agglomeration and solid recirculation in the wall region being well captured.

As shown in Fig. 5. (d) to (f), the core-annular flow structure, particle agglomeration, and solid recirculation are well captured in all three cases. However, upon close examination, particularly for the case with a mass flow rate of 7.0 kg/s, an unexpected reversal in particle velocity near the wall region is observed. Further examination of the results in Fig. 4. (b) indicates that within certain radial positions, particle velocity decreases from the center to the sides, while a reverse trend is detected in other positions. This inconsistency suggests that the uncertainties or approximations within the CG CFD-DEM model become significant when the gas-solid flow is denser. The reason is that the CG CFD-DEM model is more suited to dilute flows where the interactions among particles might be insignificant and hence ignorable. However, when particle interactions play a key role in dense flows, the uncertainties or approximations in the coarse-grained model become apparent. Similar conclusions have been reported by Chu and others (Chu et al., 2016). The results and analysis indicate that for the

cases studied in this paper, the applicable range is when the solid mass flow rate is less than approximately 5.54 kg/s.

| (a) 20 mm | (b) 25 mm | (c) 30 mm | (d) 2.0 kg/s | (e) 5.54 kg/s | (f) 7.0 kg/s |
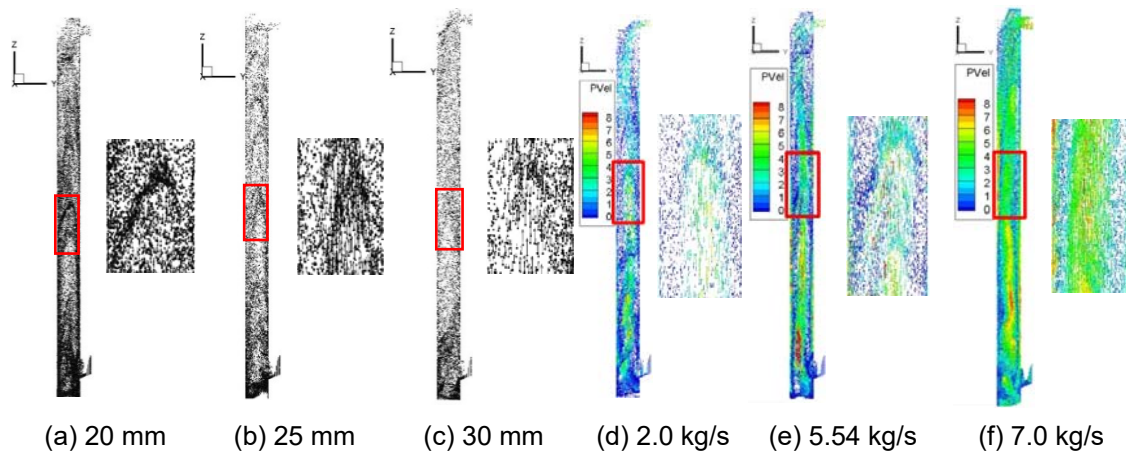
Fig. 5. Different model particle sizes and solid mass flow rates, the solid particle flow pattern.

4. Conclusions

In this work, the CG CFD-DEM model is employed to simulate the gas-solid two-phase flow within an industrial-scale Circulating Fluidized Bed (CFB) riser. The research investigates typical flow features such as axial pressure gradients, velocity differentials, solid concentrations, back-mixing, and clustering phenomena. The CG CFD-DEM approach has successfully captured flow patterns observed in large-scale CFB risers, with simulation outcomes showing good correspondence with experimental data. This model serves as a robust tool for predicting the performance of industrial-scale CFBs under various operational conditions, particularly in dilute flow regimes. Nonetheless, the model requires a substantial number of particles for accurate simulation and may introduce errors or uncertainties at higher solid mass flow rates.

5. References

Breault, R. W., Panday, R., Shadle, L. J., et al. Preface. Powder Technology, 2010. 203(1), 1-2.

Che, H., Werner, D., Seville, J., et al. Evaluation of coarse-grained CFD-DEM models with the validation of PEPT measurements. Particuology, 2023. 82, 48-63.

Chu, K., Chen, J., Yu, A. Applicability of a coarse-grained CFD–DEM model on dense medium cyclone. Minerals Engineering, 2016. 90, 43-54.

Huang, X., Jin, X., Dong, L., R., et al. CPFD numerical study on tri-combustion characteristics of coal, biomass and oil sludge in a circulating fluidized bed boiler. Journal of the Energy Institute, 2024. 113, 101550.

Li, Z. Numerical study of particle-fluid flow in complex pipe systems [Ph.D thesis]. Melbourne, Australia: Monash University. 2016.

Li, Z., Wu, Y., Wang, Y., et al. Simulation of non-spherical particles stirring process in stirred tanks. Powder Technology, 2024. 434, 119345.

Tang, R., Zou, Z., Xu, J., et al. Simulation of the L-valve in the circulating fluidized bed with a coarse-grained discrete particle method. Particuology, 2024. 90, 266-280.

Wang, C. High density gas-solids circulating fluidized bed riser and downer reactors [Ph.D thesis]. Ontario, Canada: The University of Western Ontario. 2013.

Wang, F., Zeng, Y., Yan, H. CFD-DEM study of impacts of the porous distributor medium on fluidization characteristics of a 2D-fluidized bed. Particuology, 2024. 87, 54-73.

Zhang, M, Chu, K., Wei, F., et al. A CFD–DEM study of the cluster behavior in riser and downer reactors. Powder Technology, 2008. 184, 151–165.

Numerical study of gas and powder flow characteristics in a filled bed of CFETR

Zhengquan Tang[1],Jian Wang[1,2,*],Mingzong Liu[1]

1.Anhui University of Science and Technology, Huainan, 232001, China

2.Institute of Plasma Physics, Chinese Academy of Sciences, Hefei 230031, Anhui, China

*E-mail of corresponding author:1501384813@qq.com

ABSTRACT

Helium-cooled solid blanket is one of the three candidate conceptual designs for the China Fusion Engineering Experimental Reactor (CFETR), and the flowability of lithium silicate powders in the pebble bed of the fusion blanket is closely related to the design of the tritium extraction system. We numerically investigated the gas-powder flow characteristics of the packed bed based on the two-way coupling of computational fluid dynamics(CFD) and the Discrete Element Method(DEM). The effects of powder radius and different rolling friction coefficients on the powder flow behaviour under different gravity directions at the same helium flow rate were analyzed and discussed. The results show that the powder with a radius of $0.11\mathrm{mm}$ has the largest remaining quantity in the fluid domain, which indicates that in the range of the studied powder radius when the radius of the powder is smaller than $0.11\mathrm{mm}$, the flowability of the powder decreases with the increase of the radius of the powder. When the radius of the powder is larger than $0.11\,\mathrm{mm}$, the flowability of the powder increases with the increase of the radius of the powder. For different rolling friction coefficients, its influence on the powder flowability is small. In contrast, in the direction of gravity, the direction of gravity with the larger angle with the direction of the Z-axis, the powder fluidity is stronger. There is a positive correlation between the direction of gravity and powder flowability.

Keywords: lithium silicate powder; computational fluid dynamics; discrete element; two-way coupling

1. Introduction

Helium-cooled solid blanket is one of the three candidate conceptual designs for the China Fusion Engineering Experimental Reactor (CFETR), and the flowability of lithium silicate powders in the pebble bed of the fusion blanket is closely related to the design of the tritium extraction system. Therefore, it is essential to study the flow and dynamic characteristics of powder and gas in the pebble bed.In terms of particle filling, Gong et al.[1] used the discrete element software to conduct a numerical simulation of particle filling, one and two-dimension simulation models which meet the voidage requirements were obtained,Meanwhile, by using different sizes of Li_4SiO_4 particles ,performing simulated stacking experiments on one and two-dimension bed,and the voidage meets design goals . In terms of gas flow analysis of pebble bed, Zhang et al.[2], Chen et al.[3,4] conducted CFD (computational fluid dynamics) - DEM (discrete element method) coupling simulation on the helium flow characteristics of randomly packed $1\mathrm{D}$ and $2\mathrm{D}$ pebble beds. The results showed that the flow rate increased in areas with large voidage and the flow rate decreased in areas with large fill rates.

However, most current research on the gas flow in the pebble bed focuses on the characteristics of the gas flow in the pebble bed where the gas flow direction is parallel to the gravity direction. In working conditions, there are also some pebble beds where the direction of gas flow is at a different angle from the direction of gravity. There is little research on the motion characteristics of the crushed powder in the

pebble beds in the gas flow.Considering the slow gas velocity in the pebble bed, based on the laminar flow model, the characteristics of the purging helium fluid in the horizontal cylindrical randomly stacked pebble bed and the movement state of the powder in the purging gas flow were analyzed in this paper. A randomly packed particle pebble bed that meets the requirements of working conditions was constructed by the DEM method. CFD-DEM two-way coupled calculation are used for the pebble bed model to obtain the velocity of helium and the powder dynamics in the pebble bed.

2 Numerical Methods

2.1 Pebble bed model in DEM

In the solid cladding of fusion reactor, pebble Li_4SiO_4 particles with a diameter of $1\,\mathrm{mm}$ is used to tritium increase. To make the model as close as possible to the working conditions, DEM discrete element method is used to simulate the particle heap in the blanket pebble bed.

The DEM software used in this paper is EDEM, and the physical parameters of Li_4SiO_4 stacked particles are shown in Table 1[2]. To lessen the influence of the wall affect on the filling rate of the pebble bed[10], a cylindrical container with a diameter of $11\,\mathrm{mm}$ and heigh of $9\,\mathrm{mm}$ was built to accommodate Li_4SiO_4 pebbles with a diameter of 1mm. At $0\,\mathrm{s}$, particles are randomly generated at the top of the container, and particle would fall into the container along gravity until the particles cannot be filled and all the particles are relatively stationary. When the accumulation of particles is finished, a force in the same direction as gravity is added at the top of the cylinder container to increase the filling rate of the pebble bed. After the completion of particle accumulation, 968 stacked particles were obtained, and the filling rate of the pebble bed was 59%. The nonlinear Hertzian contact model was selected to calculate the contact force of particle-wall and particle-particle interactions in simulation. The DEM packed bed model and projection of particle positions on the XY plane were shown in $\mathrm{Fig.1}$.

Table 1. Physical parameters of Li4SiO4 for DEM simulation

Physical parameters	value
Diameter (mm)	1
Poisson's ratio	0.24
Young's modulus (GPa)	90
Density (kg/m3)	2323
Coefficient of Collision recovery	0.3
Coefficient of Static friction	0.2
Coefficient of rolling friction	0.01
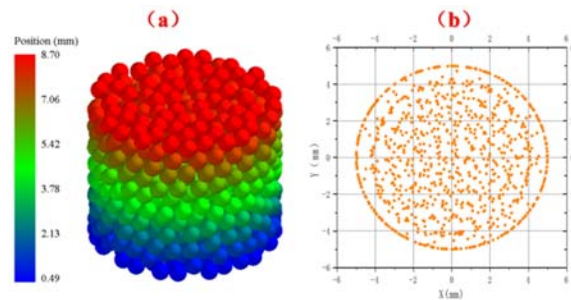
(a)Packed bed model in DEM(b) Projection of accumulated particles on XY plane

Fig. 1. Calculation model

2.2 Fluid domain reconstruction and mesh generation

FLUENT-EDEM coupling was used to calculate helium-entrained Li_4SiO_4 powder flowability in pebble bed. As the helium flow velocity in the pebble bed is slow (about $0.02 \sim 2.0\,\mathrm{m/s}$) [2], Li_4SiO_4 particles

with a particle size of 1 mm can be regarded as static in the simulation process. The position information of particles was exported by EDEM, and its spherical center coordinates and end point coordinates was imported into Spaceclaim to model the Li_4SiO_4 pebble bed model. Then Li_4SiO_4 particles was extracted from the pebble bed through a Boolean operation. At the same time, the particle size of the inlet and outlet sections was extended the distance of four times the particle size and three times[4] to obtain the final fluid domain.

The contact points of particle-particle and particle-wall in the pebble bed belong to geometry with thickness of 0. When modeling the fluid domain, the contact points must be treated. Reddy et al.[8] studied the diameter reduction method. They found that when the particle diameter is reduced by less than 2%, the flow rate at the particle gap is basically 0. Therefore, the diameter reduction method was chosen in this paper, to treat the contact points in meshing process. Particle diameter experienced a reduction of 1%. That is, the particle diameter is reduced to 0.99 mm. The reconstructed fluid domain model is shown in $\mathrm{Fig.\,2}$.
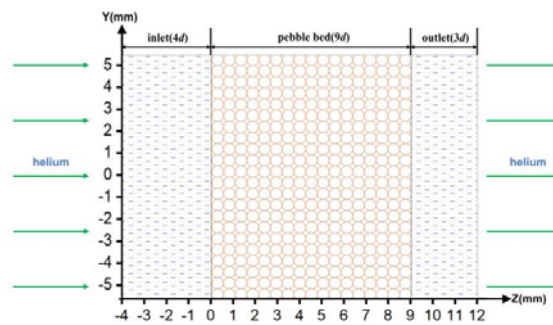
Fig. 2 Reconstructed fluid domain model

Generally, the velocity range of helium purging in the pebble bed is $0.02 \sim 2.0\,\mathrm{m/s}$ [2], the Reynolds number in the fluid domain is much less than 2300, and the FLUENT-EDEM coupling interface cannot be used for steady-state calculation. Therefore, the transient laminar model was used to analyze the flow field and powder dynamics characteristics. Because of the complex structure of the fluid domain, compared with the tetrahedral mesh, the iterative calculation in the boundary layer is uneasy to converge. Hence the polyhedral mesh is used to divide the fluid domain[11]. Four sets of mesh with mesh quantities of 932,000, 1210,000, 1962,000, and 2200,000 were generated. The inlet and outlet pressure drop in the pebble bed under the inlet flow rate of 0.2 m/s and operating pressure of 101 kPa[2] are shown in Table 2. When the mesh quantity exceeds 1982,000, the calculation error is less than 0.06%. The mesh division results and details could be seen in $\mathrm{Fig.\,3}$.

Table 2. Mesh independence verification

The number of mesh	Pressure drop /(Pa/m)
932,000	1658.14
1210,000	1662.57
1962,000	1665.65
2200,000	1666.57
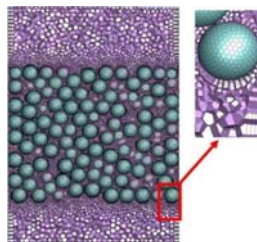
Fig. 3 Mesh division results and mesh details

3. Results and Discussion

3.1 Velocity analysis of helium

When helium inlet flow velocity is $0.3m/s$ and the gravity direction was along the negative direction of the Y-axis, the velocity distribution of YZ face after $t = 2s$ of helium blowing in the pebble bed is shown in Fig.4a. The flow velocity was small in the area with small particle-particle voids, and the minimum flow velocity is almost 0. While in the area with larger voids, the flow velocity became larger, and the maximum flow velocity was about 10 times more than the inlet flow velocity. The reason for this phenomenon is that when the gas flows through the area with small voids, the flow resistance is larger and the flow velocity is smaller. Instead, when the flows through the area with large voids, the flow resistance is smaller and the flow rate increases greatly, the phenomenon can also be observed in the velocity flow diagram depicted in Fig.4b. Therefore, the simulation results presented in this paper are consistent with the actual situation.

(a)Velocity distribution of YZ plane   (b) Velocity streamline distribution of YZ plane
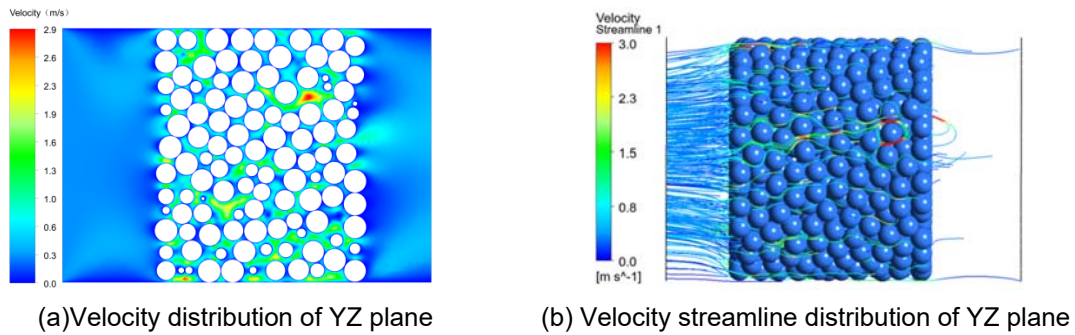
Fig.4 Velocity and its streamline distribution of YZ plane

3.2 Powder dynamics analysis

During the operation of the pebble bed in a blanket, Li_4SiO_4 particles in the pebble bed are easily broken to form powder and mixed with other powders retained in the pebble bed, generating many powders with different friction coefficients, which will move with the purge gas in the pebble bed. At the same time, there are also different angles between the direction of airflow and the direction of gravity in the actual working conditions, which will affect the normal operation and tritium breeding efficiency. This section mainly discusses the influence of gravity direction on powder fluidity under different rolling friction coefficients. Based on the coupling calculation of EDEM and FLUENT, the simulation model of gas-solid two-phase flow is established. The physical parameters of the powder are the same as those of Li_4SiO_4 particles. The shape of the powder is spherical and the diameter is 0.05mm. Eight different rolling friction coefficients were set in the fluid domain, and the gravity direction was different in each case. By changing the rolling friction coefficient and the angle between gravity and the Z-axis, the influence of gravity direction on powder fluidity was analyzed.

Fig.5 shows that at $t = 2s$, the remaining amount of powder with different rolling friction coefficients in the pebble bed changes with the angle in the direction of the Z-axis. With the increase of the angle between the gravity direction and the Z-axis direction, the remaining total powder quantity within various rolling friction coefficient decreases, however, the reduction of each group is similar, which indicates that the influence on powder fluidity is small. In the gravity direction, The fluidity of the powder increases as the angle between the direction of gravity and the Z-axis increases, indicating that the angle between the gravity direction and the axial direction of the pebble bed is positively correlated with the powder fluidity within the studied range. The main reason for this phenomenon is that when there is an angle between the gravity direction and the axial direction of the pebble bed, the powder will move toward the edge of the pebble bed. However, the porosity at the edge of the pebble bed is larger, and the powder is

not easy to be intercepted in the process of movement, so the greater the angle between the gravity direction and the Z-axis direction, the stronger the powder fluidity.

N: the remaining quantity of powder in the fluid domain
G: the magnitude of the angle of gravity with the direction of z-axis
v: the coefficient of friction of powder rolling
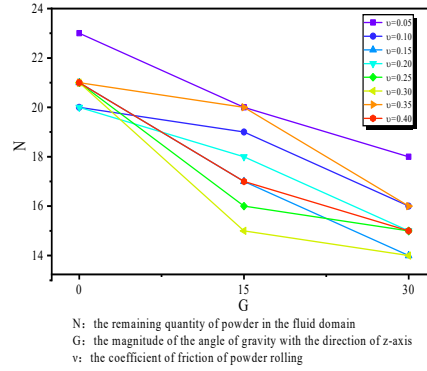
Fig. 5 Effect of gravity direction on powder number at different rolling friction coefficients

Since the particle size of the broken powder produced by Li_4SiO_4 particles cannot all be equal in actual working conditions, and the powder fluidity may also change with the powder particle size distribution, the flow channel may be blocked by a larger powder, and then prevent other powders from flowing through the void, and ultimately lead to the reduction of powder fluidity. In this paper, several particles of different sizes are purged into the fluid domain. In general, particle sizes should be uniformly distributed within each particle size group. In order to simplify implementation, The particle sizes of the powder group were $0.05mm$, $0.08mm$, $0.11mm$, $0.14mm$, $0.17mm$, $0.20mm$, $0.23mm$ and $0.26mm$, and the number of spherical powders in each group was 100. Other simulation settings and boundary conditions were kept the same as the previous section. The influence of particle size on fluidity was studied and illustrated in $Fig.6$, where N is the amount of powder remaining in the fluid domain when $t = 2s$, and R is the particle radius.

N: the remaining quantity of powder in the fluid domain
R: the radius of powder
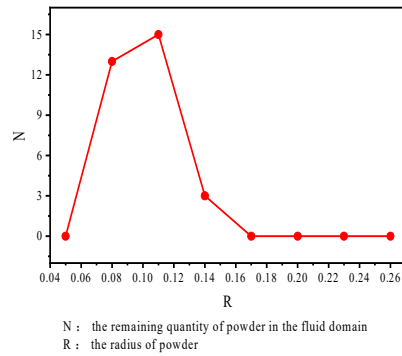
Fig. 6 Effect of size on powder number

For the Li_4SiO_4 powder, the influence of particle size on fluidity is obvious, while the change trend is not just monotonous. It can be seen that the powder with radius of $0.11mm$ has the largest remaining amount in the fluid domain and the minimum fluidity. When the radius of the powder is less than $0.11mm$, the fluidity of the powder decreases with the increase of the radius of the powder. Although the smaller powder is easier to fluidize than the larger powder, its fluidity should be higher, but the higher fluidity will also lead to the possibility of the powder being intercepted by the pebble bed. Thus, the retention of powder in the pebble bed increases and the fluidity characterization decreases. When the radius of the powder is greater than $0.11mm$, the fluidity of the powder increases with the increase of the radius of the powder, indicating that the fluidization effect of the powder begins to dominate the fluidity, and the interception effect gradually weakens with the increase of the particle size. At the end of the simulation,

all large particles ($R > 0.17mm$) were blown out of the packed bed, while some small particles were intercepted and filled in the packed bed. The reason may be attributed to the large particles having a large momentum exchange term, which makes it easier to pass through the void of the packed bed with a larger speed.

4. Conclusion

The flow characteristics of gas and powder in the packed bed were studied by CFD-DEM two-way coupled calculation. The numerical method was described in detail, including the control equation, DEM model, CFD model establishment and coupling program. The benchmark test is carried out to verify its effectiveness. The effects of powder radius and different rolling friction coefficients on the powder flow behaviour under different gravity directions at the same helium flow rate were analyzed and discussed. The results show that the powder with a radius of $0.11mm$ has the largest remaining quantity in the fluid domain, which indicates that in the range of the studied powder radius when the radius of the powder is smaller than $0.11mm$, the flowability of the powder decreases with the increase of the radius of the powder. When the radius of the powder is larger than $0.11mm$, the flowability of the powder increases with the increase of the radius of the powder. For different rolling friction coefficients, its influence on the powder flowability is small. In contrast, in the direction of gravity, the direction of gravity with the larger angle with the direction of the Z-axis, the powder fluidity is stronger. There is a positive correlation between the direction of gravity and powder flowability.The results of this paper may provide partial insights into powder dynamics in pebble beds.

References

[1] B. Gong, et al., Discrete element modeling of pebble bed packing structures for hccb tbm. Fusion Eng. Des. 121, 256-264 (2017).
[2] Zhang. B, Xia. Z, Zhou. Z. DEM-CFD Coupled Simulation for Determination of Character of Heat and Mass Transfer and Purge Gas Flow in Li4SiO4 Pebble Bed. Atomic Energy Science and Technology. 55(8): 1367-1375(2021).
[3] CHEN. Y, CHEN. L, LIU. S. Flow characteristics analysis of purge gas in binary mixed pebble bed of water-cooled ceramic blanket for CFETR. Nuclear Fusion and Plasma Physics. 37(04): 452-456(2017).
[4] Y. Chen. Flow Characteristics Study of Purge Gas in the Pebble Beds of Water Cooled Ceramic Blanket. University of Science and Technology of China, 2017.
[5] BAI. L, HAN. C, XU. Y, et al. Numerical simulation and experimental study of CFD-DEM in bubbling fluidized bed basedon different drag models. Journal of drainage and irrigation machinery engineering. 40(1): 49-54(2022).
[6] P. Langston, A. R. Kennedy, Discrete element modelling of the packing of spheres and its application to the structure of porous metals made by infiltration of packed beds of nacl beads. Powder Technol. 268, 210-218 (2014).
[7] A. de Klerk, Voidage variation in packed beds at small column to particle diameter ratio. Aiche J. 49, 2022-2029 (2003).
[8] R. K. Reddy, J. B. Joshi, Cfd modeling of pressure drop and drag coefficient in fixed and expanded beds. Chemical Engineering Research and Design 86, 444-453 (2008).
[9] J. Zhao, T. Shan, Coupled cfd–dem simulation of fluid–particle interaction in geomechanics. Powder Technol. 239, 248-258 (2013).
[10] J. Reimann, D. Ericher, G. Wörner, Influence of pebble bed dimensions and filling factor on mechanical pebble bed properties. Fusion Eng. Des. 69, 241-244 (2003).
[11] Jian Wang. Study on Packing , Crushing Behavior and Evolution Law of Granular Material in Pebble Bed of Fusion Reactor [D]. University of Science and Technology of China, 2021.
[12] K. Feng, et al., Current progress of chinese hccb tbm program. Fusion Eng. Des. 109-111, 729-735 (2016).

A COMPREHENSIVE MODEL FOR BIOMASS GASIFICATION IN A CIRCULATING FLULIDIZED BED USING ASPEN PLUS

Hao Shi[1], Yaji Huang[1 *], Shuaijie Qi[1], Huikang Song[1], Hu Pan[1]

Key Laboratory of Energy Thermal Conversion and Control of Ministry of Education, School of Energy and Environment, Southeast University, Nanjing, 210096, China

* heyyj@seu.edu.cn

Abstract

The potential offered by biomass to upgrade into more valuable products is now being more widely recognized around the world. In this work, a comprehensive model was developed by Aspen Plus to simulate gasification process in a circulating fluidized bed (CFB) gasifier. The model involves sub-models for temperature-dependent pyrolysis products evolution equilibrium, biofuel fluidization and gasification controlled by reaction kinetics. By comparing with previous experimental data, results show that the model predicts pyrolysis products and final syngas with reasonable accuracy, after which products composition and evaluation parameters are calculated. Sensitivity studies are carried out for exploring the impact of equivalence ratio, temperature and steam/biomass mass ratio on gasification as well. This model provides additional design and simulation insight for CFB gasifier modelling in future.

1. Introduction

Biomass gasification is a complex process in which chemical reactions as well as heat and mass transfer mechanisms take place[1]. It is not only time-consuming but also costly for experimental process optimization of a certain biofuel, because many factors affect gasification behavior[2]. Also, gasification simulating based on existing experimental data which is reported on industrial scale is now popular, arising from its flexibility and accuracy. Simulation can easily determine process parameters, avoid undesirable operational conditions and support process optimization[3].

Among all process simulation tools, Aspen Plus have been widely employed in biomass gasification for its high flexibility and low calculation cost in optimizing operational conditions [4]. St|fif~x&zuiwɛky&fsi%it|siwɛky%lfxɳɘhfyɽts%wjfhytwɑr tijɑx%hfs%gj%jxyfgɑɒxmji%ɳs%{fwɩzx%r jymtix%ɳf%zxɳsl%Fxujs [5]. Mt|j{jwɒ|mjs%ɲɣhtr jx%yt%hɳwhzɑfɳsl%kɑɒnin;ji%gji%+HKG.%lfxɳɘhfyɽts%ɳuwthjxxjx%fwj%y~uɳhfɑɒ%gzmɑ|ɳm%Lɳɒgx%wjfhytwx%ɳmfy%t{jwɑttp%ymj%yjr ujwfyzwj⒉ijujsijsy%u~wtɑxnx%ɯlfxɳɘhfyɽts%fsi%kɑɒni%gjmf{ɩtwɳɑsxnij%ymj%wjfhytw[6].

The CFB model presented in this paper involves sub-models for temperature-dependent pyrolysis products evolution equilibrium, biofuel fluidization and gasification controlled by reaction kinetics. Tar cracking and pyrolysis products compositions are considered. Fluid dynamics and reaction kinetics are integrated to simulate gasification performance as well. This model provides new design for CFB gasifier modelling in future.

2. Materials and modelling methods

2.1 Biomass materials

The biomass chosen in simulation is the leach orujillo, which is consist of olive oil waste, reported by previous research, and the proximate analysis and ultimate analysis are chosen as well[7]. The average particle size of orujillo sample is measured as 1.89mm.

2.2 Pyrolysis products evolution equilibrium sub-model

Gɳtr fxx%kzjɑȶzsijwɭtjx%fs%ɳsɭɲfɕxyflj%tk⒟iw~ɳsl%fsi%u~wtɑɒxx%ɳsxnij%ymj%wjfhytwȼ%Fx% yjr ujwfyzwj%ɳɒxjx⒉moisture is released around 150℃ and it is believed that validates begin to escape from biomass at 300℃. In fact, devolatilization and pyrolysis is an extremely

complex process. Gasification in circulating fluidized bed can be regarded as isothermal condition at high temperature. It means devolatilization and pyrolysis can be simplified to be independent of heating rate, while solely determined by temperature. Therefore a pyrolysis products evolution lumping equilibrium model is investigated, containing empirical formulas and selected experimental data from the literatures. The adapted empirical relationships shown in Table 2 were derived from analyses of final products for various biomass pyrolysis evolution at certain temperature, rather than focusing on heating rate and kinetics.

The decomposition products include water vapor, pyrolysis gas, char and tar. Pyrolysis gas is consist of $H_2, CO, CH_4, CO_2, N_2, SO_2$ and H_2O. Arising from the low content of C_2H_4(typical wt%=1%) and other C_xH_y(typical wt%=0.5%) in decomposition products, only CH_4 is considered in this model to simplify modelling calculation. The whole mass balance and element balance are strictly calculated in Table 1, where T means pyrolysis temperature(℃), ω refers to values in proximate and ultimate analyses, and Y presents yield(wt%).

Table 1. Empirical equations for pyrolysis products evolution equilibrium

Variables(wt%)		Equation	References
Gas	Y_{H2}	=1.145*(1-exp(-0.0011*T))^9.384*100%	[8]
	Y_{CO}	=(0.8247-0.0025*T+0.00000255*T^2)*100%	[8]
	Y_{CH4}	=(0.1414-0.0004*T+3.75*10^(-7)*T^2)*100%	[8]
	Y_{CO2}	=(0.5284+0.0013*T-1.84*10^(-6)*T^2)*100%	[8]
	Y_{N2}	= ω_N	-
	Y_{SO2}	=64/32* ω_S	-
	Y_{H2O}	= $\omega_{moisture}$	-
Char	Y_{char}	=(0.106+2.43*exp(-0.005*T))*100%	[6,8]
	$Y_{C,char}$	=(0.93-0.92*exp(-0.0042*T))*100%	[6,8]
	$Y_{H,char}$	=(-0.0041+0.1*exp(-0.0024*T))*100%	[6,8]
	$Y_{O,char}$	=100- $Y_{H,char}$ -$Y_{C,char}$	-
Tar	Y_{tar}	=100-Y_{char}-Y_{gas}	-
	$Y_{C,tar}$	= ω_C-$Y_{C,gas}$-$Y_{C,char}$	-
	$Y_{H,tar}$	= ω_H-$Y_{H,gas}$-$Y_{H,char}$	-
	$Y_{O,tar}$	= ω_O-$Y_{O,gas}$-$Y_{O,char}$	-

2.3 Fluid dynamics

To simulate gasification in the CFB, the "Fluidbed" unit in Aspen Plus was used to deal with fluidizing and circulating regime and all parameters are the same as the settings in literature[7]. According to García-Ibañez's settings of CFB experiments[7], the height and diameter of the CFB reactor is 6.5m and 0.2m respectively. The biofuel particle can be classified as Geldart A[9], and the paper provides more details. Minimum fluidization velocity u_{mf} is used for approximate calculation by Wen's method in a wide range of Re conditions[10].

$$Re_{mf} = 33.7 * \sqrt{(1 + 3.6 * 10^{-5} * Ar)} - 1 = \frac{u_{mf}*d_p}{v_f} \tag{2-1}$$

$$Ar = \frac{g*d_p^3}{v_f^2} * \frac{\rho_s - \rho_f}{\rho_f} \tag{2-2}$$

The transport disengagement height(TDH) model are given in the literature[11] where d_b means the diameter of a bubble at the surface of the bottom zone.

$$TDH = 13.8 * d_b \tag{2-3}$$

The particles are partially elutriated from the bed by exploding bubbles at the bed surface. If the freeboard is higher than TDH, particle related elutriation coefficient($k_{\infty,i}$) is dependent on the fluidizing gas velocity, the particle velocity and the solid mass fraction, and the equation is as following where *A,B* are user-defined factors, more information involved in literature[12].

2.4 Combustion and reduction reaction kinetics

Gasification and combustion in circulating fluidized gasifier is fully controlled by Arrhenius kinetic reactions which is listed as Table 2, including Boudouard, Water-gas, Steam reforming reactions, etc. The involved C come from carbon in char calculated previously.

Table 2. Chemical reactions and kinetic parameters

Reactions	A（s^{-1}）	n	E_a（kJ/kmol）	References
$C + CO_2 = 2CO$	4.4	1	1.62e8	[1]
$C + H_2O = CO + H_2$	15170	1	1.2162e8	[2]
$C + 0.5 O_2 = CO$	2.3	1	9.23e7	[1]
$C + 2 H_2 = CH_4$	0.004189	0	1.92e7	[3]
$CO + 0.5 O_2 + 0 H_2O = CO_2$	1.3e8	0	1.256e8	[13]
$CO + H_2O = CO_2 + H_2$	2780	0	1.26e7	[14]
$CO + 3 H_2 = CH_4 + H_2O$	312	0	3e7	[13]
$H_2 + 0.5 O_2 = H_2O$	2.2e9	0	1.09e8	[13]
$CH_4 + H_2O = CO + 3 H_2$	6.09e14	0	2.57e8	[13]
$CO_2 + H_2 = CO + H_2O$	95862	0	4.66e7	[14]
$CH_4 + 1.5 O_2 = CO + 2 H_2O$	5.01e11	0	2.03e8	[13]
$C+O_2=CO_2$	0.000916	1	4.69e6	[15]

2.5 Aspen modelling assumptions and process

After combination of all sub-models, the Aspen Plus CFB modelling is shown as Fig.1. Feeding biomass is set as non-conventional (NC) components. The decomposition and pyrolysis results, conventional C (carbon particle) and conventional gas, are calculated in MATLAB by pyrolysis products evolution equilibrium sub-model and then transmitted to the unit PREDECOM, TARDECOM and CHARDECO via MATLAB/Aspen connection server. Unit SPLIT1, SPLIT2 and SPLIT3 are set to separate components to different stream.
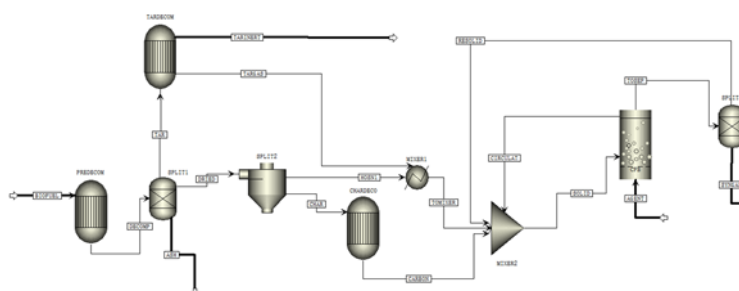
Fig.1. CFB gasification process flow diagram in Aspen Plus

Feeding biomass is firstly decomposed into ash, inert tar, reactive C solids and gases. It is necessary to decompose tar and char in order to derive reactive components. In TARDECOM, H_2, CO, CH_4, CO_2 are considered as tar cracking gas components, while phenol(C_6H_5OH) is chosen as inert tar and accounts for 15% of total tar, lower than experimental data[16,17].The ratio of moles of CO and CO2 is inversely related with their molecular mass[4].

Gasifying agents flow AGENT stream enter reactor while reactive components from biomass as SOLID stream and gasification take place in CFB zone. Remaining solid, acting as tear stream CIRCULAT, goes to MIXER2 and then reenter CFB reactor to simulate the circulation. Calculation stops at simultaneous convergence of both tear streams and design specifications.

2.6 Process evaluation parameters

Several evaluation parameters are calculated to evolute the gasification process as following.

LHV is defined as heat released by complete fuel combustion, excluding latent heat of water vaporization, calculated as following with unit MJ/Nm^3. In the equation, i means respective gas while ω means its molar fraction or volume fraction(%)[5].

$$LHV_{gas} = \Sigma LHV_i * \omega_i \qquad (2\text{-}4)$$

SGY is a fundamental parameter estimating the gasification process product, where Y represents yield of respective gas, with unit Nm^3/kgfuel[18].

$$SGY_{gas} = \Sigma Y_i \tag{2-5}$$

Cold gasification efficiency (CGE) represents the ratio of syngas LHV to biofuel LHV[18].

$$CGE = \frac{LHV_{gas}}{LHV_{biofuel}} * 100\% \tag{2-6}$$

Two operation parameters Equivalence ratio (ER), Steam/biomass mass ratio (S/B) are used as operational variables to control gasification characteristics [18]:

$$ER = \frac{[\dot{m}_{air}/\dot{m}_{biofuel}]_{actual}}{[\dot{m}_{air}/\dot{m}_{biofuel}]_{stoich}} \tag{2-7}$$

$$S/B = \dot{m}_{steam}/\dot{m}_{biofuel} \tag{2-8}$$

3. Results and discussion

3.1 Validation with experimental data

In order to validate the accuracy of Aspen Plus comprehensive model, three set of experimental data reported in literature were used, which collected from olive oil waste fluidized bed gasification[7]. The operation parameters are listed in Table 3.

Table 3. Simulation parameters of different gasification conditions

Variables	Units	Values		
Test numbers		Mod.1	Mod.2	Mod.3
ER	-	0.59	0.67	0.73
Biomass mass flow	kg/h	64	51	47
Agent(air) mass flow	Nm³/h	164	149	149
$T_{gasification}$	℃	800	800	800

Fig.2 presents the comparison of simulation result against the experimental data for each of the following syngas species : CO, CO_2, H_2, CH_4 and N_2. As is illustrated, the comprehensive model prediction results of major syngas compositions are reasonably close to experimental data. For each component, the absolute error of prediction is within 1.5%. Case Mod.2 is chosen as the typical case for further exploration based on change of operational parameters.,
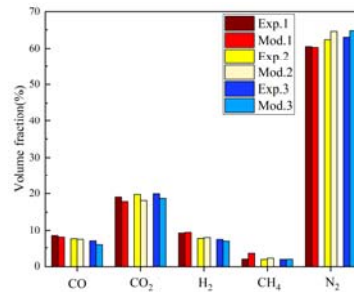
Fig. 2. Comparison of syngas composition between simulation results and experimental data.

3.2 Sensitivity studies for operational variables

To explore the impact of operational variables on syngas compositions and gasification evaluation parameters, the following sensitivity studies for ER, gasification temperature and S/B are conducted. Fig.3 shows the effect of ER on syngas compositions and gasification evaluation parameters. When ER increases, behavior in reactor transform from gasification to combustion gradually, contributing to contents of CO,H_2 and CH_4 decrease. Though syngas yield remarkably increases, CGE drops to 51%, which means less energy is saved in syngas.
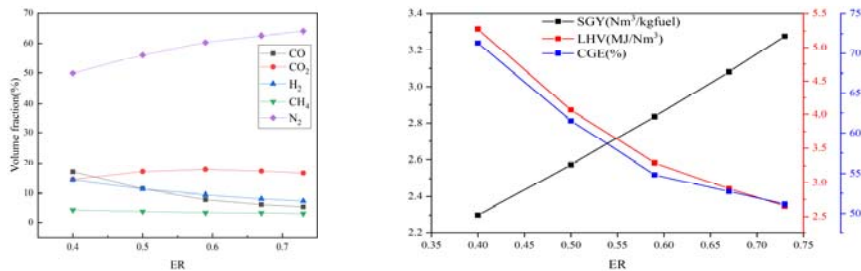
Fig. 3. Effect of ER on syngas compositions and gasification evaluation parameters.

When S/B ratio goes up as Fig.4, water-gas and methane reforming reaction are prompted, leading to the rapid increase of H_2 content and CGE. When S/B>0.2, LHV remains almost unchanged. As a result, appropriate vapor feeding significantly promotes gasification, analogous to previous work[5].
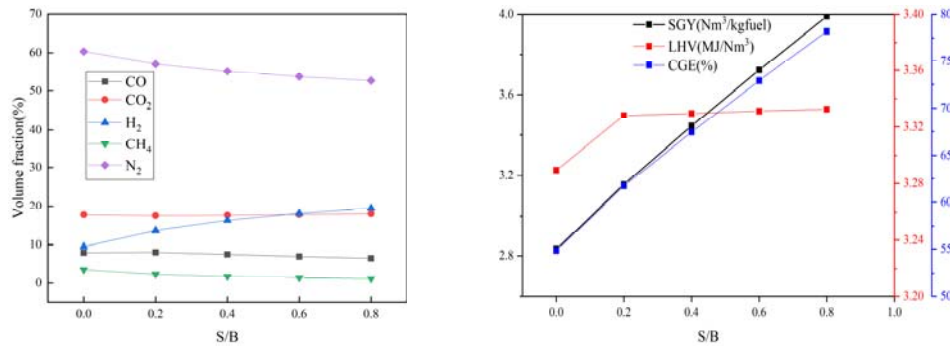
Fig. 4. Effect of S/B on syngas compositions and gasification evaluation parameters.

As gasification temperature rises, temperature-dominated methane reforming and water-gas shift reaction are sensibly prompted, so H_2 and CO contents increase. In Fig.5, notably, at 800℃ CGE and LHV are the lowest and that is the temperature range we should avoid. The simulation result will undergo comparison and verification in our subsequent experiments.
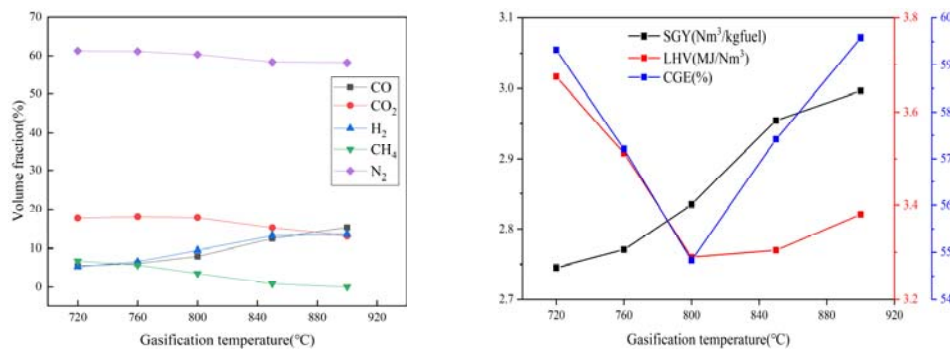
Fig. 5. Effect of gasification on syngas compositions and gasification evaluation parameters.

Superficial and void gas velocity and pressure are selected to show the possibility of fluidization characteristics calculation by Aspen Plus in Fig.6. It is illustrated that the bottom zone has a height of 1.5m, according to the pressure loss of 3000Pa. The TDH is almost 2m, above which the pressure remain remain unchanged.
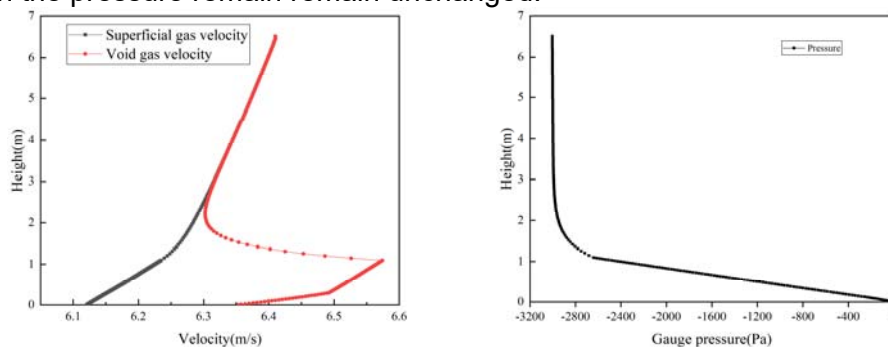
Fig. 6. Fluidization parameters calculated by Aspen Plus model

4. Conclusion

The research proposes a comprehensive model of CFB in Aspen Plus, involving sub-models for temperature-dependent pyrolysis products evolution equilibrium, biofuel fluidization and gasification controlled by reaction kinetics. Assessment on simulation results are carried out

to check modelling accuracy and feasibility in gasification products prediction and fluidization characteristics calculation in Aspen Plus. Main outcomes are listed as follows.

1.Comparing with experimental data, results show that the model predicts syngas compositions with max absolute error controlled within 1.5%, indicating the feasibility and accuracy of decomposing gasification into first-step pyrolysis and following kinetic reactions.

2.Sensitivity studies are carried out for exploring the impact of ER, S/B and gasification temperature on gasification behavior. Sensitivity analyses on evaluation parameters indicates that proper ER and relatively high S/B and temperature will promote gasification.

Acknowledgment

References

[1] Kumar M., Ghoniem A. Multiphysics Simulations of Entrained Flow Gasification. Part II: Constructing and Validating the Overall Model. Energy Fuels. 2012.26,464–79.
[2] Salem A., Paul M. An integrated kinetic model for downdraft gasifier based on a novel approach that optimises the reduction zone of gasifier. Biomass and Bioenergy. 2018.109,172–81
[3] Sharma A. Modeling and simulation of a downdraft biomass gasifier 1. Model development and validation. Energy Conversion and Management .2011.52,1386–96.
[4] Ratnadhariya J., Channiwala S.. Three zone equilibrium and kinetic free modeling of biomass gasifier – a novel approach. Renewable Energy.2009.34,1050–8.
[5] Fernandez-Lopez M, Pedroche J, Valverde JL, et al. Simulation of the gasification of animal wastes in a dual gasifier using Aspen Plus®. Energy Conversion and Management .2017.140,211–7.
[6] Tavares R, Monteiro E, Tabet F, et al. Numerical investigation of optimum operating conditions for syngas and hydrogen production from biomass gasification using Aspen Plus. Renewable Energy. 2020.146:1309–14.
[7] García-Ibañez P, Cabanillas A, Sánchez J. Gasification of leached orujillo (olive oil waste) in a pilot plant circulating fluidised bed reactor. Preliminary results. Biomass and Bioenergy. 2004.27,183–94.
[8] Neves D, Thunman H, Matos A,et al. Characterization and prediction of biomass pyrolysis products. Progress in Energy and Combustion Science .2011.37,611–30.
[9] Geldart D. Types of gas fluidization. Powder Technology. 1973.7,285–92.
[10] Wen C., Yu Y. A generalized method for predicting the minimum fluidization velocity. AIChE Journal 1966.12,610–2.
[11] Fournol A., Bergougnou M., Baker C. Solids entrainment in a large gas fluidized bed. Can Journal of Chemical Engineering .1973.51,401–4.
[12] Colakyan M, Levenspiel O. Elutriation from fluidized beds. Powder Technology .1984.38,223–32.
[13] Rabea K, Michailos S, Akram M, et al. An improved kinetic modelling of woody biomass gasification in a downdraft reactor based on the pyrolysis gas evolution. Energy Conversion and Management .2022.258,115495.
[14] Gómez-Barea A, Leckner B. Modeling of biomass gasification in fluidized bed. Progress in Energy and Combustion Science .2010.36,444–509.
[15] Wu Y, Zhang Q, Yang W,et al. Two-Dimensional Computational Fluid Dynamics Simulation of Biomass Gasification in a Downdraft Fixed-Bed Gasifier with Highly Preheated Air and Steam. Energy Fuels .2013.27,3274–82.
[16] Boroson ML, Howard JB, Longwell JP, et al. Product yields and kinetics from the vapor phase cracking of wood pyrolysis tars. AIChE Journal .1989.35,120–8.
[17] Rath J, Staudinger G. Cracking reactions of tar from pyrolysis of spruce wood. Fuel .2001.80,1379–89.
[18] Guo F, Dong Y, Dong L, et al. Effect of design and operating parameters on the gasification process of biomass in a downdraft fixed bed: An experimental study. International Journal of Hydrogen Energy .2014.39,5625–33.

MODELING OF FLOW HYDRODYNAMICS IN A NOVEL CIRCULATING TURBULENT FLUIDIZED BED

Xu Li, Wenbin Li*, Zhongli Tang, Donghui Zhang

The Research Center of Chemical Engineering, School of Chemical Engineering and Technology, Tianjin University, Tianjin 300072, China

* E-mail of corresponding author: richard@tju.edu.cn

Abstract

The circulating turbulent fluidized bed (CTFB) is a newly discovered fluidization system that combines the well gas-solid mixing properties of conventional turbulent beds (TFB) with the continuous operation features of circulating fluidized beds (CFB). Modeling of the hydrodynamic behaviors of CTFB with Geldart group B particles has been performed based on the Eulerian-Eulerian approach integrated with the kinetic theory of granular flow (KTGF). Three turbulent models have been adopted in order to investigate the influence of macroscopic turbulent viscosity of particles in the model prediction. It is shown that the $k - \varepsilon - k_p{}' - \varepsilon_p{}' - \theta$ model considering particle turbulent viscosity at both micro and macro scales show satisfactory agreements with measurements. Then, the effect of mesoscale structure on the hydrodynamics are investigated by comparing the predictions of Energy-Minimization Multi-Scale (EMMS) model and Huilin-Gidaspow drag model. The parameters in KTGF including particle collision parameter of restitution (e_{ss}) and particle-wall specularity coefficient (ϕ) also affect the simulation of the hydrodynamic characteristics of CTFB. It is found that drag models have an effect on the selection of parameters in KTGF and wall boundary condition. Simulation results showed that these parameters have little effect on axial differential pressure (ΔP) profile when the EMMS model was used, but have a pronounced influence on ΔP using Huilin-Gidaspow drag model. Different systems also affect the choice of these parameters. e_{ss} from 0.85 to 0.95 entails a noticeable impact in solid holdup distribution in the top part of the CTFB riser while the solid holdup on the bottom has more sensitivity to e_{ss} than that on the top in the CFB and TFB. The specularity coefficient (ϕ) plays but a minor role in the holistic flow characteristics.

1. Introduction

The atmospheric carbon dioxide levels have increased appreciably and its effect on climate is forcing humanity to consider CO_2 capture technologies. Carbon capture and storage are reliable tools [1]. For nearly a century, fluidized beds nominated as an efficient method to remove CO_2 from flue gases have been the backbone of the processing industries [2]. The circulating turbulent fluidized bed (CTFB) is a newly discovered fluidization system that combines the gas-solid mixing properties of conventional turbulent fluidized beds (TFB) with the continuous operation features of circulating fluidized beds (CFB) [3]. Nevertheless, there still lacks systematic investigation in some areas in terms of equipment optimization and amplification. To optimize and scale up a fluidization system, it is crucial to understand the hydrodynamics and flow characteristics of the multiphase flow in the fluidized bed reactor [4,5]. To lighten the burden for experiment, numerical simulation have been proposed for investigating multiphase flow. As one of the most commonly used numerical methods, the Euler –Euler based TFM model regards both fluid and particle phases as continuous and completely interpenetrating, describes solid rheology through the kinetic theory of granular flow (KTGF) and characterizes the interaction between particles and gas by a drag model [6]. There have been studies on the models and the sensitivity of relative parameters in the TFB, CFB and BFB system [7–9], but specific empirical correlation such as drag model and parameters about solid viscosity is only suitable for specific operating conditions. It is difficult to be extended to other systems, therefore, loses its generalization [10]. For CTFB, a novel system, the choice

of model and the setting of empirical parameters need to be reconsidered. Mesoscale structures (such as clusters) in gas–solid fluidized beds significantly affect macroscopic hydrodynamic behavior. The effect of clusters is usually considered in drag models, while the influence of clusters on viscosity should also be taken into account.

In the present work, Euler-Euler two-fluid model in combination with KTGF is used to study the hydrodynamic behavior of a circulating turbulent fluidized bed riser with Geldart B particles. Turbulence models and drag models including Huilin-Gidaspow drag model and the energy minimization multi-scale (EMMS) model are discussed. The Johnson and Jackson wall boundary condition with different specularity coefficients and the KTGF with different restitution coefficients are used and their effects on the hydrodynamic behavior of the bed are investigated.

2. Numerical procedure

2.1 The model equations

The system hydrodynamics behavior was simulated using the five main governing equations (conservation of mass, momentum, energy, species and solid phase fluctuating energy). The constitutive equations for the solid particle was used via KTGF. For the momentum exchange coefficient, the Huilin-Gidaspow model and EMMS model were compared.

2.2 Computational domain and boundary conditions

The riser for the CTFB has an inner diameter of 0.0635 m and a height of 4.3 m. The simulation is performed in a 2D cylindrical space. Table 1 lists bed dimensions and operating conditions. The experimental data was obtained by Korea Research Institute of Chemical Technology (KRICT) [11,12].

Table 1. Adsorber dimensions and operating conditions of the unit.

•	values
D (m)	0.0635
H (m)	4.3
F_g (m^3 h^{-1})	10.5
y_{CO2}	0.12
G_s (kg m^{-2} s)	5.26
d_p (m)	1.5E-4
ρ_s (kg m^{-3})	1700

2.3 Grid-size independence analysis

For the simulation procedure, firstly, the grid-independency and the simulation time tests were conducted to investigate the hydrodynamics model with high accuracy and less time consuming. In this study, the reactor system was simulated by ANSYS FLUENT software. The computational cells of the reactor system with 117424 (42 x 2795), 51543 (28 x 1911) and 29988 (23 x 1397) cells were tested for the grid independency. The minimum appropriate number of computational cells required was 51543 by simulating.

3. Simulation results and discussion

3.1 Turbulence model

Gas–particle two-fluid model (TFM) treated the particle phase as a continuous fluid based on the Eulerian method in which enclosing the stress of particle phase in the particulate momentum equation was a key problem. Various methods were put forward considering different enclosing methods that the kinetic theory of granular flow (KTGF) has gradually become the basis of these methods. KTGF was originally developed for

pure granular flow [13]. The effects of clusters caused by the transfer of turbulent energy between two phases were not taken into account. Some researchers enclosed the stress of particulate phase by only considering the microscopic viscosity of particles using KTGF, which showed approximately agree with measurements in bubbling fluidized bed (BFB) but unsuitable in TFB and CTFB et al. That is because in BFB the turbulent effect is weak so the microscopic viscosity plays a dominant role, but when the particle turbulence is intense and obvious phenomena of particle agglomeration and fragmentation are existed such as in TFB and CTFB system, it is not optimal for only using KTGF to enclose the stress of particulate phase. Another method was based on the closure of the particulate turbulent equation. Two different methods is employed. One is using $k - \varepsilon$ model which is same as gas phase (in this paper called $k_p - \varepsilon_p$ model), the other is $k_p{}' - \varepsilon_p{}'$ model which accounts for the presence of particles turbulence [13]. Four different models have been adopted in order to investigate the influence of macroscopic turbulent viscosity of particles in the model prediction. They are:

A: θ model, in which the effect of macroscopic turbulent viscosity of particles is ignored and only using KTGF to enclose the stress of particulate phase.

B: $k - \varepsilon - \theta$ model in which turbulent viscosity of gas is considered by $k - \varepsilon$ and viscosity of particles is simulated by θ model.

C: $k - \varepsilon - k_p - \varepsilon_p - \theta$ model, in which the particle viscosity is considered by both $k_p - \varepsilon_p$ model and KTGF.

D: $k - \varepsilon - k_p{}' - \varepsilon_p{}' - \theta$ model [13], in which $k_p{}' - \varepsilon_p{}'$ equations represent the transfer of turbulent energy of particle phase and the granular temperature equation is utilized to simulate the collisions between particles.

As shown in figure 2(a, b), both A model and B model set the viscosity of particles by only KTGF, so their effective viscosity of particles (μ_e) are close leading the similar simulations of their ΔP. The kinetic theory describes the motion of a single particle, so it cannot model the flow in larger space scale, such as the motions of clusters, which generally exist in risers [13]. For C model and D model, they consider the viscosity of particles on microcosmic scale and macroscopic scale respectively. As shown in figure 2(c), the particle turbulent viscosity ($\mu_{s,t}$) of C model maintain steady fluctuations, while $\mu_{s,t}$ of D model fluctuates more at the bottom than the top. That is because there are more particles near the inlet and the particle fluctuation is stronger. The C models obscures the difference between gas-solid phases which leads to the disparities between simulations and experiments.
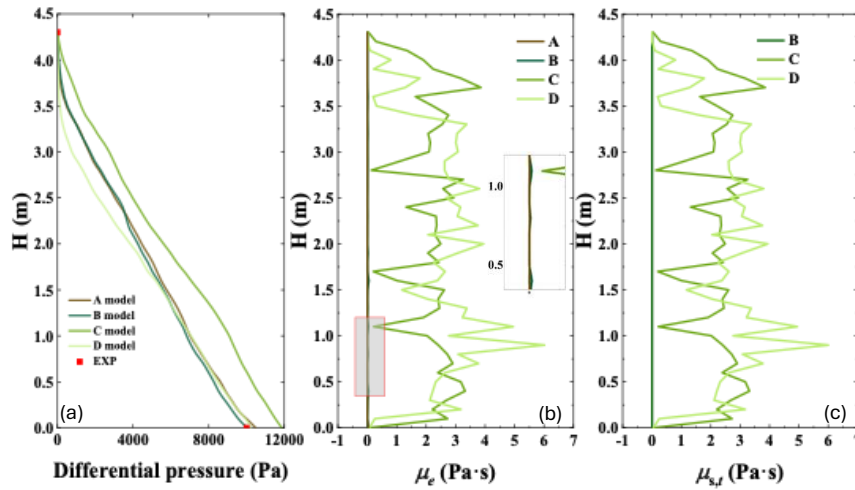
Fig. 2. The comparisons of predicted results by different turbulence models.

3.2 Drag model

Drag force is the predominant force in gas-solid fluidized bed reactors that affects hydrodynamics behavior. Due to the lack of consideration for mesoscale structures, the gas-solid drag force is often overestimated using traditional drag models. In order to successfully predict the flow characteristics, the energy minimization multi-scale (EMMS) model is used to improving the accuracy of simulation by taking into account the fluid flow involving particle agglomerations [14,15]. To assess the sensitivity of drag force models on the CTFB hydrodynamics, we have investigated two different drag models, Huilin-Gidaspow and EMMS.

Figure 4 represents the time-averaged axial solid volume fraction profiles plotted against the height in riser and time-averaged axial differential pressure profiles. The results of Huilin-Gidaspow drag model and EMMS model show significant differences, indicating that the hydrodynamics behavior is sensitive with the consideration of meso-scale structure. This work of simulation reduced computational time by performing local initialization. The solid mass of equilibrium in the riser was roughly estimated based on the pressure drop, then an initial solid volume fraction was set. This may result in inconsistencies between experimental data and simulation. Huilin-Gidaspow drag model over-predicted the bed expansion heights due to overprediction of the drag force, which is also investigated in the previous literature [16,17]. In the following work, the effect of parameters are investigated for both Huilin-Gidaspow drag model and EMMS model. The sensitivity of flow characteristics to parameters based on KTGF and the influence of drag models on parameters will both be investigated.
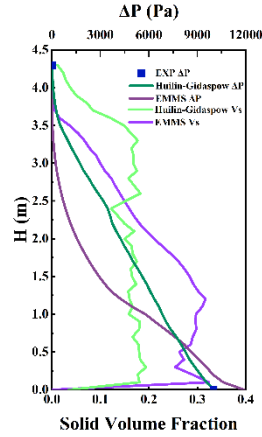
Fig. 4. Time-averaged axial solids holdup and differential pressure profiles predicted using different drag models.

3.3 Sensitivity of parameters

The frictional interaction between the wall and solid particles, termed as specularity coefficient in wall boundary theory by Johnson and Jackson, and particle–particle restitution coefficient depicting momentum transfer or energy dissipation between colliding particles are important in numerical predictions of gas–solid flow. Nevertheless, there is no consensus on the value of specularity coefficient and restitution coefficient. Besides, the formation of mesoscale heterogeneous structures has a significant effect on the constitutive laws as proven in many studies [10], but the concern of parameter sensitivity was almost based on single particle without considering the effect of cluster. It is also worth exploring. Therefore, a series of simulations were performed to explore the qualitative behavior of the above discussed model parameters, respectively based on Huilin-Gidaspow drag model and EMMS model.

3.3.1 Specularity coefficient

In the Johnson-Jackson model, the influence of solid wall friction and its roughness on the shear force is computed using specularity coefficient. The specularity coefficient is defined as the fraction of collisions that pass momentum to the wall boundary and specified between zero and unity. Similar trends were noticed using both two drag models that increasing the value of φ results in a higher solids concentration near the walls due to less friction between particles and walls, as shown in figure 5(a). Figure 5(c) shows the differential pressure profiles at different specularity coefficients (φ = 0.9, 0.5, 0.1, 0.05) when the Huilin-Gidaspow drag model was used and the differential pressure profiles at five specularity coefficients of 0.99, 0.9, 0.5, 0.1 and 0.01 using EMMS model. For Huilin-Gidaspow drag model, the values of specularity coefficient from 0.9 to 0.1 resulted in a negligible impact on the differential pressure, yet specularity coefficient below 0.05 resulted in a slight but distinguishable impact. Compared with Huilin-Gidaspow drag model, simulations employing EMMS model has less sensitivity with specularity coefficient. This is significantly different from CFB. Zhou et al. [18] found that EMMS model is more sensitive to specularity coefficient. That is because CTFB has the characteristics of high solid holdup, and gas–solid interaction is much larger than the interaction between particles and wall, so the effect of particle–wall interaction on the flow behavior was hardly observable. Similar to TFB, CTFB exhibits a weaker sensitivity to the specularity coefficient compared with restitution coefficient.
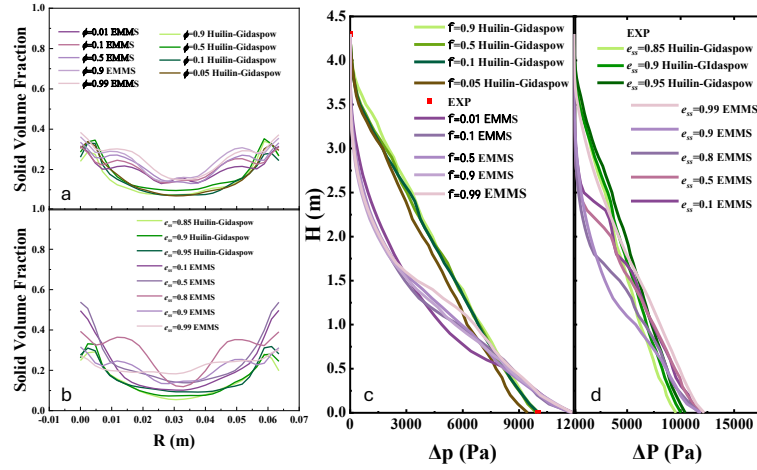
Fig. 5. Predictions for particle–particle restitution coefficient and specularity coefficient.

3.3.2 Restitution coefficient

The particles restitution coefficient (e_{ss}) is referred as tunning variable in simulating [13]. Its value ranges between 0 and 1, where $e_{ss} = 0$ shows inelastic inter-particle collisions, while $e_{ss} = 1$ represents a perfectly elastic collision. There is no consensus on choosing the best value of the restitution coefficient for different operating conditions. In this section, a special concern is dedicated to the effect of restitution coefficient.

As it can be seen into figure 5(d), particles restitution coefficient (e_{ss}) varying from 0.1 to 0.99 based on EMMS model resulted in a slight but more distinguishable impact on differential pressure distribution than Huilin-Gidaspow drag model. From figure 5(b), it is observed that decreasing e_{ss} resulted in more heterogeneous distributions in the bed using EMMS model, because more mechanical energy dissipation resulting from inelastic inter-particle collisions, thus attaching more particles in the bed, which further results in a more heterogeneous bed. The sensitivity of e_{ss} is negligible using Huilin-Gidaspow drag model. The reason is the drag force was over-predicted, when the Huilin-Gidaspow drag model was used, and the impact of collision between particles is inconspicuous.

Restitution coefficient varying from 0.85 to 0.95 entails a noticeable impact in solid holdup distribution in the top part of the CTFB riser. This numerical result is against with CFB and TFB in which the bottom part has more sensitivity to particles restitution coefficient [7,14].

4. Conclusion

Accurate simulation of gas–solid flow behavior in CTFB risers depends on the proper description of all possible intra- and interphase interactions. In this work, an EE-TFM approach coupled KTGF was implemented to study the gas–solid flow hydrodynamic in the CTFB riser. Different CFD model simulations were conducted while investigating the sensitivity of CFD model parameters (macroscopic viscosity, drag coefficient, specularity coefficient and particle–particle restitution coefficient) to accurately predict the CTFB riser hydrodynamic profile.

1. The consideration about turbulence viscosity of particles by both turbulence model and KTGF is superfluous. Using $k - \varepsilon - k_p{}' - \varepsilon_p{}' - \theta$ model which considers particle turbulent viscosity at both micro and macro scales will be efficient to improve the simulation.
2. The drag force models show the most substantial influence on the hydrodynamics behavior of the CTFB. The simulations employing EMMS model are more sensitive with parameters of KTGF than Huilin-Gidaspow drag model.
3. The simulation of CTFB exhibits significantly different sensitivity to parameters compared to CFB and TFB. Their distinct characteristics of hydrodynamic should be predicted by CFD model with different parameters. e_{ss} from 0.85 to 0.95 entails an impact in solid holdup distribution in the upper section of the CTFB riser, while

in the CFB and TFB the solid holdup on the bottom has more sensitivity to e_{ss} than that on the top. The specularity coefficient (ϕ) has a minor influence on the overall flow characteristics.

Acknowledgment

References

Wilberforce, T., Olabi, A., Sayed, E., et al. Progress in carbon capture technologies. Science of The Total Environment. 2021. 761, 143203

Nouri, M., Rahpaima, G., Nejad, M., et al. Computational simulation of CO_2 capture process in a fluidized-bed reactor. Computers & Chemical Engineering. 2018. 108, 1–10

Zhu J. Circulating turbulent fluidization—A new fluidization regime or just a transitional phenomenon. Particuology. 2010. 8, 640–644

Tebianian, S., Dubrawski, K., Ellis, N., et al. Investigation of particle velocity in FCC gas-fluidized beds based on different measurement techniques. Chemical Engineering Science. 2015. 127, 310–322

Zhang, Y., Ren, P., Li, W., et al. Turbulent mass transfer model for the simulation of liquid-solid CFB risers and its verification. Powder Technology. 2021. 377, 847–856

Van, W., Schouten, J., van, d., et al. Comparative analysis of CFD models of dense gas–solid systems. AIChE Journal. 2001. 47, 1035–1051

Chang, J., Wu, Z., Wang, X., et al. Two- and three-dimensional hydrodynamic modeling of a pseudo-2D turbulent fluidized bed with Geldart B particle. Powder Technology. 2019. 351, 159-168

Xiaoxue, J., Shuyan, W., Qinghong, Z., et al. Granular restitution coefficient-based kinetic theory computations of bubbling fluidized beds. Powder Technology. 2021. 394, 825–837

Uwitonze, H. CFD simulation of hydrodynamics and heat transfer characteristics in gas–solid circulating fluidized bed riser under fast pyrolysis flow condition. Applied Thermal Engineering. 2022. 212, 118555

Wang, J. A Review of Eulerian Simulation of Geldart A Particles in Gas-Fluidized Beds. Industrial & Engineering Chemistry Research. 2009. 48, 5567–77

Park, J., Won, W., Jung, W., et al. One-dimensional modeling of a turbulent fluidized bed for a sorbent-based CO_2 capture process with solid–solid sensible heat exchange. Energy. 2019. 168, 1168–1180

Park, Y. Energy recoverable multi-stage dry sorbent CO_2 capture process. Energy Procedia. 2014. 63, 2266-2279

Zheng, Y., Wan, X., Qian, Z., et al. Numerical simulation of the gas–particle turbulent ow in riser reactor based on $k - \varepsilon - k_p - \varepsilon_p - \theta$ two-fluid model. Chemical Engineering Science. 2001. 56, 6813-6822

Yang, N., Wang, W., et al. CFD simulation of concurrent-up gas–solid flow in circulating fluidized beds with structure-dependent drag coefficient. Chemical Engineering Journal. 2003. 96, 71–80

Zhou, W., Zhao, C., Duan, L., et al. Two-dimensional computational fluid dynamics simulation of coal combustion in a circulating fluidized bed combustor. Chemical Engineering Journal. 2011. 166, 306–314

Adnan, M. Validation and sensitivity analysis of an Eulerian-Eulerian two-fluid model (TFM) for 3D simulations of a tapered fluidized bed. Powder Technology. 2022. 396, 490-518

Lu, L., Konan, A., Benyahia, S. Influence of grid resolution, parcel size and drag models on bubbling fluidized bed simulation. Chemical Engineering Journal. 2017. 326, 627–639

Zhou, X. Effect of wall boundary condition on CFD simulation of CFB risers. Particuology. 2013. 11, 556–565

REGULATION MECHANISM OF CHEMICAL REACTION FOR COAL CATALYTIC HYDROGASIFICATION IN FLUIDIZED BED

Weiwei Li*

School of Chemistry and Chemical Engineering, North University of China, Taiyuan 030051, China

*Email:*liweiwei197@126.com*

Abstract

Catalytic coal hydrogasification is an efficient method for converting coal into natural gas. However, the deployment of this technology at large scale is constrained by high cost of pure hydrogen. Utilizing raw gas in place of hydrogen has the potential to significantly reduce cost. Nonetheless, the presence of steam and carbon dioxide in raw gas may unfavorably impact on the hydrogasification reaction, thereby changing carbon conversion and methane yield. A mathematical model for catalytic coal hydrogasification in a fluidized bed has been developed, incorporating both pressurized hydrodynamics behaviors (bubble and bed expansion height) and the kinetic models of catalytic reactions. This model enables predictions of gas composition distribution along the bed height. Furthermore, it elucidates the interaction between the reactions. The effect of carbon dioxide on methane composition and carbon conversion were discussed. The contribution ratios were analyzed, such as of reaction related to methane, carbon conversion, carbon dioxide and carbon monoxide. The model may provide a guideline for the development of coal catalytic hydrogasification.

1. Introduction

With the increased demand of nature gas in China, the technology of coal to nature gas had aroused more and more attention. The coal hydrogasification was the most promising technology with high methane yield and thermal efficiency, comparing with catalytic coal gasification and two-step methods [1].

Suitable reactor and catalyst were very important for coal hydrogasification. Different reactors had been developed for this process, including fixed bed, fluidized bed and entrained flow bed. With the high heat transfer rate and easily controlled reaction time in fluidized bed, it was more suitable reactor for coal hydrogasification. Many catalysts had been tested in these process, such as single component catalyst: Na_2CO_3, K_2CO_3, Ca catalyst ($Ca(OH)_2$, CaO, $Ca(CH_3COO)_2$, $CaCO_3$, $CaCl_2$, CaF_2) [3, 4]); two-components catalyst: Ni-Ca, Fe-Ca, Cu-Ca, Co-Ca, Co-K, Co-Mg; three-components catalyst:: Cu-Ni-Ca, and the dispose catalyst: biomass ash. Table 1 showed the typical catalysts used in coal hydrogasification. As shown in Table 1, the catalyst of Co-Ca showed the high performance with carbon conversion and methane component of 91.3% and 78.8%, respectively.

Table 1 The typical catalysts used in coal hydrogasification

Ref.	Coal	Catalyst	T (℃)	P (MPa)	C (%)	CH$_4$ (%)
Jiang et al.[1]	Bituminous coal	CaO	800	3	-	16.9-70.3
Yan et al. [2]	Fugu bituminous coal	Ni-Ca	850	3	80.8	66.8
Yan et al. [2]	Fugu bituminous coal	Fe-Ca	850	3	61.5	49.3
Yuan et al. [3]	Fugu bituminous coal	Fe	750	1	48.85	33.15
Yuan et al. [3]	Fugu bituminous coal	Fe-Ca	750	1	58.47	46.71
Sun et al. [4]	De-ash Yili Coal	Cu-Ca	850	2	-	20.6-60.6
Qu et al. [5]	Fugu bituminous coal	Co-Ca	850	3	91.3	78.8

Note: - is not available.

However, the big obstacle to develop the Co-Ca catalyzed coal hydrogasification was the used pure hydrogen as gasification agent. To reduce the cost and enhance the utilization of hydrogen, the three-stage fluidized bed was developed, as shown in Fig.1. The fluidized bed was divided into three sections: catalyzed hydropyrolysis, catalyzed hydrogasification and In-site hydrogen supply. The coal with Co-Ca was pyrolysized to produce relative light tar and

methane under H_2 atmosphere. And then, most coal with H_2-rich agent to produce methane. The gasification reside could be gasified under H_2O and O_2 in the bottom gasifier to produce H_2 and realized the in-site hydrogen supply. During this process, the cost of hydrogen decreased. The produced H_2-rich gas contained CO and CO_2, which may reacted with H_2 to produce methane, therefore the hydrogen utilization increased.
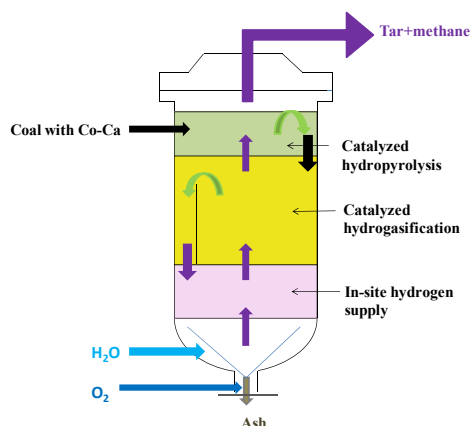
Fig. 1 Three-stages fluidized bed for coal catalyzed hydrogasification

Under the pure H_2, only reaction R1 ($C+2H_2=CH_4$) happened. The supply in-site gas in three-stages fluidized bed contained CO, H_2O and CO_2, which may change chemical reaction pathway. However, few works were conducted on this aspect. Feng et al. [6] had conducted the methane generation under H_2/CO_2 mixed atmosphere. The CO_2 conversion and carbon conversion could be about 90% and 72%, respectively. The methane yield under mixed atmosphere increased to 188% compared with 77.4% at pure hydrogen. Latter, the methane generation under H_2/H_2O mixed atmosphere was also conducted [7]. The Co-Ca firstly catalyzed C-H_2O reaction, and inhibited the C-H_2 reaction, which made the selectivity of CH_4 decreased and CO_X increased. However, the suitable CO_2 addition amount and the contribution ratio of C-H_2 (R1), CO_2-H_2 (R4) and CO-H_2 (R5) to methane were still unknown. These were very difficult to study by experiment.

Some author had used CFD and CPFD to reveal the coal catalyzed hydrogasification performance. Xia et al. [8] has analyzed the bubble size could be 2-8 mm. The predicted hydrodynamics behaviors (bubble size and bed expand ratio) by CFD were compared with empirical correlations to show its correctness. The particle temperature and size were well simulated at various times. The effect of pressure on particle temperature, methane composition and carbon conversion were further conducted by Yao et al. [9]. The suitable pressure was about 3MPa after balanced the reaction intensification and hot spot. Recently, Gu et al. [10] had analyzed the coal deposition during fluidized bed for coal catalyzed hydrogasification. The effects of particle size and particle density on hydrodynamics behaviors were specially considered. The suitable particle size was around 20-80 μm.

However, almost no works were conducted on the interaction among different reactions, which was much important for methane and carbon conversion. The novelty of this work was to establish model to reveal the chemical reactions interaction roles in Co-Ca catalyzed coal hydrogasification process, including reactions related to methane, carbon conversion, CO_2 and CO. The proposed model for Co-Ca catalyzed coal hydrogasification in a bubbling fluidized bed could serve as an invaluable tool for selection suitable agent to produce methane.

2. Experiment and model

2.1. Experiment

To make the simulation process more clearly, the experimental process of catalyzed coal hydrogasification process in bubbling fluidized bed gasifier was shown as follows. The coal with Co-Ca catalyst reacted with gasification agent to produce methane. The pure hydrogen or mixed with carbon dioxide was well distributed in the fluidized bed. After coal reacted with hydrogen or carbon dioxide, the methane-rich gas was generated. The tar and water in the product gas were separated by cold traps using ethylene glycol and ice water, respectively.

More detailed experimental process for catalyzed coal hydrogasification in bubbling fluidized bed were shown in the work of Feng et al [6].

2.2. Empirical model

2.2.1 Model assumption

To simply the simulation process, some assumptions were made, which was shown as follows:

(1) The model was one dimension at steady state.

(2) Based on gas and particle movement and two-phase theory, the gasifier was divided into two sections: one for bubble zone and the other for freeboard zone. The boundary line was the bed expansion height. The bubble zone was subdivided into bubble and emulsion. The plug flow and well mixed flow were assumed in bubble zone and freeboard zone, respectively.

(3) The particle size was spherical, uniform and constant during catalytic hydrogasification.

(4) The reactions rated were controlled by chemical reaction and mass transfer.

(5) The hydropyrolysis was instantaneously completed.

2.2 2 Hydrodynamic model

The mainly characteristic hydrodynamic behaviors in fluidized bed was minimum fluidization velocity, bed expansion ratio (Hf/Hmf), bubble diameter (Db), and bubble velocity (ub), with the expressions were shown in Table 2.

Table 2 The expression of mainly hydrodynamic behaviors

Item	Expressions
Minimum fluidization velocity	$\dfrac{d_p u_{mf} \rho_g}{\mu} = [C_1^2 + C_2 \dfrac{d_p^3 \rho_g (\rho_p - \rho_g) g}{\mu^2}] - C_1$
Expansion height	$\dfrac{H_f}{H_{mf}} = 1 + \dfrac{21.365(u_0 - u_{mf}^*)^{0.738} d_p^{1.006} \rho_s^{0.376}}{(u_{mf}^*)^{0.937} (M_f P_r)^{0.126}}$
Bubble size	$D_b = D_{bm} - (D_{bm} - D_{b0}) \exp(-\dfrac{0.3h}{D_t})$
Bubble velocity	$u_b = u_0 - u_{mf} + 0.711(g D_b)^{0.5}$

2.2 3 Chemical reaction model

The used kinetic models of chemical reactions were shown in Table 3.

Table 3. Kinetic models of chemical reactions

Chemical reaction	Reactions	Rates Expression	Ref
R1 Hydrogasification	$C+2H_2=CH_4$	$\dfrac{dC_{CH_4}}{dt} = 0.000855 \exp(\dfrac{-39.43}{Tp}) P_{H_2}^{0.508}(1-X)$	[11]
R2 Carbon dioxide gasification	$C+CO_2=2CO$	$\dfrac{dX}{dt} = 6.05 \times 10^6 \exp(\dfrac{-25182}{Tp}) P_{CO_2}^{0.264}(1-X)^{2/3}$	[12]
R3 Steam gasification	$C+\alpha H_2O=(2-\alpha)CO+(\alpha-1) CO_2+\alpha H_2$	$\dfrac{dX}{dt} = 2.39 \times 10^2 \exp(-12900/RT_P) P_{H_2O} / (1+3.16\times10^{-2}$ $\exp(30100/RT_P) P_{H_2O} + 5.3\times10^{-3} \exp(59800/RT_P) P_{H_2}$ $+82.5\times10^{-6} \exp(96100/RT_P) P_{CO}) \rho_s F_C / M_B \alpha(1-X)$	[13]
R4 Inverse water gas shift reaction	$CO_2+H_2= CO+H_2O$	$K_{eq} = \dfrac{P_{CO_2} P_{H_2}}{P_{CO} P_{H_2O}} = 0.0265 \exp(\dfrac{3956}{T})$	[12]
R5: Carbon monoxide methanation	$CO+3H_2= CH_4+H_2O$	$\dfrac{dC_{CH_4}}{dt} = \dfrac{4.444 C_{CO} C_{H_2}}{(1+1.606 C_{CO})^2}$	[14]
R6: Carbon dioxide methanation	$CO_2+4H_2=CH_4+2H_2O$	$\dfrac{dC_{CH_4}}{dt} = 6 K_6 C_{CO_2} C_{H_2}$	[15]

3. Results and Discussion

3.1. Model validation

The established model was firstly compared with the gas composition using H_2 alone or H_2/CO_2 as gasifying agent. As shown in Fig. 2, the simulated CH_4, CO, CO_2 and carbon conversion are in good agreement with the experimental values.

(a) CH_4 (b) Gas composition   (c) Carbon conversion
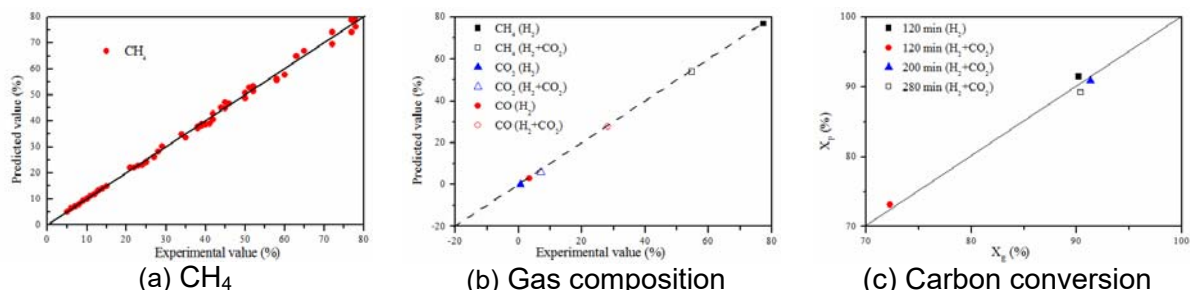
Fig .2 Comparison of experimental results with model predication

It was clearly shown in Fig.2 (b) that with introducing CO_2, the simulated CO increased much from 2.9% to 27.6% and CH_4 decreased from 76.8% to 53.9%, which may because some CO_2 conversed into CO and H_2 partial pressure decreased. As shown in Fig. 2 (c), with introducing CO_2, the simulated carbon conversion at reaction time of 120 min quickly decreased from 91.5% to 73.1%, but not much different at reaction time of 200 min, which may because at initial stage, the $C-H_2$ reaction is largely inhibited by adding CO_2, with the reaction time increased, CO_2 may reacted with C to produce CO and make the carbon conversion increased.

3.2 Model predication

The gas composition of H_2, CO, CO_2 and CH_4 changed along with the bed height using H_2 alone and H_2/CO_2 as gasifying agent, shown in Fig. 3 (a) and (b), respectively. As shown in Fig. 3 (a), the simulated methane content increases quickly to 45.5% with the increase of bed height to 25 cm. And then it slowly increased to 77.3% at bed height of 100 cm. Hydrogen content continuous decreased to 18.7% mainly due to the consumption of methane reaction. Few carbon dioxide and carbon monoxide were detected mainly caused by hydropyrolysis. As shown in Fig. 3 (b), with introducing 10%CO_2, the methane increased rate became slowly, at the same bed height of 25 cm, the simulated methane was only 31.7%. As the bed height increased from 0 to 100 cm, the simulated CO_2 decreased slowly from 10% to 7.2%, CO increased from 0 to 27.9%, H_2 decreased from 90% to 15.1%.

(a) H_2 alone   (b) H_2+CO_2
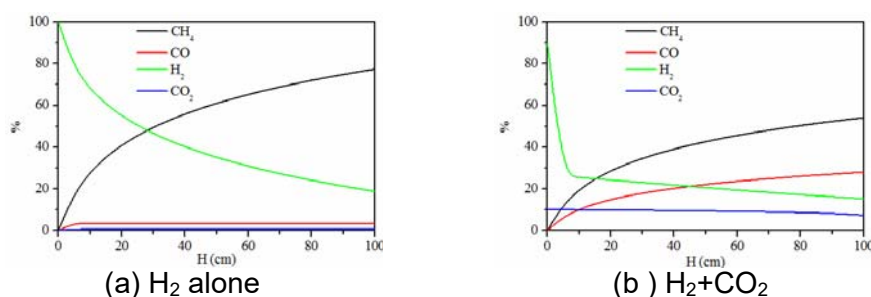
Fig .3 Gas composition along with bed height

3.3 Reaction analysis

3.3.1 Reaction contributed to methane

There are three reactions contributed to methane: $C+2H_2=CH_4$ (R1), $CO_2+4H_2=CH_4+2H_2O$ (R4) and $CO+3H_2=CH_4+H_2O$ (R5). When using H_2 as gasifying agent alone, the $C-H_2$ was the only way to produce methane. However, with adding CO_2, the methane generated way may change. Fig.4 (a) showed the contribution ratio of the three reactions. With the increased carbon dioxide concentration from 10% to 30%, the contribution ratio of R1 decreased from 97% to 62%, the contribution ratio of R4 and R5 increased from 2% to 30%, and 1% to 8%, respectively. After introducing CO_2, the reaction rate of $C-H_2$ decreases,

mainly due to the decrease in hydrogen partial pressure. The main source of CH_4 came from the C-H_2 reaction, and the proportion decreased, resulting in a decrease in the total CH_4 content.

(a) contributed to methane   (b) contributed to carbon conversion
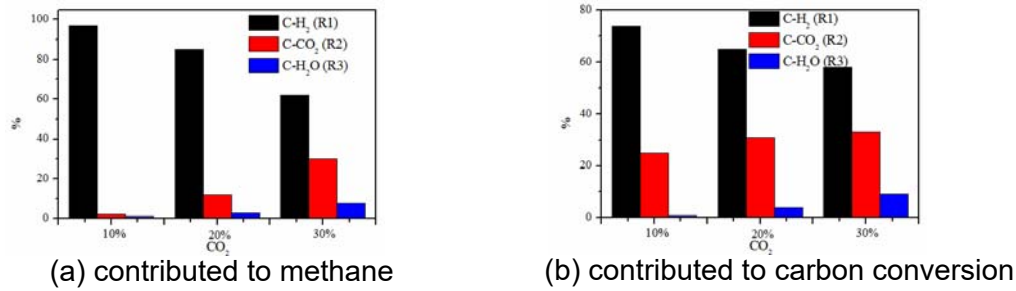
Fig .4 Effect of carbon dioxide on reactions

3.3.2 *Reaction contributed to carbon conversion*

There are three reactions contributed to carbon conversion: $C+2H_2=CH_4$ (R1), $C+CO_2=2CO$ (R2) and $C+\alpha H_2O=(2-\alpha)CO+(\alpha-1)CO_2+\alpha H_2$ (R3). When using H_2 as gasifying agent alone, the carbon conversion came from C-H_2 (R1). However, with adding CO_2, the carbon dioxide and steam may react with carbon and made carbon conversion increased. Fig. 4(b) showed the contribution ratio of the three reactions. With the increased carbon dioxide concentration from 10% to 30%, the contribution ratio of R1 decreased from 74% to 58%, the contribution ratio of R2 and R3 increased from 25% to 33%, and 1% to 9%, respectively. These meant with introducing CO_2, some carbon reacted with CO_2, but most of carbon reacted with hydrogen.

3.3.3 *Reactions related to CO_2*

There are three reactions consumed CO_2: $C+CO_2=2CO$ (R2), $CO_2+4H_2=CH_4+2H_2O$ (R4), and $CO_2+H_2=CO+H_2O$ (R6). One reaction generated CO_2: $C+\alpha H_2O=(2-\alpha)CO+(\alpha-1)CO_2+\alpha H_2$ (R3). Fig .5 showed the contribution ratio of the four reactions. With the increased carbon dioxide concentration from 10% to 30%, the contribution ratio of R2 increased from 29% to 39%, the contribution ratio of R4, R6 and R3 decreased from 13% to 9%, 54% to 50%, and 3.25% to 1.5% respectively. With the increase of CO_2 concentration, the reaction rate of R2 (C-CO_2) increases, rapidly consuming CO_2, while R6 (shift reaction) has little change, the proportion of R4 (CO_2+4H_2) and R3 (C-H_2O) decreases.

(a) related to CO_2 (b) related to CO
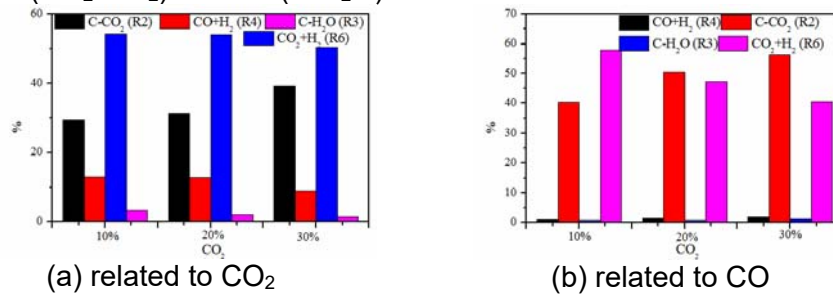
Fig .5 Effect of carbon dioxide on reactions

3.3.4 *Reactions related to CO*

There are three reactions generated CO: $C+CO_2=2CO$ (R2), $C+\alpha H_2O=(2-\alpha)CO+(\alpha-1)CO_2+\alpha H_2$ (R3) and $CO_2+H_2=CO+H_2O$ (R6). One reaction consumed CO: $CO+3H_2=CH_4+H_2O$ (R5). Fig.5 (b) showed the contribution ratio of the four reactions. With the increased carbon dioxide concentration from 10% to 30%, the contribution ratio of R2, R3 and R5 increased from 40.4% to 56%, 0.67% to 1.2% and 1% to 1.88%, respectively. The contribution ratio of R6 decreased from 57.9% to 40.6%.

With the increase of CO_2 concentration, the proportion of R5 (CO-H_2) slightly increased, consuming less CO. The reaction rate of R2 (C-CO_2) increased, producing a large amount of CO, while R6 (shift reaction) decreased much and R3 (C-H_2O) slightly increased.

4. Conclusion

A one dimension steady state model was established to simulate the coal catalytic hydrogasification. The simulated CH_4, CO, CO_2 and carbon conversion are in good agreement with the experimental values. With introducing 10% CO_2, the methane increased rate became slowly, at the same bed height of 25 cm, the simulated methane was only 31.7%. At carbon dioxide concentration of 30%, the contribution ratios of reactions to methane were 62% (C-H_2, R1), 30% (CO_2-H_2, R4) and 8% (CO-H_2, R4). The contribution ratios of reactions to carbon conversion were 58% (C-H_2, R1), 33% (C-CO_2, R2) and 9% (C-H_2O, R3). Carbon dioxide was mainly consumed by reverse waster gas shift reaction (R4). Carbon monoxide was mainly generated from reverse waster gas shift reaction (R4) and Carbon dioxide gasification (R2).

Acknowledgment

References

[1] Jiang JT, Liu QY, Liu ZY, Superior catalytic effect of calcium oxide on the hydrogasification of char for CH_4, Fuel 180 (2016) 737-742.

[2] Yan S, Bi JC, Qu X, The behavior of catalysts in hydrogasification of sub-bituminous coal in pressured fluidized bed, Applied Energy 206 (2017) 401-412.

[3] Yuan SF, Zhang N, Qu X, Bi JC, Cao Q, Wang JL, Promoted catalysis of calcium on the hydrogasification reactivity of iron-loaded subbituminous coal, Fuel 200 (2017) 153-161.

[4] Sun H, Wang JT, Bi JC, Zhang R, Qu X, Zhang JL, Zhang JS, Investigating the Cu-based catalysts for char catalytic hydrogasification and its recovery, Fuel 294 (2021) 120567.

[5] Qu X, Yan S, Yan XQ, Zhang JS, Zheng Q, An YB, Role of cobalt and calcium on coal catalytic hydrogasification in a pressurized fluidized bed, Fuel 239 (2019) 347-356.

[6] Feng J, Yan S, Zhang R, Gu SM, Qu X, Bi JC, Characteristics of Co-Ca catalyzed coal hydrogasification in a mixture of H_2 and CO_2 atmosphere, Fuel 324 (2022) 124486.

[7] Feng J, Gu SM, Zhang R, Qu X, Bi JC, Effect of steam on cobalt-calcium catalyzed coal hydrogasification, Fuel Processing Technology 249 (2023) 107868.

[8] Xia ZH, Yan S, Chen CX, Qu X, Bi JC, Three-dimensional simulation of coal catalytic hydrogasification in a pressurized bubbling fluidized bed, Energy Conversion and Management 250 (2021) 114874.

[9] Yao ZP, Song XD, Yan S, Xia ZH, Chen CX, Qu X, Bi JC, Numerical study in the pressure effects on coal catalytic hydrogasification in the bubbling fluidized bed, Fuel 346 (2023) 128383.

[10] Gu SM, Feng J, Zhang R, Qu X, Evolution of char structure during cobalt-calcium catalyzed coal hydrogasification and its impact on gas-solid hydrodynamics of gasifier, Powder Technology 433 (2024) 119273.

[11] Yan S. Fundamental study on coal catalytic hydrogasification in a pressurized fluidized bed. Tauyuan: Institute of Coal Chemistry, Chinese Academy of Science, 2019.

[12] Z.Y. Liu, Y.T. Fang, S.P. Deng, J.J. Huang, J.T. Zhao, Z.H. Cheng, Simulation of pressurized ash agglomerating fluidized bed gasifier using Aspen plus, Energy Fuels, 26 (2012) 1237-1245.

[13] J.C. Bi, C.H. Luo, K.I. Aoki, S. Uemiya, T. Kojima. A numerical simulation of a jetting fluidized bed coal gasifier, Fuel 76 (1997)285-301

[14] Pradeep KA, James RK, William HM, Methanation over transition-metal catalysts. 4. Co/Al_2O_3 rate behavior and kinetic modeling. Journal of Molecular Catalysis A: Chemical 122 (1997) 1-11.

[15] Joanna T, Roman Dj, Model of activation of the cobalt foil as a catalyst for CO_2 methanation. Journal of Molecular Catalysis A: Chemical 122 (1997) 1-11.

FLOW-REACTION COUPLED MP-PIC SIMULATION IN AN INDUSTRIAL MTO REGENERATOR

Shiyu Bai, Yongmin Zhang*

State Key Laboratory of Heavy Oil Processing, China University of Petroleum, Beijing, Fuxue Road 18, Changping District, Beijing 102249 China

*Email of corresponding author: zhym@cup.edu.cn

Abstract

Methanol to olefins (MTO) technology using partial regeneration has a strict requirement on the coke content of regenerated catalysts. This study simulated the flow and reaction in an industrial-scale MTO turbulent fluidized bed regenerator based on the multi-phase particle in cell (MP-PIC) method. To ensure the accuracy of the simulation, the simulation parameters were derived from industrial conditions and measurements of industrial catalysts. Meanwhile, key internals in the regenerator were preserved as much as possible. The simulation results show that the apparent bed density, temperature, and flue gas composition obtained from the simulation are in good agreement with industrial data. Additionally, the average coke content of regenerated catalysts is basically consistent with the actual measurement results. There is a significant distribution of the coke content of regenerated catalysts, with approximately one-third of catalysts falling within the target coke content range. This coke content distribution is closely related to the residence time of catalysts, with an ideal residence time ranging from 883 s to 2660 s. By Optimizing the residence time distribution (RTD), it is possible to achieve an optimal coke content distribution. This study successfully provides valuable experience and simulation ideas for the design and optimization of industrial MTO regenerators.

1. Introduction

MTO technology developed in recent years has provided an interesting and promising way to produce light olefins. MTO regenerator generally adopts a fluidized bed process. Due to the presence of an induction period for methanol conversion on molecular sieve catalysts(Yuan et al., 2019), MTO regeneration process typically employs partial burning(Tian et al., 2015). Regenerated catalysts with excessively low or high coke content are unable to exhibit optimal catalytic performance upon being returned to the reactor. Therefore, further studies on the regeneration process are crucial for accurately controlling the degree of coke burning and optimizing reactor performance.

Computational particle fluid dynamics (CPFD) is a numerical simulation method proposed by Snider (2007), which is based on the Euler-Lagrange method and utilizes the MP-PIC model(Andrews and O'rourke, 1996) to handle the particle phase. This method offers significant advantages when simulating industrial fluidization systems involving billions of particles. Many authors(Berrouk et al., 2017; Singh and Gbordzoe, 2017; Yang et al., 2021a; Yang et al., 2021b) have utilized the MP-PIC model to conduct numerical simulations on the gas-solid hydrodynamic and reaction kinetic characteristics in industrial fluid catalytic cracking (FCC) regenerators and these studies have analyzed the regeneration performance of the regenerators, providing empirical guidance for the optimization of FCC regenerators.

This study aims to simulate an industrial MTO regenerator using the commercial software Barracuda 21.0.1 based on the MP-PIC model, focusing on the coke content characteristics of regenerated catalysts and the relationship between the coke content and the residence time, to provide suitable simulation ideas and experience for the design and optimization of MTO regenerators in the future.

2. Model and simulation setup

2.1 Governing equations and reaction kinetics model

The governing equations used for the implementation of the MP-PIC model are given by Andrews and O'rourke (1996) and Snider (2001). This study adopts the EMMS drag model for turbulent conditions and detailed equations can refer to Yang et al. (2021b). In addition, the kinetic model proposed by Arbel et al. (1995) is adopted as the coke burning kinetic model for MTO in this study. The subsequent simulation results prove the feasibility of this drag model and this coke burning kinetic model.

2.2 Geometry model, meshing and boundary conditions

(a) Geometric model   (b) Mesh   (c) Boundary conditions
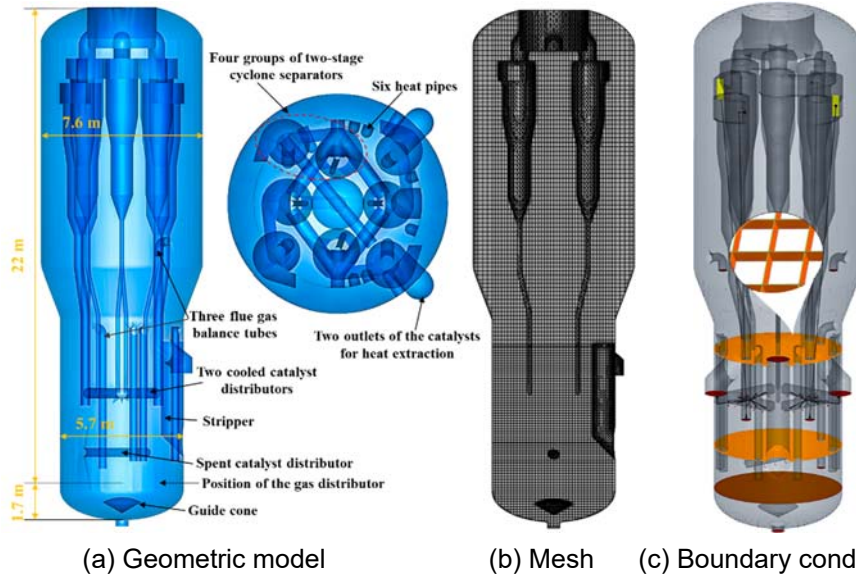
Fig. 1. Geometric model, mesh and boundary conditions of the MTO regenerator

The geometric model of the regenerator is shown in Fig. 1(a). To align as closely as possible with the industrial condition, the proportional modeling is carried out based on an industrial-scale regenerator. Four groups of two-stage cyclone separators, two cooled catalyst distributors, a spent catalyst distributor, a stripper, six heat pipes, three flue gas balance tubes and double-layer mesh grids were retained in the regenerator. Fig. 2 depicts the axial distribution of the average solid holdup under two different cell numbers: 340992 and 484056. From Fig. 2, in the range of 10 m above the gas distributor, the axial distribution of the average solid holdup is virtually identical for both grid counts. Furthermore, the solid holdup in the dense phase zone falls in the acceptable range of industrial data fluctuations. Considering both simulation accuracy and time consumption, a cell count of 340,992 is adopted for subsequent simulation. Additionally, Fig. 1(b) shows the middle section mesh of the regenerator.
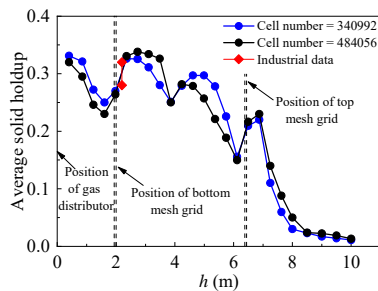
Fig. 2. Comparison of the axial distribution of average solid holdup under two different cell numbers
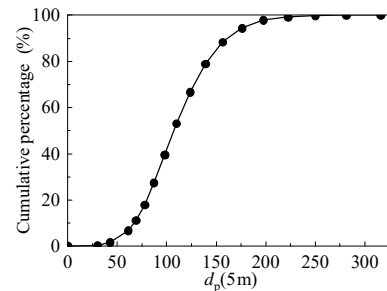
Fig. 3. Cumulative size distribution of the MTO particles

The particle densities of regenerated catalysts and spent catalysts used in the simulation are 1258 kg/m^3 and 1208 kg/m^3, respectively, and the average coke contents are 2.55 wt% (composed of 2.48 wt% carbon and 0.07 wt% hydrogen) and 8.27 wt% (composed of 7.77 wt% carbon and 0.5 wt% hydrogen), respectively. The two catalysts have the same particle size distribution, as shown in Fig. 3. Fig. 1(c) shows boundary conditions of the regenerator.

The air consisting of 21 mol% O_2 and 79 mol% N_2 is injected into the regenerator from the main air inlet at the bottom, with an inlet mass flow rate of 49.13 t/h and an air temperature of 418 K. The spent catalysts with a mass flow rate of 80.64 t/h are injected into the regenerator from the spent catalyst distributor under the action of lifting gas with a mass flow rate of 3.63 t/h. Both the spent catalysts and the lifting gas have a temperature of 749 K. Catalysts exit from two outlets of catalysts for heat extraction with a total mass flow rate of 300 t/h and is returned to the regenerator from two cold catalyst distributors under the action of lifting gas with a total mass flow rate of 5.54 t/h at a temperature of 720 K. Additionally, three flue gas balancing inlets are set as flow BCs, through which the fluidizing gas flows at a total mass flow rate of 2.35 t/h. Both the fluidizing gas and the lifting gas used in the simulation are N_2. The double-layer mesh grids in the regenerator and the underlying gas distributor are set by the virtual baffles in the Barracuda, and other numerical parameters are shown in Table 1.

Table 1. Numerical parameters in the simulation

Items	Value
Close pack volume fraction	0.56
Total number of particle clouds	1.7233×10^6
Initial pressure (Pa)	181325
Initial temperature (K)	933
Initial catalyst inventory (t)	68
Initial time step (s)	0.008
Start time for averaging (s)	3500
Simulation time (s)	4500

3. Results and discussion

3.1 Model validation

Table 2 exhibits a comparison between simulation results and industrial data. The industrial data were obtained from the real-time monitoring of the distributed control system during the normal operation of the MTO regenerator, encompassing apparent bed densities, temperatures at various locations above the gas distributor, and flue gas composition at the primary-stage cyclone entrances. It is evident that the average apparent bed densities in both the dense phase zone and the freeboard area fall in the industrial fluctuation range. The simulated average temperatures at the four locations in the regenerator and the average proportions of flue gas components at the four primary-stage cyclone entrances align closely with the industrial data, exhibiting minimal relative errors. The above comparisons indicate the accuracy of the MP-PIC model in simulating the gas-solids reactive flow system in this study.

Table 2. Comparison between the simulated results and industrial data

Items	Simulated results	Industrial data	Relative error (%)
Average apparent bed density in the dense bed (kg/m^3)	365	350~389	--
Average apparent bed density in the upper freeboard (kg/m^3)	6.9	2.3-9.5	--
Average temperature at a height of 1.3 m (K)	939	943	0.5
Average temperature at a height of 4.8 m (K)	930	933	0.3
Average temperature at a height of 13 m (K)	929	920	1
Average temperature at a height of 20 m (K)	928	908	2.2
Average mass proportion of CO in the flue gas (%)	8.73	8.70	0.3
Average mass proportion of CO_2 in the flue gas (%)	11.10	11.40	2.6
Average mass proportion of H_2O in the flue gas (%)	4.70	4.30	9.3

Average mass proportion of O₂ in the flue gas (%)	0	0	0

3.2 Axial distribution of solid holdup

Fig. 4 displays the contour of average solid holdup on the central axial plane of the regenerator. It can be observed that air cushions with lower solid holdup appear in the zones below each mesh grid. These air cushions are similar to the effects produced by other horizontal grids(Yang et al., 2021b; Yang et al., 2019), so they can suppress the solid exchange between the upper and lower zones separated by mesh grids, thereby reducing axial solid backmixing. These air cushions correspond to the steep decreases in solid holdup seen in Fig. 2. Additionally, Fig. 2 also shows a steep decrease in solid holdup at a height of approximately 4.2 m. This is attributed to the presence of two cooled catalyst distributors that occupy a portion of the gas flow space, resulting in a notable increase in the local gas velocity in that height zone and this leads to the steep decrease in solid holdup. Overall, the axial distribution of the average solid holdup is consistent with the typical distribution pattern of a turbulent fluidized bed(Venderbosch, 1998).
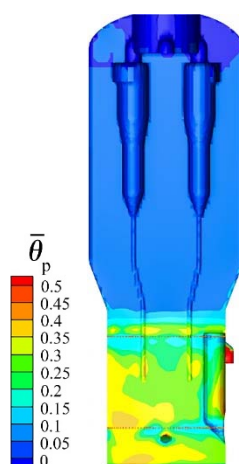
Fig. 4. Axial contour of average solid holdup ($\bar{\theta}_p$) in the regenerator

3.3 Coke content of regenerated catalysts
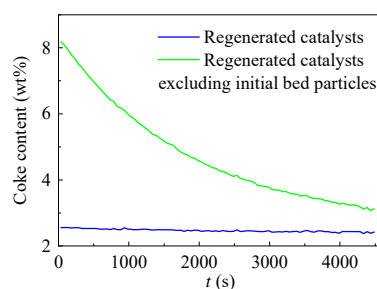
Fig. 5. Changes of the average coke content of regenerated catalysts

Fig. 5 shows changes of the average coke content of regenerated catalysts with time. When including initial bed particles, the average coke content of regenerated catalysts remains between 2.39 wt% and 2.55 wt% over 4500 s. However, in the absence of initial bed particles, the average coke content of regenerated catalysts gradually decreases from 8.27 wt% to 3.1 wt%, with a decreasing rate of decline. The nominal mean residence time of particles in the regenerator is 3035 s. As is well known, the flow pattern of solids in a dense fluidized bed approaches that of a typical Continuous Stirred Tank Reactor model(Yang et al., 2021a). There is a long tail in the RTD of catalysts, indicating that it would take a considerable time for initial bed particles in the regenerator to be replaced. By 4500 s, there are 22 % of initial bed particles remaining in the regenerator, indicating that the regenerator has not reached a true equilibrium operating state, but the difference between the two curves is only approximately 0.6wt%. Therefore, it can be reasonably predicted that the simulation results at 4500 s are very close to the results under the real equilibrium operation

state, and the simulation to this state requires a lot of computing resources. Considering comprehensively, simulating to 4500 s can basically ensure accuracy and economy.

Fig. 6 illustrates the coke content distribution of regenerated catalysts excluding initial bed particles at six distinct moments. Notably, there exists a significant coke content distribution in regenerated catalysts at each time point. From 50 s to 4500 s, the peak of the coke content distribution gradually shifts from high to low, and it becomes basically stable after 3500 s. According to studies of Liu (2015), when the coke content of regenerated catalysts is kept between 1 wt% and 4 wt%, the catalyst activity and selectivity to light olefins of catalysts can be well maintained. It can be seen from Fig. 6(f) that the mass ratio of regenerated catalysts with coke content in the range of 1 ~ 4wt% in the MTO regenerator is 36.9 % at 4500 s. This mass ratio can be used as an evaluation index to simulate the optimization effect of the regenerator in the future.
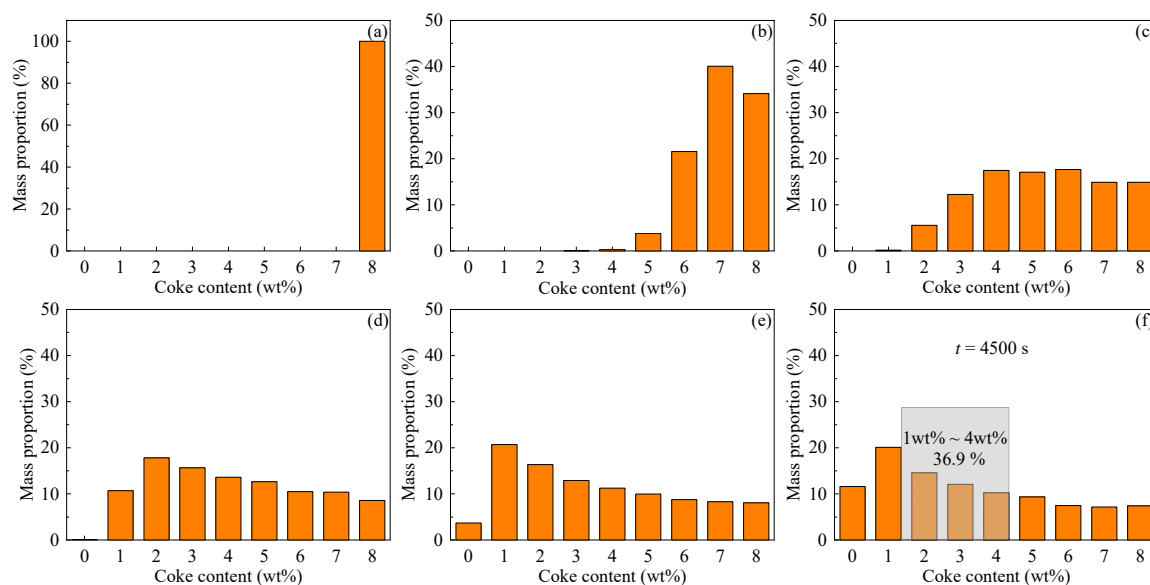
Fig. 6. Coke content distributions of regenerated catalysts at different time: (a) 50 s, (b) 500 s, (c) 1500 s, (d) 2500 s, (e) 3500 s, (f) 4500 s

3.4 Effect of residence time on the coke content of regenerated catalysts
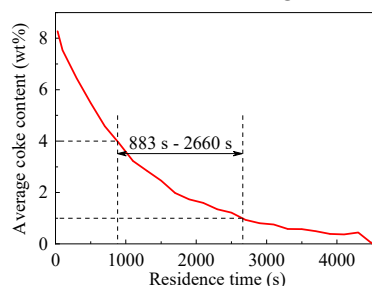
Fig. 7. Relationship between the average coke content of regenerated catalysts and the corresponding residence time

The residence time of catalysts in the regenerator has a significant effect on the coke content of regenerated catalysts. To investigate the relationship between the two, sampling and statistical analysis were conducted on regenerated catalysts (excluding initial bed particles) discharged from the regenerated catalyst outlet between 7490 s and 7500 s. Fig. 7 shows the relationship between the average coke content of regenerated catalysts and their corresponding residence time. As the residence time of regenerated catalysts increases, the corresponding average coke content gradually decreases, and the burning rate gradually decreases with the reduction of coke content. When the coke content of regenerated catalysts is between 1wt% and 4wt%, the residence time of the catalyst in the regenerator is

between 883s and 2660s. When the residence time is less than 883 s and more than 2660 s, the coke deposited on the catalyst shows insufficient combustion and excessive combustion, respectively. Therefore, measures should be taken to make the residence time of the catalyst as long as possible between 883 and 2660 s, which is conducive to maintaining the coke content of regenerated catalysts in a suitable state, thus helping the MTO reaction to proceed better.

4. Conclusion

Based on the MP-PIC method and coke burning kinetics model, the gas-solid flow-reaction coupling in an industrial MTO regenerator was successfully simulated, and the simulation results are in good agreement with the industrial data. This study established a simulation foundation for the optimization research of MTO industrial regenerators. There is a significant coke content distribution in MTO regenerated catalysts. About one-third of the coke content of regenerated catalysts is within the target range, and there is a considerable proportion of components with too low (<1wt%) and too high (>4wt%) coke content. This distribution is closely related to the RTD of regenerated catalysts. The coke content of regenerated catalysts gradually decreases with the increase of the RTD. By optimizing the RTD, especially increasing the proportion of catalysts with residence time between 883 s and 2660 s, it is expected to achieve the optimal regulation of the coke content distribution.

Acknowledgment

References

Andrews, M. J., O'rourke, P. J. The multiphase particle-in-cell (MP-PIC) method for dense particulate flows International Journal of Multiphase Flow. 1996. 22, 379-402.

Arbel, A., Huang, Z., Rinard, I. H., et al. Dynamic and Control of Fluidized Catalytic Crackers. 1. Modeling of the Current Generation of FCC's. Industrial & Engineering Chemistry Research. 1995. 34, 1228-1243.

Berrouk, A. S., Huang, A., Bale, S., et al. Numerical simulation of a commercial FCC regenerator using Multiphase Particle-in-Cell methodology (MP-PIC). Advanced Powder Technology. 2017. 28(11), 2947-2960.

Liu, Z. Methanol to Olefins. Beijing: Science Press. 2015.

Singh, R., Gbordzoe, E. Modeling FCC spent catalyst regeneration with computational fluid dynamics. Powder Technology. 2017. 316, 560-568.

Snider, D. M. An Incompressible Three-Dimensional Multiphase Particle-in-Cell Model for Dense Particle Flows. Journal of Computational Physics. 2001. 170(2), 523-549.

Snider, D. M. Three fundamental granular flow experiments and CPFD predictions. Powder Technology. 2007. 176(1), 36-46.

Tian, P., Wei, Y. X., Ye, M., et al. Methanol to Olefins (MTO): From Fundamentals to Commercialization. ACS Catalysis. 2015. 5(3), 1922-1938.

Venderbosch, R. The role of clusters in gas-solids reactors. An experimental study. 1998.

Yang, Z., Zhang, Y., Liu, T., et al. MP-PIC simulation of the effects of spent catalyst distribution and horizontal baffle in an industrial FCC regenerator. Part II: Effects on regenerator performance. Chemical Engineering Journal. 2021a. 421.

Yang, Z., Zhang, Y., Oloruntoba, A., et al. MP-PIC simulation of the effects of spent catalyst distribution and horizontal baffle in an industrial FCC regenerator. Part I: Effects on hydrodynamics. Chemical Engineering Journal. 2021b. 412.

Yang, Z., Zhang, Y., Zhang, H. CPFD simulation on effects of louver baffles in a two-dimensional fluidized bed of Geldart A particles. Advanced Powder Technology. 2019. 30(11), 2712-2725.

Yuan, X., Li, H., Ye, M., et al. Kinetic modeling of methanol to olefins process over SAPO-34 catalyst based on the dual-cycle reaction mechanism. AIChE Journal. 2019. 65(2), 662-674.

HYDRODYNAMIC CHARACTERISTICS OF FRACTAL NANOPARTICLE AGGLOMERATES ALIGNED STREAMWISE

Niannian Liu[1], Jinglu Yan[2*]

1 Department of Engineering Mathematics, University of Bristol, Bristol BS8 1QU, United Kingdom

2 School of Energy Science and Engineering, Harbin Institute of Technology, Harbin 150001, China

Email: liuhuanpeng@hit.edu.cn

Abstract

This paper explores hydrodynamic interaction characteristics between nanoparticle agglomerates in fluidization beds. A realistic heterogeneous permeability model for nanoparticle fluidized agglomerates (NFAs) is used by the multi-scale complex structure within NFAs and fractal theory. As for two typical shielded cases of NFAs, the hydrodynamic information is obtained and investigated preliminarily. The effects of permeability, Reynolds number, and separation distance on the shielding effects of NFAs are discussed. A quantitative comparison of the deviation from solid spheres is also given. The results of this study can better establish the basic hydrodynamic system of multi-scale NFAs and provide theoretical guidance for the operating parameters of nanoparticle fluidized beds.

1. Introduction

Nanoparticle fluidization bed technology plays a crucial role in many industrial processes, including the chemical engineering, pharmaceutical engineering, and materials engineering. However, nanoparticles frequently form agglomerates during the fluidization due to the strong cohesive forces between nanoparticles (Chaouki et al., 1985). Experimental studies have long observed that nanoparticle fluidized agglomerates (NFAs) exhibit multi-scale heterogeneous structures, and their hydrodynamic characteristics of NFAs are distinct from those of impermeable or homogeneous porous materials (Johnson et al., 1996; Masliyah & Polikar, 1980; Matsumoto & Suganuma, 1977; Wang et al., 2021; Wang et al., 2002). In practice, NFAs are rather small and friable and the fluidization conditions are complex. This makes it difficult to experimentally obtain hydrodynamic characteristics of the NFAs and their smaller scales. Numerical simulation offers the possibility to solve this problem with the development of computational techniques. The hydrodynamic characteristics of NFAs have been the focus of extensive numerical studies, often treating NFAs as permeable or solid spheres to understand the hydrodynamic characteristics. Vanni believes that NFAs can be modeled as a homogeneous sphere with constant porosity equal to the surface value, which works well for fractal dimensions greater than 2 (Vanni, 2000). However, Woodfield and Bickert found that the hydrodynamics of heterogeneous NFAs can be lower than the hydrodynamics of homogeneous NFAs in creeping flows (Woodfield & Bickert, 2001). This highlights the importance of considering heterogeneous permeability to accurately predict hydrodynamics characteristics of NFAs. To accurately describe the heterogeneous structures of NFAs, stepwise-varying permeability model with several concentric shells of different permeability values is proposed in initial studies (Ooms et al., 1970). But this model may introduce systematic errors since it is not continuously varying along the radial direction. NFAs often form through the particle-cluster regime, which results in NFAs with well-defined centers and radially varying porosity and permeability. Then a more realistic approach involves radially varying permeability models, which allow for a continuous change in permeability with radial distance from the center of NFAs. Vanni adopted this radially varying

permeability model to simulate the creeping flows past agglomerates and revealing that permeability increases quadratically with the radial distance from the center (Vanni, 2000). Previous studies that have used this model have all generally addressed only low Reynolds number (Re) or creeping flows. In actual industrial, intermediate Reynolds number scales are inevitable. Once intermediate Re are reached, inertial forces and viscous forces significantly influence flow characteristics. Therefore, it is necessary to conduct more detailed studies in this Re range. In addition, a large number of dense phase regions often exist inside the fluidized bed equipment. This means that hydrodynamic interactions between NFAs are unable to be ignored. The interactions between NFAs tend to cause the drag force on the each NFA is attenuated, which is called shielding effect (Debye & Bueche, 1948). To the best of our knowledge, shielding effects between NFAs over a wide range of Re have not been studied with radial varying permeability models. Considering this, the radial varying permeability model is adopted to study the hydrodynamic interactions between NFAs. This study contributes to a better understanding of the hydrodynamic behaviors of NFAs at the agglomerate scale and provides theoretical guidance for the optimization of fluidized bed equipment parameters.

2. Methods

2.1 Radially varying permeability model

Recently, it is reported that some NFAs formed by particle-cluster regime follow fractal-like properties (Sorensen, 2001). Based on fractal theory, NFAs should have a well-defined center with radially varying porosity and permeability. To more accurately model the hydrodynamic characteristics of heterogeneous NFAs, a model using a power-law relationship between radial position and permeability is proposed.

According to the fractal theory and the relationship between the mass of a NFA and nanoparticles, the average solid volume fraction porosity $\bar{\varepsilon}_{r_a}$ can be derived as

$$m_{NFA} = V_{NFA}\rho_{NFA} = N_p V_p \rho_p \tag{1}$$

$$N_p = k \left(\frac{d_{NFA}}{d_p}\right)^{D_f} \tag{2}$$

$$\bar{\varepsilon}_{NFA} = 1 - \bar{\phi}_{NFA} = 1 - \left(\frac{r_{NFA}}{r_p}\right)^{D_f - 3} \tag{3}$$

Where m is the mass, V is the volume, ρ is the density, N is the total particle number, D_f is the fractal dimension of NFAs, $\bar{\phi}_{NFA}$ is the average solid volume fraction porosity inside the NFAs, and k is the prefactor. The subscript NFA and p indicate the properties of NFAs and nanoparticles inside the NFAs. Assuming that the volumes of the spherical regions of radius r and $(r + \Delta r)$ within a NFA are V_r and $V_{r+\Delta r}$, respectively. Meanwhile, the respective average porosity $\bar{\varepsilon}_r$ and $\bar{\varepsilon}_{r+\Delta r}$ can be calculated from Eq.(3). Thus, the average porosity of the spherical-shell element with thickness Δr is as follows:

$$\bar{\varepsilon}_{\Delta r} = \frac{\bar{\varepsilon}_{r+\Delta r} V_{r+\Delta r} - \bar{\varepsilon}_r V_r}{V_{r+\Delta r} - V_r} \tag{4}$$

When $\Delta r \to 0$, $\bar{\varepsilon}_{\Delta r}$ is the average porosity of the spherical shell with infinitely small thickness, which can be considered as the local porosity at the radius r. Then the local porosity ε_r at the radial distance r within the NFA is as follows:

$$\varepsilon_r = \begin{cases} 0.26, & r \leq r_c \\ 1 - \dfrac{D_f}{3}(\dfrac{r}{r_p})^{D_f - 3}, & r > r_c \end{cases} \tag{5}$$

Considering the fact that the porosity of tightly packed monosized spheres is not lower than 0.26 (Vanni, 2000), r_c is the critical radius when ε_r is 0.26.

The local permeability at the radial distance of r is obtained by the Carman-Kozeny model by:

$$K_r = \frac{\varepsilon_r{}^3 d_p'{}^2}{180(1 - \varepsilon_r)^2} \tag{6}$$

Previous study (Wang et al., 2021; Wang et al., 2002) showed that the structures of NFAs are built up by multi scales. It is reported that the permeability should be estimated using the size of simple agglomerates (d_p') rather than nanoparticle sizes (Zhu et al., 2005). Based on the previous study (Liu & Wang, 2021), the values of d_p and d_p' are set to be 25 nm and 7.6 µm respectively. According to this radially varying permeability model, the local permeability increases continuously along the radial direction.

2.2 Governing equations

The flow outside NFAs is described by the mass conservation equations and Navier-Stokes equation for the steady-state and incompressible flow as follows:

$$\nabla \cdot \boldsymbol{U} = 0 \tag{7}$$

$$\rho(\boldsymbol{U} \cdot \nabla)\boldsymbol{U} + \nabla P = \mu \nabla^2 \boldsymbol{U} \tag{8}$$

The internal flow of the NFAs is modeled by the Brinkman's extension of Darcy's law by:

$$\nabla P = -\left(\frac{\mu}{K}\right)\boldsymbol{U} + \mu \nabla^2 \boldsymbol{U} \tag{9}$$

2.3 Boundary conditions

The boundary conditions at the outer boundary and the interface between inner region and outer region of the NFAs are given by:

$$\boldsymbol{U} = \boldsymbol{U}_\infty; P = P_\infty \tag{10}$$

$$\boldsymbol{U}|_{fluid} = \boldsymbol{U}|_{porous}; \nabla \boldsymbol{U}|_{fluid} = \nabla \boldsymbol{U}|_{porous}; \tau|_{fluid} = \tau|_{porous} \tag{11}$$

where $\boldsymbol{U}$ is the velocity; P is the pressure; τ is the shear stress; $\boldsymbol{U}_\infty$ and P_∞ are the velocity and pressure of the free stream. The equations are discretized using the second-order upwind scheme and the pressure is solved by the SIMPLE algorithm. The convergence is assumed to be achieved when the residuals decreased to ≤ 10^{-6} for all equations.

2.4 Shielding effect

The force acting on the NFAs is obtained by using stress integral method in the spherical coordinate system:

$$
\begin{aligned}
F_d = &\int_0^{2\pi} \int_0^{\pi} \left(-P|_{r=\frac{d_{NFA}}{2}} \cos\theta \right) \times \left(\frac{d_{NFA}}{2} \right)^2 \sin\theta \, d\theta d\varphi \\
&+ \int_0^{2\pi} \int_0^{\pi} \left(\mu_f \left[r \frac{\partial}{\partial r}\left(\frac{U_\theta}{r} \right) + \frac{1}{r}\frac{\partial U_r}{\partial \theta} \right] \Big|_{r=\frac{d_{NFA}}{2}} \cos\theta \right) \\
&\times \left(\frac{d_{NFA}}{2} \right)^2 \sin\theta \, d\theta d\varphi
\end{aligned}
\tag{12}
$$

Then the degree of shielding effects can be quantified by a coefficient λ, which derived by:

$$\lambda = 1 - \frac{F_{d,i}}{F_{d,iso}} \tag{13}$$

where the subscripts i is the i-th NFA in the free stream direction for the NFAs aligned streamwise, and the subscripts iso is the single isolated NFA. Therefore, according to the above definition, the shielding effect represents the deviation of pressure drop and velocity gradient between shielded NFAs and the single isolated NFA. To study the shielding effects of NFAs, pressure and velocity profiles and λ of the shielded NFAs are mainly given and analyzed here.

2.5 Computation domain

Fig. 1 gives two typical shielded cases for NFAs for this study: a NFA sandwiched between two NFAs in front and behind (case 1), and a NFA shielded by two NFAs upstream (case 2). A typical procedure is to model NFAs as spherically symmetric entities consisting of spherical particles (Vainshtein & Shapiro, 2005), and all spherical NFAs in this study have the same diameter. In this study, for two typical cases, the separation distance of two adjacent NFAs is normalized by $L^* = L/d_{NFA}$.
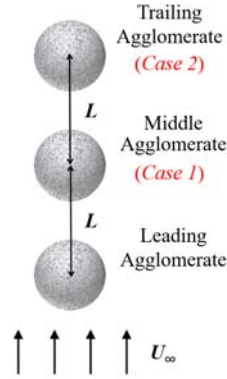
Fig. 1. Schematic diagram for computational domain.

3. Results

3.1 Flow field and pressure field
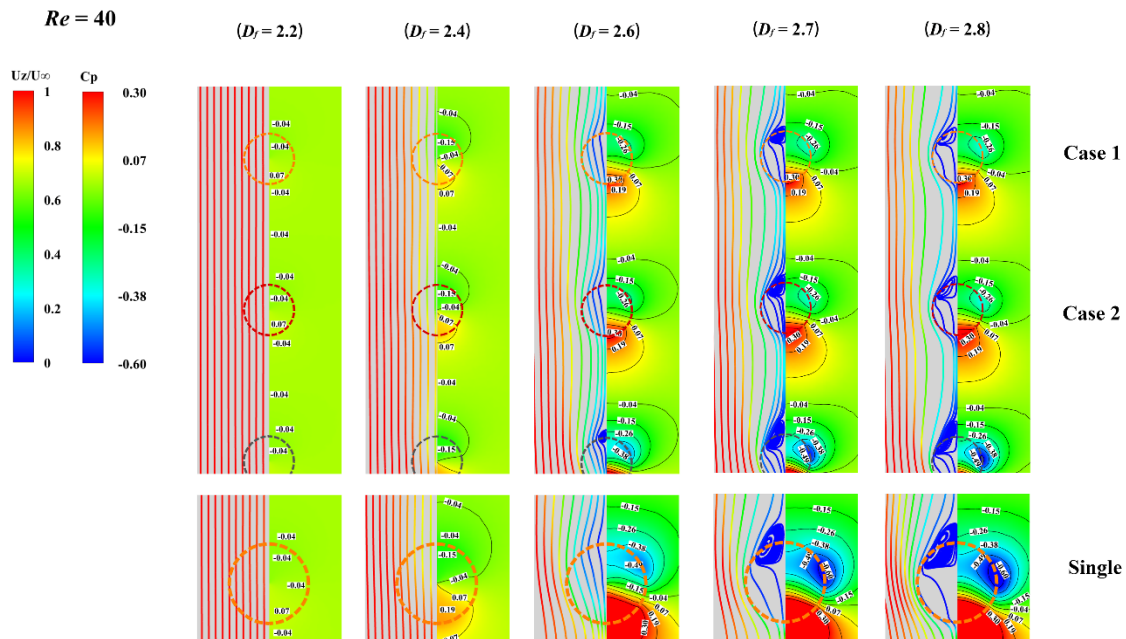
Fig. 2. Streamlines and pressure coefficients of the NFAs and single isolated NFA at Df = 2.2~2.8 when Re = 40 and L* = 3.

Fig. 2 shows the hydrodynamic behaviors of the NFAs in two shielded cases and the single isolated NFA at D_f = 2.2~2.8 when Re = 40 and L^* = 3. The local velocity is normalized by the free stream velocity. The pressure coefficient C_p is defined as the ratio of the local pressure to the free-stream dynamic pressure (Rimon & Cheng, 1969). For D_f = 2.2, the streamlines are straight and the fluid velocities are almost equal to U_∞, indicating a "no-NFA" condition, similar to "no-spheres" for homogeneous permeable spheres (Wu et al., 2004). The pressure field of the NFA in two cases is mostly unchanged compared to the single isolated NFA, indicating the weak shielding effects for two cases. As D_f increases, the fluid encounters greater resistance entering and penetrating the NFA, resulting in a velocity

attenuation compared to the single isolated NFA. The velocity attenuation into and through the NFA is the same in case 1 but larger in case 2, indicating case 2 has a stronger shielding effect than case 1. As D_f increases to 2.6, the velocity attenuation into and through the NFA is more significant and the pressure distribution in two cases is more deviated from that in the single isolated NFA. This indicates the shielding effects in two cases are enhanced as D_f increases from 2.2 to 2.6. When D_f increases to 2.8, the velocity attenuation and the pressure distribution deviation in two cases are similar. This reflects that the shielding effects for two cases tend to be stable as D_f increases when D_f > 2.6.
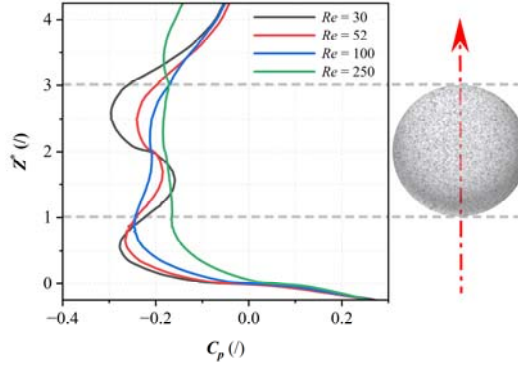
Fig. 3. Centerline pressure profiles of NFAs at Re = 30~250 when NFAs closed proximity.

Fig. 3 shows that the pressure profile fluctuation on the centerline of the shielded NFA as at Re = 30~250 when the NFAs are close proximity. The pressure profile fluctuation tends to be gradually stable with increasing Re. This is exactly due to the swallowing effect (Tsuji et al., 2003) that occurs as Re increases to 250 when NFAs are close proximity. This greatly reduces the pressure drop in the whole shielded NFA and its pressure value is close to that in the rear hemisphere of the leading NFA. Therefore, when the NFAs are close proximity, the swallowing effect at a higher Re of 250 causes the NFA to be a greater shielding effect.

3.2 Shielding effect coefficient
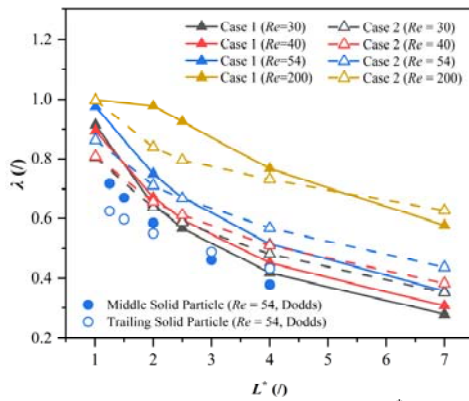
Fig. 4. Variation of λ with L^*.
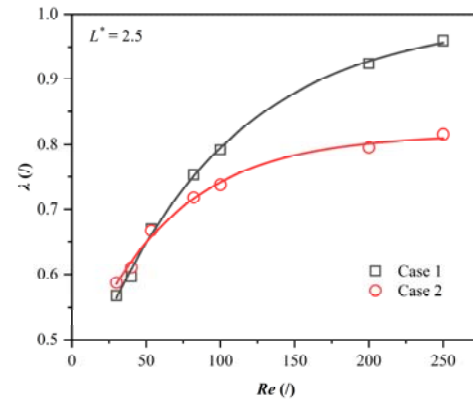
Fig. 5. Variation of λ with Re.

Fig. 4 shows λ of NFAs changes with L^* at different Re. It is found that λ and L^* are negatively correlated in two cases. Comparing with λ of solid particles from previous studies (Dodds et al., 2020), λ of two cases with considering heterogeneous permeability is larger. Therefore, studying the hydrodynamic characteristics of NFAs with solid sphere model tends to bring the errors, and the heterogeneous structures within NFAs should be not ignored. Fig. 5 also shows λ of NFAs changes with Re at L^* = 2.5. As Re increases, λ of two cases follows an exponential growth pattern.

4. Conclusion

This paper preliminarily investigates the hydrodynamic interaction characteristics between NFAs. Based on the fractal theory and the multi-scale heterogeneous structures within NFAs, the radially varying permeability model for a wide range of Re is adopted. Two representative shielded cases for the NFA are considered, where case 1 and case 2 refers

to a NFA sandwiched between two NFAs in front and behind and a NFA shielded by two NFAs upstream, respectively. Some preliminary conclusions of flow fields, pressure fields, and shielding effect coefficients for NFAs are given in this study. The results show that the effect of radially varying permeability of NFAs on shielding effects is significant. The "no-NFA" condition exhibits at D_f = 2.2. As D_f increases to 2.6, the shielding effects are enhanced. when D_f > 2.6, the shielding effects tend to be stable as D_f increases. At a high Re of 250, a stronger shielding effect of the shielding NFAs due to the swallowing effect from the leading NFA. λ of two cases are exponentially positively correlated with Re and negatively correlated with L^*. It should be noted that the effect of internal heterogeneous permeability should be evaluated when studying the hydrodynamic characteristics of NFAs.

Acknowledgment

References

Chaouki, J., Chavarie, C., Klvana, D., et al. Effect of interparticle forces on the hydrodynamic behaviour of fluidized aerogels. Powder Technology. 1985. 43, 117-125

Debye, P., Bueche, A. Intrinsic viscosity, diffusion, and sedimentation rate of polymers in solution. The Journal of Chemical Physics. 1948. 16, 573-579

Dodds, D., Sarhan, A., Naser, J. Experimental and numerical study of drag forces on particles in clusters. Powder Technology. 2020. 371, 195-208

Johnson, C. P., Li, X., Logan, B. E. Settling velocities of fractal aggregates. Environmental Science & Technology. 1996. 30, 1911-1918

Liu, H., Wang, S. Fluidization behaviors of nanoparticle agglomerates with high initial bed heights. Powder Technology. 2021. 388, 122-128

Masliyah, J. H., Polikar, M. Terminal velocity of porous spheres. The Canadian Journal of Chemical Engineering. 1980. 58, 299-302

Matsumoto, K., Suganuma, A. Settling velocity of a permeable model floc. Chemical Engineering Science. 1977. 32, 445-447

Ooms, G., Mijnlieff, P. F., Beckers, H. L. Frictional Force Exerted by a Flowing Fluid on a Permeable Particle, with Particular Reference to Polymer Coils. The Journal of Chemical Physics. 1970. 53, 4123-4130

Rimon, Y., Cheng, S. Numerical solution of a uniform flow over a sphere at intermediate Reynolds numbers. The Physics of Fluids. 1969. 12, 949-959

Sorensen, C. M. Light Scattering by Fractal Aggregates: A Review. Aerosol Science and Technology. 2001. 35, 648–687

Tsuji, T., Narutomi, R., Yokomine, T., et al. Unsteady three-dimensional simulation of interactions between flow and two particles. International Journal of Multiphase Flow. 2003. 29, 1431-1450

Vainshtein, P., Shapiro, M. Mobility of permeable fractal agglomerates in slip regime. Journal of colloid and interface science. 2005. 284, 501-509

Vanni, M. Creeping flow over spherical permeable aggregates. Chemical Engineering Science. 2000. 55, 685-698

Wang, S., Liu, H., Yang, C., et al. Experimental investigation on the microstructure of fluidized nanoparticle agglomerates by TEM image analysis. The Canadian Journal of Chemical Engineering. 2021. 99, 1125-1136

Wang, Y., Gu, G., Wei, F., et al. Fluidization and agglomerate structure of SiO2 nanoparticles. Powder Technology. 2002. 124, 152-159

Woodfield, D., Bickert, G. An improved permeability model for fractal aggregates settling in creeping flow. Water Research. 2001. 35, 3801-3806

Wu, R., Chung, H., Lee, D. Hydrodynamic drag forces on two porous spheres moving along their centerline. Chemical Engineering Science. 2004. 59, 943-950

Zhu, C., Yu, Q., Dave, R. N., et al. Gas fluidization characteristics of nanoparticle agglomerates. AIChE Journal. 2005. 51, 426-439

Session C：

Measurements and

instrumentation

PARTICLE MOVEMENT IN A CIRCULATING FLUIDIZED BED VIA ELECTRICAL CAPACITANCE VOLUME TOMOGRAPHY AND PARTICLE IMAGING VELOCIMETRY

Lennard Lindmüller[1]*, Stefan Heinrich[1], Jorg Theuerkauf[2], Yuan Yao[3], Yi Fan[3], Pedram Pakseresht[3]

1 Hamburg University of Technology, Hamburg, Germany

2 Engineering and Process Science, Core R&D, the Dow Chemical Company, Midland, MI, USA

3 Engineering and Process Science, Core R&D, the Dow Chemical Company, Lake Jackson, TX, USA

*Email: lennard.lindmueller@tuhh.de

Abstract

Despite many years of research on circulating fluidized bed (CFB) systems, the flow behavior of single particles and clusters in the riser section is still not fully understood. A reason for this is the complexity of particle movement at high velocities, which leads to difficulties for online measurement systems. For model development and optimization of existing processes, a better understanding of this topic is of major interest.

In this work, one tomographic and two invasive measurement systems are compared: a 24-electrode electrical capacitance volume tomography (ECVT) system, capacitance probes, and a borescopic high-speed camera particle imaging velocimetry (PIV) system. The experiments focus on fast fluidization in an 8-m high and 10-cm diameter acrylic glass riser in a CFB system with Geldart Group A particles. The ECVT and capacitance probe measurements mostly agreed regarding the radial solids volume fraction trends. Variations in gas velocity, solid circulation rate, and total particle holdup result in different axial and radial concentrations in the riser. With borescopic PIV, mostly upward movement in the radial center was detected. Horizontal and vertical particle movement could be evaluated separately. With all measurement systems, a 2-cm wide core flow was observed in the fully developed region.

1. Introduction

Understanding particle movement in CFBs is a major research interest for simulation and design of new industrial facilities. Small improvements in gas-solid contacting result in tremendous benefits for processes like fluid catalytic cracking (FCC). Most measurement techniques focus on bubbling fluidized beds but can also be used in other fluidization regimes. Experimental techniques for non-invasive measurement of bubbles in fluidized beds are PIV and X-ray fluoroscopy, which work by taking a series of two-dimensional images (McKeen and Pugsley, 2003; Agu et al., 2019). In both cases, very limited information can be obtained about the three-dimensional shape of the bubbles. Therefore, information about the fluidization behavior at the wall zone is the primary outcome of these measurements. In addition, PIV experiments often use rectangular facilities with very large width to depth ratios to increase the visibility of the bubbles. This further increases the effect of the wall zone on the results. More complex methods such as Positron Emission Particle Tracking (PEPT) (Stein et al., 2000), Magnetic Resonance Imaging (MRI), Radioactive Particle Tracking (RPT) or X-ray tomography can provide a three-dimensional image of a fluidized bed, but these costly systems cannot be universally applied to all particle types (Penn et al., 2018). Electrical

capacitance measurements are used to determine the solid fractions within the fluidized beds. The working principle of this measurement method is the change in the dielectric constant due to the change of solid concentration in an electric field between two electrodes, which are arranged in a circular configuration on the exterior of the fluidized bed. By pairing capacitance plates that span several axial layers, the spatial resolution can be increased. This method is known as electrical ECVT, which is used in this work (Warsito et al., 2007).

Most methods were applied for bubbling bed systems with Geldart B particles. For Geldart A particles, not many works were published due to problems of measuring small particles at higher gas velocities. This work advances the understanding of particle motion of Geldart A particles in a CFB riser during fast fluidization. A non-invasive ECVT system is compared to capacitance probes and a borescopic high-speed camera PIV system. With the benefit of each measurement system, radial solid concentration profiles as well as time-averaged movement directions of particles are determined and described.

2. Materials

At Hamburg University of Technology, a cold model CFB facility is operated. For flow observation, the riser and loop seal are made of acrylic glass (PMMA). The riser is 8-m high with 10-cm inner diameter. Measurements were conducted for fast fluidization (u_{gas} = 2.3 m/s) at a height of 7 m (fully developed region, negligible exit effect). Fig. 1. shows an illustration and pictures of the CFB facility. As bed material, Y-zeolite (Geldart A, d_{Sauter} = 91 μm, $\rho_{particle}$ = 1.88 g/cm^3, ρ_{bulk} = 0.87 g/cm^3, u_{mf} = 0.33 cm/s) was used. To prevent particle loss from the fines, a filter is installed at the exit of the cyclone.
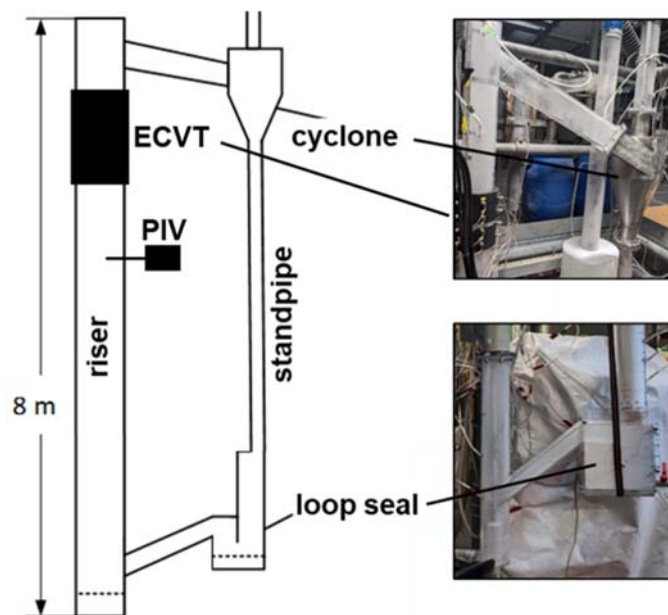
Fig. 1. Cold flow CFB at Hamburg University of Technology.

3. Methods

3.1 Electrical Capacitance Volume Tomography

The ECVT system used in this study is the *4R&D Coldflow* by *Tech4Imaging*. The sensor has an inner diameter of 110 mm and is 215 mm high, while the measurement range is 110x224 mm. With a spatial resolution of 20x20x20 voxels for the measurement area, the resulting voxel size is 5.5x5.5x11 mm. The sensor shown in Fig. 2 consists of 24 electrodes arranged in 4 layers.

ECVT is a soft-field technique, which means that the magnitude, accuracy, and precision of measurements can vary greatly depending on the exact location within the sensor region where the measurement is taken.

For example, due to the reduced number of voxels and increased distance from the electrode plates, the accuracy and precision of measurements taken at the radial center of the ECVT sensor is lower than at the wall zone (Warsito et al., 2007). In our work, the measurement data are evaluated with a new method for detecting size and velocity of phases of interest, like bubbles, slugs, or particle clusters. The phase detection method was developed based on the successes of studies from recent bubble sizing and velocity publications while also addressing some of the shortcomings of their applied methods. Most methods define limits for the solid volume fraction beneath which a bubble is defined. The novel 3D fluxion method detects phases of interest by measuring the rate of change of the solid volume fraction for every

Fig. 2. ECVT sensor on lower part of CFB riser.

voxel and frame (Watson et al., 2024). Radially, all voxels with the same distance from the center are combined at each respective radial position, resulting in 35 data points from the given 20x20 X-Y coordinate grid. Since 20 voxels are generated in the Z-axis, 20 data points are used axially. For validation of the radial solid concentration profiles, capacitance probes were used. The probes were developed and built at Hamburg University of Technology (Wiesendorf and Werther, 2000). All presented results are time averaged from 120 s long measurements.

3.2 Borescopic PIV technique

For PIV measurements, a high-speed camera (model NX4-S2 from Imaging Solutions) was used. The camera can capture 3,000 frames per second at full resolution of 992x1016 pixels and up to 16,000 frames per second at reduced resolution. After several iterations, the final experimental data for u_g = 2.3 m/s was acquired at 12,000 frames per second, with 160x168 pixels per picture. The whole PIV setup can be seen in Fig. 3. Mounted in the camera is a borescope (length = 0.6 m, d = 10 mm, d_{lens} = 9 mm), which can be positioned in different radial positions in the CFB riser. In addition to the borescope's internal xenon light, LED strips on a wedge-shaped holder were mounted on the top of borescope lens to improve lighting in the riser. The wedge shape was used to minimize the impact on the particle flow. Measurements at center position at different depths (in cm): 0 (center), 1, 2, 3, 4, and 4.7 (wall). At each position, 20 videos with 200 frames were captured and evaluated. Image processing was done in the *MATLAB*-based application *PIVLab* (Thielicke and Stamhuis, 2014).
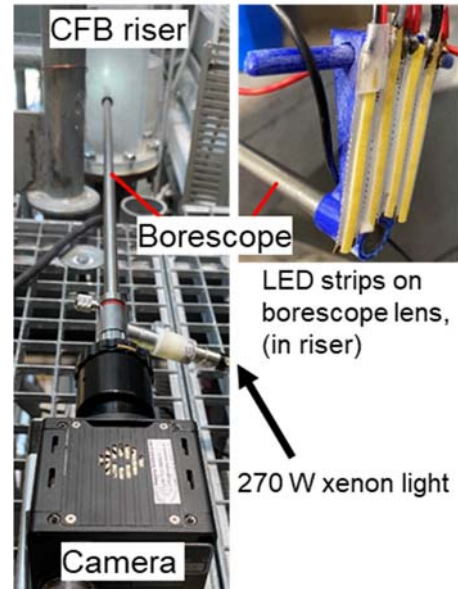
Fig. 3. PIV setup connected to CFB riser.

4. Results

4.1 Solid volume fractions via capacitance measurement

ECVT measurements were done for different riser velocities from u_{gas} = 2.3 - 4.5 m/s. Fig. 4 shows a comparison of radial solid volume fraction profiles measured with ECVT and four capacitance probes at u_{gas} = 2.3 m/s. In comparison, the solid concentrations (volume fractions) from ECVT were significantly higher than the ones obtained from capacitance probes. The reason for this might be that the signal from such low solid concentrations is not strong enough to be detected by the ECVT sensor. It is also likely that the image reconstruction parameters are not optimized yet for solid concentrations this low. Analysis of low gradients of the trends between 0 and 1 cm determined that the core region of steady-state flow at the fully developed region of the riser is about 1 cm in the radial direction. This indicates a large influence of wall effects on particles up to 4 cm into the riser.
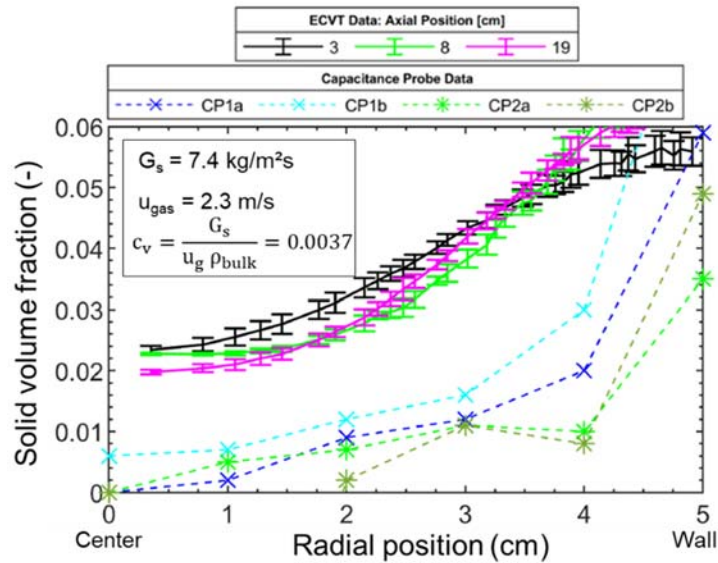
Fig. 4. Comparison of ECVT and capacitance probes.

ECVT measurements also showed that increasing solid holdup in the whole system from 15 kg to 20 kg led to an increase of solid volume fraction at 7 m height from 0.001 to 0.02 at the center and up to 0.6 at the wall. Increasing the solid circulation rate by increasing loop seal velocity while keeping the riser gas velocity constant also led to higher solid concentrations in the riser top. Higher gas velocities in the riser led to higher solid fractions near the wall and lower solid fractions in the core region. This is attributed to higher entrainment rates in the center and more wall friction at higher gas velocities. Thus, this proves that ECVT can be used for fast fluidization measurements of Geldart A particles. However, unlike bubbles in a bubbling fluidized bed, single clusters in a CFB cannot be tracked with the 3D fluxion phase detection method. The reason for this is likely the high volatility and complexity of particle clusters and the limited time resolution of ECVT.

4.2 Particle directional tendencies via PIV

Due to the small particle size and the requirement for good lighting at high gas velocities, the tracking of single particles with the borescopic high-speed camera was difficult. With the used equipment, only images sharp enough for evaluation at u_{gas} = 2.3 m/s could be obtained. Improved lighting and a high-speed camera capable of capturing more frames per second should enable measuring the motion of single particles at higher gas velocities. Since only particle movement parallel to the borescope lens can be captured, particle movement to and from the lens cannot be captured. Furthermore, despite having a manual focus to a 3 mm distance from the lens, particle movement in the background was still observable. This led to underestimations of particle velocity by a factor of > 50. Despite this limitation, the relative directional tendencies of the particle trajectories can be compared to each other. Fig. 5 shows

particle trajectory directions at different radial positions. Very little to no horizontal movement was observed in the central regions of the riser (0 cm). This changes significantly with decreasing distance from the riser wall. In this region the horizontal motion intensifies and transitions to a more chaotic state due to wall friction.
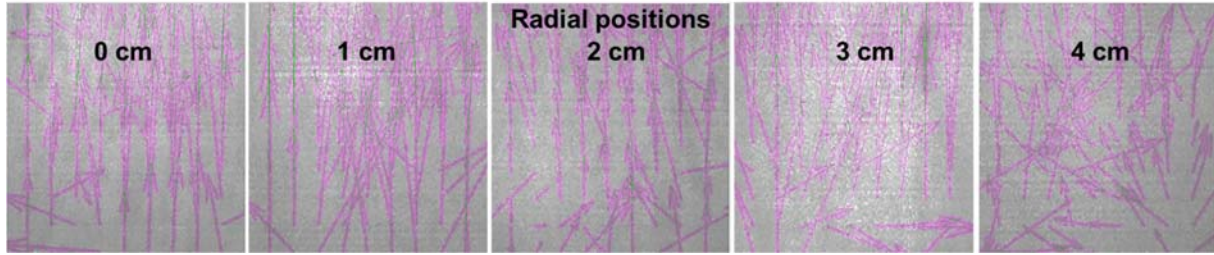
Fig. 5. Directional tendencies of particles measured with PIV.

In the next step, the movement vectors were separated into their sidewards and upwards components to distinguish between horizontal and vertical translation. For horizontal particle velocities, absolute values are used. For vertical particle velocities, the upward and downward flow is evaluated. Fig. 6 shows the resulting particle velocities over radial position. Here, the underestimation of particle velocity can be clearly seen. The velocities of the particles in the vertical direction are generally known to far exceed those in the horizontal direction, which could not be observed with the setup. A reason for this might be that particles with lower velocities are more visible and better distinguishable in the frame-by-frame analysis. Thus, for lower particle velocities, a more reliable velocimetry could be done.
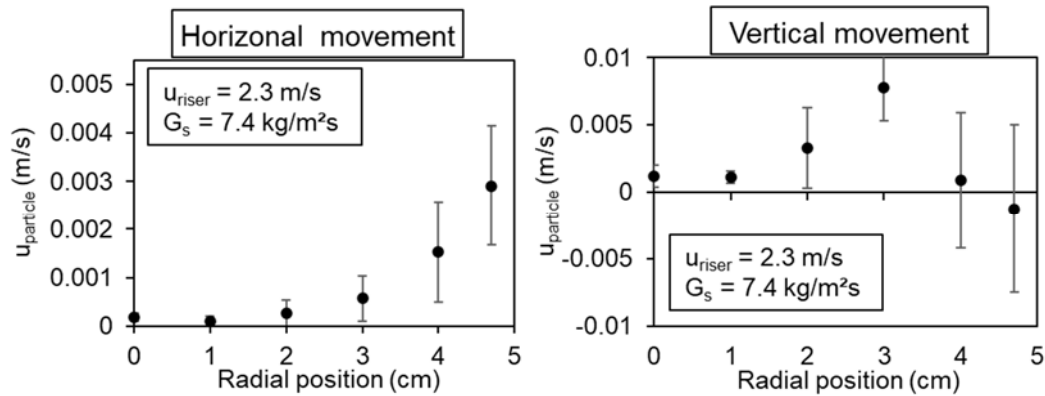
Fig. 6. Separate horizontal and vertical particle velocities measured with PIV.

Both the horizontal and vertical particle velocities show higher deviations closer to the wall. This indicates a less uniform particle flow in all directions, which comes from wall friction. The horizonal particle velocity (left and right movement from lens) is close to zero at the center and increases closer to the wall, which corresponds to the observations in Fig. 5. The measured trend for the vertical particle velocities is not that clear. Generally, in CFB risers, the vertical particle velocity is highest in the center. At the wall, the velocity is much lower and perhaps even negative, which was confirmed by visual observations. This effect can be seen in Fig. 6. Due to lower particle velocities closer to the wall, the images were sharper and, thus, a more reliable velocimetry could probably be measured. Based on the small velocity deviations (vertically and horizontally) and low horizontal velocities at 0 and 1 cm, the uniform core flow in the fully developed region occurred in the inner 2 cm of the riser. This confirms the results obtained with ECVT and capacitance probes.

5. Conclusion

For the first time, an ECVT system and borescopic high-speed camera particle imaging velocimetry (PIV) were directly compared for measuring the flow behavior of Geldart A particles during fast fluidization. Low solid concentrations in the fully developed region, small particle size, and limited time resolution of the measurement systems led to measurement inaccuracies. Despite that, the solid concentration profiles and directional tendencies could be evaluated.

Varying gas velocities in the riser, solid circulation rates, and a total particle mass in the system lead to different concentration profiles, which could be evaluated with ECVT. With borescopic PIV, radial profiles of solid movement vectors could be generated. Horizontal and vertical particle movement could be evaluated individually. With all measurement systems, a 2-cm wide core flow was observed in the fully developed region. Thus, in a 10-cm riser, the wall effect influences most of the riser area. The combination of the systems is promising for further understanding particle flows and clustering in CFBs. Due to the fast generation of results, the methods can be easily used for the validation of CFD-DEM simulations. For systems with larger particles and lower gas velocities, much clearer results are expected.

Acknowledgment

References

Agu, C.E., Tokheim, L.-A., Eikeland, M., Moldestad, B.M. Improved models for predicting bubble velocity, bubble frequency and bed expansion in a bubbling fluidized bed. Chemical Engineering Research and Design. 2019. 141, 361–371.

McKeen, T., Pugsley, T. Simulation and experimental validation of a freely bubbling bed of FCC catalyst. Powder Technology. 2003. 129 (1-3), 139–152.

Penn, A., Boyce, C.M., Kovar, T., Tsuji, T., Pruessmann, K.P., Müller, C.R. Real-Time Magnetic Resonance Imaging of Bubble Behavior and Particle Velocity in Fluidized Beds. Industrial & Engineering Chemistry Research. 2003. Res. 57 (29), 9674–9682.

Stein, M., Ding, Y., Seville, J., Parker, D. Solids motion in bubbling gas fluidised beds. Chemical Engineering Science. 2000. 55 (22), 5291–5300.

Thielicke, W., Stamhuis, E.J. PIVlab – Towards User-friendly, Affordable and Accurate Digital Particle Image Velocimetry in MATLAB. Journal of Open Research Software. 2014. 2.

Warsito, W., Qussai, M., Fan, L.-S. Electrical Capacitance Volume Tomography. IEEE SENSORS JOURNAL. 2007. 7 (4), 525–535.

Watson, B., Lindmüller, L., Heinrich, S., Theuerkauf, J., Yao, Y., Fan, Y. Dynamic bubble tracking in fluidized beds via electrical capacitance volume tomography. Chemical Engineering Journal. 2024. 150461.

Wiesendorf, V., Werther, J. Capacitance probes for solids volume concentration and velocity measurements in industrial fluidized bed reactors. Powder Technology. 2000 110 (1-2), 143–157.

PARTICLE TRACKING VELOCIMETRY STUDY OF WET PARTICLE FLOW IN A PSEUDO TWO-DIMENSIONAL FLUIDIZED BED

Zhiyang Ma[1,2], Yi Xu[1,2], Qiuya Tu[1], Haigang Wang[1,2*]

1. State Key Laboratory of Coal Conversion, Institute of Engineering Thermophysics, Chinese Academy of Sciences, Beijing 100190, China

2. University of Chinese Academy of Sciences, Beijing, 100049, China

*Email: wanghaigang@iet.cn (H.G. Wang)

Abstract

In the particle preparation, likes drying, coating and granulation, the flow characteristics of wet particles in the fluidized bed are extremely complex due to the effect of water content. It is essential to investigate the flow characteristics of wet particles for optimizing process efficiency and ensuring high end-point product quality. In this research, a high-speed camera was employed to conduct experimental investigation for wet particles flow within a pseudo two-dimensional fluidized bed. The flow dynamics of wet particles under different water contents and different inlet gas velocities were investigated. The particle tracking velocimetry (PTV) measurements were explored to observe the particle movement in specific regions, including velocity distribution and particle concentration. A digital imaging method, i.e. Voronoi method, was utilized to address particle allocation challenges, providing a foundation for calculating intricate parameters such as solid-phase flow field, and particle velocities. These parameters were calculated based on the essential information derived from the Lagrangian trajectories of particle, which enriched the understanding of complex interactions in wet particle flow dynamics system.

1. Introduction

As one of the most common production equipment, fluidized bed reactors are widely used in various industries such as chemistry, energy, food and pharmaceuticals (Azmir *et al.*, 2020; Zambrano *et al.*, 2020; Alobaid *et al.*, 2022). Moreover, many fluidized bed reactors involve moisture, resulting in the presence of wet particles, which complicates gas-solid flow dynamics, such as those used for petro-chemical, granulation, drying and coating processes in pharmaceutical. There are two types of moisture in wet particles, i.e., bound water within the particles and free water on the particle surfaces (Mezhericher *et al.*, 2008). When wet particles collide, the free water on the particle surfaces forms liquid bridges, leading to particle agglomeration (Tang *et al.*, 2020). This can result in non-uniformity and localized blockages inside the bed, which affects the uniformity and stability of fluidization, making it challenging to control. Additionally, the presence of moisture alters the interactions between particles and gas. Factors such as surface tension and liquid evaporation are affected. These changes impact the mass and heat transfer between the gas and solid phases and thus influence the overall performance and efficiency of fluidized beds (Ma *et al.*, 2023). Therefore, investigating the flow characteristics of wet particles is crucial for ensuring the smooth operation and maintaining product quality in the process.

Particle tracking velocimetry (PTV) is an image-based measurement technique designed to accurately measure the velocity and trajectories of moving objects. PTV operates on the Lagrangian measurement principle, which entails tracking the displacement of each particle at different moments and calculating particle velocity through displacement analysis (Baek *et al.*, 1996). PTV technique has been widely used in various fields involving liquid-solid and gas-solid two-phase flow, such as rollers, dams and fluidized beds. However, it should be noted that PTV technique is limited to some extent to the situation that it can only be applied to the reactors with transparent vessel.

2. Experimental setup

2.1 Experimental test facility

Fig. 1 shows a pseudo two-dimensional fluidized bed experimental test platform, which includes a fluidized bed, gas supply system and image acquisition system. The fluidized bed is divided into two sections: an upper cube and a lower conical segment, both constructed from acrylic plates. The upper cube has a height of 800 mm, while the lower section is characterized by a conical shape with a height of 200 mm and a bottom angle of inclination measuring 70°. Overall, the fluidized bed stands at a height of 1000 mm, with a bed thickness of 30 mm.
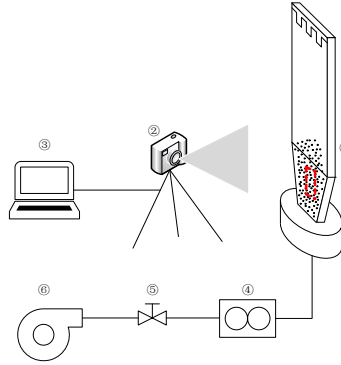
Fig. 1. The pseudo 2D fluidized bed experimental test platform. (1) Fluidized bed, (2) Digital camera, (3) Computer, (4) Rotor flowmeter, (5) Valve, (6) Roots rotors blower.

The gas supply system comprises several components, including a Roots blower, air supply conduits, rotor flowmeter, and control valves. Inlet air velocity is modulated by varying the frequency of the blower, while a flowmeter ensures precise measurement of this velocity. Throughout experiments, a constant frequency is maintained to stabilize the inlet air velocity, ensuring reliable data acquisition. Once the velocity stabilizes and aligns with the target, pertinent data is extracted for in-depth analysis.
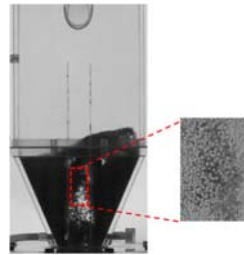
Fig. 2. The central region of the bed.

A high-speed CCD camera (Phantom VEO 710L) is used to capture the trajectory of particles. The high-speed camera is set in front of the bed. Besides, NANLITE Forza 300 high-frequency light source lighting system is set at the front of the bed to provide uniform lighting and ensure the clarity of the image. The primary function of the camera is to observe the central region of the bed (approximately 50 mm above the bottom), focusing on the process of particle upward transport induced by ascending bubbles, as shown in Fig. 2. Therefore, the sampling rate is configured to capture 1000 frames per second, with a resolution of 400 × 600, resulting in approximately 240,000 pixels in total.

2.2 Experimental conditions and materials

The selected experimental material is sugar, with the particle diameter (d_p) ranging between 1 mm and 1.2 mm. The loose bulk density of the particles is 820 kg/m³, belonging to Geldart class D particles. The total weight of dry solid particles is 0.3 kg. The initial water content of dry particle is around 1.13 %. Through adding different amounts of water, the particles have different water content after fully mixing. Moreover, different inlet gas velocities are controlled by adjusting the frequency of the blower, enabling the exploration of the flow characteristics of wet particles. Details of the experimental test conditions are given in Table 1.

	Table 1 Test conditions		
Case No.	Dry granule weight (kg)	Initial granule water contet (%)	Inlet gas velocity (m/s)
Case 1	0.30	Dry (1.13)	3.5, 4.0, 4.5
Case 2	0.30	2.25	3.5, 4.0, 4.5
Case 3	0.30	3.3	3.5, 4.0, 4.5
Case 4	0.30	4.43	3.5, 4.0, 4.5
Case 5	0.30	5.89	3.5, 4.0, 4.5
Case 6	0.30	6.54	3.5, 4.0, 4.5
Case 7	0.30	7.67	3.5, 4.0, 4.5

3. Particle tracking velocimetry

3.1 Determination of particle centroids

Fig. 3 (a) shows an image of a single particle with a size of 20 × 20 pixels. Besides, Fig. 3 (b) shows the target image of the particle group in the bed with a size of 400 × 600 pixels. The single particle image is used to scan the target image frame by frame, and the correlation coefficient matching method is used to identify the particles. When the correlation coefficient exceeds a certain threshold, it can be identified as a particle. Fig.3 (c) demonstrates the number of particles identified under different correlation coefficients. As the correlation coefficient increases, the number of particles identified gradually decreases. Particularly, when the correlation coefficient exceeds 0.6, the number of identified particles decreases sharply, and the change near this threshold is relatively flat. However, when the correlation coefficient is lower than 0.6, there will be more overlapping recognition particles. Therefore, in order to ensure accuracy, the correlation coefficient of 0.6 is selected for subsequent particle recognition operations. Fig.3 (d) shows the successfully identified particles, which cover almost all the target articles and meet the requirements of experimental operation.
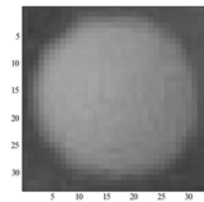
(a) A single particle
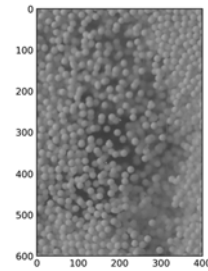
(b) Target image of the particle group

(c) The number of identified particles
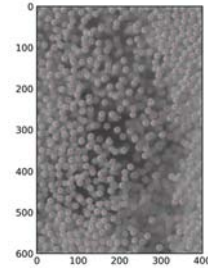
(d) Iidentified particles

Fig. 3. Detection of particle position.

3.2 PTV based on the Voronoi method

The Voronoi diagram, also known as the Dirichlet diagram, is composed of continuous polygons formed by perpendicular bisectors connecting adjacent points (Aurenhammer *et al.*, 2000). According to the identified particle center position as the feature point, the Voronoi structure diagram is constructed in image I_1, as shown in Fig. 4 (a). The Voronoi structure divides the plane into many polygons based on the feature points, where the distance from any point within a polygon to the feature point within that region is minimal, which can be expressed as

$$d(x, P_i) \leq d(x, P_k) \quad x \in V_i \quad i \neq k \tag{1}$$

where P_i is any feature point within the plane, and V_i is a Voronoi polygon constructed by the feature point P_i. P_k represents any other feature point except P_i. In addition, each feature point can construct a Voronoi star structure S_i with the surrounding feature points, as illustrated in Fig. 4 (b).

The Voronoi structure has strong stability. When the particles move gradually along their trajectories, the Voronoi polygon and the Voronoi star structure also change regularly, and the difference in the continuous image is small. Based on this characteristic, the simulation reconstruction of particle trajectory can be realized. The Voronoi diagram constructed based on the particle positions in the next image I_2, after a time interval Δt, is depicted in Fig. 4 (c). Additionally, the star structure S_j is the optimal match with S_i, as shown in Figure 4 (d).

(a) Voronoi structure diagram in I_1 (at time T)

(b) Voronoi star structure S_i of feature point P_i

(c) Voronoi structure diagram in I_2 (at time T+Δt)

(d) The difference between Voronoi star structure S_i and S_j
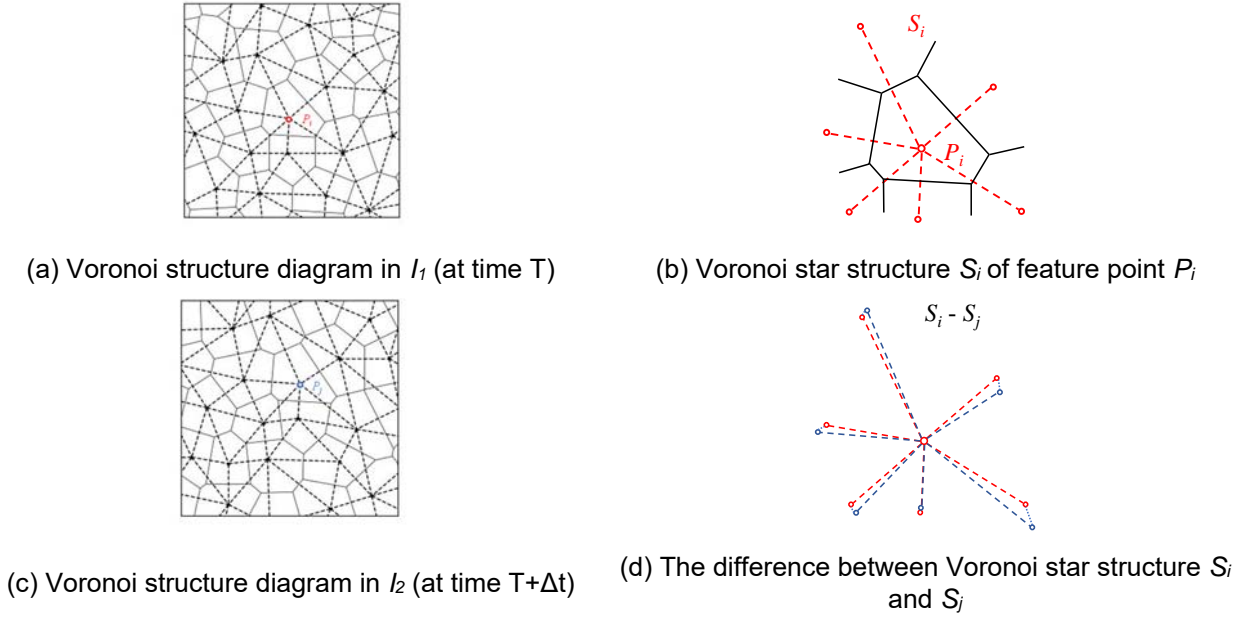
Fig. 4. The Voronoi structure.

The velocity of particles can be determined by analyzing their positions across two consecutive images captured by the high-speed camera. In this process, the Voronoi star structures of feature points in the initial frame image are compared with those in the subsequent frame image. The optimal matching point is identified as the one with the smallest difference in Voronoi star structures between the two frames, which can be expressed as

$$match(P_{i,1}) = \min(dif_s(S_i, S_j)) \tag{2}$$

where $dif_s(S_i, S_j)$ is the difference of Voronoi star structures S_i and S_j, which can be calculated by

$$dif_s = \underset{k_1=1\cdots m}{median}\left[\underset{k_2=1\cdots n}{\min} \left|(\boldsymbol{r}_{k1,1} - \boldsymbol{r}_{0,1}) - (\boldsymbol{r}_{k2,2} - \boldsymbol{r}_{0,2})\right| \right] \tag{3}$$

where k_1 = 0 and k_2 = 0 are the centers of the stars S_1 and S_2, respectively. Besides, $k_1 = 1 \cdots m$ and $k_2 = 1 \cdots n$ are the extremities of stars S_1 and S_2. $|r| = (x^2+y^2)^{\frac{1}{2}}$ is the usual Euclidean norm. The minimal median corresponds to the best match.

Fig. 5 shows the composition of the Voronoi diagrams of two consecutive images. Red points are the center positions of particles in the first frame, and blue points indicating the center positions of particles recognized after a time interval of Δt. By comparing Voronoi stars through Voronoi imaging method, the displacement vector of particles can be obtained, as shown in

Fig. 5 (b). Therefore, this computational method can be effectively utilized for the subsequent analysis of particle flow characteristics.

(a) Voronoi diagrams of two consecutive images   (b) Displacement vectors
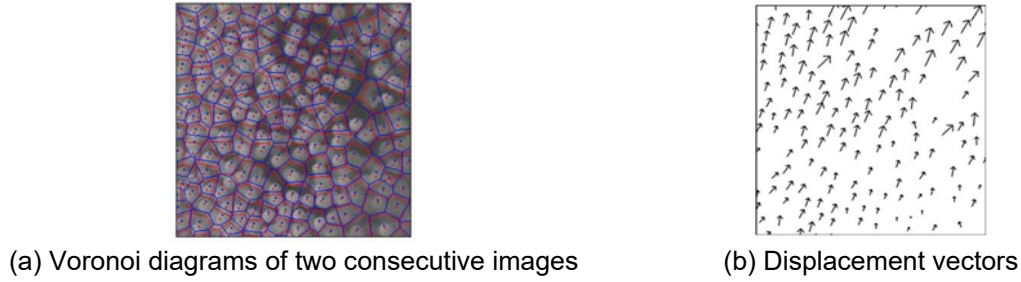
Fig. 5. The Voronoi structure and displacement vectors.

4. Results and discussions

4.1 Minimum fluidization velocity

The minimum fluidization velocity (U_{mf}) is one of the most fundamental parameters describing the characteristics of gas-solid flow (Zhu *et al.*, 2023). Therefore, U_{mf} of particles with different water content is first determined by measuring the change of bed pressure drop during the reduction of inlet gas velocity. Fig.6 illustrates the pressure drop curves of particles with different water contents, which reflects the change of bed pressure drop with the decrease of inlet velocity. U_{mf} is defined as the transition velocity from the constant pressure in the well fluidization stage to the linear decrease of pressure drop in the packed bed stage (Yates, 1996; Zhu *et al.*, 2023). The initial water content of dry particle is around 1.13 %, and the corresponding minimum fluidization velocity is 1.41 m/s. And U_{mf} of the wet particles at different water content levels, i.e., 2.25 %, 3.30 %, 4.43 %, 5.89 %, 6.35 %, 7.67 %, equals to 1.63 m/s, 2.07 m/s, 2.26 m/s, 2.29 m/s, 2.50 m/s and 2.54 m/s, respectively. With the increase of particle water content, U_{mf} and the constant bed pressure drop are both observed to gradually increase. This is because the addition of water increases the bed weight and the cohesion between particles, which makes it more difficult for the particles to be fluidized.
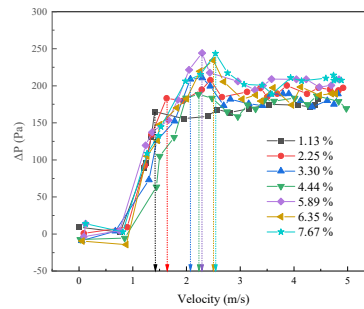
Fig. 6. The relationship of gas velocity and bed pressure drop.

4.2 Particle trajectories and particle velocities

PTV technique can effectively capture the Lagrangian trajectory of the particles, which is an important basis for obtaining particle flow characteristics. Fig. 7 (a) shows the particle trajectories over 20 time steps (Δt = 0.02s), which has good readability. Besides, the color coding represents the velocity magnitude of the moving particles. At the top of the image region, the particles velocities are relatively fast and flow out of the region. Fig. 7 (b) shows the time-averaged velocities of particles under different particle water content, within 2 s recording time. The average particle velocity increases with increasing inlet gas velocity. Moreover, as moisture increases, the particle velocity increases first and then decreases gradually. When the particle moisture content is high, the weight of wet particles increases, and the liquid bridge force on the particles surface increases, forming particle agglomeration, which inhibits the flow of wet particles and reduces the particle velocity.
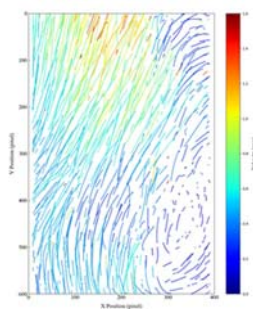
(a) Particle trajectories over 20 time steps   (b) Time-averaged particle velocities

Fig. 7. Particle trajectories and average particle velocities under different moisture.

5. Conclusions

In this research, PTV technique based on Voronoi method was used to realize the identification and matching of particles. Moreover, the particle flow under different water content and inlet gas velocities was further explored. Lagrangian trajectories of particles were obtained to explore the influence of water content on particle flow, such as particle velocity. It was observed that lower water content levels facilitate particle flow, while higher water content levels result in a reduction in particle velocity.

Acknowledgment

References

Alobaid, F., N. Almohammed, M. Massoudi Farid, J. May, P. Rößger, A. Richter and B. Epple. Progress in CFD Simulations of Fluidized Beds for Chemical and Energy Process Engineering. Progress in Energy and Combustion Science. 2022. 91.

Aurenhammer, F. and R. Klein. Voronoi Diagrams. Handbook of computational geometry. 2000. 5, 201-290.

Azmir, J., Q. Hou and A. Yu. CFD-DEM study of the effects of food grain properties on drying and shrinkage in a fluidised bed. Powder Technology. 2020. 360, 33-42.

Baek, S. J. and S. J. Lee. A new two-frame particle tracking algorithm using match probability. Experiments in Fluids. 1996. 22, 23-32.

Ma, Z., Q. Tu, Z. Liu, Y. Xu, R. Ge and H. Wang. CFD-DEM investigation of the gas-solid flow characteristics in a fluidized bed dryer. Chemical Engineering Research and Design. 2023. 196, 235-253.

Mezhericher, M., A. Levy and I. Borde. Heat and mass transfer of single droplet/wet particle drying. Chemical Engineering Science. 2008. 63, 12-23.

Tang, T., T. Wang, Q. Gao and Y. He. Flow and heat mass performances of wet particle drying process based on liquid volume-varying bridge force. International Journal of Heat and Mass Transfer. 2020. 148, 119037.

Yates, J.. Effects of temperature and pressure on gas-solid fluidization. Chemical engineering science. 1996. 5, 167-205.

Zambrano, D., J. Soler, J. Herguido and M. Menéndez. Conventional and improved fluidized bed reactors for dry reforming of methane: Mathematical models. Chemical Engineering Journal. 2020. 393, 124775.

Zhu, X., Y. Liu, X. Jiang, H. Wang, Z. Wang, Z. Bai and R. Ocone. Effects of pressure and particle size on bubble behaviors in a pseudo 2D pressured fluidized bed with Geldart A/B, B and D particles. Chemical Engineering Journal. 2023, 470. 143904.

Session D：

Catalytic reaction and novel

reaction process

OPTIMIZING PROCESS PARAMETERS OF CIRCULATING FLUIDIZED BED REACTOR FOR DME CARBONYLATION TO MA REACTION UTILIZING FER CATALYST

Ji Young Nam[1], Ji Yong Kim[1], Jong Wook Bae[1], Dong Hyun Lee[1*]

[1]*School of Chemical Engineering, Sungkyunkwan University (SKKU), 2066 Seobu-ro, Jangangu, Suwon, Gyeonggi-do 16419, Republic of Korea*

Email: dhlee@skku.edu

Abstract

C1-carbon fuel is used by the Carbon Capture, Utilization (CCU) technology to reduce atmospheric CO_2 emissions. The objective of this study was to utilize C1-carbon fuel to produce ethanol, through an indirect ethanol production method. The indirect ethanol production method is preferred because of its better conversion efficiency, selectivity, and the higher cost of noble metal catalysts]. In this approach, zeolite-based catalysts are used in the production of methyl acetate (MA) from dimethyl ether (DME). This reaction involves rapid deactivation, making it possible to anticipate long-term operation by employing a circulating fluidized bed (CFB) reactor to repetitively conduct reactions and regenerate the catalyst. The catalytic reaction experiment was conducted in a fluidized bed reactor (inner diameter (I.D.) = 24.3 mm), and the regeneration experiment was conducted in a fixed bed regime (I.D. = 7 mm) by changing the gas injection direction. This study focused on the hydrodynamics characteristics of the ferrierite (FER) catalyst in CFB apparatus with an L-valve (Bubbling fluidized bed: I.D. = 0.08 m, height = 0.6 m; Riser: I.D. = 9.0 mm, height = 2.6 m). The reaction and regeneration experiments obtained a deactivation constant of 9.08×10^{-6} 1/s and a regeneration constant of 0.02 1/s, respectively. Hydrodynamic characteristics (solid circulation rate and axial solid holdup, etc.) were investigated to optimize the flow rate in the L-valve and riser using catalyst particles in CFB. Solid particles circulated smoothly without plugging when the riser maintained a flow rate range of 1.6 - 2.4 m/s and the L-valve operated between 0.39 - 0.66 L/min. The findings from this fundamental research offer potential applications in operating CFB systems under high-temperature and high-pressure conditions.

1. Introduction

The utilization of C1-carbon fuel is a technology used by CCU to reduce atmospheric CO_2 emissions (Christensen & Bisinella, 2021). The indirect ethanol production method is preferred because of its better conversion efficiency, selectivity, and it is cost-effective unlike using the costly noble metal catalysts (Liu et al., 2022). During this process, zeolite-based catalysts are used to convert dimethyl ether (DME) into methyl acetate (MA), following the mechanism outlined in equation (1) below

$$\text{DME carbonylation to MA: } CH_3OCH_3 + CO \rightarrow CH_3COOCH_3 \qquad (1)$$
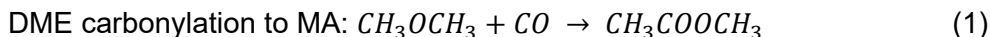
To resolve the issue of rapid catalyst deactivation, a circulating fluidized bed (CFB) reactor is employed, enabling repetitive reaction cycles and catalyst regeneration for sustained operational performance. CFB is utilized in a variety of industries for both catalytic and noncatalytic gas-solid reactions (e.g., crude oil cracking and coal combustion) (Jiang et al., 1991). In CFB, the operational flow rate range is wide, and the gas injection velocity is high, resulting in a large solid processing capacity. The gas is maintained in a plug flow, minimizing back mixing. The contact efficiency between gas and solid is high, and the contact is uniform, resulting in a high reaction conversion rate and heat transfer rate (Lim et al., 2013). The DME

carbonylation to MA using ferrierite (FER) has an induction period, necessitating operation in a bubbling fluidized bed (BFB) with a relatively extended residence time (Kim et al., 2022), while catalyst regeneration, which is relatively fast, is carried out in the riser. The catalyst particles are moved through an L-valve, which is a type of nonmechanical valve (Basu & Cheng, 2000), using nitrogen.

In this study, fundamental research was conducted to ascertain the optimal operating conditions of CFB for DME carbonylation to MA. Catalytic reaction and regeneration experiments were conducted using a bubbling fluidized bed with an inner diameter (I.D.) of 24.3 mm and a fixed bed with an I.D. of 7 mm. Previous reaction experiments were conducted on catalysts produced by the spray-drying method without a binder (Sung et al, in press). The experiments were conducted within a temperature range of 210-270 ^{o}C, a pressure range of 10 - 60 bar, a space velocity range of 350-1750 L/(kg$_{cat.}$·h), and a CO/DME molar ratio range of 3 - 70. As temperature, pressure, and CO/DME ratio increased, the DME conversion rate increased, following the principles of Le Chatelier's principle. On the contrary, an increase in space velocity led to a decrease in the DME conversion rate. This is attributed to the reduction in residence time. For process economics and bubbling fluidized bed regime, 260 ^{o}C, 20 bar, 1500 L/(kg$_{cat.}$·h), and CO/DME molar ratio were set to 20. Regeneration experiments were conducted in the temperature range of 300 - 500 ^{o}C, confirming that the catalyst's activity was nearly equivalent to that of the raw material at 500 ^{o}C

In this study, the investigation was carried out on bentonite spray-dried ferrierite (BT-S-FER) catalyst particle produced via the spray-drying method while incorporating a binder into the FER catalyst to mitigate catalyst deactivation effects. The focus of the investigation was to analyze of the hydrodynamic properties of the FER catalyst in a circulating fluidized bed system, which comprised a bubbling fluidized bed (0.08 m in I.D. and 0.6 m in height) and a riser (9.0 mm in I.D. and 2.6 m in height), with the assistance of an L-valve. The investigation also focused on examining the hydrodynamic properties relevant to optimal operational conditions, such as solid circulation rate and axial solid holdup. The outcomes of this fundamental investigation indicated potential utility in employing CFB systems under both high temperature and high pressure.

2. Experimental

2.1 Experimental apparatus

The study on the characteristics of DME carbonylation to MA reaction on catalyst particles was conducted in a fluidized bed regime using the reaction gas with a 1-inch (0.0243 m) reactor and 10 g of catalyst particles. Following the reaction experiments, regeneration studies were conducted in a fixed bed regime with air at 3/8 inch (0.007 m). Considering the economic feasibility of the process, both experiments were conducted under pressure at 20 bar, and operating conditions for temperature, reaction gas composition, and space velocity were set based on the results of prior experiments.

Fig. 1 shows a schematic diagram of the CFB apparatus used to investigate the solid circulation characteristics of the catalyst particles and a conceptual diagram of the DME to MA reaction. The experimental equipment was utilized to simulate the DME carbonylation to MA system under high temperature and pressure conditions. The right fluidized bed simulates the DME to MA reaction reactor, and the left riser simulates the regeneration reactor. The L-valve was used to control catalyst circulation rate and to prevent gas mixing between the two reactors. In the solid circulation characteristics experiment, air was used for fluidization and solid circulation. Pressure drop tabs were installed on the riser, BFB, and L-valve to measure pressure drop.

The operation was conducted at BFB (I.D.= 0.08 m) with a flow rate condition of a bubbling fluidized bed regime. The gas flow rate at the L-valve (I.D.= 0.009 m) was set to control the amount of solid being introduced into the riser. In the riser, particles are carried to a fast fluidization regime at a high gas flow rate, collected by a cyclone, and circulated to the BFB.

Particles that bypass capture in the cyclone accumulated in the bag filter. The opening area fraction of the distributor plate used when injecting air into BFB was 0.4.
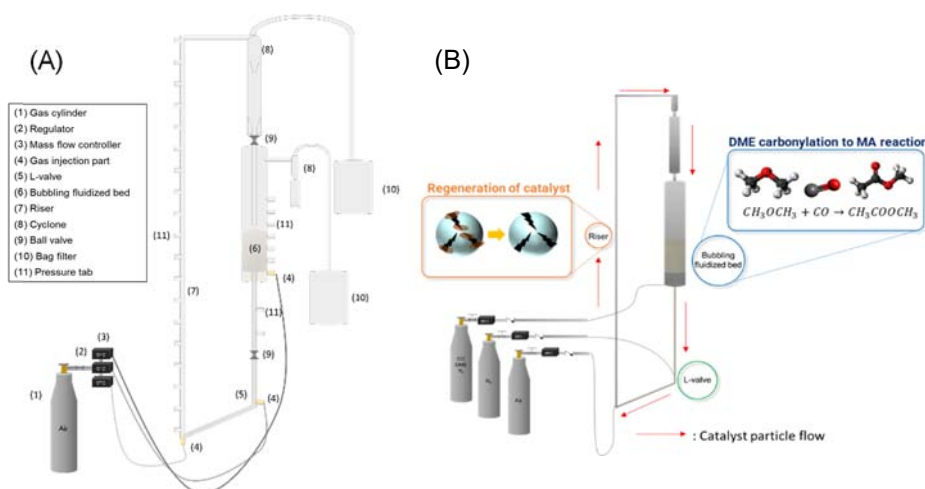
Fig. 1. (A) Schematic diagram of the CFB apparatus, (B) Conceptual diagram of DME to MA in the CFB process

2.2 Catalyst particles

 The BT-S-FER catalyst particles that were used in the experiment were manufactured by spray-drying method using bentonite as a binder and ferrierite at a weight ratio of 3% of the bentonite. The size distribution of BT-S-FER catalyst particles is shown in Table 1. The mean diameter of BT-S-FER particles was 151 μm. The skeletal density (ρ_s), particle density (ρ_p), and bulk density (ρ_b) of the particles were 1699.5 kg/m^3, 549.9 kg/m^3, and 359.9 kg/m^3, respectively. According to Geldart classification (Geldart, 1973), BT-S-FER particles are particles of the Geldart A group. The minimum fluidization velocity (u_{mf}) of the catalyst particles was measured by measuring the pressure drop according to the flow rate and height in a 2 inch acrylic column and was determined to be 0.0054 m/s.

Table 1. Size distribution of BT-S-FER particle

Sieve mesh size, [μm]	Mass fraction [-]
75-90	0.034
90-106	0.031
106-125	0.066
125-150	0.207
150-200	0.662

3. Results and discussion

3.1. Solid circulation rate

To determine the circulating velocity of catalyst particles in a CFB, experiments were conducted using the experimental apparatus shown in Fig. 1 (a), where the velocities of the riser and L-valve were varied. In the BFB, air was injected at a velocity of 3 u_g/u_{mf}, while the L-valve was operated within the range of 0.26 - 0.92 L/min. To ensure stable transport of particles, the riser was operated at 2 - 7 times the terminal velocity (0.8 - 2.8 m/s) for particles with the largest diameter. Among the operating conditions, only the conditions where particle circulation progresses in a steady state are presented in Table 2. At a riser velocity of 0.8 m/s, the drag force is lower than the gravity force, so catalyst particles do not circulate due to particle transport problems within the riser. At a riser velocity of 2.8 m/s, the pressure in the riser is higher than the pressure in the L-valve, preventing smooth particle circulation. If the flow rate injected into the L-valve is less or more than the appropriate amount, it does not circulate in a steady state.

Table 2. Solid circulation rate of BT-S-FER

$u_{g,riser}$[m/s] ($u_{g,riser}/u_t$ [-])	G_s [kg/(m^2·s)] ($u_{g,L-valve}$: 0.39 [L/min])	G_s [kg/(m^2·s)] ($u_{g,L-valve}$: 0.66 [L/min])
1.6 (4.24)	23.52	24.13
2 (5.31)	22.43	22.49
2.4 (6.37)	22.98	23.13

3.2. Axial profile of solid holdup

To assess the real-time circulation under high temperature and high pressure, basic data was obtained by measuring the pressure drop with a pressure drop tab according to the height of the riser. This provided fundamental data for estimating solid holdup based on the pressure drop values, as shown in Fig. 2. Steady-state circulation was observed exclusively under the conditions specified in Table 2, which enabled the illustration of axial solid holdup for these conditions. Prior investigations involved conducting experiments within a riser (height= 6 m) under conditions of high density (u_g= 4 – 8 m/s and G_s= 200 – 425 kg/(m^2·s)) (Issangya, 1998; Issangya et al., 1999). Consistent with prior research, this study observed a low level of solid holdup within the riser. At the bottom of the riser, particles enter from the L-valve, showing a high solid holdup of about 0.2, and then at the top, the particles rise almost constantly, maintaining a solid holdup of 0.05.
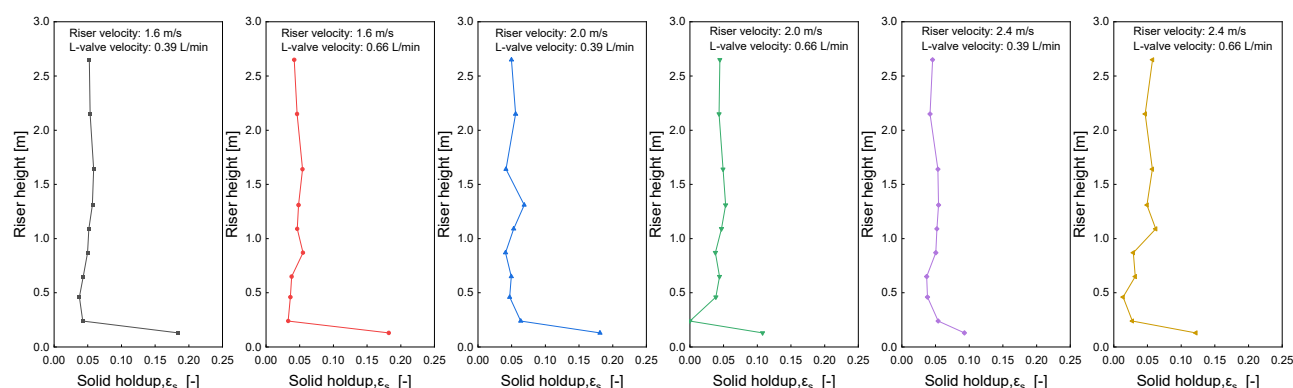
Fig. 2. Axial profile of solid holdup in riser

3.3 Reaction and regeneration of BT-S-FER

In a prior experiment, regeneration was conducted within the temperature range of 300 – 500 °C. The experiment revealed that after undergoing regeneration five times at 500 °C, the reactivity of the catalyst closely resembled that of the raw catalyst. The regeneration experiment was conducted under 500 °C, 20 bar, space velocity 2000 L/(kg$_{cat}$·h), and using air as regeneration gas. The profile graph over time of reaction and regeneration is shown in Fig. 3. DME conversion under reactive operating conditions was up to 70.7%, and selectivity to MA, the desired product, was 93.8%. According to time, the catalyst was deactivated, it was regenerated and subsequently a profile was drawn. Each reaction constant is computed differently based on the corresponding reaction condition, necessitating calculations specific to each condition.

Experiments on each reaction and regeneration process provided deactivation constant (k_d) and regeneration constant (k_r) of 9.08×10^{-6} and 0.02 1/s, respectively. Quantitatively the optimum size ratio for this study can be obtained through equation (2) below.

$$\frac{W_1}{W_2} = \left(\frac{k_r}{k_d}\right)^{1/2} \frac{e^{R_r/2} - e^{-R_r/2}}{R_r} \quad or \quad W_1 = \frac{F_s(e^{R_r/2} - e^{-R_r/2})}{(k_r k_d)^{1/2}} \tag{2}$$

[a]

260°C, 20bar, GHSV 1500 L/kg$_{cat}$/h, CO/DME/N$_2$ 90/4.5/5.5

[b]
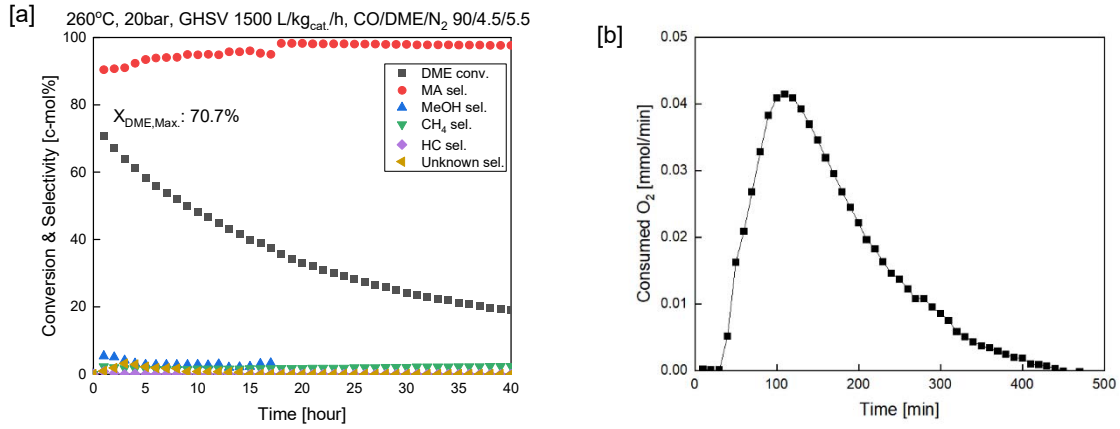
Fig. 3. (a) DME conversion and product selectivity with time on stream, (b) Oxygen consumption rate

Solid flux (F$_s$) was used as a value when the solid circulation rate (G$_s$) was calculated 24.13 kg/(m·s^2) in section 3.2. The ratio of the weight of particles in the reactor to the weight of particles in the regenerator was determined as 770. During Gs measurement in CFB, particles were filled to a height of 0.3m above the distributor plate in BFB, resulting in a particle mass of 542 g. This ratio was used to compute a particle mass of 0.7 g within the riser. However, pressure drop measurements indicated a riser particle mass of 9.85 g, underscoring the need for further investigation, including adjustments to bed height to achieve alignment with measured values.

4. Conclusion

In this study, experiments to determine the reaction and circulation flow characteristics of the produced BT-S-FER catalyst particles were conducted. By obtaining the reaction and regeneration constants under the relevant reaction experiment conditions, the approximate inventory weight within the BFB and riser can be obtained. To investigate the conditions for maintaining the stable circulation of catalyst particles, an experiment was performed by changing the flow rates of the L-valve and riser. The L-valve was operated in the range of 0.26 - 0.92 L/min and 2 - 7 times the terminal velocity (0.8 - 2.8 m/s). As a result, It was confirmed that it was stable when operating at the riser velocity of was 4 - 6 u$_{g,riser}$/u$_t$ and the L-valve velocity was 0.39 - 0.66 L/min. Reaction and regeneration constants were obtained through each experiment, and the inventory ratio in the reactor and regenerator was calculated to be 770. Additional research is required to optimize inventory in BFB and riser. The results of this fundamental study indicate potential application in employing CFB apparatus under conditions with both high temperature and high pressure.

Acknowledgment

Abbreviations

BFB	Bubbling fluidized bed
BT-S-FER	Bentonite spray-dried ferrierite
CCU	Carbon Capture, Utilization
CFB	Circulating fluidized bed
DME	Dimethyl ether
FER	Ferrierite
I.D.	Inner diameter
MA	Methyl acetate

Nomenclature

d_p	Particle diameter, [-]
F_s	Solid flux, [kg/s]
G_s	Solid circulation rate, [kg/(m·s^2)]
k_d	Deactivation constant, [1/s]
k_r	Regeneration constant, [1/s]
P	Pressure, [bar]
SV	Space velocity, [L/(kg$_{cat}$ ·h)]
T	Temperature, [°C]
u_g	Superficial velocity, [m/s]
u_{mf}	Minimum fluidization velocity, [m/s]
u_t	Terminal velocity, [m/s]
X_{DME}	DME conversion, [%]

References

Basu, P., & Cheng, L. An analysis of loop seal operations in a circulating fluidized bed. Chemical Engineering Research and Design, 2000, 78, 991–998.

Christensen, T. H., & Bisinella, V. Climate change impacts of introducing carbon capture and utilisation (CCU) in waste incineration. Waste Management, 2021, 126, 754–770.

Geldart, D. Types of Gas Fluidization. Powder Technology, 1973, 7, 285–292.

Issangya, A. S. Flow dynamics in high density circulating fluidized beds. (Ph.D. diss.). Univ. of British Columbia, Vancouver, BC. 1998

Issangya, A. S., Bai, D., Bi, H. T., Lim, K. S., Zhu, J., & Grace, J. R. Suspension densities in a high-density circulating #uidized bed riser. In Chemical Engineering Science 1999, 54, 5451-5460

Jiang, P., Bi, H., Jean, R. H., Fan, L. S. Baffle effects on performance of catalytic circulating fluidized bed reactor. AIChE Journal, 1991, 37, 1392－1400.

Kim, S., Jung, H. S., Lee, W. B., Bae, J. W., Park, M. J. Process modeling of syngas conversion to ethanol and acetic acid via the production of dimethyl ether and its carbonylation. Korean Journal of Chemical Engineering, 2022, 39, 3204–3213.

Kim, J. Y., Li, Z. J., Jung, H. S, Nam, J. Y., Woo, C. S., Bae, J. W., Lee, D. H., Integration of process optimization, TEA and LCA for dimethyl ether carbonylation to methyl acetate in a fluidized bed reactor. in press.

Liu, G., Yang, G., Peng, X., Wu, J., Tsubaki, N. Recent advances in the routes and catalysts for ethanol synthesis from syngas. Chem Soc Rev. 2022, 51, 5606–5659.

Lim, J. H., Lee, D. H., Chae, H. J., Jeong, S. Y. Pressure change and control of the solid circulation rate of Geldart A particles in a small diameter L-valve. Powder Technology, 2013, 243, 139–148.

CO-REDUCTION OF HEMATITE BY COCONUT SHELL CHARCOAL AND HYDROGEN IN FLUIDIZED BED

（Jiehan Zhang[1], Shiyuan Li[1*], Linwei Wang[1]

School of Energy and Environmental Engineering, University of Science & Technology Beijing, Beijing 100083, China.

Email: lishiyuan@ustb.edu.cn

Abstract

Utilizing bioenergy and hydrogen in iron and steel production offers significant potential achieving carbon neutrality and positive synergistic effects. This study investigates the synergistic effect and kinetic analysis of coconut shell char (CSC) and hydrogen co-reduction for hematite in a fluidized bed. The results show that more addition amount of CSC and higher reduction temperature both improves the hematite reduction degree. The reduction degree increases from 62.0% to 82.3% when the addition range of 0% to 10% at 60 minutes, 700°C. For 1.25% CSC addition, the temperature increases from 700°C to 900°C, promoting the reduction degree improves by 15.4% within 60 minutes. It is also found that hydrogen and CSC have synergistic effect during hematite reduction process. Throughout the entire range of experimental temperatures, the additions of CSC at 1.25% and 2.5% both demonstrate a positive synergistic effect, which indicates a higher reduction degree than the simple sum of the two. However, if the CSC addition exceeds 2.5%, synergistic effect is positive below 800°C and negative at higher temperatures. The further experimental results suggest that the variation in synergistic effect can be attributed to the indigenous alkali metals in CSC, as well as the aggregation of reduced products. Furthermore, the kinetics analysis present that the whole reduction process is controlled by a combination of internal diffusion and interfacial chemical reactions. The activation energy of the reduction reaction decreases significantly by 53.4 kJ·mol^{-1} when the addition amount exceeds 2.5%, in comparison with lonely hydrogen reduction. This study provides a new approach for fluidized bed iron ore reduction. The use of CSC not only improves the carbon-based reduction process but also provides the heat for the reduce reaction. Additionally, it can alleviate the particle agglomeration at the range of 700-850°C in fluidized bed.

1. Introduction

Steel is vital to modern economies and so over the coming decades global demand for steel is expected to grow to meet rising social and economic welfare needs. Iron and steel industry is currently responsible for about 8% of global final energy demand and 7% of CO_2 emissions. Iron and steel producers have a major opportunity to reduce energy consumption and greenhouse gas emissions as well as develop more sustainable products [1,2]. Correspondingly, the transition from the conventional BF process using a carbon-based reducing agent to iron production through hydrogen in a fluidized bed has been considered the main route for decarbonizing the steel industry [3,4]. However, the utilization of fluidized bed technology in the ironmaking process increased particle size of products to cause sticking and de-fluidization, which hampered the industrial application of fluidized bed direct reduction process using hydrogen [5,6]. The adhesion performance happens intrinsically from the sintering of new precipitated reduced iron, with the potential to rapidly spread throughout the entire fluidized bed to decrease reduction effect. Maintaining the fluid state of the particles is crucial for achieving a significant reduction degree [7]. Addressing particle adhesion requires initiating measures during the iron precipitation on the product's surface. Numerous techniques have been suggested to mitigate the adhesion of reduced iron for fluidized bed reduction. For instance, research has explored coating ore particles with inert oxides (such as

CaO and MgO) and carbon. Nevertheless, applying inert oxides for coating hematite fines can significantly diminish the reaction rate [8]. And the high pore structure and carbon-based properties of biomass enable its use as a coating material to reduce particle aggregation and function as a reducing agent [9].

Currently, reduced iron ore powder using biomass finds utility in three distinct applications. Firstly, biomass char can be used as reducing agent during reduction process, which replaces coal and coke in in iron- and steelmaking. However, a lot of alkali metals in the biomass char can lead to undesirable product bonding at higher temperatures, rendering it unsuitable for the fluidized bed metallurgical process [10-12]. Secondly, applying biomass into blast furnaces can reduce the CO_2 emission comparing to coal, but decrease reduction efficiency [13]. Moreover, biomass is typically utilized as an additive in combination with iron ore powder to create pellets. These mixed pellets require additional reducing gas as a medium for gas-solid reduction, leading to increased energy consumption and higher economic costs [14]. Therefore, many studies use the syngas produced from biomass pyrolysis as a reducing gas to participate in the process of reducing iron [15]. This process integrates biomass pyrolysis and iron ore powder reduction, enhancing particle properties by employing biomass as a flux, and it diminishes energy consumption through the utilization of pyrolysis gas. This process has the potential to efficiently reduce iron using biomass, offering substantial environmental benefits [16,17]. However, this technology exhibits certain limitations [18,19]: 1) it may generate Fe-C compounds, thereby complicating the procedure; 2) an elevated substitution rate of biomass for coke breeze may lead to vertical sintering and a reduction in the yield of reduced iron; 3) High-quality iron requires H_2, yet the pyrolysis gas from biomass typically contains various components, including CH_4, alkanes, olefins, and C-O gas. The utilization of such gas for iron reduction remains unexplored by researchers. Therefore, we adopt other process to use biomass energy in steel production, not only the dependence of the steel industry on fossil energy will be reduced but also the abandoned biomass will be appropriately handled. This study offers an alternative complement pathway, i.e., biomass char is mixed with iron ore powder and reduced by hydrogen in fluidized bed, which combines the biomass utilization and the H_2-based DRI route. In addition, the co-reduction of the two factors may cause some synergistic effects to promote/inhibit the reduction process of hematite [20], but there are fewer studies on biomass char-H_2 gas for DRI production in a fluidized bed.

In this study, the reduction process of hematite with coconut shell charcoal and hydrogen in a micro-fluidized bed was investigated. We discussed the effects of the reduction temperature and the amount of coconut shell charcoal on the reduction products, and both two reduction conditions affected the synergistic effect between coconut shell charcoal and hydrogen on hematite reduction. The differences of synergistic effect were explored from the following two aspects: including the effect of alkali metals in coconut shell charcoal and the bonding of reduction products. This study provides a new strategy for fluidized bed hydrogen reduction of iron ore powder. Specifically, it involves applying a coating of coconut shell charcoal on the surface of reduced iron to mitigate particle adhesion, maintain fluidization efficiency, and enhance the degree of reduction at elevated temperatures.

2. Synergistic effect between CSC and H_2

According the previous results, the introduction of CSC into hematite can significantly improve the reduction degree, especially with higher CSC additions. According to previous research, the improvement of reduction degree for mixture samples can be attributed to the synergistic effect between carbon-based and fluidized hydrogen gas. Furthermore, the literature suggested that the difference between experimental and theoretical values of reduction degree can confirm the interaction among various factors [21]. Figure 1 illustrates the difference between the experimental and theoretical values of reduction degree at different temperatures and with varying CSC additions. When the CSC addition was 1.25% and 2.5%, the synergistic reduction of biomass-charcoal and fluidized H_2 displayed positive cooperativity at the whole experimental temperature in this study. However, when CSC addition exceeded

5%, the synergistic effect of biomass-charcoal and fluidized H_2 became thoroughly complex. In the case of H-5CSC, the synergistic effect showed positive cooperativity at temperatures below 800°C and converted into negative cooperativity above that temperature. Additionally, with the CSC addition increased (about 10%), the synergistic effect shifted to a lower conversion temperature. As a result, we observed that the synergistic effect varies with temperature depending on the amount of CSC addition. Our hypothesis is that the presence of alkali metal and the aggregation of reduced particles are responsible for the difference in the synergistic effect at different CSC addition levels. We speculate that at lower CSC addition levels, alkali metal promotes the reduction process, resulting in a positive cooperativity at the whole experimental temperature, while for higher CSC addition levels, it promotes particles aggregation at increased reduction temperature to generate a negative cooperativity. Next, we will discuss the synergies from two different aspects.
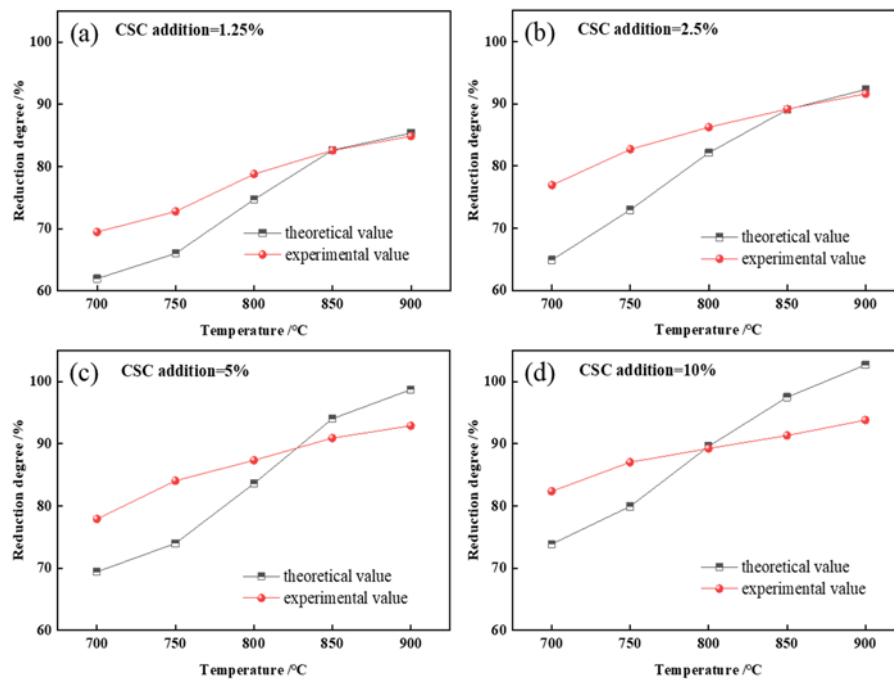
Figure 1 The difference between experimental and theoretical values with different CSC additions

3. Reason for synergistic effect

3.1 Effects of alkali metal at lower addition on synergistic effect

In general, biomass char ash contains a high level of alkali metal (mainly K, Na, Ca et al.), which can actively engage in the reduction reaction during the iron ore powder reduction process [22]. And the process includes the formation of carbonates to facilitate the reduction process and the amalgamation with reduced iron at higher reduction temperature (>850°C), leading to an increase in particle size, which hinders the continued reduction. Figure 2(a) shows the reduction degree under the 1.25% addition amount of CSC and deashing CSC (without alkali metal). When the hematite was reduced in a fluidized bed using a deashing CSC, the introduction of d-1.25CSC only acted as a carbon material, and the reduction degree increased by 4.5% when the reduction temperature rose from 700°C to 900°C. However, for the mixture sample of hematite and CSC, the reduction degree increased by 12.4% with increased reduction temperature, which was significantly higher than the reduction using deashing CSC. The reduction results of hematite and its mixture (with CSC and deashing CSC) using hydrogen at different temperature is shown in Figure 2(b). For instance, when considering the reduction degree of hematite using deashing CSC under a hydrogen atmosphere, it exhibited an intermediate level between H-1.25CSC and H_2 reduction without CSC. At higher reduction temperatures, the reduction degree for H-d-1.25CSC rose from 63.9%

to 78.7%. However, this increase in reduction degree was notably lower than that observed in the H-1.25CSC sample. From these results it was clear that the positive cooperativity between CSC and hydrogen at the lower CSC addition amount was mainly to blame the alkali metal of CSC, which was presumed to be possibly related to the following aspects [23]: Initially, alkali metals can act as catalysts in the reduction reaction at higher temperatures (in this study, T> 750°C), reducing the activation energy and enhancing heat conduction to facilitate the occurrence of the reduction reaction. Conversely, alkali metals can react with carbon in CSC, generating alkali metal carbonates that serve as reducing agents in the reduction process. Consequently, these findings elucidate the positive synergistic effect of hematite reduction in a fluidized bed using both hydrogen and CSC across the entire reduction temperature range, with CSC additions of 1.25% and 2.5%.
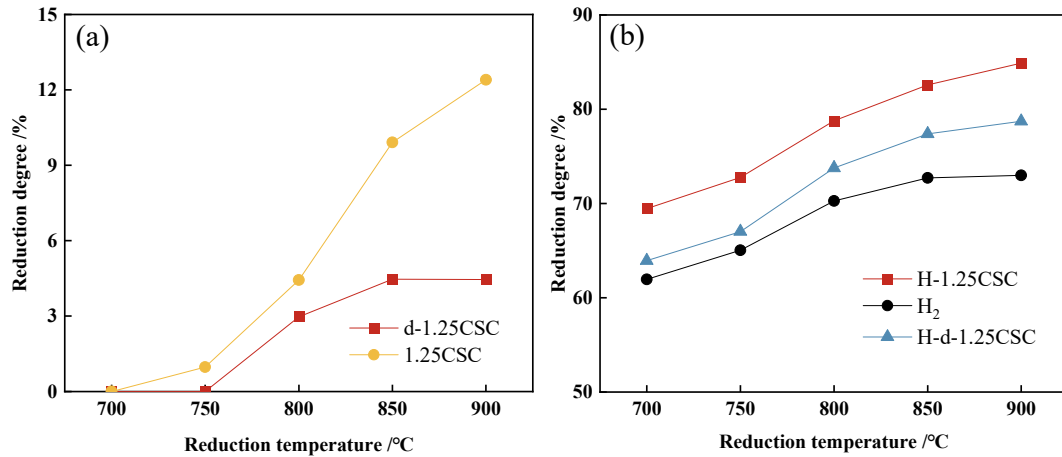
Figure 2 The effect of CSC without alkali metal on reduction degree: (a) CSC reduction lonely and (b) co-reduction of CSC and hydrogen (reduction time= 60 min).

3.2 Effects of products aggregation at higher addition on synergistic effect

As shown in Figure 1(c) and (d), at reduction temperatures of 850°C and 900°C, the experimental values were consistently lower than their theoretical counterparts, particularly with higher CSC additions (>5%). This discrepancy is speculated to be linked to the agglomeration of reduced particles at elevated temperatures. Therefore, the particle size of reduction products at different experimental conditions is shown in Figure 3. Figure 3(a) shows the particle size of raw materials (hematite and CSC) and the products for single reduction using CSC with different addition amount. At a reduction temperature of 900°C, in comparison to raw hematite, the values of Dv(50) and Dv(90) increased by 5.8 μm and 19.3 μm, respectively, for the 1.2% CSC reduction alone. However, the two values exhibited a more significant increase of 22.8 μm and 61.3 μm, respectively, during the reduction with a 10% CSC addition. Consequently, the synergistic effect shifted to negative one when the CSC addition exceeded 5% at 800°C, which was primarily attributed to the constraint on gas diffusion and heat transfer resulting from the increased particle size of the reduced products [15-17]. Furthermore, Figure 3(b) presents the particle size results for the various samples reducing under H_2 atmosphere (with or without CSC). It can be obvious seen that the significant increase of particle size using H_2 reduction, especially for the increase in of Dv(50) and Dv(90), which was related to the direct iron-iron contact at particle surfaces to cause the sticking of iron particles [38]. The introduction of CSC into hematite can decrease the particle size of reduced products under H_2 atmosphere, but the particle size increased with the more CSC addition obviously. For example, the Dv(50) and Dv(90) values for H-1.25CSC decreased by 27.0 μm and 68.6 μm, respectively, compared to hydrogen reduction without CSC, which is more likely blame to the formation of a thin carbon layer on the particle surface, isolating the metal iron to hinder the direct iron-iron contact. So, it was helpful for decreasing the aggregation of metal iron particles to promote reduction process. Nevertheless, the findings indicated a 15 μm increase in the average particle size of the reduced products for H-10CSC compared to H-1.25CSC. An increase in particle size of reduced products was attributed to

the presence of alkali metals in the carbon, and K, Na elements may form fluxes at high temperatures, which combined with the surface of reduced iron to promote the bonding possibility [22]. In addition, the intensifying competition reaction between CSC and CO_2 decreased reducing rate to limit particles reduction. In summary, the above results suggested that the negative cooperativity at higher CSC addition and temperature (>5%, 800℃) was blame to the gas-solid mass transfer limitation due to particles bonding and competition reaction.
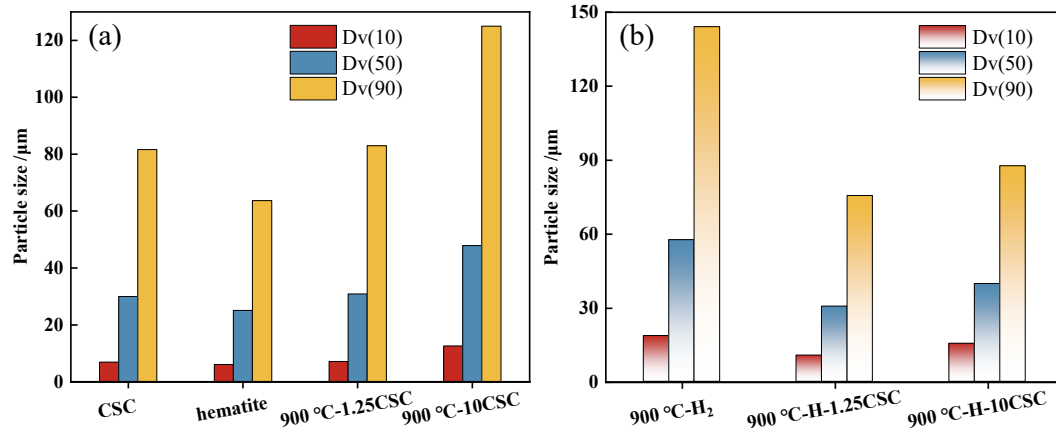
Figure 3 The particle size distribution of (a) raw samples and reduction products without H_2 and (b) reduction products under H_2 atmosphere.

4. Conclusion

In this work, the co-reduction of hematite powder using biomass char and hydrogen in a micro-fluidized bed was investigated. During the hematite reduced by CSC and H_2, it was speculated that there may be synergistic effect between CSC and hydrogen during hematite reduction. And the difference between experimental and theoretical values confirmed the possibility. For instance, when the addition was less than 2.5%, positive synergistic effect was observed throughout the reduction temperature range. And at higher temperature (>800℃), the synergistic effect shifted to negative one while the CSC addition was 5% and 10%. We explained the above results in two ways: On one hand, the existence of alkali metal in CSC can promote reduction rate due to the carbonate formation (including K_2CO_3, Na_2CO_3, et al.). And the negative synergistic effect at higher CSC addition and temperature is related to the particle aggregation to hinder the gas-solid transfer. Therefore, a fluidized bed process using hydrogen and CSC as reducing agent can promote the synergistic effect to increase reduction degree and decrease product bonding.

Acknowledgment

References

[1] Chen YS, Tian T. Experimental Study on Hydrogen Selective-Reduction of Niobium Containing Iron Ore Powder. Advanced Materials Research. 2014;941-944:157-64.

[2] Metolina P, Ribeiro TR, Guardani R. Hydrogen-based direct reduction of industrial iron ore pellets: Statistically designed experiments and computational simulation. International Journal of Minerals, Metallurgy and Materials. 2022;29(10):1908-21.

[3] Luo S, Yi C, Zhou Y. Direct reduction of mixed biomass-Fe2O3 briquettes using biomass-generated syngas. Renewable Energy. 2011;36(12):3332-6.

[4] Boretti A. The perspective of hydrogen direct reduction of iron. Journal of Cleaner Production. 2023;429.

[5] Scharm C, Küster F, Laabs M, Huang Q, Volkova O, Reinmöller M, et al. Direct reduction of iron ore pellets by H_2 and CO: In-situ investigation of the structural transformation and

reduction progression caused by atmosphere and temperature. Minerals Engineering. 2022;180.

[6] Souza Filho IR, Springer H, Ma Y, Mahajan A, da Silva CC, Kulse M, et al. Green steel at its crossroads: Hybrid hydrogen-based reduction of iron ores. Journal of Cleaner Production. 2022;340.

[7] Spreitzer D, Schenk J. Fluidization behavior and reducibility of iron ore fines during hydrogen-induced fluidized bed reduction. Particuology. 2020;52:36-46.

[8] Liu P, Liu B-g, Zhang L-b, Peng J-h. Particle motion simulation and pulverized coal injection combustion simulation of titanomagnetite pellets in rotary kiln for reduction process with coal. Journal of Iron and Steel Research International. 2022;29(6):891-906.

[9] Zaini IN, Nurdiawati A, Gustavsson J, Wei W, Thunman H, Gyllenram R, et al. Decarbonising the iron and steel industries: Production of carbon-negative direct reduced iron by using biosyngas. Energy Conversion and Management. 2023;281.

[10] Xu N, Tan G, Wang H, Gai X. Effect of biochar additions to soil on nitrogen leaching, microbial biomass and bacterial community structure. European Journal of Soil Biology. 2016;74:1-8.

[11] Ubando AT, Chen W-H, Ong HC. Iron oxide reduction by graphite and torrefied biomass analyzed by TG-FTIR for mitigating CO_2 emissions. Energy. 2019;180:968-77.

[12] Zuo H-b, Hu Z-w, Zhang J-l, Li J, Liu Z-j. Direct reduction of iron ore by biomass char. International Journal of Minerals, Metallurgy, and Materials. 2013;20(6):514-21.

[13] Han H, Duan D, Yuan P, Li D. Biomass reducing agent utilisation in rotary hearth furnace process for DRI production. Ironmaking & Steelmaking. 2015;42(8):579-84.

[14] Guo D, Li Y, Cui B, Chen Z, Luo S, Xiao B, et al. Direct reduction of iron ore/biomass composite pellets using simulated biomass-derived syngas: Experimental analysis and kinetic modelling. Chemical Engineering Journal. 2017;327:822-30.

[15] Bagatini MC, Kan T, Evans TJ, Strezov V. Iron Ore Reduction by Biomass Volatiles. Journal of Sustainable Metallurgy. 2021;7(1):215-26.

[16] Huang Z, Shu Y, Li Y, Huang B, Yi L, Jiang T. External moisture enhanced synergistic conversion of biomass and iron sand for the green production of metallic iron. Journal of Cleaner Production. 2023;418.

[17] Guo D, Zhu L, Guo S, Cui B, Luo S, Laghari M, et al. Direct reduction of oxidized iron ore pellets using biomass syngas as the reducer. Fuel Processing Technology. 2016;148:276-81.

[18] Gan M, Fan X, Chen X, Ji Z, Lv W, Wang Y, et al. Reduction of Pollutant Emission in Iron Ore Sintering Process by Applying Biomass Fuels. ISIJ International. 2012;52(9):1574-8.

[19] Carvalho MMO, Cardoso M, Vakkilainen EK. Biomass gasification for natural gas substitution in iron ore pelletizing plants. Renewable Energy. 2015;81:566-77.

[20] Yi L, Zhang N, Hao H, Wang L, Xiao H, Li G, et al. Synergetic conversion laws of biomass and iron ore for syngas and direct reduced iron co-production. Journal of Cleaner Production. 2022;363.

[21] Zhang J, Yang H, Kang G, Yu J, Gao S, Liu Z, et al. The synergistic effect on the product distribution for the co-pyrolysis of tannery wastes. Fuel. 2022;322.

[22] Cao Z, Xu Q, Kang H, Shi J, Lu X, Chen B, et al. Insights into direct reduction iron using bamboo biomass as a green and renewable reducer: Reduction behavior study and kinetics analysis. Science of The Total Environment. 2023;880.

[23] Ye Q, Li G, Peng Z, Augustine R, Pérez MD, Liu Y, et al. Microwave-assisted self-reduction of EAF dust-biochar composite briquettes for production of direct reduced iron. Powder Technology. 2020;362:781-9.

Circulating Experiments on Catalytic Characteristics of Iron-rich Fly Ash under Biomass-volatile-fired Fluidized Bed Conditions

Bingjun Du[1], Yuchen Ma[1], Weiqin Lu[1], Xueyu Tang[1], Junfu Lyu[1], Xiwei Ke[2]*

[1]*Key Laboratory for Thermal Science and Power Engineering of Ministry of Education, Department of Energy and Power Engineering, Tsinghua University, Beijing 100084, China*

[2]*Beijing Huairou Laboratory, Beijing 101499, China*

*Email: *kexw@mail.tsinghua.edu.cn*

Abstract

Oxygen carriers have been widely used in chemical looping processes to promote the mixing of fuel and oxidant, improve combustion/conversion efficiency, and reduce pollutant emissions. Among various oxygen carriers, iron-rich fly ash shows great potential with abundant reserves and considerable redox and catalytic activity. However, the oxygen-carrying/catalytic performance of the iron-rich fly ash still needs to be further studied. This study aims to determine the catalytic performance of iron-rich fly ash on the fluidized bed combustion process of the biomass-volatile gas. The Indonesian lignite ash was selected as the target sample along with other coal ashes and typical oxygen carriers, and their compositions and pore characteristics were analyzed before the experiments. Circulating experiments were conducted on a bubbling fluidized bed reactor under different ash particle sizes and bed temperatures. The biomass-volatile gas, which consisted of H_2, CH_4, and CO, was fed into the reactor according to the sequence of the "Ar-volatile-Ar-O_2" cycle under given experimental conditions, and then the concentrations of the gases in the exhaust were recorded as a function of time. Results showed that Indonesian coal ash has high adsorption capacity and conversion rates for volatiles and oxygen comparable to steel slag and ilmenite due to its high iron content (mainly in Fe_2O_3 form) and good pore characteristics.

1. Introduction

Oxygen carriers are substances with strong oxygen-carrying capacities and significant redox reactivities and thus can achieve continuous and efficient redox cycles between oxidizing and reducing agents by introducing gas-solid sub-reactions with lower activation energies (Ishida, Zheng & Akehata, 1987). There have been wide applications of various oxygen carriers in the fields of chemical looping combustion (CLC), chemical looping gasification (CLG), chemical looping reforming (CLR), chemical looping hydrogen generation (CLHG), and oxygen carrier aided combustion (OCAC), in which cases these oxygen carriers have been proved to greatly improve reaction kinetics and combustion/conversion efficiencies and significantly reduces pollutant emissions. (Thunman et al., 2013; Yu et al., 2019)

Many scholars have explored the characteristics and effectiveness of various oxygen carriers including ilmenite (Thunman et al., 2013), steel slag (Attah et al., 2021), hematite (Pineau, Kanari & Gaballah, 2006), and multiple metal ores or oxides including Fe (Mattisson et al., 2004), Mn (Ryden et al., 2016), Cu (Diego et al., 2004) or other elements (Li et al., 2006; Yu et al., 2019). Among these substances, iron-based oxygen carriers have attracted wide attention considering their low costs and high redox reactivities and mechanical strengths. Beside various kinds of natural ores and synthetic catalysts, one high iron-content substance should be paid more attention to: iron-rich coal ash, which shows great potential to be an excellent oxygen carrier for the following reasons:

①Coal ash is one of the staple solid wastes in the industry that has a huge amount to be disposed of every year in China, so its utilization is cheap and yields economic and environmental benefits;

②Coal ash has a scouring and cleaning effect on the contaminated layer on the heating surface in the equipment considering its suitable particle size (1 μm ~ 500 μm), good anti-wear performance, and stability;

③Good pore characteristics and rich iron content in iron-rich coal ash usually indicate strong oxygen-carrying capacity and redox reactivity. Besides, coal ash is also usually rich in minerals such as Al, Ca, and Mg, which can act as co-catalysts and help form alkali metal compounds with higher melting points to alleviate sintering and agglomeration of bed materials (this is more important for OCAC process in the boiler);

These characteristics determine the potential industrial use of coal ash as an excellent oxygen carrier in the future. For example, the oxygen-carrier aided combustion based on iron-rich fly ash (FeAsh-OCAC) is expected to achieve high-efficiency, low-pollutant-emission biomass combustion in CFB boilers. However, at present, few studies delved into the practical oxygen-carrying/catalytic performance of iron-rich coal ash, and the feasibility of relative technique in industrial scenarios remains to be further studied. This study takes Indonesia lignite ash as an example of iron-rich coal ash and determines its oxygen-carrying capacity and catalytic performance in the biomass-volatile combustion process. Redox circulating experiments were conducted on a bubbling fluidized bed reactor for different materials and temperatures, yielding a qualitative and quantitative description of the oxygen-carrying and combustion assistance ability of the iron-rich coal ash under different conditions. The lignite ash, along with other coal ash and typical oxygen carriers before and after the experiment were characterized using XRD (X-Ray Diffraction), XRF (X-Ray Fluorescence), and pore structure analysis methods and compared.

2. Experiment Settings

2.1 Sample Preparation and Characterization

2.1.1 Sample Preparation

This experiment used five typical and potential oxygen carriers: Indonesian lignite ash (IN), Jiaocheng coal ash (JC), Shuozhou coal ash (SZ), steel slag (SS), and ilmenite (IL). Indonesian lignite has a large consumption in China and produces a large amount of iron-rich lignite ash every year. The main research object of this paper is Indonesian lignite ash, and the other four substances are used for comparison. The Indonesian lignite was crushed to about 1 cm particles and then laid on an iron tray with a thickness of about 2 cm and fed into a Muffle furnace to burn (850℃ for 6 h). The lignite in the iron tray was turned over every two hours to ensure that the lignite was burned thoroughly. The lignite ash generated was then sieved for more than 3 h. All materials were sieved into five particle size ranges: 105~125 μm, 125~150 μm, 150 ~180 μm, 200~250 μm, 250~300 μm. The preparation processes of JC and SZ were the same. IL was directly sieved for 1 h, and SS was first crushed and then sieved for 1 h. Only the 150~180 μm particle size range groups of these oxygen carriers were used. The particle size range of the sieved IN was measured via a Malvern laser particle size analyzer. The analysis result showed that the Dv (50) of the sieved IN is 210 μm, which met the expectation and could be used for following experiments.

2.1.2 Composition analysis

The compositions of all the materials were analyzed via XRD and XRF methods. The test result of XRF for all materials are shown in Fig. 1(a) and Table 1. In terms of mass fraction, the order of element contents (in oxide forms) of IN from high to low is Fe_2O_3, SiO_2, Al_2O_3, CaO, MgO, and other elements. Compared to the other two coal ashes (JC and SZ), IN has significantly higher Fe_2O_3 content (even higher than IL, but lower than SS) and lower SiO_2 and Al_2O_3 content, proving that it is an iron-rich coal ash. Moreover, IL has an extremely higher TiO_2 content than other materials and has lower SiO_2 and Al_2O_3 content than IN. SS also has lower SiO_2 and Al_2O_3 content than IN but has the highest CaO content.

The test spectrum of XRD for all materials is shown in Fig. 1(b). The three coal ashes (IN, JC, and SZ) have similar mineral phases (that is, Fe_2O_3, SiO_2, $MgFe_2O_4$, and $CaSO_4$). Because the iron content of SS and the Titanium content of IL are higher, there are more compounds formed between Fe (or Ti) and other elements.
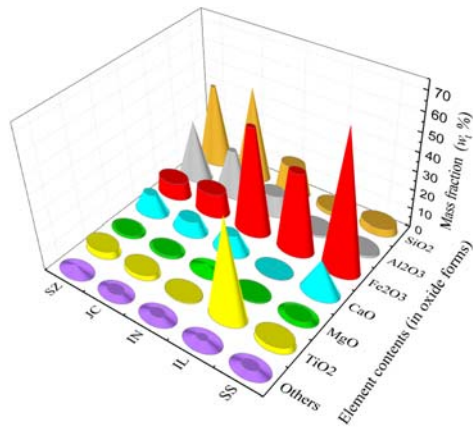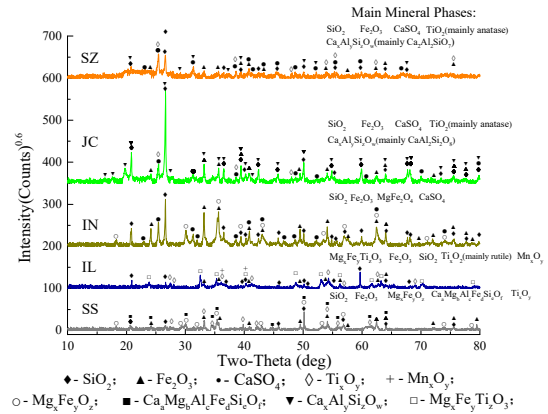
(a)XRF result   (b)XRD result

Fig. 1. Analysis results of different materials used in the experiment

Table 1 Specific result of XRF analysis of different materials used in the experiment

Material	Fe_2O_3 (Wt%)	SiO_2 (Wt%)	Al_2O_3 (Wt%)	CaO (Wt%)	MgO (Wt%)	TiO_2 (Wt%)	Others (Wt%)
SS	72.20 ±0.22	3.97 ±0.10	1.08 ±0.05	17.15 ±0.19	1.08 ±0.05	3.15 ±0.09	1.37 ±0.70
IL	41.47 ±0.25	2.27 ±0.07	1.01 ±0.05	0.200 ±0.010	0.287 ±0.014	51.59 ±0.25	3.173 ±0.644
IN	54.40 ±0.25	16.40 ±0.19	10.45 ±0.15	9.44 ±0.15	3.38 ±0.09	0.671 ±0.033	5.259 ±0.863
JC	12.47 ±0.17	48.75 ±0.25	23.79 ±0.21	6.73 ±0.13	0.675 ±0.034	2.72 ±0.08	4.865 ±0.874
SZ	8.82 ±0.14	41.70 ±0.25	30.97 ±0.23	10.27 ±0.15	0.604 ±0.030	3.84 ±0.10	3.796 ±0.900

2.1.3 Pore structure analysis

Through the nitrogen adsorption test (using the BET method) and theoretical calculation, the test results of pore structure analysis of each material are shown in Table 2. It can be seen that Indonesian lignite ash has the highest porosity and larger specific surface area and pore volume than iron-rich SS and IL, which has a positive impact on adsorption and gas-solid reaction on the material surface.

Table 2 Specific results of pore structure analysis of different materials used in the experiment

Material	Specific surface area ($m^2 \cdot g^{-1}$)	Pore volume ($cm^3 \cdot g^{-1}$)	Average pore diameter (nm)	Porosity (%)
IN	7.1598	0.023870	13.7717	7.9092
SS	0.6277	0.002219	17.0672	0.9581
IL	2.3862	0.008165	13.5556	3.5404
JC	6.1016	0.035098	22.8747	6.1016
SZ	7.3055	0.027979	18.0851	7.3055

2.2 Experimental System

The diagram of the entire experimental system is shown in Fig. 2. The reducing gas cylinder used in this experiment, referring to the pyrolysis products of straw, consisted of 25.61% H_2, 37.74% CH_4, and 36.65% CO. The oxidizing gas, referring to air, was obtained by mixing the gas from O_2 and Ar gas cylinders with a volume ratio of 21:79. The inlet gases first flew through the mass flowmeters (Qixing Huachuang D07-19B), and the flowmeters were connected to an external automatic controller (customized by Shanxi Clean Energy Research Institute of Tsinghua University) to achieve precise real-time control of flow rates of all gas paths.
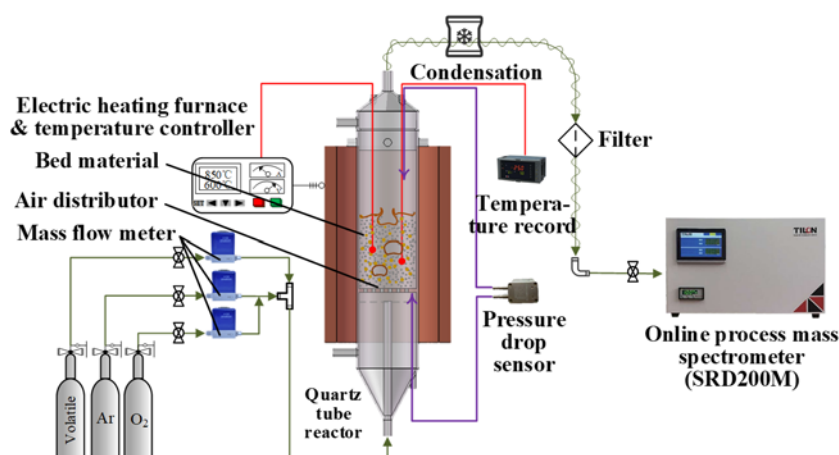
Fig. 2. Experimental system diagram

The reaction process occurred in a quartz tube (made by Jiangsu Donghai Jinpute Photoelectric Technology Co. Ltd.) heated by an electric vertical furnace (made by Shanghai Yuzhi Electromechanical Device Co. Ltd.). Gases were fed into the quartz tube from the bottom pipe to 3 cm below the air distributor in the middle of the quartz tube. Then the gas streams flew through the air distributor and fluidized the material particles (along with adsorption and reaction processes) on the air distributor. The exhaust exited the quartz tube through the top central branch pipe. Moreover, the quartz tube also has branch tubes for bed pressure drop and bed temperature measurements.

The exhaust was filtered and condensed to remove fine particles and steam, then fed into the TILON online mass spectrometer to achieve continuous quantitive gas analysis.

2.3 Experiment Procedure

Before the experiment began, 14 g of one material (3 cm height of IN in the quartz tube, not mixed with quartz sand) was added into the quartz tube on the air distributor. After setting the temperature of the vertical furnace at 700℃, a stream of Ar with a flow rate of 0.5 L/min was fed into the tube to purge the gas path. Then open the TILON online mass spectrometer. The gas types and correlated molecular masses were $H_2(2)$, $CH_4(15)$, $CO(28)$, $O_2(32)$, $Ar(40)$, and $CO_2(44)$. When the temperature reached the preset value, start feeding the oxidizing and reducing gases, and control the flow rate to ensure the gas flow velocity in the quartz tube was slightly larger than 0.08 m/s, which is the minimum fluidization velocity. The gases were fed circularly into the tube in the order of "Ar 5 min - reducing gas 40 min - Ar 5 min - oxidizing gas 40 min". In some cases, the input gas types were switched after the concentrations were basically stable during the experiment. After three cycles, switch the inlet gas to pure Ar and raise the preset temperature of the furnace to 800℃ and 900℃ and then repeat the circulating experiment procedure above. After the entire circulating experiment was done, close the mass spectrometer and the furnace, then keep the flow of Ar with a flow rate of 0.5 L/min to cool the tube. After the tube was cooled to room temperature, stop Ar feeding and take out the material particles in the tube for later characterization. The reaction tube was then cleaned with anhydrous ethanol for the experiment of the next material. After a set of experiments, the signal intensity data of the mass spectrometer was saved and converted into Excel file format for subsequent data processing.

3. Results and Discussions

3.1 Redox reactivity of IN

Figure 3(a) shows different gas concentrations as a function of time in two cycles for both the IN experiment group and the blank group (using quartz sand as bed material) at 800℃. Compared to the blank group, under the influence of IN, concentrations of each gas at the same reaction time significantly decreased, the climbing rate of gas concentrations also slowed down, and the required time for gas concentrations to reach stability was significantly extended, indicating that IN has large gas adsorption capacity and strong redox reactivity, and significant heterogeneous redox reactions occurred on its surface during the experiment.

These reactions mainly include reactions of reducing gases with active oxygen atoms on the IN surface:

$$CH_4 + 4O^* = CO_2 + 2H_2O$$
$$H_2 + O^* = H_2O$$
$$CO + O^* = CO_2$$
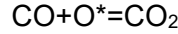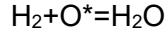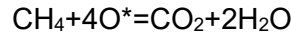
And reactions of oxygen dissociation on the IN surface to form active oxygen atoms.

$$O_2 + 2(^*) = 2O^*$$

| (a)IN and blank experiment at 800°C | (b)Blank experiment under different temperatures | (c)IN under different temperatures |
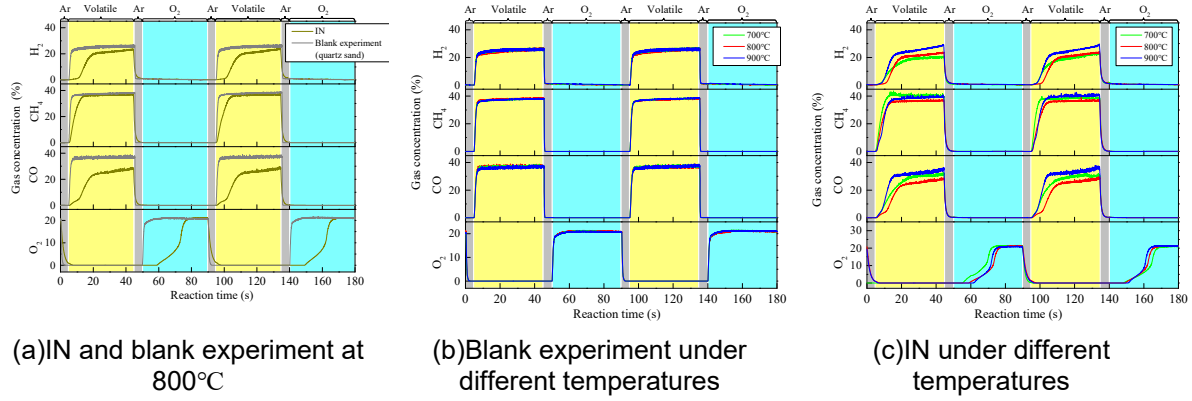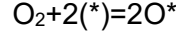
Fig. 3. Gas concentrations as a function of time for IN and the blank experiment

At different temperatures, gas concentrations as a function of time in two cycles for the blank group and the IN experiment group are shown in Fig. 3(b) and Fig. 3(c), respectively. For the blank experiment group, the influence of temperature on gas concentrations is insignificant. For the IN experiment group, the global trends for different gases are basically the same. For some working conditions, some gas concentrations (such as CO concentration) did not reach the equilibrium concentration of the blank experiment at the end of the ventilation time, indicating that the gas may still be reacting slowly at this time. Furthermore, at 800°C, the concentration of each gas is relatively lower, indicating that IN has better redox reactivity at this temperature.

In order to further analyze the redox reactivity of IN and other materials, the following indexes were introduced for quantitative description.

(1) Adsorption capacity. The adsorption capacity for gas X of material Y per gram can be defined as:

$$C_{X,Y} = \frac{1}{m_Y}\left[\sum_{t_{j,0}=t_i}^{t_s} c_{X,0}(t_{j,0})\dot{Q}_0(t_{j,0})\Delta t_{j,0} - \sum_{t_{k,Y}=t_i}^{t_s} c_{X,Y}(t_{k,Y})\dot{Q}_Y(t_{k,Y})\Delta t_{k,Y}\right]$$

Where the subscript X represents the gas type, Y represents the material type, and 0 represents the blank experiment group. m_Y is the mass of the material (equal to 14 g for all types). $c_{X,0}$ and $c_{X,Y}$ are the concentrations of gas X in the tube (unit mol/m³) for the blank group and the material Y experimental group, respectively. $\Delta t_j(\Delta t_k)$ is the time interval between $t_j(t_k)$ and $t_{j+1}(t_{k+1})$. t_i is the time when the concentration of gas X in the blank experiment begins to rise. t_s is the time when the concentration of gas X in the experiment of material Y rises to 95% of the maximum concentration in a cycle (the units of time are all s).

In order to simplify the calculation, it is assumed that under the same temperature and pressure conditions, the gas velocity in the tube is fixed. Therefore, the flow rate of the mixed gas in the tube is also fixed:

$$\dot{Q}_0(t_{j,0}) = \dot{Q}_Y(t_{k,Y}) = \dot{Q} = \frac{\pi}{4}d^2 v$$

Where d = 40 mm. Under the conditions of 700°C and 114.881 kPa in the blank experiment, the gas velocity in the tube is controlled at v = 0.08 m/s. Assuming that the mixed gas obeys the ideal gas hypothesis, then:

$$\dot{Q}(\text{m}^3/\text{s}) = 1.187 \times 10^{-5}\frac{T(\text{K})}{p(\text{kPa})}$$

The absorption capacity of IN for different gases can be obtained through calculation (the results calculated from the two cycles in Fig. 3 are averaged, as shown in Table 3). It can be seen from the data in the table that at 800℃, the absorption capacities of IN for all gases are relatively higher, which may be related to the increase of adsorption and reaction rates, decrease of residence time, and decrease of porosity due to sintering and agglomeration as the temperature increases. The detailed mechanism remains to be further studied.

Table 3. Absorption capacities for different gases of Indonesian lignite ash

Temperature (℃)	Absorption capacities for H_2 (mol/g)	Absorption capacities for CH_4 (mol/g)	Absorption capacities for CO (mol/g)	Absorption capacities for O_2 (mol/g)
700	0.0174	0.0026	0.0229	0.0213
800	0.0184	0.0070	0.0335	0.0235
900	0.0096	0.0063	0.0176	0.0208

(2) Conversion rate. The conversion rate for gas X of material Y can be defined as:

$$\alpha_{X,Y} = \frac{\sum_{t_{j,0}=t_i}^{t_s} c_{X,0}(t_{j,0})\dot{Q}_0(t_{j,0})\Delta t_{j,0} - \sum_{t_{k,Y}=t_i}^{t_s} c_{X,Y}(t_{k,Y})\dot{Q}_Y(t_{k,Y})\Delta t_{k,Y}}{\sum_{t_{j,0}=t_i}^{t_s} c_{X,0}(t_{j,0})\dot{Q}_0(t_{j,0})\Delta t_{j,0}} = \frac{\sum_{t_{j,0}=t_i}^{t_s} c_{X,0}(t_{j,0})\Delta t_{j,0} - \sum_{t_{k,Y}=t_i}^{t_s} c_{X,Y}(t_{k,Y})\Delta t_{k,Y}}{\sum_{t_{j,0}=t_i}^{t_s} c_{X,0}(t_{j,0})\Delta t_{j,0}}$$

The conversion rate of IN for different gases can be obtained through calculation (the results calculated from the two cycles in Fig. 3 are averaged, as shown in Table 4). It can be seen from the data in the table that IN has a high O_2 conversion rate, indicating that it is a good oxygen carrier. Similarly at 800℃, the conversion rates of IN for all gases are basically higher.

Table 4. Absorption capacities for different gases of Indonesian lignite ash

Temperature (℃)	Absorption capacities for H_2 (mol/g)	Absorption capacities for CH_4 (mol/g)	Absorption capacities for CO (mol/g)	Absorption capacities for O_2 (mol/g)
700	43.14	17.75	40.76	69.93
800	39.66	26.45	48.63	73.84
900	18.03	17.39	25.35	70.40

3.2 Comparison between different materials

Figure 4 compares the gas concentration trends as a function of time in two cycles for different material experiments at 800℃. Compared with the blank experiment, the concentration of all gases at the same reaction time decreased due to different grades of adsorption and surface reaction on material particles. For iron-lean materials (such as the other two coal ashes JC and SZ), the gas concentrations did not decrease significantly and quickly reached stability, which indicated poor redox reactivity. However, the gas concentration trends of Indonesian lignite ash were significantly different from the two coal ashes, which were more similar to those of SS and IL with higher iron content, indicating that its redox reactivity should be significantly stronger than JC and SZ.

Figure 5 summarizes the gas concentration trends as a function of time in two cycles for different material experiments under different temperatures. For iron-lean JC and SZ, the temperature has no significant effect on the time for gas concentrations to reach stability. For iron-rich SS and IL, the concentration trends for different gas types are relatively complicated. With the increase of reaction temperature, CH_4 concentrations for different material groups generally decreased at the same reaction time, while H_2 and CO concentrations generally increased, indicating that these materials may have certain catalytic effects on the partly oxidation reaction of CH_4, especially under high temperature and for iron-rich materials (such as SS and IL) after injecting reducing gas into the tube for a certain period (Yu et al., 2019). For these material groups under high temperatures, CH_4 concentrations first increased and then decreased, while H_2 and CO concentrations first increased rapidly and then increased slowly. However, these trends are not significant for IN.
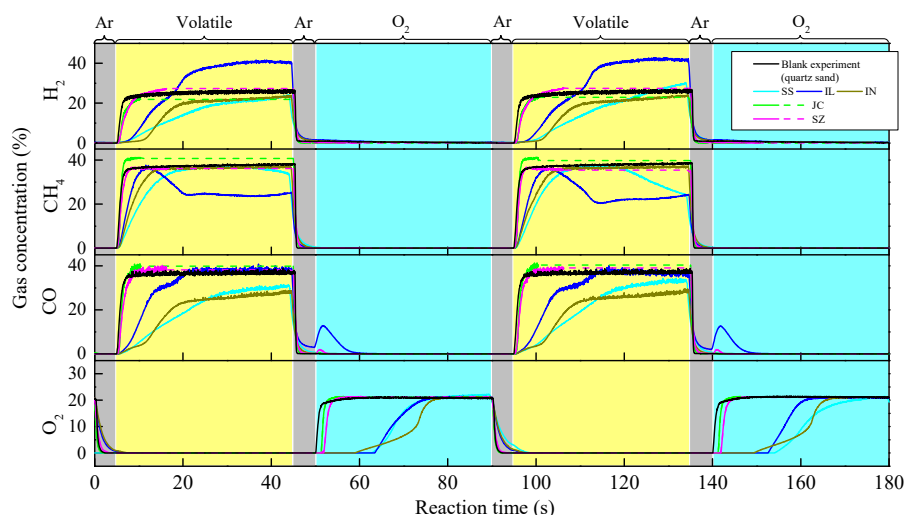
Fig. 4. Gas concentrations as a function of time for different material groups at 800℃, The dashed line indicates that the input gas types were switched after the concentrations were basically stable during the experiment, and the concentrations of these gases were regarded unchanged in this time range

The absorption capacities and conversion rates for different materials, gases, and temperatures can be obtained through calculation (the results calculated from the two cycles in Fig. 5 are averaged, summarized in Fig. 6 and Fig. 7). According to these quantitative analysis, the absorption capacities and conversion rates of IN are significantly higher than those of iron-lean JC and SZ coal ashes. Meanwhile, some values can be comparable to or even better than SS and IL, indicating the potential of Indonesian lignite ash as an excellent oxygen carrier.

(a)SS

(b)IL

(c)IN

(d)JC

(e)SZ
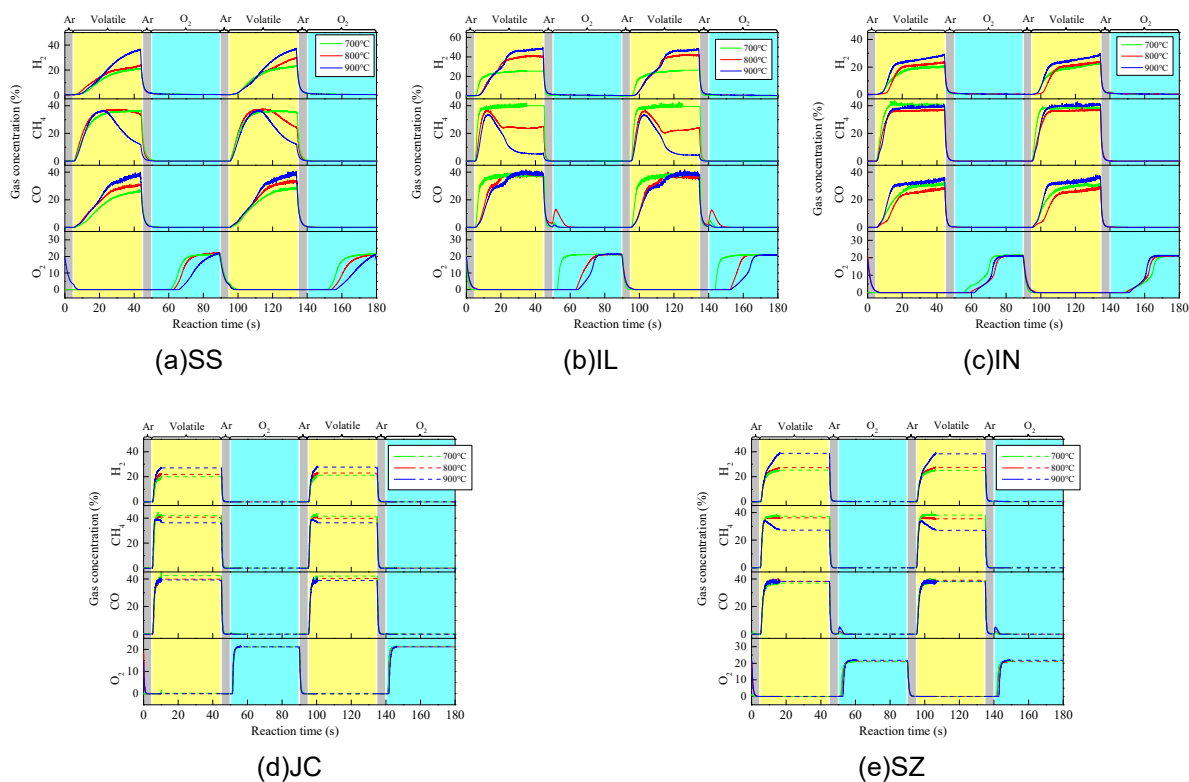
Fig. 5. Gas concentrations as a function of time for different material groups under different temperature

(a)Adsorption capacities for H_2 (b)Adsorption capacities for CH_4 (c)Adsorption capacities for CO   (d)Adsorption capacities for O_2
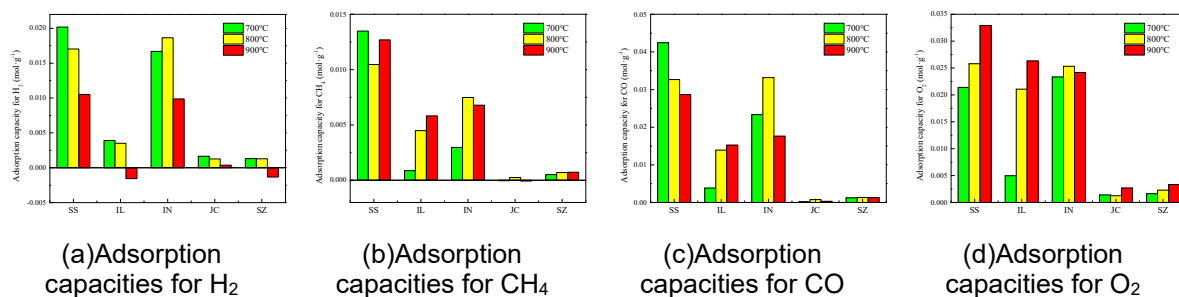
Fig. 6. Comparison of carrying capacity for different gases of different materials

(a)Conversion rates for H_2 (b)Conversion rates for CH_4 (c)Conversion rates for CO   (d)Conversion rates for O_2
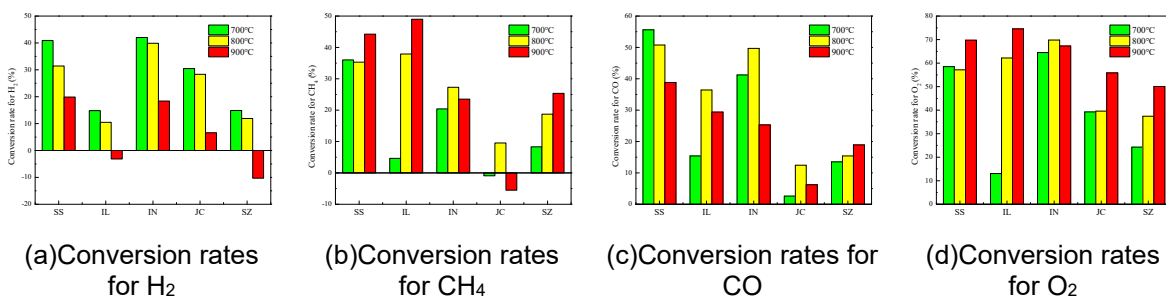
Fig. 7. Comparison of conversion rates for different gases of different materials

4. Conclusion

In order to confirm the potential of iron-rich coal ash as an oxygen carrier, this research conducted circulating experiments on the redox reactivity of different materials under different temperatures, in which iron-rich Indonesian coal ash, along with other coal ashes and typical oxygen carriers, experienced circulating redox process between biomass-volatile reducing gas and oxygen. Results show that Indonesian coal ash is an excellent oxygen carrier with high adsorption capacity and conversion rates for various reducing gas and oxygen comparable to typical oxygen carriers such as steel slag and ilmenite, which is mainly attributed to its high iron content (mainly in Fe_2O_3 form) and good pore characteristics. Considering there are more benefits for coal ash utilization such as waste disposal and potential abilities to improve operation performances and reduce NO_x emission(which remains to be further studied), it has promising industrial applications such as being an additive to improve combustion characteristics of biomass-fired CFB boilers.

Acknowledgment

References

Attah, M., Hildor, F., Yilmaz, D., et al. Vanadium recovery from steel converter slag utilised as an oxygen carrier in oxygen carrier aided combustion (OCAC). Journal of Cleaner Production. 2021. 293, 126159.

Diego, L., Francisco, G., Juan, A., et al. Development of Cu-based oxygen carriers for chemical-looping combustion. Fuel. 2004. 83(13),1749~1757.

Ishida M., Zheng D., Akehata T., Evaluation of a chemical-looping-combustion power-generation system by graphic exergy analysis, Energy. 1987. 12, 147–154.

Mattisson, T., Johansson, M., Lyngfelt, A., Multi cycle reduction and oxidation of different types of iron oxide particles application to chemical-looping combustion. Energy Fuels, 2004. 18(3), 628~637.

Pineau A., Kanari N., Gaballah I., Kinetics of reduction of iron oxides by H_2-part I: low temperature reduction of hematite, Thermochim. Acta. 2006. 447, 89–100.

Ryden, M., Hanning, M., Corcoran, A., et al. Oxygen carrier aided combustion (OCAC) of wood chips in a semi-commercial circulating fluidized bed boiler using manganese ore as bed material. Applied Sciences-Basel. 2016. 6(11), 347-347.

Yu, Z., Yang, Y., Guan, G., et al. Iron-based oxygen carriers in chemical looping conversions: a review. Carbon Resources Conversion. 2019. 2(1): 23-34.

Session E：

Combustion, pyrolysis and gasification

Numerical Simulation of Tar Conversion Process in Biomass Fluidized Bed Gasification Based on MP-PIC Method

Chun Wang, Qi Chen, Haiping Yang, Yingquan Chen, Hanping Chen, Xianhua Wang*

State Key Laboratory of Coal Combustion, Huazhong University of Science and Technology, Wuhan 430074, Hubei, China
Email: wangxianhua@hust.edu.cn

Abstract

This paper explores the generation and conversion processes of tars during fluidized bed gasification of biomass with a reactive multiphase particle-in-cell (MP-PIC) numerical model coupling with a tertiary tar (phenol + naphthalene + benzene) conversion model. The results show that the spatial and temporal scale distributions of these three types of tars in gasifier are non-uniform due to the strong irregular gas-solid interaction. During the gasification process, the primary tar is easily cracked and converted into other tars, and increasing steam to biomass ratio (S/B) and gasification temperature can reduce tar by enhancing steam reforming reaction and tar cracking reaction. A greater S/B (≥1.2) or a higher temperature (≥870°C) can effectively promote the conversion of secondary tar. And there is an optimal value of bed high for tar conversion，especially for naphthalene and benzene. This study could help lowering initial tar content in the fluidized bed gasifier.

1. Introduction

In the face of the new situation of accelerating the evolution of global energy to the direction of low-carbon and zero-carbon, implementing the new requirements of carbon peak and carbon neutrality, developing and utilizing non-fossil fuels, and steadily promoting the diversified development of biomass energy are the main ways to achieve a green and low-carbon energy transformation[1]. And, fluidized bed (FB) is a widely used gasifier in numerous biomass energy utilization devices, especially in industrial applications, which can convert low-quality biomass feedstocks into a versatile syngas[2]. FB has a wide applicability of raw materials, high gasification intensity, high heat and mass transfer efficiency and good potential of amplification[2]. However, as a by-product which is inevitable and difficult to remove during the gasification process, tar seriously affects the quality of syngas and is a key bottleneck restricting the application of biomass gasification technology[3]. And the generation and conversion of tar are closely related to the design and operation of FB gasifier. At the experimental level, researchers obtained tar content and composition at the outlet of FB gasifier through continuous or discontinuous measurement methods, and removed the tar by using catalysts inside or outside the gasifier. Benedikt et al.[4] established a valid correlation between gas components in the product gas and its tar content through online measurement in a dual FB to optimize operating parameters of gasification. Meng et al.[5] used a synthesized high abrasion resistant olivine as in-situ catalyst in a circulating FB gasifier. Compared with traditional bed material of silica sand, the tar content was reduced by 40.6%. Diego et al.[6] used four different catalytic filters for in situ removal of the real tar produced in a dual FB gasifier. They investigated the effects of temperature and velocity inside the reactor on tar removal rate, with a value of up to 95% at 850 °C.

However, traditional experimental research methods are often time-consuming and laborious, with long cycles and high costs. And there may be some interference factors (e.g. reactor structure, heat preservation, measurement method) that are difficult to eliminate during the experiment[7]. It is also difficult to understand the internal situation of the FB gasifier. Therefore, numerical simulation method provides a powerful tool to explore the generation and conversion of tar inside FB gasifier. Gerber et al.[8-10] used the Euler-Euler method and 2D Euler-Lagrange method to model a bubbling FB with char as bed material, exploring the effects of different pyrolysis models and operating parameters on the tar content at the

reactor outlet. They found that the operating parameters and model parameters had a significant impact on the tar content in the product gas. However, tar information inside the FB wasn't discussed in the study. Chen et al.[11] established a new tar cracking model based on a multi-step kinetic scheme through reactive molecular dynamics (MD), and combined computational fluid dynamics (CFD) to explore the high-temperature pyrolysis process of thick biomass particles. The improved model significantly improved the prediction accuracy of pyrolysis process. This study temporarily ignored the influence of other reactions such as devolatilization during gasification and used two-dimensional simplified simulation, which is expected to be applied in the simulation of three-dimensional actual FB. Mellin et al.[12] studied the specific components of tar as much as possible in a two-dimensional FB model, considering 134 substances and 4169 reactions, and thoroughly explored the rapid pyrolysis reactions of the products after secondary pyrolysis, such as free radical concentration. However, there is a lack of mutual conversion relationship between tar compositions, and it is difficult to consider detailed tar reactions in an actual three-dimensional FB simulation.

In order to explore the evolution process of tar in biomass FB gasification, a three-dimensional numerical model of biomass steam gasification in a spouted FB gasifier considering tar conversion is established based on the multiphase particle-in-cell (MP-PIC) approach, and used to investigate the effects of different S/B, gasification temperature, and initial bed height. This study preliminarily clarifies the generation and conversion of tars in biomass FB gasification, it contributes to the design and optimization of low-tar FB gasifiers in the future.

2. Mathematical model

2.1 Governing equations

In this work, a reactive MP-PIC model for biomass gasification is developed by the Eulerian-Lagrangian method, which is coupled with the gas-particle interactions, intensive heat tranfer and complex chemical reactions (especially the tar conversion reactions). In this model, the gas phase is described by solving the Navier-Stokes (N-S) equations in the Eulerian framework, while the solid phase is tracked by solving the Newton's law of motion as computational particles within the Lagrangian framework. And the two phases are coupled with the source term in the equations to exchange mass, momentum and energy. The gas turbulence is solved using the Large-eddy Simulation (LES). The detailed equations can be seen from previous studies[13, 14]. Based on relevant literatures[15-17], this work makes several assumptions: a) bed material and biomass particles are assumed spherical without deformation; b) heat conduction is neglected; c) particles are isothermal without thermal gradients; d) global reaction kinetics are used without elementary reactions.

2.2 Reaction kinetics

This work considers the drying, devolatilization, homogeneous and heterogeneous reactions of biomass in FB, and specifically introduces a tertiary tar (phenol + naphthalene + benzene) conversion model to study the generation and conversion processes of tars during biomass gasification. The specific reaction path is depicted in Fig.1.
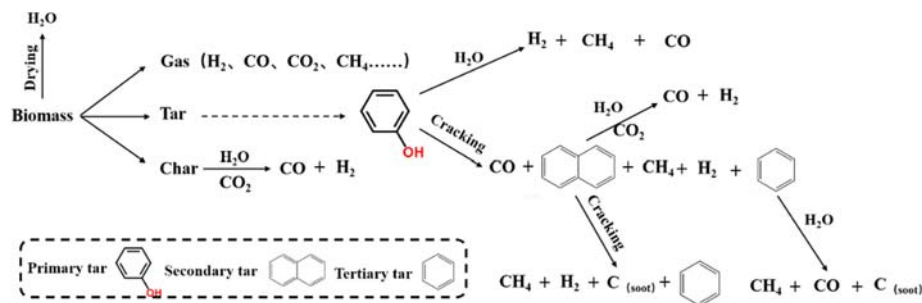
Fig. 1. Mechanism for the model of biomass gasification and tar conversion.

The reaction kinetic models are listed in Table 1, the heterogeneous reactions are described using the kinetic-diffusion mechanism, while the remaining reactions are formulated via the first-order Arrhenius laws[18-21].

Table 1. Reaction models used in this work

Reaction	Kinetics parameters
Drying	
$Moisture\ in\ Biomass_{(s)} \rightarrow H_2O(g)$	$r_1 = 5.13 \times 10^{10} e^{(-10585/T_p)} m_{moisture}$
Devolatilization	
$Biomass_{(dry)} \rightarrow Ash + Char + Volatiles(CO, CO_2, H_2, CH_4, Tar...)$	$r_2 = 5 \times 10^6 e^{(-14433/T_p)} m_{volatile}$
Heterogeneous reactions	
$C + CO_2 \rightarrow 2CO$	$A_{CO_2} = 8.3 s/(m \cdot K), E_{CO_2} = 4.37 \times 10^7 J/kmol, \beta_{CO_2} = 1.0$
$C + H_2O \rightarrow CO + H_2$	$A_{H_2O} = 45.6 s/(m \cdot K), E_{H_2O} = 4.37 \times 10^7 J/kmol, \beta_{H_2O} = 1.0$
Homogeneous reactions	
$CH_4 + H_2O \rightarrow CO + 3H_2$	$r_5 = 3 \times 10^8 T^0 e^{-15024/T} [CH_4][H_2O]$
$CO + H_2O \leftrightarrow CO_2 + H_2$	$r_6 = 2.78 \times 10^3 e^{-1515.52/T} ([CO][H_2O] - [CO_2][H_2]/(0.029 e^{(4089/T)}))$
Tar conversion reactions	
$C_6H_6O + 3H_2O \rightarrow 4CO + 2CH_4 + 2H_2$	$r_7 = 1 \times 10^7 e^{-12028/T} [C_6H_6O][H_2O]^3$
$C_6H_6O \rightarrow CO + 0.4C_{10}H_8 + 0.15C_6H_6 + 0.1CH_4 + 0.75H_2$	$r_8 = 1 \times 10^7 e^{-12028/T} [C_6H_6O]$
$C_{10}H_8 + 5CO_2 + 5H_2O \rightarrow 15CO + 9H_2$	$r_9 = 4.3 \times 10^{13} e^{-39932/T} [C_{10}H_8]^{0.2} [H_2]^{0.3}$ (modified)
$C_{10}H_8 \rightarrow 7.38C + 0.275C_6H_6 + 0.97CH_4 + 1.235H_2$	$r_{10} = 3.39 \times 10^{14} e^{-42098/T} [C_{10}H_8]^{1.6} [H_2]^{-0.5}$
$C_6H_6 + 2H_2O \rightarrow 1.5C + 2.5CH_4 + 2CO$	$r_{11} = 3.39 \times 10^{16} e^{-53284/T} [C_6H_6]^{1.3} [H_2O]^{0.2} [H_2]^{-0.4}$

3. Numerical condition

3.1 Model description

In this work, parameters for the 3D reactor model are sourced from a lab-scale interconnected FB system for biomass gasification at Southeast University, as shown in Fig.2 (a)[22]. The reactor primarily comprises a spout-fluid bed (as a gasifier) and a high velocity FB (as a combustor). And in this work, the high velocity FB has been simplified and replaced by a thermal wall for heating, as shown in Fig.2 (b), the cross-section of the spout-fluid bed is rectangular with 40 ×230 mm², and a height of 1500 mm. And the bottom is connected a 60° conical gas distributor with an inlet tube of 20mm diameter, through which biomass particles and steam are fed into the spout-fluid bed. The biomass particle used in this work is pine and the bed material is silicon sand. And the material properties and main operating parameters are set based on the experimental data of Song et al[22]. In simulation, the top of the reactor is set as a pressure boundary condition, where gas and particles can leave the reactor through the pressure boundary. An injection boundary condition is set at the bottom of gas distributor, where biomass, protective gas, and steam are injected into the reactor together. Walls are set as constant temperature boundary condition to provide heating for gasification[23].
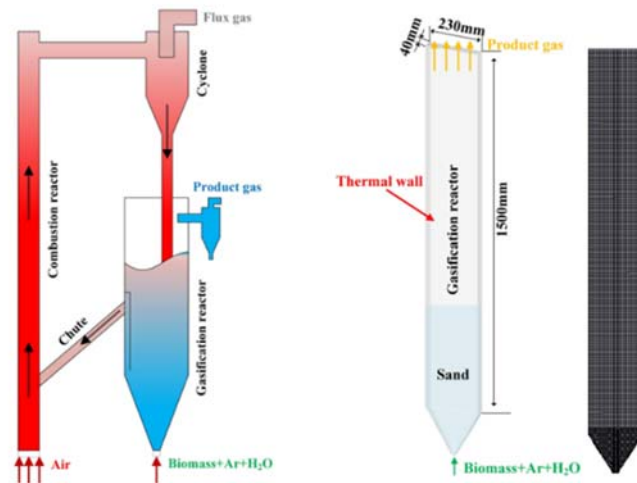
Fig. 2. Model setup: sketch and geometric model with boundary parameters.

3.2 Model validation

Firstly, four sets of grids with different thicknesses are divided for grid independence verification. The distribution of solid holdup along the vertical height under different grids is shown in Fig.3 (a). Except for the coarse grid, the solid holdup of other grids is similar. Considering the calculation speed and simulation accuracy, mediate grid number is selected for subsequent simulations. The comparison of the dry gas and tar content between numerical simulation results and experimental results is shown in Fig.3 (b). It can be seen that the numerical simulation results are basically consistent with the experimental results. The error is mainly due to the simplification of three-dimensional model and chemical reaction model[24]. The MP-PIC model in this work is reasonable and reliable for the simulation of biomass FB gasification process.
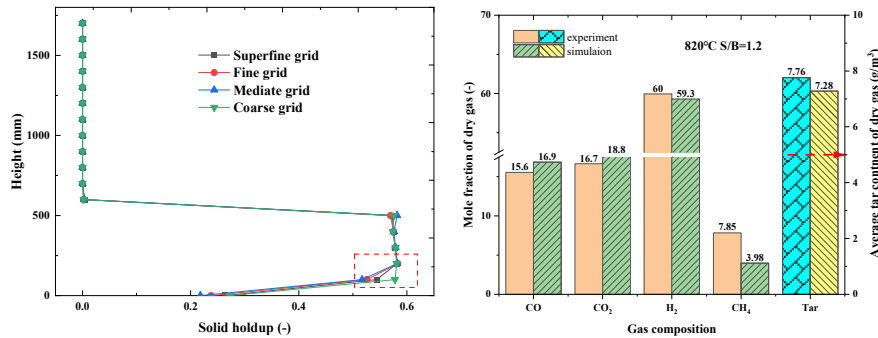
Fig. 3. Model validation: grid independence validation and model validation.

4. Results and discussion

4.1 Tar flow pattern

The instantaneous distribution of particles and tars in the FB is shown in Fig.4. From Fig.4 (a), it can be seen that during the gasification process, bubbles continuously generate, expand, rise, and rupture from the bottom, thereby carrying biomass particles and mixing with the bed material. Biomass tends to accumulate on the surface of the bed, with some particles are blown to the upper part of the bed and then fall from the sidewall. And due to the strong gas-solid flow, heat and mass transfer, and chemical reactions in the FB, transient gas-solid flow is not completely symmetrical[25]. From Fig.4 (b), Fig.4 (c), and Fig.4 (d), it can be seen that three types of tars mainly generate on the surface of the bed, where biomass accumulates, and undergoes cracking and transform at the upper part of the bed, with non-uniform distributions at both spatial and temporal scale.
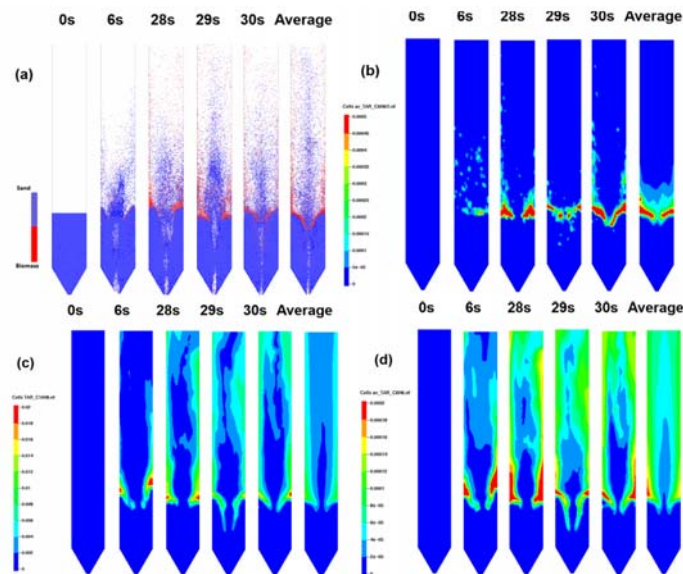
Fig. 4. Instantaneous distribution of flow pattern: (a) particle species; (b) C_6H_6O; (c) $C_{10}H_8$; (d) C_6H_6.

4.2 Tar distribution

The distribution of tars in the FB is shown in Fig.5. In the vertical direction, there is a sudden rise of tar content above the surface of the bed, and among these three types of tars, the phenol (primary tar) ratio is the least (about 0.01%), and the naphthalene (secondary tar) ratio is the highest (about 98.5%). In the horizontal direction, the overall distribution of tar is like U-shaped, which is similar to the distribution of biomass particles in Fig.4. Phenol only exists in a narrower area of the bed surface, while naphthalene and benzene exist in a wider area above the bed, indicating that most phenol is converted into naphthalene on the bed surface, and then slowly converts into benzene (about 1%) along the vertical height.
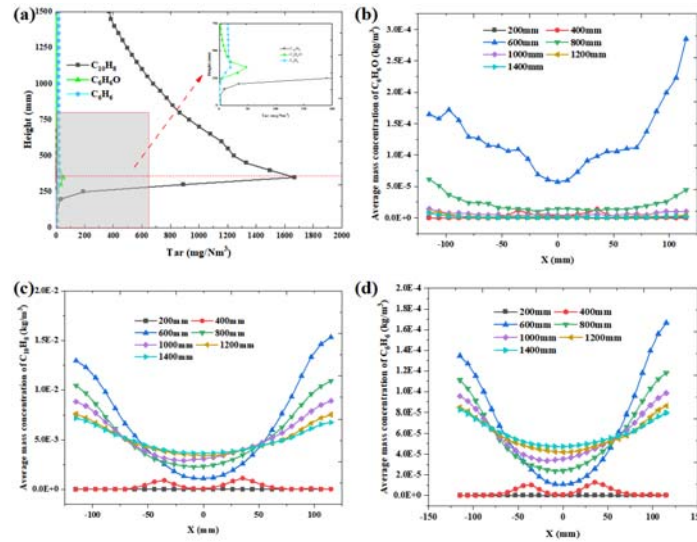
Fig. 5. Average mass concentration of tar distribution profile: (a) vertical distribution of tars; (b) horizontal distribution of C_6H_6O; (c) horizontal distribution of $C_{10}H_8$; (d) horizontal distribution of C_6H_6.

4.3 Effect of operating parameters
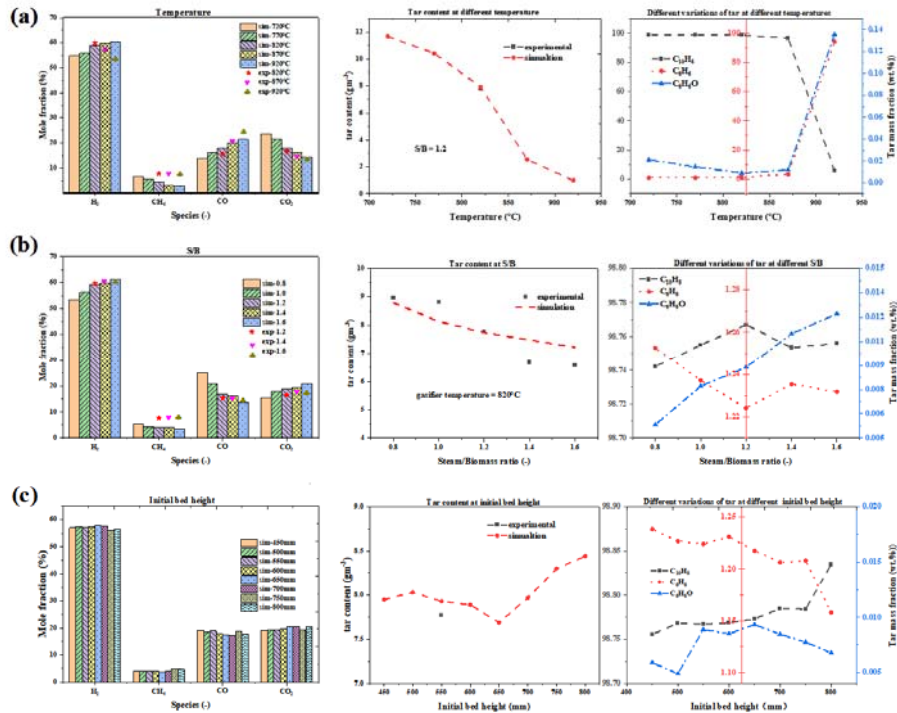
Fig. 6. Effect of operating parameters on the composition of syngas and tar: (a) temperature; (b) S/B; (c) initial bed height.

The distributions of syngas compositions, tar content, and tar compositions under different operating parameters (temperature, S/B, and initial bed height) are shown in Fig.6. It can be seen that the increase of S/B (0.8~1.6) can enhance the steam reforming reaction of tar, resulting in the decrease of overall tar content (8.83~7.26 g/m^3). When S/B is increased from 0.8 to 1.2, the relative amounts of naphthalene and phenol gradually increase. When S/B is greater than 1.2, naphthalene gradually decreases and is converted into benzene. The temperature has the most significant impact on the tar content and tar conversion, increasing the gasification temperature (720°C~920°C) can significantly reduce the tar content (11.67~0.98 g/m^3). The relative amounts of these three types of tars are stable below 870°C, and a large amount of naphthalene (about 94%) is converted into benzene when the temperature exceeds 870°C. The initial bed height of the FB has an optimal value (650mm) for the lower tar yield. Below the optimal value, the heat transfer of the bed material slows down and the conversion rate of biomass decreases. Above the optimal value, the tar residence time and the conversion degree from secondary tar to tertiary tar decrease.

5. Conclusion

This study used MP-PIC method to study the evolution behavior of tars during biomass gasification in FB, preliminarily clarifies the generation and conversion of tars, it will contribute to the design and optimization of FB gasifier for lower tar yield in the future. The results show that the generation and cracking conversion of tar depend on the gas-solid flow pattern and the mixing form between the bed material and biomass particles. During the gasification process, the primary tar is easily cracked and converted into other tars, and the content of primary tar in the exported tar is very low. It is possible to promote the conversion of secondary and tertiary tars as much as possible under an optimal gasification condition, including suitable temperature, S/B, and initial bed height.

Acknowledgment

References

[1] Ndrc. 14th Five-year plan for renewable energy development[R]. National Energy Administration, 2022.
[2] Chew J W, Lamarche W C Q, Cocco R A. 100 years of scaling up fluidized bed and circulating fluidized bed reactors. Powder Technology. 2022, 409: 117813.
[3] Devi L, Ptasinski K J, Janssen F J J G. A review of the primary measures for tar elimination in biomass gasification processes. Biomass and Bioenergy. 2003, 24(2): 125-140.
[4] Benedikt F, Kuba M, Schmid J C, et al. Assessment of correlations between tar and product gas composition in dual fluidized bed steam gasification for online tar prediction. Applied energy. 2019, 238: 1138-1149.
[5] Meng J, Wang X, Zhao Z, et al. Highly abrasion resistant thermally fused olivine as in-situ catalysts for tar reduction in a circulating fluidized bed biomass gasifier. Bioresource Technology. 2018, 268: 212-220.
[6] Diego L F, Garcia-Labiano F, Gayan P, et al. Tar abatement for clean syngas production during biomass gasification in a dual fluidized bed. Fuel Processing Technology. 2016, 152: 116-123.
[7] Wang S, Hu C, Luo K, et al. Multi-scale numerical simulation of fluidized beds: Model applicability assessment. Particuology. 2023, 80: 11-41.
[8] Gerber S, Behrendt F, Oevermann M. An Eulerian modeling approach of wood gasification in a bubbling fluidized bed reactor using char as bed material. Fuel. 2010, 89(10): 2903-2917.
[9] Gerber S, Oevermann M. A two dimensional Euler–Lagrangian model of wood gasification in a charcoal bed – Part I: model description and base scenario. Fuel. 2014, 115: 385-400.
[10] Gerber S, Oevermann M. A two dimensional Euler-Lagrangian model of wood gasification in a charcoal bed — Part III: Parameter influence and comparison. Powder Technology. 2017, 310: 163-174.

[11] Chen T, Ku X, Li T, et al. High-temperature pyrolysis modeling of a thermally thick biomass particle based on an MD-derived tar cracking model. Chemical Engineering Journal. 2021, 417: 127923.

[12] Mellin P, Yu X, Yang W, et al. Influence of Reaction Atmosphere (H2O, N2 , H2 , CO2 , CO) on Fluidized-Bed Fast Pyrolysis of Biomass Using Detailed Tar Vapor Chemistry in Computational Fluid Dynamics. Industrial & Engineering Chemistry Research. 2015, 54(33): 8344-8355.

[13] Snider D M, Clark S M, O'Rourke P J. Eulerian–Lagrangian method for three-dimensional thermal reacting flow with application to coal gasifiers. Chemical Engineering Science. 2011, 66(6): 1285-1295.

[14] Zhu X, Wang Z, Ocone R, et al. MP-PIC simulation on CO_2 gasification of biomass in a pilot plant circulating fluidized bed gasifier. Fuel. 2023, 332: 125992.

[15] Zhou M, Wang S, Luo K, et al. Three-dimensional modeling study of the oxy-fuel co-firing of coal and biomass in a bubbling fluidized bed. Energy. 2022, 247: 123496.

[16] Wan Z, Yang S, Hu J, et al. Numerical analysis of wood air gasification in a bubbling fluidized gasifier with reactive charcoal as bed material. Renewable Energy. 2022, 188: 282-298.

[17] Tokmurzin D, Nam J Y, Park S J, et al. Three-Dimensional CFD simulation of waste plastic (SRF) gasification in a bubbling fluidized bed with detailed kinetic chemical model. Energy Conversion and Management. 2022, 267: 115925.

[18] Yang S, Liu X, Wang S, et al. Eulerian-Lagrangian simulation study of the gas-solid reacting flow in a bubbling fluidized coal gasifier. Chemical Engineering Journal. 2021, 426: 130825.

[19] Yang S, Liu X, Wang S. CFD simulation of air-blown coal gasification in a fluidized bed reactor with continuous feedstock. Energy Conversion and Management. 2020, 213: 112774.

[20] Ding H, Ouyang Z, Su K, et al. Investigation of gas-solid flow characteristics in a novel internal fluidized bed combustor by experiment and CPFD simulation. Advanced Powder Technology. 2023, 34(3): 103962.

[21] Ji P, Feng W, Chen B. Production of ultrapure hydrogen from biomass gasification with air. Chemical Engineering Science. 2009, 64(3): 582-592.

[22] Song T, Wu J, Shen L, et al. Experimental investigation on hydrogen production from biomass gasification in interconnected fluidized beds. Biomass and Bioenergy. 2012, 36: 258-267.

[23] Yan L, Lim C J, Yue G, et al. Simulation of biomass-steam gasification in fluidized bed reactors: Model setup, comparisons and preliminary predictions. Bioresource Technology. 2016, 221: 625-635.

[24] Gupta S, Choudhary S, Kumar S, et al. Large eddy simulation of biomass gasification in a bubbling fluidized bed based on the multiphase particle-in-cell method. Renewable Energy. 2021, 163: 1455-1466.

[25] Wang S, Luo K, Fan J. CFD-DEM coupled with thermochemical sub-models for biomass gasification: Validation and sensitivity analysis. Chemical Engineering Science. 2020, 217: 115550.

ESTIMATION OF BED DRAINAGE DISCHARGE TO PREVENT AGGLOMERATION BASED ON EXPERIMENTAL DATA AND CALCULATIONS OF CHANGES IN POTASSIUM CONTENT IN THE BED

Georgy Ryabov*, Dmitriy Litun, Oleg Folomeev, Elena Shorina

All Russia Thermal Engineering Institute, Avtozavodskay14, Moscow, Russia

Corresponding Author: G. Ryabov georgy.ryabov@gmail.com, GARyabov@vti.ru

Abstract

The study of the agglomeration of 4 types of biomass was carried out in the fixed bed. The experimental techniques and characteristics of biomass are described. The influence of temperature on the proportion of formed agglomerates was established. The microstructure and chemical composition of agglomerated particles were studied using a scanning electron microscope equipped with an energy dispersive microanalysis system. The obtained data are compared with the results of similar experiments carried out under fluidized bed conditions. To assess the drainage of the bed, the equations of material balance and the balance of sodium and potassium compounds were written. The calculation techniques and calculated data obtained with use of them on the behavior of the potassium concentration in the bed under various conditions are presented.

1. Introduction

Bed agglomeration is among the most important issues when combusting biomass, primarily agricultural and some industrial waste, in a fluidized bed (FB) with sand as traditional bed inventory. It can lead to sintering of bed material and to defluidization. The processes of bed agglomeration have been studied for over 20 years, but the same problems still arise during the boilers operation [1]. Author's analyzed [2], the world-wide studies aimed at identifying the basic laws of agglomeration processes in fluidized bed boilers during of biomass combustion. It was shown that the alkaline ash components, which react with silicates and form low-melting eutectics, have the greatest effect on the agglomeration processes. Therefore, the determination of the critical concentration of the most low melting eutectics in the bed—primarily potassium in the compound with silicon—the formation of which gives rise to sintering of particles, is among the most important problems.

Data on the critical concentration vary widely. It was reported in [3] that the critical concentration of K_2CO_3 in the bed at temperatures above 800°C is 1 wt %, which corresponds to 0.6 wt % of potassium in the corresponding chemical form. In [4], critical potassium concentrations in the bed were determined on the basis of the results of corn cobs combustion in an FB boiler, which were in the range from 1.25 wt % at 800°C to 0.93 wt % at 850°C. A review of measures used to prevent agglomeration is given in [1, 5, 6]. In addition to the use of co-firing technology with coal and the use of various additives and bed materials, the increasing of bed drainage with a corresponding addition of fresh inert material is a traditional way to prevent bed agglomeration. In [7], the data of domestic studies were analyzed to draw up the following recommendations for preventing bed agglomeration: the creation of the increased bed drainage and the addition of fresh sand.

2. The experimental techniques and characteristics of biomass

We wanted to get answers to the following questions: what happens if you put a mixture of biomass ash and sand in a furnace and make a temporary exposure? How to bring conditions closer to reality? Will the structure of the formed agglomerates be similar to those obtained during combustion in a fluidized bed? Can such experiments without fluidization be similar to experiments with fluidization?

The experiments were carried out in a laboratory furnace on biomass ash, sand, and a mixture of sand and ash with a sample weight of 5 g. A layer of material was poured onto a substrate with a bed height at the level of 2–3 particle diameters (1–2 mm). The temperature range was 670–900 °C. Exposure of samples varied from 15 minutes to an hour at a constant temperature. Then the samples were taken out, cooled, and the unsintered material was weighed. Sunflower husk ash # 1 from Elevator LLC (Kumertau), sunflower husk pellet ash # 2 (Tambov), wood construction waste ash # 3 (Moscow region) and peat pellet ash # 4 were used as biomass. The composition of ash is presented in Table 1.

Table 1 - Compositions of the ashes of various origins wt %.

Components	# 1	# 2	# 3	# 4
SiO_2	2,94	14,32	9,46	50,50
TiO_2	0,05	0,36	0,32	0,68
Al_2O_3	0,85	2,83	1,52	15,15
Fe_2O_3	0,5	11,45	5,11	9,11
CaO	26,98	11,31	35,17	11,20
MgO	14,16	8,19	4,25	2,71
K_2O	36,46	25,73	3,96	1,30
Na_2O	0,74	3,44	0,62	0,45
P_2O_5	5,27	6,81	2,31	1,77
SO_3	12,05	7,57	7,31	7,13
CO_2	-	7,99	26,8	-

Preliminary experiments showed that the exposure time from 15 minutes to 1 hour did not play a significant role. It was customary to conduct experiments with an exposure of 1 hour. It is important to choose the ash concentration in the mixture with sand. For this, experiments were carried out on mixtures with an ash content of 5 to 50% at a temperature of 850–900 °C. It turned out that for ash (1) the influence of the ash fraction is not significant - in all cases, almost complete sintering occurred. When starting an FB boiler, only sand is in the bed, then, in the process of operation, it is partially replaced by fuel ash. As applied to coals with high ash content, the stabilization occurs after about 2 days of operation [8]. For biomass with low ash content, this process is longer. The content of SiO_2 in the bottom ash decreases significantly, and in the case of a small agglomeration after one week of operation it becomes equal to 92.4% [7]. This means that in bottom ash (with SiO_2 content in biomass ash of 26.6%) there is almost 9% of biomass ash. As a result, we can conclude that the accepted value of the ash concentration in the mixture with sand of 5% quite well reflects the real situation for FB boilers. An increase in the concentration of potassium and sodium was carried out by adding a solution of KCl and NaCl, followed by drying at room temperature. Methodically, our approach is similar to that applied in [3]. The experiments were carried out with the addition of KCl solutions of different concentrations (from 3 to 36%) to the ash (4). The concentration of potassium in a mixture with sand was from 538 ppm to 8450 ppm.

3. The calculation techniques experimental result and discussio

It should be noted that for all ashes there is a background fraction of agglomerated particles at low temperatures. If we take peat pellet ash (4) as completely non-agglomerating ash, then this value is 3-5%. Apparently, this is due to the adhesion of a small fraction of particles to the metal grid during heat treatment. With a subsequent increase in temperature, the proportion of agglomerates only slightly increases. This temperature roughly corresponds to the melting temperature of potassium tetra- and disilicates. Agglomerates at relatively low temperatures are not strong and may disintegrate. However, even the intensification of mass transfer in a fluidized bed only slows down this process in time. On fig. 1 shows the effect of temperature on the proportion of agglomerates for ash (1), (2) and ash (4) with the addition of the maximum amount of potassium and sodium.

All curves almost coincided, which is not surprising, since the concentration of alkaline elements in the mixture is very high and is in a narrow range of 1.08–1.53%. The last series of experiments involved a change in the bed material. Next, the analysis of the unloaded agglomerates during the heat treatment of ash 1 with sand was performed using an electron

microscope. Of interest is the microstructure of large, not yet completely melted particles of ash #1 and sand (Fig. 2). Analysis of the microstructure shows that there are both completely melted large particles and rough agglomerated groups of particles.
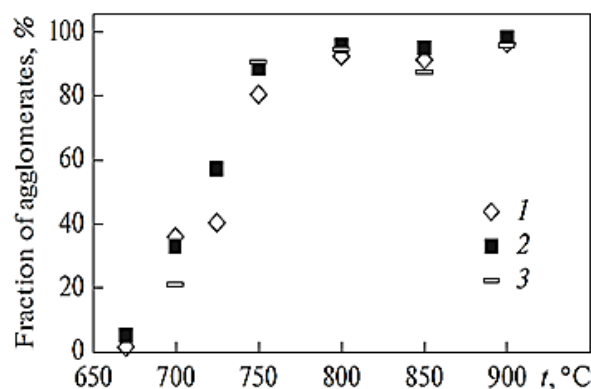
Fig. 1. Temperature dependences of the fraction of the agglomerates for (1) ash no. 1, (2) ash no. 2, and (3) ash no. 4 with the maximum amounts of potassium and sodium.
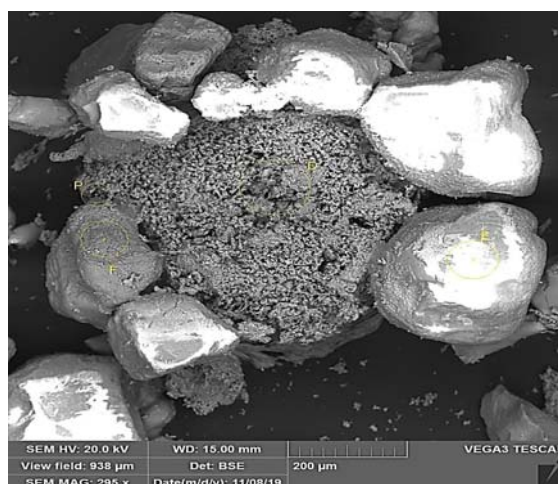
Fig.2. Microstructure of large incompletely melted particles

Table 2 shows the characteristic concentrations of elements on the surface of particles in the zones according to Fig. 2. The microdispersion analysis of the zones on the surface of these particles showed that the porous groups of particles (region F) contain a lot of calcium, potassium, and magnesium, while the melted particles contain much more silicon and oxygen. This is typical for all processing temperatures, despite significant fluctuations in concentrations across zones.

Table 2. Data on the elements share on the surface of particles in different zones of Fig. 2.

	D zone	E zone	F zone
O	64.32	54.96	38.50
Na	1.20	1.06	0.77
Mg	0.53	1.11	4.10
Al	2.50	1.51	0.50
Si	23.51	27.34	2.21
P	0.19	0.51	1.76
S	0.58	1.07	10.05
K	5.71	8.46	24.61
Ca	1.07	2.22	15.03
Cr	0.09	0.34	1.11
Fe	0.30	1.41	1.37
Summa	100.00	100.00	100.00

The authors of [9] believe that the smooth appearance of the film indicates that it was melted during combustion. As our experiments show, smooth particles can become smooth even without combustion. As a result, it can be stated that the appearance and composition of the agglomerates in our experiments are close to those characteristic under fluidization. The accumulation of potassium in the bed at different temperatures was analyzed in [9]. Knowing the test rig sizes, the mass of sand, the consumption of biomass and the potassium content, it is possible to calculate the values of the limiting concentrations for different bed temperatures. Such a calculation was made both for the conditions of the particles accumulation and taking into account the decrease in potassium concentrations. Figure 3 shows a comparison of our data with the data [9], as well as the results of [4, 10]. Our data give the lowest value of critical concentrations, especially for bed temperatures below 800 °C. At the same time, it should be noted that in [4, 9, 10], the critical concentrations correspond to the loss of fluidization, and not to the beginning of bed agglomeration.
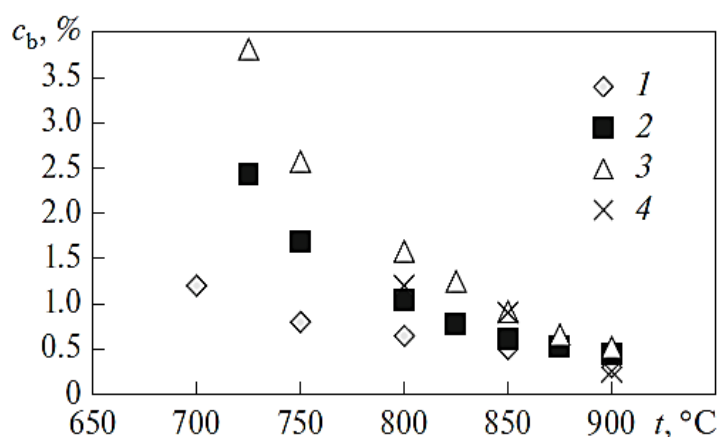
Fig. 3. Critical concentration of potassium in the bed as a function of the temperature for (1) the data obtained in this study, (2) the data [9] when taking into account a decrease in the potassium concentration, (3) the data [9] in accordance with the material balance, and (4) the data [4, 10].

It is of interest to study the change in the potassium concentration in the bed during operation of FB boilers. This task is important for the practice of using one of the methods to prevent agglomeration – bed drainage.

4. The calculation techniques and calculated data

The first attempt to estimate the required bed drainage rate was made in [7]. This approach is based on the analogy of a fluidized bed and steam bubbling in the drum. There is similar to the calculation of the salt balance in the drum of a boiler with natural circulation. It should be remembered that continuous and periodic water blowdowns from the boiler drum are necessary in order to maintain the required quality of steam and boiler water. The continuous blowdown usually requires 0.5–1% of the steam rate, and the intermittent blowdown can entail up to 5% of it. The equation for changing the concentration of potassium in the bed can be written as follows:

$$M\frac{dc_b}{d\tau} = G_a c_a a_{entr.a} + G_a c_{entr} - \left(1 - a_{entr.a}\right)G_a c_{dr} - G_{entr} c_{bs} + G_s c_{sr} \quad (1)$$

Where M is the mass of the bed, kg; c_b, c_a, c_{dr}, and c_{bs} are the concentrations of potassium in the bed, fuel ash, bed drainage, and bed sand, respectively; τ is the time, s; G_a is the fuel ash flow rate, kg/s; a_{entr} is the fraction of the entrained sand; G_{entr} is the entrained sand discharge rate, kg/s; G_s is the added sand flow rate, kg/s; and c_s is the concentration of potassium in the added sand.

The flow rate of the incoming ash is

$$G_a = B_c A_c \quad (2)$$

225

Where B_c is the calculated fuel consumption rate, kg/s, and A_c is the ash content

The mass of the bed is determined by cross-sectional area F_b (m^2) of the bed, its height h_b (m), and bulk density ρ_s (kg/m^3) according to the following formula:

$$M = F_b h_b \rho_s \tag{3}$$

The cross section of the bed is selected based on velocity U_b (m/s) in the bed. The formula for calculating the cross-sectional area of the bed can be written as follows:

$$F_b = \frac{B_c \beta_b V_g}{U_b} \frac{273 + t_b}{273} \tag{4},$$

Where V_g is the theoretically required volume of gases, m^3/rg; and t_b is the temperature in the bed, °C, β_b –air fraction in the layer from theoretically necessary.

Ratio K of the mass of the bed to the flow rate of the incoming ash depends on the fuel properties and the gas velocity in the bed, while the fuel consumption is reduced as follows:

$$\frac{M}{B_c A_c} = K = \frac{h_b B_c \beta_b V_g}{B_c A_c U_b} \frac{273 + t_b}{273} \tag{5}$$

It was found that the K ratio for fluidized bed varies within a fairly narrow range of 60–110 h^{-1}.

The fraction of entrainment is 0.95, of which 0.07 falls on sand (the fraction of the entrained fuel ash is 0.88). Under these conditions, it can be assumed that $c_s = 0$ and $c_{dr} = c_b$. Hence, equation (1) is simplified and can be written as follows:

$$K \frac{\Delta c_b}{\Delta \tau} = 0.12 c_a - c_b (0.07 + a_{dr}) \tag{6}$$

Where $\Delta \tau$ is the time interval, s; and $a_{dr} = G_{dr}/G_a$. If there is no additional drainage and no sand addition, then $a_{dr} = 0.05$.

Calculations were performed for the two types of biomass: bark and wood waste (BWW) produced by a pulp and paper mill (PPM) (the content of potassium in ash is approximately 10% [7]) and sunflower husks with the characteristics given in Table 1. The results of calculations during the co- combustion of sunflower husks and anthracite culm (AC) are shown in fig. 4. This account was made based on the data [10], which showed that in a bed of iron ore with a Fe$_2$O$_3$ concentration of 39%, the critical concentration increases by about 3 times. In our experiments, it also increased by about 3 times at 50% Fe$_2$O$_3$ in the bed to 1.6% at a temperature of 850 °C.
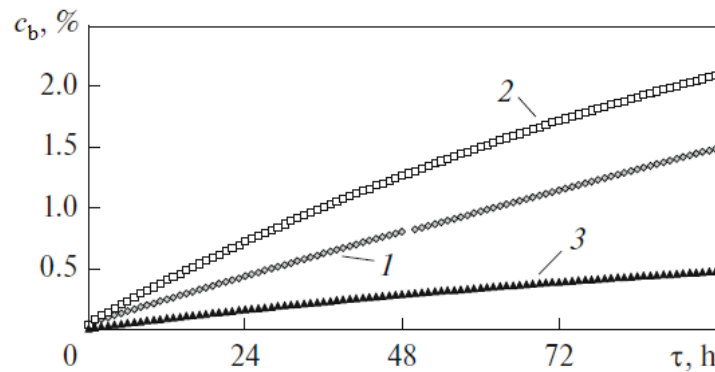
Figure 4. Co-combustion of husks and coal (AC)
(1) separate combustion of husks, (2) co-combustion of husks together with AC and (3) co-combustion of husks with coal when taking into account iron oxides in AC

This means that about 2/3 of potassium reacts with iron oxides, respectively, the conditional concentration of potassium in the bed, leading to agglomeration, decreases proportionally. With such a simplified assessment, it turns out that the co- combustion of AC and sunflower husks does not lead to agglomeration.

Conclusions

The results of experiments on the proportion of agglomerated particles at different temperatures and concentrations of alkaline elements in the bed are presented. The onset temperature of agglomeration depends to the greatest extent on the potassium concentration. At a high concentration of potassium in the ash, agglomeration occurs already at 750 °C. Agglomerates at relatively low temperatures are not strong and may disintegrate. When replacing the bed material from sand to iron oxides and their mixture with sand, agglomeration occurs only at high temperatures (850 °C or more), and the critical concentration of potassium in the bed increases by a factor of 3 or more.

The results are compared with similar experiments during fluidization, the mechanisms of agglomeration, the effect of fluidization rate, particle size and excess air are considered. It can be stated that the appearance and composition of the agglomerates in our experiments are close to those characteristic under fluidization conditions. Based on the comparison, it was noted that experiments with a fixed bed give the lowest value of critical concentrations, especially for conditions of relatively low bed temperatures - below 800 °C.

A calculation procedure has been developed and calculated data on the change in the potassium concentration in the bed under various conditions are presented. It is shown that for BWW, an increase in drainage flow to 1% of fuel consumption reduces the concentration of potassium in the layer by 40%. To burn husks, a much larger bed drainage is required – 5%. The results of calculations during the combustion of sunflower husks and anthracite culm (AC) showed that for conditions of 50% combustion of husks and 50% AC in terms of heat, agglomeration sharply decreases due to the high content of iron oxides in AC ash.

References

[1] F. Scala. Particle agglomeration in fluidized beds: Mechanisms, early detection and possible countermeasures, in Proc. 12th Int. Conf. on Fluidized Bed Technology, Kraków, Poland, May 23–26, 2017 (Fundacja dla Akademii Górniczo-Hutniczej im. Stanisława Staszica, Kraków, 2017), pp. 65–76.

[2] G. A. Ryabov and D. S. Litun. Agglomeration during fluidized bed combustion and gasification of fuels, Therm. Eng. 66, 635–651 (2019). https://doi.org/10.1134/S0040601519090040.

[3] P. Yrjas, C. Sevonius, and M. Hupa. Bed agglomeration due to addition of KCl and K_2CO_3 — First results from a laboratory fluidized bed reactor, in Proc. 21st Int. Conf. on Fluidized Bed Combustion, Naples, Italy, June 3–6, 2012, pp. 203–210.

[4] B. G. Grubor, S. N. Oka, M. S. Ilic, D. Dakic, and B. Grubor. Biomass FBC combustion — Bed agglomeration problems. in Proc. 13th Int. Conf. on Fluidized Bed Combustion, Orlando, Fla., May 7–10, 1995 (American Society of Mechanical Engineers, New York, 1995), Vol. 1, pp. 515–522.

[5] V. Mettanant, P. Basu, and J. Butler. Agglomeration of biomass fired fluidized bed gasifier and combustor. Can. J. Chem. Eng. 87, 656–684 (2009).

[6] Y. Niy, H. Tan, and S. Hui. Ash-related issues during biomass combustion: Alkali-induced slagging and related countermeasures. Prog. Energy Combust. Sci. 52, 1–61 (2016). https://doi.org/10.1016/j.pecs.2015.09.003.

[7] G. A. Ryabov, D. S. Litoun, and E. P. Dik. Agglomeration of bed material: Influence on efficiency of biofuel fluidized bed boiler. Therm. Sci. 7 (1), 5–16 (2003). https://doi.org/10.2298/TSCI0301005R.

 [8] Su-Xia Ma, Jun Guo, Wei-Ming Chang, Guang-Xi Yue, and Hai Zhang.The dynamic balance of bed material size distribution in start-up process for circulating fluidized bed boiler. in Proc. 22nd Int. Conf. on Fluidized Bed Combustion, Turku, Finland, June 14–17, 2015 (Juvenes Print, Turku, Finland, 2015), pp. 788–796.

[9] W. Lin, K. Dam-Johansen, and F. Frandsen. Agglomeration in bio-fuel fired fluidized bed combustors. Chem. Eng. J. (Amsterdam, Neth.) 96, 171–185 (2003). https://doi.org/10.1016/j.cej.2003.08.008.

[10] B. Grubor, M. Ilec, and D. Dakic. Hematite — A definite solution for FB combustion of biomass, in Proc. 3rd Int. Heat and Mass Transfer Forum (MIF-96), Minsk, May 20–24, 1996 (Inst. Teplo- i Massoobmena im. A. V. Lykova, Minsk, 1996), pp. 227–234.

SLUDGE ASH PERFORMANCE OF OXYGEN-CARRYING AND CATALYSIS ON WET SLUDGE GASIFICATION

Sheng Yao, Kun Wang, Peng Ni, Xiaoying Yuan, Yusheng Zhang, Cuiping Wang*

Clean Energy Lab, Shandong University of Science and Technology, Qingdao, Shandong Province, China, 266590

* wangcuiping@tsinghua.org.cn

Abstract

In the city sewage treatment process, polymeric iron is commonly used as coagulant, which finally enters the sludge and causes a rich iron content sludge. During the sludge incineration process, the sludge particles always shrink and burn into strengthened ash, which could be oxygen carriers (OCs) in chemical looping for its iron oxide component. The redox multi-cycle experiments using incinerated sewage sludge ash (ISSA) particles as OCs in Thermal Gravimetric Analysor (TGA) with alternate CO/Air atmosphere was carried out, and the iron oxide in ISSA has a stable oxygen carrying capacity of 3-10%, which is suitable to be an OC for chemical looping gasification (CLG) of wet sludge. Moreover, in a lab-scale fluidized bed reactor, the multi-cycle reactions of gasification of sludge particles and air regeneration of OCs were carried out using ISSA particles as bed materials and oxygen carriers. With the accumulation of sludge ash particles in the bed, the hydrogen content in the syngas component shows a decreasing trend from 35-37% after the third cycle and a significant decrease after five cycles. The content of methane (9-15%) and carbon dioxide (around 40%) gases remains stable. The optimal O/C (oxygen content of iron oxide in ISSA to carbon content in sludge) is determined according to the flow rate in the third cycle, so the best circulating rate of ISSA to act as OC is 3-5, the oxygen carrier capacity in each redox cycle is similar with that of TGA. The components of ISSA after five cycles in the fluidized bed was analyzed by XRD. The iron-based component was mainly magnetic oxide, and after air oxidation, it was mainly ferric oxide. The CLG of sludge under the ISSA OCs in the fluidized bed reactor has been verified the ideal OC properties of sludge ash for its rich-Fe content to prepare the hydrogen-rich syngas.

1. Introduction

Sludge is the main by-product in the process of sewage treatment. With the rapid development of urbanization and industrialization, the output of sludge is increasing year by year. Faced with severe environmental protection requirements, improper disposal and utilization of sewage sludge is the key for waste resource and reduce environmental pollution. Therefore, the realization of harmless disposal and resource utilization of sludge is a practical problem to be solved urgently. Polymeric iron is one of the widely and economic used municipal sewage treatment agents, with the characteristics of fast floc formation, high floc density, fast settling speed in sludge, some bound water is closely linked to the mud, making it difficult to reduce the moisture content to a very low level using conventional mechanical methods. Due to the long dehydration time and large footprint required by low-temperature drying, as well as the high energy consumption of high-temperature drying, it is accompanied by secondary pollution of odor and dust. Therefore, it is significant to directly utilize high wet sludge (HWS) as a resource.

The purpose of thermochemical conversion is to reduce the volume of sludge and recover the energy and substances with added value. Blending incineration of sludge with coal is the most widely used thermochemical conversion method in recent years, so sludge incineration plants will concentrate on producing a large amount of ISSA. The inorganic substances in sludge are

retained in the solid phase in ISSA, while the ISSA produced by sludge using polymeric iron flocculants is rich in Fe_2O_3 and CaO. These two components have high reaction activity and are commonly used as catalyst materials, which have the potential to become catalysts and OC, and are one of the ways for ISSA resource utilization.

In chemical looping technology, OC provides lattice oxygen in the fuel reactor, reducing or avoiding direct contact between air and fuel, which can reduce and control the generation of thermal nitrogen oxides. When OC is regenerated in the air reactor, it releases heat to prompt the gasification reaction to continue and save external heat sources. Therefore, CLG of sludge is of economic advantages. In this study, HWS produced by polymeric iron was chemically looping gasified in a fluidized bed reactor to prepare syngas. The catalytic performance and oxygen carrying capacity of ISSA were comprehensively studied using the OC prepared by rich in iron oxide ISSA.

2. Materials and methods

2.1 Fuel analysis and ISSA OC preparation

The HWS used in this study was taken from a municipal sewage treatment plant in Qingdao. The industrial and elemental analyses of HWS are shown in the Table 1.

Table 1. Proximate analysis and ultimate analysis of raw materials.

Sample	Proximate analysis(wt.%)			Ultimate analysis(wt.%)					
	M_{ar}	V_{ar}	FC_{ar}	A_{ar}	C_d	H_d	N_d	S_d	O_d*
HWS	79.82	10.03	1.33	8.82	22.82	3.52	3.43	2.30	24.22

Mechanical extrusion of HWS into strips, using a disc granulation mechanism to prepare HWS particles with a particle size of 1-2mm, as raw materials for preparing OC and gasification experiments. Part of the HWS particles were incinerated in a muffle furnace at 850 ℃ to obtain ISSA. ISSA with a particle size of 0.6-0.9mm was selected using laboratory standard sieving as the OC for gasification experiments. To ensure the ideal fluidized state of OC in the fluidized bed reactor, Al_2O_3 particles with a particle size of 0.9-2.0mm were selected as the material layer and placed on the distribution plate. As an inert carrier, Al_2O_3 particles have a regular surface, making it easy to separate them from OC and sludge gasification ash for sampling and analysis of the reacted OC and sludge gasification ash.

2.2 OC characteristic

The XRF analysis of ISSA is shown in Table 2. The main chemical components are Si, Fe, P, Ca, S, Al, Mg and other elements, and the Fe oxides content reach to about 20.1%, and the CaO and SO_3 contents are very higher, the exist components should be CaO and $CaSO_4$.

Table 2. Contents of main elements by XRF.

Item	SiO_2	Fe_2O_3	P_2O_5	CaO	SO_3	Al_2O_3	MgO	K_2O	TiO_2	MnO	ZnO	SrO	V_2O_5
Wt(%)	29.52	20.1	16.73	12.66	7.25	6.38	4	1.7	1	0.26	0.25	0.1	0.06

The XRD analysis of ISSA is shown in Fig 1. Fe_2O_3 is the main form of Fe element present in ISSA.
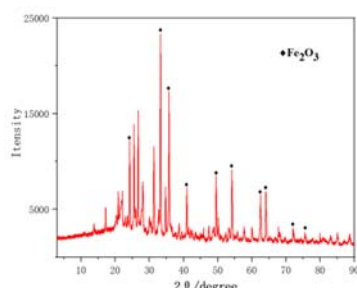
Fig. 1. XRD patterns of ISSA.
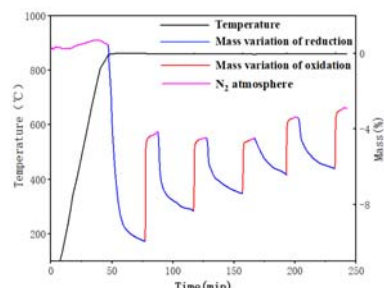
Fig. 2. OC's multi cycle redox under CO/Air in

2.3 Analysis of the oxygen-carrying capacity of the ISSA OC

The OC prepared by ISSA rich in iron oxide was subjected to CO/air multi-cycle redox experiments in a thermogravimetric analyzer to quantitatively study the oxygen carrying performance of OC.

 As shown in Fig. 2, the five oxygen-release and oxygen-obtaining cycles of ISSA OC is stable, and the oxygen carrying capacity of OC was about 3-10%, and showed a decreasing trend with redox cycles, especially, in the first cycle, the oxygen releasing arrived 10%, more than the theoretical oxygen content in FeO_x in ISSA OC, so the $CaSO_4$ and manganese oxide in ash also release its oxygen as the OC, but did not recover the oxygen transferring in next cycles.

2.4 The ISSA OC used for HWS gasification
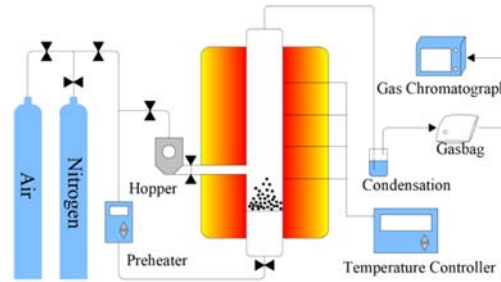
Fig. 3. Schematic illustration of the fluidized bed reactor.

The experimental system is shown in Fig.3. Under the oxygen and heat carrying effect of ISSA OC, HWS undergoes pyrolysis and gasification processes successively. The main reactions, including Fe_2O_3 in OC reacted with the gas-phase components, are shown in Table 3.

Table 3. The main reactions of HWS in fluidized bed reactors.

Name of reaction	Chemical equation	NO.
Water-gas shift reaction	$CO+H_2O \rightarrow CO_2+H_2$	R1
Steam methane reforming	$CH_4+H_2O \rightarrow CO+3H_2$	R2
Tar cracking	$Tar \rightarrow CO+H_2+C_nH_m$	R3
Reduction reaction	$CO+3Fe_2O_3 \rightarrow 2Fe_3O_4+CO_2$	R4
	$H_2+3Fe_2O_3 \rightarrow 2Fe_3O_4+H_2O$	R5
Partial oxidation of methane	$CH_4 + 3Fe_2O_3 \rightarrow 2Fe_3O_4 + CO +2H_2$	R6

So the gasous components include H_2, CO, CO_2, little CH_4 and remainder H_2O. The optimal gasification conditions were obtained according to the calorific value of synthesis gas and the hydrogen content in gas product.

$$CVS = V_{H_2} \times CVS_{H_2} + V_{CO} \times CVS_{CO} + V_{CH_4} \times CVS_{CH_4}$$

CVS is the Calorific Value of syngas, V_{H2}, V_{CO}, V_{CH4}, which represent the average gas content of H_2, CO, and CH_4 at different time points.

(1) The HWS is put into the spiral feeding device connected to the fluidized bed reactor. (2) Put part of OC and some Al_2O_3 particles into the reactor to form a bed material layer, and nitrogen gas with a flow rate of 1L/min was inflowed for 30 minutes to discharge the air from the reactor. (3) The fluidized bed reactor starts to be heated up at a heating rate of 10 ℃/min, and the temperature inside the furnace rises to 850 ℃. (4) Nitrogen gas preheated by a gas preheating device with a flow rate of 6L/min is sent to the fluidized bed reactor to achieve the fluidized state of the bed material. (5) The HWS particles was fed into the reactor and the gasification begins, the spiral feeding device was controlled to quantitatively inject HWS into the fluidized bed reactor. (6) OC was reduced and the synthesis gas was collected every a period with a gas bag. (7) Switch the intake conditions and introduce compressed air at a rate

of 6L/min for 15 minutes, causing OC to be oxidized. In the fluidized bed reactor, OC was successively reduced and oxidized to form a cyclic process.

A total of five bags of HWS gasification synthesis gas were collected, and the catalytic characteristics and oxygen carrying capacity of ISSA were analyzed and evaluated by the gas phase composition and OC performance. The oxidized OC separated from Al_2O_3 was analyzed by SEM detection to compare the morphological changes with the fresh OC. Beside the CLG tests, a control group was carried out, and HWS was directly gasified in the fluidized bed reactor with Al_2O_3 as an inert carrier and no OC added, also proceeded under 850 ℃ and collected five gas bags.

3. Results and discussions

3.1 Analysis of gasification performance

The synthesis gas component obtained from HWS at 850 ℃ were shown in Fig.4 .
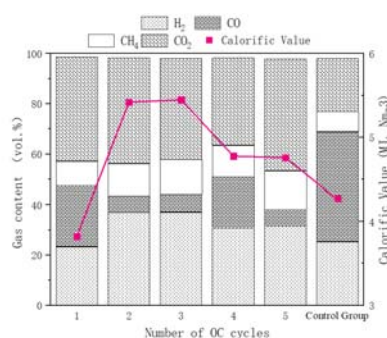
Fig. 4. The gas content and calorific value of syngas with OC cycles increasing.

In Fig 4, the content and components in the synthesis gas are statistically analyzed. In Fig 4, it can be seen that the participation of OC in the gasification process of HWS is clear and a significant change is shown with the number of cycles increasing. The calorific value of the synthesis gas shows a trend of first increasing and then decreasing. The peak heat value of the synthesis gas is obtained during the third cycle closely related to the composition and content of combustible gas in the synthesis gas. In the first cycle, OC provides the most oxygen for the gasification reaction, resulting in a large amount of carbon being transferred to CO_2, while hydrogen is fully burned and not transferred to CH_4. Instead, it is absorbed by the drying equipment of the gas collection device in the form of water molecules, resulting in a high content of CO_2 in synthesis gas, while the content of CO is significantly lower than that of the control group. At the same time, the calorific value of the synthesis gas is lower than that of the control group. As the number of OC cycles increases, the ability to provide oxygen element gradually weakens. Hydrogen element is not completely burned. The calorific value of synthesis gas has significantly increased compared to the first cycle of OC and the control group. In the third cycle of OC participating in pyrolysis gasification, the calorific value reaches its peak, and the component content of hydrogen is the highest, the content of hydrogen components in the synthesis gas obtained from the third cycle of OC increased significantly from 23.24% in the first cycle to 37.03% in the third cycle, compared to the control group of 25.23%. From this, it can be concluded that the optimal number of cycles for obtaining high-quality hydrogen-rich syngas is for OC participated in the CLG gasification of HWS in a fluidized bed reactor until the third cycle.

In Fig 4, the content of each gas component collected in the second and third cycles obeyed basically the similar rule. The reason for this phenomenon is that HWS gasification under ISSA OC has the optimized oxygen transferring capacity in these two cycles. The gasification ash generated can also serve as a new oxygen element for the gasification process, compensating for the weakened oxygen carrying capacity of the OC prepared by ISSA. This indicates that HWS can provide new OC after several chemical looping cycles in the fluidized bed reactor and continue to participate in the reaction. The calorific value of the synthesis gas obtained after the third cycle of OC significantly decreased, but the calorific value was still higher than that of the control group. This is because the oxygen carrying capacity of OC severely decayed after three cycles, but not completely fail. To prepare high-quality hydrogen-rich syngas, for the OC no longer has excellent oxygen carrying performance after three cycles. After experiencing the fourth and fifth cycles in OC, the hydrogen content in synthesis gas begin to decrease quickly, while the carbon conversion rate began to fluctuate.

3.2 Microscopic appearance evolution of OC

In Fig 5, the microstructure of OC before and after undergoing five redox cycles is compared. It can be inferred that, the irregular surface of the OC particles varied very few, but sinter appeared, The original microstructure presents a slender rod-shaped state and after five cycles, structural collapse, sintering and agglomeration into large granular morphology. The reason is related to the mineral substances in HWS with different melting points react each other in a high-temperature environment, and the melting point of the mixture decreases, resulting in a change in surface structure. This causes a little produced coke by HWS to easily adhere to the surface of the particles, leading to the blockage of surface pores of OC and the absence of surface active sites that can participate in the gasification process, which reduced oxygen carrying capacity and catalytic performance of OCs.

(a) Before	(b) After
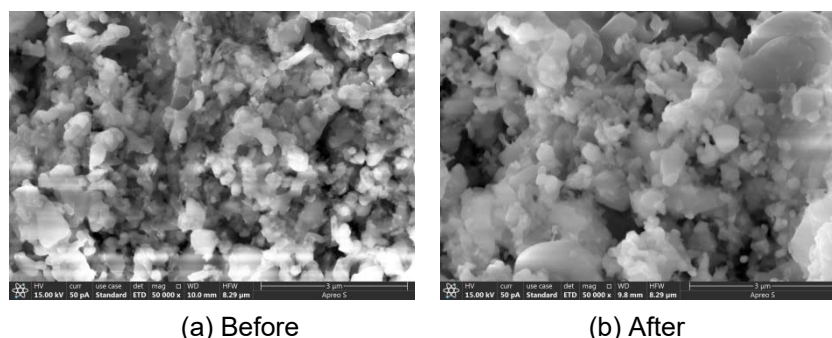
Fig. 5. SEM images before and after OC cycle in CLG.

4. Conclusion

The Fe element in ISSA mainly exists as Fe_2O_3. The ISSA OC for CLG can significantly improve carbon conversion and gasification rate. OC plays a catalytic role in the CLG process and provides oxygen element.

The ability of OC to provide oxygen for HWS gasification gradually weakens during the gasification cycle. But, HWS gasification can produce new sludge ash OC and continue to participate in the CLG reactions.

Except for the first cycle of OC, the synthesis gas of HWS has a higher content of hydrogen and a higher calorific value compared to the synthesis gas by HWS gasification without OC. In the third cycle of CLG, the synthesis gas is of the highest effective gas composition and calorific value. So the sludge ash particles could circulated from the sludge gasification to air reactor and then back to gasifier at least three times before discharged to outside.

Acknowledgment

References

Lee, Duu-Jong.Measurement of Bound Water in Waste Activated Sludge:Use of the Centrifugal Settling Method[J].Journal of Chemical Technology and Biotechnology,1994,Vol.61(2): 139-144

Hu, Mian;Hu, Hongyu;Ye, Zhiheng;Tan, Suqin;Yin, Ke;Chen, Zhong;Guo, Dabin;Rong, Hongwei;Wang, Junliang;Pan, Zhiyan;Hu, Zhong-Ting.A review on turning sewage sludge to value-added energy and materials via thermochemical conversion towards carbon neutrality.[J].Journal of Cleaner Production,2022,Vol.379(1): 134657

Sun Guozhen;Liang Wenzheng;Wang Kun;Li Jialu;Cui Weiwei;Yang Laishun;Yue Guangxi.Investigation on hydrogen-rich syngas preparation from high wet sludge mixed with sawdust based on iron oxygen carrier[J].Fuel,2023,Vol.343: 127853

Xu, Fang;Xing, Xinxin;Gao, Shuaifei;Zhang, Wenqi;Zhu, Lin;Wang, Yinfeng;Chen, Jianbiao;Chen, Haijun;Zhu, Yuezhao.Direct chemical looping gasification of pine sawdust

using Fe2O3-rich sludge ash as an oxygen carrier: Thermal conversion characteristics, product distributions, and gasification performances.[J].Fuel,2021,Vol.304: 121499

Ortiz, María;de Diego, Luis F.(ldediego@icb.csic.es);Abad, Alberto;García-Labiano, Francisco;Gayán, Pilar;Adánez, Juan.Hydrogen production by auto-thermal chemical-looping reforming in a pressurized fluidized bed reactor using Ni-based oxygen carriers.[J].International Journal of Hydrogen Energy,2010,Vol.35(1): 151-160

Song, T (Song, Tao); Wu, JH (Wu, Jiahua); Zhang, HF (Zhang, Haifeng); Shen, LH (Shen, Laihong).Characterization of an Australia hematite oxygen carrier in chemical looping combustion with coal[J].INTERNATIONAL JOURNAL OF GREENHOUSE GAS CONTROL,2012,Vol.11: 326-336

Ottosen, Lisbeth M;Kirkelund, Gunvor M;Jensen, Pernille E.Extracting phosphorous from incinerated sewage sludge ash rich in iron or aluminum[J].Chemosphere,2013,Vol.91(7): 963-969

A. T. Harris;S. A. Scott;J. S. Dennis;A. N. Hayhurst;J. F. Davidson.The Gasification of Sewage Sludge in Bubbling Fluidized Beds[A].17th International Conference on Fluidized Bed Combustion[C],2003

Nimit Nipattummakul;Islam Ahmed;Somrat Kerdsuwan;Ashwani K. Gupta;.High temperature steam gasification of wastewater sludge[J].Applied Energy,2010,Vol.87(12): 3729-3734

Huang, Z (Huang, Zhen);He, F (He, Fang);Zheng, AQ (Zheng, Anqing);Zhao, K (Zhao, Kun);Chang, S (Chang, Sheng);Zhao, ZL (Zhao, Zengli);Li, HB (Li, Haibin).Synthesis gas production from biomass gasification using steam coupling with natural hematite as oxygen carrier.[J].Energy,2013,Vol.53: 244-251

Wu, Jiahua;Shen, Laihong;Xiao, Jun;Wang, Lei;Hao, Jiangang.Chemical looping combustion of sawdust in a 10 kWth interconnected fluidized bed[J].CIESC Journal,2009,Vol.60(8): 2080-2088

ON THE MECHANICAL STABILITY OF BIOMASS PELLETS WITH DIFFERENT INITIAL DENSITIES AFTER FLUIDIZED BED PYROLYSIS

Abdullah Sadeq[1]*, Shen Wang[2], Marian Schmitt[1], Hannah Sophia Rothberg[1], Swantje Pietsch-Braune[1], Stefan Heinrich[1]

[1]Hamburg University of Technology, Institute of Solids Process Engineering and Particle Technology, Hamburg, Germany

[2]Key Laboratory of Energy Thermal Conversion and Control of Ministry of Education, Southeast University, Nanjing, China

*abdullah.sadeq@tuhh.de

Abstract

In this study, wood pellets of different densities were investigated for their mechanical properties before and after pyrolysis. Pyrolysis of these pellets was performed on the one hand in a fluidized bed at high nitrogen gas flow rate and on the other hand in a fixed bed at low nitrogen gas flow rate at a temperature of 900 °C in each case. It was found that the properties of the resulting pellet char depend on the pyrolysis specifications and the pellets initial density at raw state. After a fixed bed pyrolysis, the char pellets have a less rough outer surface than pellets after pyrolysis in a fluidized bed. Although these pellets have also shrunk to a small extent during the fluidization process, they have a pinecone-like structure due to a high number of large cracks on the surface leading to a larger diameter than pellet chars from the fixed bed process. It was observed that pellets with an initial higher density retained their cylindrical shape and a smoother surface after pyrolysis than pellets with an initial lower density. Accordingly, the pellets with a high density at raw state showed a higher stability than pellets with a lower initial density. This indicates that using wood pellets with an initial high density can lead to less undesired fines and therefore less losses of material during a fluidized bed pyrolysis.

1. Introduction

Wood pellets, made from wood sawdust and wood shavings are used as an alternative biofuel because of their significant lower emission of the climate-relevant carbon dioxide compared to fossil fuels. These pellets can be burned using many technologies, such as home heating stoves or institutional boiler systems.

Wood pellets can also be used to produce environmentally friendly synthesis gas (syngas) and replace natural gas. Pyrolysis, a thermochemical process at temperatures of about 900 °C, enables the conversion of biomass into syngas and char (remaining solid phase). The fluidized bed is an efficient process for converting wood pellets into the above-mentioned components [1]. It offers advantages such as high miscibility and the sand particles in the reactor (bed material) are in direct contact with the wood pellets, enabling better heat transfer compared to e.g. fixed bed reactors.

During the fluidized bed process, a major challenge arises from the increase in the fines content due to thermal and mechanical stress on wood pellets [2,3]. The resulting different particle size distribution affects the process dynamics. Furthermore, losses occure due to elutriation of the unreacted fines from the reactor [4]. While studies about the properties of raw wood pellets being mechanically stressed are available [5,6], the literature on wood pellets for pyrolysis in fluidized bed applications is limited. A previous study [7] showed that the devolatilization of wood pellets resulted in macroporous charcoal pellets. The final structure

and stability of the pellets therefore appears to be independent of whether the fluidized bed process is carried out with bed material (sand) or without bed material at high gas flow rate (HFR). The process without bed material at a low gas flow rate (LFR), on the other hand, lead to less severe structural damage. In the mentioned study [7] tests were carried out with commercial wood pellets of different composition and porosity. In addition, no information about the pelleting parameters was available. However, further investigations are necessary to determine a correlation between the pelleting settings and the properties of the resulting wood pellets during pyrolysis. For this purpose, wood pellets of different densities were produced using dies with different ratios of press channel diameter to length. The properties of the wood pellets before and after fixed bed and fluidized bed pyrolysis were compared.

2. Characteristics of wood pellets

3.1 Wood shavings

The wood shavings from Pfeifer Holz GmbH (Uelzen, Germany) were prepared in collaboration with Amandus Kahl GmbH & Co. KG (Reinbek, Germany). Firstly, the wood shavings were milled using the roller mill type 33-390 with two rollers and a roller speed of 2.28 m/s was set at 166 rpm. After milling, the wood shavings were moistened and soaked for 12 hours. Before pelleting, the wood shavings were mixed with water in an MIT turbomixer to reach a water content of 9 wt.-%.

3.2 Wood pellets

The investigated wood pellets were produced with a flat die press type 14-175 from Amandus Kahl GmbH & Co. KG. To achieve different densities, dies of different press channel lengths were used to densify the wood shavings (Figure 1).
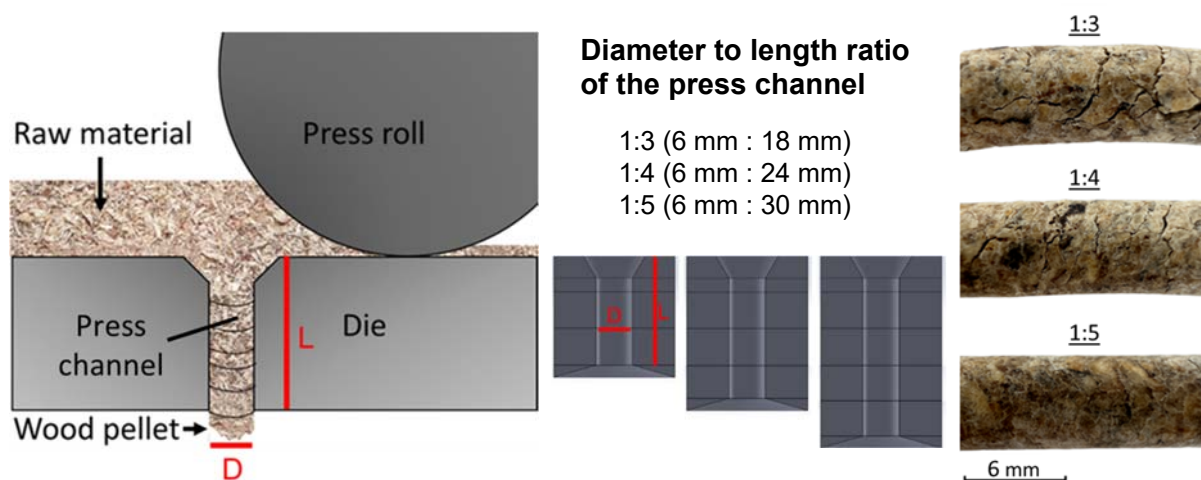
Figure 1. Scheme of the pelleting process (left), geometry of the dies (middle) used for the densification of wood pellets of different densities (right).

Therefore, these pellets consist of wood shavings of identical composition and wood shaving size distribution ($x_{50,3}$ = 571 µm). A high pellet density is associated with high mechanical stability of wood pellets in the raw state. For example, a diameter (6 mm) to length (30 mm) ratio of 1:5 of the press channel leads to high density pellets (hereafter referred to as 1:5 pellets) with a significantly higher compressive strength compared to pellets produced with a die of press channels with a ratio of 1:4 or 1:3 (see Table 1). The high density pellets show a smoother surface compared to the 1:3 pellets, which show a high number of cracks.

3. Pyrolysis

The pellets were treated with nitrogen gas to remove oxygen from the pores. Then, pyrolysis in a fluidized bed with sand as bed material and a nitrogen gas flow of 2 l/min at 900 °C (16 cm/s superficial gas velocity) was carried out for three minutes. Pyrolysis was also conducted as a fixed bed without bed material at a low nitrogen gas flow of 0.1 l/min at 900 °C (0.3 cm/s superficial gas velocity) for three minutes. A sketch of the plant is shown in Figure 2.
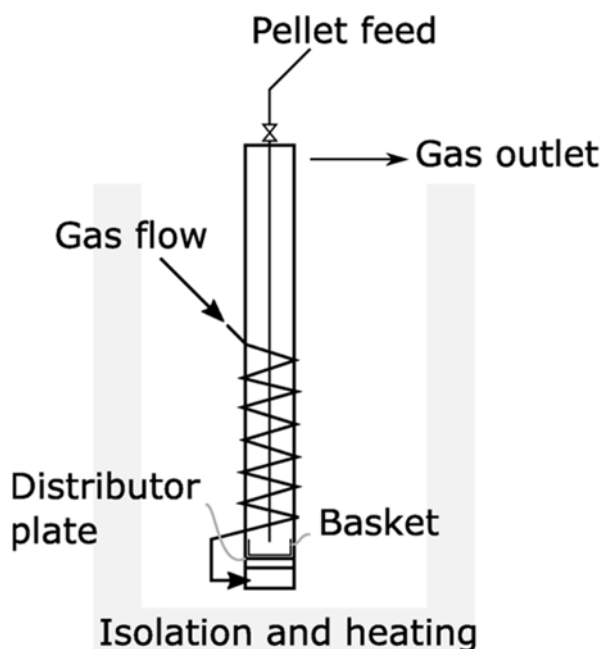
Figure 2. Scheme of the fluidized bed apparatus [7].

4. Comparison of wood pellets before and after pyrolysis

It was found that the resulting pellet charcoal structure depends on the pyrolysis process specifications and the pellets density at raw state. In the fixed bed process, the pellets shrink both radially and longitudinally. Scanning electron microscopy (SEM) images at different states of pellets were taken using the device Supra from the company Carl Zeiss Microscopy GmbH (Jena, Germany). From SEM images it can be seen that they have a less rough outer surface than pellets after pyrolysis in a fluidized bed (Figure 3).

Table 1.Wood pellet properties before and after pyrolysis.

Press channel D/L ratio	[-]	1:3	1:4	1:5
Raw				
Pellet diameter	[mm]	6.36 ± 0.06	6.14 ± 0.06	6.1 ± 0.03
Apparent density $\rho_{app.}$	[g/cm³]	1.144	1.195	1.289
Fixed bed pyrolysis				
Pellet diameter	[mm]	4.72 ± 0.36	4.25 ± 0.17	4.40 ± 0.2
Apparent density $\rho_{app.}$	[g/cm³]	0.4583	0.6276	0.8392
Fluidized bed pyrolysis				
Pellet diameter	[mm]	5.59 ± 0.16	5.34 ± 0.12	5.10 ± 0.2
Apparent density $\rho_{app.}$	[g/cm³]	0.3714	0.3711	0.3934

Although pellets from fluidized bed process have also shrunk, they have a pinecone-like structure due to a high number of large cracks on the surface leading to a higher diameter (Figure 4) and lower apparent density. This significantly higher damage of the structure can be attributed to the high air velocity during the fluidized bed process and the contact between sand particles and pellets enables a faster heat transfer. µCT measurements were conducted using the µCT 35 apparatus from SCANCO Medical AG (Switzerland). The µCT images show that the sand particles are not only located on the surface of the pellet, but are also located in the pores of the pellet (white dots in Figure 4).
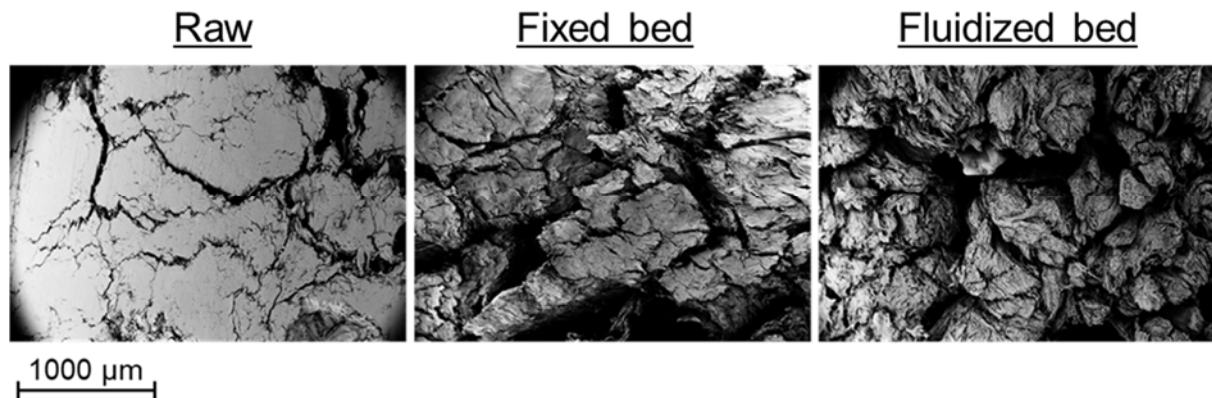
Figure 3. Scanning electron microscopy images of wood pellets in their raw state, after fixed bed pyrolysis and after fluidized bed pyrolysis.
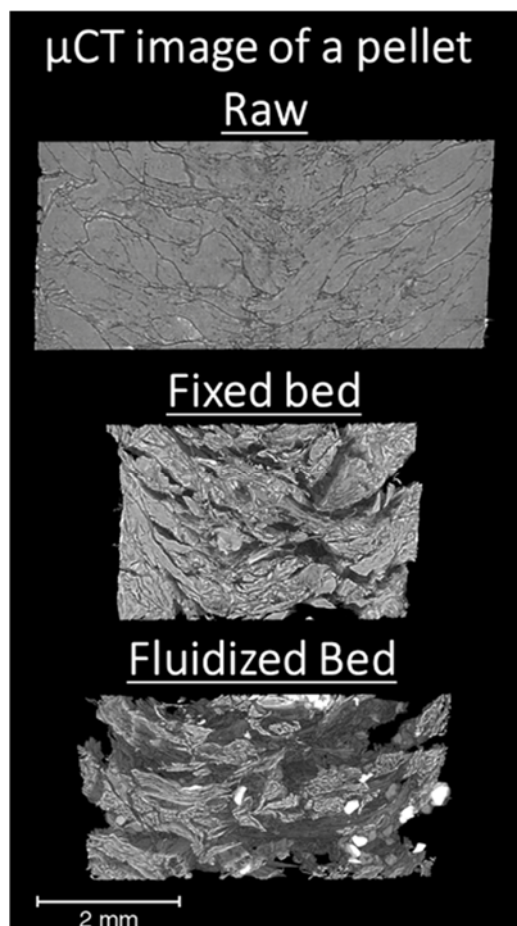
Figure 4. µCT images of the longitudinal cross cut of wood pellets before and after pyrolysis in fixed bed and fluidized bed.

The initial density of the pellets plays a major role, as a low density of the pellet leads to more sand particles to be found in the center of the pellet. Large pores also lead to an accumulation of larger sand particles, while smaller sand particles accumulate in pellets with small pores. These effects prevent the porosity of the pellet chars from being determined using typical methods such as mercury porosimetry. As the pellet charcoals consist of large pores, the spatial resolution of 6 µm of the µCT scans is sufficient. A newly developed post-processing enabled to exclude the the sand particles, which have a high density, during porosity determination. In Figure 5, the porosity of the pellets in the raw and pyrolyzed state is compared. A significant difference in porosity can be observed between the pellets in the raw state, which results from the different press channel length of the dies used during pelleting. A longer press channel leads to a higher back pressure and therefore more compact wood pellets [8]. While the wood pellets 1:4 and 1:5 have a porosity of about 5-6%, the porosity of 1:3 pellets is over 10%. Their initial porosity seems to have an effect on their behavior during fixed-bed pyrolysis. The increase in porosity of 1:3 pellets is significantly greater than that of 1:4 and 1:5 pellets. This shows that high porosity pellets have suffered severe structural damage due to the thermal effects. Here, the porosity of 1:3 pellet charcoal is between 30 and 60%, whereas the porosity of 1:4 and 1:5 pellet chars is below 40%.
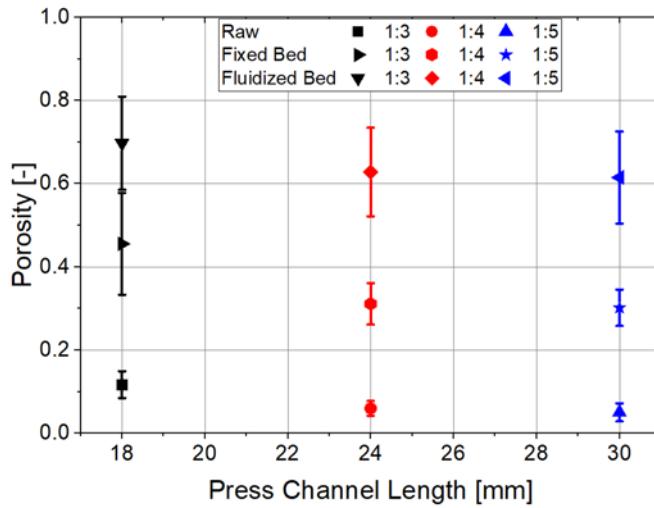
Figure 5. Porosity of wood pellets in their raw state and after pyrolysis.

During the fluidized bed process, high air velocity contributes to greater disintegration of the wood shavings from the pellet matrix. Due to the higher dynamics during fluidization, this results in a significantly higher porosity for the pellet charcoals 1:3, 1:4 and 1:5 than for the fixed bed process. However, only moderate differences in porosity can be observed between 1:3, 1:4 and 1:5 pellets. The high standard deviation also indicates a high heterogeneity of the pellet structure due to some local disintegration of wood shavings. In order to investigate their mechanical stability, a maximum number of 100 drop tests were conducted with 20 pellet charcoals from a specific height until pellet breakage occurred. In accordance to the more uniform structure of the pellets after fixed bed pyrolysis, a higher kinetic energy, approximated from the drop tests as described in [7], was required for breakage. The drop tests with the 1:5 pellet charcoals after a fixed bed pyrolysis had to be repeated significantly more often than with the 1:3 pellets. Two of the 20 1:5 pellet charcoals did not break after 100 drop tests, while all of the 1:3 pellets broke. The reason why the value of the 1:4 pellets is similar to that of the 1:3 is that 6 out of 20 1:4 pellet charcoals could not be considered as they did not break at all. This indicates a higher stability of the 1:4 pellet charcoals. The high standard deviation shows a high degree of structural heterogeneity. As the heterogeneity of the pellet structure is more pronounced after a fluidized bed process, there are very large outliers in the kinetic energy.
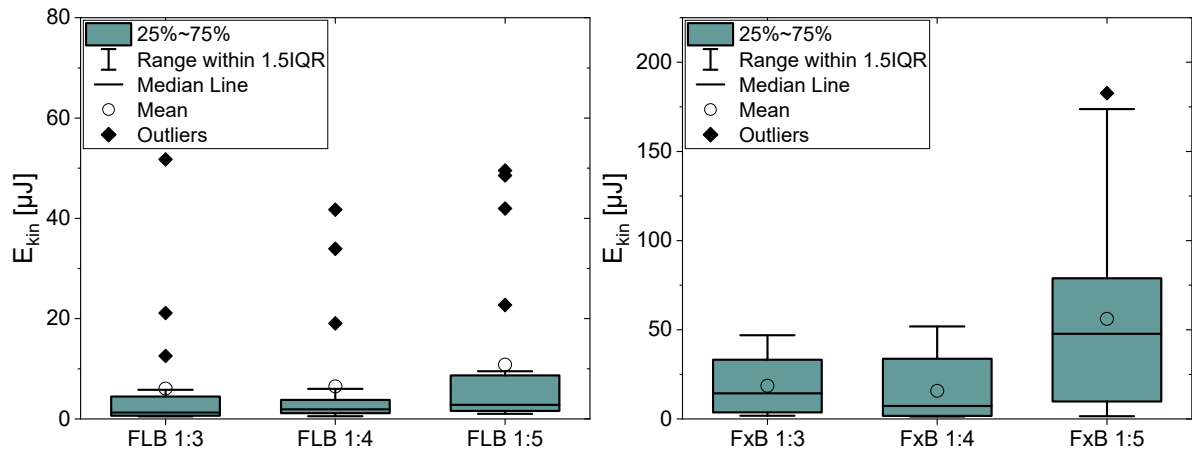
Figure 6. Kinetic energy required for breakage of pellet chars from fluidized bed pyrolysis (left) and fixed bed (right).

The results show that the setting of a higher press channel length tends to have an influence on the structure and stability of pellet charcoals after a fixed bed process. However, high velocity of heated air, such as in the fluidized bed process, lead to very large structural damage and porosities, so that no significant differences in stability between 1:3, 1:4 and 1:5 can be determined.

4. Conclusion

It has been shown that wood pellets in a fixed bed pyrolysis tend to exhibit slightly less structural damage compared to fluidized bed pyrolysis as the latter comes along with high air velocity resulting in a larger heterogeneity in the structure. These different structures after pyrolysis can also be recognized in a variation in stability, as a higher kinetic energy is required to break pellet charcoals from a fixed bed process. Differences in the initial density of the wood pellets also have a slight influence, but the impact by the pyrolysis process is more significant. Although trends are apparent, further ongoing studies with additional investigation of the compression behavior and internal structure of pellet charcoals will provide a better understanding of the correlation between pelleting process and pellet structure after pyrolysis.

Acknowledgment

References

[1]   A. Molino, S. Chianese, D. Musmarra, Biomass gasification technology: The state of the art overview, Journal of Energy Chemistry 25 (2016) 10–25. https://doi.org/10.1016/j.jechem.2015.11.005.

[2]   F. Scala, R. Chirone, P. Salatino, 6 - Attrition phenomena relevant to fluidized bed combustion and gasification systems, in: F. Scala (Ed.), Fluidized Bed Technologies for Near-zero Emission Combustion and Gasification, Woodhead Publishing Ltd, Cambridge, 2013, pp. 254–315.

[3]   F. Scala (Ed.), Fluidized Bed Technologies for Near-zero Emission Combustion and Gasification, Woodhead Publishing Ltd, Cambridge, 2013.

[4]   P. Ammendola, R. Chirone, G. Ruoppolo, F. Scala, The effect of pelletization on the attrition of wood under fluidized bed combustion and gasification conditions, Proceedings of the Combustion Institute 34 (2013) 2735–2740. https://doi.org/10.1016/j.proci.2012.06.008.

[5]   A. Sadeq, D. Heinrich, S. Pietsch-Braune, S. Heinrich, Influence of oscillating water content on the structure of biomass pellets, Powder Technology 426 (2023) 118631. https://doi.org/10.1016/j.powtec.2023.118631.

[6]   A. Sadeq, A. Frank, M. Tyslik, J. Jägers, S. Pietsch-Braune, V. Scherer, S. Heinrich, Influence of cyclic water content changes during long-term storage on the mechanical stability of wood pellets, Powder Technology 428 (2023) 118866. https://doi.org/10.1016/j.powtec.2023.118866.

[7]   K. Jarolin, S. Wang, T. Dymala, T. Song, S. Heinrich, L. Shen, M. Dosta, Characterizing devolatilized wood pellets for fluidized bed applications, Biomass Conv. Bioref. 13 (2023) 5133–5150. https://doi.org/10.1007/s13399-021-01486-x.

[8]   R. Čolović, Đ. Vukmirović, R. Matulaitis, S. Bliznikas, V. Uchockis, V. Juškienė, J. Lević, Effect of die channel press way length on physical quality of pelleted cattle feed (2010).

REACTION KINETICS OF BIOGENIC FUEL
FOR CHEMICAL LOOPING

Marian Schmitt*, Lennard Lindmüller, Stefan Heinrich

Institute of Solids Process Engineering and Particle Technology,

Hamburg University of Technology (TUHH), Germany

*Email: marian.schmitt@tuhh.de

Abstract

In the course of efforts to reduce emissions of carbon dioxide and to meet the global climate targets, the chemical looping combustion process (CLC) has increasingly received more attention over the years after originally being designed to produce pure CO_2. In recent years CLC has been investigated as a way to capture CO_2 from the combustion without the need for any extra processing steps. CLC uses an oxygen-carrier that is circulated between two fluidized bed reactors. The oxygen carrier provides oxygen in the fuel reactor by reduction and gets reoxidized in the air reactor. Therefore, CO_2 sequestration is already implemented in the process and no extra gas treatment is necessary [1].

The accurate kinetic description of the fuel devolatilization and char gasification within the CLC process is of great importance, especially for modelling the fuel reactor. Due to the fact, that during gasification of biomass in the in-situ gasification-CLC (ig-CLC) process both the devolatilization and char gasification occur simultaneously, the experimental setup has to be designed to investigate these behaviors separately.

In this work the devolatilization and subsequent char gasification of woody biomass were studied under fluidized conditions in a lab scale hot plant. To mimic ig-CLC process conditions, both CO_2 and H_2O gasification were considered, comparing inert bed and reactive bed conditions respectively. Kinetic parameters were derived from the experimental results and compared with common models. Process parameters like temperature and particle size distribution were varied to study their effects on the kinetic behavior of the gasification.

1. Introduction

The implementation of the Paris climate targets is closely linked to the german coal phase-out act. This stipulates that fossil fuels should be replaced by the use of biogenic fuels. Recently, the combustion of biomass in combination with CCS has gained in importance and is known as BECCS (Biomass Energy with Carbon Capture and Sequestration). With this process, a negative CO_2 balance can be achieved and there is the prospect of a significant reduction in the concentration of CO_2 in the atmosphere [2].

Solid biofuels will therefore become increasingly important for achieving climate targets in the future. However, their use in fluidized bed plants poses a challenge. The efficiency of CLC plants is reduced due to the poor interaction between the two solids, the insufficient contact time of the oxygen carrier with the high volatile amount in comparison to coal and the slow decomposition of the solid coke when solid fuels are used.
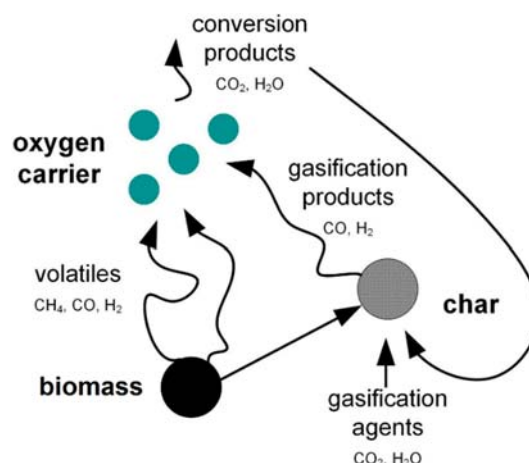
Fig. 1.1: Schematic of biomass gasification process steps (modified from [1]).

In addition, the fluidization of biomass with a wide particle size distribution is difficult in conventional fluidized bed reactors. Furthermore, ash residues and their melting behavior can lead to an agglomeration of oxygen carriers and subsequently to defluidization [3]:

$$C + CO_2 \rightleftharpoons 2\,CO \qquad (1.1)$$
$$C + H_2O \rightleftharpoons CO + H_2 \qquad (1.2)$$

The gasification of solid fuels in the CLC process can be conceptually divided into two separate mechanisms: Degassing and gasification, as shown in Fig 1.1. First, the solid fuel is dried and devolatilized, i.e. the gaseous components are released. The remaining solids are referred to as coke, which can then be gasified using steam (equation 1.1) or carbon dioxide (equation 1.2). In this work, the degassing (or de-volatilization) is performed ahead of the main experiments, in which the reaction kinetics of the biomass coke are measured and quantified. To get insight into the kinetics of both possible gasification types, they have been studied in separate experiments using inert and reactive bed material. Furthermore, coal gasification was realized in a spouted bed setup as well.

2. Experimental Setup

2.1 Lab scale plant

To study the gasification in a controllable environment, CLC conditions were produced in the lab scale hot plant shown in Fig 2.1. The plant consists of a chrome-nickel tube with a length of 500 mm and 53 mm in diameter. Using two PID controllers, a 4 kW electrical heating unit can heat the plant up to 1100 °C. Fluidization gases are pre-heated in a coil like pipe routing and given into the reactor through a gas distributor made from sintered metal.

To control the process, temperatures are measured at different points in the reactor, namely below and above the gas distributor, in the freeboard phase of the reactor and in the outgas stream. Pressures are also measured between these points as pressure differences and additionally a total pressure inside the reactor is measured in comparison towards the atmosphere.

Solenoid valves are used to switch the inflow between reducing, oxidizing and inert gases. Rotameters are used to control the volumetric flow rates of the singular gases.
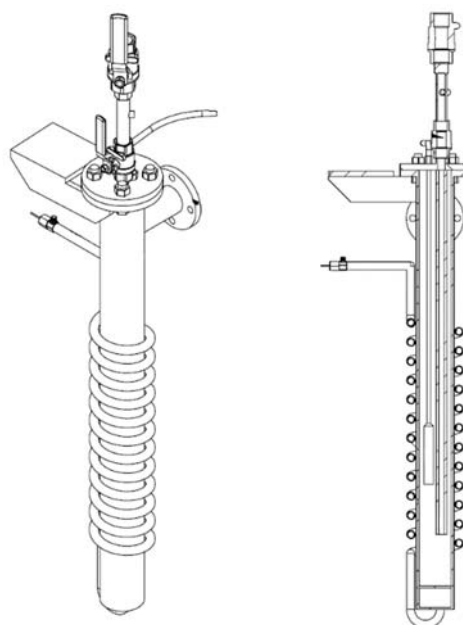
Fig. 2.1: Exterior and sectional view of the lab scale hot plant.

2.2 Online gas analytic

The exhaust gas is first channeled through a ceramic filter. This is followed by a filter consisting of a glass filled with filter wadding to separate coarse particles and an air filter with a hydrophobic PTFE membrane with a pore size of 0.2 μm to separate fine particles. As a result, the residual moisture is removed from the exhaust gas by cooling it to a dew point temperature of approx. 2-3 °C in a sample gas conditioner. The dry and cooled exhaust gas flow is then passed through an inline adsorber filter series circuit consisting of two adsorption filter units for removing nitrogen oxides and a filter unit for separating fine particles (< 0.1 μm). The downstream vacuum pump conveys the exhaust gas further through a universal filter to remove the remaining solid impurities before the exhaust gas is fed to the exhaust gas analysis modules.

At this point, part of the volume flow is passed through a stationary process gas analyzer. This consists of four individual modules connected in series, where the volume concentrations of the exhaust gas components, such as methane, carbon monoxide, carbon dioxide and hydrogen, are measured. The CO_2, CO and CH_4 are measured nondispersive infrared sensors (NDIR). H_2 is quantified with a thermal conductivity detector using values of the other modules to correct for the change in thermal conductivity.

2.3 Solid feeding system

A sluice was used to ensure that no atmospheric oxygen could be introduced into the process. For this purpose, the above-bed feeder was extended by two ball valves with a connection for a nitrogen purge flow in the center. When the sample was introduced, the lower ball valve could be closed and the sample and sample chamber could be flushed with nitrogen. After closing the upper valve and reaching a fixed overpressure in the airlock, the sample could be injected into the process through the overpressure. The initial volumetric flow rate of inert gas was kept constant during the whole experimental procedure. This can be observed in lower values of measured total CO_2 concentration in the outflow.

3. Material

3.1 Biomass and coke

Milled softwood pellets by the company POWERPELLETS were used as biogenic fuel. These were reduced in size using a ball mill and then degassed. Degassing was carried out in the actual process plant at 900 °C for 1 hour. In the process, 300 g of shredded biomass was flowed through with a pre-heated nitrogen flow of 5.6 l/h. At the end of the process time, the entire system was allowed to cool down to below 100 °C with a further flow of nitrogen. The coke obtained was then removed, crushed, classified and divided into five size fractions.

The particle size distributions were determined using a Camsizer type X2 by the company Retsch. In Fig 3.1 (left) the mass-related cumulative PSD is plotted against the particle diameter. Particles smaller than 50 µm were defined as dust and excluded from the gasification experiments. Particles larger than 1.8 mm were crushed again and assigned to the other fractions.

The Ultimate Analysis was conducted by using a NCHS-Analyzer (Vario Macro Cube by Elementar). For the Proximate Analysis, the following analyses were conducted: Moisture content was determined using a Precisa EM120-HR moisture analyzer [4]. Ash content was analyzed according to DIN 51719 [5], and volatile content was assessed following DIN 51720 [6]. All results of these analysis are shown in Table 3.1.

Table 3.1. Proximate and Ultimate Analysis of raw biomass and biomass coke.

Proximate Analysis		raw	coke
Moisture	wt-% (raw)	8.1	3.2
Volatiles	wt-% (raw)	76.6	1.7
Ash	wt-% (raw)	0.1	1.5
Fixed Carbon	wt-% (raw)	15.1	93.6
Ultimate Analysis		raw	coke
N	wt-% (raw)	<0.1	0.39
C	wt-% (raw)	47	89
H	wt-% (raw)	6.5	0.4
S	wt-% (raw)	<0.2	<0.2
O	wt-% (raw)	38.4	7.4

3.2 Bed material

Both inert bed material and oxygen carrier was used to conduct experiments to derive reaction kinetics. Quartz sand (H31) was used as inert bed material and a synthetic CuO-based oxygen carrier on Al_2O_3, with 9% CuO, was used as reactive bed material. The mass-related cumulative PSD is shown on the of Fig 3.1 (right) and all other bed material properties are listed in Table 3.2.
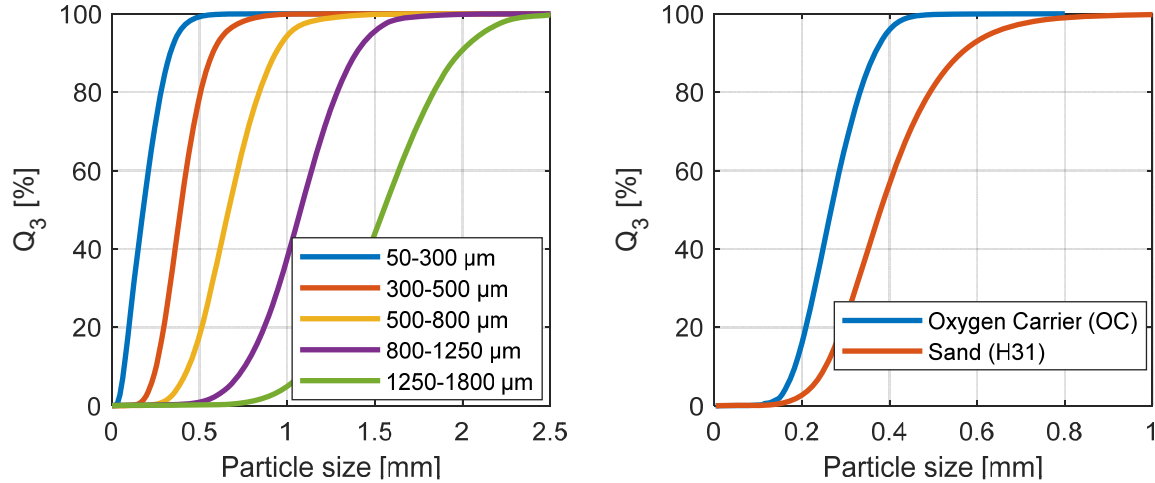
Fig. 3.1: Cumulative mass-based particle size distribution of manufactured biomass coke particles (left) and Cumulative mass-based particle size distribution of bed materials used.

Table 3.2. Bed material properties of inert sand H31 and oxygen carrier (OC).

Bed material properties			OC	H31
Solid density	ρ_s	[kg/m³]	3858.1	2648.9
Sauter diameter	d_{sa}	[µm]	276.6	400.1
Porosity	ε	[-]	0.74	0.44
Bulk density	ρ_{bulk}	[kg/m³]	1043.8	1487.5
Bed volume	V	[cm³]	33	33
Min. fluidization velocity	u_{mf}	[m/s]	2.3	5.7

4. Spouted bed operation

In order to be able to quantify the influence of the reactor design on the results, a conical spouted bed was proposed in addition to the reactor type already shown in Fig 2.1.

In spouted beds, the fluidization gas is not fed over the entire cross-sectional area of the bed, but only through a gap or nozzle. This creates a fountain in the middle of the bed, in which the particles are accelerated upwards and then fall back down the reactor wall, as shown in Fig 4.1. Due to this back-mixing, spouted bed plants generally exhibit higher heat and mass transfer, which strongly favors sterically hindered chemical reactions [7]. Spouted beds also tend to have lower pressure drops over the bed height, which would be beneficial to upscaling processes, because less energy would be required for the fluidization.

Preliminary tests with this reactor design have already been evaluated with regard to carbon conversions during combustion. It was shown that total conversion, conversion rates and degree
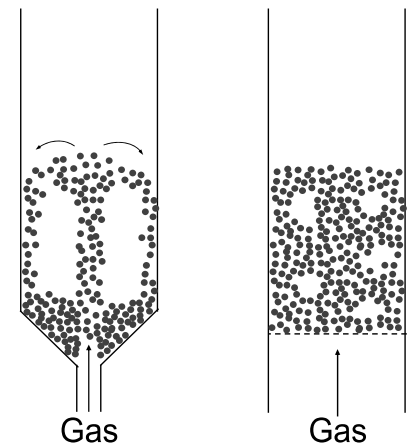
Fig. 4.1: Schematic of fluidized and spouted bed operation in comparison.

of conversion in the spouted bed were increased in comparison to the fluidized bed setup.

In order to determine the stability of the spout non-optically, a stability analysis was carried out using the Fast Fourier Transformation (FFT) according to equation 4.1 [8]:

$$F(k) = \sum_{j=1}^{N} x(j)e^{-i\frac{2\pi}{N}(j-1)(k-1)} \qquad (4.1)$$

For this purpose, a high-frequency pressure sensor was used to record the total relative pressure of the system compared to its atmosphere at different operating temperatures. Using the FFT, this signal can be transferred to the frequency domain and the peak distribution can be used to make a statement about the stability of the spout. By using low-pass and high-pass filters, peaks in the low frequency range (<5 Hz) can be eliminated, as these are only predominantly caused by particle movements in the fixed bed. In the case of a stable operating point, a clear single dominant peak can be recognized in the range of 5-15 Hz, as the particle movements in the fountain are shown in this frequency range.

5. Results

5.1 Stability Analysis

Fig 5.1 shows the pressure signal recorded at 2.5 kHz on the left and the corresponding representation in the frequency range after the FFT has been carried out on the right.
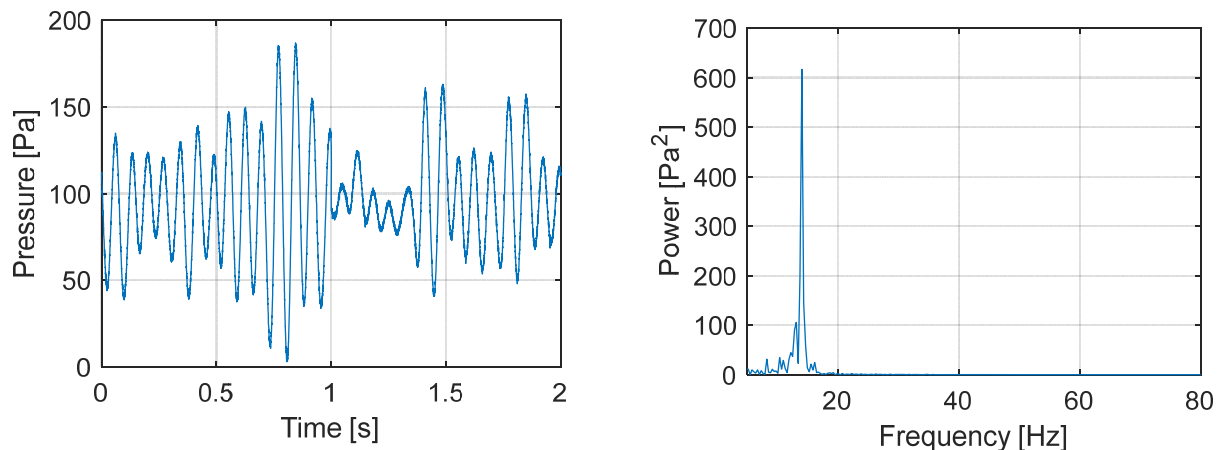
Fig. 5.1: Total relative pressure signal against atmosphere over time (left) and transformed signal in using FFT (right) for nitrogen fluidization with H31 sand at 800 °C and 4.4 L/min.

Using this method, stable working ranges could be determined for different gases and flow rates as a function of temperature. The data shown in Fig 5.1 is an example of the stability analysis with nitrogen at 800 °C and a flow rate of the fluidization gas of 4.4 L/min.

5.2 Carbon conversion

By balancing the total carbon in the process, the carbon conversion for different particle size distributions could be analyzed. Fig 5.2 shows the carbon conversion over time for different particle sizes at 1000 °C in an inert sand bed, which is fluidized by a 50/50 Vol.-% mixture of CO_2 and N_2. As expected, the increased specific surface area of the coke particles and the improved mixability of these with the bed material leads to accelerated heat and mass transfer and consequently to an increased reaction rate. The associated reaction rates are shown in Table 5.1. Furthermore, total conversion during combustion studies could be increased by up to 24 % using the developed spouted bed setup. The high rate of back-mixing that was achieved with the new setup also led to an increase in conversion rates by up to 17 %.

PSD [μm]	conversion rates [1/s]
300-500	0.0035
500-800	0.003
800-1250	0.0027
1250-1800	0.0024

Tab. 5.1: Evaluated carbon conversion rates for different particle size distributions at 1000°C in inert sand and 50 Vol.-% CO_2 atmosphere.
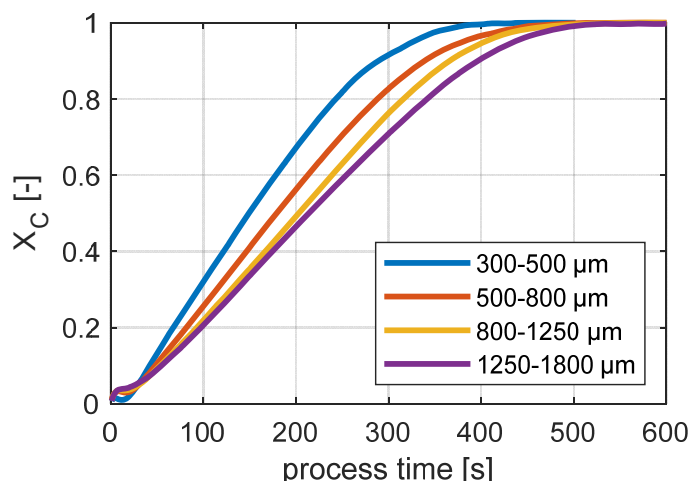
Fig. 5.2: Relative carbon conversion for different PSDs at 1000°C in inert sand and 50 Vol.-% CO_2 atmosphere.

6. Conclusion

First initial experiments with inert bed material and using carbon dioxide as gasification agent have been carried out successfully and it has been shown, that the particle size distribution is a driving factor for the conversion rates of said gasification. Further investigation especially regarding different reaction temperature will allow for a derivation of reaction parameters such as activation-energy and reaction rate constant. In addition, a new type of spouted bed reactor design was planned and put into operation. Through pressure-based stability analyses, stable operating ranges were determined for all relevant process conditions such as temperature, gas species, bed material and gas velocity. In future, this will enable further investigation of the reactions already investigated in the fluidized bed and a comparison with these.

Acknowledgment

References

[1] J. Haus, M. Goltzsche, E.-U. Hartge, S. Heinrich, and J. Werther, 'Gasification kinetics of lignite char in a fluidized bed of reactive oxygen carrier particles', *Fuel*, vol. 236, pp. 166–178, Jan. 2019, doi: 10.1016/j.fuel.2018.08.151.

[2] J. Adánez and A. Abad, 'Chemical-looping combustion: Status and research needs', *Proc. Combust. Inst.*, vol. 37, no. 4, pp. 4303–4317, 2019, doi: 10.1016/j.proci.2018.09.002.

[3] L. Lindmüller, J. Haus, and S. Heinrich, 'High Volatile Conversion in a Chemical Looping Combustion System with Three Different Biomasses', *Energy Fuels*, vol. 36, no. 17, pp. 9529–9537, Sep. 2022, doi: 10.1021/acs.energyfuels.2c00901.

[4] 'DIN 51718:2002-06, Prüfung fester Brennstoffe_- Bestimmung des Wassergehaltes und der Analysenfeuchtigkeit', Beuth Verlag GmbH. doi: 10.31030/9226705.

[5] 'DIN 51719:1997-07, Prüfung fester Brennstoffe_- Bestimmung des Aschegehaltes'. Beuth Verlag GmbH. doi: 10.31030/7346447.

[6] 'DIN 51720:2001-03, Prüfung fester Brennstoffe_- Bestimmung des Gehaltes an Flüchtigen Bestandteilen'. Beuth Verlag GmbH. doi: 10.31030/9065360.

[7] K. B. Mathur and P. E. Gishler, 'A technique for contacting gases with coarse solid particles', *AIChE J.*, vol. 1, no. 2, pp. 157–164, Jun. 1955, doi: 10.1002/aic.690010205.

[8] N. Mostoufi, G. Kulah, and M. Koksal, 'Flow structure characterization in conical spouted beds using pressure fluctuation signals', *Powder Technol.*, vol. 269, pp. 392–400, Jan. 2015, doi: 10.1016/j.powtec.2014.09.028.

CHARACTERISTICS OF GLASS FIBERS AND CARBON FIBERS RECOVERED FROM SCRAP WIND TURBINE BLADES BY CFB TECHNOLOGY

Siyang Yan[1], Lei Feng[1], Senxiang Liu[1], Wenhui Zhao[1], Suxia Ma[1,2,3], Ruixue Feng[1,2,3]*

1 Key Laboratory Cleaner Intelligent Control on Coal & Electricity, Ministry of Education, College of Electrical and Power Engineering, Taiyuan University of Technology, Taiyuan 030024, PR China;

2 Shanxi Key Laboratory of Clean and Efficient Combustion and Utilization in the Circulating Fluidized Bed, Taiyuan University of Technology, Taiyuan 030024, PR China;

3 Taiyuan Boiler Group Co., Ltd, Taiyuan 030008, PR China

Email: fengruixue@tyut.edu.cn

Abstract

Glass fiber reinforced plastic (GFRP) and carbon fiber reinforced plastic (CFRP) from wind turbine blades (WTB) was fragmented and fluidized by circulating fluidized bed (CFB) aiming at studying the fluidized behavior and corresponding products. The raw material with a cracked size of around 25 mm experiences a decomposing process with temperature ranging in 500-900 °C. Regular and well-organized fiber is seen in SEM of solid product, and no eroded or fractured fiber observed. It was investigated that with the increase of temperature, the polymerization increased and particles wrapped the fibers decreased, thus improved the purity of collected fibers. Present temperature was not high enough for the carbon fibers to graphitize.

1. Introduction

The recycling and recovery of materials from end-of-life wind turbine blades (WTB) have become critical with the rapid expansion of renewable energy. The WTB are mainly manufactured using thermoset matrix materials such as epoxy, vinyl ester resins, or unsaturated polyester resin [1], with the glass fiber (GF) and carbon fiber (CF) embedded. Due to the high economic value and sustainability of glass fiber reinforced polymer (GFRP) and carbon fiber reinforced polymer(CFRP), many studies focus on the fiber recycling by means of mechanical, thermal, and chemical recycling[2-4]. Thermal recycling mainly includes three methods: pyrolysis, fluidized bed and microwave pyrolysis[5]. The circulating fluidized bed (CFB) is a thermal oxidative process using air as fluidizing gas for decomposing the composite matrix by air heat flow of high temperature. Pickering et al. [4,6] first proposed fiber recycling technology using fluidized bed and concluded that at 450 °C the strength loss of recycled glass fibre (rGF) was measured as 50%[7], while for recycled composite fiber (rCF) it was 25% at 550°C[8]. Guo et al. [9] investigated the pyrolysis behavior and corresponding pyrolysis products of printed circuit board plastic particles in CFB, and analyzed the gas products, liquid products, and solid residues. Meng et al.[10] evaluated the energy and environmental impacts of CF recycling by a fluidized bed process and reuse to manufacture a CFRP material. Moreover, recent researches have highlighted the potential of recycled GF from WTB in various applications, including asphalt modification[11], reinforcement for waste phosphogypsum[12] and so on. Previous researches show the possibility to decompose WTB in CFB, however, the CFB technology and fluidized behavior needs to be further studied to optimize the experimental parameters for promising industrial potential.

This study aims at investigating the characterization of the quality of the recovered GF and CF from scrap WTB through CFB method, including the surface contamination and surface chemistry of the fibers by SEM, function groups of fibers by FTIR, and crystal of fibers by XRD.

Through experiments and characterization analysis, insights will be gained into the influence of temperature on product yields. By leveraging the insights from previous study, this study seeks to find a proper temperature for recycle fibers through CFB experiments and recycle GF and CF more efficiently and environmentally friendly.

2. Experiments

2.1 Raw materials

The chemical compound of WTB was measured via X-ray Fluorescence, and the result was shown in Table 1. The CaO shown in table was considered as the limestone and dolomite composed glass fiber in WTB, and the SiO_2 represented the main composition of glass fiber in WTB. The composition of carbon of WTB was absent from Table 1, which was out of the range of XRF detection.

Table 1. Chemical compound of WTB

Wt%	MgO	Al_2O_3	SiO_2	P_2O_5	SO_3	ClO_2	K_2O	CaO	Fe_2O_3	TiO_2
WTB	2.715	12.804	53.552	0.544	0.133	0.538	0.411	28.259	0.579	0.296

2.2 CFB experiments

Fig. 1. presents the process of recovering fibers from WTB, which consists of the fracture of raw material, decomposing process in CFB, and characterization analysis of products. The raw materials were fractured into small pieces with a cracked size of around 25 mm and then sent into CFB. The composition of the CFB system is shown in the figure Fig. 1. Scrap GF and CF composite material is fed into a 700 mm silica sand bed with heated air. While the polymer in the composite volatilizes through cyclone, the flaky solid products are collected from freeboard.
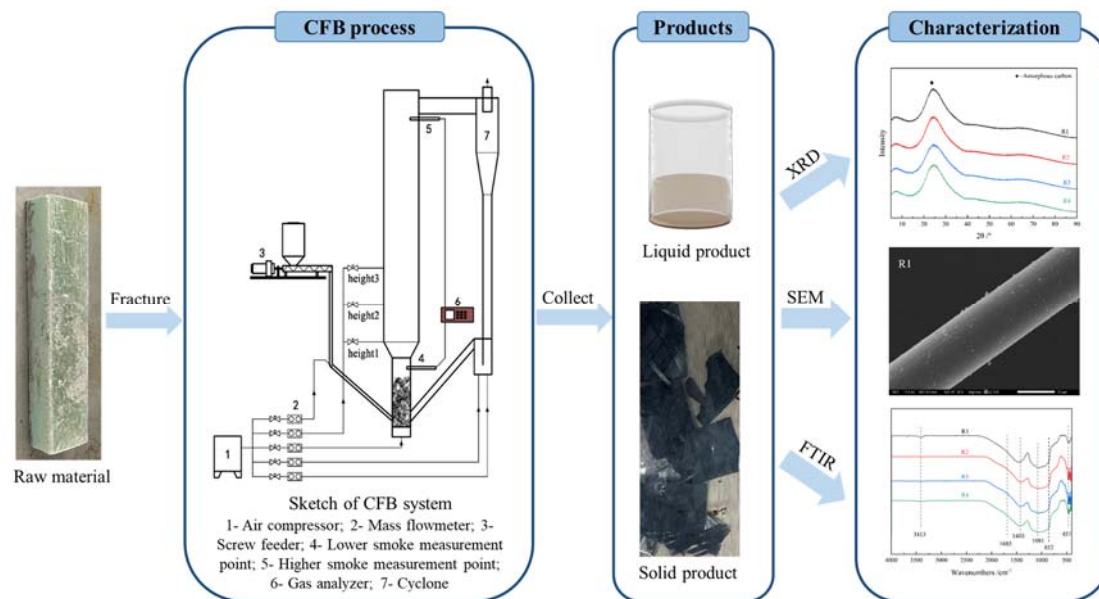
Fig. 1. Sketch diagram of recovering fibers from wind turbine blades.

Experimental conditions are shown as Table 2. With four experiments carried out, each temperature range is 100 °C, covering 500-900 °C. The heating time is set to 3h, and fluidization velocity is 0.5 m/s.

Table 2. Experimental conditions of CFB.

Sample	Temperature °C	Time /h
R1	500-600	3
R2	600-700	3
R3	700-800	3
R4	800-900	3

3. Results and discussion

3.1 FTIR analysis

The FTIR analysis results of sample R1-R5 were shown in Fig.2. The absorption peak at 3413cm^{-1} represented the stretching vibration band of O-H and N-H in samples, noteworthy, the appearance of absorption band of O-H indicate the high combustion temperature enhanced the evaporation rate of liquid products in WTB, and retained a small amount of O-H and N-H in liquid products on the surface of the solid products[9]. The characteristic peak at 852cm^{-1} represented the antisymmetric vibration of thermoset epoxy groups, considering that the glass fiber was the main compound in WTB, the peak at 852cm^{-1} indicated the present of Si-O group in glass fiber, and the peak at 457cm^{-1} represented the present of Si-O-Si as glass fiber in WTB[11]. The adsorption peak at 1081cm^{-1} and 1685cm^{-1} evidenced the C=O in samples[12].
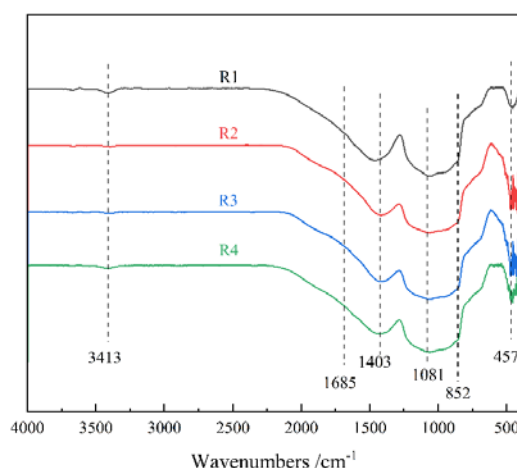
Fig. 2. FTIR curves of samples R1-R4.

3.2 XRD analysis

The XRD result curves of sample R1-R4 were shown in Fig.3. The peak with an 2θ of 20°-40° represented the amorphous carbon in sample, which appeared in all samples tested. The characteristic peak of amorphous peak represented the carbon fiber in WTB, however, no characteristic peaks of graphite were observed in XRD curves, which indicated that the combustion temperature of circulating fluidized bed was insufficient for carbon fiber in samples to graphitize. As the combustion temperature of circulating fluidized bed increased, the width of the amorphous carbon characteristic peak decreased, which might be attributed to a slight increase in the polymerization of amorphous carbon at high temperatures. Based on the FTIR result discussed previously, the peak of SiO_2 and limestone contained in the glass fiber was absent from the XRD curves because the amorphous carbon peak overlapped it.
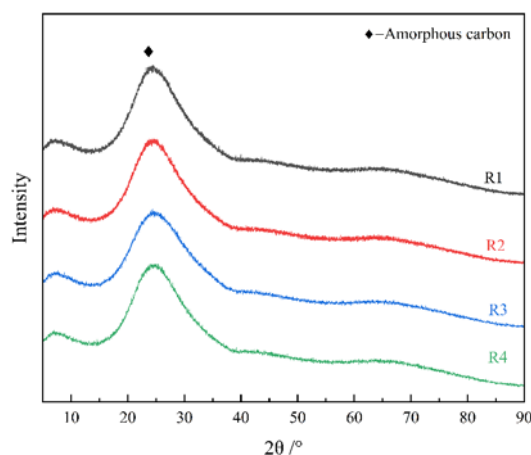
Fig. 3. XRD curves of samples R1-R4.

3.3 SEM analysis

Fig. 4 and Fig.5 demonstrated the microstructure of WTB in different magnification, respectively. Fig.4 showed that the fibers were relatively intact and did not fracture at combustion temperatures of circulating fluidized bed. Fig.5 showed the microstructure of fiber under higher magnification, and it's clear to be seen that the fiber was wrapped with fine practices, resulted in a high roughness of the fiber surface. As can be seen in Fig.5, the number of fine particles wrapped on the fiber surface decreases significantly as the combustion temperature increases, the surfaces of the fibers were not eroded and exhibited no fractures or cracks at high magnifications. Since the residue on the fiber surface gradually decreases at high temperatures, which indicated that higher combustion temperatures improved the purity of the fiber. Simultaneously, the circulating fluidized bed treatment method enables the fibers retain their integrity remarkably.
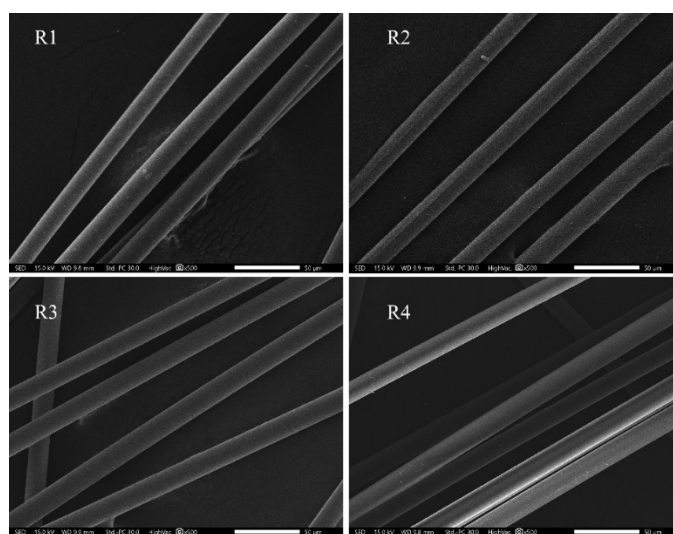
Fig. 4. Sketch of CFB system.
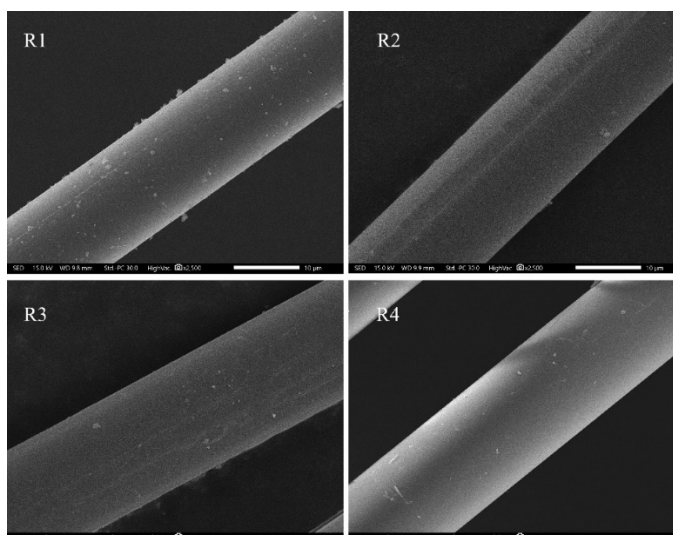
Fig. 5. Sketch of CFB system.

4. Conclusion

This study recycled glass fibers and carbon fibers from wind turbine blades through CFB in a temperature range of 500-900 °C. Glass fibers and carbon fibers are obtained in all the experiments that we carried out in present study. Characterization method such as FTIR, XRD and SEM are used to investigate the fluidized behavior, product characteristics of fibers, through which we drawn the following conclusions. 1) With the increase of temperature, the polymerization increases according to the FTIR analysis. 2) Present temperature is not high

enough for the carbon fibers to graphitize according to the XRD analysis. 3) The fibers were not eroded or fractured, and the increasing temperature decreased the wrapped particles, thus improved the purity of collected fibers.

Acknowledgment

References

Mishnaevsky Jr L, Branner K, Petersen H, et al. Materials for Wind Turbine Blades: An Overview. Materials. 2017. 10, 1285

Beauson J, Lilholt H, Brøndsted P. Recycling solid residues recovered from glass fibre-reinforced composites – A review applied to wind turbine blade materials. Journal of Reinforced Plastics and Composites. 2014. 33(16), 1542-1556

Pimenta S, Pinho S T. Recycling carbon fibre reinforced polymers for structural applications: Technology review and market outlook. Waste Management. 2011. 31(2), 378-392

Pickering S J. Recycling technologies for thermoset composite materials—current status. Composites Part A: Applied Science and Manufacturing. 2006. 37(8), 1206-1215

Rathore N, Panwar N L. Environmental impact and waste recycling technologies for modern wind turbines: An overview. Waste Management & Research. 2023. 41(4), 744-759

Pickering S J, Kelly R M, Kennerley J R, et al. A fluidised-bed process for the recovery of glass fibres from scrap thermoset composites. Composites Science and Technology. 2000. 60(4), 509-523

Yip H L H, Pickering S J, Rudd C D. Characterisation of carbon fibres recycled from scrap composites using fluidised bed process. Plastics, Rubber and Composites. 2002. 31(6), 278-282

Jiang G, Pickering S J, Walker G S, et al. Surface characterisation of carbon fibre recycled using fluidised bed. Applied Surface Science. 2008. 254(9), 2588-2593

Guo Q, Yue X, Wang M, et al. Pyrolysis of scrap printed circuit board plastic particles in a fluidized bed. Powder Technology. 2010. 198(3), 422-428

Meng F, Mckechnie J, Turner T A, et al. Energy and environmental assessment and reuse of fluidised bed recycled carbon fibres. Composites Part A: Applied Science and Manufacturing. 2017. 100, 206-214

Nie Y, Liu Q, Xiang Z, et al. Performance and Modification Mechanism of Recycled Glass Fiber of Wind Turbine Blades and SBS Composite-Modified Asphalt. Applied Sciences, 2023. 13(10), 6335

Yang L, Zhao W, Wang D, et al. Surface-Treated Recycling Fibers from Wind Turbine Blades as Reinforcement for Waste Phosphogypsum. Molecules. 2022. 27(24), 8668

FOULING AND CORROSION IN RETROFIT CFB WITH INCREASING SHARE OF WASTE

Kyösti Vänskä[1]*, Emmi Kallio[1], Marcin Kost[2], Alexander Kuhn[3], Jochen Ströhle[3], Bernd Epple[3], Vesna Barišić[1]

1 Research and Development Department, Sumitomo SHI FW Energia Oy, FI-78201 Varkaus, Finland

2 Fortum Power and Heat Polska Sp. z o. o., ul. Antoniego Słonimskiego 1A, 50-304 Wrocław, Poland

3 Institute for Energy Systems and Technology, Technical University Darmstadt, Otto-Berndt-Str. 2, 64287 Darmstadt, Germany

*kyosti.vanska@shi-g.com

Abstract

This paper presents results from field and pilot measurements conducted to study the effect of increasing shares of waste-derived fuel in mixtures with hard coal on fouling and corrosion. Field measurements were conducted in a CFB unit in Zabrze, Poland with a power generation capacity of 75 MW_{el}, and a heat generation capacity up to 139 MW_{th}. This boiler is designed to combust a mix of solid recovered fuel (SRF) (locally sourced municipal solid waste, up to 40 %$_{LHV}$), biomass, and coal to provide heat and power. Field tests were carried out with two fuel mixtures: SRF 40 – 45 %$_{LHV}$ range, and SRF 45 – 50 %$_{LHV}$, with the rest being hard coal. Each test campaign lasted 5 days. Pilot tests were conducted in a 1 MW_{th} CFB pilot plant at the Technical University Darmstadt. Pilot tests were carried out during the combustion of a mixture of 80 wt% SRF and 20 wt% hard coal, as well as during mono-firing of coal and SRF. Fouling and corrosion were studied by utilizing air cooled probes, most equipped with multiple metal alloy coupons, located in the furnace and the convective pass. The progress of corrosion was also followed by utilizing electrochemical online corrosion measurement system, which allow real time corrosion monitoring. Pilot and field tests both confirmed a high impact of increasing share of SRF on fouling and corrosion, in case of studied hard coal above 40 %$_{LHV}$.

1. Introduction

Power and industrial decarbonization have become national to global top-priority missions, calling for a variety of solutions to reduce, capture, utilize and store CO_2. Currently, most of coal-fired power plant operators in the EU are either actively seeking or implementing retrofit solutions, which decrease CO_2 output while assuring economic viability and sustainability of their operations. Partial or complete substitution of coal with alternative fuels, such as waste-derived fuels, e.g., solid recovered fuel (SRF), is becoming a common practice globally.

The combustion of waste-derived fuels is an attractive alternative to coal due to their low or even negative price, their permanent availability along with the moderate carbon footprint. Thanks to their renowned flexibility, circulating fluidized bed (CFB) combustors are particularly suitable for such retrofitting. The drawback of increased waste-shares for all boilers is, however, an increase in fouling and material wastage in the furnace as well as in the convective section that can lead to undesirable shutdowns and costly maintenance. In co-firing of coal and waste, up to a certain share, coal may synergically minimize deposit formation and growth and suppress the deposition of corrosive species from the waste. The beneficial effects and favorable shares of the fuel mixture depend on both, coal and waste properties as well as on overall boiler features such as layout, steam properties, materials selection, etc. [Haaf et al., 2022].

The target of this study was to evaluate fouling and corrosion in retrofit units for which partial or complete substitution of coal with waste-derived fuels is considered. Tests were carried out by using air cooled fouling and corrosion probes which included several different base and weld overlay (WOL) metal alloy coupons. The online corrosion probe used in the tests is based on linear polarization resistance method [Mahanen et al., 2015]. Analyses of the metal coupons included visual inspections, analysis of the electrochemical corrosion signal data, fouling rate by weighing the coupons with deposits, analysis of the formed deposits and corrosion layers by scanning electron microscopy with energy dispersive X-ray spectroscopy (SEM-EDS), and corrosion rate by weighing the coupons after cleaning by glass bead blasting.

2. Field Tests

Field tests were conducted at the CFB unit in Zabrze, Poland, in November 2022. The fuels fired were Polish bituminous coal and SRF, processed from municipal and industrial wastes, class 3 – 4 (EN 15359:2011). Tests were carried out by using 40 – 45 $\%_{LHV}$ SRF, 45 – 50 $\%_{LHV}$ SRF and 45 – 50 $\%_{LHV}$ SRF with limestone (LS) feeding with – the rest of the fuel mix being coal. Each fuel mix test lasted 5 days.

2.1 Furnace

A fouling probe was inserted on the furnace wall at an elevation of ~14, 19 and 24 m above the grid. The exposure time was 2 hours and the probe included one steel coupon with 2% chromium (2Cr). The target coupon surface temperature was 325 °C. The appearance of the coupons after each exposure and the relative material loss rates are shown in Fig. 1. In all test points, the deposits were mainly composed of calcium sulphates (Ca, S), aluminum silicates (Al, Si) and alkali chlorides (Na, K, Cl). At all elevations, chlorine was found enriched next to the metal causing corrosion of the coupons. The material loss was lowest at 14 m where it was mostly due to corrosion, and at 19 and 24 m it appeared to be due to a combination of erosion and corrosion. The material loss increased with the increase of the SRF share in the fuel mixture.

* Test done with 1Cr coupon and 2.5 h exposure.
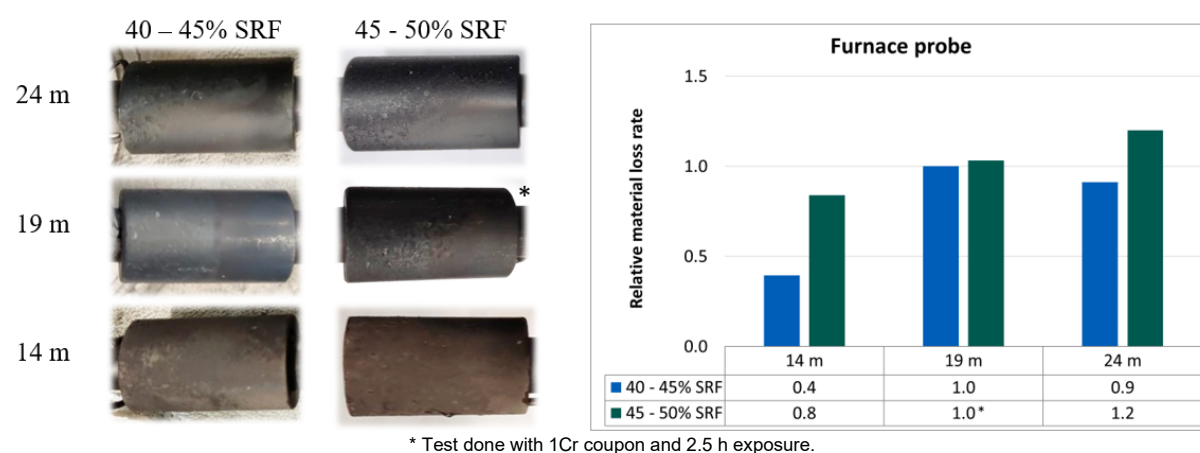
Fig. 1 The furnace probe 2Cr coupon after each exposure and relative material loss rates.

2.2 Convective pass

A fouling probe was installed just above the convective superheater-2 (SH2), where it was subject to soot blowing. The exposure time during each test was 48 hours. The probe included five coupons: 1Cr, 9Cr, 18Cr-11Ni, 25Cr-20Ni and 22Cr-60Ni (WOL). The target coupon surface temperature was 450 °C. Fouling was heaviest during limestone feeding. In all test points, the deposits were mostly composed of calcium sulphates (Ca, S) and alumina silicates (Al, Si) together with lesser amounts of alkali chlorides (K, Na, Cl), iron (Fe) and titanium (Ti). Only traces of heavy metals (Zn, Cu) were seen during analysis. During limestone feeding, the deposits had highest calcium and chlorine amounts. Chlorine was found enriched next to the metal occasionally together with alkalis (Na, K), causing corrosion of the samples. The

visual appearance of the coupons after each exposure and relative material loss rates are shown in Fig. 2. The material loss was highest when limestone was fed which could be due to the highest chlorine content in the deposits but also more frequent soot blowing, which can accelerate oxidation and erosion of the coupons.
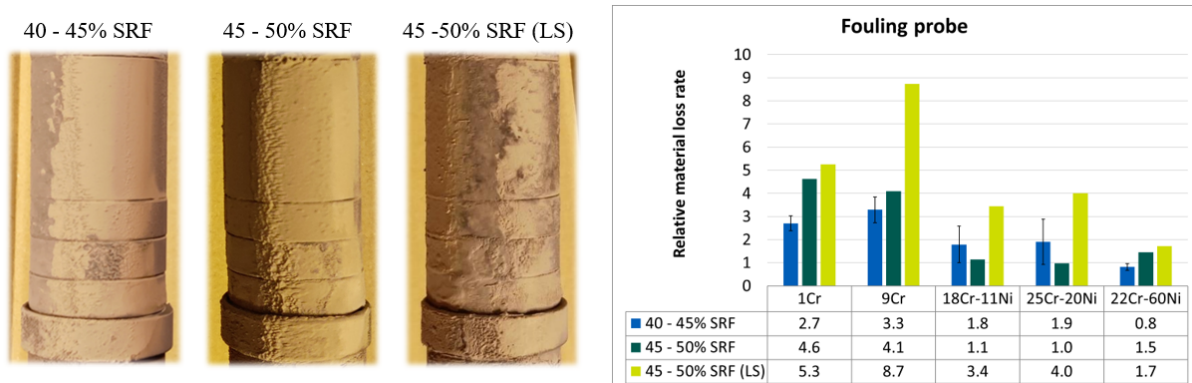
Fig. 2 The fouling probe after each exposure and relative material loss rates of the coupons.

A corrosion probe was installed just above the SH2 in the week before the actual test campaign was started and it stayed installed during the entire test campaign. The coupons on the probe were 1Cr and 18Cr-11Ni and the target coupon surface temperature was 450 °C. Just before the test campaign started, the boiler had a two-day planned shutdown. The appearance of the coupons after exposure as well as the measured electrochemical corrosion signal are shown in Fig. 3. Deposits were thickest on the wind side, which was less exposed to soot blowing compared to the lee side. The soot blowing can be seen periodically decreasing the corrosion rates.
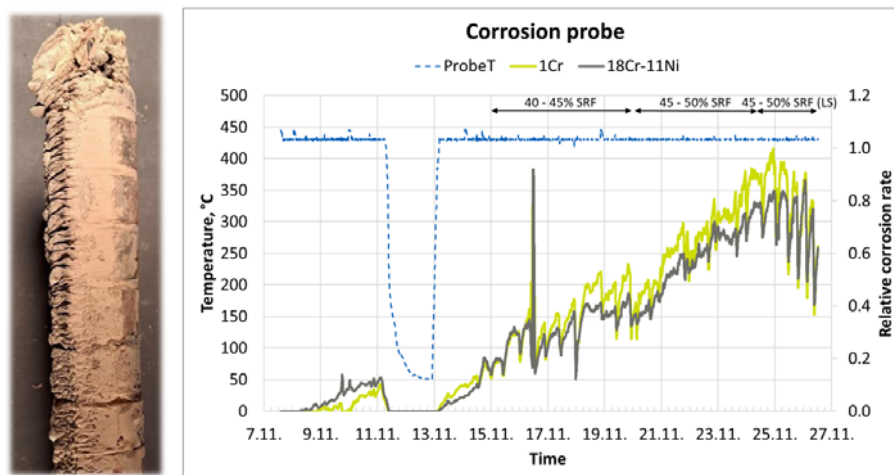
Fig. 3 The corrosion probe after the exposure from the right side and electrochemically measured relative corrosion rates of 1Cr and 18Cr-11Ni in the convective pass.

Based on the signal, an increase of the SRF share in the fuel mix increased corrosion. During limestone feeding, the soot blowing frequency was increased due to higher fouling, thus corrosion rates appear to be decreasing. The signal during the entire test campaign indicates that the higher alloyed 18Cr-11Ni performed only slightly better than 1Cr. A cross section of the coupons was analyzed by SEM-EDS. The deposits were mainly composed of calcium sulfates (Ca, S), with some aluminum silicates (Al, Si) and small amounts of iron (Fe), alkalis (Na, K) and chlorine (Cl), no heavy metals were found. Chlorine was enriched in the same locations as alkalis, indicating the presence of alkali chlorides. Chlorine was found on the metal-oxide interface causing active oxidation of the coupons.

3. Pilot Tests

Pilot tests were conducted at the CFB600 1 MW$_{th}$ pilot plant in Darmstadt (TUDA), Germany in March 2023. The fuels used during the tests were Polish bituminous coal and German SRF of MCI type (municipal, commercial, industrial waste). Tests were carried out with 100 wt% coal, fuel mix of 80 wt% SRF and 20 wt% coal, and 100 wt% SRF [Kuhn et al, 2024].

3.1 Furnace

A furnace probe was installed at an elevation of ~5 m above the grid. The exposure time in each test was 20 hours, and the probe included four coupons, one carbon steel (CS) base metal and three weld overlays: CS, 22Cr- 60Ni (WOL), 30Cr-9Ni (WOL) and 16Cr-5Ni (WOL). The target coupon surface temperature was 325 °C. The appearance of the coupons immediately after exposure, the deposit compositions and the relative material loss rates are given in Fig. 4. The deposits' composition includes, with 100% coal: mainly sulphur (S) with traces of Si, Al, K, Ca; 80% SRF: alkali and calcium sulphates (K, Na, Ca, S), with some alkali chlorides, no heavy metals (HMs); and 100% SRF: alkali chlorides (K, Na, Cl), calcium sulphate (Ca, S) and some HMs (Cu, Zn). When SRF was fired the main corrodent of the coupons were alkali chlorides - in 100% SRF firing, HMs (Cu, Zn) may have also contributed to corrosion. Mixing coal with waste had a beneficial effect on reducing material loss rates by lowering Cl in the deposits. In all cases 22Cr- 60Ni (WOL) was found to be the best performing alloy.

Furnace probe (Weight-%)	Na	S	Cl	K	Ca	Cu	Zn
100% Coal	0.0	20.0	0.0	0.7	0.3	0.0	0.0
80% SRF	20.7	17.6	1.2	10.0	2.9	0.0	0.0
100% SRF	11.0	9.0	22.0	9.7	9.6	4.7	2.5

Furnace probe (Relative material loss rate)	CS	22Cr-60Ni	30Cr-9Ni	16Cr-5Ni
100% Coal	1.0	0.7	1.8	2.1
80% SRF	2.0	1.2	1.5	2.9
100% SRF	10.8	2.9	6.5	16.1
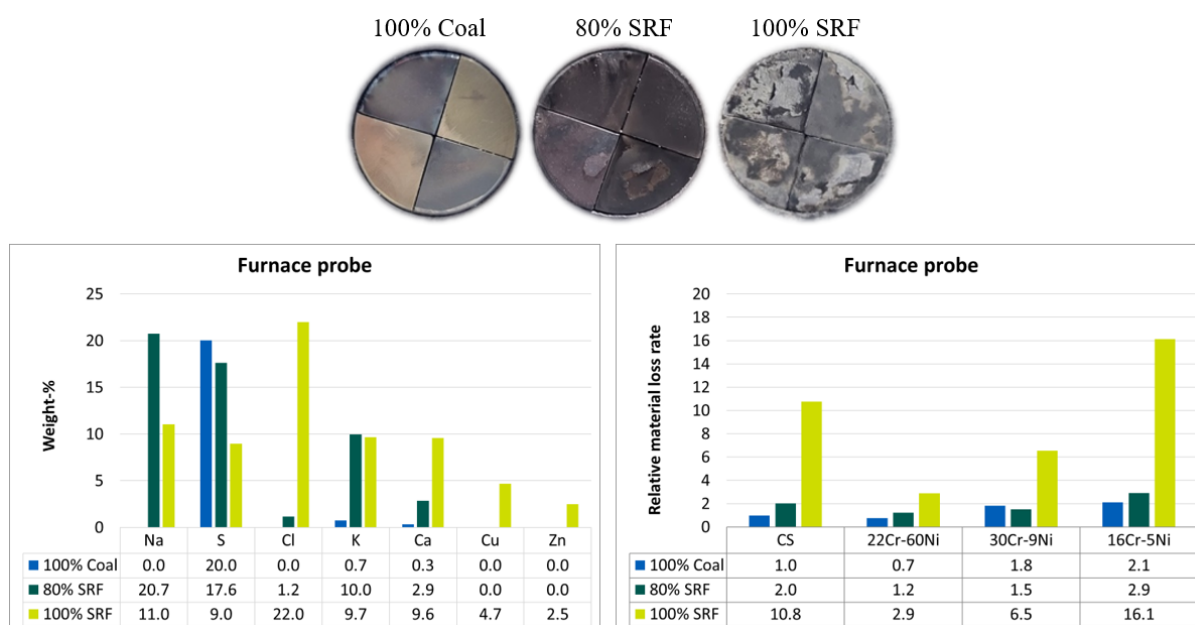
Fig. 4 The furnace probe after each exposure, deposit composition and relative material loss rates of the coupons.

3.2 Convective pass

The fouling probe and the corrosion probe were installed in the convective pass after the cyclone before the heat exchanger. The exposure time in each fouling probe test was 20 hours. The corrosion probe was not removed during the test campaign. The test coupons in the fouling probe were: 1Cr, 9Cr, 18Cr-11Ni, 25Cr-20Ni and 22Cr-60Ni (WOL). The target coupon surface temperature was 450 °C. Immediately after each exposure, the coupons were visually inspected. With 100% coal deposits were formed only on the lee side, with 80% SRF all around the coupons and with 100% SRF more on the wind side. With 80% SRF deposits were more powdery than deposits formed with 100% SRF. By increasing the share of SRF fouling rates increased and with 100% SRF heavy fouling occurred. The deposits' composition includes, with 100% coal: aluminosilicates (Al, Si), alkali and calcium sulphates (K, Ca, S), no Cl or HMs

were found; 80% SRF: alkali and calcium sulphates (K, Na, Ca, S), aluminosilicates (Al, Si), some Cl and Zn, no other HMs; and 100% SRF: alkali chlorides (K, Na, Cl), calcium sulphate (Ca, S), aluminosilicates (Al, Si) and some HMs (Cu, Zn). Alkali chlorides were the main corrodent of the coupons when SRF was fired. The appearance of the coupons after each exposure, relative fouling rates, deposit compositions and relative material loss rates of the coupons are shown in Fig. 5. The material loss increased by increasing the share of SRF. Coal had reduced chlorine in the deposits, and thus the material wastage rates were much lower with the mix than with 100% SRF. Additionally, with 100% SRF heavy metals Cu and Zn were found in deposits, and especially copper was found enriched on the metal surface, which may have contributed to corrosion.

100% Coal **80% SRF** **100% SRF**

Fouling probe

100% Coal	1.0
80% SRF	7.5
100% SRF	20.8

Fouling probe

Weight-%

	Na	Al	Si	S	Cl	K	Ca	Cu	Zn
100% Coal	0.0	15.0	22.1	1.8	0.0	2.9	2.7	0.0	0.0
80% SRF	5.9	7.6	5.9	11.9	2.3	10.8	7.4	0.0	0.7
100% SRF	7.2	9.3	3.5	5.9	13.0	11.5	5.2	7.0	1.6

Fouling probe

Relative material loss rate

	1Cr	9Cr	18Cr-11Ni	25Cr-20Ni	22Cr-60Ni
100% Coal	1.0	0.7	0.6	0.1	0.4
80% SRF	7.8	11.4	2.9	2.4	2.8
100% SRF	33.2	50.1	13.2	13.8	16.8
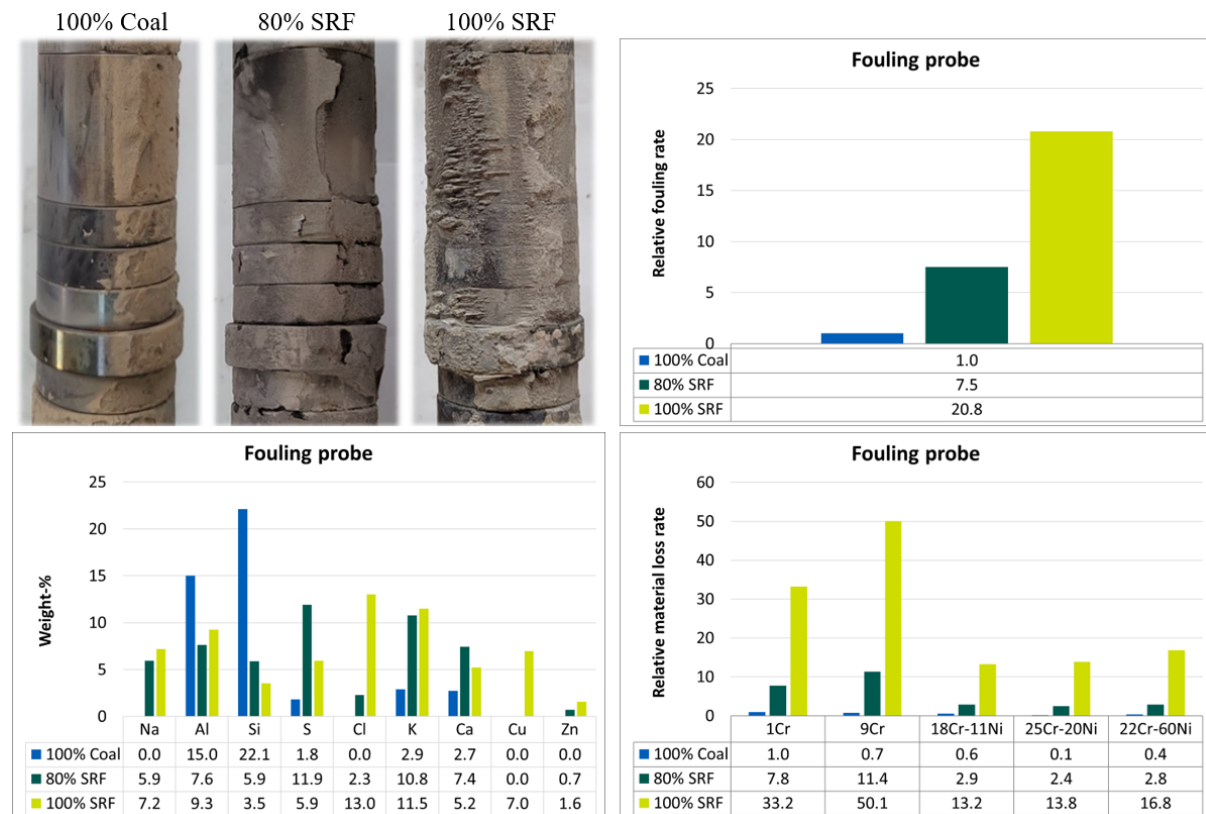
Fig. 5 The convective pass fouling probe from the top after each exposure, flue gas is coming from the left, relative fouling rates, deposit compositions and relative material loss rates of the coupons.

The corrosion probe was installed next to the fouling probe with the target coupon surface temperature of 450 °C. The coupons on the probe were made of 1Cr and 18Cr-11Ni. The appearance of the coupons after exposure and measured relative electrochemical corrosion rates are shown in Fig. 6. During 100% coal firing, corrosion was below the detection limit. Corrosion increased quickly after SRF was introduced and further increased when shifted to 100% SRF firing. The increase in the corrosion signal occurred with delay, which is probably due to less corrosive deposits formed on the coupon surface prior to the SRF test periods. The flue gas temperature was also seen to clearly be affecting the corrosion signal. Throughout the entire test campaign, 18Cr-11Ni was better performing than 1Cr. The cross section of the coupons was analyzed by SEM-EDS. The deposits were mainly composed of calcium sulfates (Ca, S) and alkali chlorides (Na, K, Cl), with some aluminosilicates (Al, Si), no heavy metals were found. Chlorine was found on the metal-oxide interface causing active oxidation of the coupons.
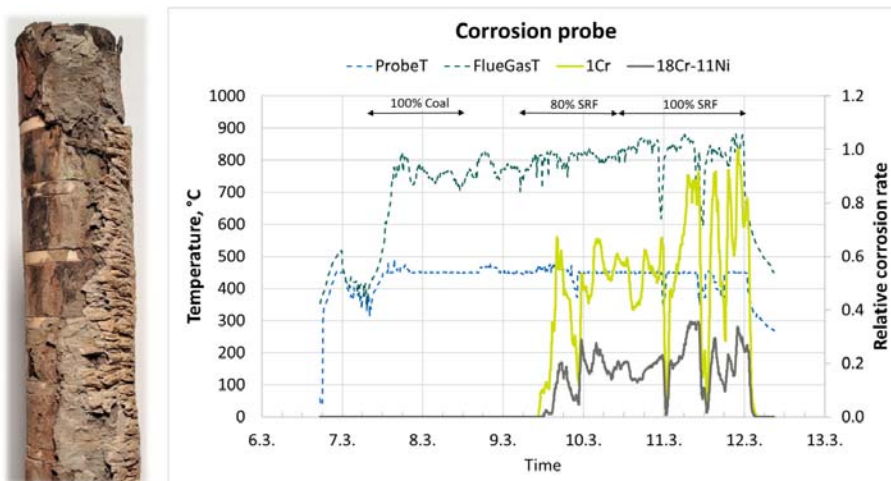
Fig. 6 The corrosion probe after the exposure from the top, flue gas is coming from the right, and electrochemically measured relative corrosion rates of 1Cr and 18Cr-11Ni in the convective pass.

4. Conclusions

When SRF was fired, corrosion was mainly due to alkali chlorides, and corrosion increased by increasing the share of SRF. In the field tests, the material loss in the furnace area increased at higher elevations due to more erosive conditions. In the convective pass, limestone feeding increased fouling and material loss, which could be due to more corrosive deposits as also more frequent soot blowing accelerating oxidation and erosion of the coupons. In the pilot tests, the best performing alloy in the furnace was the weld overlay 22Cr-60Ni (WOL) which material loss was still moderate with 100% SRF. In the convective pass, fouling was moderate with 80% SRF and high with 100% SRF. The performance of the higher alloyed grades (18Cr-11Ni, 25Cr-20Ni and 22Cr-60Ni (WOL)) was quite similar. For them to be applicable with 100% SRF, temperatures would need to be lowered.

Acknowledgment

References

Haaf, M., Barišić, V., Coda Zabetta, E., Kost, M., Bartosz, M., Ströhle, J., Epple, B., Retrofitting Fluidized Bed Power Plants for Waste-Derived Fuels and Novel Process Concepts, Proceedings of the 24th Fluidized Bed Conversion Conference, 8-11 May 2022, Sweden.

Mahanen, J., Vänskä, K., Coda Zabetta, E., Corrosion monitoring in commercial CFBs, Proceedings of the 22nd International Conference on Fluidized Bed Conversion Volume 1 (2015) p. 198- 207, ISBN: 978-952-12-3222-0.

Kuhn, A., Langner, E., Hülsbruch, D., Kallio, E., Söderholm, A., Barišić, V., Ströhle, J., Epple, B., Experimental Investigation of Combustion Characteristics During Co-Combustion of Solid Recovered Fuel and Coal in a 1 MW$_{th}$ Circulating Fluidized Bed Reactor, 14th European Conference on Industrial Furnaces and Boilers, 2-4 April 2024, Portugal.

Gasification of sewage sludge samples in the laboratory scale bubbling fluidized bed

Yermakhan Gabdulkarimuly[1], Sultan Ybray[1,4], Dhawal Shah[2], Michal Jeremias[3], Yerbol Sarbassov[1]

[1]*Mechanical and Aerospace Engineering, School of Engineering and Digital Sciences, Nazarbayev University, Kazakhstan;*
[2]*Chemical and Materials Engineering, School of Engineering and Digital Sciences, Nazarbayev University, Kazakhstan;*
[3]*VTT Technical Research Center of Finland Ltd., Ruukinmestarintie 2 02330, Espoo, Finland*
[4]*Department of Heat Power Engineering S. Seifullin Kazakh AgroTechnical Research University, Kazakhstan;*
Email: ysarbassov@nu.edu.kz

Abstract

Waste-to-Energy is a key concept towards circular economy and sustainability. Among several ways, thermal treatment of municipal sewage sludge (SS) is a carbon-neutral process and provides significant volume reduction of sludge waste. Moreover, with recent global interest towards hydrogen production, gasification of sewage sludge as waste fuel and its optimisation becomes essential. In this work, pre-dried sewage sludge samples collected from the wastewater treatment plant of Astana city, Capital of Kazakhstan, were tested for the gasification processes in the indigenously-developed laboratory scale bubbling fluidized bed rig. Gasification tests were carried out in air, with three bed temperatures: 650 $^\circ$C, 750 $^\circ$C, and 850 $^\circ$C, and at two equivalence ratios (ER) of 0.2 and 0.3. A systematic study of various parametric conditions was carried out in order to determine most efficient and optimum operating conditions. Results of this study shows better performance at higher reactor temperatures, and at 0.2 ER.

Keywords: Bubbling fluidized bed, gasification, sewage sludge, syngas

1. Introduction

Sewage sludge is the solid waste stream of wastewater treatment plants. Conventional utilization methods of sewage sludge include its usage as fertilizer, which was a common practice around the globe (Gao et al., 2020). However, due to the presence of toxic metals and other pollutants, these methods have become less attractive and require significant improvements. In addition, the ever-increasing volumes of sewage sludge worldwide makes it challenging problems to solve. Ferrentino et al. (2023) reported that globally the annual dry sewage sludge production rate is 45 million tons. This huge amount, which will further increase due to global population growth, highlights the significance of alternative utilization methods of sewage sludge. Among the three traditional thermal methods of treating the sludge, i.e., incineration, pyrolysis and gasification, gasification has amassed significant interest recently due to it being a possible pathway for production of hydrogen.

Fluidized bed technologies are well suited for gasification of waste fuels into carbonaceous materials and syngas (Shahabuddin et al., 2020). During gasification, air, steam, or their combination could be used as the gasifying and fluidizing agent (Zhang et al. 2020). Air gasification has been used widely and well known as the basic gasification technique due to its simplicity (Ghani et al., 2009). In the air environment, gasification occurs in the presence of O_2,

which leads to an increased formation of carbon dioxide in the syngas. The authors further investigated the effects of temperature (700 - 900 ^oC), equivalence ratio (0.16-0.46), gas velocity (2 - 3.33 m/s), static bed height (10 - 30 mm) on hydrogen composition of the syngas after air gasification under fluidized bed condition. Results of these experiments revealed that higher temperatures favor H_2 concentration in the syngas. Khan et al. (2022) have simulated gasification in the presence of air at different temperatures and equivalent ratios for improvement of hydrogen yield and conducted lab scale experiments to obtain real data. Their experiments revealed an optimum equivalent ratio of 0.25 at 850^oC for high H_2 concentration.

Several studies in the past have worked on steam gasification of various fuels and biowaste fuels, wherein the reaction of water with the volatiles form an additional hydrogen. Therefore, addition of steam to the air gasification increases the H_2 production. Franco et al. (2003) identified the relationship between syngas composition and reactor temperature & steam to fuel ratio (STF) in a steam gasifier fluidized bed reactor using forestry biomass. These authors found that H_2 generation was increased by 10-20% with the increase of temperature from 700 to 900 ^oC, while slightly decreasing the CO and hydrocarbons concentrations. STF ratio was found to be optimal in a range of 0.6-0.7 for greater syngas yield and H_2 formation. Lee et al. (2018), investigated the effects of steam flow rate on syngas composition in a fluidized bed reactor with a thin, 76 mm inner diameter. The reactor was set to 1000 ^oC, gasifying the 3 g of sewage sludge with variable steam input from 2.5 to 20 g/min. Their results showed that the gasification rate is directly proportional to the steam flow. The optimum steam flow rate for syngas generation was determined to be 5 g/min.

Although several studies have been performed to investigate the efficiency of the gasification of the biomass, few studies were conducted on gasification of sewage sludge. In addition, optimum operating parameters for higher hydrogen yield still need to be explored experimentally. Thus, this research explores the composition of syngas generated from gasification of sewage sludge under fluidized bed condition. The aim of this paper is to evaluate the effect of operating parameters for the individual components of syngas. The focused operating parameters are temperature and ER. Through comprehensive review of current achievements and empirical methods, this paper contributes to development of waste to energy technology through optimizing the process parameters.

2. Materials and Methods

2.1 Sample preparation and characterization

Sewage sludge was collected from Astana Su Arnasy, the wastewater treatment plant (WTP) of Astana city. The samples were dried at 110 ^oC until the weight of the sample became constant. Post-drying the samples were grinded to the desired particle diameter of 0.4 - 0.5 μm as suggested by Khan et al. 2022. 400 g of sand with particle diameter of 0.4 - 0.5 μm was used as the bed material. Ash content was determined based on the ASTM D7582 standard. The samples were thermally treated in a muffle furnace at a temperature of 550 °C for one hour, and volatile matter content was determined using ISO 18134-3:2023. The ultimate analysis of the tested SS was performed using the UNICUBE® micro elemental analyzer. Thermal degradation behavior of sewage sludge pyrolysis was determined by using thermogravimetric analyzer under nitrogen environment.

2.2 Bubbling fluidized bed (BFB) gasifier setup
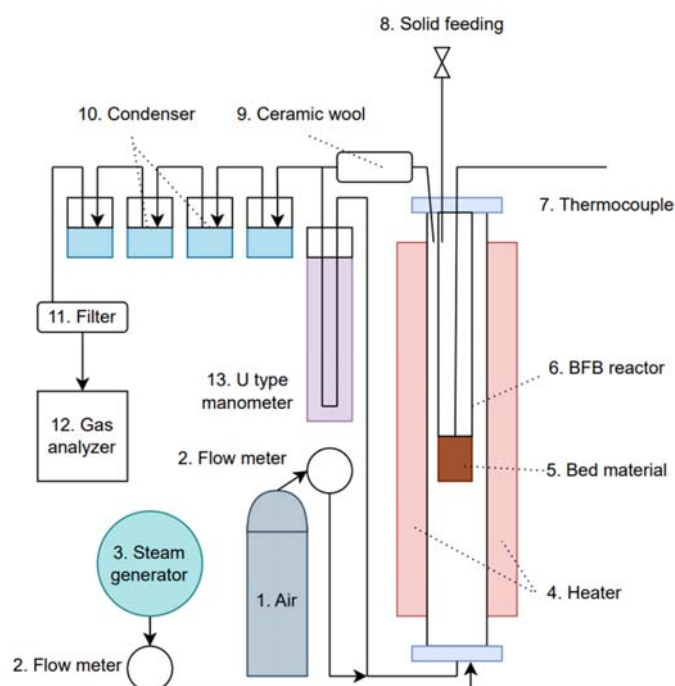
Fig. 1. Experimental setup of the designed bubbling fluidized bed gasifier.

Sewage sludge gasification was carried in a lab scale bubbling fluidized bed reactor with inner diameter and height of 55 mm and 800 mm, respectively. The schematic illustration of the BFB reactor is shown in Fig. 1. Uniform air and steam flow was introduced through the bottom of the reactor and was controlled using Bronkhorst flow meters. Batch feeding of solid sewage sludge samples were performed from the top of the reactor. The temperature of the reactor was controlled using an external (Nabertherm) heater. The produced syngas passed through an isopropanol solution filled in 4 serial impinger bottles, serving as a condenser to filter the syngas from tar and solid particles. Lastly, a gas analyzer (CDL-TeCora ARCMULTI-01) was used for measuring and recording the syngas composition. Table 1 shows the main experimental conditions of this study. Each experiment used 15 g of sewage sludge samples and were repeated 3 times.

Table 1: Experimental conditions used for gasification of the sewage sludge

Operating parameter	Value
Temperature °C	650; 750; 850
Equivalence ratio	0.2; 0.3
SS particle diameter, µm	0.4-0.6

3. Results & discussion

3.1 Thermal properties of samples

The results of the proximate and ultimate analysis of the pre-dried sewage sludge are taken from our previous study and shown in table 2 (Aidabulov et al., 2023). SS is characterized by relatively low moisture content 2.27% and high ash content 32.22%. Ash content reduces the low heating value, but the high volatile matter content 62.82% indicates high thermal decomposition potential. The results are comparable to studies Elbl et al. (2023), Tic et al. (2018).

Table 2. Proximate and ultimate analysis of Astana's pre-dried sewage sludge, (Aidabulov et al., 2023)

Proximate Analysis (wt%)		Ultimate Analysis (wt%, Dry Ash Free)	
FC	2.69	Carbon	48.21
VM	62.82	Hydrogen	5.69
Ash	32.22	Nitrogen	5.49
Moisture	2.27	Sulfur	1.62
HHV (daf), (MJ/kg)	18.87	Oxygen (by difference)	38.99

Based on the TGA analysis, the behavior of thermal degradation of SS was obtained. Fig 2 shows the thermogravimetric (TG) and differential thermogravimetric (DTG) curves for the pre-dried sewage sludge as a function of the temperature at a heating rate of 10 ^{o}C/min under nitrogen atmosphere. In the TG–DTA curves, three distinct regions were identified.
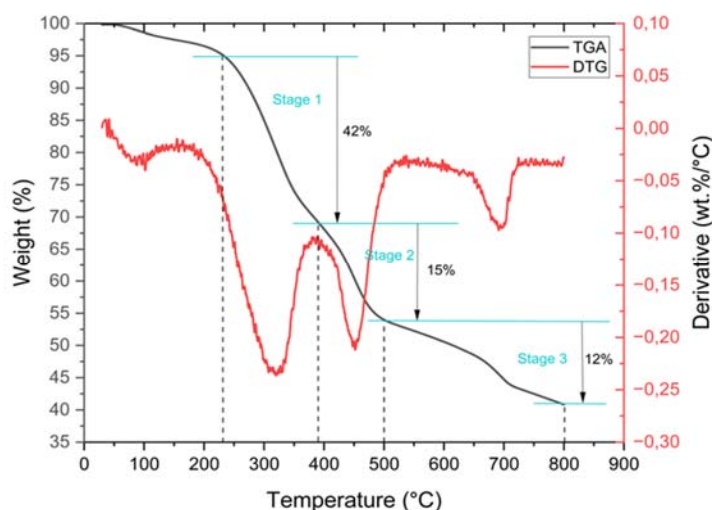
Fig. 2. TGA and DTA graphs for pre-dried sewage sludge under nitrogen environment at 10 ^{o}C/min

The initial weight loss of about 3% is related to the loss of physically adsorbed water molecules at temperatures lower than 120 ^{o}C. The maximum rate of water loss occurred at 109 ^{o}C.

Correspondingly, an endothermic peak appeared, and heat was absorbed by water evaporation. The second weight loss region occurred in the range of 232–380 $^{\circ}$C, about 42% of the total weight of sewage sludge weight loss. In this temperature range main components such as proteins and carboxyl groups decompose. Lastly, in the temperature range from 500 to 800 $^{\circ}$C, sewage sludge sample showed a weight loss of 12.0% of its original mass, slowly approaching a final residue weight of 40.9%. This stage might be attributed to the decomposition of inorganic materials.

The analysis results in fig. 3 show that the total weight loss was only 3.5%. The analysis can be divided into three main stages of decomposition. The first stage is from 21 to 330 degrees with a mass loss of 0.75%. The second main is from 330 to 450 with a weight loss of 1.5%. The third final one is from 450 to 900 with a weight loss of only 1.25%. Based on the data obtained, it can be concluded that the conversion coefficient is very high during air gasification of SS.
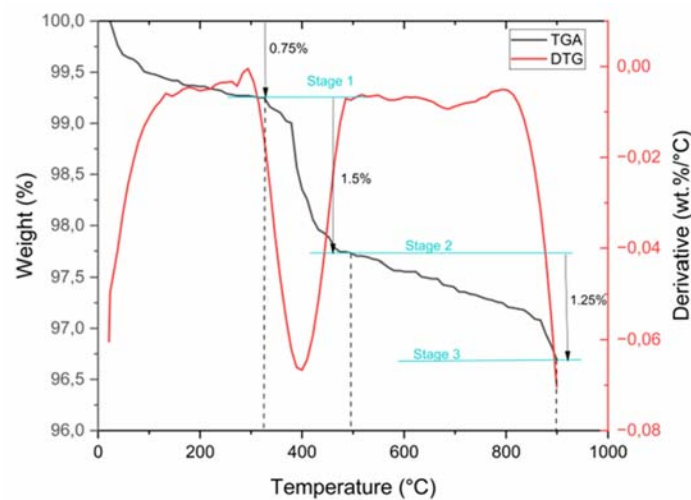
Fig. 3. TGA and DTA graphs sewage sludge ash after air gasification at 650 C under oxygen environment at 10 $^{\circ}$C/min

3.2 Effect of temperature and equivalence ratio on syngas composition

Table 3 shows the effect of temperature and varying ER on the produced syngas composition. The results of air gasification shows that the increase of the bed temperature was directly proportional to the hydrogen concentration, which increased from 5.8% to 18.2%, and inversely proportional with CO and CO_2 composition. This trend indicates that the reaction mechanisms involving H_2 and CO are optimized for a maximum temperature of 850 $^{\circ}$C, the maximum temperature tested in this study. Conversely, formation of CH_4 and CO decreased with an increase of the temperature from 650 to 850 $^{\circ}$C. Negligible effects were observed from the experiments with different ER. This is due to the small difference in equivalence ratio. Since the optimum ER was found to be in a range of 0.2 - 0.3, in order to see the correlation between syngas composition and ER, further experiments are needed at different ERs. A key point to highlight herein is that the gas analyzer detects CO, CO_2, CH_4, O_2 and N_2 from its sensors and H_2 is computed as a residual. Thus, although hydrogen is a key component of the remaining syngas, its purity can be a concern.

Table 3. Composition of syngas obtained from gasification of sewage sludge under various operating conditions

Gas composition (vol%)	ER	650 ºC	750 ºC	850 ºC
CH_4	0.2	24.2	23.1	21.8
	0.3	23.4	21.2	19.1
H_2	0.2	7.3	14.9	17.1
	0.3	5.8	12.4	18.2
CO	0.2	9.7	5.8	6.5
	0.3	7.6	5.4	5.1
CO_2	0.2	11.2	10.4	8.7
	0.3	13.5	12.6	11.2
O_2	0.2	5.3	4.4	5.8
	0.3	5.5	4.9	4.3
N_2	0.2	42.3	41.4	40.1
	0.3	44.2	43.5	42.1

3.3 Effect of gasifying agent on mass balance

Table 4 shows effects of gasifying agents to the char and tar yield. Introduction of steam increased the production of syngas, however it also led to the increase in tar yield which is an undesirable result and decrease in char yield. In order for comprehensive analysis of effects of a gasifying agent, more experiments under different operating parameters are needed.

Table 4. Results for the mass balance at ER=0.2; T=650C.

Input (g)	Output (g)

SS	Air	Steam	Char	Tar	Syngas
15	68	-	3.1	2.3	77.6
15	68	7.5	2.9	4.1	83.5

3.4 Composition of ash and the influence of its elements on gasification

Fig. 4 shows the XRF analysis of sewage sludge ash at 550 and 810 C. The elements are listed in decreasing order of abundance, with silicon dioxide (SiO2) being the most abundant element (24.02 - 25.15%) and strontium oxide (SrO) being the least abundant element (0.18%).
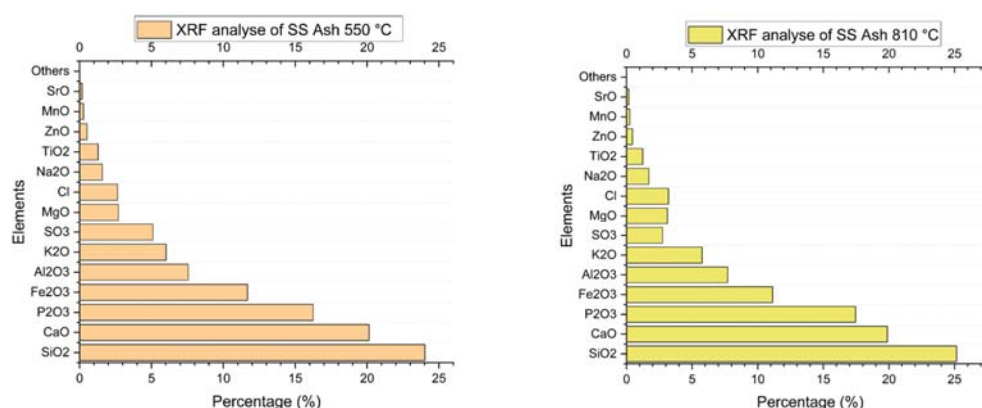
Fig.4. Results of XRF analysis of SS ash oxides

Here are some of the key components identified in the sewage sludge ash and their potential effects on the gasification process. Calcium oxide (CaO): Can act as a catalyst in the gasification process and promote the formation of hydrogen (Li et al., 2021). Silicon dioxide (SiO2): Can act as an inert material in the gasification process. It may reduce the efficiency of the process by absorbing heat. (Yang et al., 2019). Iron and aluminum oxides (Fe_2O_3, Al_2O_3) have been shown to act as catalysts in the gasification process. Studies have demonstrated the development of $Fe_xO_y/CaO\text{-}\gamma\text{-}Al_2O_3$ catalysts capable of achieving a high conversion rate (99.95%) for steam gasification of methoxy-4-methylphenol, a model biomass-derived tar, at a relatively low temperature of 500°C. (Uddin et al., 2008), (Torres et al., 2020)

4. Conclusion

In this paper the composition of syngas obtained from air gasification under bubbling fluidized bed conditions were investigated. Gasification experiments were conducted with the sewage sludge samples in a lab-scale setup. The results show the dominant effect of the temperature for syngas composition and small effect of ER. The maximum hydrogen concentration was obtained to be 18.2% at 850 °C and at an ER 0.2, while CH_4 was reduced to 21.8% of the syngas. In order to

better understand the process of gasification, more experimental campaigns are required. Furthermore, air gasification combined with steam will be conducted and with variable sewage sludge moisture content.

Acknowledgements

References

Aidabulov M, Zhakupov D, Zhunussova K, Temireyeva A, Shah D, Sarbassov Y. Thermal Characterization, Kinetic Analysis and Co-Combustion of Sewage Sludge Coupled with High Ash Ekibastuz Coal. Energies. 2023; 16(18):6634. https://doi.org/10.3390/en16186634

Elbl, P., Baláš, M., Lisý, M., & Lisá, H. (2023). Sewage sludge and digestate gasification in an atmospheric fluidized bed gasifier. Biomass Conversion and Biorefinery. https://doi.org/10.1007/s13399-023-04276-9

Ferrentino, R., Langone, M., Fiori, L., & Andreottola, G. (2023). Full-Scale Sewage Sludge Reduction Technologies: A Review with a Focus on Energy Consumption. Water, 15(4), 615. https://doi.org/10.3390/w15040615

Franco, C., Pinto, F., Gulyurtlu, I., & Cabrita, I. (2003). The study of reactions influencing the biomass steam gasification process☆. *Fuel*, *82*(7), 835–842. https://doi.org/10.1016/s0016-2361(02)00313-7

Ghani, W. a. W. a. K., Moghadam, R. A., Salleh, M. a. M., & Alias, A. B. (2009). Air gasification of agricultural waste in a fluidized bed gasifier: Hydrogen production performance. Energies, 2(2), 258–268. https://doi.org/10.3390/en20200258

Khan, M. A., Naqvi, S. R., Taqvi, S. a. A., Shahbaz, M., Ali, I., Mehran, M. T., Khoja, A. H., & Juchelková, D. (2022). Air gasification of high-ash sewage sludge for hydrogen production: Experimental, sensitivity and predictive analysis. International Journal of Hydrogen Energy, 47(88), 37374–37384. https://doi.org/10.1016/j.ijhydene.2021.11.192

Lee, U., Dong, J., & Chung, J. N. (2018). Experimental investigation of sewage sludge solid waste conversion to syngas using high temperature steam gasification. Energy Conversion and Management, 158, 430–436. https://doi.org/10.1016/j.enconman.2017.12.081

Li, H., Wang, Y., Zhou, N., Dai, L., Deng, W., Liu, C., ... & Ruan, R. (2021). Applications of calcium oxide–based catalysts in biomass pyrolysis/gasification–a review. Journal of cleaner production, 291, 125826. https://doi.org/10.1016/j.jclepro.2021.125826

Quan, C., Kamran, K., & Williams, P. T. (2020). Thermochemical conversion of sewage sludge: A critical review. Progress in Energy and Combustion Science, 79, 100843. https://doi.org/10.1016/j.pecs.2020.100843

Shahabuddin, M., Alam, T., Krishna, B. B., Bhaskar, T., & Perkins, G. (2020). A review on the production of renewable aviation fuels from the gasification of biomass and residual wastes. Bioresource Technology, 312, 123596. https://doi.org/10.1016/j.biortech.2020.123596

Tic, W. J., Guziałowska-Tic, J., Pawlak–Kruczek, H., Woźnikowski, E., Zadorożny, A., Niedźwiecki, Ł., Wnukowski, M., Krochmalny, K., Czerep, M., Ostrycharczyk, M., Baranowski, M., Zgóra, J., & Kowal, M. (2018). Novel concept of an installation for sustainable thermal utilization of sewage sludge. Energies, 11(4), 748. https://doi.org/10.3390/en11040748

Torres, C., Rostom, S., & de Lasa, H. (2020). An Eco-Friendly Fluidizable Fe x O y/CaO-γ-Al2O3 Catalyst for Tar Cracking during Biomass Gasification. *Catalysts*, *10*(7), 806. https://doi.org/10.3390/catal10070806

Uddin, M. A., Tsuda, H., Wu, S., & Sasaoka, E. (2008). Catalytic decomposition of biomass tars with iron oxide catalysts. *Fuel*, *87*(4-5), 451-459. https://doi.org/10.1016/j.fuel.2007.06.021

Yang, J., Ma, L., Yang, J., Guo, Z., Liu, H., Zhang, W., & Wang, L. (2019). Gasification performance and mechanism of high-silicon phosphogypsum oxygen carrier in chemical looping gasification. Energy & fuels, 33(11), 11768-11780. https://doi.org/10.1021/acs.energyfuels.9b02042

Zhang, Y., Wan, L., Guan, J., Xiong, Q., Zhang, S., & Jin, X. (2020). A review on Biomass Gasification: Effect of main parameters on char generation and reaction. Energy & Fuels, 34(11), 13438–13455. https://doi.org/10.1021/acs.energyfuels.0c02900

SIGNIFICANCE OF THE GAS RELEASE ON THE MIXING OF LARGER PARTICLES IN BUBBLING FLUIDIZED BEDS

Azka Rizwana Siddiqui[1]*, Jing Shi[1], Anna Köhler[2],

Diana Carolina Guío-Pérez[1], David Pallarès[1]

[1] *Division of Energy Technology, Department of Space, Earth, and Environment,*

Chalmers University of Technology, SE-412 96 Gothenburg, Sweden

[2] *BioShare AB, Karlstad (Sweden)*

* azkar@chalmers.se

Abstract

The mixing of larger particles (e.g. fuel particles) in dense regions of bubbling fluidized bed units is governed by the interplay of buoyancy forces and the drag from the surrounding solids, whose movement is induced by the bubble flow. The contribution of the gas released from the converting particles (from e.g. drying or devolatilization) to their own mixing is often overlooked. This experimental study aims to evaluate the influence of the gas release from larger particles on their mixing with the bed solids. In this work, experiments are performed in a fluid-dynamically scaled cold flow model resembling typical conditions for the thermochemical conversion of solid fuels (more specifically, the pyrolysis of biomass at 700 °C in a bed of sand fluidized by flue gas). Magnetic particle tracking is used to obtain the trajectory of a large particle resembling biomass properties, while freely moving in the bed. The work uses tracer particles loaded with dry ice to yield a gas release that mimics that of a biomass particle during drying and devolatilization, and compares them with particles of similar physical properties but without the ability to release gas. Different fluidization velocities are examined, revealing that the gas-releasing tracers tend to a deeper immersion within the dense bed at low fluidization velocities, whereas higher fluidization velocities render the gas-releasing tracers more buoyant.

Keywords: Solids mixing, Solids segregation, Fluid-dynamic scaling, Stefan flow, Fluidized bed

1. Introduction

Fluidized beds are extensively used in various industrial processes (e.g. thermochemical conversion of fuels, synthesis, calcination of ores, particle drying and coating, agglomeration, etc.) owing to their efficient mixing capabilities and high heat and mass transfer rates. Understanding the intricate dynamics of particle mixing within fluidized beds is crucial for optimizing their performance and enhancing process efficiency. Previous investigations have given valuable insights into understanding the mixing dynamics in fluidized beds of particles other than the bulk solids. Bubbles have shown to play a pivotal role in the mixing dynamics of fluidized beds, with much research done on understanding the solids mixing/segregation dynamics driven by them (Woollard & Potter, 1968). The bubbles are integral to the behavior of dense fluidized beds, but they not only emerge from the fluidization gas, called exogenous bubbles. Bubbles can also arise from gases that are produced by the chemical reactions or physical transformation of materials in the bed, these are known as endogenous bubbles. Existing research indicates quite some similarities in the structure and behavior of both types of bubbles (Iannello, Macrì, et al., 2023). Several studies have looked at biomass particles to explore the characteristics of endogenous bubbles (resulting from the drying and devolatilization processes) and their role in uplifting fuel particles to the bed surface (Fiorentino et al., 1997; Iannello et al., 2022; Iannello, Bond, et al., 2023; Salatino & Solimene, 2017;

Solimene et al., 2003). These investigations focused on beds under minimum fluidization conditions and with the gas-releasing particles being fed under the bed (Fiorentino et al., 1997; Iannello, Bond, et al., 2023), thereby making it possible to observe their lifting enhancement by the formation of the endogenous bubbles.

However, fluidized bed operation under typical industrial conditions involves fluidization numbers (FN, defined as u/u_{mf}) well beyond 1, and the feedstock feeding above the bed. Moreover, larger particles (such as fuel in thermochemical conversion processes) are prone to be readily segregated to the surface of the bed due to their comparatively lower densities. It is thus of critical importance to comprehend the impact of gas release from such larger feedstock particles on its mixing and under the representative conditions of industrial units (i.e. lighter larger feedstock, above bed feeding, bubbling conditions), even in the scenarios where the formation of endogenous bubbles may not occur.

This research aims to investigate the significance of gas release on the mixing behavior in bubbling fluidized beds of particles larger and lighter than bulk solids. To attain this, experiments are carried out at fluid-dynamically downscaled conditions using a gas-releasing tracer as a reference for a biomass particle undergoing a typical pyrolysis process. The tracer is fed at the top of the bed and different fluidization velocities are applied in the study.

2. Experimental Setup

Fig. 1 schematizes the cold flow model used in this work, featuring a cross-section of 0.17×0.17 m^2 and a 0.04 m-high bed (at rest) consisting of air-fluidized bronze particles with an average size of 189 µm and a density of 8492 kg/m^3 (yielding a minimum fluidization velocity of 0.084 m/s). By applying laws for fluid-dynamic scaling (Glicksman et al., 1994), this set-up resembles pyrolysis at 700 °C in a large-scale bed (0.71×0.71 m^2 and a height of 0.16 m) of sand fluidized by flue gas. Table. 1 lists the scaling of operational conditions and gas and solids properties.

Table. 1: Scaling of operational conditions and gas and solids properties.

Parameters		Hot Reactor		Cold Reactor	
Operating Parameters	Temperature [°C]		700		20
	Pressure [atm]		1		1
	Minimum Fluidization Velocity [m/s]		0.17		0.084
Fluidizing Gas	Density [kg/m^3]	Flue Gas	0.36	Air	1.20
	Viscosity [N/m.s]		4.07e-5		1.83e-5
Bed Material	Density [kg/m^3]	Sand	2600	Bronze	8492
	Particle Size [µm]		789		189
Fuel Particle	Density [kg/m^3]	Biomass	300 – 700	Synthetic Tracer	990 – 2300
	Particle Size [mm]		1 – 90		0.26 – 23.76
Scaling factors (cold/hot)	Length				0.24
	Time				0.49
	Mass				0.05

To investigate the significance of the gas release of larger particles in the bed on their mixing, two types of tracer particles are used: gas-releasing tracers and blank tracers. The tracers selected for the study are cylinders of 12 mm in diameter with an L/D ratio of 1.5 and a density of ~2000 kg/m^3. The gas-releasing tracers consist of a cylindrical case holding a small cylindrical magnet in the center and containing dry ice in both ends. The cylinder is closed with porous caps to allow the release of sublimated CO_2, to mimic the release of gas (i.e., of moisture and volatiles during drying and devolatilization). The blank tracers are constructed in

the exact same way but omitting the dry ice filling. Four fluidization numbers are tested: FN 1.5, 2, 3.5, and 5.
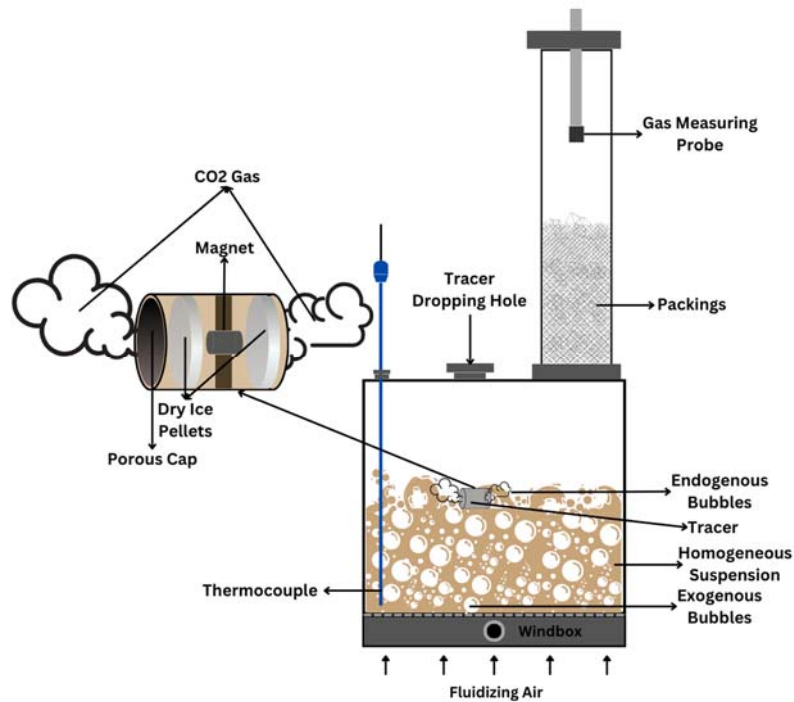
Fig. 1: Experimental setup and depiction of the gas-releasing tracer.

The magnetic particle tracking (MPT) technique (Sette et al., 2015) is used to track the position and orientation of the tracer particle. This technique provides the spatial location of a magnetic tracer with an accuracy of 1 mm, and for this work, a sampling rate of 20 Hz is applied. The core of the tracer consists of a 3×3 mm cylindrical magnet, for which a magnetic field is detected by eight sensors placed outside the bed walls. The gas-releasing tracer is tracked until all the CO_2 sublimates - approximately 15 - minutes and the experiment is repeated 5 times for every set of conditions to ensure the statistical robustness of the acquired data. Blank tracers are tracked for at least 60 minutes. The mixing behavior of the tracers is characterized through the probability density function (PDF) of their vertical location in the bed.

The gas release rate from the tracers is monitored by means of a probe sampling (at 1 Hz) the concentration of CO_2 at the gas exit duct. To ensure representative sampling, packings were placed upstream of this probe, promoting mixing in the outlet gas stream, and thereby eliminating local concentration biases. The time delay characteristic of the measurement system is assessed and accounted for in the data processing. These concentration measurements are later used to analyze the influence of the CO_2 release rate on the mixing. The bed temperature is monitored with a thermocouple to ensure uniform conditions throughout the experiment and in between repetitions.

3. Results and Discussion

As shown in Fig. 2, the probability distribution of vertical locations for FN=2 indicates that the gas-releasing tracer predominantly takes positions slightly below the bed surface, while the blank tracer is observed to be more likely to float on the surface of the bed. Additionally, the gas-releasing tracer exhibits a wider distribution of vertical positions, suggesting enhanced vertical mixing. This finding suggests enhanced contact between the gas-releasing particles and the bed solids suspension, which has the potential to alter heat transfer and mass transfer in comparison to particles without significant gas release. These aspects need to be added to the consideration of the presence of a Stefan flow when evaluating the mass and heat transfer between the particle and the surrounding bed.
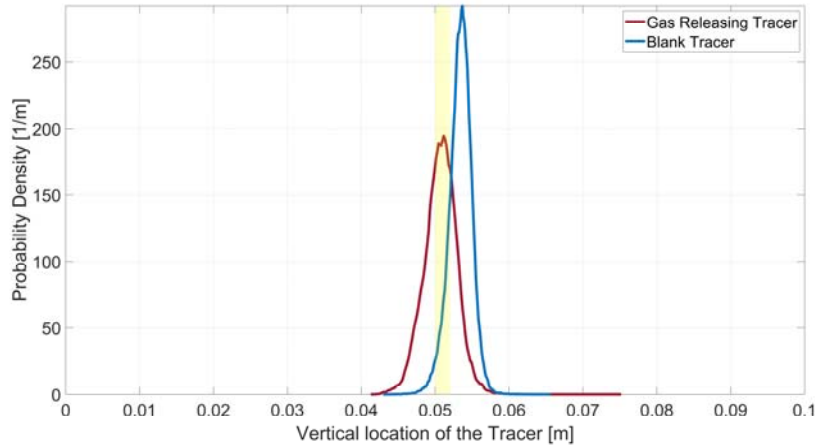
Fig. 2: PDF of the vertical location of the tracer. The yellow band indicates the bed surface interval. FN=2.

In order to further understand the effect of the gas release on the particle-bed mixing, the average vertical position of the tracer is plotted against the release rates of CO_2 and is shown in Fig. 3. The data plotted for gas release rate equal to zero, corresponds to the blank tracer as an allusion. In contrast, the gas-releasing tracer penetrates deeper into the dense bed at intermediate release rates, while for the highest release rates, a tendency of increased buoyancy is observed, although the limited number of data points for such high release rates must be noted.
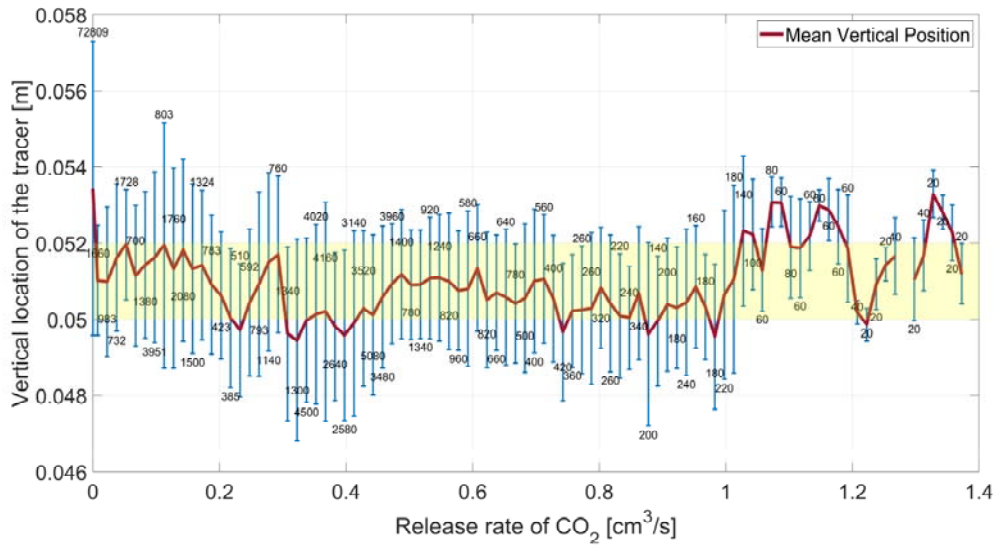
Fig. 3: Vertical position of tracers as a function of the release rate of CO_2. FN=2. The bars indicate the standard deviation in the data distributions corresponding to each release rate bin, and number tags indicate the amount of data points in each distribution. The yellow band indicates the bed surface interval.

According to measurements by Iannello et al. (2023), the local velocity of volatiles released from biomass at hot conditions ranges within 0.01-0.1 m/s. In this study, the gas release rates attained (refer to the x-axis in Fig. 3 for release rates in the cold model) reach velocities which on an up-scaled basis correspond to values up to 0.02 m/s.

Fig. 4 compares the vertical distributions of gas-releasing and blank tracers for all the fluidization velocities tested. Note that for gas-releasing tracers, the data contains the whole range of releasing rates. The general shift of the distributions towards higher values as the fluidization velocity is increased is attributed to the bed expansion, which sets the bed surface level at a higher location. As seen in the figure, for lower fluidization velocities (FN≤2) the gas-

releasing tracer is found to immerse the dense bed more than blank tracers. However, under higher fluidization conditions (FN≥3.5) the gas-releasing tracers exhibit a slightly higher buoyancy than blank tracers. This contrasting impact of the gas release at different fluidization velocities can be explained by the following: at higher fluidization velocities, the excess gas velocity becomes sufficiently large to generate a bubble flow that dominates the fluid-dynamics of the bed, making the influence of the gas released from the particle negligible. Thus, the gas-releasing tracers behave roughly the same as blank tracers.
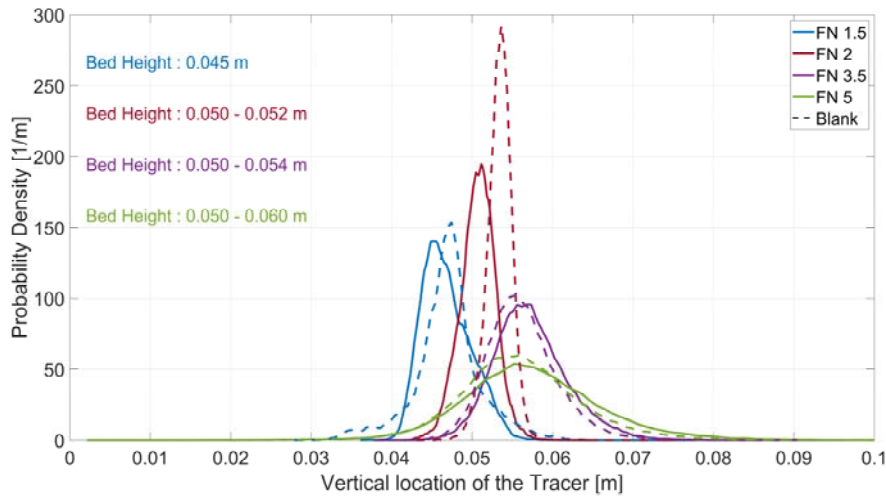
Fig. 4: Probability density function of the vertical location of the tracers for different fluidization numbers. Dashed curves indicate blank tracers.

Fig. 5 exemplifies typical horizontal tracer trajectories for FN=5. As seen, the blank tracer tends to remain in the same horizontal position only fluctuating across the vertical dimension. Instead, the gas-releasing tracers show strong lateral dispersion, with trajectories covering wide areas of the horizontal cross-section of the bed.
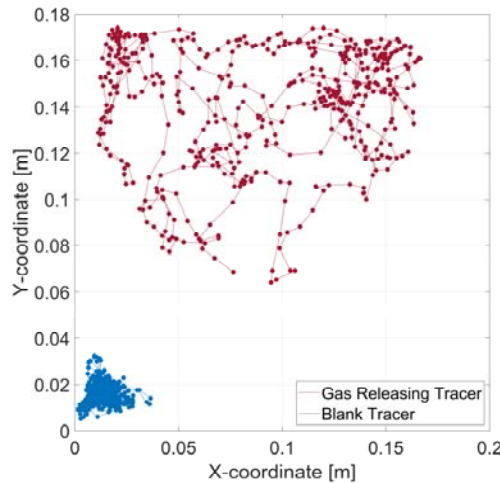
Fig. 5: Horizontal trajectories of the two types of tracers used. Data representing 25 s (500 data points). FN=5.

The horizontal dispersion coefficients of the particle, under each FN value have been calculated using the Einstein equation for a length threshold of 0.02 m and are presented in Table. 2 below. At lower fluidization conditions (FN ≤ 2), the lateral dispersion is too small to make meaningful comparisons. At FN=3, the dispersion coefficient is comparatively similar for both tracers. However, at FN=5, the dispersion coefficient for the gas-releasing tracer is nearly 40% larger than that of the blank tracer, thus the impact of the gas release overcomes the constraints of bed dynamics at FN values above 3.5.

Table. 2: Horizontal particle dispersion coefficients for tested fluidization numbers.

Tracer	Horizontal dispersion coefficient (m^2/s)			
	FN 1.5	FN 2	FN 3.5	FN 5
Gas-releasing	1.42e-05	2.04e-05	4.04e-04	1.1e-03
Blank	8.19e-07	1.97e-04	4.57e-04	7.90e-04

4. Conclusion

The significance of gas released from the particles on the mixing of larger and lighter particles is studied at different fluidization conditions. Magnetic particle tracking is used in a fluid-dynamically downscaled unit to precisely measure and then analyze the movement of gas-releasing particles and non-releasing particles. Results show that at low fluidization velocity, the gas-releasing tracers are more immersive into the dense bed than the blank tracers. While, at higher fluidization numbers the difference between gas-releasing and blank tracers becomes insignificant in terms of vertical mixing. Analysis of the horizontal tracer trajectories at higher fluidization velocities illustrates a higher horizontal mixing rate of gas-releasing tracers compared to blank tracers, which typically were trapped in corner regions. This insight also sets the direction for future work exploring the impact of higher gas release rates and the lateral mixing of gas-releasing tracers.

Acknowledgment

References

Fiorentino, M., Marzocchella, A., & Salatino, P. (1997). Segregation of fuel particles and volatile matter during devolatilization in a fluidized bed reactor—II. Experimental. *Chemical Engineering Science*, *52*(12), 1909–1922. https://doi.org/10.1016/S0009-2509(97)00019-5

Glicksman, L. R., Hyre, M. R., & Farrell, P. A. (1994). Dynamic similarity in fluidization. *International Journal of Multiphase Flow*, *20*(SUPPL. 1), 331–386. https://doi.org/10.1016/0301-9322(94)90077-9

Iannello, S., Bond, Z., Sebastiani, A., Errigo, M., & Materazzi, M. (2023). Axial segregation behaviour of a reacting biomass particle in fluidized bed reactors: experimental results and model validation. *Fuel*, *338*(October 2022), 127234. https://doi.org/10.1016/j.fuel.2022.127234

Iannello, S., Foscolo, P. U., & Materazzi, M. (2022). Investigation of single particle devolatilization in fluidized bed reactors by X-ray imaging techniques. *Chemical Engineering Journal*, *431*(P1), 133807. https://doi.org/10.1016/j.cej.2021.133807

Iannello, S., Macrì, D., & Materazzi, M. (2023). A comprehensive assessment of endogenous bubbles properties in fluidized bed reactors via X-ray imaging. *Powder Technology*, *413*(October 2022), 118013. https://doi.org/10.1016/j.powtec.2022.118013

Salatino, P., & Solimene, R. (2017). Mixing and segregation in fluidized bed thermochemical conversion of biomass. *Powder Technology*, *316*, 29–40. https://doi.org/10.1016/j.powtec.2016.11.058

Sette, E., Pallarès, D., Johnsson, F., Ahrentorp, F., Ericsson, A., & Johansson, C. (2015). Magnetic tracer-particle tracking in a fluid dynamically down-scaled bubbling fluidized bed. *Fuel Processing Technology*, *138*, 368–377. https://doi.org/10.1016/j.fuproc.2015.06.016

Solimene, R., Marzocchella, A., & Salatino, P. (2003). Hydrodynamic interaction between a coarse gas-emitting particle and a gas fluidized bed of finer solids. *Powder Technology*, *133*(1–3), 79–90. https://doi.org/10.1016/S0032-5910(03)00080-9

Woollard, I. N. M., & Potter, O. E. (1968). Solids mixing in fluidized beds. *AIChE Journal, 14*(3), 388–391. https://doi.org/10.1002/aic.690140310

ALTERNATIVE BED MATERIALS FOR HIGH ALKALI FUELS AND TORREFACTION OF BIOMASS: DOES IT REDUCE THE RISKS OF FUEL ASH SLAGGING, BED AGGLOMERATION, FOULING AND CORROSION IN COMBUSTION?

Dmitry Klimov[1]*, Sergey Kuzmin[1], Oleg Milovanov[1], Sergey Grigoriev[1], Artem Ryzhenkov[1], Vadim Kokh-Tatarenko[1]

Affiliation and address National Research University "Moscow Power Engineering Institute"-scientific center "Wear resistance", Russia, Moscow, Krasnokazarmennaya st. 17, building 1

*Email: klimovd.ce@gmail.com

Abstract

Biomass is considered as a renewable energy source. Sunflower seed hulls (SSH) are formed during the shelling of seeds and account for approximately 18–20 wt.% of the mass of processed seeds. The high lignin content in SSH results in a high combustion heat value for this type of waste, approximately 20.10 MJ/kg. SSH is difficult to use as fuel, because its ash contains alkali (K, Na) and alkaline earth (Ca, Mg) metals, as well as Si, S, Al, P and Cl. Agglomeration is one of the operational problems in fluidized bed combustion of biomass, which is caused by interaction between bed materials (e.g. silica sand) and the biomass ash with a high content of potassium species. The paper analyses two techniques that can contribute to stable boiler operation during SSH combustion: 1) replacement of silica sand with quartz-free material (olivine), 2) pre-treatment of biomass before combustion by torrefaction.

1. Introduction

During biomass fluidized bed combustion, the common problem is agglomeration of inert material particles and biomass ash, leading to de-fluidization and boiler stoppage (Anicic B et al., 2018). Combustion of agricultural wastes has been particularly challenging as this biomass typically contains elevated alkali content in the ash (Scala F., 2018). Such types of biomass include sunflower seed hulls (SSH). SSH has a moisture content below 10 %, an ash content of 1.98 - 2.22 %, and a calorific value of about 18 MJ/kg (Perea-Moreno M. – A. et al., 2018). The volumes of sunflower processed make SSH one of the cheapest sources of thermal energy (Perea-Moreno M. – A. et al., 2018). SSH ash contains alkali (K, Na) and alkaline - earth (Ca, Mg) metals, as well as Si, S, Al, P and Cl [9]. This causes rapid growth of ash deposits and corrosion of convective heating surfaces of boilers, as well as agglomeration of inert material particles during fluidized bed combustion of sunflower husks (Raclavska H. et al., 2011).

Agglomeration is frequently seen in biomass fluidized bed combustion and gasification using silica sand as an inert bed material (Visser, H. J. M. et al., 2008) due to the formation of fusible compounds from the interaction of biomass ash and SiO_2. The replacement of SiO_2 based bed material with alternative materials containing aluminium, calcium, magnesium and iron can slow down the agglomeration. Such alternative materials include olivine ($(MgFe)_2SiO_4$) (Almark M. and Hiltunen M., 2005). The temperature of de-fluidization onset was increased in some biofuels burning in an olivine fluidized bed compared to burning in a silica sand bed. In some cases, such as wheat straw burning, this effect could not be achieved. This means that additional studies of combustion processes of different types of biomass, including SSH in an olivine fluidized bed, are needed.

Biomass torrefaction can increase the heat of combustion of biomass, reduce the cost of grinding biomass for co-firing with coal, and impart hydrophobic properties to biomass, which simplifies biomass transport and storage (Abelha P. et al., 2019, Nebyvaev A. et al., 2023). However, fluidized bed combustion processes of thus prepared SSH have not been studied.

The aim of this paper is to comparatively study the combustion process of raw SSH and torrefied SSH in fluidized bed of silica sand and olivine.

2. Materials, facility and experimental procedure

2.1 Materials.

Silica sand and olivine were used as bed material. The silica sand had a particle size of 0.6 - 0.8 mm and a bulk density of 1416 kg/m^3. The chemical composition of the silica sand was as follows: Na_2O – 1,4 %, K_2O – 2,8 %, CaO – 0,6 %, MgO – 0,5 %, Al_2O_3 – 7,0 %, Fe_2O_3 - 2,2 %, SiO_2 – 84,9 %, P_2O_5 – 0,1 %, TiO_2 – 0,3 %. The average particle size of olivine was 0.34 mm. Olivine had a density of 3300 kg/m^3 and a bulk density of 2000 kg/m^3. The use of silica sand and olivine allowed burning SSH in the same boiler without changing the blower fan at a fluidization number of 3.5 - 4.0. The chemical composition of olivine was as follows: MgO – 50 %, SiO_2 – 42 %, $FeO + Fe_2O_3$ – 7 %, Al_2O_3 – 0,5 %, CaO – 0,2 %, free silica < 0,1, impurities – 0,3 %.

SSH was burnt in the combustion chamber. SSH had the following characteristics: moisture content - 8.24 %, ash content - 2.06 %, S - 0.02 %, C - 48.2 %, H_2 - 5.71 %, N_2 - 0.7 %, O_2 - 35.07 %, volatile matter - 70.48 %, net calorific value - 17.88 MJ/kg. The chemical composition of sunflower husk ash was as follows: SiO_2 – 1.24%, TiO_2 – 0.02%, Al_2O_3 – 0.36%, Fe_2O_3 – 0.43%, CaO – 6.39%, MgO – 12.05%, K_2O – 38.99%, Na_2O – 0.93%, P_2O_5 – 11.72%, SO_3 – 6.1%, Cl – 1.77%.

Proximate analysis of the sample was performed according to ASTM standards, while the ultimate analysis was implemented using Leco TruSpec® CHN ultimate equipment with Leco TruSpec® S module. The higher heating value was determined by IKA C2000 calorimeter.

An index was calculated to evaluate the potential for bed agglomeration during SSH combustion (Vamvuka . and Zografos D., 2004):

$$BAI = \frac{Fe_2O_3}{Na_2O + K_2O}$$

Agglomeration should be noted when the raw SSH is burned in a fluidized bed of silica sand, as the BAI < 0.15 (Vamvuka . and Zografos D., 2004).

The burning characteristics of the raw and torrefied sample as well as the effects of temperature on the weight loss characteristics during torrefaction were determined using a thermal analyzer which is TA Instruments SDTQ 600 model device. The behavior of raw SSH throughout the heating period is illustrated in Fig. 1 (TGA and DSC curve's). The mass loss graph (Fig.1) shows that the torrefaction temperature should not exceed 250 ºC, as SSH mass loss increases dramatically at higher temperatures.
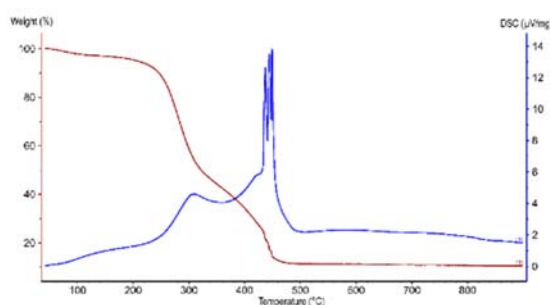
Fig. 1. Effects of torrefaction temperature on the weight recovery and the heat flow.

2.2. Facility.

Sunflower husk torrefaction process was carried out in a heart-type reactor. The scheme of the reactor is shown in Fig. 2.
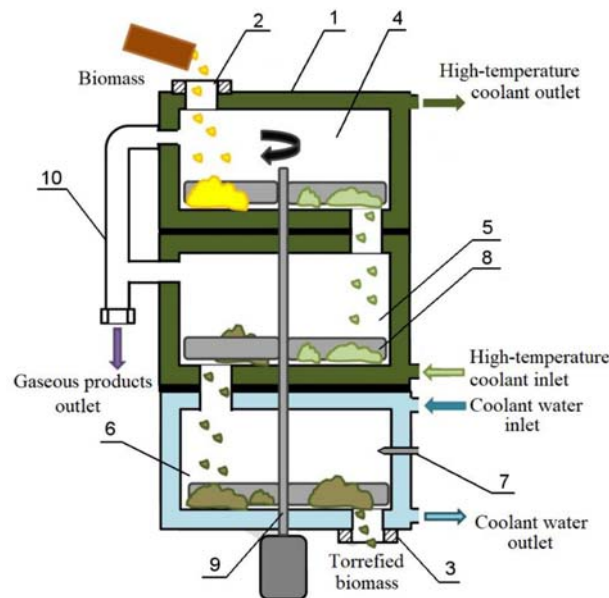
Fig. 2. Scheme of a heart-type reactor for the torrefaction of SSH

Liquid high-temperature coolant with a temperature of 300 ºC is fed into the jacket of the reactor 1. A portion of raw SSH is loaded into reactor 1 through unit 2, and moved through plates 4, 5 and 6 with the help of agitator 9. On plate 6, the torrefied SSH is cooled by finely atomized water supplied through nozzles 7. On plate 6, the SSH is cooled down to 80 ºC. The water is evaporated and water vapour is discharged from the reactor through the pipeline 10.

The study of sunflower husk combustion process was carried out in an industrial boiler of 2 MW capacity equipped with a fluidized bed combustion chamber. The scheme of the boiler is shown in Fig. 3.
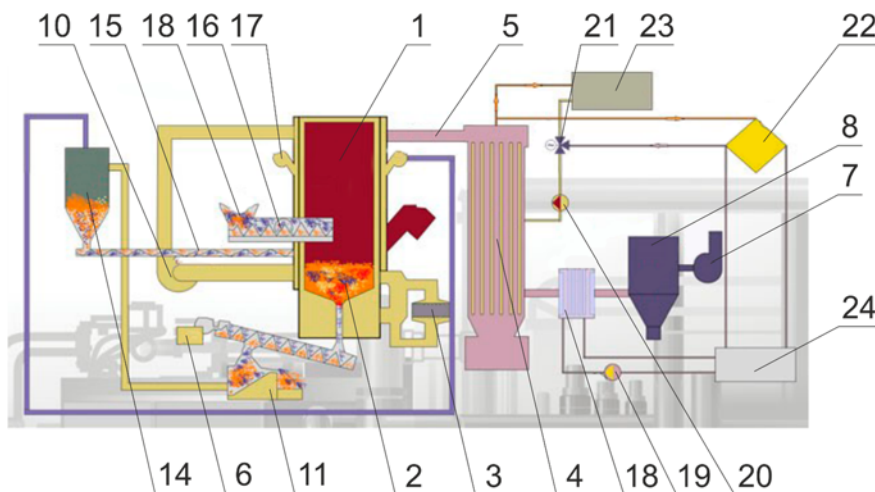
1. Combustion Chamber, 2. Inert Bed, 3. Calorifier Unit, 4. Heat Exchanger, 5. Transition, 6. Inert Discharge Auger, 7. Smoke Fan, 8. Cyclone, 9. Burner, 10. Air Blower, 11. Separator, 12. Inert Return Fan, 13. Fuel Storage Hopper, 14. Inert Storage Hopper, 15. Inert Feed Auger, 16. Fuel Feed Auger, 17. Fan, 18. Utilizer, 19. Utilizer Pump, 20. Thermal Oil Pump, 21. Three-way Valve. 22. Heat consumer. 23. ORC. 24. Heating and hot water circuit

Fig 3. FBC boiler

The boiler features a combustion chamber with "bottom circulation" of inert material. At accumulation of ash in the fluidized bed the auger 6 is switched on (Fig. 3) and fed the inert material into the separator 11. The separator 11 removes the formed agglomerates. Then the inert material by means of the fan 12 returns to the hopper 14 and to the boiler combustion chamber.

2.3. Experimental procedure.

SSH torrefaction was carried out at a temperature of 250 ºC for 1 hour. SSH was combusted at a bed temperature of 750 - 800 ºC at a fluidization number of 3.5 - 4.0 (minimum fluidization velocity of 0.8 m/s). Samples of bed material (silica sand or olivine) were taken through the combustion chamber door approximately every 4 hours and their fractional composition was analyzed. In transition 5 (Fig. 2) the probe of the "Vario Plus Industrial" gas analyzer was placed. With the help of this probe the temperature of flue gases and the content of O_2, CO and CO_2 were determined.

3. Results and discussion.

3.1. Results of analyses of torrefied SSH.

SSH obtained by torrefaction had the following characteristics and composition: moisture - 3,11 %, ash content - 3,83 %, S - 0,01 %, C - 51,7 %, H_2 - 5,85 %, N_2 - 0,74 %, O_2 - 34,76 %, volatile matter - 65,08 %, net calorific value - 20,85 MJ/kg. The chemical composition of the torrefed SSH ash was as follows: SiO_2 – 2,42 %, TiO_2 – 0,03 %, Al_2O_3 – 0,8 %, Fe_2O_3 – 1,37 %, CaO – 11,88 %, MgO – 6,35 %, K_2O – 39,16 %, Na_2O – 0,35 %, P_2O_5 – 4,13 %, SO_3 – 8,9 %, Cl – 1,16 %, loss on ignition of ash sample – 23,45 %. Agglomeration of silica sand particles and SSH ash (BAI = 0.035) should also be seen during combustion of torrefied SSH.

3.2. Results of study of SSH combustion in silica sand fluidized bed.

About 70 hours after the start of boiler operation at combustion of raw and torrefied SSH significant fluctuations of O_2, CO and CO_2 concentrations in flue gases were noted (Fig. 4). This meant the de-fluidization process.
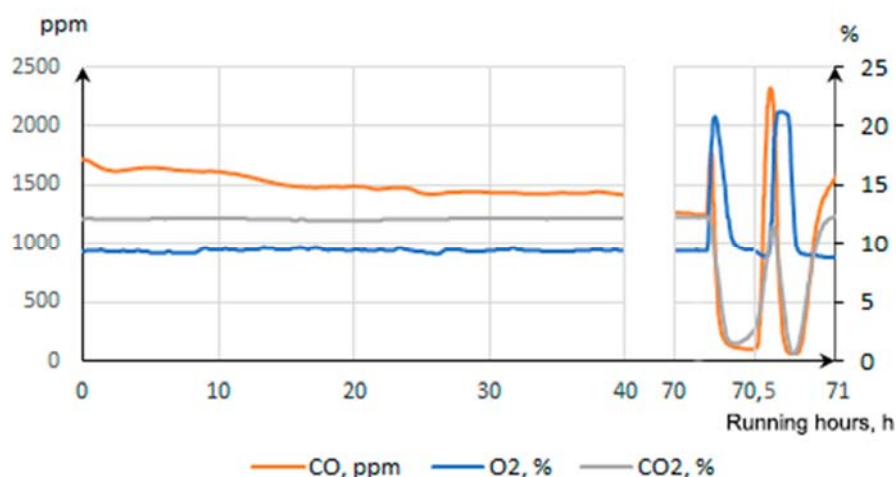
Fig. 4. Variation of CO, CO_2 and O_2 concentration in flue gases during combustion of SSH in a silica sand fluidized bed

In fact, when analyzing the samples of inert material taken from the combustion chamber, agglomerates in the form of balls of different diameters from 2 - 3 mm to 6 - 7 mm were found. The proportion of agglomerates formed in the fluidized bed after 70 hours of continuous operation of the boiler was about 30 %. This made further operation of the boiler impossible. The agglomerates were very hard and contained a core and a shell. The SiO_2 content in the agglomerate core (69.25 g/kg) was 7.93 times higher than in its shell (8.73 g/kg), and the K_2O content was 1.8 times higher in the shell (219.32 g/kg) than in the bed core (122.18 g/kg). I.e.

in the beginning a low-melting eutectic of silicon compounds contained in the sand and potassium contained in the husk ash is formed, which glues the sand particles together. In the second step this agglomerate germ is covered with molten ash. The replacement of raw SSH with torrefied SSH did not affect the agglomerate formation process.

3.4. Results of study of SSH combustion in olivine fluidized bed.

At combustion of raw and torrefied SSH in olivine fluidized bed no dramatic fluctuations of CO, CO_2 and O_2 concentrations were registered (Fig. 5) at long (during 600 hours) continuous operation of the boiler. It should be noted that the concentration of CO in flue gases at combustion of raw SSH reached 2000 ppm (Fig. 5 a), while at combustion of torrefied SSH the concentration of CO did not exceed 350 ppm (Fig. 5 b). This means that SSH torrefaction allows burning this fuel with higher efficiency.

(a) Raw SSH   (b) Torrefied SSH
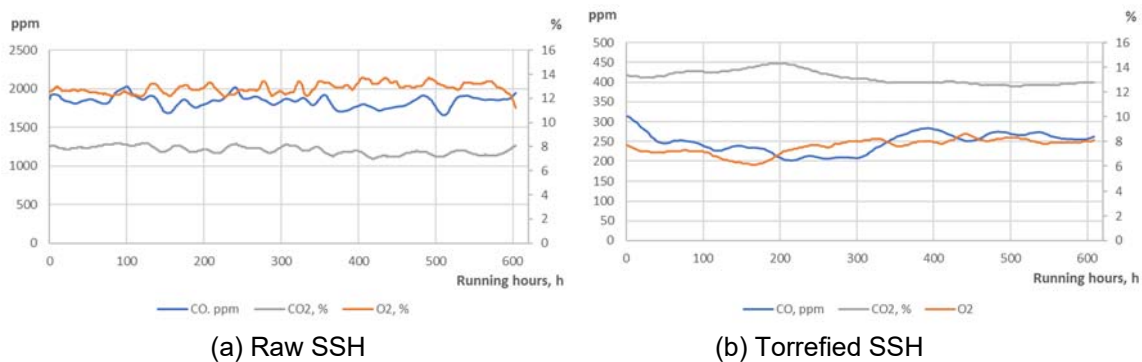
Fig. 5. Variation of CO, CO_2 and O_2 concentration in flue gases during combustion of SSH in olivine fluidized bed

The fraction composition of olivine fluidized bed at SSH combustion changes during the first 58 hours of boiler operation (Fig. 6). It is obvious that in the first few tens of hours of operation of the fluidized bed combustion chamber very small fractions of olivine are taken out of the bed. No formation of agglomerates of fuel ash and olivine particles was found.
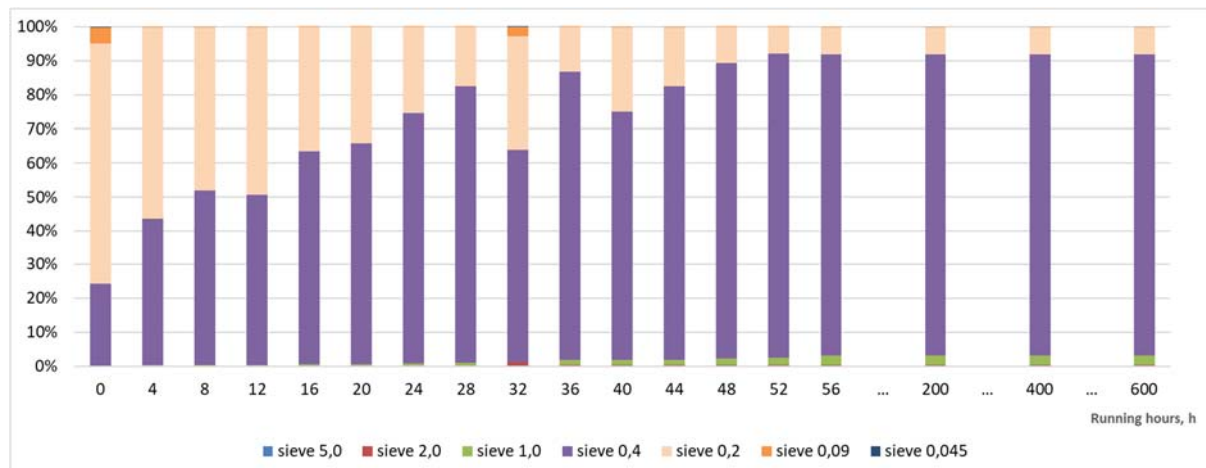
Fig. 6. Variation in fraction composition of olivine bed during SSH combustion

When a mixture of aspen and willow was combusted in the olivine fluidized bed, no agglomerate formation was also detected (Almark M. and Hiltunen M., 2005). At the same time potassium compounds in the olivine fluidized bed did not accumulate. However, the content of potassium compounds in the ash deposits in the convective heat exchanger tubes increased, which was more than twice as high as the content of potassium compounds in these deposits when burning aspen-willow mixture in silica sand fluidized bed.

In our case, the content of potassium compounds in ash deposits in the pipes of the convective heat exchanger was 181.85 g/kg when SSH was burnt in a silica sand fluidized bed, and 324.16 g/kg when burnt in an olivine bed. I.e. in the olivine fluidized bed, potassium compounds do not accumulate, but are carried out of the combustion chamber and deposited in the tubes of the convective heat exchanger. However, these deposits were friable and they did not interfere with stable operation of the boiler.

4. Conclusion

Combustion of SSH in a silica sand fluidized bed leads to formation of agglomerates of ash and inert material about 72 hours after boiler start-up. Replacement of the raw SSH with torrefied SSH does not affect the de-fluidization process.

No agglomerate formation occurs with prolonged (600 hours) combustion in olivine fluidized bed as with SSH in any form. Potassium compounds in the olivine bed do not accumulate, but are carried out of the combustion chamber and deposited in the tubes of the convective heat exchanger in the form of friable ash deposits. These ash deposits do not interfere with the normal operation of the boiler.

When burning torrefied SSH, CO emissions into the atmosphere are about 4.25 times lower than when burning raw SSH. Chlorine content in torrefied SSH is 1.5 times lower than in the raw SSH. This suggests less intensive corrosion of convective heating surfaces of the boiler when burning torrefied SSH.

In summary, replacement of silica sand with olivine and torrefaction of SSH allow to significantly increase reliability and environmental compatibility of the combustion process of this type of fuel in the fluidized bed.

Acknowledgment

References

Anicic B., Lin W., Kim Dam-Johansen K. – D., Wu H. Agglomeration mechanism in biomass fluidized bed combustion – Reaction between potassium carbonate and silica sand, Fuel Processing Technology 173 (2018) 182–190

Scala F. Particle agglomeration during fluidized bed combustion: Mechanisms, early detection and possible countermeasures, Fuel Processing Technology 171 (2018) 31–38.

Perea-Moreno M. – A., Francisco Manzano-Agugliaro F., Perea-Moreno A.- J. Sustainable Energy Based on Sunflower Seed Husk Boiler for Residential Buildings, Sustainability 2018, 10, 3407.

Raclavska H., Juchelkova D., Roubicek V., Matysek D. Energy utilisation of biowaste — Sunflower-seed hulls for co-firing with coal, Fuel Processing Technology 92 (2011) 13–20.

Visser, H. J. M.; Hofmans, H.; Huijnen, H.; Kastelein, R.; Kiel, J. H. A. Biomass Ash - Bed Material Interactions Leading to Agglomeration in Fluidized Bed Combustion and Gasification. Prog. Thermochem. Biomass Convers. 2008, 272–286.

Almark M., Hiltunen M. Alternative bed materials for high alkali fuels, Proceedings of FBC2005 18th International Conference on Fluidized Bed Combustion May 22-25, 2005, Toronto, Ontario, Canada.

Abelha P., Vilela C. M., Nanou P., Carbo M., Janssen A., Leiser S. Combustion improvements of upgraded biomass by washing and torrefaction, Fuel 253 (2019) 1018–1033.

Nebyvaev, A.; Klimov, D.; Ryzhenkov, A.; Brulé, M. Preliminary Results of Innovative Two-Stage Torrefaction Technology Applied for Thermochemical Treatment of Sunflower Husk. Processes 2023, 11, 2486.

Vamvuka D., Zografos D. Predicting the behaviour of ash from agricultural wastes during combustion, Fuel, 2004, 83, 2051–2057.

THE RELATIONSHIP BETWEEN SOLID CHARACTERISTICS AND SEGREGATION IN A TERNARY FLUIDIZED BED FOR THE GASIFICATION OF A WASTE OF THE OLIVE OIL INDUSTRY

Rossella Girimonte [1]*, Daniele Sofia [1]

[1]*Department of Computer Engineering, Modeling, Electronics and Systems, University of Calabria, Via P. Bucci cubo 39/c Rende (CS), 87036, ITALY*

*Email: *rossella.girimonte@unical.it*

Abstract

Conversion of biomass into syngas is usually operated in fluidized beds of inert material, with the purpose of achieving a stable fluidization regime with high performances. During the process, the production of secondary products such as tars is often encountered, with serious problems resulting from their condensation and aerosol formation, causing corrosion, fouling or even clogging of engines or turbines and also deactivation of the catalysts used in downstream operations. A reduction of the content of tars in syngas can be achieved by integrating specific catalysts (e.g. Olivine) in the gasification reactor; the fluidized bed is thus formed by a ternary mixture (biomass, inert and catalyst) and controlling the mixing state of its components becomes a difficult task due to differences in particle density, size and shape of the various materials. Though focused on the case of a specific biomass, crushed olive pits produced by the olive oil industry, the present study analyses the effects of the diversity of particle diameter, density and shape in a ternary mixture of biomass, sand and olivine on segregation of the three components. Since the particle density increases from the biomass to sand and then to olivine, the average sizes of the three particulate solids were chosen in the opposite order to explore the possibility of contrasting as much as possible the tendency to segregation due to the density differences. Two main cases are explored: the first mixture is characterized by a significant volume fraction of the olive pits (the biomass), fixed at a value of 0.7, while the other components fractions are let vary; in the second case, more interesting for industrial applications, the fraction fixed at a value of 0.7 is that of sand (the inert component). The results obtained from experiments devoted to determining the variations of the internal voidage of the mixtures as well as their characteristic velocities of fluidization are discussed.

1. Introduction

Fluidized bed reactors play a pivotal role in the thermochemical decomposition of biomass, owing to their ability to ensure high rates of heat and mass transfer, flexibility in utilizing different energy sources, and ease of separating volatile components produced during operation. These reactors provide an efficient platform for biomass gasification, a process in which an inert material such as silica sand, alumina, or calcite is added to the solid of interest to assist in its fluidization and enhance the heat transfer process at temperatures typically ranging from 600-900°C or even higher. Biomass gasification results in the production of fuel gases with low-to-medium heating value, containing significant amounts of CO, H_2, CH_4, CO_2, H_2O, and N_2, along with secondary products like tars, inorganic compounds (alkali metals, nitrogen, sulfur, and chlorine compounds), and solid particles. Tars pose one of the most challenging secondary products as they can cause particle agglomeration, catalyst deactivation, and hot corrosion of metal surfaces both in gasifiers and downstream systems.

The issue of tar formation has been addressed in various literature reviews, focusing not just on preventing their formation but also on converting them directly in the gasification reactor (Gómez-Barea et al., 2010). The use of catalysts, such as Ni-based olivine, olivine, and calcined dolomite, has been shown to significantly reduce tar content in syngas (Devi et al., 2005a,b), highlighting the importance of effective gas-solid contact time and local mixing conditions of the solid components in the reactor (Cui and Grace, 2007). Our study focuses not only on a specific biomass case, such as crushed olive pits produced by the olive oil industry (Miranda et al., 2008), but also broadly explores the effects of solid property diversity on segregation phenomena in a three-component bed typical of gasification processes. It investigates how to mitigate segregation through a suitable choice of particle size of the mixture components, for which no specific constraints exist. This approach is of general interest, as it analyzes the effects of solid property diversity on segregation phenomena occurring in a bed of this type in gasification processes.

2. Materials and Methods

2.1 Components, binary and ternary mixtures

Before analyzing the behavior of the ternary mixture of interest, that of the three binary systems formed by the various pairs of its components was investigated. In each of them, the 'packed component' (i.e. that having higher u_{mf}) coincides with the bigger one, although its density is lower than that of the 'fluidized' component. To this regard, Tables 1 and 2 report all the properties of the components and of the binary beds investigated, in terms of the density, size and shape ratio of their solids as well as the difference of fluidization velocity between them.

Table 1. Properties of the experimental solids.

Solid	ρ [kg/m^3]	Sieve size [μm]	d [μm]	ϕ [-]	d_{SV} [μm]	ε_{mf} [-]	u_{mf} [cm/s]
Olive pits (OP)	1380	1400-2000	1925	0.80	1540	0.402	59.0
Sand (S)	2610	710-800	821	0.60	493	0.488	33.5
Olivine (O)	3200	360-600	500	0.50	250	0.527	18.5

Table 2. Properties of the binary mixtures investigated.

Mixture (LBP-HSF)	ρ_P/ρ_F	$(\phi d)_F/(\phi d)_P$	ϕ_F/ϕ_P	$u_{mf,P}-u_{mf,F}$ [cm/s]	k [-]
OP1540-O250	0.43	0.16	0.63	40.5	0.406
OP1540-S493	0.53	0.32	0.75	25.5	0.157
S493-O250	0.82	0.51	0.83	15.0	0.083

Ultimately, ternary mixtures of various composition were prepared and used in the experiments. As specified in Table 3, a first series of tests was carried out on beds with a volume fraction of Olive Pits equal to 0.7 and a variable ratio of the fractions of Olivine and Sand in the remaining part. This choice appeared interesting to study because both binary systems with Olives Pits have signaled the presence of the minimum voidage at this volume fraction, a favorable condition for the easier suspension of the components in the mixture. In the second case, regarded mixtures for which the volumetric fraction of Sand was fixed at the value of 0.7, an usual value for real gasification, the aim was that of analyzing how olivine, the catalyst added to the mixture of biomass and inert as the third component, could assume a role of regulator of the mixing-segregation phenomena between biomass and Sand.

2.2 Experimental Apparatus and Procedures

Experiments were conducted in a Perspex fluidization column with a porous distributor, using air as the fluidizing agent (Girimonte et al., 2019). Pressure drop and bed height were adjusted and measured to study fluidization. A layering method ensured homogeneity, with air flow increased to fluidize the bed, then decreased to return it to a fixed state. Characteristic

fluidization velocities were determined by typical diagrams of ΔP versus the superficial gas velocity. The "freezing" procedure allowed for analysis of component segregation and concentration along the column, by separating and weighing horizontal particle layers to determine their volume fraction. This approach provided detailed insights into mixing and segregation effects under similar fluid dynamic conditions. (Formisani et al., 2008).

Table 3. Properties of the ternary mixtures investigated.

Mix OP1540/S493/O250	x_{OP} (vol)	x_S (vol)	x_O (vol) [-]	ε_0	u_{if}	u_{ff}
0.7/0.05/0.25	**0.7**	0.05	0.25	0.391	22.1	51.6
0.7/0.15/0.15	**0.7**	0.15	0.15	0.389	25.8	55.3
0.7/0.25/0.05	**0.7**	0.25	0.05	0.393	33.2	55.3
0.25/**0.7**/0.05	0.25	**0.7**	0.05	0.426	27.6	38.7
0.15/**0.7**/0.15	0.15	**0.7**	0.15	0.437	24.0	38.7
0.05/**0.7**/0.25	0.05	**0.7**	0.25	0.450	22.1	35.0

3. Results and discussion

3.1 Binary mixtures

Packing characteristics are influenced by factors like particle size, shape, friction, surface chemistry, and agglomeration, with particle size distribution being the most critical. Researchers aim to understand how this affects packing density and to identify the optimal particle composition for maximum density. However, rigorous and accurate model for the packing of complex particle systems (e.g., multi-component and non-spherical particles) is yet to be developed (Kwan et al., 2015). Since it is practically impossible to devise empirical relationships for predicting the effect of the shape of the two solids on the packing characteristics of their mixtures, the curves of ε_m were determined experimentally and they are illustrated in Fig. 2a in function of the volume fraction of the Fluidized component for all three binary systems. Among the pure components, OP1540 exhibits the lowest voidage (0.402), while O250 the highest value (0.527), since the first has a more regular shape than the second. All trends of bed voidage always exhibit a minimum at intermediate values of x_F, a circumstance that signals that an optimal component proportion exists for the density of the particulate bulk to reach a maximum level. Mixtures with OP1540 as Packed component show a common trend until a minimum value at $x_F=0.3$, is reached, but at increasing Fluidized fraction the trend branches off forward to distinct levels, the higher being those with the more irregular solid, O250. Mixture S493-O250, made with both more irregular components, instead has an overall distinct trend on a higher level with the same minimum in the region of low x_F. (Girimonte et al., 2019).

The position of the minimum suggested exploring as a basic case the ternary mixture originating from that of OP-S with a prevalence of Olive Pits at the content fixed to 0.7, with the content of Olivine increased from zero to 0.3 completely replacing Sand with Olivine in order to reach the system OP-O at minimum voidage. The second basic case, starting from OP-S with a prevalence of Sand at the content fixed to 0.7, with the content of Olivine increased from zero to 0.3 completely replacing Olive Pits with Olivine in order to reach the system S-O at minimum voidage. The first case shows an equal value of the bed voidage independently on kind of fluidized component, probably because in the bulk structure prevails the OP component and the volume penetration effect exhibits the maximum reduction of voidage already at $r_d=0.3$. In the second case, the voidage condition for the initial binary OP-S mixture is smaller than the final S-O, so the change of the OP component (biggest and more spherical) with the smallest and irregular Olivine could introduce new effects on the equilibrium of mixing/segregation of the components.
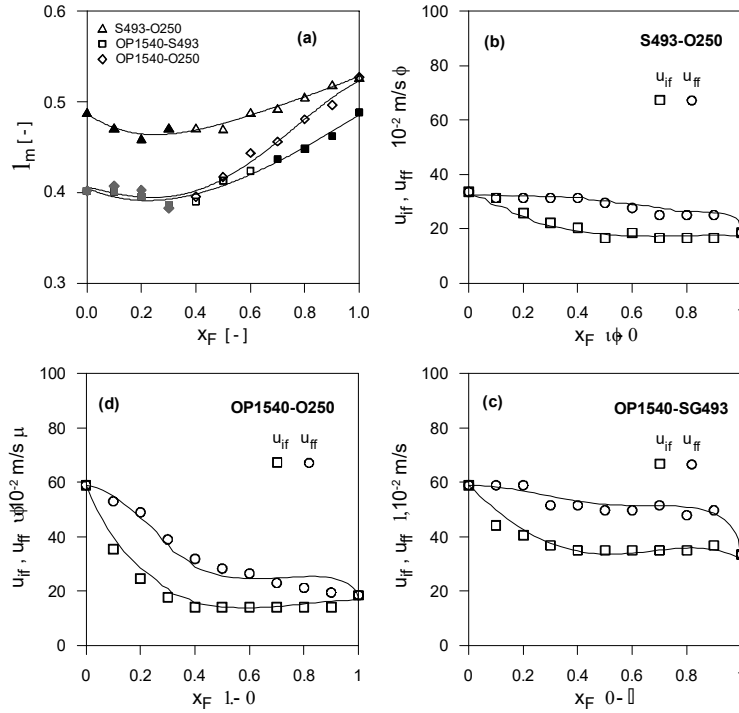
Fig. 2. Bed voidage and characteristic fluidization velocities versus xF

for all the binary mixtures examined.

The initial and final velocities at varying x_F are illustrated in Fig. 2 (b-d) for the three binary mixtures investigated in order of decreasing r_d. Minimum fluidization velocities are influenced by the particle diameter more than the component density: in fact, O250, the densest but the smallest has the lowest value of u_{mf}. The trend of the initial fluidization velocity rapidly decreases in the range of lower x_F: in peculiar way for the OP1540-O250 and OP1540-S493 systems. This depends on the bed voidage trend that in this range decreases until its minimum point. For values superior of 0.3, u_{if} remains almost constant at the value of the minimum fluidization velocity of the Fluidized component, because, although voidage increases, the drag area of finer particles also increases, with an effect of counterbalance.

In fact, all systems exhibit the characteristic behavior of size-segregating mixtures (Formisani, 2011), because the variation is controlled by the bed voidage trend, but mixture S493-O250 (Fig. 2b), which has the minor variation of the voidage in function of the composition, shows a residual behavior of the density-segregating. For the u_{ff} trend, at low x_F the size ratio prevails on density ratio as segregating factor, and its role increases gradually from S493-O250 to OP1540 O250. Formisani et al. 2011 have shown that the width of the velocity interval, i.e. the difference (u_{ff}-u_{if}), increases with the difference (d_P-d_F) but decreases with the difference (ρ_F-ρ_P), since the fluidized component is always the denser solid. Moreover, size ratio influences the voidage variation and then the characteristic velocities: among the clearly size-segregating mixtures, i.e. OP1540-S493 and OP1540-O250, the first mixture has the highest width because the effect of bed voidage is minus evident. Curves on the experimental trends are determined by means equations of the model (Girimonte et al., 2019). They show high predictability since they use the experimental curves of voidage, by which the effect of irregular shape of particles can be take account on. The values of the best-fitting parameter k, necessary for the calculation of u_{ff} trend are 0.406, 0.157 and 0.083 for the mixtures at decreasing size ratio. These values can describe the spontaneous tendency to stratification of the components during a slow defluidization pattern (Girimonte et al., 2019).

3.2 Ternary mixtures
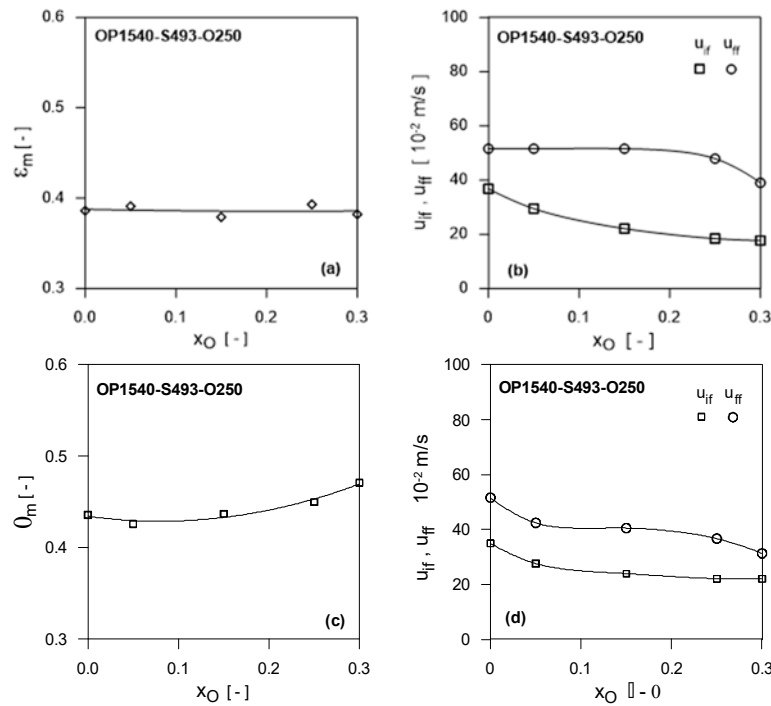
Fig. 3. Bed voidage and characteristic fluidization velocities versus x_O

for both ternary mixtures examined.

As regards the ternary beds with a volume fraction of 0.70 of Olive Pits, the dependence of system voidage on the composition of the remaining 30% is illustrated in Fig. 3(a). The diagram clearly shows that ε_m is practically unaffected by the variation of Olivine fraction; as a consequence, the shape of the fluidization velocities interval of the ternary mixture, reported in Fig. 3(b), is very similar to that typical of two-component mixtures subject to density segregation, probably because the substitution with Olivine increases the role of the density ratio on the initial velocity, which decreases almost linearly and gets constant the final velocity at value of u_{mf} of Olive Pits, abundant component in the initial mixture OP1540-S493.

Rather different trends are found with the second mixture, i.e. that with 70% Sand. When the composition of the remaining 30% of the bed is let vary by progressively increasing the amount of Olivine, an increase of system voidage is observed that exerts its influence also on the fluidization velocity diagram of the ternary bed. Then it appears similar to that of binary size-segregating mixtures. The disappearing of Olive Pits in favour of Olivine decreases the effect of the density difference and makes effective the role of voidage on the final fluidization velocity. For both cases, an analysis of the component distribution at value of operating velocity over u_{ff} have been realized. Diagrams of axial profiles at varying Olivine fraction are shown in Figures 4 and 5.
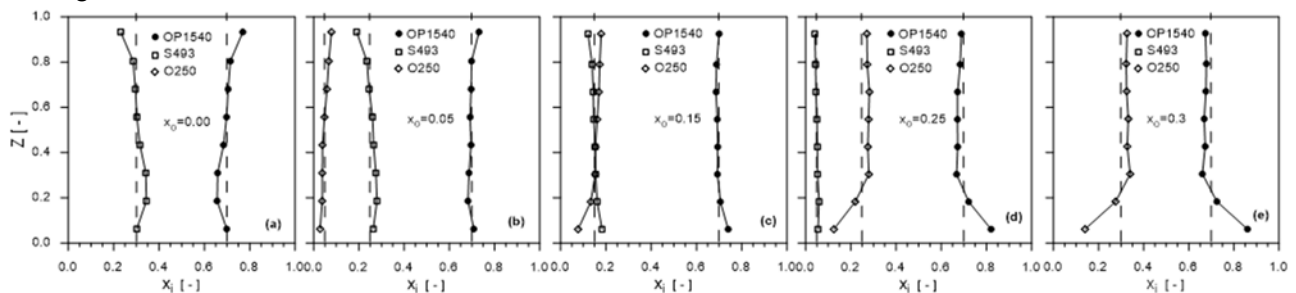
Fig. 4. Component profile at varying Olivine fraction for the ternary mixture rich of Olive Pits.

The two cases highlight opposite effects at increasing of the Olivine fraction: when mixture is rich of Olive Pits, this substitution moves the system towards a behavior more segregating because both, density and size, become really different between the biggest component and the smallest; for the mixture rich of Sand, the presence of Olivine, in place of Olive Pits, allows that system become more mixed, because it reduces its density and size difference. Excluding the binary cases (a) and (e) from the sequence shown in Fig.4 and 5, it is possible to indicate that mixing condition was obtained at low fraction of Olivine (i.e. 5-15%) when in the mixture was abundant the biomass. On the contrary, for practical case study, as that of the ternary mixture rich in Sand, mixing condition was obtained at high fraction of Olivine (i.e. 15-25%).
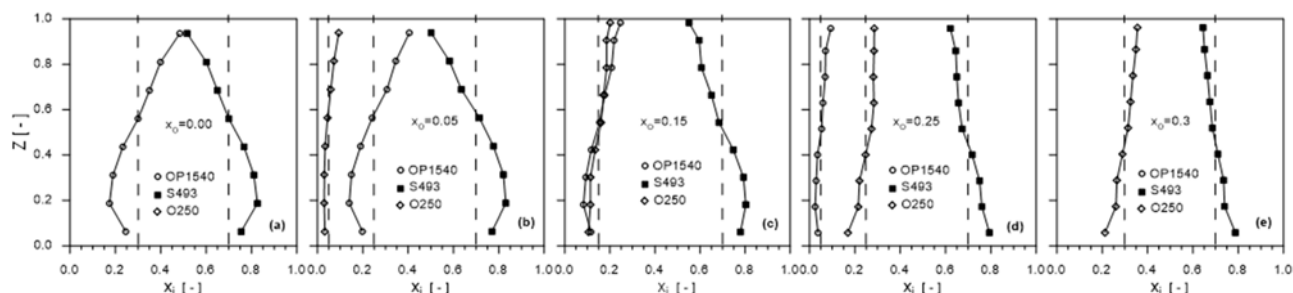
Fig. 5. Component profile at varying Olivine fraction for the ternary mixture rich of Sand.

4. Conclusion

Using Olivine particles, which are smaller and denser than Sand and biomass, allows for control over component distribution in fluidized beds by tapping into size-segregation dynamics. The behavior of ternary mixtures mirrors that seen in binary systems: biomass-rich mixtures act like density-segregating systems, while Sand-rich ones resemble size-segregating systems. This difference is due to varying voidage at different Olivine concentrations. Segregation is more pronounced with larger size ratios, where low Olivine concentrations favor mixing in biomass-rich systems, and high concentrations do so in Sand-rich systems, consistent with theoretical predictions.

References

Cui, H., Grace, J.R. Fluidization of biomass particles: a review experimental multiphase flow aspects. Chemical Engineering Science. 2007. 62, 45-55.

Devi, L., Ptasinski, K.J., Janssen, F.J.J.G., van Paasen, S.V.B., Bergman, P.C.A., Kiel, J.H.A. Catalytic decomposition of biomass tars: use of dolomite and untreated olivine. Renewable Energy. 2005a. 30, 565-587.

Devi, L., Craje, M., Thüne, P., Ptasinski, K.J., Janssen, R.J.J.G. Olivine as tar removal catalyst for biomass gasifiers: catalyst characterization. Applied Catalysis A: General. 2005b. 294, 68-79.

Formisani B., Girimonte R., Longo T., The fluidization process of binary mixtures of solids: Development of the approach based on the fluidization velocity interval. 2008. Powder Technology. 185, 97-10.

Formisani, B., Girimonte, R., Vivacqua V. Fluidization of mixtures of two solids differing in density or size. AIChe Journal. 2011, 57, 2325-2333.

Girimonte, R., Formisani, B., Vivacqua, V. Application of the theory of binary fluidization to solids of irregular shape: Choosing the granulometry of sand in processes for energy production from wastes of the olive oil industry, Powder Technology. 2019. 345, 563-570.

Gómez-Barea, A., Ollero, P., Leckner, B. Optimization of char and tar conversion in fluidized bed biomass gasifiers. Fuel. 2010. 103, 42-52.

Kwan, A.K.H., Wong, V., Fung, W.W.S. A 3-parameter packing density model for angular rock aggregate particles Powder Technology. 2015. 274, 154–162.

Miranda, T. Esteban, A., Rojas, S., Montero, I., Ruiz, A. Combustion analysis of different olive residues, Int. J. Mol. Sci. 2008. 9, 512–525.

EFFECT OF PREHEATING MODIFICATION UNIT AIR EQUIVALENT RATION ON COMBUSTION AND NO$_X$ EMISSION IN CIRCULATING FLUIDIZED BED

ZIhua Tang[1,2], Guoliang Song[1,2]*, Weijian Song[1], Haiyang Wang[1,2], Yi Han[1,2]

[1]*State Key Laboratory of Coal Conversion, Institute of Engineering Thermophysics, Chinese Academy of Sciences, Beijing 100190, China*
[2]*University of Chinese Academy of Sciences, Beijing 100049, China*

*Email: Songgl@iet.cn

Abstract

The preheating modified combustion technology has a broad prospect in improving the flexibility of circulating fluidized bed (CFB), but the effect of air equivalent ratio of preheating modified unit (PMU) on combustion and NO$_x$ emission of CFB is not fully understood. Therefore, the CFB experimental platform with PMU was used to carry out the preheating modified combustion conditions of Shenmu coal, and the impact of three different PMU air equivalent ratios (λ_{PMU}), namely 0.30, 0.35, and 0.40, on the combustion and NO$_x$ emission of CFB, was investigated. The experimental results showed that the appropriate increase of λ_{PMU} was conducive to the conversion of fuel-N to N$_2$, thereby further reducing the NO$_x$ emission. When the λ_{PMU} increased from 0.3 to 0.4, the proportion of fuel-N conversion to N$_2$ in PMU increased from 44.6% to 65.5%, and the final NO$_x$ emission concentration was reduced by about 15%. In addition, increasing λ_{PMU} decreased the particle size of modified char. The finer the modified char entered CFB, the more likely it was for particle agglomeration to occur, which had a more positive effect on reducing NO$_x$. The experimental results also showed that increasing λ_{PMU} increased the average temperature of PMU, but had little effect on the temperature distribution of CFB. Besides, the CO emission concentration in flue gas and the carbon content in fly ash decreased with the increase of λ_{PMU}.

1. Introduction

In recent years, the construction of a new power system with new energy as the main body is accelerating. By the end of 2023, China's installed capacity of solar power and wind power reached 609.49 million kW and 441.34 million kW, respectively, with year-on-year growth of 55.2% and 20.7% [1]. However, the instability of wind power and solar power has brought serious harm to the safe and stable operation of the power system [2]. To ensure the safe and stable operation of the power system, thermal power units must perform depth peak regulation.

Although CFB units have the advantages of a wide load regulation range and low cost of pollutant control [3], there is still much room for improvement in NO$_x$ emission control under low load. Under low loads, to maintain a normal fluidization state, the secondary air volume is significantly reduced, thus greatly weakening the effect of air classification on NO$_x$ emission reduction [4]. In addition, the inlet temperature of CFB cyclone separator is usually lower than 800℃ under low loads, which is out of the temperature window of selective non-catalytic reduction (SNCR) reaction, resulting in a significant decrease in NO$_x$ reduction efficiency, and at the same time causing ammonia escape, equipment corrosion and other problem [5]. Therefore, it is of great significance to develop NO$_x$ emission reduction technology under the low load of CFB.

The existing approaches for controlling NO$_x$ emission at low CFB load are essentially of two types. The first is to optimize the position of the SNCR system, to improve the NO$_x$ reduction efficiency of the SNCR system under low load [6,7]. The second is to strengthen the effect of air classification under low loads. By appropriately raising the position of the secondary air nozzle, the height of the bottom reduction zone can be extended, thus reducing

the emission of NO_x [8]. The flue gas recirculation technology introduces tail flue gas into the furnace to reduce the primary air volume and increase the secondary air volume, thus strengthening the air classification effect and achieving the purpose of reducing NO_x emission [9]. In addition, the fluidization state reconstruction technology reduces the minimum fluidized air volume of CFB by reducing the particle size of the bed material and fuel, which significantly reduces the oxidation atmosphere in the dense phase zone and improves the classification effect of secondary air, thus reducing the NO_x emission [10]. Preheating modified combustion technology combines staged fuel and air combustion with CFB combustion, that is, fuel undergoes anoxic combustion in PMU before burning with oxygen-rich fluidized air in CFB [11]. In previous studies, fuel preheated and modified by PMU was fed into pulverized coal furnace for combustion, and the effects of λ_{PMU}, fuel particle size, and fuel type on NO_x emission from pulverized coal furnace were thoroughly studied [12-14]. However, the effects of preheated modified fuel generated in a strongly reducing atmosphere on CFB combustion and NO_x emission have never been studied.

To research the effect of λ_{PMU} on CFB combustion and NO_x emission, experiments were carried out on a small experimental platform. The temperature distribution and combustion effect of CFB under preheating modified combustion technology and different λ_{PMU} were concerned. The migration and transformation paths of fuel-N in PMU were analyzed. In addition, the effects of modified char characteristics at PMU outlet and fuel-N migration and conversion path on the NO_x emission of CFB were studied. This paper provides a certain reference for CFB to further reduce NO_x emission under low loads.

2. Experiment

2.1 Material for experiment

In this experiment, Shenmu bituminous coal with particle sizes ranging from 0 to 0.355 mm was used as fuel. The results of the proximate analysis and ultimate analysis of Shenmu bituminous coal are shown in Table 1. In addition, the wide screening quartz sand was used as the bed material of CFB, and its particle size range was 0-1 mm.

Table 1. Proximate analysis and ultimate analysis of Shenmu bituminous coal.

Proximate analysis					Ultimate analysis				
M_{ad} %	A_{ad} %	V_{ad} %	FC_{ad} %	$Q_{ad, net}$ MJ/kg	C_{ad} %	H_{ad} %	O_{ad} %	N_{ad} %	S_{ad} %
8.12	5.48	27.14	59.26	26.96	71.51	3.45	10.21	0.87	0.36

2.2 Experimental system
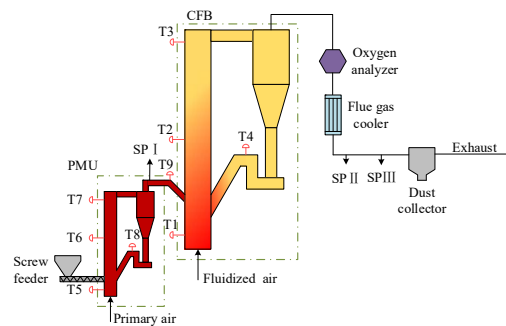
Fig. 1. Schematic diagram of the experimental system

Fig. 1 shows the experimental system used in this experiment. The PMU, CFB, and other auxiliary equipment are the main components of the experimental system. The PMU is a small CFB with an inner diameter of 68 mm and a height of 1500 mm for the riser. The furnace of the CFB has an inner diameter of 150 mm and a height of 4000 mm. The PMU and CFB are arranged with 5 and 4 thermocouples respectively, as shown in Fig. 1. Other auxiliary equipment includes a screw feeder, oxygen analyzer, flue gas cooler, and dust collector. In addition, there are three sampling points (SP) in the experimental system, the positions are

shown in Fig. 1. SPⅠ is used to collect modified char and high-temperature coal gas, SPⅡ and SPⅢ are used to collect flue gas and fly ash, respectively.

2.3 Experimental conditions and sample analysis

During the experiment, the λ_{PMU} and total excess air coefficient can meet the requirements of the experimental conditions by adjusting the air volume and the coal supply. Table 2 shows the operating parameters of each experimental condition. In Table 2, λ_{CFB} and λ represent the CFB air equivalent ratio and total excess air coefficient, respectively.

Table 2 Experimental conditions parameter

Case	Coal supply （kg/h）	Air volume in PMU （Nm³/h）	Air volume in CFB （Nm³/h）	λ_{PMU}	λ_{CFB}	λ	O₂ （%）
1	5.0	10.8	32.4	0.3	0.9	1.2	3.5
2	5.0	12.6	30.6	0.35	0.85	1.2	3.5
3	5.0	14.4	28.8	0.4	0.8	1.2	3.5

During the stable operation of the experimental condition, the coal gas composition and flue gas composition were respectively measured by the coal gas analyzer and the flue gas analyzer (Testo 350), and the concentration of NH_3 and HCN in the coal gas was measured by the gas detection tube. At the same time, the modified char and fly ash were respectively collected at the SPⅠ and SPⅢ. After the experiment, particle size analysis, proximate analysis, and ultimate analysis of the collected modified char, and proximate analysis and ultimate analysis of the collected fly ash were carried out.

3. Results and discussion

3.1 Effect of λ_{PMU} on combustion

Fig. 2 presents the temperature distributions of PMU and CFB under different λ_{PMU}. It can be seen from Fig. 2(a) that the temperature in the PMU increases with the increase of the λ_{PMU}, while the temperature difference between the top and bottom of the PMU riser decreases with the increase of the λ_{PMU}. On the one hand, this is because the increase in the λ_{PMU} causes the combustion share in the PMU to increase, on the other hand, because the increase in the λ_{PMU} improves the ability of the primary air to entrain the material, and more heat can be carried to the top of the riser. As can be seen from Fig. 2(b), when λ_{PMU} is in the range of 0.3~0.4, the temperature in the CFB hardly changes. When λ_{PMU} is 0.3, 0.35 and 0.4, the average temperature of the CFB is 817.4℃, 827.2℃ and 826.9℃, respectively. At lower λ_{PMU}, more fuel is burned in the CFB. As λ_{PMU} increases, more fuel is burned in the PMU, but the heat released by fuel combustion is carried to the CFB. Therefore, changes in λ_{PMU} have little effect on the temperature distribution within the CFB.
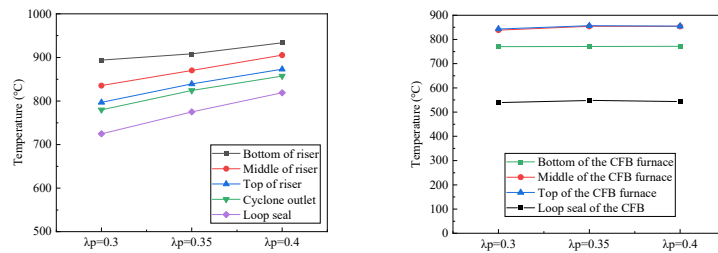
(a) PMU temperature distribution (b) CFB temperature distribution

Fig. 2. Temperature distribution of PMU and CFB under different λ_{PMU}

Fig. 3 shows the coal gas composition and particle size of modified char under different λ_{PMU}. From Fig. 3(a), it can be found that the content of CO and H_2 increases with the increase of λ_{PMU}, while the content of CH_4 decreases slightly with the increase of λ_{PMU}. According to the calculation, the heat value of coal gas increases with the increase of λ_{PMU}, and the heat value of coal gas is 1.32 MJ/Nm³, 1.83 MJ/Nm³, and 1.90 MJ/Nm³ when λ_{PMU} is 0.3, 0.35 and 0.4, respectively. This indicates that the appropriate increase of λ_{PMU} can promote the conversion of pulverized coal to combustible coal gas. When λ_{PMU} is 0.3, the ability of primary air to entrain

solid particles is weak, and more pulverized coal accumulates at the bottom of PMU, which is easy to form a local oxygen-rich zone, prompting pulverized coal to burn and generate more CO_2. With the appropriate increase of λ_{PMU}, the fluidized state in PMU is improved, the local oxygen-rich zone is reduced, the modified effect of pulverized coal is enhanced, and the heat value of coal gas is increased. Fig. 3(b) presents that the particle size of pulverized coal is greatly reduced after modification, and the particle size of the modified char further decreases with the increase of λ_{PMU}. In the PMU, the fuel is broken under the dual action of collision and release of volatiles, so the particle size is reduced. When λ_{PMU} increases, the fuel experiences a more intense collision degree, the thermal stress of the fuel increases due to the increase in the average temperature, and the volatiles are released more completely. Therefore, a proper increase of λ_{PMU} can further reduce the particle size of modified char.

(a) Coal gas composition   (b) Modified char particle size
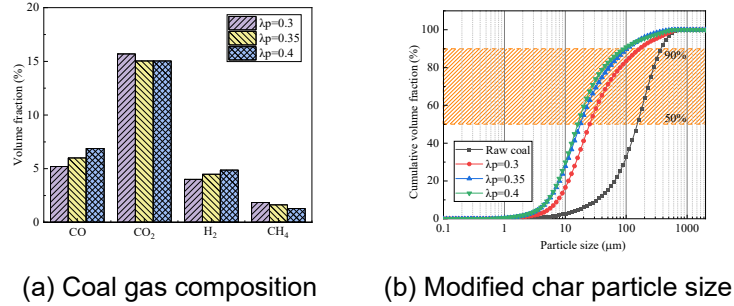
Fig. 3. Coal gas composition and particle size of modified char under different λ_{PMU}

The carbon content of fly ash and CO emission concentration under different λ_{PMU} are shown in Fig. 4. As can be seen from Fig. 4 the carbon content of fly ash and CO emission concentration show a decreasing trend with the increase of λ_{PMU}. When λ_{PMU} is in the range of 0.3~0.4, there is little difference in temperature within the CFB, and the residence time becomes the main factor affecting the CO emission concentration. With the decrease of λ_{PMU}, the CO content released in PMU gradually decreases, while the CO content released by modified char in CFB gradually increases. More CO released in CFB means that the residence time of CO decreases. Therefore, the CO emission concentration decreases with the increase of λ_{PMU}. In addition, the increase of λ_{PMU} reduces the particle size of modified char, which is conducive to the rapid combustion of modified char in CFB. Therefore, the carbon content of fly ash decreases with the increase of λ_{PMU}.
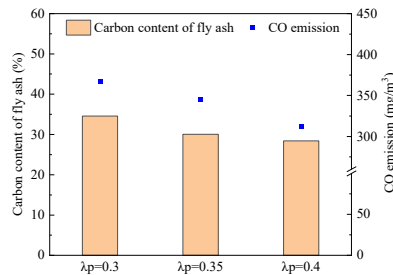
Fig. 4. Carbon content of fly ash and CO emission under different λ_{PMU}

3.2 Effect of PMU air equivalent ratio on NO_x emission

PMU is in a strongly reducing atmosphere and no NO_x is generated. The proportions of fuel-N remaining in modified char, converted to the gas phase, converted to N_2, converted to NH_3, and converted to HCN are defined as R_s, R_G, R_{NH3}, R_{HCN}, and R_{N2}, respectively. Fig. 5 shows the proportion of fuel-N converted into other nitrogen-containing substances in the PMU. As shown in Fig. 5 (a), as λ_{PMU} increases, the proportion of fuel-N remaining in the modified char decreases, while the proportion of fuel-N converted to the gas phase and N_2 increases. In raw coal, fuel-N exists in polymer organic matter. As λ_{PMU} increases, the concentration of O_2 in the PMU increases, and the char is more prone to oxidation, so more fuel-N is converted to the gas phase instead of remaining in the modified char. In addition, it is worth noting that the conversion ratio of fuel-N to N_2 increases with the increase of λ_{PMU}, which indicates that

an appropriate increase of λ_{PMU} is conducive to the conversion of fuel-N to N_2. It can be seen from Fig. 5(b) that R_{NH3} and R_{HCN} both show a downward trend as λ_{PMU} increases. At a lower λ_{PMU}, the concentration of O_2 in PMU is low, resulting in the enrichment of a large amount of H radicals in PMU, and the nitrogen-containing aromatic ring hybridization triggered by H radicals is the primary condition for the formation of NH_3 and HCN. With the increase of λ_{PMU}, the amount of H free radicals decreases. Therefore, R_{NH3} and R_{HCN} decrease as λ_{PMU} increases. In addition, NH_3 and HCN are easily oxidized under high temperatures and aerobic conditions, and the consumption rate of NH_3 and HCN will increase with the increase of oxygen concentration. For the above two reasons, the conversion ratio of fuel-N to NH_3 and HCN decreases with λ_{PMU}.

(a) $R_S/R_G/R_{N2}$ for different λ_{PMU} (b) R_{NH3}/R_{HCN} for different λ_{PMU}
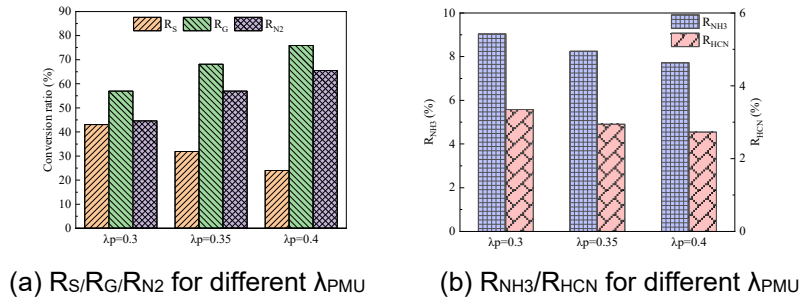
Fig. 5 Fuel N conversion ratio under different λ_{PMU} in PMU

NOₓ in flue gas is formed in CFB. Fig. 6 presents the NO_x emission concentration (@6% O_2) in flue gas and the conversion of fuel-N to NO_x (R_{NOx}) at different λ_{PMU}. It can be seen from Fig. 6 that with the increase of λ_{PMU}, both the NO_x emission concentration and R_{NOx} show a downward trend. When λ_{PMU} is 0.3, the ratio of fuel-N to N_2 in the PMU is low, more fuel-N remains in the modified char, and the content of NO_x precursors (NH_3 and HCN) measured at the PMU outlet is higher. In the atmosphere of strong oxidation of CFB, more NH_3, HCN and more fuel-N remaining in the modified char will produce more NO_x. Therefore, the NO_x emission concentration in flue gas is relatively high. With the increase of λ_{PMU}, the proportion of fuel-N converted to N_2 in PMU increases, and the content of NH_3, HCN, and the fuel-N remaining in the modified char decreases, so the emission of NO_x is reduced. In addition, with the increase of λ_{PMU}, the concentration of CO and H_2 entering the CFB increases, and the particle size of modified char decreases. The increase of CO and H_2 concentration is conducive to the reduction of NO_x in CFB. The smaller the particle size of the modified char, the more likely the particle agglomeration phenomenon, which makes the formation of a local reducing atmosphere inside the particle group, thereby promoting the reduction of NO_x [15]. Therefore, the lowest NO_x emission concentration and R_{NOx} at λ_{PMU} of 0.4 are due to the optimal conversion of fuel-N to N_2 in the PMU at this air equivalence ratio, and the best NO_x reduction conditions in the CFB.
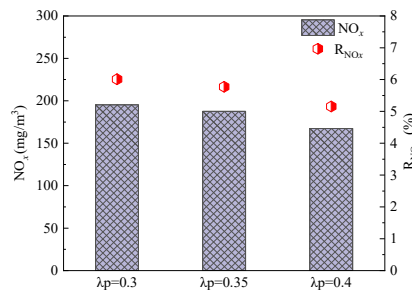
Fig. 6 Fuel-N conversion ratio in PMU under different λ_{PMU}

4. Conclusion

This paper explores the influence of λ_{PMU} on CFB combustion and NO_x emission under preheating modified combustion technology for the first time. The main conclusions are as follows:

1) Appropriately increasing the λ_{PMU} can increase the temperature of PMU and increase the heat value of coal gas produced by PMU. In addition, the increase of λ_{PMU} will reduce the particle size of the modified char.

2) The increase of λ_{PMU} has almost no effect on the temperature distribution of CFB but can reduce the emission concentration of CO in flue gas and the carbon content of fly ash.

3) Preheating modified combustion technology has a good control effect on the directional conversion of fuel-N to N_2, thereby reducing the emission of NO_x.

4) λ_{PMU} will affect NO_x emission concentration under preheating modified combustion technology. Appropriately increasing the λ_{PMU} makes more fuel-N to be converted to N_2, thereby further reducing NO_x emissions.

Acknowledgment

References

National Energy Administration. Statistics of the national power industry in 2023 [EB/OL]. (20244.01.26) https://www.nea.gov.cn/2024-01/26/c_1310762246.htm.

Olatomiwa, L., Mekhilef, S., Ismail, MS., et al. Energy management strategies in hybrid renewable energy systems: A review. Renewable & Sustainable Energy Reviews. 2016. 62, 821-35.

Huang, Z., Deng, L., Che, D. Development and technical progress in large-scale circulating fluidized bed boiler in China. Frontiers in Energy. 2020. 14(4), 699-714.

Hou, Y., Liu, H., Shen, Q., et al. Numerical Simulation of the Influence of CFB Boiler Secondary Air Optimization on NO_x Emission Under Low Load [J/OL]. PCSEE. 1-11 (2024.02.29).

Li, Q., Wu, Y., Yang, H., et al. Simulation and optimization of SNCR process. CIESC Journal. 2013. 64(05), 1789-96.

Yang, J., Wang, J., Wang, P., et al. Characterization and Mitigation of NO_x Emissions Across a Wide Load Range in Supercritical 350 MW Circulating Fluidized Bed Boiler [J/OL]. Clean Coal Technology. 1-10 (2024.02.09).

Liu, X., Deng, B., Zhang, S., et al. Operation and optimization technology of deep peak for 330 MW CFB boiler units. Clean Coal Technology. 2022. 28(12), 87-93.

Zheng, W., Zhang, M., Zhang, Y., et al. The effect of the secondary air injection on the gas-solid flow characteristics in the circulating fluidized bed. Chemical Engineering Research & Design. 2019. 141, 220-8.

Zhang, S., Zhang, S., Zhang, J., et al. Performance Research on Deep Peak Regulation with Flue Gas Recirculation in a 330 MW CFB Boiler. Clean Coal Technology. 2021. 27(01), 291-298.

Li, J., Zhang, M., Yang, H., et al. The theory and practice of NO_x emission control for circulating fluidized bed boilers based on the re-specification of the fluidization state. Fuel Processing Technology. 2016. 150, 88-93.

Zhu, J., Ouyang, Z., Lyu, Q. An Experimental Study on NO_x Emissions in Combustion of Pulverized Coal Preheated in a Circulating Fluidized Bed. Energy & Fuels. 2013. 27(12), 7724-9.

Liu, W,, Ouyang, Z., Song, W., et al. Experimental Research on Combustion Characteristics and NO_x Emission of Three Kinds of Solid Fuels Preheated by a Self-Preheating Burner. Energy & Fuels. 2019. 33(9), 8483-90.

Ouyang, Z., Ding, H., Liu, W., et al. Effect of the Primary Air Ratio on Combustion of the Fuel Preheated in a Self-preheating Burner. Combustion Science and Technology. 2022. 194(6), 1247-64.

Ding, H., Ouyang, Z., Zhang, X., et al. The effects of particle size on flameless combustion characteristics and NO emissions of semi-coke with coal preheating technology. Fuel. 2021, 297.

Xiao, Y., Song, G., Song, W., et al. Experimental Research on the Conversion of Fuel Nitrogen in the Post combustion Chamber of the Circulating Fluidized Bed. Energy & Fuels. 2021. 35(3), 2416-24.

Experimental study on the co-production of gas and char during the partial gasification of biomass in a bench-scale circulating fluidized bed gasifier

Xinyu Yuan[1,2], Zhiping Zhu[1,2,3, *], Xiaobin Qi[1,2,4, *], Xiaofang Wang[1,2,3], Chen Chen[4,5]

1. State Key Laboratory of Coal Conversion, Institute of Engineering Thermophysics, Chinese Academy of Sciences, Beijing 100190, China

2. University of Chinese Academy of Sciences, Beijing 100049, China

3. Shanxi Engineering Research Center of Coal Clean, Efficient Combustion and Gasification, Datong 037000, China

4. Shanxi Key Laboratory of Coal Flexible Combustion and Thermal Conversion, Datong 037000, China

5. Datong Institute of Coal Clean and Efficient Utilization, Datong 037000, China

*Email: * zhuzhiping@iet.cn

* qixiaobin@iet.cn

Abstract

In order to investigate the feasibility of co-production of gas and char using circulating fluidized bed (CFB) technology, partial gasification experiments of two biomass, walnut and apple branches, were carried out on a 20 kg/h CFB gasifier. The impacts of reaction atmosphere including oxygen to carbon ratio and steam were mainly investigated. The results show that the partial gasification process was relatively stable, with a uniform temperature distribution in the furnace. In the experiments, there found an opposite effect of oxygen to carbon ratio on the quality of gas and char, indicating the possibility of improving the quality of gas or char by optimizing the operation parameters. Despite the calorific value of gas was reduced at a higher oxygen to carbon ratio, such as the calorific value reducing from 1270 to 736 kcal/Nm^3 at the oxygen to carbon ratio increasing from 0.11 to 0.44, the pore structure of char was improved. The intervention of steam promoted the development of pore structure of char. Besides of high carbon content above 84%, it is also found that the char was characterized with a high proportion of mesoporous structure above 55%, enabling the char to have certain adsorption capacity. For walnut shell, the char was of an iodine adsorption value of 262 mg/g and a methmethene blue adsorption value of 23 mg/g, while for apple branches the two values were 201 and 22 mg/g, respectively. It indicates that the char may be used as activated char. This work preliminarily verifies that the co-production of gas and char can be achieved using CFB technology.

1. INTRODUCTION

Biomass has advantages over traditional energy because of its renewability, wide distribution and low pollution, and the use of biomass energy in developing countries accounts for 35% of total energy use and 13% of global use[1]. Biomass gasification is a process of partial oxidation reaction of biomass solids with air, oxygen, steam and other gasification agents under high temperature environment. After drying, pyrolysis, oxidation and reduction, lignin, cellulose and hemicellulose components in biomass are converted into CO, H_2, CH_4 and other flammable gases, and biochar and bio-oil are generated at the same time[2]. Biomass gasification equipment is mainly divided into two categories of fixed bed and fluidized bed. Compared with fixed bed, fluidized bed gasifier has the advantages of uniform furnace temperature, large heat capacity in bed, high heat transfer and combustion intensity in bed, and strong adaptability of raw materials[3]. It is suitable for gasification of various biomass raw materials to co-produce gas and biochar.

In view of the advantages of fluidized bed, there have been many studies on the utilization of biomass by fluidized bed boilers. Luis et al.[4] studied the energy and exergy balance of beech wood gasification in a pilot fluidized bed reactor with CO_2 and steam as gasification agents and biochar and sand as bed materials at a temperature range of 600-900 ℃. Karatas et al.[5][6] carried out gasification experiments on cotton stalk, hazelnut shell, walnut shell, and pistachio shell on a bubbling fluidized bed with air and water vapor as gasification agents, respectively, and investigated the effects of air equivalent ratio and steam to biomass mass flow ratio on gasification performances. Martinez et al.[7] used grape seed as raw material to analyze the effects of different operating parameters (such as steam to carbon (S/C) ratio, CO_2 adsorption capacity, and adsorbent to biomass ratio) on the synthesis gas composition and coke conversion in a 30 kW bubbling fluidized bed gasifier. The effects of high steam-to-carbon ratio and the use of CO_2 adsorbent with high adsorption capacity on H_2, CO and CO_2 contents in syngas were evaluated. Lan et al.[8] carried out biomass gasification experiments in a self-designed fluidized bed, and analyzed the effects of different factors on the composition and calorific value of the combustible gas, including equivalent ratio, bed temperature, catalyst addition, and steam.

The distribution and physicochemical properties of biomass thermal conversion products (char, gas, and tar) depend on the reaction conditions. Many researchers have carried out research on biomass co-generation. Ma et al.[9] achieved the gasification polygeneration of wood chips in a 190 kWe dual-air stage downdraft fixed bed pilot plant and obtained three-phase products including gas, charcoal, and liquid extract. Kramreiter et al.[10] used a 125 kW two-fire fixed-bed gasifier to study the effects of the type of wood chips, power, and air flow distribution on the gas composition, tar content in gas, and carbon content in ash. Chen et al.[11] studied the influences of pyrolysis temperature on the pyrolysis characteristics of tobacco waste and results showed that the three-phase products were in relative equilibrium at the pyrolysis temperature of 650 ℃. Besides, it is found that the pyrolysis process can be divided into three stages: degradation (250-450 ℃), reforming (450-650 ℃), and polycondensation (>650 ℃).

By regulating the thermal conversion process, biomass can be transformed into gas and biochar (namely gas-char co-production of biomass) for heating and power generation and preparation of carbon materials, which helps to realize the high-value utilization of biomass and has a good development prospect. However, there is currently still limited research on biomass gasification polygeneration based on fluidized bed. Against this background, in this work, the gasification polygeneration of two types of biomass (apple branch and walnut shell) was attempted on a bench-scale fluidized bed experimental device. The effects of gasification atmosphere (oxygen-carbon ratio and steam atmosphere) on the gasification performance, and distribution characteristics and physicochemical properties of gas-solid products were explored. The aim of this work is to provide theoretical guidance for high-efficiency gasification polygeneration and high-value utilization of biomass.

2 Experimental equipment and research methods

2.1 Experimental materials and bed materials

Apple tree branch (ATB) and walnut shell (WS) were employed as raw materials. The biomass particles were crushed and sieved to the particle size of 0-4 mm. Table 1 gives the property analysis results of biomass. Boiler bottom slag with a particle size ranging from 0.10 to 0.71 mm was selected as the experimental bed material.

Table 1. Proximate analysis and ultimate analysis of apple tree branches and walnut shells

Sample	Proximate analysis （wt.%, ar）				Ultimate analysis （wt.%, ar）				
	M	A	V	Fd	C	H	O	N	S
ATB	8.75	0.74	73.91	16.61	45.35	4.56	40.28	0.31	0.01
WS	8.17	0.17	75.15	16.51	46.98	4.57	39.87	0.24	-

Note: ar represents the received basis.

2.2 Experimental facility

The gasification experiments were carried out on a bench-scale circulating fluidized bed experimental device, diagram of which is shown in Fig. 1. This experimental system mainly

includes circulating fluidized bed, downer, and auxiliary systems (including feeding, air supply, heating, cooling, measurement, and so on). During the experiments, the auxiliary thermal system was turned on to maintain the circulating fluidized bed in a certain temperature range. The downer was not activated and only served as the tail pipe.
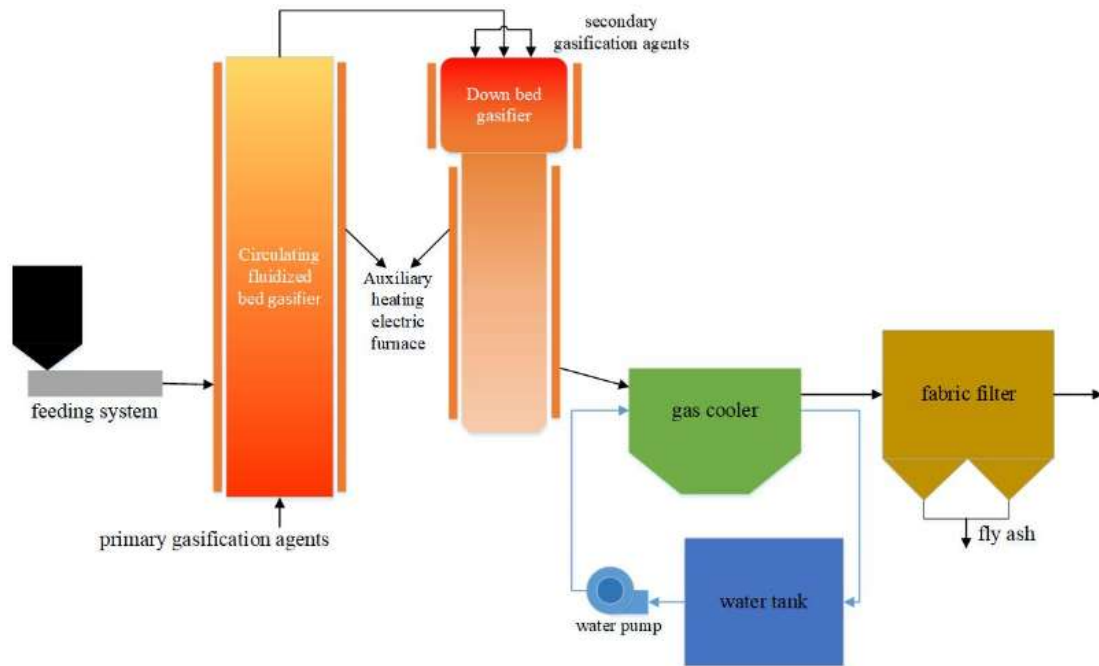
Fig. 1. Diagram of circulating fluidized bed experimental device

2.3 Experimental condition and sample characterization

In experiments, influences of biomass type and reaction atmosphere were investigated. According to the operating conditions, as shown in Table 2, the four test conditions carried out are named WS-1, ATB-1, ATB-2, and ATB-3, respectively.

Table 2. Experimental completion condition

Operating parameter	Experimental condition			
	WS-1	ATB-1	ATB-2	ATB-3
Biomass	walnut shell	apple tree branch		
Oxygen-carbon ratio (O$_2$/C)，mol/mol	0.11	0.14	0.44	0.33
Steam-carbon ratio (S/C)，mol/mol	0	0	0	0.60
Circulating fluidized bed bottom temperature，℃	~730	~827	~835	~832

For each condition, after stable operation for more than 20 minutes, the gas was sampled at the outlet of cyclone by air bag, to then off-line detect the volume fraction of CO, H$_2$, CH$_4$, CO$_2$, and N$_2$ in the gas by a gas chromatography. Besides, biochar samples were collected from the bottom of the riser of circulating fluidized bed.

The biochar samples were characterized by proximate and ultimate to obtain their chemical compositions, by nitrogen adsorption test using automatic gas adsorption analyzer to obtain the pore structure, and by adsorption tests of iodine and methylene blue respectively according to Chinese Standard GB/T 12496.8-2015 and GB/T12496.10-1999 to obtain the adsorption characteristics.

2.4 Data processing

Gas yield (Y_g) refers to the volume of gas produced by feedstock per unit mass, calculated according to the principle of nitrogen balance：

$$Y_g = Q_a/(W_c \cdot X_{N_2}) \ (Nm^3/h) \quad\quad （1）$$

where Q_a is N$_2$ flow rate (Nm^3/h); W_c is the feed rate (kg/h); X_{N_2} is the volume percentage of N$_2$ in the combustible gas (%), obtained by difference according to the detected gas

compositions.

Char yield (Y_C) refers to the mass of biochar produced per unit mass of raw material, calculated according to the principle of ash balance：

$$Y_C = X_{A1}/X_{A2} \text{ (kg/kg)} \hspace{2cm} (2)$$

where X_{A1} is the ash content in raw materials (%), X_{A2} is the ash content in biochar (%).

3 Results and discussion

3.1 Gas and biochar yield
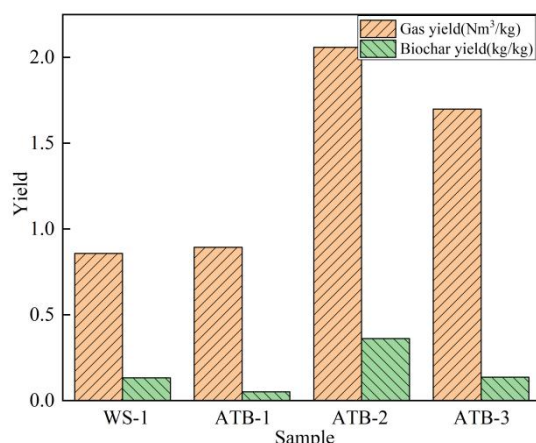
Fig. 2. Gas and biochar yields under different conditions

According to Fig. 2, the gas and biochar yields in the case of WS-1 (O_2/C: 0.11 mol/mol) are 0.858 Nm^3/kg and 0.13 kg/kg, respectively. At similar O_2/C (0.14 mol/mol), the gas yield of ATB was also similar (0.89 Nm^3/kg). In addition, with the increase of O_2/C, the gas yield of ATB increased, and the gas yield reached 2.06 Nm^3/kg at the O_2/C of 0.44 mol/mol.

3.2 Gas composition

(a) Gas components   (b) LHV
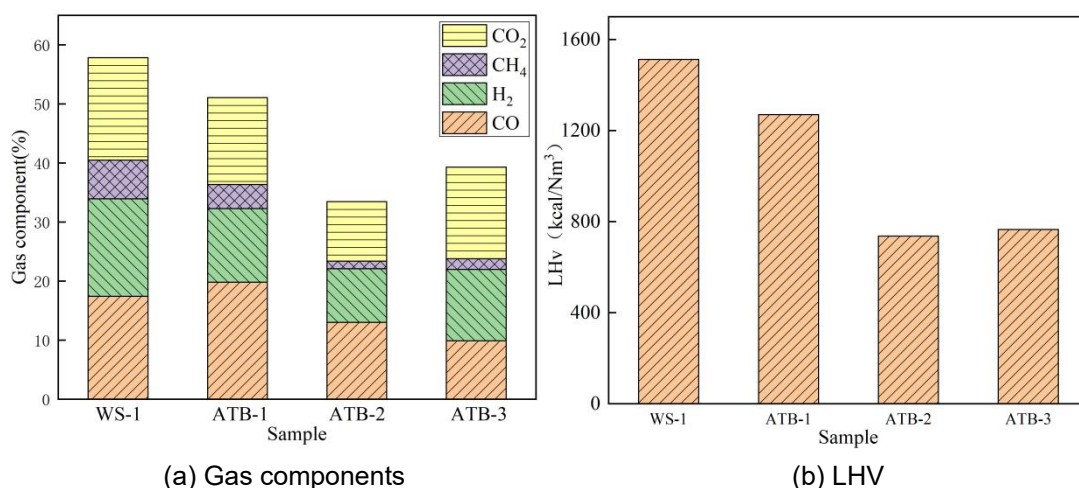
Fig. 3. Gas components and its LHV under different conditions

Fig. 3 shows the gas components and corresponding low heating value (LHV) under different conditions. It can be seen that under the condition of lower O_2/C, the concentration of combustible gas is higher. For WS, when the O_2/C is 0.11 mol/mol, the concentration of combustible gas can reach 40.46% and the LHV is 1512.3 kcal/Nm^3. For ATB, when O_2/C is 0.14 mol/mol, the combustible gas concentration can reach 36.35%, and the LHV is 1269.9 kcal/Nm^3. When the O_2/C increased from 0.14 mol/mol to 0.44 mol/mol, the combustible gas concentration and corresponding LHV decreased significantly, mainly because the increased oxygen intensifies the oxidation reaction of the gas, consuming CH_4 and CO and producing CO_2. Further focusing on the case of ATB-3, it is found that the concentrations of H_2 and CO_2 increase while a decrease in that of CO. It is because the steam intervention greatly

strengthens the water-gas conversion reaction ($CO+H_2O ->CO_2+H_2$). The introduction of steam is conducive to the production of hydrogen-rich gas. Hyungseok et al.[12] also showed a similar phenomenon in their experimental research.

3.3 Pore structure of biochar

(a) Specific surface area   (b) Pore volume
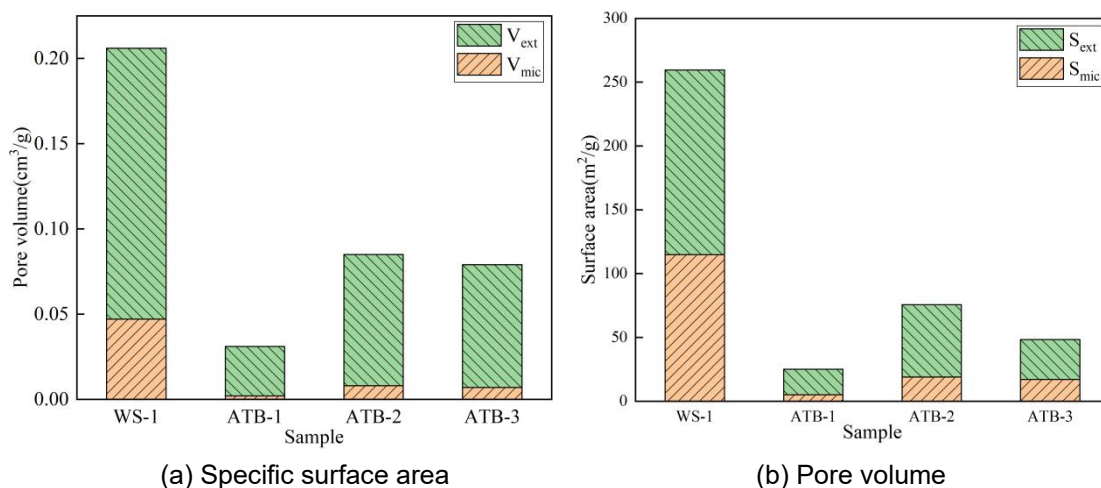
Fig. 4. Pore structure of biochar under different conditions

According to Fig. 4, it can be seen that the pore structure of biochar obtained from WS is more developed than that from ATB, with a specific surface area reaching 259.6 m^2/g and pore volume reaching 0.21 cm^3/g. The pore structure of the two types of biochar is mainly mesoporous, of which corresponding surface area accounts for more than 55% and pore volume accounts for more than 77%. Compared with the case of WS-1, the mesoporous proportion for the cases of ATB is higher, of which corresponding surface area and pore volume accounting for 65% and 90%, respectively. As the O_2/C increases from 0.14 mol/mol to 0.44 mol/mol, the specific surface area and pore volume of biochar increase, and the pore structure gets developed. This may be because the increase of air flow makes the surface gasification reactions more intensified, forming pores at reaction sites on the surface of particles.

3.4 Adsorption characteristics of biochar
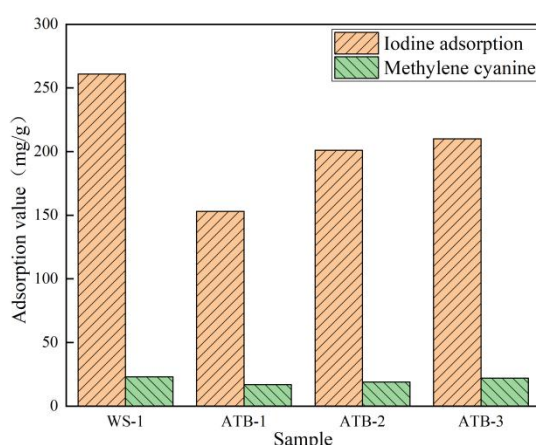
Fig. 5. Adsorption characteristics of biochar under different conditions

Fig. 5 shows the iodine adsorption value and methylene blue adsorption value of biochar under different conditions. It can be seen that the adsorption capacity of WS biochar is higher than that of ATB, and the iodine adsorption value reaches 261 mg/g and the methylene blue adsorption value reaches 23 mg/g. When the O_2/C increases from 0.14 mol/mol to 0.44 mol/mol, the adsorption capacity of ATB biochar increase, for instance, the iodine adsorption

value increases from 153 mg/g to 201 mg/g and the methylene blue adsorption value increases from 17 mg/g to 19 mg/g. Steam can further enhance the adsorption capacity of biochar, and the adsorption value of methylene blue for the case of ATB-3 increases to 22 mg/g.

4 Conclusions

(1) When the O_2/C increases from 0.14 mol/mol to 0.44 mol/mol during the gasification of apple tree branch, more combustible gas is consumed, resulting in a decrease in the low heating value of gas. In this case, the gas and biochar yields increase and both pore structure and adsorption capacity of biochar are improved.

(2) The gas compositions were improved directionally during the gasification of apple tree branch at the S/C of 0.6 mol/mol because the addition of steam strengthens the water-gas conversion reaction ($CO+H_2O ->CO_2+H_2$). Meanwhile the gas and biochar yields increase, as well as the adsorption capacity of biochar.

Acknowledgment

REFERENCES

[1] Renato Godinho, Michela Morese, Olivier Dubois, et al. IEA Bienergy Annual Repor 2019. Finland: International Energy Agency. 2019.

[2] Kumar A, Jones D D, Hanna M A. Thermochemical biomass gasification: a review of the current status of the technology[J]. Energies. 2009. 2(3), 556-581.

[3] Asadulah M, Miyazawa T, Ito S, et al. Demonstration of real biomass gasicaion drastically promoted by efective catalystyl. Applied Catalysis a-General. 2003. 246 (1), 103-116.

[4] Luis R, Lokmane A, Balkydia C, et al. Exergetic study of beech wood gasification in fluidized bed reactor using CO_2 or steam as gasification agents[J]. Fuel Processing Technology. 2020. (prepublish), 106664.

[5] KARATAS H, AKGUN F. Experimental results of gasification of walnut shell and pistachio shell in abubbling fluidized bed gasifier under air and steam atmospheres[J]. Fuel. 2018. 214, 285-292.

[6] KARATAS H, OLGUN H, AKGUNF. Experimental results of gasification of cotton stalk and hazelnut shell in a bubbling fluidized bed gasifier underair and steam atmospheres[J]. Fuel. 2013. 112, 494-501.

[7] Martínez I, Kulakova V, Grasa G, et al. Experimental investigation on sorption enhanced gasification (SEG) of biomass in a fluidized bed reactor for producing a tailored syngas[J]. Fuel. 2020. 259,116252.

[8] Lan W, Chen G ,Zhu X, et al. Research on the characteristics of biomass gasification in a fluidized bed[J]. Journal of the Energy Institute. 2019. 92(3), 613-620.

[9] Ma Z,Zhang Y,Zhang Q, et al. Design and experimental investigation of a 190 kW e biomass fixed bed gasification and polygeneration pilot plant using a double air stage downdraft approach[J]. Energy. 2012. 46(1), 140-147.

[10] Kramreiter R, Url M, Kotik J, et al. Experimental investigation of a 125 kW twin-fire fixed bed gasification pilot plant and comparison to the results of a 2 MW combined heat and power plant (CHP)[J]. Fuel Processing Technology. 2008. 89(1), 90-102.

[11] Chen H P, Lin G Y, Chen Y Q, et al. Biomass pyrolytic poly generation of tobacco waste: productcharacteristics and nitrogen transformation[J]. Energy and Fuels. 2016. 30(3), 1579-1588.

[12] Hyungseok N, Shuang W,K.C. S, et al. Enriched hydrogen production over air and air-steam fluidized bed gasification in a bubbling fluidized bed reactor with CaO: Effects of biomass and bed material catalyst[J]. Energy Conversion and Management. 2020. 225,113408.

STEAM/OXYGEN BIOMASS GASIFICATION IN A PILOT TWO-STAGE FLUIDIZED BED GASIFIER

Long Cheng[1], Lei Zhang[1], Ruixu Wang[1], Junnan Chao[1],
Sahand Nekoeian[1], Nazanin Charchi Aghdam[1], Zhijie Fu[1], Xiaoyang Wei[1],
Milad Taghavivand[1], Shida Liu[1], Haiyan Wang[1], Jing He[1], Jiantao Li[1], Yang Liu[1],
Markus Hughes[1], Yumeng Zhang[1], Bhavya Nagda[1], Maria Cortazar[4],
Gorka Elordi[4], Suarez Cardona[4], Mayra Alejandra[4], Leire Olazar Barona[4],
Santiago Orozco Hernandez[4], Jan Becker[5], Antoine Escudie[6],
Chunbao Zhou[1], Zhangke Ma[1], Shoushi Bo[1]
Kevin Smith[1], Naoko Ellis[1], Robert Legros[2], Wenli Duo[3], Jim Lim[1], Xiaotao Bi[1]*

[1]Department of Chemical and Biological Engineering, University of British Columbia, 2360 East Mall, Vancouver, BC, V6T 1Z3, Canada

[2]Department of Chemical Engineering, Polytechnique Montreal, 2500 chemin de Polytechnique, Montreal, QC, H3T 1J4, Canada

3 FPInnovations, 2665 East Mall, Vancouver, BC, V6T 1Z4, Canada

[4]Department of Chemical Engineering, University of Basque Country, Bilbao, Spain

[5]TUM School of Natural Sciences, Technical University of Munich, D-85748, Lichtenbergstr. 4 Garching, Germany

[6]Institut national Polytechnique de Toulouse, Emile Monso, 31030 Toulouse, France

*Email: tony.bi@ubc.ca

Abstract

Renewable natural gas, produced via gasification of waste woody biomass, has been considered as a pipeline-quality green fuel which is fully compatible with the existing natural gas transmission infrastructure. Gasification has been widely recognized as an efficient thermochemical technology to convert biomass into green gas fuels. However, reducing the tar content and inert gas fraction is still a great challenge for generating high-quality syngas from biomass gasification (Cortazar et al., 2023). In this context, controlling the interaction between the main products of biomass during pyrolysis and the subsequent biochar gasification and tar reforming reactions has been reported to be an effective way to reduce tar concentration from biomass gasification (Han et al., 2018). On this basis, a new design of a two-stage fluidized bed system, consisting of a bubbling fluidized-bed pyrolyzer and a riser gasifier, has been proposed for the production of high-quality syngas for lime kiln use or RNG production. In this work, a pilot-scale steam-oxygen two-stage fluidized bed pilot facility, capable of processing 30 kg/h of woody biomass, has been commissioned and tested. The effect of various process parameters, including reactor temperatures, equivalent ratio (ER) and steam-to-biomass ratio (S/B), on the gasifier performance in terms of syngas yield and composition, and tar yield has been studied systematically, with typical gasifier performance results reported in this paper.

1. Introduction

With the growing global energy demand and rising fossil fuel crises, interest in the exploitation of biomass as a carbon-neutral and renewable energy source has increased in the past decade. Among all the biomass conversion processes, gasification has emerged as an attractive option for syngas production due to its superior efficiency compared to other thermochemical processes. Theoretically, biomass-derived syngas can be utilized as a renewable fuel in a wide range of applications, such as the production of renewable natural gas. However, reducing the tar level and inert gas fraction in syngas still remains a great

challenge for the commercialization of biomass gasification technologies. In general, raw biomass-derived syngas needs to be subjected to secondary tar removal treatment to meet the demand for downstream applications. Meanwhile, the tar content generated during gasification depends significantly on gasification conditions (temperature, residence time, type of gasifying agents, and bed material) and gasifier configurations.

To date, a variety of gasifier configurations have been explored for biomass gasification, with the most common ones being fixed/moving bed (updraft, downdraft, and crossdraft), entrained-flow and fluidized bed gasifiers. Fixed/moving bed gasifiers have been traditionally used for biomass gasification due to their simple and robust design. However, atmospheric fixed bed gasifiers have limited capacity and are sensitive to particle size range. Entrained flow gasifiers generally operate at high temperatures (up to $1700^{\circ}C$) and high pressure (20-70 bar), which produces a relatively low tar content gas (Cortazar et al., 2023). However, entrained flow gasifiers are more suitable for dry feedstock with very small particle sizes (< 0.4 mm). On the other hand, fluidized bed gasifiers (mainly bubbling-, circulating-, and dual-fluidized beds) are relatively versatile for feedstocks with wide particle size distribution and have a more uniform and controllable temperature distribution and higher gas-solids contact efficiency. However, due to relatively lower operating temperature (typically between 800-$900^{\circ}C$), tar yield is considerable. Another major problem associated with fluidized bed gasifiers is the low thermal efficiency due to incomplete carbon conversion.

The dual fluidized bed design has been introduced for biomass gasification to alleviate the negative impact of volatiles on char gasification (Kunii et al., 1977). It has been proposed that separating the combustion and gasification of solid fuel in the dual fluidized bed reactors can effectively lower inert gas fraction, improving the calorific value of syngas. Nonetheless, during gasification, a number of different reactions occur simultaneously and interact mutually inside the gasifier, resulting in a complex reaction network. Meanwhile, it has been widely recognized that decoupling the thermochemical reaction network can potentially promote the desired reactions for tar removal (Zhang et al., 2010). In this regard, two-stage or staged gasification with reaction decoupling have been proposed to effectively reduce the tar content by preventing short-circuiting of tar single-stage fluidized beds by forcing the tar vapour generated from the first stage through a second stage, and by physically decoupling the pyrolysis and gasification reactions to facilitate the interaction between tar and solid char particles in the second stage (Brandt et al., 2000; Kersten et al., 2003). It has been widely agreed that char produced in the pyrolysis stage is not only the reactant for gasification but also a promising tar removal catalyst in the second stage. However, char is consumed during the gasification process, and its properties can vary significantly depending on the gasification conditions, biomass feedstock, thermal annealing and presence of various gasifying agents. Therefore, sustaining the stable catalytic reactivity of char for tar removal through balancing the fresh char supply and the consumption from char gasification is critical in two-stage gasification.

Although the two-stage gasification technology has been shown to have the potential to produce high quality syngas with low tar content, there still exist some problems in scaling up the staged gasification technologies. Therefore, a new pilot biomass gasification system based on the two-stage concept was developed and commissioned in this study to validate the potential of two-stage gasification, as illustrated in Fig. 1. Steam and oxygen were employed as the gasifying agents to produce high quality N_2-free syngas with high gasification efficiency (He et al., 2015). The ultimate goal of this study is to develop a two-stage fluidized bed gasification technology for high quality syngas production.
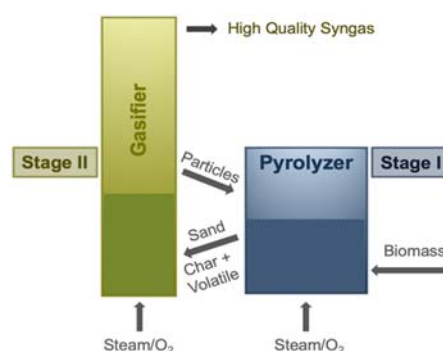
Fig. 1: Conceptual diagram of two-stage biomass gasification process

2. Experimental

2.1 Biomass Feedstock

Wood pellets of an initial diameter of 6 mm and length of 10-50 mm of a mixture of spruce, pine and fir (SPF, Pinnacle Renewable Energy Inc., Armstrong, Canada) were utilized in this study. The proximate and ultimate analyses of the SPF sawdust pellet are given in Table 1.

Table 1: Proximate and ultimate analyses of SPF pellets

Proximate Analysis (wt.%)				Ultimate Analysis (wt.%, daf)					LHV (MJ/kg)
Moisture	VM^d	FC^d	Ash^d	C	H	N	O	S	
6.8	82.4	16.9	0.6	50.1	5.9	0.2	43.8	0	19.7

Note: VM-volatile matters; FC-fixed carbon; daf-dry and ash free basis; ^{d} dry basis

2.2 Pilot Process Design and Operation

In this study, a pilot-scale two-stage fluidized bed gasifier has been designed and built with a feeding capacity of 30 kg/h. The system mainly consists of a screw feeder, a bubbling fluidized bed (BFB) pyrolyzer, a riser gasifier, a loop seal, two nature gas burners for start-up, two-stage cyclones, a syngas cooler, and a bag-house filter, as shown in Fig. 2. An overflow pipe was used to connect the pyrolyzer and gasifier. The effective heights of the pyrolyzer and gasifier are 1.9 m and 6 m, respectively.
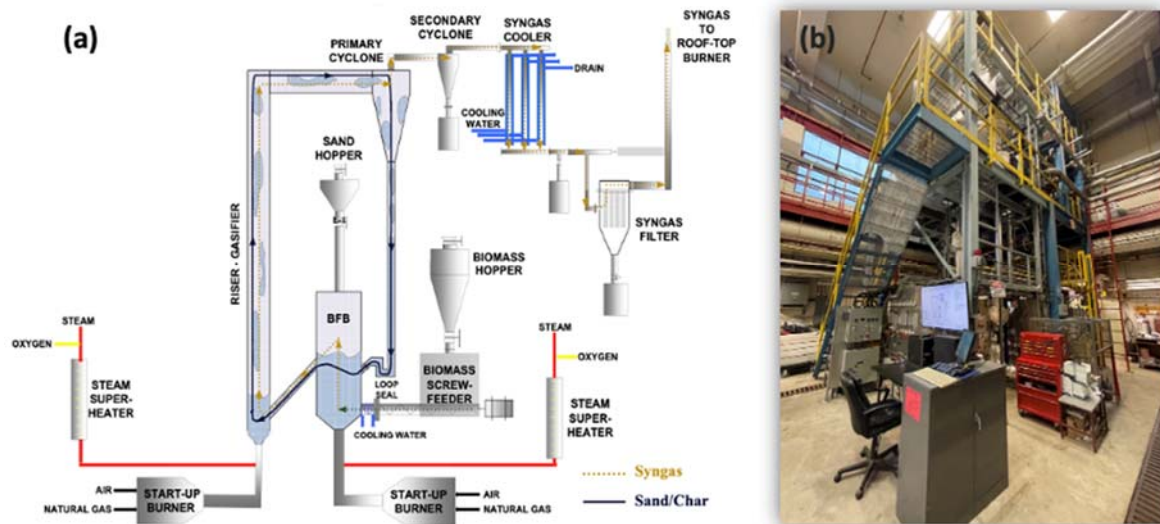
Fig. 2: (a) Schematic diagram and (b) the pilot-scale two-stage gasification facility

Silica sand particles with a size range of 100-150 μm are loaded into the pyrolyzer as the fluidization media and heat carrier. The pyrolyzer and gasifier are pre-heated to ~600°C by natural gas burners. During the preheating, air was used as the fluidizing medium. After the temperature reached the target values, biomass pellets from the hopper were gradually fed into the pyrolyzer through the screw feeder to initiate biomass combustion, further elevating the system temperature required for gasification. After the entire system reached the required temperatures, steam and oxygen were introduced into the system at controlled flow rates, with air injection shut off gradually. In this study, different oxygen and steam feed rates were employed to study the effect of equivalence ratio (ER) and steam to biomass ratio (S/B) on the gasifier performance. During the pilot experiment, the temperature and pressure of the system were continuously monitored by thermocouples and pressure transducers located at different reactor heights.

Meanwhile, after the biomass pellet is introduced into the pyrolyzer, pyrolysis takes place in the first stage bubbling fluidized bed in the presence of steam and oxygen, where the release

of volatiles and char oxidation reactions help to lower the primary tar content and provide heat for endothermic pyrolysis, as shown in Fig. 3. Consequently, the resulting pyrolysis gas together with the biochar and sand overflow to the gasifier, forming a dynamic hot char/sand bed, further enhancing tar cracking/reforming into smaller molecules within the process. Whereas the catalytic effect of char on tar removal could be strongly correlated to the gasifier conditions (temperature and type of gasifying agents) and to pore size, specific surface area, surface functionality, the mineral spices and content of the char (Abu El-Rub et al., 2008), as illustrated in Fig. 3. Afterwards, the un-reacted biochar and sand were entrained and captured by the primary cyclone, and circulated back to the pyrolyzer through the standpipe. Whereas the resulting syngas passed through cyclones, syngas cleaning units and a water scrubber for further conditioning, in order to clean up the syngas to meet the requirement for RNG synthesis.
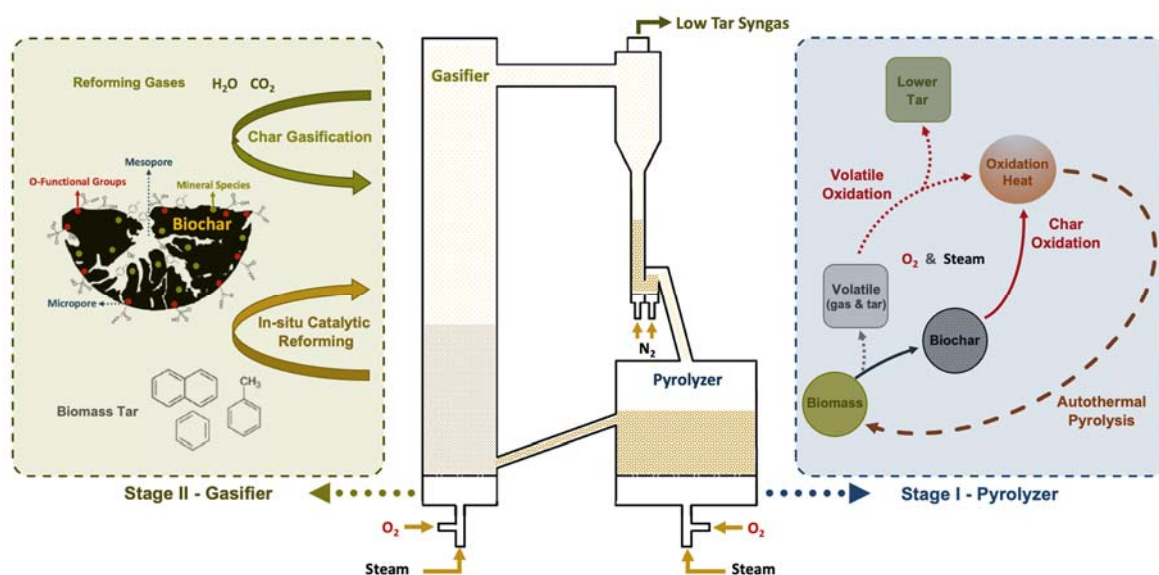
Fig. 3: Concept of tar reduction in two-stage fluidized bed gasification

After stable operating condition was reached, syngas was sampled through a gas sampling train where the non-condensable gas was metered and purified prior to gas analysis using a gas chromatograph (GC) equipped with a thermal conductivity detector (TCD). Meanwhile, tar samples were collected through impinger bottles filled with isopropanol according to the tar protocol. Subsequently, an aliquot of the collected tar solution was evaporated using a rotatory evaporator at 65°C, and the resulting residue was weighed to determine the tar content.

3. Results and Discussion

3.1 Operation Stability

In this study, the new two-stage fluidized bed pilot gasifier was tested using oxygen and steam as the gasifying agents. During operation, the ER value was controlled by regulating the oxygen flow rate while the steam-to-biomass ratio (S/B) was varied by adjusting the steam flow rate. Before each run, the entire pilot experimental device was gradually preheated to the required temperature. Fig. 4(a) shows the temperature profile of the first-stage pyrolyzer and second-stage gasifier, which normally takes about 24-28 h to reach target temperature due to the larger thermal capacity and the significant heat loss.

The operation stability can be determined by the temperature fluctuation inside the gasifier. During gasification, the variations in temperatures can be influenced by biomass size and moisture content. Fig 4(b) shows the temperature profile for the first-stage pyrolyzer and the second-stage gasifier during stable operation at a feeding rate of 30 kg/h with an ER of 0.3. It can be seen that both temperatures are relatively stable within the testing period, showing that the pilot staged gasifier is able to run smoothly under steady-state conditions. This also verifies the operational feasibility of the new two-stage gasification system.
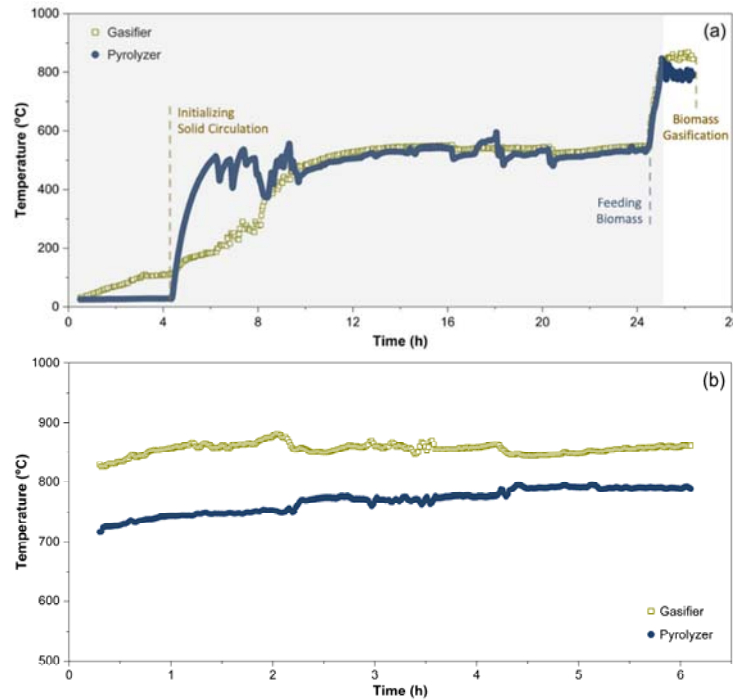
Fig. 4: Temperature profiles of pyrolyzer/gasifier during (a) start-up and (b) steady-state gasification

3.2 Influence of ER on Gasification Temperature

The reactor temperature during gasification is an important factor for influencing the gasifier's performance, because it has a strong effect on the gasification products. Although elevating the gasification temperature has been widely reported to reduce the tar level, it could also be detrimental to the syngas quality by lowering the calorific value and generating more CO_2. In addition, higher gasification temperatures may lead to bed material agglomeration, causing the non-uniform gasifier temperature profile and premature shut-down (Mettanant et al., 2009).

The gasification temperature of biomass pellets at various ER, with other operational variables kept constants, has been recorded from pilot tests. As shown in Fig. 5(a), the gasification temperature is strongly correlated with ER. Both the pyrolyzer and gasifier temperatures generally increase with the total ER, which can be attributed to the enhanced energy released from the active oxidization reactions. In addition, it is noted that the temperature in the pyrolyzer is ~100°C lower than that in the gasifier, which is mainly due to the occurrence of the endothermic drying and pyrolysis processes in the pyrolyzer. Meanwhile, it was found that the temperature in the gasifier dense phase zone decreases after the gasifier ER increases from 0.30 to 0.35, indicating that less heat was released from char/volatile oxidation in the dense phase zone (Fig. 5(b)). This could be due to increased superficial gas velocity with the rising ER, which decreases the residence time of char in the dense phase zone.
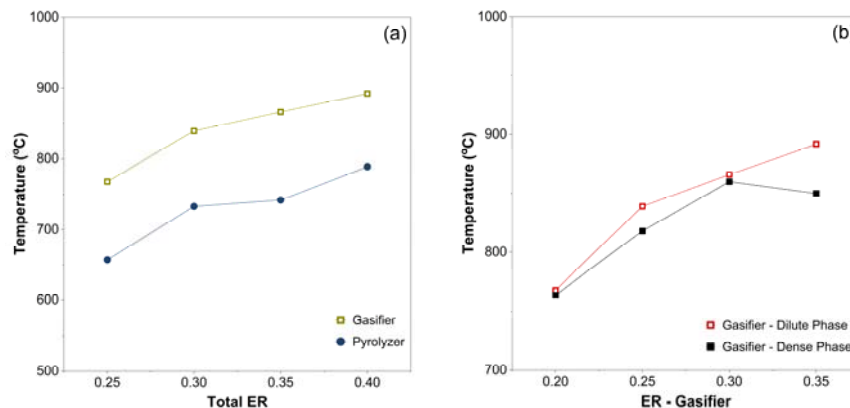
Fig. 5: Effect of ER on (a) gasifier/pyrolyzer temperatures and (b) dense/dilute phase zones in gasifier

300

3.3 Performance of the Two-Stage Fluidized Bed Gasifier

Table 2 shows the typical operating conditions and the key performance data, and the corresponding operating temperature profiles during gasification are shown in Fig. 4(b). As generally recognized, ER value is the most crucial operating variable for optimizing gasification operations (Cortazar et al., 2023). Theoretically, increasing the oxygen concentration in the gasifier would not only reduce the tar level but also oxidize the effective components (H_2 and CO) in the syngas. Hence, there should be an optimal ER for producing high quality syngas.

Based on a series of pilot biomass gasification tests, it has been verified that the suitable operating conditions for the new two-stage fluidized bed gasifier are an ER around 0.35 with a steam-to-biomass ratio of ~1. The volume fractions of H_2, CO, CH_4, and CO_2 in the produced dry syngas were about 19.5%, 36.0%, 6.5% and 38.0%, with a LHV of ~9.3 MJ/Nm^3. The tar content was determined to be around 2.0 g/Nm^3, which is much lower compared to the single-stage design (typically ~25-30 g/Nm^3) (Li et al., 2018), verifying that the two-stage design could lower the tar content substantially by prolonging the residence time of tar in the reactor. Those pilot testing results also provide the basis for future studies on identifying the suitable operating range for each stage to produce high quality syngas.

Table 2: Typical performance of the pilot two-stage fluidized bed gasifier

Main Operating Conditions		Gas Composition and Tar Yield	
Feeding Rate (kg/h)	30	H_2 (vol.%)	19.5
Steam to Biomass Ratio	1/1	CO (vol.%)	36.0
ER - Stage I Pyrolyzer	0.05	CH_4 (vol.%)	6.5
ER - Stage II Gasifier	0.30	CO_2 (vol.%)	38.0
Temperature - Stage I Pyrolyzer (^oC)	750-790	LHV (MJ/Nm^3)	9.3
Temperature - Stage II Gasifier (^oC)	850-870	Tar (g/Nm^3)	2.0

4. Conclusion

A new two-stage gasification process consisting of a bubbling fluidized bed pyrolyzer and a riser gasifier has been studied for producing low-tar and high calorific syngas. Results from a series of pilot biomass gasification experiments verified that the two-stage gasifier can produce clean syngas with lower tar level. Further studies are being undertaken to identify the suitable operating range for each stage with different biomass feedstock.

References

Abu El-Rub, Z., Bramer, E. A., & Brem, G. Experimental comparison of biomass chars with other catalysts for tar reduction. Fuel. 2008. 87, 2243–2252

Brandt, P., Larsen, E., Henriksen, U. High tar reduction in a two-stage gasifier. Energy and Fuels. 2000. 14, 816–819

Cortazar, M., Santamaria, L., Lopez, G., et al. A comprehensive review of primary strategies for tar removal in biomass gasification. Energy Conversion and Management. 2023. 276,

Han, Z., Geng, S., Zeng, X., et al. Reaction decoupling in thermochemical fuel conversion and technical progress based on decoupling using fluidized bed. Carbon Resources Conversion. 2018. 1, 109

He, T., Han, D., Wu, J., et al. Simulation of biomass gasification and application in pilot plant. Energy Technology. 2015. 3, 162–167

Kersten, S. R. A., Prins, W., Van der Drift, B., et al. Principles of a novel multistage circulating fluidized bed reactor for biomass gasification. Chemical Engineering Science. 2003. 58, 725–731

Kunii, D., Hasegawa, M., & Fukuda, J. Research and development of circulation system between fluidized beds for application of gas-solid reactions. Second Pacific Chemical Engineering Congress. 1977, 77

Li, Y. H., Chen, Z., Watkinson, P., et al. A novel dual-bed for steam gasification of biomass. Biomass Conversion and Biorefinery. 2018. 8, 357–367.

Mettanant, V., Basu, P., & Butler, J. Agglomeration of biomass fired fluidized bed gasifier and combustor. Canadian Journal of Chemical Engineering. 2009. 87, 656–684

Zhang, J., Wang, Y., Dong, L., et al. Decoupling gasification: Approach principle and technology justification. Energy and Fuels. 2010. 24, 6223–6232

EXPERIMENTAL INVESTIGATION INTO THE EFFECT OF BED TEMPERATURE AND ATMOSPHERE AND THE ROLE OF CHAR ON THE QUARTZ PARTICLE AGGLOMERATION IN A BFB

Xiaofei Long[1], Jianbi Li[1,*], Shengqi Yuan[1], Lin Mei[2], Xiaofeng Lu[1], Tao Yan[3], Dongke Zhang[4]

[1]Key Laboratory of Low-grade Energy Utilization Technologies and Systems, Ministry of Education of PRC, Chongqing University, 174 Shapingba Main street, Shapingba, Chongqing 400044, China

[2]Chongqing Special Equipment Inspection and Research Institute, Chongqing 401121, China

[3]Key Laboratory of Electromechanical Equipment Security in Western Complex Environment for State Market Regulation, Chongqing 401121, China

[4]Centre for Energy (M473), The University of Western Australia, 35 Stirling Highway, Crawley, WA 6009, Australia

*Email: jianbo.li@cqu.edu.cn

Abstract

Agglomeration of bed material in circulating fluidised bed (CFB) during combustion or gasification of high-alkali fuel has been a practical challenge in industrial practice. This work therefore investigates systematically the effect of temperature and atmosphere on the agglomeration of quartz bed particles. Experimentations were conducted in a lab-scale bubbling fluidised bed at temperatures 700-900 °C at air equivalence ratios of 1.61-0.53. By characterising the mineralogy and morphology of the bed particles, results show that agglomeration of quartz particles in oxidising atmosphere did not occur at 700°C but incurred at 800-900 °C due to the formation of Na silicates bridging the bed particles. This highlights the effect of temperature and Na in initiating particle agglomeration. In gasification atmospheres, de-fluidisation of the bed occurred in advance in comparison to the case in oxidising atmosphere. In particular concern, char particles with molten ash were found to be the main precursor in initiating agglomeration. This is also proved by separate experiments sending either Na_2CO_3-doped coal particles or coal ash. FactSage calculation revealed that more slag-liquid phase are formed at higher temperatures, confirming the presence of low melting-point $Na_6Fe(SO_4)_4$ and $Na_2Si_4O_9$ in initiating agglomeration. This would provide a few strategies such as reducing bed temperature and avoiding local deflagration to mitigate agglomeration of bed particles in CFB burning high alkali fuel.

1. Introduction

Fluidised Bed (FB) or Circulating Fluidised Bed (CFB) is one clean and trustworthy technology for utilization of multi-component fuels, due to its characterisations including intensive gas-solid flow, low furnace temperature and specific recirculation circuit [1]. These require a series of solid materials to be remained in the furnace or to be recirculated along bed, freeboard and circulating loop [2]. However, agglomeration of these solid materials would occur occasionally, due to ash-bed interaction [3, 4], which induces the retention of bed particles in bed while reduces the amount of circulating ash. This issue becomes trickier to be managed when fuels enriching in alkali metals are utilised [5, 6]. Once efficient measures have not applied timely, the presence of agglomerates would bring about uneven fluidisation locally [7, 8], and subsequently the formation of hotspots in furnace. Local defluidisation and overheating would further deteriorate the agglomeration of bed particle [9, 10]. To solve this supposed "positive feedback" mechanism, a comprehensive understanding on the factors that facilitate or mitigate bed particle agglomeration is required.

Agglomeration of bed particles induced by alkali metals in FB is found be affected by many factors including fuel ash chemistry [11], nature of bed materials [4], fluidisation velocity [5], particle size [12], operating temperature [9] and reaction atmosphere [13]. These strategies could be divided into two categories, namely, regulating fluidisation velocity and particle size is a physical process regulation, while other strategies belong to chemical reaction regulation. Physical process regulation could mitigate but not avoid particle agglomeration, since they make no sense to prevent the formation of viscous substance. On the contrary, chemical reaction regulation aims at avoiding the generation of melt materials, being believed as a thorough solution. Specifically, high-alkali fuel ash enriching in Ca were found to have low intendency to induce bed agglomeration [14]. Similarly, bed materials comprised of Ca, Mg and Al were also found to mitigate agglomeration [15, 16]. These minerals could dilute the content of alkali or avoid the formation of alkali silicates melt [4]. However, considering the wide usage of quartz bed material in FB, owing to its low price [17], for specific fuel, the regulation of temperature or atmosphere is a more effective means.

This work therefore investigates experimentally the effect of temperature and atmosphere, as well as the role of char on quartz particle agglomeration, aiming at revealing the ash-bed interaction during utilization of high-alkali fuel in fluidised bed. Systematic characterisations on the mineralogy and morphology of quartz particles and their agglomerates and thermodynamic calculations were conducted, which would provide an improved understanding on the mechanism of bed particle agglomeration during FB combustion of high alkali fuels.

2. Experimental and analysis

2.1 Second Level of Headings

The experimentation was carried out in a lab-scale fluidised bed (FB), which can be found in our previous work [1]. Briefly, the quartz reactor is 1000 mm in height with an inner diameter of 40 mm. And a perforated plate was posited at a height of 300 mm to enable the loading and fluidisation of bed particles. Furthermore, an electricity-controlled furnace was equipped to heat the reactor and maintain a stable temperature within experimental time. And a K-type thermocouple and two pressure transducers were installed to monitor the temperature and pressure variation of the bed during experiment.
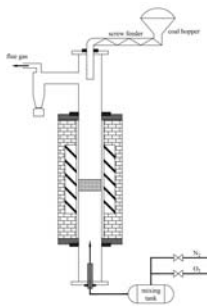
Fig. 1. Schematic diagrams of the FB systems

In a typical run, 30 g quartz in a cut-size of 0.21-0.25 was filled into the reactor, forming a static height of 21 mm. Synthesis gas with a fluidisation velocity of 0.27 m/s (1.8 Umf), was then supplied to maintain a bubbling state in the bed. Once the target temperature was reached, coal sample was continuously fed into the reactor in fixed rates, or coal ash was fed intermittently with an interval of 1 min. Detail settings in varying conditions can be seen in Table 2. Meanwhile, pressure drops over the bed were monitored to evaluate the fluidisation state in the bed, and typical pressure drops in the case of stable fluidisation and defluidisation can be seen in Fig. 2. Clearly, the pressure drops in Fig. 2(a) waved in the range of 1200-1600 Pa, while that in Fig. 2(b) decreased sharply at experimental time of 40 mins and then maintained in a stable value, confirming the occurrence of bed defluidisation [2]. Experiments stopped until 100 g coal sample or equivalent coal ash have been sent into the reactor or at the time of defluidisation. After experimentation, bed particles were discharged from the

reactor and cooled by pure nitrogen, immediately, to avoid ash sintering and post-combustion of char in the cooling stage.
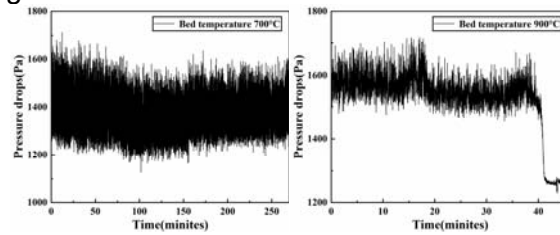
Fig. 2. Typical pressure drops in the case of (a) stable fluidization and (b) defluidisation

Table 1. Proximate and ultimate analysis of ZD, and its ash chemical composition

Proximate analysis (dry basis, wt%)				
M_{ar}	V_d	FC_d	A_d	Low heating value (MJ kg^{-1}, ar)
15.6	30.07	64.84	5.09	21.66
Ultimate analysis (dry basis, wt%)				
C_d	H_d	O	N_d	S_d
75.45	3.51	14.69	0.69	0.57
Ash chemistry (wt%, dry basis)							
SiO_2	Al_2O_3	Fe_2O_3	CaO	SO_3	MgO	Na_2O	K_2O
11.7	6.7	5.9	32.5	27.9	7.5	4.9	0.4

Table 2. The fluidization state after experimentation in varying conditions

Run #	Samples	Bed temperature (°C)	ERs	Defluidisation (yes or no)
1		700	1.40	No
2		800	1.40	Yes
3			1.61	Yes
4	ZD		1.40	Yes
5		900	1.06	Yes
6			0.76	Yes
7			0.53	Yes
8	ZD ash	800	1.40	No
9		900	1.40	Yes
10	Washed ZD	900	1.40	No
11	Washed ZD+1%Na_2CO_3	900	1.40	Yes

The carbon content in the bed particles was determined using a muffle furnace in accordance with CB212-2001. Moreover, a Bruker X-ray diffraction (XRD) with Cu Kα radiation was used to identify the mineral phases in the bed particle collected after experimentation. These samples were ground into fine powders and then analysed in XRD at a rate of 5°C/min within 5°-90°/2θ at an accelerating voltage of 40 kV and a current of 40 mA. The crystalline phases were then identified and analysed by using the X′Pert HighSocre Plus software in the search-match mode. Besides, a Quattro S scanning electron microscopy (SEM) coupled with energy dispersive X-Ray spectroscopy (EDX) was also used to observe the morphological characteristics and provide a semi-quantitative elemental composition analysis of the bed particles. Furthermore, thermodynamic equilibrium calculation was performed by using FactSage 8.2 to calculate the amount of slag-liquid phase at elevated temperatures[18], with the ash chemistry of quartz and Zhundong ash being the inputs and FactPS and FToxide databases being the references.

3. Results and discussion

3.1 Effect of bed temperature on agglomeration

To verify the effect of bed temperature on particle agglomeration and bed defluidisation, the fluidization status in the final of experiment and the weight ratio of Na/Si at the time of defluidisation have been presented in Table 2 and Fig. 3. It is seen that, when ZD was fed,

bed defluidisation did not occur at bed temperature 700 °C, but happened at bed temperature 800 and 900 °C. Moreover, bed temperature 800°C led bed defluidisation at a Na/Si ratio of 3.96 ‰, but decreased to 2.44 ‰ at 900 °C, suggesting that higher bed temperature would accelerate defuidisation [9]. However, when ZD ash was fed, bed defluidisation happened at a remarkable high Na/Si ratio of 5.55 ‰ at bed temperature 900 °C, but did not occur at bed temperature 800 °C. This implies that the absence of char might be able to delay the onset of bed defluidisation, or enven avoid the occurance of bed defluidisation. This which will be further discussed in Section 3.3.
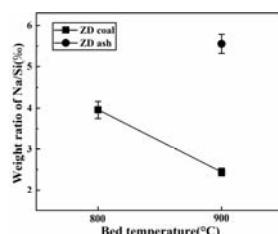
Fig. 3 The weight ratio of Na and Si at the time of defluidisation at bed temperature 800 and 900 °C with ZD and ZD ash input in Runs 2, 4 and 9

Fig. 4 shows the morphological features and EDX analysis of the bed particles collected at bed temperature 700-900 °C. As shown in Fig. 4(a-b), bed particles collected at bed temperature 700 °C were all discrete, being coated by ash particles in micro-sizes, indicating the absence of agglomerates. This is consistent with the results in Table 2, confirming that agglomerates were rarely found at this temperature. As bed temperature increased to 800 and 900 °C, agglomerates consisting of several bed particles were found (Particles A-C). Closer images show that the surfaces of agglomerates were smooth (Fig. 4(e) and Fig. 4(h)), without the presence of ash particles in micro-sizes, indicating that ash particles had been melted in the FB reactor. EDX analysis revealed that the ash particles on the surface of bed particles at 700 °C was comprised of Ca, S and Si in notable contents, as well as Na, Mg and Fe, suggesting that coal ash had been deposited on or reacted with bed particles. However at 800 and 900 °C, the surface of bed particles mainly consisted of Si, Ca and Na (e.g., spots 5, 6, 9 and 10), with decreased S contents in comparison to that at 700 °C, indicating the decomposition of sulfates and the presence of Na/Ca silicates. This is consistent with previous study [19, 20], confirming the role of Na/Ca silicates in initiating quartz particles agglomeration during ZD combustion.
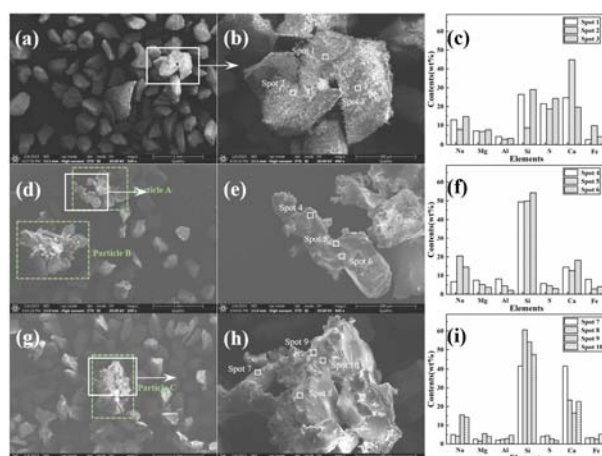
Fig. 4 Bed particles collected after experimentation at bed temperature (a-c) 700, (d-f) 800°C. and (g-i) 900 °C in Runs 1, 2 and 4

Fig. 5 illustrates the mineral phases that identified in the bed particles collected at bed temperature 700-900 °C. As shown in the Figure, SiO_2 was identified to be the dominant mineral phase in these bed particles, confirming their identify as quartz bed materials. Meanwhile, $CaSO_4$, Fe_2O_3, $Na_2Si_2O_5$ and $NaAlSiO_4$ were also identified in the bed particles collected at 700 °C, confirming the interaction between coal ash and quartz and the formation of Na silicate and aluminosilicate. These Na-based minerals of

low melting points were expected to be molten at temperature higher than 700 °C [21], contributing to bed particle agglomeration. However, when bed temperature increased to 800 and 900 °C, the peak of $Na_2Si_2O_5$ was disappeared, while that of $CaSO_4$ and $NaAlSiO_4$ were presented in lower intensities. This is consistent with SEM-EDX analysis, being attributed to the decomposition of $CaSO_4$ and the transition into amorphous phase transition of silicates and aluminosilicates [22].
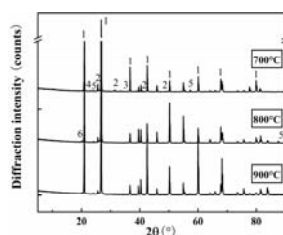
Fig. 5 XRD patterns of the bed particles at bed temperature 700-900 °C in Runs 1, 2 and 4. 1- SiO_2, 2-$CaSO_4$, 3-Fe_2O_3, 4-$Na_2Si_2O_5$, 5-$NaAlSiO_4$, 6-$CaAl_4O_7$

3.2 Effect of atmosphere on agglomeration

Fig. 6 shows the weight ratio of Na/Si at the time of defluidisation at ERs 1.61-0.53 and bed temperature 900 °C. Note that bed defluidisation happened in all Runs at bed temperature 900 °C, as shown in Table 2. However, the weight ratio of Na/Si inducing bed defluidisation were 2.44-2.48 ‰ at ERs 1.61 and 1.40, but decreased to 2.10 ‰ at ER 1.06 and futher reduced to 1.90-1.92 ‰ at ERs 0.76 and 0.53, showing a progressive decrease of Na/Si ratio at defluidisation with decreased ERs. This suggests that reducing atmosphere would increase the propensity of bed defluidisation.
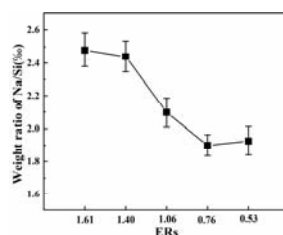
Fig. 6 The weight ratio of Na and Si at the time of defluidisation at 900 °C and ERs 0.53-1.61

To verify the effect of atmosphere on particle agglomeration, the morphological feature and EDX analysis of the agglomerates collected in gasification atmosphere were also performed, as shown in Fig. 7. It is seen that the agglomerate in Fig. 7(a-b) were comprised of three or more irregular bed particles (eg., Spots 1 and 3), with porous particles (eg., Spots 2, 4 and 5) acting as binder. This is differed from the agglomerates collected in oxidation atmosphere (Fig. 4(g-h)). EDX analysis revealed that the irregular bed particles were enriched in Si (ca. 80 wt%), confirming their identify as quartz. The porous particles, however, were rich in C (ca. 30.0 wt%), Fe (ca. 22.2 wt%), Ca (ca. 12.2 wt%), Na (ca. 8.6 wt%), S (ca. 8.2 wt%) and Si (ca. 9.7 wt%), indicating the presence of unreacted char and the enrichment of Na/Ca/Fe. This suggests that the unreacted carbon contribute to sodium retention, by means of being bound to the coal matrix [23, 24]. Once char was depleted, these porous particles might be transformed into molten ash consisting of Na, Ca, Si and Fe (e.g., Spot 7) to bridge bed particles, as shown in Fig. 7(c). This implies the role of char in acting as intermediation to facilitate bed particle agglomeration. Accordingly, the contribution of reducing atmosphere on particle agglomeration could be attributed to that less oxygen contents prolongs the residence time of carbon in FB reactor [25]. This point is also supported by the increased carbon contents with decreased ERs, as shown in Fig. 7(e).
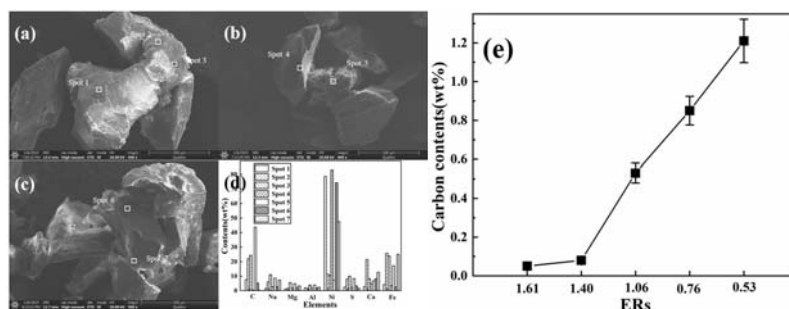
Fig. 7 Typical SEM images and EDX analysis of the agglomerated particles in gasification atmosphere and carbon content in the bed particles collected at ERs 0.53-1.61

Fig. 8 presents the identified *minerals in the bed particles collected* at ERs 1.61-0.53. It is seen that SiO_2 was the dominant mineral phase in these Runs due to the usage of quartz bed material. In addition, $CaSO_4$, Fe_2O_3, $CaAl_4O_7$ and Mg_2SiO_4 were also found in oxidation atmosphere at ERs 1.61, 1.40 and 1.06. However in gasification atmosphere at ERs 0.76 and 0.53, mineral phases not only $CaSO_4$, Fe_2O_3 and $CaAl_4O_7$ but also $Na_6Fe(SO_4)_4$ were identified. This is consistent with EDX analysis in Fig. 7, implying that iron had been participated in the reaction with Na-based compounds in gasification atmosphere [26], forming Na/Fe compounds of low melting-points. This might contribute to the bed defluidsation in advance at reducing atmosphere.
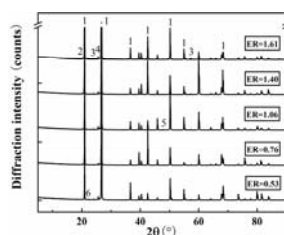
Fig. 8 XRD patterns of the bed particles at bed temperature 900 °C and ERs 1.61-0.53. 1-SiO_2, 2-$CaAl_4O_7$, 3-Fe_2O_3, 4-$CaSO_4$, 5-Mg_2SiO_4, 6-$Na_6Fe(SO_4)$

3.3 Role of char on agglomeration

To comprehend the role of char in agglomeration, washed ZD removing sodium has been prepared. Simplify, ZD was washed using ultrapure water and diluted hydrochloric acid to remove its water-soluble sodium and acid-soluble sodium [27]. EDX analysis on the ash of washed ZD was available in supplementary material S1, and sodium content was identified to as low as 2.89 wt%, confirming the efficiency of sodium removing. Moreover, FB experimentation with washed ZD input was also performed, and no defluidisation occurred even though 100 g coal sample had been feed into reactor. This suggests that washed ZD cannot solely induce bed defluidisation. However, when washed ZD loaded with 1% Na_2CO_3 was fed into reactor, bed defluidisation happened at a Na/Si ratio of 2.29 ‰ (shown in Fig. 10), which was slight lower than that when ZD was fed, and much lower than that with ZD ash input. This confirms that sodium was the key factor in initiating quartz particle agglomeration, by means of forming sodium silicates of low melting point [20, 28], whereas char could accelerate this process and cause bed defluidisation in advance [9].
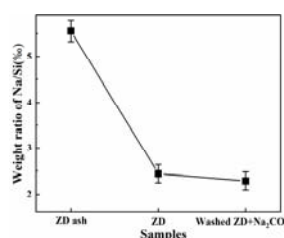
Fig. 9 The weight ratio of Na and Si at the time of defluidisation when different samples were fed

Fig. 10 shows the morphological features and EDX analysis on the bed particles with washed ZD and washed ZD loaded with Na_2CO_3 input. It is seen that the bed particles collected in Run 10 distributed dispersedly, with no sign of agglomeration, confirming that the low potential of washed ZD in inducing particle agglomeration. Closer images show that the surface of bed particles was quite clean without ash particle adhering on, suggesting that ash particles after acid-treated were less prone to deposit on or react with quartz particles. This has been further confirmed by EDX analysis that the regions on bed particle surface were rich in Si (ca. 86.9%), but were depleted in other elements. However when Na_2CO_3 was mixed into washed ZD, agglomerates were frequently found among bed particles (Fig. 11(d)), showing a severe propensity of particle agglomeration. Bed particles in agglomerates were found to be coated by molten ash and ash particles in micro-sizes (Fig. 11(e)), and to be connected by molten bridge (Areas A-B) comprising of Si and Na (ca. 18.4 wt%). This is similar to the finding in Run 4 (Fig. 4(h)), confirming the key role of Na in initiating particle agglomeration.
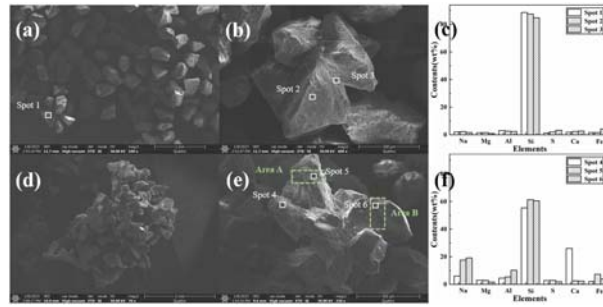
Fig. 10 The morphological feature and EDX analysis of the bed particles when washed ZD and washed ZD loaded with Na_2CO_3 were fed

To verify the role of char in facilitating particle agglomeration in both oxidation and gasification atmosphere, the mixture of ZD and quartz had been placed in a fixed bed reactor in oxidation and gasification atmosphere for 3 mins, and then discharged from the reactor and cooled rapidly using pure nitrogen. Fig. 11 shows the morphology and EDX analysis of the mixture of ZD and quartz. As shown in Fig. 11(a), residue char had been coated by dozens of quartz particles in the size below 1 mm, and acted as a core of agglomerates. Closer image in Fig. 11(b) shows that a solid neck (Area A) was formed between residue char and quartz particle, which contributed to stable agglomerates structure. The elemental compositions of the neck, as identified by EDX, was comprised of Si and C, as well as Fe, Ca, Al, Mg and Na in invisible contents. Such phenomenon was also found in gasification atmosphere, as shown in Fig. 11(d-f), indicating that char contribute to particle agglomeration in both oxidation and gasification atmosphere. However, since residue char was less present in CFB in oxidation atmosphere in comparison to that in gasification atmosphere (shown in Fig. 7), the role of char on agglomeration in oxidation atmosphere was expected to be lessened.
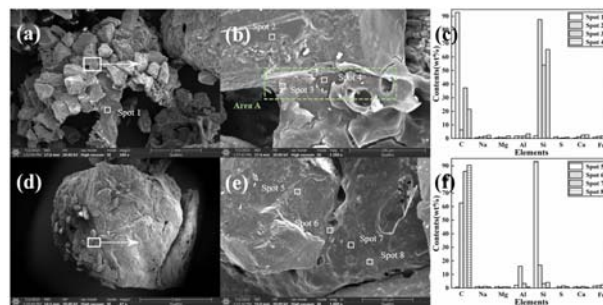
Fig. 11 SEM images and EDX analysis of the mixture of ZD and quartz in (a-c) oxidation and (d-f) gasification atmosphere

3.4 Formation of liquid phase

The transition of minerals and the formation of slag-liquid phase in ZD ash at elevated temperatures were calculated and the results are given in Fig. 12. As shown in this Figure, the relative mass of minerals at different temperatures varied, despite the minerals in oxidation and gasification atmosphere were roughly the same. Specially, slag-liquid phase was formed at 1150 °C and further increased to 20% at 1269 °C in oxidation atmosphere due to the decomposition or fusion of $Na_2CaAl_4O_8$. However in gasification, slag-liquid phase was formed at 993 °C and increased to 20% at 1254 °C due to the generation of Na/Ca silicates melt, showing a relatively lower liquefying temperature compared to the conditions in oxidation atmosphere. This indicates that gasification atmosphere had a positive effect in accelerating slag-liquid phase formation, and thus promoted particle agglomeration and bed defluidisation. However, the temperature at slag-liquid phase was formed is notably higher than the operating temperature of the FBC reactor, which cannot account for the presence of liquid bridge observed in this work, as well as in previous literature reports [19]. This could be attributed to either ash-bed interaction or overheating on the surface of residue char [9, 29], which will be discussed, furtherly.

As such, the composition of quartz bed material was taken into account, to calculate the formation of liquid phase in the mixture of quartz and ZD ash. As shown in Fig. 12(c), the slag-liquid phase presented at 940 °C in oxidation atmosphere, and increased to 20 wt% at 1018 °C, along with the decomposition or fusion of feldspar. Subsequently, the amount of slag-liquid phase reached 23.4 wt% at temperature 1140 °C, which is mainly due to the fusion of $CaSiTiO_5$ and $CaMgSi_2O_6$, $Ca_3Fe_2Si_3O_{12}$ and $CaSiTiO_5$.

Eventually, the amount of slag-liquid phase reached to 54.6 wt% at 1240 °C, and all minerals excluding SiO_2 had been fused into liquid phase. Similar observations on the formation of minerals were also found in gasification atmosphere. Note that the liquefying temperature when quartz was introduced reduced by ca. 250 °C, suggesting that the interaction between coal ash and quartz bed material could promote the formation of slag-liquid phase, consistent with the observations in Fig. 4.
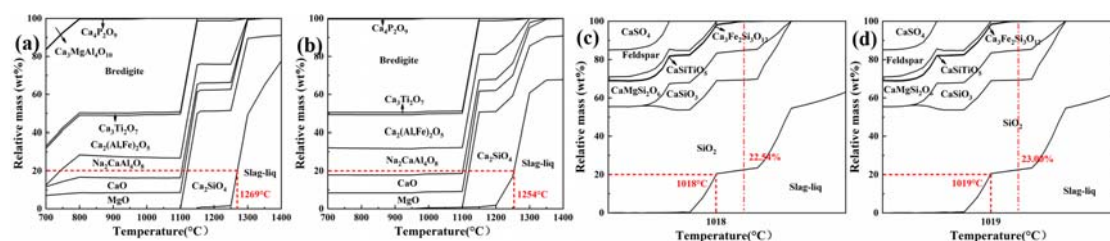
Fig. 12 Formation of slag phase and minerals of ZD ash in (a) oxidation and (b) gasification atmosphere and formation of slag phase and minerals when quartz was mixed with ZD ash in (c) oxidation and (d) gasification atmosphere

Furthermore, temperature on char particle is also a point that requires special concern [30]. As shown in Fig. 14(a), the temperature with slag-liquid formation was obviously higher than the set temperature of 800 and 900 °C, which is inconsistent with the occurrence of bed defluidisation as well as SEM analysis. This implies that agglomeration of quartz particles was formed at temperature much higher than set temperatures. Similar phenomenon have also been reported when biomass was combusted in lab-scale fluidised bed [30-32], or when coal was combusted in utility boiler [33]. Speculate the reason, local hotspot in furnace or excess temperature on char particle were the culprit of overheating. Considering the relatively small reactor size of FB reactor and stable fluidisation state (shown in Fig. 2), excess temperature on char particle was the main factor of overheating. Tthe difference between ambient temperature and the temperature on char particle varied in a wide range of 29-317 °C due to several factors including fuel sample, atmosphere and particle size. Specifically, fuel of low carbonization degree showed a high temperature difference up to 317 °C. This could be attributed to their combustion activity. Moreover, higher oxygen content and decreased particle size were also confirmed to promote higher temperature difference [25]. For Zhundong lignite used in this work, its carbonization degree was comparable to that of Kosovo lignite, and its size distribution was comparable to that of south African coal. Accordingly, the temperature on char particle during the combustion/gasification process of Zhundong is expected to exceed the set temperature by ca. 200 °C, with the estimated amount of liquid phase to be 22.54%. This might be another reason for bed particle agglomeration and bed defluidisation.

4. Conclusion

This work experimentally investigated the effect of temperature and atmosphere on quartz particle agglomeration during ZD lignite was utilized in a lab-scale fluidized bed, aiming to comprehending the role of char on quartz particle agglomeration. Results show that agglomeration of quartz particles in oxidising atmosphere did not occur at 700°C but incurred at 800-900 °C due to the formation of Na silicates bridging the bed particles. This highlights the effect of temperature and Na in initiating particle agglomeration. In gasification atmospheres, de-fluidisation of the bed occurred in advance in comparison to the case in oxidising atmosphere. In particular concern, char particles with molten ash were found to be the main precursor in initiating agglomeration. This is also proved by separate experiments sending either Na2CO3-doped coal particles or coal ash. FactSage calculation revealed that more slag-liquid phase are formed at higher temperatures, confirming the presence of low melting-point Na6Fe(SO4)4 and Na2Si4O9 in initiating agglomeration. This would provide a few strategies such as reducing bed temperature and avoiding local deflagration to mitigate agglomeration of bed particles in CFB burning high alkali fuel.

Acknowledgment

References

[1] Yue G, Cai R, Lu J, Zhang H. From a CFB reactor to a CFB boiler – The review of R&D progress of CFB coal combustion technology in China. Powder Technology. 2017;316:18-28.

[2] Zhang H, Lyu J, Yue G. A review on research and development of CFB combustion technology in China. Powder Technology. 2023;414.

[3] Scala F. Particle agglomeration during fluidized bed combustion: Mechanisms, early detection and possible countermeasures. Fuel Processing Technology. 2018;171:31-8.

[4] Long X, Li J, Wu Q, Lu X, Zhang Y, Li D, et al. Inhibiting agglomeration of bed particles in CFB burning high-alkali fuel: Experiment, mechanisms and criteria for recirculating bottom ash or selecting alternative bed materials. Energy. 2024;289.

[5] Bartels M, Lin W, Nijenhuis J, Kapteijn F, van Ommen JR. Agglomeration in fluidized beds at high temperatures: Mechanisms, detection and prevention. Progress in Energy and Combustion Science. 2008;34(5):633-66.

[6] Niu Y, Tan H, Hui Se. Ash-related issues during biomass combustion: Alkali-induced slagging, silicate melt-induced slagging (ash fusion), agglomeration, corrosion, ash utilization, and related countermeasures. Progress in Energy and Combustion Science. 2016;52:1-61.

[7] Long X, Li J, Lu X, Zhang K, Zhang D. An experimental investigation into the effect of sodium salts on quartz particle agglomeration and bed defluidisation in a bubbling fluidised bed. Powder Technology. 2023;426.

[8] Chaivatamaset P, Sricharoon P, Tia S. Bed agglomeration characteristics of palm shell and corncob combustion in fluidized bed. Applied Thermal Engineering. 2011;31(14-15):2916-27.

[9] Lin W, Dam-Johansen K, Frandsen F. Agglomeration in bio-fuel fired fluidized bed combustors. Chemical Engineering Journal. 2003;96(1-3):171-85.

[10] Scala F, Chirone R. Characterization and early detection of bed agglomeration during the fluidized bed combustion of olive husk. Energy & Fuels. 2006;20(1):120-32.

[11] Ohman M, Nordin A, Skrifvars BJ, Backman R, Hupa M. Bed agglomeration characteristics during fluidized bed combustion of biomass fuels. Energy & Fuels. 2000;14(1):169-78.

[12] Ma J, Liu D, Chen Z, Chen X. Agglomeration characteristics during fluidized bed combustion of salty wastewater. Powder Technology. 2014;253:537-47.

[13] He Z, Saw WL, van Eyk PJ, Nathan GJ, Ashman PJ. Interactions between Quartz Sand and Wood Doped with either K or Na Salts under Steam Gasification and Combustion Atmospheres. Industrial & Engineering Chemistry Research. 2020;59(4):1712-22.

[14] Piotrowska P, Grimm A, Skoglund N, Boman C, Öhman M, Zevenhoven M, et al. Fluidized-Bed Combustion of Mixtures of Rapeseed Cake and Bark: The Resulting Bed Agglomeration Characteristics. Energy & Fuels. 2012;26(4):2028-37.

[15] Qi X, Song G, Yang S, Yang Z, Lyu Q. Exploration of effective bed material for use as slagging/agglomeration preventatives in circulating fluidized bed gasification of high-sodium lignite. Fuel. 2018;217:577-86.

[16] Faust R, Sattari M, Maric J, Seemann M, Knutsson P. Microscopic investigation of layer growth during olivine bed material aging during indirect gasification of biomass. Fuel. 2020;266.

[17] Kirnbauer F, Hofbauer H. Investigations on bed material changes in a dual fluidized bed steam gasification plant in Güssing, Austria. Energy & Fuels. 2011;25(8):3793-8.

[18] Li J, Long X, Zhu H, Liu Z, Lu X, Zhang D. Investigation into the fusibility of biomass ashes and their mineral phase transformations at elevated temperatures by using the HT-XRD technique. Biomass and Bioenergy. 2023;173.

[19] Liu Z, Li J, Long X, Lu X. Mechanisms and characteristics of ash layer formation on bed particles during circulating fluidized bed combustion of Zhundong lignite. Energy. 2022;245.

[20] Sevonius C, Yrjas P, Lindberg D, Hupa L. Impact of sodium salts on agglomeration in a laboratory fluidized bed. Fuel. 2019;245:305-15.

[21] Vassilev SV, Baxter D, Vassileva CG. An overview of the behaviour of biomass during combustion: Part II. Ash fusion and ash formation mechanisms of biomass types. Fuel. 2014;117:152-83.

[22] Chi H, Pans MA, Sun C, Liu H. Effectiveness of bed additives in abating agglomeration during biomass air/oxy combustion in a fluidised bed combustor. Renewable Energy. 2022;185:945-58.

[23] Song G, Song W, Qi X, Lu Q. Transformation Characteristics of Sodium of Zhundong Coal Combustion/Gasification in Circulating Fluidized Bed. Energy & Fuels. 2016;30(4):3473-8.

[24] Takuwa T, Mkilaha ISN, Naruse I. Mechanisms of fine particulates formation with alkali metal compounds during coal combustion. Fuel. 2006;85(5-6):671-8.

[25] Bu C, Pallarès D, Chen X, Gómez-Barea A, Liu D, Leckner B, et al. Oxy-fuel combustion of a single fuel particle in a fluidized bed: Char combustion characteristics, an experimental study. Chemical Engineering Journal. 2016;287:649-56.

[26] Shu X, Li J, Zhu M, Liu Z, Lu X, Zhang Z, et al. An experimental investigation into bed particle agglomeration and ash deposition during circulating fluidized bed gasification of Zhundong lignite. Journal of the Energy Institute. 2021;96:192-204.

[27] Li X, Li J, Wu G-G, Bai Z-Q, Li W. Clean and efficient utilization of sodium-rich Zhundong coals in China: Behaviors of sodium species during thermal conversion processes. Fuel. 2018;218:162-73.

[28] Kosminski A, Ross DP, Agnew JB. Reactions between sodium and silica during gasification of a low-rank coal. Fuel Processing Technology. 2006;87(12):1037-49.

[29] Manovic V, Komatina M, Oka S. Modeling the temperature in coal char particle during fluidized bed combustion. Fuel. 2008;87(6):905-14.

[30] Gatternig B, Karl J. Investigations on the mechanisms of ash-induced agglomeration in fluidized-bed combustion of biomass. Energy & Fuels. 2015;29(2):931-41.

[31] Olofsson G, Ye ZC, Bjerle I, Andersson A. Bed agglomeration problems in fluidized-bed biomass combustion. Industrial & Engineering Chemistry Research. 2002;41(12):2888-94.

[32] Chirone R, Miccio F, Scala F. Mechanism and prediction of bed agglomeration during fluidized bed combustion of a biomass fuel: Effect of the reactor scale. Chemical Engineering Journal. 2006;123(3):71-80.

[33] Li D, Ahn S, Kim R-G, Li J, Jung S, Jeon C. Formation of agglomerates with core–shell structure in a large-scale CFB boiler. Fuel. 2023;332.

BIOMASS AND WASTE VALORIZATION
VIA ADVANCED DUAL FLUIDIZED BED GASIFICATION

Miriam Huber[1,2,3], Florian Benedikt[2*], Daniel Hochstöger[1,3], Katharina Fürsatz[1,4], Matthias Binder[1,3], Matthias Kuba[1], Christoph Pfeifer[2], Tobias Pröll[2], Thomas Karl Hannl[1,2]

1 BEST - Bioenergy and Sustainable Technologies GmbH, Inffeldgasse 21b, A-8010 Graz

2 University of Natural Sciences and Life Sciences, Vienna (BOKU), Institute of Chemical and Energy Engineering, Muthgasse 107/I, A-1180 Vienna

3 Institute of Chemical, Environmental and Bioscience Engineering, TU Wien, Getreidemarkt 9/166, A-1060, Vienna

4 Thermochemical Energy Conversion Laboratory, Department of Applied Physics and Electronics, Umeå University, SE-901 87 Umeå

*E-Mail: florian.benedikt@boku.ac.at

Abstract

The coupling of biomass and waste gasification with downstream synthesis processing is widely acknowledged as key technology for a sustainable energy transition in the future. Therefore, the process units that have been well-developed for woody biomass such as dual fluidized bed gasification (DFB) and Fischer-Tropsch (FT) synthesis are further developed towards utilization of alternative feedstocks such as waste assortments and agricultural residues. This extended focus comes with additional operational challenges regarding the fluidized bed reactor design related to ash-rich fuels and fuels with high shares of volatiles. Due to a wide range of operational risks and challenges, the main focus of scientific investigations relates to aspects and operating conditions such as tar formation and conversion, evolution of inorganic components from varying ash compositions and key parameters regarding DFB processes e.g. fluidization regimes and control of the bed material circulation.

A research facility to investigate coupled DFB and synthesis processing in demo-scale has been erected and commissioned as part of the Syngas Platform Vienna in recent years. The facility comprises a 1 MW advanced DFB reactor based on the design developed at TU Wien, where increased performance parameters e.g. cold gas efficiency and in-situ tar conversion could be observed. The parametric and analytical setup at the Syngas Platform Vienna allows for the investigation of a wide range of different biogenic and waste feedstocks and for determining the functionality of process subunits such as the countercurrent column in the gasification reactor and the product gas cleaning with regards to scale-up and long-term experimental campaigns. In combination with a 250 kW FT-synthesis pilot plant and other downstream synthesis units, comprehensive research evaluating full process chains from feedstock to final product is conducted. Furthermore, partial flows of the product gas are used in lab-scale facilities to investigate and develop advanced procedures for gas cleaning, biological gas upgrading, and gas upgrading/separation.

1. Introduction

The recent advances in the field of energy and resource conversion research have intensified their focus on the utilization of biomass and waste as feedstock for the generation of sustainable energy carriers. The need for these efforts arises from the needs to tackle some of the most essential challenges we face as humanity, i.e., the ongoing climate change, depletion of critical resources, and the urge to elevate living standards of the vast communities in the global developing countries. Energy conversion and resource recovery based on biomass and waste feedstock could enable the valorization of sustainable bioresources and

inevitable wastes to promote the transition out of the presently fossil-based energy system and provide energy carriers and resources where these feedstocks accrue [1,2].

Classifying all kinds of biomass, agricultural residues, and wastes was shown to be a rather complicated matter since it is difficult to generalize their feedstock properties into groups based on the key characteristics, e.g., heating value and ash composition [3]. However, these characteristics are essential for the design of a suitable conversion process to address potential risks related to the composition of the derived products and to the process operability [4,5]. A facility for the reliable conversion of different feedstocks into product gas suitable for subsequent use as energy carrier or synthesis reactant must be capable of providing a high degree of flexibility in its conversion process as well as in the gas conditioning pathway.

Dual fluidized bed (DFB) steam gasification represents a promising option for this task. Its functionality provides the advantages of autothermic process control through the combination of an endothermic gasification reactor and an exothermic combustion reactor, enhanced contact of gas and solids (both of which due to the use of a granular bed material), and an overall lower conversion temperature in a more homogenous temperature field compared to reference conversion processes [6]. The sum of benefits suggests that common issues linked to the combustion and gasification of biogenic residues and waste feedstocks such as tar formation, ash melting, and noxious emissions can be prevented in DFB gasification. Furthermore, the spatial separation of combustion and gasification processing enables the production of a gasification product gas of higher energetic and chemical value, facilitating subsequent processes such as syntheses and gas purification, and a flue gas exiting the combustion reactor with comparably low emissions [7].

DFB gasification systems have been developed scientifically by several different research institutions and commercialized for the conversion of woody biomass feedstocks in CHP operation. Additionally, subsequent processing such as Fischer-Tropsch synthesis (FTS), methanation, and hydrogen production were investigated in pilot-scale setups using the product gas from DFB gasification [8]. However, as the economics of plants solely using woody biomass represent a fragile basis for the commercialization of the technology, increasing efforts have been made to use DFB gasification for the valorization of biogenic and industrial wastes. Scientific research up to 100 kW gave a detailed prospect for the opportunities and challenges when using a wide range of different feedstocks. The aim of this contribution is to present the status quo of knowledge and development of DFB gasification systems for waste valorization that motivated the erection of the 1 MW demo-scale plant at the Syngas Platform Vienna.

2. Methodology

2.1. DFB Steam Gasification

The working principle of dual fluidized bed (DFB) steam gasification builds on the gas-impermeable but solid-permeable interconnection of a gasification reactor (GR) and a combustion reactor (CR) as shown in Figure 1. In this setup, a certain fuel is inserted into the GR, where the endothermic process of gasification takes place. Residual char and bed material are transported into the CR, where the exothermic combustion of the char releases heat to be taken up by the bed material. The recycling of the bed material into the GR allows for an overall autothermic operation of the DFB steam gasification process [9]. The reactor interconnection is implemented by chute or loop seal installations between the reactors. While the lower connection transports the bed material from the GR, commonly operated as bubbling fluidized bed (BFB), to the CR, the upper connection takes advantage of the circulating fluidized regime in the CR to transport coarse ash and bed material separated by a cyclone back to the GR. Additional installations in the reactors that have been researched and developed in recent years, especially by a research group at TU Wien, include a countercurrent flow column (CCC), where recirculated bed material enters the GR in a column comprising constrictions for enhanced gas-solid contact, and loop seal (LS) installations as gas-tight, syphon-like reactor interconnection units for the solids transport [4]. The developed process was named advanced dual fluidized bed (aDFB) gasification.
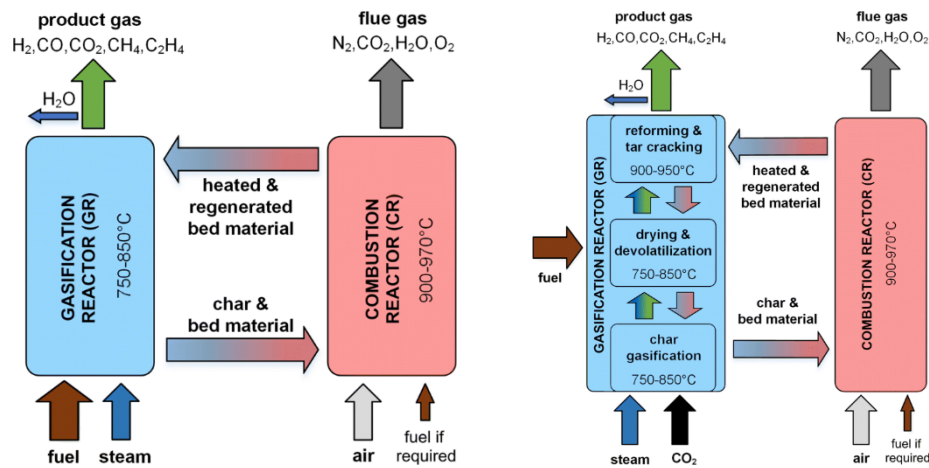
Figure 1: Scheme of the basic principle of the (left) DFB steam gasification process and the (right) aDFB gasification process [6].

2.2. 1 MW demo-scale plant

The 1 MW demo-scale aDFB gasification system erected and situated at the industrial site of Wien Energie in Simmering, Vienna is depicted as process flow sheet in Figure 2. The visualization includes the entire process chain from the DFB gasification and combustion reactors to the coarse gas cleaning units. The reactor design was based on the 100 kW aDFB reactor at TU Wien and comprises some of its functional installations such as the CCC and radiation coolers. In the following, the individual operation units in the separated lines of product and flue gas of the 1 MW aDFB demo-scale plant are described in greater detail.
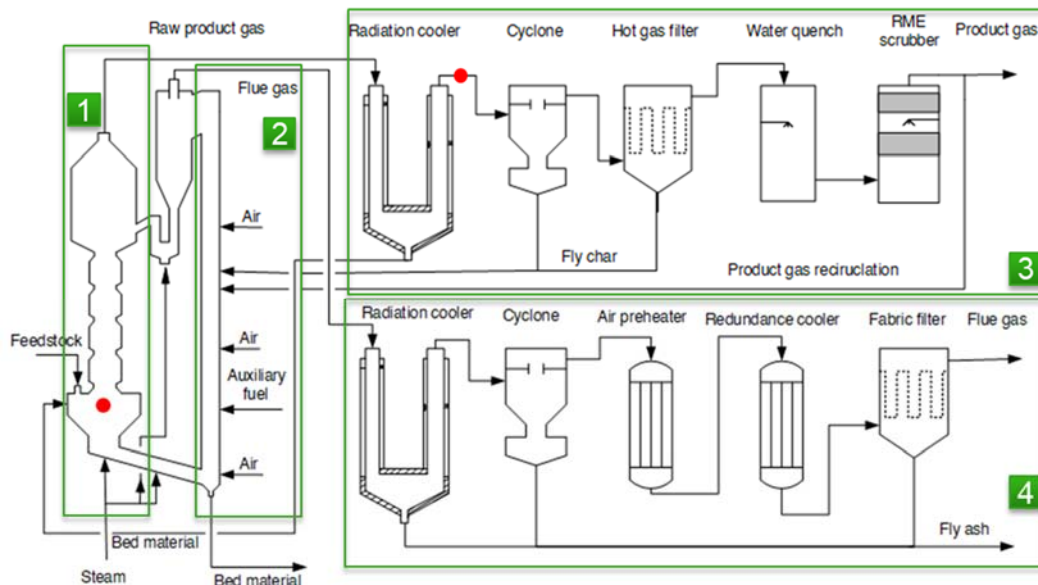
Figure 2: Simplified process flow sheet of the DFB steam gasification system. Adapted from [10].

The gasification reactor (GR, "1" in Figure 2) comprises a BFB section, with a cross-sectional area of 0.31 m² in the bottom and a freeboard with a maximum cross-section of 1.48 m², and a CCC section on top with 5 built-in constrictions (area constriction from 0.17 to 0.06 m²) for enhanced particle hold-up and gas-solid contact over a height of 4.8 m. The reactor is about 11 m high in total and fueled by on-bed feeding of the feedstock and steam nozzles supply the fluidization and reaction agent for the process. The combustion reactor (CR, "2" in Figure 2) comprises a CFB column with a bottom area of 0.05 m² and a 0.11 m² main column above, equipped with air supply nozzles in 3 stages of height to control the solids circulation and with auxiliary fuel supply (heating oil, product gas, scrubber emulsion) to control the temperature profile. Both reactors are coated with refractory lining on the inside wall as protective layer for

the steel construction. The lower reactor connection for transporting bed material and fuel char to the CR is realized as chute to handle heterogenous fuel chars and larger impurities such as rocks and nails.

The primary stages of the gas cleaning are identical for product gas from the GR (PGC, "3" in Figure 2) and flue gas from the CR (FGC, "4" in Figure 2). Radiation coolers are employed for initial cooling down to 450-550 °C and gravity separation of coarse solids in the gas streams followed by cyclones. The thermal energy in the flue gas is then used for preheating the CR input air, thereby being cooled, and passed through a bag filter. The solid residues of these cleaning stages are then gathered cumulatively in flow bin containers. For the product gas, the steps after cyclone separation include a hot gas ceramic candle filter and a two-stage scrubbing unit with an initial water quench followed by a biodiesel scrubber for separation of condensable hydrocarbons, water, and therein soluble gas impurities. The solid residues, i.e., fly char, dust, and bed material, as well as the exhausted biodiesel emulsion are recirculated into the CR.

The process media used in the 1 MW plant comprise several gaseous agents (air, N_2, steam), biodiesel, and heating oil as liquids, and a broad variety of solids when it comes to the options of possible fuels and bed materials. The reactor is designed to be capable of dealing with a wide range of fuel properties as found in alternative biomass, biogenic residues, and waste materials such as the water content, the ash content, the ash composition, and the share of volatile matter. Olivine is mostly used as bed material due to its capability of forming Ca-enriched layers beneficial for the kinetics of essential gasification reactions such as the water-gas-shift. Ca needed for this layer formation can be derived directly from the fuel conversion process or supplied by Ca-additives.

2.3. Process analytics

In-situ and ex-situ process analytics are employed at the Syngas Platform Vienna to determine the metrics and key performance indicators (KPI) of the aDFB gasification process. Naturally, the input quantities and qualities for the gaseous, liquid, and solid process media are measured and controlled. Furthermore, the process is monitored continuously by temperature and pressure measurements distributed over the height of both reactors and along the gas cleaning pathways of product and flue gas. The energetic key figures of the process are determined by pre-process analysis of the fuel, e.g., heating value and ash composition, and calibrated feeding systems. Orifice plates and online gas measurements are installed for determining the gas quantities and qualities. KPI's defining the process that are monitored as derivative of the mentioned analytics are the steam to fuel ratio, the product gas yield, the water conversion, and the cold gas efficiency.

Ex-situ analyses include the sampling of entities during the aDFB operation, which are then analyzed in external facilities. Entities that can be sampled are the product gas, from the gasification process at different stages of conversion and gas cleaning from the freeboard in the gasifier to the post-scrubber gas, and solid residues as they accrue in different parts of the system. The product gas properties analyses can be categorized into main components analysis, i.e. CO_2, CO, H_2, CH_4, and impurities analysis, i.e., tar hydrocarbons and inorganics such as NH_3. The solid residues, mainly consisting of ash, char, and bed material, can be analyzed for their chemical composition, mineralogical characteristics, and physical morphology.

3. Exemplary Results & Discussion

An evaluation of the process performance of the Syngas Platform Vienna is exemplified by analytical determination of the tar reforming capabilities of the CCC. For this purpose, the results of the impurities analysis for tar at two different positions in the process are considered: the gas in the freeboard section of the gasifier and after the radiation cooler, highlighted with red dots in Figure 2. The sample extraction and measurement were conducted according to the requirements of the Tar Protocol with minor adaptions to the specifics of the DFB gasification process including a sampling set-up as shown in Figure 3.
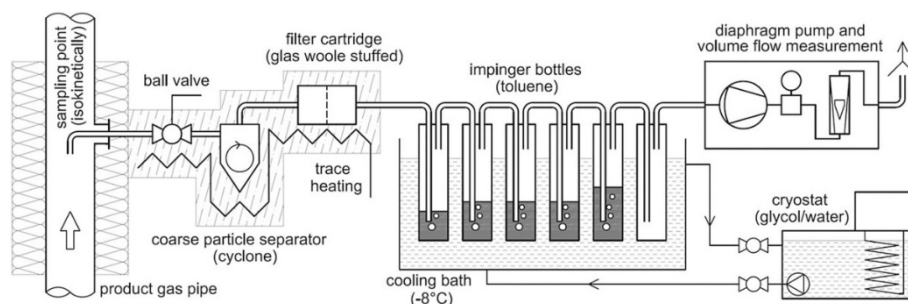
Figure 3: Overview scheme of the tar sampling setup. Adapted from [11].

As the reactor design promotes the applications of alternative and waste feedstocks, the product gas impurities of bark gasification are compared to the benchmark feedstock wood chips. The gravimetric and GCMS tar concentrations for both sampling points are presented in Figure 4. For both woody biomasses, 1 MW of feedstock input was supplied and led to similar gravimetric tar levels in the freeboard. In addition, the GCMS tar content is similar at the respective process stage. After the CCC, GCMS tars are reduced to about half of the initial concentration, i.e., from 30 g/Nm^3_{db} to 15 g/Nm^3_{db} GCMS tar content for wood chips and bark. Hence, the CCC significantly decreases the tar concentration for the applied feedstocks, corresponding to the findings of [4,12,13]. The effect of product gas dilution contributes to this outcome, since the promotion of gasification reactions in the CCC increases the total product gas volume.
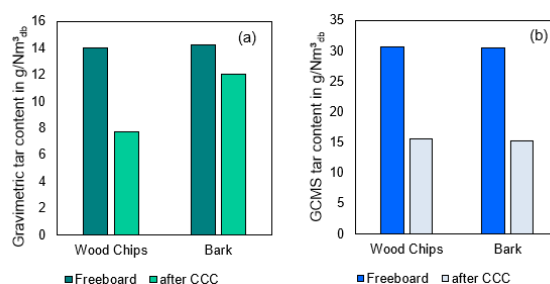
Figure 4: Gravimetric tar (a) content and GCMS (b) tar content of wood chips and bark in the freeboard and after the CCC

A detailed evaluation of measured GCMS tar species showed different behavior of individual tar species. While secondary tars, which are the product of decomposition of the primary tars formed during feedstock devolatilization [14], decrease consistently to below 50 % of their initial concentration (1h-indene) or a non- detectable amount (phenol) after the CCC, a divergent behavior occurred for higher molecular PAH tar i.e. naphthalene and pyrene. An increase occurred for every sample, leading to the conclusion of tar reformation and recombination reactions appearing in the CCC, induced by the increased residence time and temperature [10]. However, this increase of heavy tars is beneficial for the subsequent coarse gas cleaning process, as their separation efficiency in the scrubber units is higher compared to the lighter tar species [15].

4. Conclusions & Outlook

Initial investigations at the Syngas Platform Vienna demonstrated the viability of converting waste and biomass residues in a 1 MW aDFB steam gasification processes. The metrics examined in the research facility allow for determination of key performance indicators (KPI) and of the functionality of process subunits such as the implemented countercurrent column (CCC) and the gas cleaning facilities. The exemplary evaluation regarding tar reforming in the CCC shows that tar concentrations could be reduced at the cost of being subject to recombination reactions increasing the share of heavy tars.

Future research will target the gasification of a variety of biomass residues to determine suitable process parameters for industrial-scale applications. The scientific focus shall include

the entire chain of biomass and waste valorization from the ecological and techno-economic assessment of possible feedstocks to the array of products of potential downstream syntheses.

Acknowledgment

References

[1]   Rezania S, Oryani B, Nasrollahi VR, Darajeh N, Lotfi Ghahroud M, Mehranzamir K. Review on Waste-to-Energy Approaches toward a Circular Economy in Developed and Developing Countries. Processes 2023;11:2566. https://doi.org/10.3390/pr11092566.

[2]   Santos SM, Assis AC, Gomes L, Nobre C, Brito P. Waste Gasification Technologies: A Brief Overview. Waste 2022;1:140–65. https://doi.org/10.3390/waste1010011.

[3]   TNO Biobased and Circular Technologies. Phyllis2, database for (treated) biomass, algae, feedstocks for biogas production and biochar, 2024. https://phyllis.nl/.

[4]   Benedikt F, Schmid JC, Fuchs J, Mauerhofer AM, Müller S, Hofbauer H. Fuel flexible gasification with an advanced 100 kW dual fluidized bed steam gasification pilot plant. Energy 2018;164:329–43. https://doi.org/10.1016/j.energy.2018.08.146.

[5]   Hupa M. Ash-Related Issues in Fluidized-Bed Combustion of Biomasses: Recent Research Highlights. Energy Fuels 2012;26:4–14. https://doi.org/10.1021/ef201169k.

[6]   Schmid JC, Benedikt F, Fuchs J, Mauerhofer AM, Müller S, Hofbauer H. Syngas for biorefineries from thermochemical gasification of lignocellulosic fuels and residues—5 years' experience with an advanced dual fluidized bed gasifier design. Biomass Convers Biorefinery 2021;11:2405–42. https://doi.org/10.1007/s13399-019-00486-2.

[7]   Benedikt F. Fuel flexible advanced dual fluidized bed steam gasification. 2020. https://doi.org/10.34726/HSS.2020.39988.

[8]   Rauch R, Hrbek J, Hofbauer H. Biomass gasification for synthesis gas production and applications of the syngas. WIREs Energy Environ 2014;3:343–62. https://doi.org/10.1002/wene.97.

[9]   Hanchate N, Ramani S, Mathpati CS, Dalvi VH. Biomass gasification using dual fluidized bed gasification systems: A review. J Clean Prod 2021;280:123148. https://doi.org/10.1016/j.jclepro.2020.123148.

[10]   Huber M, Benedikt F, Karel T, Binder M, Hochstöger D, Egger A, et al. Tar conversion and recombination in steam gasification of biogenic residues: The influence of a countercurrent flow column in pilot- and demonstration-scale. Fuel 2024;364:131068. https://doi.org/10.1016/j.fuel.2024.131068.

[11]   Wolfesberger-Schwabl U, Aigner I, Hofbauer H. Mechanism of Tar Generation during Fluidized Bed Gasification and Low Temperature Pyrolysis. Ind Eng Chem Res 2012;51:13001–7. https://doi.org/10.1021/ie300827d.

[12]   Mauerhofer AM, Schmid JC, Benedikt F, Fuchs J, Müller S, Hofbauer H. Dual fluidized bed steam gasification: Change of product gas quality along the reactor height. Energy 2019;173:1256–72. https://doi.org/10.1016/j.energy.2019.02.025.

[13]   Kolbitsch M. First fuel tests at a novel 100 kWth dual fluidized bed steam gasification pilot plant. Technische Universität Wien, 2016.

[14]   Milne TA, Evans RJ, Abatzaglou N. Biomass Gasifier "'Tars'": Their Nature, Formation, and Conversion. 1998. https://doi.org/10.2172/3726.

[15]   Thunman H, Seemann M, Berdugo Vilches T, Maric J, Pallares D, Ström H, et al. Advanced biofuel production via gasification – lessons learned from 200 man-years of research activity with Chalmers' research gasifier and the GoBiGas demonstration plant. Energy Sci Eng 2018;6:6–34. https://doi.org/10.1002/ese3.188.

SURFACE ADJUSTMENT OF BIOCHAR BY CO_2 GASIFICATION UNDER FIXED AND FLUIDIZED BED CONDITIONS

Florian J. Müller[1]*, Camila Rodríguez M.[1], Eugen Schöfbänker[1], Franz Winter[1]

Technische Universität Wien, Institute of Chemical, Environmental and Bioscience Engineering. Getreidemarkt 9/166, 1060 Wien, Austria

*E-mail: florian.johann.mueller@tuwien.ac.at

Abstract

This paper explores how torrefaction and CO_2 gasification can be combined to create biochar with a high surface area from *Pinus sylvestris* wood pellets. Raw pellets were pretreated in a torrefaction process at 300 °C before conducting biomass CO_2 gasification experiments under various operating conditions. Gasification was performed under fixed and fluidized bed conditions at temperatures between 800 to 900 °C and biomass residence times of 15 or 25 minutes. Biomass burn-off and BET surface areas were analyzed individually and combined to determine the surface yield per raw *Pinus sylvestris* feedstock. Higher temperatures, higher biomass residence times, and fixed bed conditions increased burn-off and BET surface areas up to 798 m²/g. Surface yield per raw biomass was instead found to be the highest from fluidized bed experiments, which yielded around 100 m²/$g_{feedstock}$ after gasification at 850 to 900 °C.

1. Introduction

Biomass CO_2 gasification is a carbon capture and utilization technology producing CO-rich gas [1]. Potential applications of such gas are for iron ore reduction in a direct reduced ironmaking shaft furnace [2] or, if sustainable hydrogen is added, as a synthesis gas for producing renewable chemicals and energy carriers [3]. If no oxygen is fed to the gasification reaction, biomass is often not fully converted, and the residual char is frequently used for energy generation [5]. The specific surface areas of typical biochars (from 0.1 to 500 m²/g) make them suited for applications like soil amendment [7] and to restore degraded sites [8]. Activated biochars with high specific surface areas of 200 to 2500 m²/g can be produced from various biomass feedstocks by thermochemical treatment and can be used for higher-value applications like catalysis, electrochemistry, or energy storage [9]. An ongoing research project on phytoremediation at TU Wien investigates the encapsulation of heavy metals in biochar. In this project, one investigated process route is a multi-stage process consisting of a torrefaction process at mild temperatures as pretreatment and a CO_2 gasification step for surface activation at high temperatures. This paper investigates the influence of CO_2 gasification operating conditions on the surface characteristics of biochar.

1.1. State of the art on surface adjustment by gasification

The manufacturing process of activated biochar generally consists of a carbonization step, creating a biochar structure with pores that are often blocked by tar compounds, and an activation step, during which these blockages are removed and the pores are widened [10]. This activation step can be realized by adding chemicals before thermal or physical activation through gasification, where oxidizing gases penetrate the structure at temperatures between 700 and 1000 °C [11]. The characteristics of the final product depend mainly on feedstock composition and process conditions such as heating rate, temperature, and residence time [12].

CO_2 and H_2O are the most common gasification agents for producing high surface area biochars because their endothermic reactions can be controlled well [13]. Chang et al. reported on the gasification of corn cob agro-waste that at 900 °C higher Brunauer-Emmett-Teller (BET) surface areas and total pore volumes were found with CO_2 as gasification agent

compared to steam (1705 vs. 1063 m²/g; 0.884 vs. 0.536 cm³/g) [14]. The opposite trend was reported at 800 °C (670 vs. 998 m²/g; 0.342 vs. 0.511 cm³/g), which can be attributed to the higher reaction rate for the steam-carbon reaction with H_2O compared to the Boudouard reaction with CO_2 [13]. Pallarés et al. reported a similar trend reversion when they studied the activation of barley straw after carbonization via pyrolysis at 500 °C [11]. BET surface area and pore volume were higher from CO_2 gasification at 800 °C (789 vs. 534 m²/g; 0.3495 vs. 0.2576 cm³/g), but higher surface area was found for steam gasification at 700 °C (211 vs. 552 m²/g). Additionally, Ngernyen et al. reported a linear increase in burn-off values and BET surface area with increasing activation time between 60 and 300 minutes for the CO_2 activation of Eucalyptus and Wattle wood [15].

Based on the presented literature, activation time and temperature were selected to investigate *Pinus sylvestris* pellets' surface evolution during CO_2 gasification. Additionally, the experiments were performed under fixed and fluidized bed conditions to examine if this would lead to different results, e.g., from differences in heat transfer.

2. Materials and methods

2.1. Experimental design

Pellets with a diameter of approximately 4 mm and varying lengths between 5 to 20 mm were produced from a mixture of *Pinus sylvestris* needles and branches (Table 1). The pellets were subjected to a pre-treatment phase by torrefaction and further activation by gasification. The torrefaction process was performed under an N_2 atmosphere and fixed bed conditions in a separate reactor with an inner diameter of 53 mm. This larger reactor was used because it enabled the production of torrefied intermediate products for all gasification experiments in a single batch. The pellets were kept at 300 °C for 45 minutes under a nitrogen flow of 0.8 Nm³/h. Quartz sand with a density of 2650 kg/m³ and a particle mean diameter determined by sieving analysis at 370 µm was used as bed material during fluidized bed experiments. CO_2 and N_2 from gas bottles were used as gaseous feed.

Table 1: Elemental analysis of raw Pinus sylvestris pellets

	Water content		C	H	N	S	O
wt%	4.6		50.0	6.9	1.1	0.7	41.3

Torrefied biochar was activated by gasification with CO_2 in a stainless-steel batch reactor with an inner diameter of 38 mm (Figure 1a). Two external half-shells electrically heated the reactor (Figure 1b). Temperatures were measured by thermocouples type K. A gas mixture of 1.6 NL/min N_2 and 0.4 NL/min CO_2 was supplied to the reactor and controlled by mass flow controllers for all experiments. Gas entered the reactor through an empty preheating section before a Quartz glass frit distributed the gas evenly into the upper section, where the activation process was carried out (reaction zone). Fuel was inserted into the reaction zone batch-wise. It was placed into a metal cage with a mesh size of approximately 500 µm, which was used for extracting the activated biochar after the experiment. Fuel was added after the reactor had reached its desired temperature.
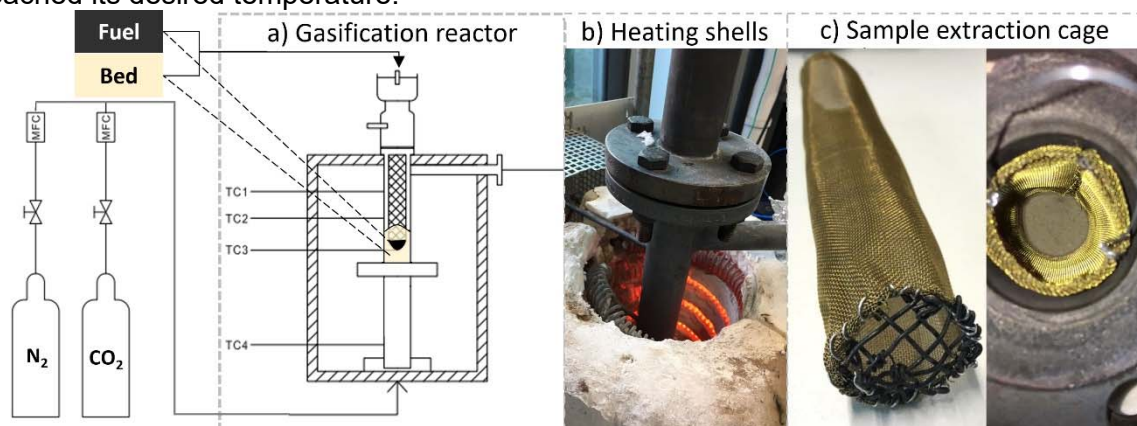
Figure 1:a) Gasification reactor schematic layout, b) Reactor with heating, c) Sample extraction cage

2

For fluidized bed experiments, fuel was submerged in Quartz sand. Fluidization equations proposed by Grace [16], Wen, and Yu [17] were used to calculate that the selected feed gas flow rate of 2.0 NL/min resulted in around 5 times the minimum fluidization velocity. Therefore, the fluidized bed conditions were achieved by forming a bubbling fluidized bed from Quartz sand particles around the fuel in the sample extraction cage (Figure 1c).

A four-step procedure was followed after the activation time to stop reactions and freeze the surface state of biochar: 1. The electrical heating was turned off, 2. CO_2 was no longer fed to the reactor (only N_2), 3. 50 mL of Quartz sand at room temperature was fed through the ball valve lock to lower the temperature in the reactor, and 4. A part of the insulation was removed to cool down the biochar faster. After the reactor had cooled down, the activated biochar samples were removed by carefully lifting the cage.

A list of the selected experimental conditions for activation is given in Table 2.

Table 2: Investigated gasification conditions

Name	Fluidization		Temperature			Activation time	
	Fluidized bed	Fixed bed	800°C	850°C	900°C	15 min	25 min
E1		X	X			X	
E2		X		X		X	
E3		X			X	X	
E4		X	X				X
E5		X		X			X
E6		X			X		X
E7	X		X			X	
E8	X			X		X	
E9	X				X	X	
E10	X		X				X
E11	X			X			X
E12	X				X		X

2.2. Sample characterization

The weight loss of the solid samples during processing is described by the burn-off value (b), which is formed from the weight before the conversion step (w_0) and the weight of the final product (w_f); see Eq. 1.

$$b = \frac{w_0 - w_f}{w_0}$$

Eq. 1

Nitrogen adsorption isotherms for surface characterization were measured using an ASAP 2020 Plus adsorption analyzer by Micromeritics for the torrefied biochar and a Belsorp Max G by Microtrac Retsch for samples after activation. These measurements were also used to determine the total pore volume. Before measurement, the activated samples were degassed under vacuum in a Belprep Vac degassing station for 24 hours at 150°C, which is suggested as degassing temperature in the European Biochar Certification [18]. The torrefied sample was degassed at 200 °C for 4 hours. Isotherm data were used to calculate a specific surface area a_{BET} following the proposed method by Brunauer-Emmett-Teller (BET) [19]. Guidelines for applying this method to microporous materials, as given in Annex C of DIN ISO 9277:2014-01, were followed for activated samples. These guidelines were proposed by Rouquerol et al. [20] and are as follows:
- C must be positive
- Application of the BET equation must be limited to the range where the term $V(1-P/P_0)$ continuously increases with P/P_0
- The P/P_0 value corresponding to the monolayer volume should be within the selected BET range.

Two further criteria were followed to select the appropriate range for multi-point BET in this analyzer:
- The first point of the fit must be at least $1 \cdot 10^{-3}$ Pa following pressure measurement sensitivity.

3

- The last point of the fit is chosen to achieve the highest correlation coefficient between data and fit.

Furthermore, light microscopy using a Keyence VHX-S650E and a VH-ZST dual zoom objective and scanning electron microscopy (SEM) were used to evaluate surface adjustments. Samples were sputtered with gold before analysis in a COXEM EM-30 Plus microscope.

Increasing the surface area further and further might not bring additional benefits for some applications, which might, for example, only need 500 m²/g to reach process demands. In such cases, optimal operating conditions to produce biochar could be identified by considering both a_{BET} and b. A surface yield parameter (y) is proposed that relates the final biochar surface area a_{BET} to the mass of *Pinus sylvestris* feedstock used for producing this biochar (Eq. 2). Higher y values indicate that higher total surface area is produced per mass of raw feedstock.

$$y = a_{BET} \cdot \left(1 - b_{torrefaction}\right) \cdot \left(1 - b_{gasification}\right) \qquad \text{Eq. 2}$$

3. Results and discussion

3.1. Biomass conversion

A burn-off value (b) of 32.64 % was recorded during torrefaction. The torrefied pellets were dark brown and softer in texture compared to the raw pellets, suggesting a slight surface degradation and the presence of tar in the pore structures. Investigations by SEM at various magnifications from x50 to x2000 confirmed that the pore structure remained relatively closed after torrefaction (Figure 2). Small hollows and irregularities were visible in the raw and torrefied samples due to the pelletization process mixing needles and branches. At the process temperature of 300 °C and under constant nitrogen flow, this weight loss was likely caused by drying and the decomposition of hemicellulose [13].
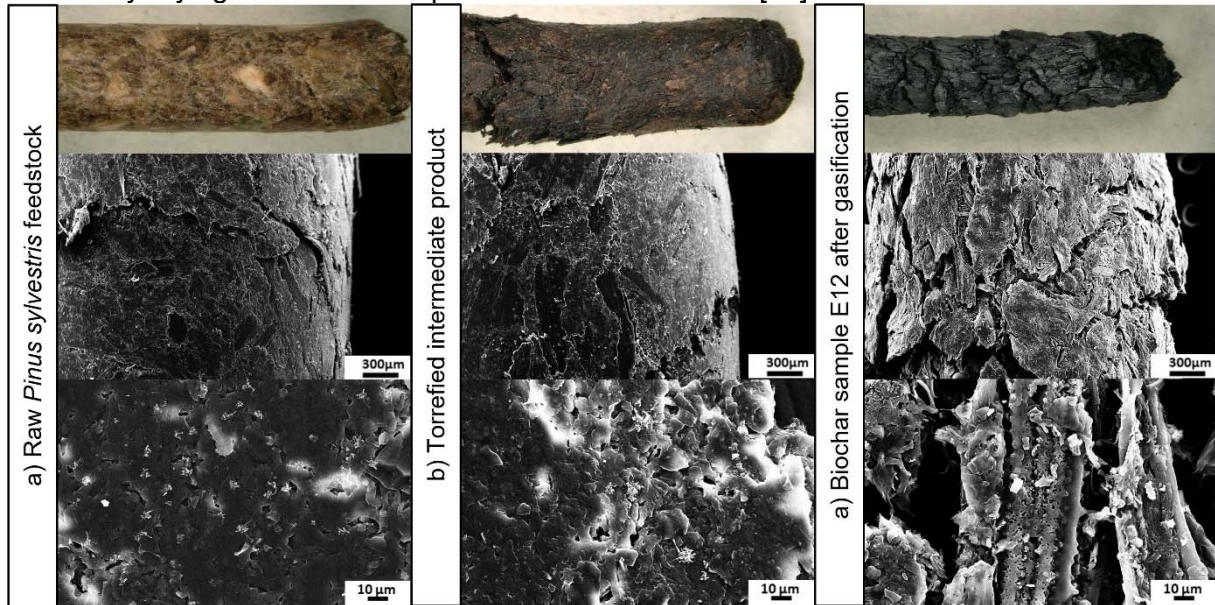
Figure 2: Evolution of Pinus sylvestris pellets during thermal processing investigated by light and scanning electron microscopy (x50, x1000 magnifications).

Significant further weight losses were recorded during gasification with CO_2 (Figure 3). Burn-off was calculated relative to the torrefied intermediate product. Biochar pellets were black and brittle after gasification, and their diameter had decreased by 25 % on average. Morphological examination under light microscopy and SEM revealed a surge in fragmentations and the development of both, narrow and larger pore structures that were not there before gasification. The inner structure showed the presence of channels and hollow areas next to each other, which might be related to solid-gas reactions with CO_2.

4
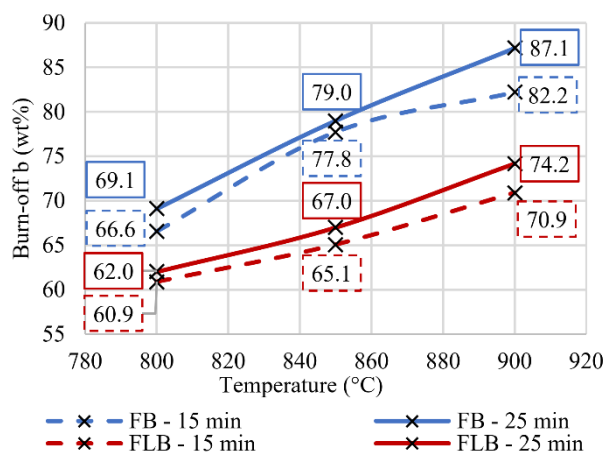
Figure 3: Burn-off during CO$_2$ gasification under various conditions. FB=Fixed bed; FLB=Fluidized bed.

The increase in biochar residence time from 15 to 25 minutes increased burn-off for fluidized bed and fixed beds experiments. Burn-off was also increased at higher temperatures. Devolatilization at high temperatures is a fast process [6], suggesting that the burn-off increase at longer residence times was a result of ongoing gas-solid reactions. Temperatures exceeding 800 °C lead to the pyrolytic decomposition of more stable biomass components [22] and also favor fixed carbon conversion by gas-solid reactions, mainly the Boudouard reaction [1]. Therefore, the increase in burn-off at higher temperatures can be attributed to a mixture of pyrolytic decomposition and reactions with the gasification agent CO$_2$.

Burn-off values across all temperatures and residence times were higher under fixed bed than under fluidized bed conditions. Various factors could influence this result, e.g., an inhibition effect of silicon in the bed material could have lowered the biomass conversion under fluidized bed conditions [1][21]. Another reason could be lower fuel-gas contact times under fluidized bed conditions, due to inconsistent fluidization and effects like gas channeling around the sample cage. Differences in heat transfer from the external heating shell to the thermocouples outside the sample extraction cage and biomass inside the cage could also lead to this result because the cage could have decreased heat transfer from the heating to the sample by hindering radial mixing. As a result, the samples' actual temperature could have been higher under fixed bed than under fluidized bed conditions.

3.2. BET surface

Multi-point fitting data, calculated BET surface areas, and total pore volumes are given in Table 3. Correlation coefficients between isotherm measurement data and selected multi-point fits were at least 0.9981.

Table 3: Surface characterization data from BET surface measurement by N$_2$ adsorption

Name	p/p$_0$		C	Isotherm data points in the fitting range	BET surface area (m²/g)	Total pore volume (cm³/g)
	Low point	High point				
Torref.	1.01E-02	0.07	46	4	0.65	9E-04
E1	1.16E-03	0.23	261	16	201	0.09
E2	1.12E-03	0.20	812	30	387	0.17
E3	1.76E-03	0.05	2902	8	608	0.25
E4	1.07E-03	0.14	1177	9	193	0.09
E5	2.13E-03	0.04	3702	6	498	0.20
E6	1.39E-03	0.05	1913	12	798	0.34
E7	3.28E-03	0.10	645	6	55	0.03
E8	1.10E-03	0.20	796	24	340	0.15
E9	1.03E-03	0.04	3811	8	482	0.20
E10	4.76E-03	0.14	655	9	240	0.11
E11	1.76E-03	0.03	4088	5	451	0.18
E12	1.44E-03	0.04	3472	7	560	0.23

5

Surface areas and total pore volume are orders of magnitude higher for biochar samples after CO_2 gasification. BET surface area and total pore volume increased with higher burn-off values. Samples prepared under fixed bed conditions generally showed higher surface areas and pore volumes than samples prepared under fluidized bed conditions. Both values were increased for samples prepared at higher gasification temperatures and solid residence times. The surface area measured after 25 minutes of fixed bed operation was around 4 times as much as the surface area after treatment at 800 °C under otherwise equivalent conditions, showing that temperature had a high impact.

This indicates two things: First, heat transfer problems under fluidized bed conditions might also explain the differences observed in surface area and pore volume compared to fixed bed conditions. Second, since the difference between 800 and 900 °C significantly impacts the thermodynamic equilibrium and reaction kinetics of the Boudouard reaction in biomass CO_2 gasification [1], these results suggest that surface area growth is largely caused by the Boudouard reaction.

While these results suggest fixed bed conditions, long solid residence times, and high temperatures for producing biochar with a high BET surface area, fixed bed conditions did not yield the highest surface area per mass of raw feedstock. Figure 4 compares the BET surface area results side-by-side with the surface yield. The second metric suggests that the yield of surface area per mass of feedstock was higher from gasification under fluidized bed conditions. Around 100 m²/g$_{feedstock}$ are found for gasification under fluidized bed conditions and at 850 °C or 900 °C. Since the BET surface area measured for these samples was also near or above 500 m²/g, fluidized bed operation seems to have an edge in yield for applications that do not need BET surface areas over 500 m²/g.
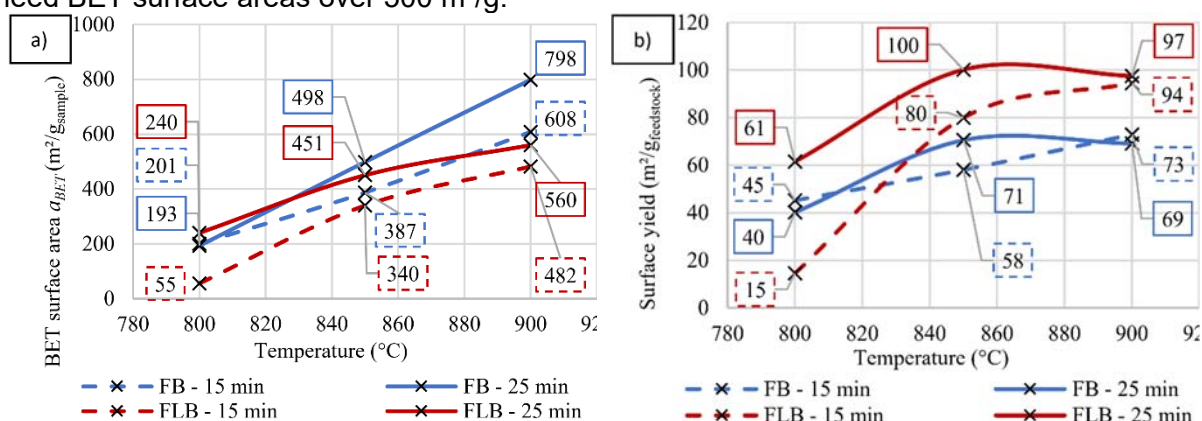
Figure 4: a) BET surface area of biochar, b) Surface yield from raw biomass to biochar.

4. Conclusion

The combination of torrefaction pretreatment and biomass CO_2 gasification produced biochar with a high surface area. CO_2 gasification increased BET surface areas by two to three orders of magnitude compared to the torrefied intermediate product. Higher temperatures and solid residence times lead to higher BET surface areas, burn-off, and surface yields. While fixed bed conditions were used to produce the highest BET surface areas and pore volumes in this work, fluidized bed conditions yielded more total surface area per raw feedstock due to lower burn-off values during gasification. Therefore, fluidized bed gasification should be considered if the biochar meets the application's demands. Further research could help to determine if the observed differences in burn-off are a system-specific result of this experimental setup. Since high temperatures and solid residence times are also favorable for utilizing CO_2 in this process, using biomass CO_2 gasification as a CCU process and for producing high-quality biochar is promising.

Acknowledgment

6

References

[1] F. J. Müller *et al.*, "CO2 conversion to CO by fluidized bed biomass gasification : Analysis of operational parameters," *Journal of CO2 Utilization*, vol. 81, no. March 2024, 2024, doi: 10.1016/j.jcou.2024.102706.

[2] A. Nurdiawati, I. N. Zaini, W. Wei, R. Gyllenram, W. Yang, and P. Samuelsson, "Towards fossil-free steel: Life cycle assessment of biosyngas-based direct reduced iron (DRI) production process," *J Clean Prod*, vol. 393, no. January, p. 136262, 2023, doi: 10.1016/j.jclepro.2023.136262.

[3] Y. H. Chan, S. N. F. Syed Abdul Rahman, H. M. Lahuri, and A. Khalid, "Recent progress on CO-rich syngas production via CO2 gasification of various wastes: A critical review on efficiency, challenges and outlook," *Environmental Pollution*, vol. 278, pp. 1–16, 2021, doi: 10.1016/j.envpol.2021.116843.

[4] A. Lampropoulos *et al.*, "Effect of Olive Kernel thermal treatment (torrefaction vs. slow pyrolysis) on the physicochemical characteristics and the CO2 or H2O gasification performance of as-prepared biochars," *International Journal of Hydrogen Energy*, vol. 46, no. 57. pp. 29126–29141, 2021. doi: 10.1016/j.ijhydene.2020.11.230.

[5] A. M. Mauerhofer *et al.*, "Conversion of CO2 during the DFB biomass gasification process," *Biomass Convers Biorefin*, vol. 11, no. 1, pp. 15–27, 2021, doi: 10.1007/s13399-020-00822-x.

[6] P. Lahijani, Z. A. Zainal, M. Mohammadi, and A. R. Mohamed, "Conversion of the greenhouse gas CO2 to the fuel gas CO via the Boudouard reaction: A review," *Renewable and Sustainable Energy Reviews*, vol. 41, pp. 615–632, 2015, doi: 10.1016/j.rser.2014.08.034.

[7] B. M. Ohsowski, K. Dunfield, J. N. Klironomos, and M. M. Hart, "Plant response to biochar, compost, and mycorrhizal fungal amendments in post-mine sandpits," *Restor Ecol*, vol. 26, no. 1, pp. 63–72, Jan. 2018, doi: 10.1111/rec.12528.

[8] M. Ahmad, S. S. Lee, S. E. Lee, M. I. Al-Wabel, D. C. W. Tsang, and Y. S. Ok, "Biochar-induced changes in soil properties affected immobilization/mobilization of metals/metalloids in contaminated soils," *J Soils Sediments*, vol. 17, no. 3, pp. 717–730, Mar. 2017, doi: 10.1007/s11368-015-1339-4.

[9] F. L. Braghiroli, H. Bouafif, C. M. Neculita, and A. Koubaa, "Influence of Pyro-Gasification and Activation Conditions on the Porosity of Activated Biochars: A Literature Review," *Waste and Biomass Valorization*, vol. 11, no. 9. Springer, pp. 5079–5098, Sep. 01, 2020. doi: 10.1007/s12649-019-00797-5.

[10] V. Benedetti, F. Patuzzi, and M. Baratieri, "Gasification Char as a Potential Substitute of Activated Carbon in Adsorption Applications," in *Energy Procedia*, Elsevier Ltd, 2017, pp. 712–717. doi: 10.1016/j.egypro.2017.03.380.

[11] J. Pallarés, A. González-Cencerrado, and I. Arauzo, "Production and characterization of activated carbon from barley straw by physical activation with carbon dioxide and steam," *Biomass Bioenergy*, vol. 115, pp. 64–73, Aug. 2018, doi: 10.1016/j.biombioe.2018.04.015.

[12] A. Korus, "Investigation of Tar Conversion Over Biomass Char," University of Lincoln, 2019. doi: https://doi.org/10.24385/lincoln.24326497.v1.

[13] P. Basu and P. Kaushal, "Biomass Gasification, Pyrolysis, and Torrefaction: Practical Design, Theory, and Climate Change Mitigation, Fourth Edition," *Biomass Gasification, Pyrolysis, and Torrefaction: Practical Design, Theory, and Climate Change Mitigation, Fourth Edition*, pp. 1–681, Jan. 2023, doi: 10.1016/C2022-0-02464-8.

[14] C. F. Chang, C. Y. Chang, and W. T. Tsai, "Effects of burn-off and activation temperature on preparation of activated carbon from corn cob agrowaste by CO2 and steam," *J Colloid Interface Sci*, vol. 232, no. 1, pp. 45–49, Dec. 2000, doi: 10.1006/jcis.2000.7171.

[15] Y. Ngernyen, C. Tangsathitkulchai, and M. Tangsathitkulchai, "Porous properties of activated carbon produced from Eucalyptus and Wattle wood by carbon dioxide activation," *Korean Journal of Chemical Engineering*, vol. 23, no. 6, pp. 1046–1054, Nov. 2006, doi: 10.1007/S11814-006-0028-9/METRICS.

[16] J. R. Grace, "Contacting Modes and Behaviour Classification of Gas-Solid and Other Two-Phase Suspensions," *Can J Chem Eng*, vol. 64, no. June, pp. 353–363, 1986.

7

[17]   C. Y. Wen and Y. H. Yu, "A generalized method for predicting the minimum fluidization velocity," *American Institute of Chemical Engineers Journal*, vol. 12, no. 3, pp. 610–612, 1966, doi: 10.1002/aic.690120343.

[18]   "Analytical Methods." Accessed: Mar. 14, 2024. [Online]. Available: https://www.european-biochar.org/en/ct/8

[19]   S. Brunauer, P. H. Emmett, and E. Teller, "Adsorption of Gases in Multimolecular Layers," 1938, Accessed: Mar. 14, 2024. [Online]. Available: https://pubs.acs.org/sharingguidelines

[20]   J. Rouquerol, P. Llewellyn, and F. Rouquerol, "Is the bet equation applicable to microporous adsorbents?," *Stud Surf Sci Catal*, vol. 160, pp. 49–56, Jan. 2007, doi: 10.1016/S0167-2991(07)80008-5.

[21]   D. Neves, H. Thunman, A. Matos, L. Tarelho, and A. Gómez-Barea, "Characterization and prediction of biomass pyrolysis products," *Prog Energy Combust Sci*, vol. 37, no. 5, pp. 611–630, Sep. 2011, doi: 10.1016/J.PECS.2011.01.001.

[22]   X. Jing *et al.*, "Evaluation of CO_2 gasification reactivity of different coal rank chars by physicochemical properties," *Energy and Fuels*, vol. 27, no. 12, pp. 7287–7293, 2013, doi: 10.1021/ef401639v.

8

Volatile releasing and ignition during oxy-combustion in fluidized bed

Chaoran Li, Tong Wang, Man Zhang, Tuo Zhou, Hairui Yang[1]*

[1] *Department of Energy and Power Engineering, Tsinghua University, Beijing 100084, China*

* E-mail of corresponding author: yhr@mail.tsinghua.edu.cn

Abstract

Oxygen-enriched circulating fluidized bed technology is symbolized by CO2 capture convenience. Volatile releasing and ignition temperature for several types of coal samples under different oxygen concentrations and bed temperatures was analysed in lab scale fluidized bed. Ar was used as inert gas to measure the volatilization characteristics of different coals and the curve of different volatilization components, including O2, CO2, CO, H2, CH4 and SO2, were recorded online. Volatile matter and oxygen play a dual role in the ignition and combustion of coal. Coal type has the primary effect, that means, coal with lower volatile normally has higher ignition temperature, while, volatile content, especially the combustible one such as CO, H2 and CH4, also plays great role.

Key words: oxygen-enriched combustion, ignition, volatile releasing, fluidized bed

1. Introduction

Oxygen fuel combustion in fluidized bed is the technology combing the advantage of oxy-fuel combustion and fluidized bed combustion, as one of the feasible measures to control CO2 emission. By pure oxygen separated from traditional air separation or Electrolyzed Water and flue gas recirculation, the CO2 concentration can be increased up to over 90% for latter capture and storage.

As an inspiring technology, Oxy-combustion in fluidized bed has attracts a lot of investigation in the past decades. Luo (Luo et al 2004) found recycling of the flue gas increases the contact of the SO2 and desulphurization sorbent, which decreases SO2 emission. The emission of the NOX is much lower because of the formation of nitrogen species was prohibited by CO2 and lack of thermal NOx (Czakiert et al 2006). While, when the oxygen increases, the ignition temperature will be greatly influenced (Chao et al 2016), so, the experience obtained for air combustion in fluidized bed can not directly used for oxy-combustion (Yang et al 2005).

The ignition temperature in fluidized bed means the lowest temperature above that the coal can be safely injected into the furnace. If the coal is fed into the furnace too early at lower temperature, the coal will not burn, which will cause slowly heating until risk of exploration, contrast, if coal fed at very high bed temperature, it will consume too much igniting oil and increase the start up cost (Hu et al 2005). So, accurately obtain the ignition temperature of coal under oxygen condition is key for fluidized bed operation.

Besides the measurement with TG-DTG (Lu et al 1997) and real fluidized bed boiler(Wang et al 2002), small scale fluidized bed can provide accurate measurement on ignition temperature (Yang et al 2005).

In this paper, in order to provide guidance for real oxy-combustion fluidized bed design, ignition temperatures of five different types of coal under different atmospheres (air, different O2 contents), were measured in a lab scale fluidized bed. By measuring the volatilization characteristics of different coals including O2, CO2, CO, H2, CH4 and SO2, the influence of volatile content on ignition temperature was also discussed.

2. Experiments

The lab scale fluidized bed consists of main reactor, temperature control system, gas system, coal feeding system, sampling system and online data recording system, as shown in Figure 1. The main reactor was made of quartz tube of 50mm inside diameter and 600 mm height, more details can be found in previous studies [Yang et al 2005 and Chao et al 2016]
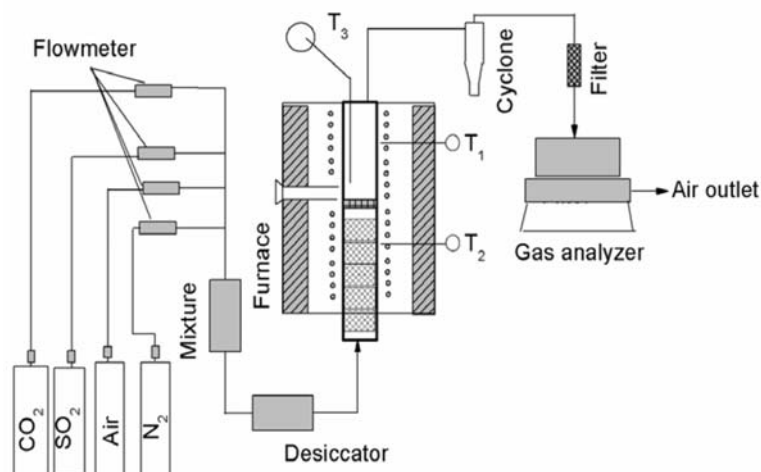
Figure 1 Lab scale of fluidized bed reactor

Because combustion characteristic, especially the ignition temperature, is influenced greatly by the measuring test rig, the operation conditions should be standardized, as listed in Table 1.

Table 1 standards for ignition temperature measurement

Fluidized gas	U/Umf	Mass of coal	Size of coal	Bed material	Bed height	Bed material size
O2/CO2	3	2g	1-2mm	Quartz sand	40mm	275-300μm

The proximate and ultimate analyses of five coal types are listed in Tables 2. The temperature in the dense bed was measured by thermocouple online. An O2 analyser and a mass spectrometer were used to measure the concentration changes of the gas compositions (especially O2, CO2, H2, CH4, CO and SO2) in the flue gas.

Table2   Ultimate and Proximate analyses of coals

Coal	Ultimate analyses, wt%					Proximate analyses, wt%				LHVar, MJ/kg
	Cad	Had	Oad	Nad	Sad	Mt	Vd	Fcd	Ad	
1	52.30	1.04	0.83	0.71	1.12	4.72	4.51	60.89	34.59	19.07
2	62.13	2.67	7.38	1.18	0.15	2.12	10.53	62.35	27.11	25.05
3	56.58	3.61	14.28	1.12	0.42	3.96	31.43	46.14	22.42	22.58
4	55.38	2.04	6.42	1.12	0.50	0.00	35.51	55.67	8.82	21.38
5	36.72	1.87	12.59	1.01	1.66	9.88	54.45	40.06	5.49	12.43

3. results and discussion

3.1 Volatile releasing for different coal

At set bed temperature of 770℃，Ar as the balance inert gas, the volatile releasing characteristic for all coals were measure with mass spectrometer, as shown in Figure 2. The gas components such ash O2, CO2, CO, SO2, H2 and CH4 were recorded on line.

It was clearly found, for coal 1 and 2, during the volatile releasing process, the gas components were very less due to the volatile content is very little. Especially for coal 1 with only 4.3% volatile content, combustible gas such as CO, H2 and CH4 were nearly zero. Relatively, the H2 content for coal 2 was higher as 3%.

Coal 3 and Coal 4 belongs to high volatile bituminous coal, and volatiles have relatively high fraction of combustible gas. For coal 3, the CO was high as 12%, as well as H2 and CH4. Comparingly,

though coal 5 has volatile content of 50%, while, the CO2 in volatile was high as 10% and the combustible gases were lower.

Volatile releasing for coal 1

Volatile releasing for coal 2

Volatile releasing for coal 3

Volatile releasing for coal 4

Volatile releasing for coal 5
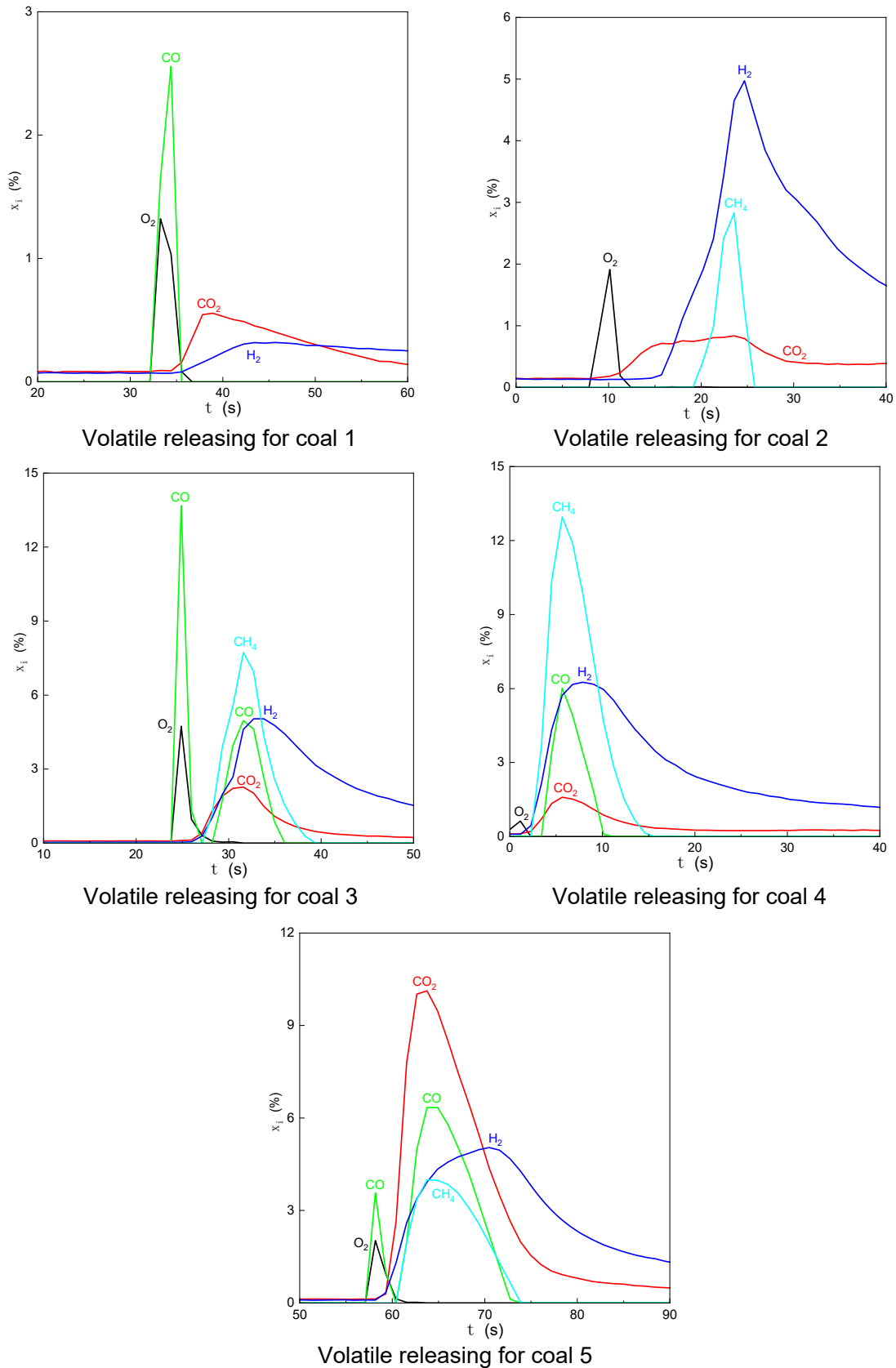
Figure 2 The volatile releasing for different coals

When the initial bed temperature was high enough, coal 3 and 4 will release volatile quickly. Once the oxygen is higher, the coals will burn quickly and consume a large amount of oxygen until to valley.

Such intensive combustion will release much heat to heat the bed material to high temperature peak, as shown in Figure 3.

3.2 Coal type effect on ignition temperature

Temperature increasing profiles

Oxygen profiles
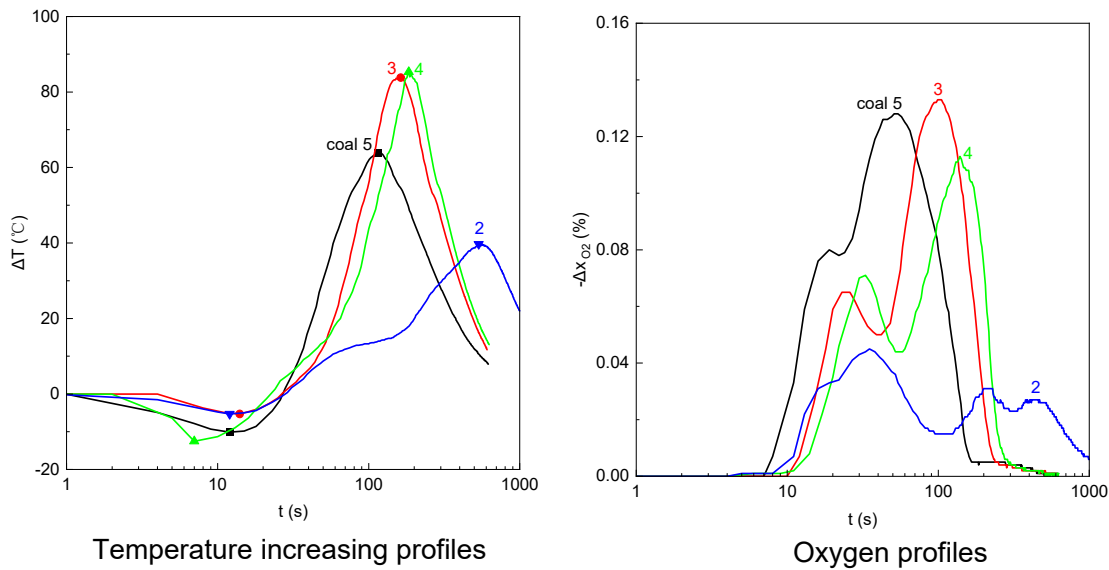
Figure 3 Volatile releasing for different coals at 508℃ and O2 of 27.8%

As shown in Figure 3, except for the coal 1, all coals can quickly burn at such temperature and oxygen content, the oxygen were consumed in short time. Comparingly, the peak of temperature increasing and the valley of oxygen were nearly simultaneously coincided. Coal 1 was very special, just because it has less volatile content of 4.3% and the ignition temperature is the highest. In this view, the volatile content has very important effect on combustion characteristic in the initial stage of coal.

3.3 Oxygen Effect on ignition temperature

Figure 4 shown the effect of oxygen on the temperature increasing profile at certain bed temperature for different coals.

Temperature profile for Coal 4 at 490℃

Temperature profile for Coal 5 at 400℃
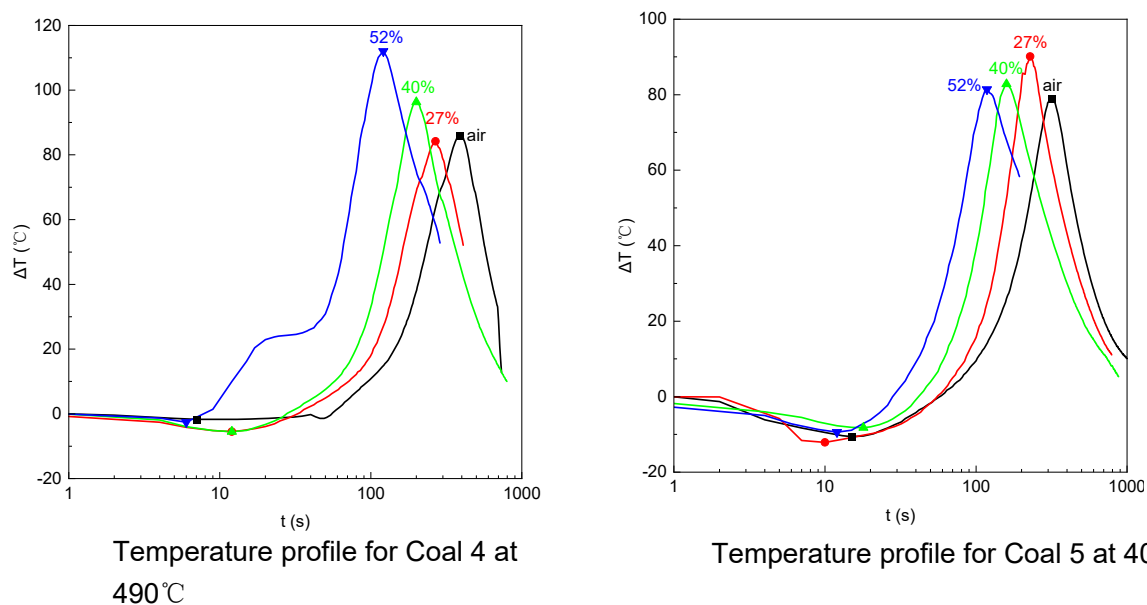
Figure 4 Temperature increasing profile under under different O2%

As mentioned above, the initial bed temperature can influence the heating rate on the coal particles, and then determine the chemical reaction rate. The oxygen content will control the partial pressure

and the gas solid diffusion rate. Combination of two effect can obviously increase the combustion and heating releasing rate, so, the ignition temperature can greatly decrease. For the same coal and at the same bed temperature, increasing of O2 content will greatly decrease the ignition temperature.

3.4 Ignition index

To evaluate the ignition characteristics in a fluidized bed system, the ignition index, Fi, can be calculated as $Fi = \frac{T_{max} - T_{min}}{t_1 + t_2}$, more information about Fi definition can be found in previous work (Yang et al 2005). The calculation results are shown in Figure 5. Higher bed temperature, Tb, and higher O2 content can lead to higher Fi because of reaction acceleration.
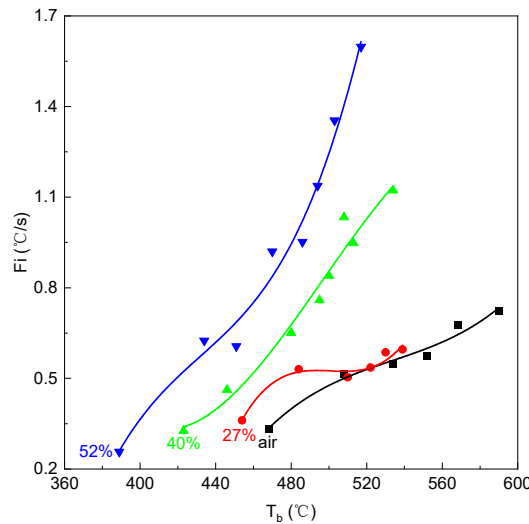
Figure 5 The influence of Tb and gas atmosphere on Fi for coal 3

3.5 Ignition temperature measured

Base on the above measurement, the ignition temperatures for all coals under different oxygen content were determined, as listed in Table 3. It is clear that, increasing the oxygen content will decrease the ignition temperature significantly. At same time, coal type has the primary effect, that means, coal with lower volatile normally has high value, while, volatile content, especially the combustible one, also plays great role.

Table 3 Ignition temperature for different coal under different Oxygen content

coal	52.7%/℃	40.6%/℃	27.8%/℃	air/℃
1	590	630	640	650
2	520	540	560	580
3	420	430	450	460
4	450	460	480	500
5	360	370	380	400

4. Conclusion

Volatile releasing and ignition temperature for 5 types of coal under different oxygen concentrations and bed temperatures was analyzed in lab scale fluidized bed.

It is clear to find, increasing the oxygen content will decrease the ignition temperature significantly. Volatile matter and oxygen contend play a dual role in the ignition and combustion of coal. Coal type has the primary effect, that means, coal with lower volatile normally has higher ignition temperature, while, volatile content, especially the combustible one such as CO, H2 and CH4, also plays great role.

Reference

Luo Zhong yang , Mao Yuru, WU Xue cheng et al ,Test study on and analysis of burning behavior for coal under atmosphere of O2/ CO2.,Thermal power generation, 33 ,(2004)

T Czakiert,Z.Bis,W Muskala,et al.Fluidized bed combustion in oxygen-enriched conditions,.The 19th inter-national Conference on Fluidized Bed Combustion.(2006.)

Chao JN, Yang HR, Wu YX, et al, The investigation of the coal ignition temperature and ignition characteristics in an oxygen-enriched FBR, Fuel 2016, 183:351-358

Yang HR, Lv JF, Zhang H, Yue GX, Guo YX. Coal ignition characteristics in CFB boiler. Fuel 2005;84:1849–53.

Hu WB, Yang HR, Lv JF, Zhang H. Determination of ignition temperature of coal by using thermogravimetry. In: Proceedings of FBC 2005 18th international fluidized bed combustion conference 2005, Toronto, Canada. p. 18–21.

Lu CM, Wang LZ, Shao YL, et al, Using thermogracimetric analysis to determind the coal ignition temperaure and combustion index, Shangdong Electiric Power, 1997, 20, 63-68
Wang ZW, Zhang CY, Experimental Research of igniting characteristics in circulating fluidized bed, Journal of Combustion Science and Technology, 2002, 8,460-471

Yang HR, Xue L,Guo YX et al,The ignition characteristic in CFB boiler, Journal of Combustion Science and Technology,2005, 236-239

O$_2$-RICH GASIFICATION OF BIOMASS MIXING A SMALL AMOUNT OF COAL IN A TWO-STAGE CIRCULATING FLUIDIZED BED GASIFIER PRODUCING H-RICH AND LOW-TAR SYNGAS

Chao Wang[b,c,1], Hanyang Li[a,1], Mengjuan Zhang[a,], Zhennan Han[b,c], Xin Jia[a], Guangwen Xu[a,*]*

[a] Key Laboratory of Resources Chemicals and Materials (Shenyang University of Chemical Technology), Ministry of Education, Shenyang 110142, China.

[b] Laboratory of Engineering Thermochemistry, Guangdong University of Technology, Guangzhou, 510006, People's Republic of China.

[c] School of Chemical Engineering and Light Industry, Guangdong University of Technology, Guangzhou, 510006, People's Republic of China.

Email: E-mail of corresponding author: zhengmengjuan_0703@syut.edu.cn (M. Zhang), gwxu@ipe.ac.cn (G. Xu).

Abstract

A small amount of coal mixing into biomass was used as feedstock in a two-stage fluidized bed gasifier for O$_2$-rich gasification producing H-rich and low-tar syngas. Double loop streams in the two-stage fluidized bed system were designed to upgrade the problem of short running time caused by coal ash agglomeration. As O$_2$-rich air was used as gasifying agent, under the condition of electric furnace temperature = 950 °C, ER = 0.35 and the coal fractions mixing into biomass = 10%, the gas composition contained of 13.31% CO, 20.21% CO$_2$, 4.21% CH$_4$, 1.07% C$_n$H$_m$, 9.77% H$_2$, and 51.43% N$_2$ with corresponding LHV of 4.85 MJ/Nm^3. And the tar content by intermittent collection gradually dropped from 1.8 g/Nm^3 to 0.012 g/Nm^3 after 6 h. The steady state of temperature, pressure and gas composition indicated that the two-stage fluidized system with double loop streams demonstrates excellent continuous running stability and technical feasibility for producing H-rich syngas from biomass and coal mixture gasification.

1. Introduction

The global trend towards low-carbon development is forcing the energy structure to shift from fossil fuels to renewable energy sources, with the hope of reducing dependence on fossil fuels while reducing carbon dioxide emissions [1]. Biomass, as the largest organic group in nature, is the only solid resource with the characteristics of fossil fuels. Biomass thermal conversion technology can convert low-grade biomass into high-energy density fuel oil and fuel gas, which only accelerates the carbon dioxide cycle during the plant's growth cycle, without producing additional carbon dioxide, and is a carbon-neutral process. The gasification of biomass with low energy density is difficult to use high-temperature gas flow bed technology [2]. At the same time, the high alkali metal and SiO$_2$-based ash content of biomass hinders the application of biomass as a gasification raw material in terms of properties, and coal gasification technology is often not suitable for the needs of large-scale biomass gasification. Therefore, medium-temperature fixed bed and fluidized bed gasification become the inevitable technical choice for large-scale and medium-scale applications [3].

The generation and control of biomass tar at medium and low temperatures has become a worldwide research hotspot and a difficult problem [4]. The tar-containing product gas from biomass not only reduces the efficiency of gasification, but also seriously affects the use of the product gas as a chemical production raw gas. The two-stage gasification technology, based on the thermochemical thought of reaction decoupling and reconstruction, has been proved to be one of the effective measures to remove tar in the reactor.

Biomass gasification as a typical thermally driven process is greatly affected by temperature, which requires the conversion process to coordinate the heat release and heat transfer within a limited time and space to form a high-energy density field. Meanwhile, air as a gasifying agent introduces nitrogen into the gasification system, affecting the quality of the producer gas using as chemical raw gas. Therefore, researchers hope to increase the energy density of the gasification system while reducing the impact of nitrogen on the product gas by using O_2/O_2-rich gasifying agent. The high-content oxygen in biomass contributes to the low energy density as gasification feedstock, making it difficult to meet the temperature requirements for tar thermolysis in self-heating gasification processes. Additionally, bio-char as fluidized bed material has two disadvantages: the low bulk density to cause poor circulation, and the limited catalytic activity of bio-char [5]. Therefore, researchers have tried to add a proportion of coal during biomass gasification, improving the system's energy density for high temperature and the catalytic activity by coal char for tar severity cracking [6].

In this work, a two-stage fluidized bed gasifier consisting of a downer pyrolyzer, a riser gasifier and a bubbling fluidized bed reactor was used for biomass gasification with O_2/O_2-rich gasifying agent producing low-tar and H-rich syngas. As shown in Figure 1, based on the principle of two-stage fluidized bed gasifier, the large particles of biomass and coal char will accumulate at the bubbling fluidized reactor to form a rich carbon reaction zone with high bulk density. And O_2/O_2-rich gasifying agent is introduced into the system as fluidizing agent from the bottom of the bubbling fluidized reactor. During the process of oxidizing gas passing through the high-temperature char bed, char occurs combustion and gasification reaction to release sufficient heat in a limited time and space, providing the system with the required high temperature. Meanwhile, the carbon-rich bed can prevent the oxidizing gasifying agent from coming into contact with the H_2-rich pyrolysis gas, effectively increasing the hydrogen content in the producer gas. In addition, the coal ash with large particle size is discharged from the bottom of the bubbling bed system, while small-size ones are circulated within the system with the heat carrier particles to increase the catalytic activity of the bio-char.
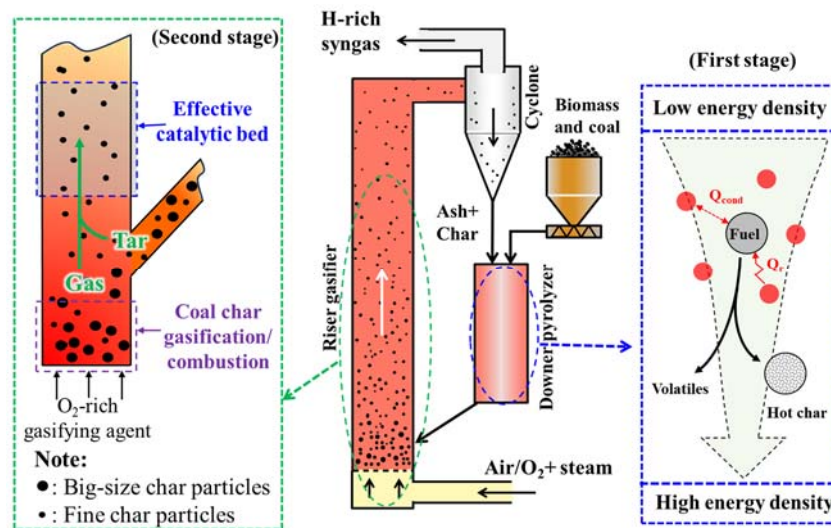
Figure 1 Schematic diagram of O_2-rich biomass gasification by two-stage fluidized bed.

2.Experimental part

2.1 The raw materials of biomass and coal

The biomass and coal feedstock for this experiment were pine pellets and Yilan coal, respectively, collecting form Jiangsu province and Heilongjiang of China. Before the experiment, the raw pine wood and Yilan coal were crushed and screened to decompose into small particles with a uniform particle size of 0.3-5 mm. As described in Table 1, the pine

chip has a volatile content of up to 75.91%, and the content of C and O element accounts for 49.89% and 43.95% of the total element composition, respectively. In comparison, the Yilan coal contains more fixed carbon and ash about 18.87% and 55.82%, respectively, as well as lower O element about 6.55%.

Table 1 Result of ultimate and proximate analyses of the raw pine chips and Yilan coal.

Sample	Ultimate analysis with ash (wt.%. ad)					LHV (MJ/kg)	Proximate analysis (wt.%. ad)			
	C	H	O*	N	S		V	A	M	FC*
Pine chips	49.89	6.12	43.95	0.04	0	19.85	75.91	0.79	8.93	14.37
Yilan coal	33.39	3.08	6.55	0.77	0.39	15.95	20.99	55.82	4.32	18.87

Note: ad: air dry basis, *: by the difference.

2.2 Biomass gasification testing facility

The two-stage fluidized bed gasifier made of stainless steel pipes consists of a downer pyrolyzer, a riser gasifier and a bubbling fluidized bed reactor. Before the gasification test, the pyrolysis and gasification reactors were heated to the specified temperature by the electric heating furnaces in accordance with heating procedures. After the temperatures reached the target values, 5 kg of white corundum particles with a particle size of 100-150 μm, as heating carrier particles (HCPs), were gradually fed into the gasification system. Under the action of air entrainment, the HCPs absorbed heat and transported it to various parts of the system. After the system temperature reached a steady state, the mixture of biomass and coal was fed into system from the top of pyrolyzer with a rate of 6 kg/h. The raw materials firstly contacted with high-temperature HCPs and entered into pyrolyzer under gravity undergoing rapid pyrolysis reaction and steam evaporation. All the generated products and HCPs were transported into the second stage through the top of the bubbling fluidized bed. In here, the big particles of char from biomass and coal shifted to the bubbling fluidized bed reactor and formed a carbon-rich bed. The required-quantity oxidizing fluidizing agent entered the system occurred combustion and gasification reactions with char, which produced heat and wore down the size of char particles. The small char and ash particles were transported into the riser to form a dynamical effective catalytic bed for tar catalytic cracking/ reforming and gas upgrading. After that, the unreacted char, ash and HCPs were captured by the cyclone separator, and circulated back to the downer pyrolyzer through the J-type valve with a 6 NL/min N_2 injection. The producer gas left the gasification system from the top of the cyclone separator. All the information on temperature and pressure was measured and continuously monitored by a sophisticated data acquisition system from thermocouples and pressure sensors mounted at specified locations of the facility.

After the test, all the tar in the acetone-washing bottles and pipelines was washed by acetone. The obtained liquid was filtrated to remove ash and evaporated to separate acetone getting the mixture of tar and water. Here, the water content was evaluated by a Coulomb meter, and the tar weight was calculated by the subtraction method. After further removing moisture by anhydrous $MgSO_4$, the detectable components in the tar were detected using gas chromatography-mass spectrometry (GC-MS, Agilent 7890B).

3. Results and discussion

The designed tests with variations of coal fraction mixing into biomass were defined as Case 1, Case 2 and Case 3 with biomass/coal ratio = 85/15, 70/30 and 55/45, respectively. The experimental operating parameters were obtained by material balance following the average element content in the mixture of biomass and coal.

Under steady state in Case 1, the temperature of pyrolyzer (T3) and gasifier (T1) were 646 ℃ and 850 ℃, respectively. As the mass fractions of coal mixing into biomass increased from 15% to 45%, the fixed carbon content in feedstock increased resulting in the average temperature of pyrolyzer (T3) and gasifier (T1) increased to 735 ℃ and 880 ℃. Meanwhile, in all cases, the pressure differential between downer (P1) and riser top (P3) was maintained

at about 3 kPa, providing the power of fine particles circulation. And the pressure difference between riser bottom (P2) and riser top (P3) was floated at about 5 kPa, causing by dynamic circulation of big-size particles in bubbling fluidized bed. However, in the actual gasification operation, the approach of biomass and coal simultaneously feed into gasification system would cause the alkali metals in the biomass to migrate to the surface of coal ash, forming coal ash agglomeration in bubbling fluidized bed zone. The generated agglomeration can limit the circulation of solid materials in the circulation fluidized bed system, ultimately leading to the shutdown of the gasification test. As shown in Table 2, the steady running time of the gasification test was hardly more than 1 hour, as well as presented a downward trend with increasing of coal fractions mixing into biomass.

Table 2 Key performance data and experimental results of gasification tests.

Condition parameter	Case 1	Case 2	Case 3
Temperature of pyrolyzer (T3) (^{o}C)	646	675	735
Temperature of gasifier (T1) (^{o}C)	850	870	880
Pressure of downer (P1) (kPa)	2	2	3
Pressure of riser bottom (P2) (kPa)	4	4	5
Pressure of riser top (P3) (kPa)	-1	-1	-1
Steady running time (min)	66	50	45
Cold gasification efficiency (%)	65%	77%	86%
LHV of producer gas (MJ/Nm^3)	6.88	7.8	8.14
Gas yield (Nm^3/kg)	1.81	1.88	1.91
Tar content (g/Nm^3)	1.72	1.19	0.17

The causes of forming agglomeration in the fluidized bed system can be inferred as follows: As displayed in Figure 2, during the pyrolysis process, the volatile alkali metals (e.g. K and Na) are released from inside the biomass particles, and reacted with SiO_2-based coal ash to form eutectic mixture [7]. And then, the non-volatile alkali metals (e.g. Ca and Al) shift to the surface of coal char increasing the bonding strength among the solid particles [8]. What's more, the agglomeration of coal char shifts to the bottom of the bubbling fluidized reactor resulting in the shutdown of solid particle circulation. The oxygen in the fluidizing agent contacting with carbon of agglomeration can release lots of heat causing local high temperature (above 1200 ^{o}C). Under that high temperature atmosphere, the coal ash can be burnt into a molten state forming serious blocks.
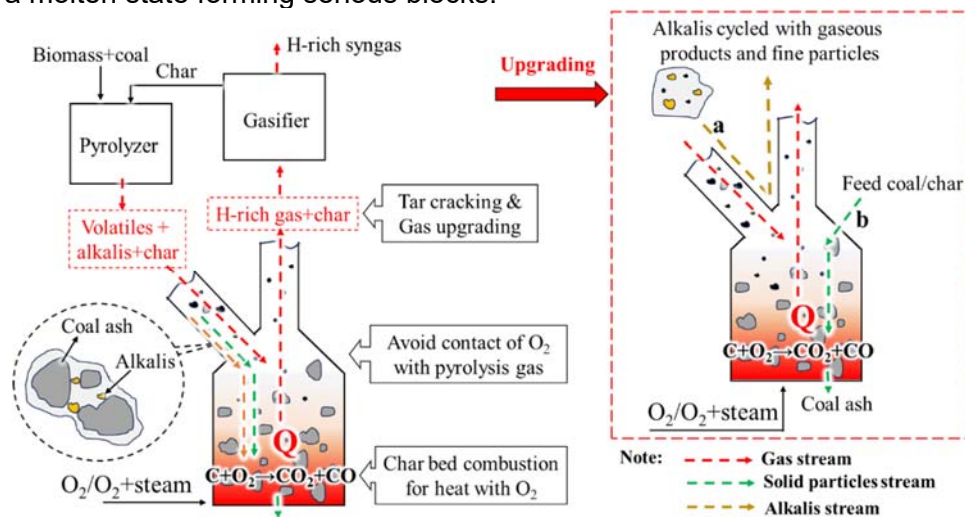
Figure 2 Schematic diagram of the coal ash forming agglomeration in the device and upgrading approach.

In order to solve the above blockage problem, an upgrading approach was proposed to move the feed port of coal to the top of the bubbling fluidized bed. By which, double loop

streams were designed to avoid the contact between alkali metals and coal char. Inhere, the alkali metals deriving from biomass participated in the cycle of pyrolysis gas in gaseous form, and the coal char can still form a carbon-rich material bed in the bubbling fluidized reactor.
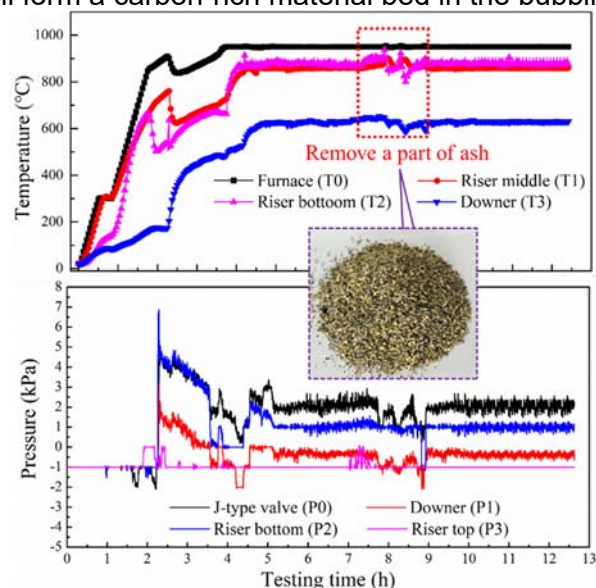
Figure 3 Variations of temperature and pressure in gasification system during the further gasification test.

The long-term continuous running of further gasification test by the above upgrading approach was carried out for 12.5 h under the condition of electric furnace temperature = 950 ^{o}C, ER = 0.35 and the coal fractions mixing into biomass = 10%. As presented in Figure 3, during the gasification process, temperatures of pyrolyzer and gasifier were maintained at 631 and 880 ^{o}C, as well as their pressures fluctuated in a small range. After 4 hours of stable biomass feeding, open the discharge port of bubbling fluidized reactor and remove part of the coal ash from the system. In that period of time, the temperature and pressure sharply fluctuated, and gradually returned to a stable state in a short time after closing the discharge valve. The obtained coal ash was well dispersed without agglomeration. It indicted that the double loop streams in two-stage fluidized system with the mixture of biomass and coal as feedstock can run stably while ensuring good gasification efficiency.
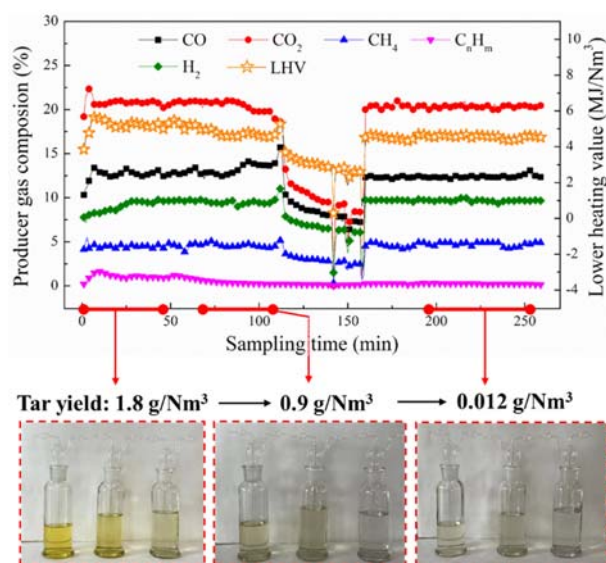
Figure 4 Time-series changes of the producer gas composition and tar content in producer gas.

Figure 4 shows the time series of gas composition and corresponding LHV during further operation. In about 20 min, the producer gas's composition became almost constant,

containing of 13.31% CO, 20.21% CO_2, 4.27% CH_4, 1.07% C_nH_m, 9.77% H_2 and 51.43% N_2 with corresponding LHV of 4.85 MJ/Nm^3. And during the process of discharge the coal ash, the gas composition changed very rapidly in response to the system variation. As the circulation of the solid material got equilibrium again, the gas composition reached the previous stable state in a short time. It indicated that the two-stage fluidized system with double loop streams has great continuous running stability and technical feasibility for the gasification of mixture of biomass and coal. Meanwhile, the tar content gradually dropped by intermittent collection from 1.8 g/Nm^3 to 0.012 g/Nm^3 after 6 h.

4. Conclusion

In this work, a two-stage fluidized bed gasifier consisting of a downer pyrolyzer, a riser gasifier and a bubbling fluidized bed reactor was used for gasification of the mixture of biomass and coal producing low-tar and H-rich syngas. During the gasification test with O_2/O_2-rich gasifying agent, as the coal fractions mixing into biomass increased from 15% to 45%, the cold gasification efficiency increased from 65% to 86%, as well as the carbon and hydrogen conversion efficiency increased from 86% to 95% and 71% to 86%, respectively. However, the approach of biomass and coal simultaneously feed into gasification system would cause the alkali metals in the biomass to migrate to the surface of coal ash, forming coal ash agglomeration in bubbling fluidized bed zone and ultimately leading to the shutdown of the gasification test. Double loop streams in two-stage fluidized system were designed for upgrading the problem of coal ash agglomeration by avoiding the contact between alkali metals and coal char. At the condition of electric furnace temperature = 950 ^{o}C, ER = 0.35 and the coal fractions mixing into biomass = 10%, the gas composition contained of 13.31% CO, 20.21% CO_2, 4.27% CH_4, 1.07% C_nH_m, 9.77% H_2, and 51.43%N_2 with corresponding LHV of 4.85 MJ/Nm^3. And the tar content by intermittent collection gradually dropped from 1.8 g/Nm^3 to 0.012 g/Nm^3 after 6 h. The steady state of temperature, pressure and gas composition indicated that the two-stage fluidized system with double loop streams had great continuous running stability and technical feasibility for the gasification of mixture of biomass and coal producing H-rich syngas.

Acknowledgment

References

[1]   Shrestha A, Mustafa AA, Htike MM, et al.. Evolution of energy mix in emerging countries: Modern renewable energy, traditional renewable energy, and non-renewable energy. Renewable Energy. 2022;199:419-32.
[2]   AlNouss A, McKay G, Al-Ansari T. Production of syngas via gasification using optimum blends of biomass. Journal of Cleaner Production. 2020;242:15.
[3]   Sapariya DD, Patdiwala UJ, Panchal H, et al.. A review on thermochemical biomass gasification techniques for bioenergy production. Energy Sources Part a-Recovery Utilization and Environmental Effects. 2021;34.
[4]   Rubinsin NJ, Karim NA, Timmiati SN, et al.. An overview of the enhanced biomass gasification for hydrogen production. International Journal of Hydrogen Energy. 2024;49:1139-64.
[5]   Lapidus AL, Shumovskii AV, Gorlov EG. Gasification of Coal and Biomass Mixtures. Solid Fuel Chemistry. 2023;57:373-80.
[6]   Ma M, Bai Y, Wei J, et al. Decoupling study of volatile–char interaction during coal/biomass co-gasification based on a two-stage fixed bed reactor: Insight into the role of O-containing compound species. Chemical Engineering Science. 2023;265:118-262.
[7]   Yao XW, Zhou HD, Xu KL, et al.. Systematic study on ash transformation behaviour and thermal kinetic characteristics during co-firing of biomass with high ratios of bituminous coal. Renewable Energy. 2020;147:1453-68.
[8]   Teixeira P, Lopes H, Gulyurtlu I, et al.. Slagging and Fouling during Coal and Biomass Cofiring: Chemical Equilibrium Model Applied to FBC. Energy & Fuels. 2014;28:697-713.

Session F:

Looping and energy storage processes

MODELLING-BASED PROOF-OF-CONCEPT FOR Ca(OH)$_2$-ENHANCED CO$_2$ CAPTURE IN A CALCIUM LOOPING PROCESS

Markus Secomandi[1]*, Borja Arias[2], Markku Nikku[1], Kari Myöhänen[1], Jouni Ritvanen[1]

[1]Lappeenranta-Lahti University of Technology, LUT School of Energy Systems,

P.O. Box 20, FI-53851 Lappeenranta, Finland

[2]CSIC-INCAR, C/Francisco Pintado Fe, 26, 33011 Oviedo, Spain

*Email: markus.secomandi@lut.fi

Abstract

Scenarios in which global warming is limited to 1.5 °C require some form of carbon dioxide removal technologies. Calcium looping (CaL) is an emerging CO$_2$ capture process in which CaO is cycled between two CFB reactors: the carbonator, in which CO$_2$ is adsorbed, forming CaCO$_3$, and the calciner, in which the sorbent is regenerated. The carbonator is typically operated at a temperature close to 650 ºC and with CO$_2$ capture efficiencies of around 90 %. This modelling study assesses a concept to improve the CO$_2$ capture efficiency of the CaL process to 99 %.

The investigated carbonator design employs a larger heat exchanger to attain a temperature drop of 100 °C over the height of the reactor. This results in a temperature of approximately 550 °C in the top region of the carbonator, thus reducing the minimum CO$_2$ concentration achievable according to the CO$_2$-CaO equilibrium. In addition, calcium hydroxide is fed in the upper part of the reactor as an additional sorbent to capture part of the remaining CO$_2$.

An in-house model is used to simulate the interconnected reactors, represented one-dimensionally by control volumes along their heights. The model features comprehensive reaction modelling, with heterogeneous and homogeneous combustion and sorbent reactions expressed by kinetic equations. Semi-empirical closure models are used for fluidised bed hydrodynamics and heat transfer.

First, a steady state balance measured in the "La Pereda" pilot is simulated and serves as a reference point. Then, a calcium hydroxide injection is added, and the resulting temperature and CO$_2$ profiles are compared with those of the reference case. The resulting CO$_2$ capture efficiency of the carbonator increases from 93 % close to 99 %.

Based on the model results, the investigated carbonator configuration offers a significant potential to further reduce CO$_2$ emissions in industrial processes. The parameters controlling the sorbent reaction rates will be calibrated with experimental data from pilot tests once available, and the validated model will be used in future large-scale studies.

Keywords: circulating fluidised bed, carbon capture, calcium looping, calcium hydroxide.

1. Introduction

Carbon capture technologies are needed to reduce emissions in hard-to-abate sectors (FCCC, 2023) such as the cement, steel and iron, and power sectors. Calcium looping is a tail-end method used to capture carbon dioxide (CO$_2$) by blowing flue gas through a bed rich in calcium oxide (CaO) (Shimizu, et al., 1999) in a CFB reactor. The CO$_2$ reacts with the CaO particles, forming calcium carbonate (CaCO$_3$), and is then circulated to a second reactor in which it is

decomposed back to CaO and CO_2, producing a concentrated stream of CO_2 that can be utilized or stored after purification. Heat is provided to the process by firing a solid fuel in the calciner, and excess heat is removed from the carbonator by heat-exchanging surfaces. Reactor conditions are dictated by the CaO-CO_2 equilibrium curve (Abanades, et al., 2015): calcining the sorbent in a stream of concentrated CO_2 under atmospheric pressure requires a temperature of 900 °C, while reducing the CO_2 concentration of the treated gas below 0.1 %-v requires a temperature of around 550 °C. However, the highest carbon capture efficiencies, defined as the ratio of CO_2 captured to the total flow of CO_2 entering the carbonator, are typically reached at temperatures between 600 and 650 °C due to the effect of temperature on the kinetics of carbonation (Dieter, et al., 2013) and the maximum carbonation conversion (Criado, et al., 2018). The equilibrium CO_2 concentration at 650 °C is 1 %-v, which corresponds to a maximum carbon capture efficiency of 90 % when treating typical flue gases with a CO_2 concentration of 10 %-v.

A method to reach a carbon capture efficiency of 99 % has been proposed (Arias, et al., 2022; CaLby2030, 2022). It consists of operating the dense bed, where most of the CO_2 is captured, at a temperature close to 650 °C and installing additional heat-transfer surfaces to reduce the temperature in the top region of the carbonator to 550 °C. This would, in principle, allow for the CO_2 capture in the dense bed to be maximized, while an injection of highly reactive calcium hydroxide ($Ca(OH)_2$) in the dilute upper region of the carbonator would capture most of the remaining CO_2, potentially increasing the total carbon capture efficiency of the carbonator to 99 %.

This paper presents a proof-of-concept for the method described. A steady-state balance measured at the La Pereda pilot is modelled and the effect of implementing a $Ca(OH)_2$ injection is simulated by using interconnected 1.5D reactor models. The study quantifies the CO_2 reduction achievable under partial load conditions and a suitable temperature profile.

2. Methodology

The reactor model used in the proof-of-concept study is a dynamic 1.5D CFB model developed at LUT (Ylätalo, et al., 2012). The reactor is divided radially into core and annulus regions and vertically into control volumes for which time-dependent heat and mass balances are written. The obtained set of differential equations is solved by the ODE solvers available in the Simulink environment. While dynamic simulations are supported by the model, in this work the reactor system is evaluated at a steady state by running the simulation to convergence. The model features homogeneous and heterogeneous chemical reactions, and the most relevant of the gas-solid reactions are presented in Table 1.

Table 1. Selected heterogeneous reactions. Reaction rates r_i in kg/s.

Reaction	Equation	ΔH_{298K} [kJ/mol]	Ref.
Calcination	$CaCO_3(s) \rightarrow CaO(s) + CO_2(g)$ $r_{calc} = k_{calc} n_{Ca} M_{CaCO_3} X_{carb}^{0.67} \left(C_{CO_2,eq} - C_{CO_2} \right)$ $k_{calc} = 2057 \exp\left(-112400/RT\right)$ $C_{CO_2,eq} = 4.137 \times 10^{12}/RT \ \exp\left(-20474/RT\right)$	178.2	(Fang, et al., 2009) (Martínez, et al., 2012) (Stanmore & Gilot, 2005)
Carbonation	$CaO(s) + CO_2(g) \rightarrow CaCO_3(s)$ $r_{carb} = k_{carb} n_{Ca} X_{CaO}^{0.1} M_{CaO} \left(X_{max} - X_{CaCO_3} \right)^{0.67} \left(C_{CO_2} - C_{CO_2,eq} \right)$ $k_{carb,CaCO_3} = 0.3429 \exp\left(-2309/T\right)$ $k_{carb,Ca(OH)_2} = 70 \exp\left(-2309/T\right)$	-178.2	Adapted from (Grasa, et al., 2009)
Dehydration	$Ca(OH)_2 \rightarrow CaO(s) + H_2O(g)$ $r_{dehy} = k_{dehy} n_{Ca} M_{Ca(OH)_2} X_{Ca(OH)_2}^{0.67}$ $k_{dehy} = 4359 \exp\left(-63200/RT\right)$	109.2	(Arias, et al., 2022)

The kinetic behaviour of the carbonation of $Ca(OH)_2$ is known to be complex (Koga & Kodani, 2018), but in this study, it was assumed to consist of the dehydration of $Ca(OH)_2$ followed by the carbonation of the nascent CaO. The rate constant for the carbonation of $Ca(OH)_2$-derived CaO was obtained by fitting the reaction model to the results of a drop-tube experiment similar to that presented in Arias et al. (2022). A full description of the remaining reactions is presented by Ritvanen et al. (2021).

The empirical correlation of Johnsson & Leckner (1995) is used to define the density profile of the main sorbent in the reactor, which is assumed to have a uniform particle size of 120 μm. The auxiliary sorbent injected in the dilute top region of the reactor is assumed to initially consist of a fine (10 μm) $Ca(OH)_2$ powder and to be in plug flow. The main sorbent entrained from the calciner is fully recirculated to the carbonator and vice-versa, whereas the auxiliary sorbent is assumed to leave the system with the gas stream through the cyclone.

A steady-state balance, as measured at the La Pereda pilot (Diego & Arias, 2020), was simulated to establish a reference case. This serves as a basis for comparing the effects of the $Ca(OH)_2$ injection. The reference case and the case with the $Ca(OH)_2$ injection will be referred to as C1 and C2, respectively. The pilot consists of two 15 m tall cylindrical reactors, with internal diameters of 0.65 and 0.75 m for the carbonator and calciner, respectively. The carbonator is cooled by four bayonet tubes hanging from the roof down to an elevation of 3 m above the grid. Because the temperature in the upper part of the carbonator was already suitable for highly efficient CO_2 capture, i.e., close to 550 °C, additional cooling surfaces were not needed and the $Ca(OH)_2$ was injected at the relatively high temperature of 350 °C, thus minimizing changes in the temperature profiles of both reactors. For this study, an injection elevation of 5 m and a $Ca(OH)_2/CO_2$ molar ratio of 3 were chosen, where the flow of CO_2 refers to the flow exiting the carbonator in the reference case. The boundary conditions of the simulated reactors are given in Table 2, and the specifications of the fired coal are given in Table 3.

Table 2. Boundary conditions of simulated reactors.

Parameter	Unit	Carbonator	Calciner
Heat exchange area	m^2	5.75	-
Hydroxide injection, C1 / C2	kg/s	0 / 0.022	-
Fuel consumption	MW_{LHV}	-	1.49
Cooling duty	kW	200	-
Heat losses, reactor walls	kW	50	50
Fluidising gas flow	kg/s	0.31	0.45
Fluidising gas O_2	m-%	3.3	23.3
Fluidising gas N_2	m-%	67.5	76.7
Fluidising gas CO_2	m-%	18.9	-
Fluidising gas H_2O	m-%	10.2	-
Fluidising gas SO_2	m-%	0.14	-
Fluidising gas temperature	°C	115	25
Loop seal air flow	kg/s	0.11	0.12
Make-up flow	kg/s	-	0.1
Make-up $CaCO_3$	m-%	-	98.6
Make-up inert	m-%	-	1.4
Density of solids	kg/m^3	2000	2000
CO_2 carrying capacity of sorbent (X_{max}), main / aux.	mol/mol	0.13 / 0.7	-
Bed pressure	Pa	8700	2300

Table 3. Specifications of the coal fired.

LHV	Proximate analysis, m-%, a.r.				Ultimate analysis, m-%, d.a.f.				
MJ/kg, a.r.	Moisture	Ash	Char	Volatiles	C	H	N	S	O
26.43	1.9	20.3	54.8	23.0	86.4	5.4	1.7	2.0	4.5

3. Results and discussion

The temperature and pressure profiles of both reactors are presented in Fig. 1, showing good agreement between experimental results and the simulation. The reference case was a partial load case, with grid gas velocities close to 2.5 m/s and a low suspension density in the upper parts of the reactors. The bottom region of the calciner is cooler due to the endothermic calcination reaction and the thermal mass of solids recirculated from the carbonator, while the carbonator has a more pronounced temperature gradient due to the installed cooling surfaces. The dashed lines show that the temperature and pressure profiles do not change dramatically when $Ca(OH)_2$ is injected. The applied $Ca(OH)_2/CO_2$ ratio leads to a net endothermic effect from the combined dehydration and carbonation reactions of the auxiliary sorbent. This, in conjunction with its relatively low feeding temperature, causes the temperature in the carbonator to decrease slightly.

(a) Temperature (°C) profiles

(b) Pressure (Pa) profiles
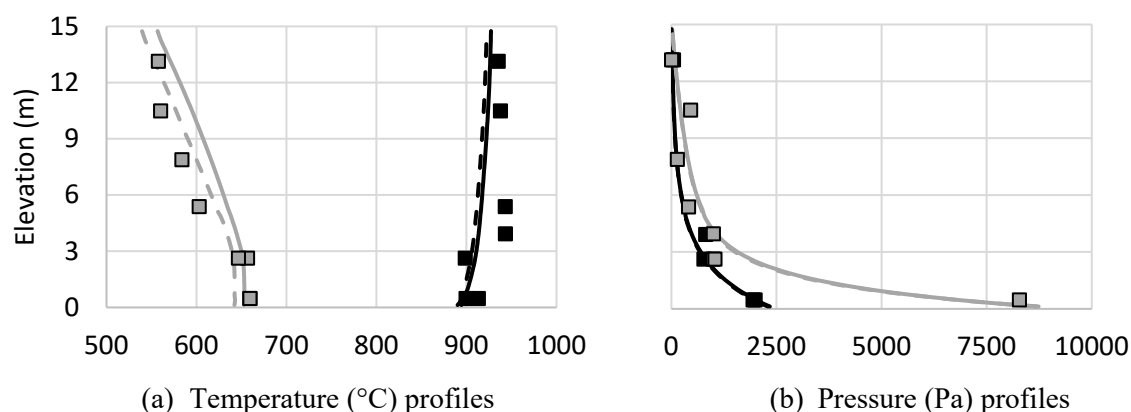
Fig. 1. Temperature and pressure profiles. Squares: measured values; Solid lines: reference case (C1); Dashed lines: simulated $Ca(OH)_2$ injection (C2). Black: calciner; Grey: carbonator.

The CO_2 the carbonation rate profiles are shown in Fig. 2. The graphs show how the partial pressure of CO_2 quickly decreases to 1 kPa in the dense bed, which is close to the equilibrium pressure. Above the dense bed, the bayonet tubes reduce the suspension temperature and, consequently, the equilibrium pressure of CO_2. However, due to the low concentration of solids, additional capture above the dense bed is limited and the pressure of CO_2 does not decrease below 0.7 kPa. The resulting carbon capture efficiency of 93 % is in good agreement with the values measured under similar conditions, which were between 85 and 96 %.

(a) Local and equilibrium CO_2 pressure

(b) Carbonation rates
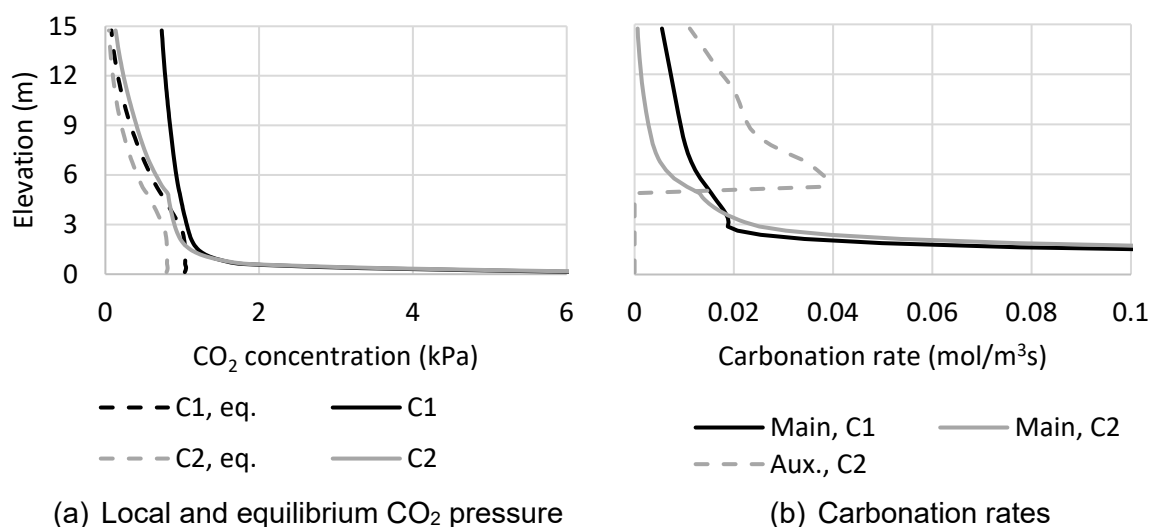
Fig. 2. CO_2 pressure and carbonation profiles of the carbonator.

When the results of C1 are compared to those of C2, the effect of the $Ca(OH)_2$ injection is clearly visible as a sharp reduction in CO_2 concentration above the injection point. The CO_2 concentration decreases from 0.9 %-v at 5 m to approximately 0.1 %-v at 15 m, resulting in an overall carbon capture efficiency of 98.6 %. The CO_2 and carbonation profiles indicate that the auxiliary sorbent has sufficient contact time with the gas for efficient carbonation, although a longer residence time might have yielded a slight improvement in the carbon capture efficiency. While the reactor model encompasses only the CFB riser, in a real plant the contact time of the auxiliary sorbent would be extended at least until the cyclone, but possibly as far as the baghouse, further increasing the amount of CO_2 captured.

The carbonation profiles of Fig. 2b also show that the $Ca(OH)_2$ injection suppresses the carbonation of the main sorbent in the upper part of the carbonator by consuming the CO_2 available. While carbonation in the freeboard of the reactor was not very significant for the overall carbon capture efficiency of the reference case studied, this could change when operating the reactor at full load, as a leaner bed and a denser freeboard would likely cause carbonation in the entrained zone to become more prominent. This could lead to a scenario where injecting the auxiliary sorbent at a higher elevation would be more efficient, as the main sorbent would be able to capture a larger share of CO_2 despite the carbonation of the auxiliary sorbent being limited.

4. Conclusion

A method to increase the carbon capture efficiency of a calcium looping process was studied using interconnected 1.5D reactor models. The results show that sufficient contact time is needed between the $Ca(OH)_2$ and flue gases for efficient CO_2 capture. They also suggest that the $Ca(OH)_2$ injection can suppress the carbonation of the main sorbent, and while this had a negligible effect on the overall carbon capture efficiency under the conditions examined, the effect could be more significant under full load conditions. Overall, the simulation results support the feasibility of the configuration studied and suggest that carbon capture efficiencies as high as 99 % could be reached under the right conditions, although the limitations of the study must be acknowledged. There is little experimental data available on the kinetics of $Ca(OH)_2$ under the conditions studied, i.e., at temperatures close to 550°C and CO_2 concentrations close to equilibrium, and the hydrodynamic interactions between the main and auxiliary sorbents have not been studied in detail. Additionally, while the model assumes perfectly mixed control volumes, achieving sufficient dispersion of the auxiliary sorbent in the radial direction could pose a practical challenge, especially in large-scale units. A better understanding of the behaviour of $Ca(OH)_2$ under CFB conditions will be reached once data from upcoming experimental campaigns becomes available, allowing the model to be properly validated and calibrated.

Disclaimer

References

Abanades, J. C. et al. Emerging CO2 capture systems. International Journal of Greenhouse Gas Control. 2015. 40, 126-166.

Arias, B., Criado, Y., Paneda, B. et al. Carbonation kinetics of $Ca(OH)_2$ under conditions of entrained reactors to capture CO_2. Industrial & Engineering Chemistry Research. 2022. 61, 3272-3277.

Arias, B., Diego, M., Criado, Y. et al. Advanced CO2 capture systems based on Calcium Looping for deep decarbonization of flue gases. GHGT-16. 2022.

CaLby2030. Decarbonising industrial processes with Calcium Looping. 2022. [Online] Available at: https://www.calby2030.eu/ [Accessed 7 November 2023].

Criado, Y. A., Arias, B. & Abanades, J. C. Effect of the carbonation temperature on the CO_2 carrying capacity of CaO. Ind. Eng. Chem. Res. 2018. 57, 12595-12599.

Diego, M. & Arias, B. Impact of load changes on the carbonator reactor of a 1.7 MWth calcium looping pilot plant. Fuel Processing Technology. 2020. 200, 106307.

Dieter, H., Hawthorne, C., Zieba, M. et al., G. Progress in Calcium Looping Post Combustion CO2 capture: Successful Pilot Scale Demonstration. GHGT-11. 2013. 48-56.

Fang, F., Li, Z.-S. & Cai, N.-S. Experiment and modeling of CO_2 capture from flue gases at high temperature in a fluidized bed eactor with Ca-sorbents. Energy & Fuels. 2009. 23, 207-216.

FCCC. First global stocktake. 2023. UAE: FCCC.

Grasa, G., Murillo, R., Alonso, M. et al. Application of the random pore model to the carbonation cyclic reaction. AIChE Journal. 2009. 55, 1246-1255.

Johnsson, F. & Leckner, B. Vertical distribution of solids in a CFB-furnace. Fluidized Bed Combustion. 1995. 1, 671-679.

Koga, N. & Kodani, S. Thermally induced carbonation of $Ca(OH)_2$ in a CO_2 atmosphere: kinetic simulation of overlapping mass-loss and mass-gain processes in a solid-gas system. Phys. Chem. Chem. Phys. 2018. 20, 26173-26189.

Martínez, I., Grasa, G., Murillo, R. et al. Kinetics of calcination of partially carbonated particles in a Ca-looping system for CO_2 capture. Energy & Fuels. 2012. 26, 1432-1440.

Ritvanen, J., Myöhänen, K., Pitkäoja, A. et al. Modeling of industrial-scale sorption enhanced gasification process: One-dimensional simulations for the operation of coupled reactor system. Energy. 2021. 226, 120387.

Shimizu, T., Hirama T., Hosoda, H. et al. A twin fluid-bed reactor for removal of CO_2 from combustion processes. Trans IChemE. 1999. 77, 62-68.

Stanmore, B. & Gilot, P. Review - calcination and carbonation of limestone during cycling for CO_2 sequestration. Fuel Processing Technology. 2005. 86, 1707-1743.

Ylätalo, J., Ritvanen, J., Arias, B. et al. 1-Dimensional modelling and simulation of the calcium looping process. International Journal of Greenhouse Gas Control. 2012. 9, 130-135.

CALCIUM LOOPING TO DECARBONIZE CO$_2$-INTENSE INDUSTRIES WITH ADDED REVENUE STREAMS

Martin Haaf*[1], Ari Kettunen[2], Edgardo Coda Zabetta[2]

[1]Sumitomo SHI FW Energia Oy (SFW), Metsänneidonkuja 10, 02130 Espoo, Finland

[2]Sumitomo SHI FW Energia Oy (SFW), Relanderinkatu 2, 78200 Varkaus, Finland

*Email: martin.haaf@shi-g.com

Abstract

Calcium Looping (CaL) is a competitive carbon capture (CC) technology due to the inherently efficient process combined with its offsetting revenue streams such as additional heat and/or power as well as calcined lime. CaL technology can be applied to virtually all carbon-intensive industries, including heat & power, cement plants as well as current and future iron- & steelmaking processes. Sumitomo SHI FW (SFW) is a global provider of solutions and services that drive the decarbonization of several industries. SFW has developed CC solutions since the late 2000s, including the CaL technology based on circulating fluidized beds (CFB). Now, we are extending the technology development to new applications, and we target commercial demonstration of SFW CaL+ with partnering customers for 2025-2027 (depending on the application case). In this conference we will outline and discuss the status of SFW CaL+ product development, related piloting and demonstration activities as well as the pathway towards commercialization of the technology.

1. Introduction

According to the Intergovernmental Panel on Climate Change (IPCC), Carbon capture (CC) is an unavoidable climate mitigation tool to reach Net-Zero emissions by 2050. The accelerated deployment of CC projects by 2030 is essential in reaching that target. The market for CC solutions is promoted by several factors, including financial and technological aspects. In the first phase of market development the focus is on capturing CO$_2$ emissions from existing power and industrial plants, with over 85 % of all CO$_2$ emissions captured during this decade from existing plants retrofitted with CO$_2$ capture equipment. Of particular interest are the steel and cement sectors, which along with the chemical sector, emit ~ 60% of all global industrial CO$_2$ emissions (IPCC, 2023).

Irrespective of the selected technology, all CC solutions add costs due to reasons such as additional equipment, additional energy to operate, and added burdens related to the storage and/or utilization of the captured CO$_2$. Independent estimates suggest that the most cost-effective CC technologies, including calcium looping (CaL) based on circulating fluidized beds (CFB), could capture CO$_2$ from industrial sources for less than 60 EUR/t$_{CO2}$. This figure could be reduced even further to below 40 EUR/t$_{CO2}$ if offsetting revenues are considered along with utilization of synergy effects, and optimized process integration. The CaL process requires oxygen, often considered to be supplied by a cryogenic air separation unit (ASU). In the current market, the oxygen could be supplied from the ever-growing fleet of electrolyser instead. Furthermore, the CaL process is in fact a net energy generator, thus enabling revenues via the sales of additional heat and/or power.

2. Calcium Looping Process Fundamentals

The CaL process decarbonizes flue gas (FG) by means of cyclic carbonation/calcination (see Eq. 1) of a Ca-based sorbent, e.g., natural, non-toxic limestone. The process fundamentals are shown in Figure 1. Accordingly, the circulating sorbent is exposed to cyclic carbonation-calcination conditions within carbonator and calciner, whereby CO$_2$ is separated from an FG stream and made available as a highly CO$_2$-enriched product gas. Typically, a CO$_2$ processing

unit (CPU) is needed for purification, compression and/or liquification of the CO_2 product gas according to the requirements set by the targeted CO_2 use/storage/transportation strategy.
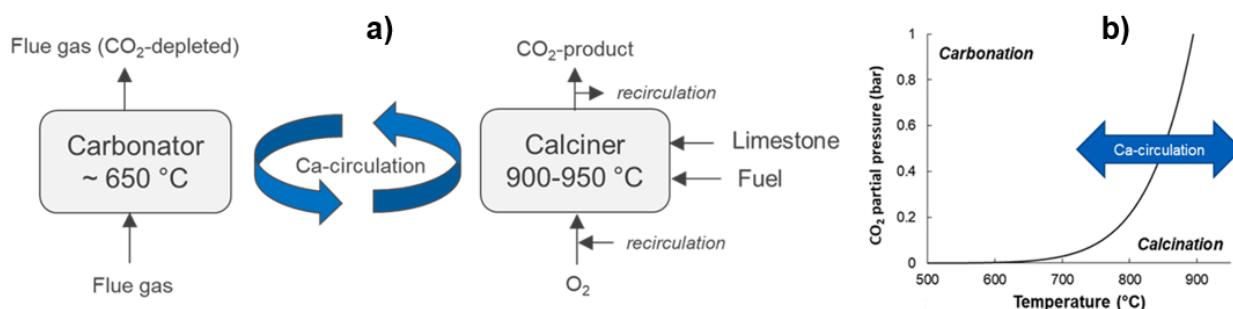
Figure 1: CaL process fundamentals (a: Simplified process scheme, b: Carbonation-calcination equilibrium partial pressure of CO_2).

The heat required to run the CaL process is supplied via oxyfuel combustion in the CFB calciner. Thereby, the inherent fuel flexibility of CFBs allows for the utilization of various fuel candidates, including sustainably sourced bio-residues and/or waste-derived fuels. The oxygen can be provided either by an ASU or as by-product from electrolysers.

$$CaO_{(s)} + CO_{2(g)} \leftrightarrow CaCO_{3(s)} \tag{1}$$

To maintain the CO_2 absorption capacity of the sorbent, and to compensate for the loss of fine sorbent from the circulation loop, a continuous stream of fresh limestone make-up is fed to the process. Deactivated sorbent and fuel ashes, often referred to as "CaL purge", are continuously discharged from the CaL process. As both reactors (carbonator and calciner) operate at relatively high temperature levels (~ 650 & 900 °C), the process excess heat can be efficiently recovered via a water/steam cycle. Alternatively, if suitable high-temperature heat sinks exist in the proximity of the CaL unit, direct heat integration scenarios can be implemented.

2. Calcium Looping Applications and Integration Synergies

The CaL process according to its basic process scheme (Fig. 1), is a multiproduct technology. In addition to the CO_2 captured from the industrial source, the process supplies additional process heat and/or power as well as calcined lime which represents a feedstock for clinker/cement manufacturing or other lime-based industries. Moreover, co-capture capabilities of acid gases within the CFB carbonator could potentially replace FG cleaning equipment within the host process. The high-temperature process heat from the CaL dual-CFB system is available at different process locations within carbonator and calciner. This allows to partially decouple the process sections that are most exposed to fuel impurities and the locations where high temperature heat is transferred. Moreover, the classical CFB combustion process has proven its dynamic flexibility in commercial installations which makes CFB-CaL also suitable for applications that require a transient flexibility from the CC system. Such requirements are exemplarily known from Electric Arc Furnace (EAF) and Argon Oxygen Decarburization (AOD) processes for the production of iron & steel.

The process concept and its integration approach into the respective host plant represents therefore one means to maximize process performance and synergy effects according to the case specific requirements. SFW CaL+ can be applied for CO_2 capture from point-source CO_2 emissions released from various industrial processes, including for instance cement, iron & steel, biomass fuelled power plants, waste incineration plants. The following section provides an overview on the application and synergies of the CaL process in hard-to-abate industrial sectors for the example of SFW CaL+ for the cement industry.

In 2020, the global production of cement was 4.2 billion tons. This has led to 2.7 billion tons of CO_2 emissions, which equals around 5-8% of global GHG emissions. The CO_2 intensity of

cement production is around 640 kg/t_{cement} (GCCA, 2022). Cement manufacturing is considered as a hard-to-abate sector as most of the CO_2 emissions are process related. More specifically, approximately, 2/3 of total CO_2 emissions originates from the calcination of calcium carbonate as part of limestone, the major substance in the feedstock (raw meal) of cement. Formation of this CO_2 emission portion occurs during the processing from raw meal to clinker, the predecessor of cement.

Among the different technology options to decarbonize cement manufacturing, the CaL process is considered relevant due to the potential process synergies (Plaza, 2020). CaL can make cement plants self-sufficient in power production and turn them into sellers of firm decarbonized electricity even after considering the power consumption of the CaL plant, including carbon processing unit (CPU) and ASU (if applicable). The CaL purge may be either used to increase cement plant production capacity, or to replace limestone in the feedstock, i.e., in the raw meal.

Fig. 2 a) shows the "tail-end" configuration of SFW CaL+ for cement plants. Hereby, the integration level of the CC unit and the host process is low. The use of CaL purge as feedstock for cement manufacturing can be considered to either increase production capacity or the partly decarbonize feedstock via the supply of calcined lime. Operating the cement plant without operating the CO_2 capture system is therefore possible. (de Lena, 2017)

Fig. 2 b) shows the "integrated" configuration of SFW CaL+ for cement plants, according to which the capture of CO_2 via CaL and manufacturing of cement (clinker) are merged into one
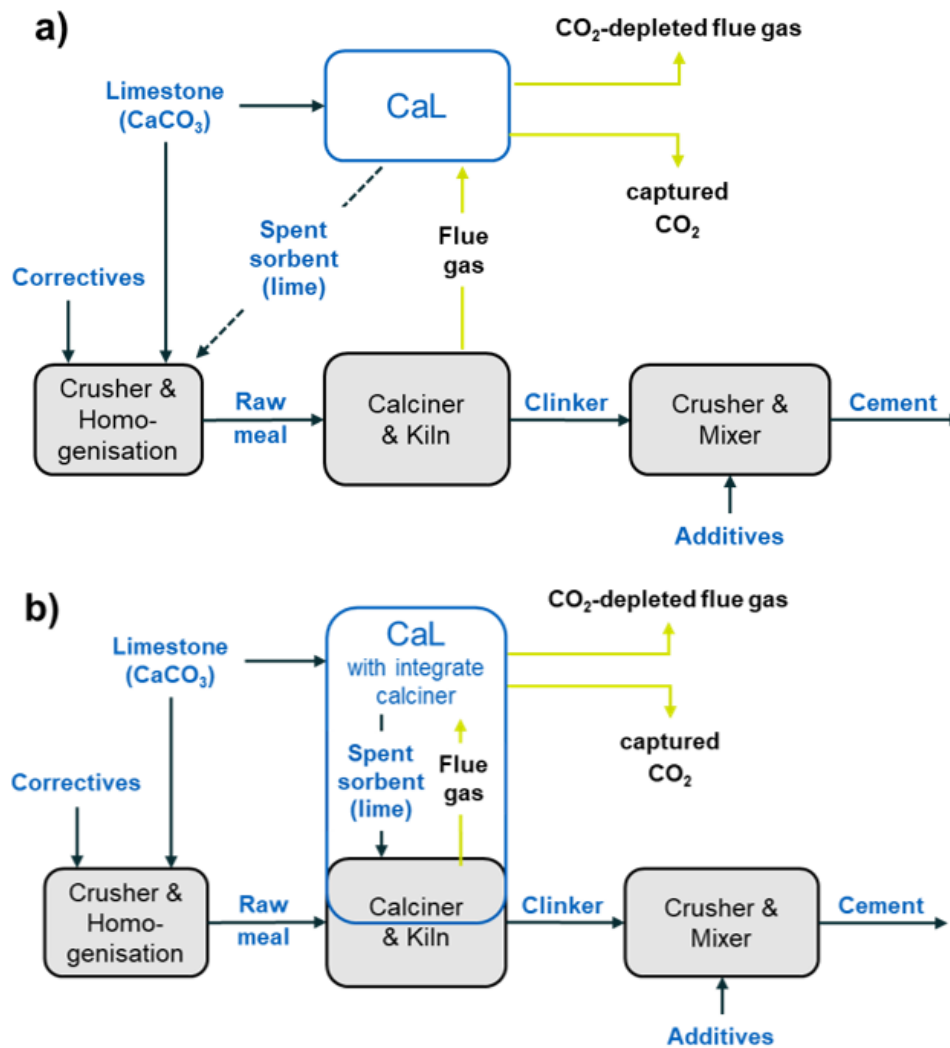
Figure 2. Options to integrated SFW CaL+ into cement production, a) "Tail-end", b) "Integrated".

process via a shared calciner. Thereby, the process synergies are maximized, which leads to a lower footprint of the CaL system along with improved key performance indicators (de Lena, 2022). In case of retrofitting integrated SFW CaL+ to existing assets, the re-use of plant components could be considered to further reduce costs.

A recent estimate showed that for a "tail-end" scenario utilizing low-cost waste-derived fuel in the CaL calciner, the levelized cost of capture can be approximately 30 EUR/t$_{CO2}$, by monetizing only power revenues and even assuming no oxygen synergies in place (SFW, 2023).

3. Roadmap Towards SFW CaL+ Commercialization

Pilot-scale testing and demonstration are vital for the development of novel technologies. SFW has developed CC solutions since the late 2000s, including the CaL technology based on CFBs, developed jointly with CSIC/HUNOSA/ENDESA over the last 10+ years.

The CaL process based on CFBs has been demonstrated already in various pilot plants up to MW-scale, leading to a technology readiness level (TRL) between 6-7, depending on the application scenario in question. As of today, the three most relevant CFB-CaL pilot plants are listed below:

- 200 kW pilot plant at University of Stuttgart, Germany (Hornberger, 2020)

- 1.0 MW pilot plant at Technische Universität Darmstadt, Germany (Haaf, 2020), based on SFW technology

- 1.7 MW plant at La Pereda power plant, Spain (Arias, 2023; Fig. 3), based on SFW technology

Figure 3: "La Pereda" 1.7 MW CaL demonstration plant (La Pereda, Spain).

SFW recently joined forces with partnering organizations in the frame of two EU-funded research projects (CaLby2030 and HERCCULES) to bring the CFB-CaL technology towards commercialization (CaLby2030, 2022; HERCCULES, 2023). Both projects directly support SFW`s roadmap for commercialization of SFW CaL+ within the coming years. Focus lies on the development and demonstration of the CaL process for hard-to-abate sectors, namely cement, iron & steel, biomass combined heat and power (BioCHP) as well as waste-to-energy (WtE). As part of these two projects, two new CFB-CaL pilot plants are designed by SFW,

which will be erected and tested. The new pilot plants will be specifically designed to demonstrate the CaL process under the conditions relevant for iron & steel industrial sectors (Kettunen, 2024) and WtE (HERCCULES, 2023). Moreover, the existing pilots in Stuttgart and La Pereda will be upgraded for conditions relevant to cement and Bio-CHP applications.

In addition to the extensive test program in the TRL 6-7 pilot plants as listed above, SFW is exploiting its vast in-house expertise, dimensioning tools and databases generated from more than 850 commercial FB combustors and gasifiers, totaling over 40 GW_e of installed power capacity (SFW, 2024). As an example of such expertise, Fig 4 shows the SFW Biomass CFB evolution, from 0.5 MW pilot-scale up to 300 MW_e CFB size class.
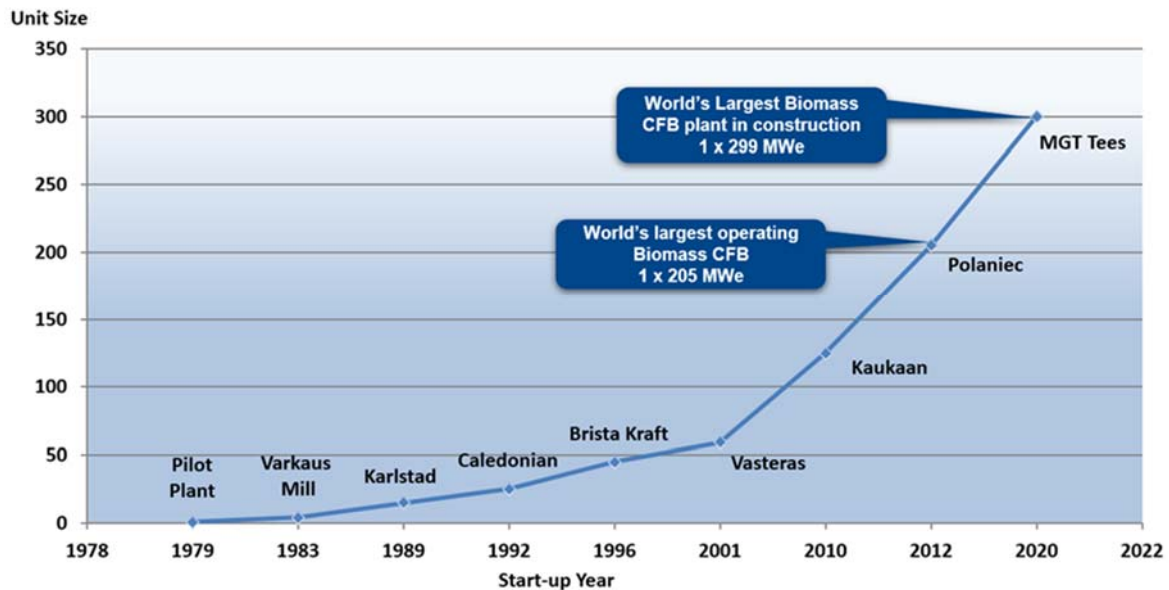
Figure 4: SFW Biomass CFB evolution (unit size in MW_e).

Further acceleration in SFW CaL+ technology demonstration is related to similarities in the mode of combustion within the CaL calciner. SFW demonstrated already CFB oxyfuel combustion in 30 MW_{th} during the 2010s at the Fundacion Ciudad de la Energia (CIUDEN, Spain), accumulating thousands of operational hours under various conditions. Based on the demonstration activities, commercial development with partners led to the completion of FEED activities and development of a readily available 300 MW_e CFB Oxyfuel power plant design (Eriksson, 2013). Now, those experiences allow us to upscale more rapidly the SFW CaL+ technology, since in both processes (CaL calciner, oxyfuel boiler) the fuel is combusted in a CFB oxyfuel environment.

4. Conclusion

The implementation of CC technologies as a climate mitigation tool is required to reach Net-Zero emissions by 2050. The accelerated deployment of CC projects by 2030, is essential in reaching that target. Sumitomo SHI FW (SFW) – as a technology forerunner – is currently expanding the SFW CaL+ technology demonstration to new applications, including Bio-CHP, WtE, cement and steel. Such demonstration is due in relevant industrial environments, in collaboration with commercial partners, and targeting commercial readiness in 2025-2027, depending on the application.

Acknowledgment

References

Arias B., Haaf M., Magdeldin M., Coda Zabetta E., Diego M.E., Lorenzo M.; DelaLlera E., Abanades J.C.; Calcium looping using CFB technology to achieve negative emissions in biomass-fired power plants. 31st European Biomass Conference & Exhibition. EUBCE 2023, 5-8 June, Bologna, Italy.

De Lena, E., Spinelli, M., Martínez I., Gatti, M., Scaccabarozzi, R., Cinti, G., Romano M.C. Process integration study of tail-end Ca-Looping process for CO_2 capture in cement plants. International Journal of Greenhouse Gas Control. 2017. 67. 71-92.

De Lena, E., Arias, B., C. Romano, M., Abanades, C. Integrated Calcium Looping System with Circulating Fluidized Bed Reactors for Low CO_2 Emission Cement Plants. International Journal of Greenhouse Gas Control. 2022. 114. 103555.

CaLby2030. https://www.calby2030.eu/. Calcium Looping to Capture CO_2 from Industrial Processes by 2030. Accessed on 06/03/2024.

Eriksson T., Gutierrez Cerezales P., Development of Flexi-Burn® CFB boiler concept for Oxy-CFB-300 Compostilla project, 3rd International Oxyfuel Combustion Conference, Ponferrada (Spain), September 9-13, 2013.

GCCA. Global Cement and Concrete Association. Concrete Future - The GCCA 2050 Cement and Concrete Industry Roadmap for Net Zero Concrete.

Haaf, M., Hilz, J., Peters, J., Unger, A., Ströhle, J., Epple, B. Operation of a 1 MW_{th} Calcium Looping Pilot Plant Firing Waste-Derived Fuels in the Calciner. Powder Technology. 2020. 372, 267-274.

HERCCULES. https://www.herccules.eu/. HERCCULES: Heroes in southern Europe to decarbonize industry with CCUS. Accessed on 06/03/2024.

Hornberger, M., Moreno, J., Schmid, M., Scheffknecht, G. Experimental investigation of the carbonation reactor in a tail-end Calcium Looping configuration for CO_2 capture from cement plants. Fuel Processing Technology. 2020. 210.

IPCC, 2023: Climate Change 2023: Synthesis Report. Contribution of Working Groups I, II and III to the Sixth Assessment Report of the Intergovernmental Panel on Climate Change. IPCC, Geneva, Switzerland, pp. 35-115, doi: 10.59327/IPCC/AR6-9789291691647.

Kettunen, A., Haaf, M., Blomqvist, M., Lundqvist, Anetjärvi, E., Ritvanen, J. A Dynamically Operated Dual CFB CaL Tailored for Carbon Capture of Future Iron & Steel Industries - Development and Model Investigation. 14th International Conference on Fluidized Bed Technology (CFB-14), 21-24 July 2024, Taiyuan, China.

Plaza, G., M., Martinez, S., Rubiera, F. CO_2 Capture, Use, and Storage in the Cement Industry: State of the Art and Expectations. Energies 2020, 13(21), 5692.

Sumitomo SHI FW (SFW), 2023. https://www.shi-fw.com/insights/articles/cementing-the-path-to-net-zero-solutions-for-reducing-the-carbon-footprint-of-concrete-production/. Cementing the path to Net Zero: Solutions for reducing the carbon footprint of concrete production. Accessed on 06/03/2024.

Sumitomo SHI FW (SFW), 2024. https://www.shi-fw.com/. Accessed on 25/03/2024.

A DYNAMICALLY OPERATED DUAL CFB C$_A$L TAILORED FOR CARBON CAPTURE OF FUTURE IRON & STEEL INDUSTRIES - DEVELOPMENT AND MODEL INVESTIGATION

Ari Kettunen[1]*, Martin Haaf[1], Malin Blomqvist[2], Magnus Lundqvist[2], Eemeli Anetjärvi[3], Jouni Ritvanen[3]

[1]*Sumitomo SHI FW Energia Oy, Relanderinkatu 201, FI-78201 Varkaus, Finland*

[2]*Swerim AB, Aronstorpsvägen 1, 974 37 Luleå, Sweden*

[3]*Lappeenranta-Lahti University of Technology LUT, LUT School of Energy Systems,*

P.O. Box 20, FI-53851 Lappeenranta, Finland

* ari.kettunen@shi-g.com

Abstract

Instances necessitating the limitation of global warming to a 1.5 °C temperature increase mandate the deployment of carbon dioxide removal technologies [1]. The steel industry presents a formidable challenge due to its substantial global contribution to greenhouse gas emissions [2]. The complexity of emissions abatement in this sector is compounded by the batch-oriented nature of the steelmaking process and the inherent variability in both flue gas flow rates and properties, which make efficient carbon capture via existing technologies challenging.

Sumitomo SHI FW (SFW) continues its pioneering efforts for the development of carbon capture technologies together with core partners. The special focus of this study is the adaptation of the well-known calcium looping process (CaL) to capture CO_2 from the steelmaking industry, which is a novel application. This study shows the fundamental stages of steel production and identifies the predominant greenhouse gas emission sources associated with it. Furthermore, it presents the steel case-specific conceptual aspects of the CaL pilot facility, which is under engineering phase and will be used for the demonstration of CO_2 capture in steelmaking. Additionally, the study provides modelling principles regarding a 1.5D dynamic simulation tool and offers preliminary simulation results relating to the time-dependent operation of the CFB-CaL process.

The simulations confirm that the dynamic nature of flue gas originating from the steel production process introduces additional complexities in managing the operation of the CaL system. Owing to the interdependence of material and heat capacity flows, specific design solutions are needed to provide sufficient operational flexibility and particular attention is necessary for developing the control strategies.

1. Introduction

Despite recent reductions in the CO_2 intensity of crude steel production, the iron and steel industry remains a significant contributor to global greenhouse gas (GHG) emissions, accounting for 7% of total emissions and up to 11% of global CO_2 emissions [2]. Each ton of steel produced emits between 1.4 to 1.85 tons of CO_2, emphasizing the pressing need for accelerated efforts to embrace low-carbon alternatives and implement energy-efficient CO_2 capture technologies.

The CFB-CaL process has been largely investigated for several years and found to be one of the most suitable carbon capture (CC) technologies for different CO_2-intensive processes. Fluctuating properties of gases emitted from the iron/steel making processes are calling extreme transient flexibility from the CC technology. The CFB combustion process has proven its dynamic flexibility in energy production. Hence, CFB-CaL is expected to be well applicable also for the integration with batch-type steel-making processes. In this work, a first-of-a-kind CaL pilot facility with high operational flexibility is designed in collaboration between SFW and SWERIM. The pilot will be connected to the steel mill, and the performance of the capture technology will be demonstrated with fluctuating exhaust gas properties, like CO_2 concentration, gas flow rate, temperature and impurities.

SFW has developed comprehensive dynamic models for the CFB processes in collaboration with LUT over 15 years. Those models are adapted for the CFB CaL processes by LUT and are utilized in this work to investigate the process's dynamic characteristics and to develop advanced control concepts that provide high CO_2 capture efficiency in all operating conditions.

2. CO_2 emissions from steel making processes

The adoption of hydrogen-based Direct Reduced Iron (DRI) stands as a promising alternative to the traditional Blast Furnace - Basic Oxygen Furnace (BF-BOF) method, representing a significant advancement in reducing CO_2 emissions from steel production. Even natural gas-based DRI presents a more favorable environmental impact compared to conventional methods. However, the transition to DRI processes involves production units like the Electric Arc Furnace (EAF) and converters such as Argon Oxygen Decarburization (AOD), which brings forth new challenges, as these methods become the primary melting routes for steel. EAF is currently the predominant route for recycled steel and represents 23% of global steel production with specific emissions between 0.2-0.5 tons of CO_2 per ton of steel. It is anticipated that by 2050, the EAF's market share will expand, driven by both increased recycling efforts and augmented DRI production.

The treatment of off-gases from EAFs and AODs poses significant challenges for conventional CO_2 capture technologies due to their highly variable nature. These gases are intermittent and dynamic, containing a high concentration of small particles and pollutants such as sulfur and chlorine components. Moreover, the gas exhibits both oxidizing and reducing properties, complicating its handling and imposing stringent demands on the material properties of potential gas-cleaning systems.

Many EAF and AOD systems currently incorporate suction-operated hoods positioned above the furnace, designed to draw all emitted gases into a gas duct. However, these hoods typically remain open to the atmosphere, allowing for the intake of false air. While this setup facilitates post-combustion of residual CO and H_2 and results in rapid gas cooling, it poses challenges from a CO_2 capture perspective by diluting the CO_2 concentration. Current gas treatment methods for EAF and AOD off-gases primarily involve thermal recovery mechanisms, such as steam production or pre-heating of solid material fed into the furnace, followed by dust removal.

For the effective implementation of a suitable CO_2 capture system to treat variable off-gases, especially those emitted by EAF and AOD processes, a comprehensive understanding of gas behavior is essential. This understanding facilitates the accurate adaption of models to typical

off-gas parameters. Figure 1 illustrates the CO_2 concentration profile, flow rate and temperature of EAF off-gases, while a corresponding depiction for AOD off-gases is provided in Figure 2.
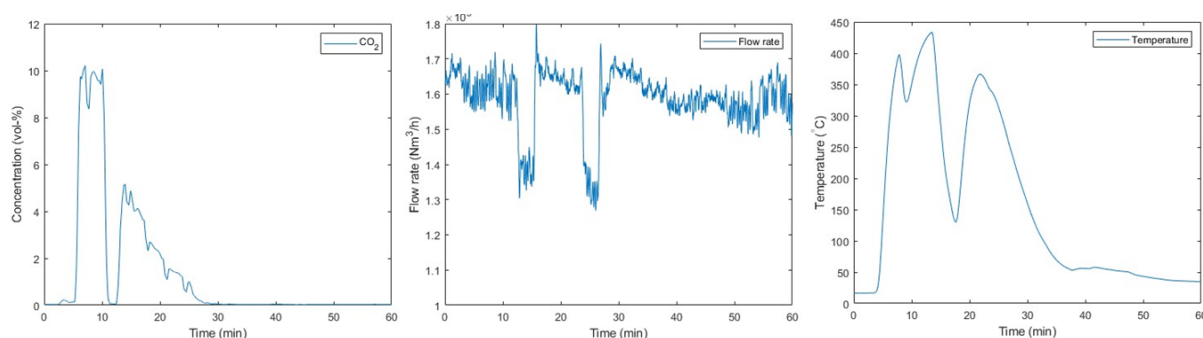
Figure 1. CO_2-concentration, flow rate and temperature of an AOD converter.
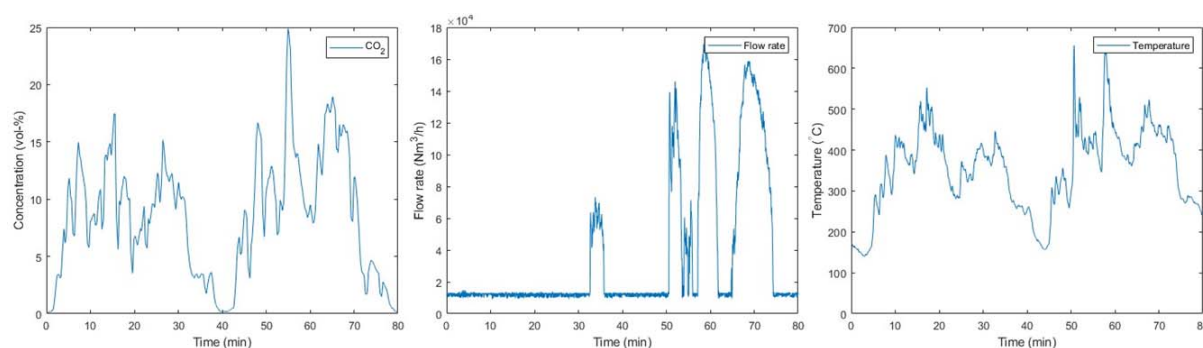
Figure 2. CO_2-concentration, flow rate and temperature of an EAF.

3. CaL pilot facility

SFW together with SWERIM is designing a first-of-a-kind CaL pilot facility to be integrated into the steel mill using EAF and AOD technology. The pilot facility will be located in Luleå, Sweden and is targeted to handle up to 250 nm^3/s of metallurgical gas including max. 10.5% of CO_2. The facility is under detailed engineering. Commissioning and testing activities are scheduled to be started in 2025.

The CaL test facility utilizes two interconnected Circulating Fluidized Bed (CFB) reactors, the carbonator and the calciner (Figure 3). Both reactor systems consist of typical CFB components and are designed based on proven commercial-scale CFB hot loop guidelines providing robust and flexible operation with various operating conditions and full scalability from pilot to commercial scale. In the carbonator, adjustable water-cooled bayonet tubes are used for the reactor temperature control according to testing needs. Heating of the calciner is provided via air combustion mode with gas (propane) which can be fed into the reactor optionally at different elevations. The test facility will be equipped with a comprehensive set of measuring ports for temperatures, pressures, and gas compositions as well as specific sampling ports for various solid materials. Key design parameters of the pilot facility are presented in Table 1.

To achieve best CO_2 capture throughout the dynamic changes in the flue gas, the CaL test facility will include sorbent storage system and controllable wall seals. As for the controllable wall seals, those will be adopted in the return leg of both calciner and carbonator. In such wall seals, fluidizing gas is used to control the material flow between the loop seal main and by-pass lines. i.e., the internal and external material flow between reactors. This is expected to provide optimal dual reactor operation even in fast transient situations.

Further, the flue gas feeding line into the carbonator will be equipped with an additional feeding system to simulate different scenarios of flue gas dust content and composition coming along with steel making exhaust gases.
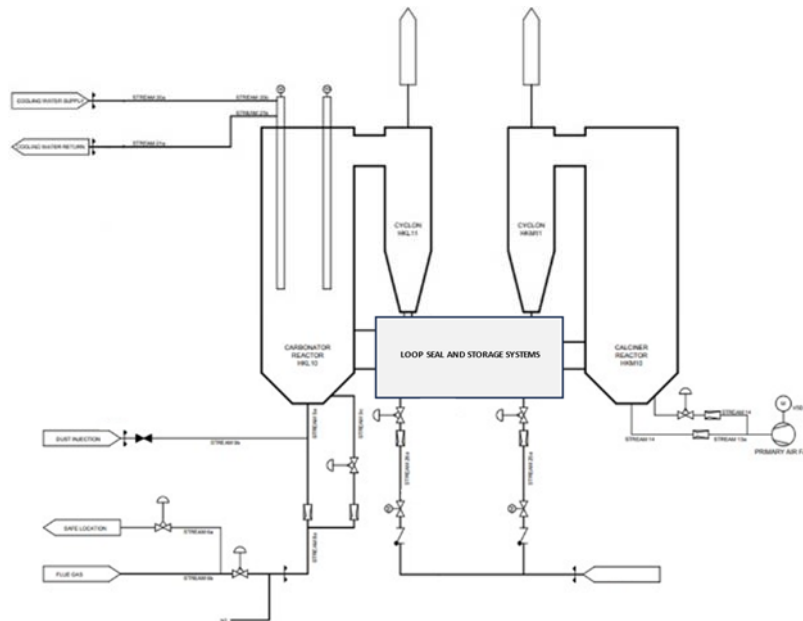
Figure 3. CaL pilot facility.

Table 1. Technical data of carbonator and calciner.

	Carbonator	Calciner
Reactor inner diameter (m)	0,32	0,37
Reactor height (m)	10,0	10,0
Design Temperature (ºC)	650	900
Gas analysis at the reactor outlet	O_2, CO_2, CO, NO_x, SO_2, H_2O	O_2, CO_2, CO, NO_x, SO_2, H_2O
Temperature and pressure measurements	At different reactor elevations, the reactor outlet and wall seal	At different reactor elevations, the reactor outlet and wall seal

4. Model investigation

4.1 Dynamic model

A time-dependent 1.5D simulation tool (Figure 4) was used to characterize the dynamics of the CaL process and to evaluate the effect of fluctuating flue gas properties on the operation of the CaL process. The simulation tool includes reactor models discretized into 1D control volumes, including mixing due to wall layer flow. The model includes time-dependent mass and energy balances, as well as the necessary closure equations for CFB hydrodynamics, heat transfer, and homogeneous and heterogeneous reactions [4]. Utilizing published test data [5], the simulation tool has been validated in the suitable operational range.
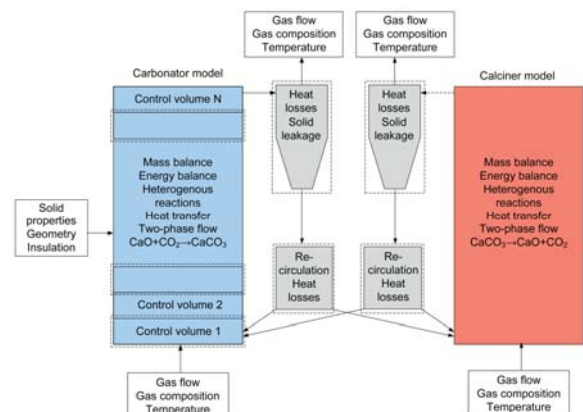
Figure 4. 1-D dynamic model frame for the calcium looping process [6].

4.2 Simulations and discussion

A model-based investigation of the process was performed for a pilot-scale CaL device [3] with reactor heights of 15 m, and carbonator and calciner diameters of 0.65 m and 0.75 m, respectively. Fluctuating flue gas flow from the steel process was simulated by varying the properties of the gas flow entering the carbonator between air and flue gas. The time series of the change is shown in Figure 5, and the feed properties are in Table 2. The simulation case is started by feeding air to the carbonator, and after 10 minutes, the conditions are linearly changed to flue gas within 1 minute, which is kept constant for 10 minutes. During the next 20 minutes, the conditions are linearly changed back to the air, and at the end, another 40-minute period is simulated using air. Fuel feeding, makeup flow of fresh limestone and air primary gas feed were kept constant, corresponding to the values of 1.7MW$_{th}$ input, 0.022 kg/s and 0.5 kg/s, respectively.
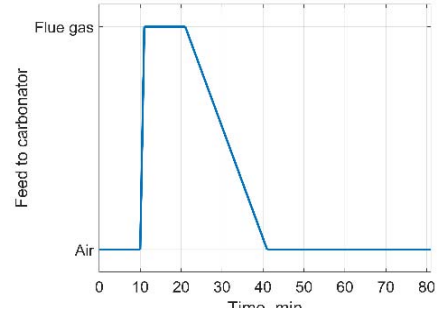
Figure 5. Time-series for the carbonator feed.

Table 2. Properties of air and flue gas feed to the carbonator.

	Feed [kg/s]	O_2 [m-%]	N_2 [m-%]	CO_2 [m-%]	H_2O [m-%]	T [°C]
Air	0.54	20.0	69.0	0.0	11.0	100
Flue gas	0.54	6.3	72.7	10.0	11.0	100 - 350

The simulated carbonator outlet temperatures versus time are shown in Figure 6a. The results show significant changes in temperature levels which are caused by the increased inlet gas temperature and by the carbonation reaction heat. Too high temperature weakens lime reaction rates as the conditions deteriorate in relation to the reaction equilibrium of the carbonation reaction (Figure 6b). The higher is the carbonator temperature increase the lower remains the CaCO3 content of the bed material entering to the calciner (Figure 6c), indicating relative decrease in CO_2 capture efficiency. These simulations show the requirement to find ways to prevent the carbonator temperature from rising as the CO_2 concentration and temperature of the flue gas stream increase.
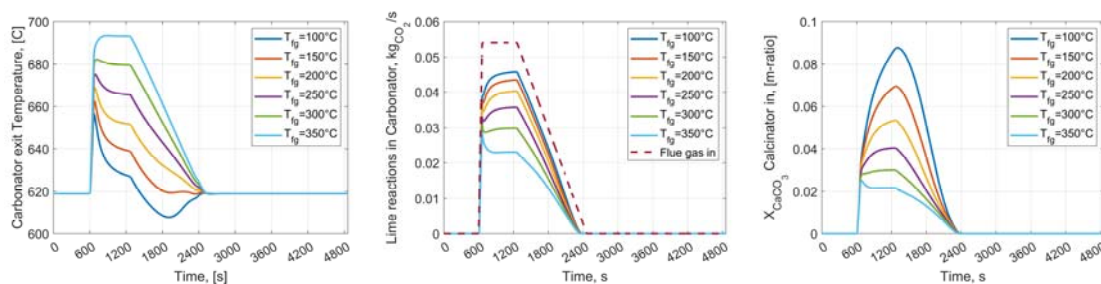
Figure 6. a) Carbonator exit temperatures, b) Lime reaction rates in the Carbonator and c) Bed material CaCO$_3$ content entering the calciner.

The storage system combined with the controllable wall seals bring extra flexibility for the CFB-CAL process. With these solutions, the reactor operations can be partially decoupled meaning that the calciner system (including ASU and CPU) can be dimensioned for the smaller capacity and hence the CAPEX and OPEX of the overall CaL system can be reduced [7]. Further, the calciner operation is not disturbed drastically during fast transients on the carbonator side which makes the calciner control easier. The CaL process provides good options for the

calciner temperature control by the fuel feed, as well as by using the possible recycling of solids through internal circulation via controllable wall seals.

5. Conclusions

Dynamics simulations done in this work indicates that the intermittent steel mill gases have remarkable effects on the carbonator behavior. The CFB-CaL process with novel solutions has superior dynamic flexibility and hence it will have good potential for the carbon capture from fluctuating exhaust gases. Dynamic performance of the CaL process will be further studied by dynamic simulations as well as demonstrated in a first of a kind pilot facility which is under designing and will be commissioned during 2025. Obtained data from the process simulations combined with test data from the pilot will provide a sound basis for the scale-up of the CaL technology for the decarbonization of the steel industry.

References

[1] IPCC, Summary for Policymakers. In: Global warming of 1.5 °C, (2018).

[2] Our World in Data. https://ourworldindata.org/emissions-by-sector, (2020).

[3] Arias, B., Diego, M.E., Abanades, J.C., Lorenzo, M., Diaz, L., Martínez, D., Alvarez, J. and Sánchez-Biezma, A., Demonstration of steady state CO2 capture in a 1.7MWth calcium looping pilot. International Journal of Greenhouse Gas Control. (2013). 18, 237-245.

[4] Ylätalo, J., Ritvanen, J., Arias, B., Tynjälä, T. and Hyppänen, T. 1-Dimensional modelling and simulation of the calcium looping process. International Journal of Greenhouse Gas Control. (2012). 9, 130-135.

[5] Diego, M. and Arias, B. Impact of load changes on the carbonator reactor of a 1.7 MWth calcium looping pilot plant. Fuel Processing Technology. (2020). 200, 106307.

[6] Ylätalo, J., Parkkinen, J., Ritvanen, J., Tynjälä, T. and Hyppänen, T. Modeling of the oxy-combustion calciner in the post-combustion calcium looping process. Fuel. (2013). 113, 770-779.

[7] Astolfi, M., De Lena, E., Casella, F. and Romano, M.C. Calcium looping for power generation with CO_2 capture: The potential of sorbent storage for improved economic performance and flexibility. Applied Thermal Engineering. (2021). 194, 117048.

Reaction Characteristics Between Modified Perovskite Oxygen Carrier and Methane Measured Using Micro-fluidized Bed Thermogravimetric Analysis Coupled with Mass Spectrometer

Yang Wang, Qiran Geng, Dan Li, Zhenshan Li*

Key Laboratory for Thermal Science and Power Engineering of Ministry of Education, Department of Energy and Power Engineering, Tsinghua University, Beijing 100084, China

E-mail: lizs@mail.tsinghua.edu.cn

Abstract

Perovskite oxygen carrier ($CaMn_{0.5}Ti_{0.375}Fe_{0.125}O_{3-\delta}$, CMTF) is an excellent oxygen carrier, which has been prepared on an industrial scale. It exhibits good reactivity with H_2, CO, and O_2. However, its reactivity with CH_4 is relatively low. In this study, CMTF oxygen carrier was modified through impregnation with NiO. The modified CMTF oxygen carriers were tested using micro-fluidized bed thermogravimetric analysis coupled with mass spectrometer. It can measure both the mass change signal of the oxygen carrier sample in the fluidization state and the gas product concentration signal simultaneously in real-time. Moreover, steam can be introduced into the reactor to investigate its effect on the performance of oxygen carriers. It was observed that impregnating with NiO can significantly enhance the reactivity of CMTF oxygen carrier with CH_4 but the catalytic effect of NiO led to severe carbon deposition. For both the modified CMTF oxygen carriers impregnated 7.5 wt.% and 1 wt.% NiO, in the absence of steam, complete oxidation of CH_4 occurred in the early stage of the reaction and partial oxidation of CH_4 took place when the mass change rate of the oxygen carrier reached half of its minimum value. Steam can effectively inhibit carbon deposition. The CMTF oxygen carrier impregnated with 1 wt.% NiO can be fully reduced in 75 s at 900 °C and the main gas product was CO_2.

1. Introduction

Chemical looping combustion (CLC) is a highly promising carbon capture technology, characterized by inherent CO_2 separation and low energy consumption[1]. Generally, a CLC unit mainly consists of three parts: air reactor, fuel reactor, and oxygen carrier. The oxygen carrier is oxidized in the air reactor while reduced in the fuel reactor[2]. It circulates between the air reactor and the fuel reactor, playing a role in the transfer of lattice oxygen and heat. Therefore, the oxygen carrier is a key material in CLC.

CLC technology has reached TRL-6, undergoing MW_{th}-scale pilot demonstrations[3]. Consequently, the required oxygen carrier for CLC units has reached a scale of tons. Liu et al.[4] developed a perovskite oxygen carrier ($CaMn_{0.5}Ti_{0.375}Fe_{0.125}O_{3-\delta}$) using industrial spray drying granulation. It exhibits high lattice oxygen transport capacity, stable reactivity, and resistance to agglomeration. Using micro-fluidized bed thermogravimetric analysis (MFB-TGA) to measure the redox kinetics of the oxygen carrier, it is found that it has excellent reactivity with H_2, CO, and O_2. However, its reactivity with CH_4 is relatively poor, achieving only 80% conversion in 300 s. Numerous researchers have discovered that Ni-based oxygen carriers exhibit good reactivity and catalytic performance towards CH_4[5-7]. Yang et al.[6] found that Ni can lower the energy barrier for CH_4 activation via DFT calculation. Chen et al.[7] investigated the effect of different Ni doping on the performance of Fe-based oxygen carriers using a fixed-bed reactor. It indicated that doping with 2 % Ni can significantly enhance the reactivity of Fe-based oxygen carriers with CH_4.

For the reaction between oxygen carriers and CH_4, the oxidation of CH_4 takes place on the surface of the oxygen carrier and consumes lattice oxygen. It results in a concentration gradient of lattice oxygen between the surface and the bulk phase, driving lattice oxygen to

50 diffuse from the bulk phase to the surface consequently[8]. Reactions of CH_4 occurring on the
51 oxygen carrier surface include complete oxidation of methane, partial oxidation of methane,
52 and catalytic methane decomposition[9]. The consumption of lattice oxygen leads to a decrease
53 in the mass of the oxygen carrier, and different reactions of CH_4 occurring at the surface
54 generate different gaseous products. Therefore, information on the conversion of the oxygen
55 carrier and the gas products should be obtained when investigating the reaction characteristics
56 of the oxygen carrier with CH_4. Micro-fluidized bed (MFB) generally has good heat and mass
57 transfer characteristics, and gas product information can be obtained[10]. However, it is difficult
58 to accurately back-calculate the oxygen carrier conversion from the gas products due to the
59 complexity of the gas products during the reaction between oxygen carriers and CH_4. MFB-
60 TGA also has good heat and mass transfer characteristics, but only oxygen carrier conversion
61 can be obtained, not gas product information[11,12]. Thermogravimetric analyzer coupled with
62 mass spectrometer (TGA-MS) can realize the simultaneous measurement of gas product and
63 oxygen carrier conversion[13]. However, due to the high resistance of heat and mass transfer in
64 TGA, the reaction situation is significantly different from that in the actual CLC reactor[14].

65   In this study, the industrial perovskite oxygen carriers modified with Ni are prepared using
66 the impregnation method. The reaction performance of oxygen carriers impregnated with
67 different Ni ratios towards CH_4 is tested with micro-fluidized bed thermogravimetric analysis
68 coupled with mass spectrometer (MFB-TGA-MS). The effect of the existence of steam on the
69 reaction characteristics is investigated and the reaction kinetics of the best-performing oxygen
70 carrier with CH_4 is measured.

71 **2. Experiment**

72 2.1 Oxygen Carriers

73   Using industrial perovskite oxygen carriers (developed by Liu et al.[4], labeled as CMTF.)
74 and $Ni(NO_3)_2 \cdot 6H_2O$ (Alfa Aesar, AR) as raw materials, modified perovskite oxygen carriers
75 were prepared via the impregnation method. The physical properties of the fresh CMTF are
76 shown in Table 1. The calculated amount of $Ni(NO_3)_2 \cdot 6H_2O$ was dissolved in 50 ml of
77 deionized water, heated in a water bath at 40 °C, and stirred to form a transparent solution.
78 Subsequently, 5 g of CMTF was transferred to the solution. Then, this mixture was heated at
79 80°C and stirred continuously until all the water was completely evaporated. The collected
80 particles were placed in a drying oven for 12 h at 120 °C. The dried particles were then calcined
81 in a muffle furnace under air at 1000 °C for 2 h, with a heating rate of 5 °C/min. After natural
82 cooling, the particles were sieved to obtain a particle size of 160 - 224 μm. The mass ratios of
83 NiO to fresh CMTF were selected to be 1wt.%, 2.5 wt.%, 5 wt.%, and 7.5wt.%, corresponding
84 to the labels of the obtained modified perovskite oxygen carriers as 1Ni@CMTF,
85 2.5Ni@CMTF, 5Ni@CMTF, and 7.5Ni@CMTF.

86
Table 1. Physical properties of the fresh perovskite oxygen carrier.

	BET (m^2/g)	Porosity (%)	True density (kg/m^3)	Particle size (um)
Fresh CMTF	0.15	45	4227	160 - 224

87 2.2 Micro-fluidized Bed Thermogravimetric Analysis Coupled with Mass Spectrometer (MFB-
88 TGA-MS)

89   As shown in Fig. 1., the MFB-TGA-MS mainly consisted of five parts: an electric furnace,
90 a quartz tube reactor, a gas supply system, a measurement system, and a steam generation
91 system. The electric furnace was used to heat the quartz tube reactor. The inner diameter of
92 the quartz tube reactor was 30 mm, and there was a sintered porous quartz plate as the gas
93 distributor inside. For the gas supply system, the gas was introduced from the bottom of the
94 reactor to fluidize the bed material, with its flow rate regulated by the mass flow controllers.
95 Gas switching was controlled using electromagnetic valves. For the measurement system, the
96 mass balance has a capacity of 1200 g with an accuracy of 1 mg, enabling real-time
97 measurement of the overall mass changes of the reactor placed on it. The differential pressure
98 transducer can measure the bed pressure drop inside the reactor, providing a means to
99 monitor the fluidization quality. The K-type thermocouple can measure the temperature inside
100 the reactor and provide feedback to the electric furnace. The mass spectrometer (TILON, LC-

D200M) is a quadrupole mass spectrometer with fast response characteristics, which can measure the concentrations of different components in the reactor exhaust gas. The hygrothermograph was used to measure the temperature and humidity of the fluidizing gas entering the reactor. The steam generation system mainly consisted of a gas washing bottle and a water bath. The temperature of the water bath was set to 30 °C. The fluidizing gas passed through the gas washing bottle and bubbled through the water, carrying steam in the gas stream consequently. According to the results of the hygrothermograph, the gas stream passing through the gas washing bottle is saturated with steam, corresponding to ~ 4.2 vol.% steam. The bypass of the gas washing bottle can control whether steam enters the reactor.
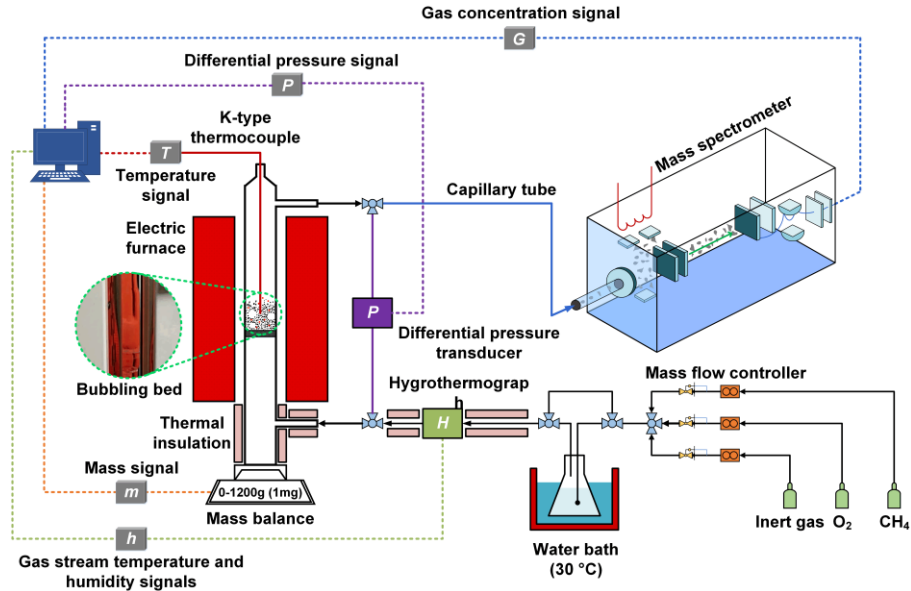
Fig. 1. Schematic diagram of the MFB-TGA-MS.

During the experiment, ~16 g silica sand with a particle size of 300 – 355 μm was added to the reactor as inert bed material. The experimental procedure was as follows: firstly, introduced oxidizing gas into the reactor and heated the reactor to the desired temperature (900/850/800 °C); secondly, added modified perovskite oxygen carriers (400 – 500 mg) to the reactor; thirdly, switched oxidizing gas to inert gas to purge for 5 s and then switched inert gas to reducing gas; finally, switched reducing gas to inert gas for 20 s and then switched inert gas to oxidizing gas to complete a redox cycle. Adding oxygen carriers under an oxidizing atmosphere can prevent oxygen uncoupling. The purpose of introducing inert gas between switching reducing and oxidizing gases was for safety and data stabilization. The flow rate of fluidizing gas was 1 NL/min, corresponding to a fluidization number of 2 – 3. Therefore, the bed material inside the reactor was in a bubbling bed state. To ensure the stability of the mass signal during gas switching, all the fluidizing gases introduced into the reactor had the same density, and the specific compositions were shown in Table 2. Before testing the performance of oxygen carriers, the activation of the oxygen carriers was carried out using 10 vol.% H_2 and 21 vol.% O_2.

Table 2. The detailed gas compositions and densities.

Gas type	Specific composition	Density (kg/m^3, 900 °C)
Inert gas	66.79 vol.% Ar + 33.21 vol.% He	0.2909
Reducing gas	20.00 vol.% CH_4 + 60.09 vol.% Ar + 19.91 vol.% He	0.2909
Reducing gas	15.00 vol.% CH_4 + 61.77 vol.% Ar + 23.23 vol.% He	0.2909
Reducing gas	10.00 vol.% CH_4 + 63.44 vol.% Ar + 26.56 vol.% He	0.2909
Reducing gas	10.00 vol.% H_2 + 21.78 vol.% Ar + 68.22 vol.% N_2	0.2909
Oxidizing gas	21.00 vol.%O_2 + 50.44 vol.% Ar + 28.56 vol.% He	0.2909

2.3 Data evaluation

The relative mass change rate (RMCR) of oxygen carriers was defined as eq. (1)

$$RMCR = \frac{m(t) - m_o}{m_o} \times 100\% \qquad (1)$$

where $m(t)$ is the mass of the oxygen carrier sample added to the reactor at the t moment. m_o refers to the mass of the oxygen carrier sample at the fully oxidized state. The conversion (X) of the oxygen carrier is defined as eq. (2). $R_{O,m}$ refers to the maximum oxygen transport capacity of the oxygen carrier.

$$X = \frac{m_o - m(t)}{m_o R_{O,m}} \qquad (2)$$

3. Results and Discussions

3.1 Performance Characteristics of Modified CMTF Oxygen Carriers

The reaction characteristics of modified CMTF oxygen carriers were tested at 900 °C and under an atmosphere of 10 vol.% CH_4 and no steam. Compared with the CMTF oxygen carrier, Ni-impregnated oxygen carriers had better reactivity with CH_4, as shown in Fig. 1 (a). The higher the ratio of impregnated Ni, the faster the reaction rate between the oxygen carrier and methane. Modified CMTF oxygen carriers can be fully reduced by CH_4 within 30 – 75 s. Moreover, Impregnating with Ni can enhance the oxygen transport capacity of oxygen carriers. However, due to the catalytic effect of Ni, catalytic methane decomposition occurred on the oxygen carrier surface leading to an increase in RMCR. The higher the ratio of impregnated Ni, the faster the reaction rate of catalytic methane decomposition.

Fig. 2 (b) and (c) show the relation between gas products and RMCR for 7.5Ni@CMTF and 1Ni@CMTF, respectively. In the initial stage of the reaction, the predominant gas product was CO2, with almost no presence of CO and H_2. It indicated that the primary reaction occurring in the early stage was the complete oxidation of CH_4. As the reaction progressed, the lattice oxygen within oxygen carriers was continuously consumed. When the lattice oxygen became insufficient to support the complete oxidation of CH_4, partial oxidation of CH_4 occurred. Because of the partial oxidation of CH_4, the concentration of CH_4 decreased and the concentration ratio of H_2 to CO was close to 2. For both 7.5Ni@CMTF and 1Ni@CMTF oxygen carriers, partial oxidation of CH_4 occurred when the RMCR reached half of its minimum value. Coincidentally, for both two oxygen carriers, the concentration of CO reached the maximum value when the RMCR reached 88 % of its minimum value. And then, the concentrations of CO and H_2 decreased as a result of the continuous consumption of lattice oxygen. When the concentration of CO had decreased to a relatively low level, the concentration of H_2 remained relatively high, indicating the catalytic methane decomposition.
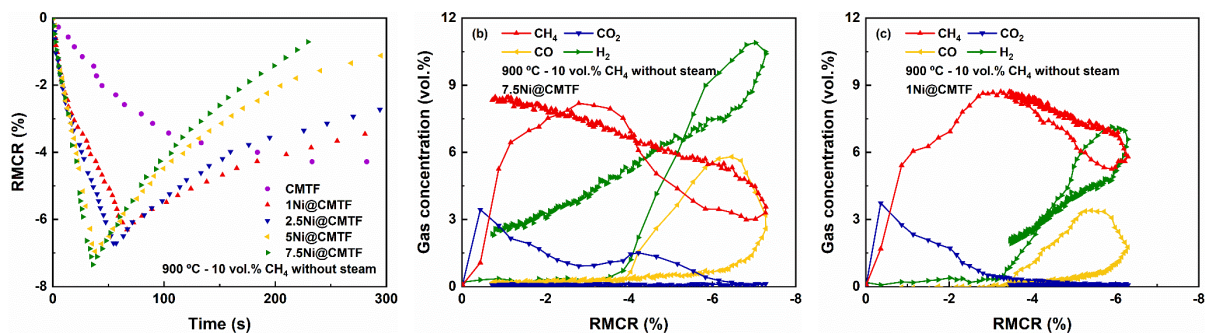
Fig. 2 Reaction characteristics of modified CMTF oxygen carriers: (a) performance of oxygen carriers impregnated with different NiO; relation between gas products and RMCR for (b) 7.5Ni@CMTF and (c) 1Ni@CMTF

3.2 The Effect of Steam

In an actual CLC system, steam is usually used as the fluidizing gas for the fuel reactor. The effect of steam on the reaction characteristics of modified oxygen carriers was investigated, which was tested at 900 °C under an atmosphere of 10 vol.% CH_4. In the presence of steam, the reaction rate between modified oxygen carriers and CH_4 was reduced compared to when steam was absent, as shown in Fig. 3 (a). For 1Ni@CMTF and

171 2.5Ni@CMTF, the minimum value of RMCR increased in the presence of steam, indicating a
172 decrease in the proportion of lattice oxygen available for reaction within oxygen carriers. For
173 5Ni@CMTF and 7.5Ni@CMTF, there was almost no effect of steam on the maximum value
174 of RMCR. Fig. 3 (b) shows a redox cycle of 1Ni@CMTF in the presence of steam. 10 vol.%
175 CH_4 was introduced into the reactor for at leather 400 s. During the oxidation stage, neither
176 CO_2 nor CO were formed, indicating no carbon deposition during the reduction stage.
177 Therefore, steam inhibited carbon deposition effectively.
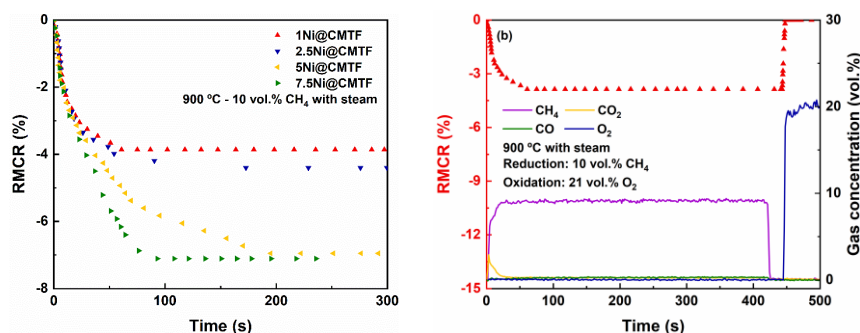
178
179 Fig. 3 Effect of steam on (a) reaction performance and (b) carbon deposition.

180 3.3 Reaction Kinetics of the Best Modified Perovskite Oxygen Carrier with CH_4

181 Considering cost and reactivity, 1Ni@CMTF was chosen as the best modified CMTF
182 oxygen carrier. Its maximum oxygen transport capacity is 3.87 wt.%. The reduction kinetics
183 of 1Ni@CMTF with CH_4 under various conditions were tested in the presence of steam, as
184 shown in Fig. 4. The effect of temperature on the reaction kinetics was significant. At 900 °C,
185 1Ni@CMTF can be fully reduced within 75 s, compared to 275 s required at 800 °C. gas
186 concentration had a minimal impact on the reaction kinetics.
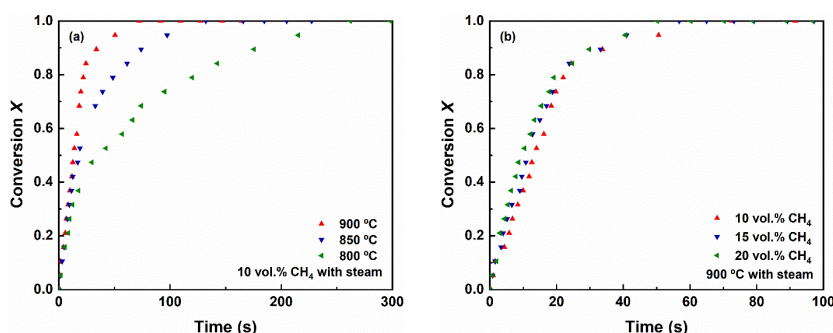
187
188 Fig. 4 Reduction kinetics of 1Ni@CMTF with CH_4 under the presence of steam: (a) effect of
189 temperature; (b) effect of CH_4 concentration.

190 Fig. 5 shows the relation between gas product and RMCR for 1Ni@CMTF. It was simpler
191 than when steam was absent. The main gas product was CO_2, which indicated that the
192 complete oxidation of CH_4 was the primary reaction. At 900 °C, H_2 was detected at the end of
193 the reaction under 10 and 20 vol.% CH_4, demonstrating that partial oxidation of CH_4 occurred.
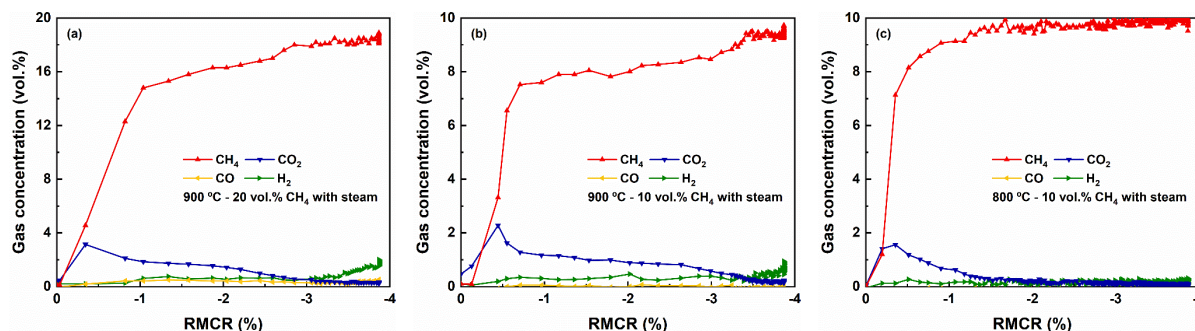
194
195 Fig. 5 Relation between gas product and RMCR for 1Ni@CMTF under different conditions.

4. Conclusion

Modified CMTF oxygen carriers exhibited significantly improved reactivity with CH_4 but the catalytic effect of NiO led to severe carbon deposition. The higher the ratio of impregnated NiO, the greater the reactivity with CH_4 and the more severe the carbon deposition. For both 1Ni@CMTF and 7.5Ni@CMTF, in the absence of steam, complete oxidation of CH_4 occurred in the early stage of the reaction and partial oxidation of CH_4 took place when the mass change rate of the oxygen carrier reached half of its minimum value. Although steam can effectively inhibit carbon deposition, it also slowed down the reaction rate between oxygen carriers and CH_4. Moreover, the presence of steam limited the reduction depth of 1Ni@CMTF and 2.5Ni@CMTF, but it had no effect on 5Ni@CMTF and 7.5Ni@CMTF. Considering cost and reactivity, 1Ni@CMTF was chosen as the best modified CMTF oxygen carrier, which had the maximum oxygen transport capacity of 3.87 wt.%. It can be fully reduced in 75 s at 900 °C and the main gas product was CO_2. Its reaction rate with CH_4 was significantly influenced by temperature, while the effect of CH_4 concentration was minimal. In summary, impregnating a minimal amount of NiO can significantly improve the reactivity of the CMTF oxygen carrier with CH_4.

Acknowledgment

References

[1] Metz, B., Davidson, O., De Coninck, H. C., et al. IPCC special report on carbon dioxide capture and storage. Cambridge: Cambridge University Press, 2005.

[2] Adánez, J., Abad, A., Garcia-Labiano, F., et al. Progress in chemical-looping combustion and reforming technologies. Progress in energy and combustion science, 2012, 38, 215-282.

[3] Adánez, J., Abad, A. Chemical-looping combustion: Status and research needs. Proceedings of the Combustion Institute, 2019, 37, 4303-4317.

[4] Liu, L., Li, Z., Wang, Y., et al. Industry-scale production of a perovskite oxide as oxygen carrier material in chemical looping. Chemical Engineering Journal, 2022, 431, 134006.

[5] Gayán, P., de Diego, L. F., Garcia-Labiano, F., et al. Effect of support on reactivity and selectivity of Ni-based oxygen carriers for chemical-looping combustion. Fuel, 2008, 87, 2641-2650.

[6] Yang, Y., Qiu, Y., Zhang, Z., et al. Ni-promoted Fe_2O_3/Al_2O_3 for enhanced hydrogen production via chemical looping methane reforming. Energy & Fuels, 2023, 37, 12788-12795.

[7] Chen, X., Zou, G., Yuan, Y., et al. Flame spray pyrolysis synthesized Ni-doped Fe/Ce oxygen carriers for chemical looping dry reforming of methane. Fuel, 2023, 343, 127913.

[8] Li, Z. First-principles-based microkinetic rate equation theory for oxygen carrier reduction in chemical looping. Chemical Engineering Science, 2022, 247, 117042.

[9] Mihai, O., Chen, D., Holmen, A. Chemical looping methane partial oxidation: the effect of the crystal size and O content of LaFeO3. Journal of catalysis, 2012, 293, 175-185.

[10] Wang, P., Bu, H., Liu, X., et al. Inexpensive composite copper ore/red mud oxygen carrier: Industrial granulation via hydroforming and multiple-cycle evaluation in chemical looping combustion. Fuel, 2024, 365, 131271.

[11] Wang, Y., Li, Z., Cai, N. Redox Reaction Kinetics of a Fe–Cu-Based Oxygen Carrier Measured with Microfluidized Bed Thermogravimetric Analysis. Energy & Fuels, 2022, 36, 9672-9686.

[12] Li, D., Wang, Y., Li, Z. Limestone calcination kinetics in microfluidized bed thermogravimetric analysis (MFB-TGA) for calcium looping. Catalysts, 2022, 12, 1661.

[13] Riley, J., Siriwardane, R., Tian, H., et al. Kinetic analysis of the interactions between calcium ferrite and coal char for chemical looping gasification applications: Identifying reduction routes and modes of oxygen transfer. Applied Energy, 2017, 201, 94-110.

[14] Stanmore, B., Gilot, P., Prado, G. The influence of mass transfer in DTG combustion tests. Thermochimica acta, 1994, 240, 79-89.

CHEMICAL LOOPING CO$_2$ CAPTURE AND CATALYTIC METHANATION OVER DUAL FUNCTION MATERIALS IN A TWIN FLUIDIZED BED REACTOR

Fiorella Massa[1], Antonio Coppola[1], Stefano Cimino[1], Fabrizio Scala[1,2,*]

[1]*STEMS, Consiglio Nazionale delle Ricerche, P.le Tecchio 80, 80125 Napoli, Italy*

[2]*DICMaPI, Università di Napoli Federico II, P.le Tecchio 80, 80125, Napoli, Italy*

*Email: *fabrizio.scala@unina.it*

Abstract

Carbon Capture and Utilization (CCU) is regarded as one of the most promising options to address the reduction of CO$_2$ emissions. This approach may be combined to a Power-to-gas technology, realizing a chemical energy storage through the production of synthetic methane, exploiting the surplus of renewable electric energy. Since one of the main drawbacks of current CCU technologies lies in energy-intensive regeneration processes, integrated CO$_2$ capture and reduction solutions have been proposed. These techniques require the use of dual function materials (DFM) combining both sorbent and catalytic properties to cyclically capture CO$_2$ from flue gas and convert into CH$_4$. So far, the concept has been investigated in discontinuous fixed-bed reactor configurations with alternate feeds. Herein we propose a chemical looping process based on the use of two interconnected fluidized beds, which would allow a steady operation of the plant. In this work we tested highly performing Lithium-Ruthenium/Al$_2$O$_3$ DFM with low Ru loading, previously developed and investigated in a fixed bed reactor. The experimental campaign was carried out in a batch lab-scale apparatus, consisting of two bubbling fluidized beds connected by a duct enabling the fast transfer of solid materials. CO$_2$ capture was carried out in one reactor at 200-400 °C, while reduction/regeneration was carried out in the other reactor at 230-300 °C under 4% H$_2$, for a total of 5 complete cycles. As expected for a chemisorption process, the CO$_2$ uptake decreased with increasing temperature, but its degree of conversion to CH$_4$ followed the opposite trend. Kinetic constraints determined the best methane yield at the highest methanation temperature (300°C). The optimal condition identified for this set of tests corresponded to the case in which both carbonation and methanation occurred at 300°C.

1. Introduction

Carbon Capture and Utilization (CCU) is regarded as one of the most promising technological options to address the reduction of CO$_2$ emissions. In the framework of energy transition, if considering CO$_2$ methanation, a CCU solution can be combined with a Power-to-gas technology to realize a chemical energy storage process using renewable hydrogen (Gotz et al., 2016). Synthetic methane can be produced via the reaction:

$$CO_2(g) + 4H_2(g) \leftrightarrows CH_4(g) + 2H_2O(g) \qquad \Delta H_r\,(298K) = -165 \text{ kJ mol}^{-1}$$
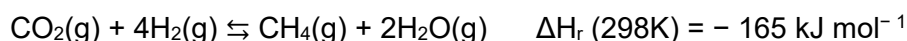
Methane is a fundamental energy carrier, socially accepted, and with a well-developed infrastructure. When considering current carbon capture technologies, the high temperature regeneration processes represent one of the main drawbacks. At the present, a CO$_2$ capture step generally involves absorption by corrosive amine solutions or solids, like alkaline metal oxides, implying an increase of the energy requirements of a power plant by 25-40% (Bobadillaa, et al., 2016). In addition, costs due to processing plants, handling and transport, must be considered (Duyar et al., 2015). In order to reduce these penalties, integrated CO$_2$ capture and reduction (CCR) solutions have been proposed (Omodolor, et al., 2020). These

chemical looping processes involve the CO_2 capture form sources like flue gases and anaerobic digestion, and its conversion into CH_4 by means of materials known as dual function materials (DFM), with both sorbent and catalytic properties. The typical applied active phases for CO_2 hydrogenation are Ni or Ru, while alkaline or alkaline earth CO_2 sorbents are investigated in the DFMs structure. Alternately, CO_2 capture on DFM and hydrogenation occur, in two steps schematically presented as follows:

$$A_nO + CO_2 \rightarrow A_nCO_3$$

$$A_nCO_3 + 4H_2 \rightarrow A_nO + CH_4 + 2H_2O$$
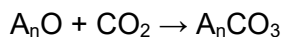
where, A = Li, Na, K, Ca, or Mg; and n = 1 or 2.

The success for this emerging technology relies on DFM characteristics such as catalytic activity, selectivity, reducibility, mechanical stability, and CO_2 capture and regeneration capacity (Cimino et al., 2022). Although Ni is the most used active phase in industrial application due to its good activity and low price, Ru supported on alumina appears to be the optimal choice for these applications, showing, unlike Ni, easy reducibility at low temperature, higher resistance to oxidation and, furthermore, favorable interaction with alkali-based sorption phases in DFM [8]. Several oxides and carbonates of Li, Na, K, Ca, Mg, Ba, La, Ce, have been tested as CO_2 sorbent phases at intermediate temperatures (200-450 °C). Based on a study reporting the following order of activity for alkali metals: Cs ≥ Li > Rb > Na ≥ K (Li et al., 1998), Cimino et al. (2020) developed a highly performing Li-promoted Ru/Al_2O_3 DFM outperforming the Na- and K- promoted counterparts, considering both CO_2 capture and methanation steps. On $Li-Ru/Al_2O_3$ DFM, superficial Li-aluminates would prevent the formation of stable, and difficult to hydrogenate, carbonate species. In this work, Li-Ru-based DFM was prepared, containing 1% of noble metal and 5% Li on commercial $\gamma-Al_2O_3$ spheres. The CCR concept was mainly studied in fixed bed reactors so far, involving the intrinsic limit due to the discontinuity of these configurations. Herein, an innovative chemical looping based on the use of dual interconnected fluidized beds is proposed to allow a steady operation of the process, where the DFM can be continuously transported between the two reactors, subjected, alternately, to the capture and hydrogenation steps.

2. Experimental

2.1 Materials

The DFM was prepared following the procedure by Cimino et al. (2022), dispersing 1%$_{wt}$ of Ruthenium by incipient wetness impregnation of a Ru(III) nitrosyl nitrate solution on commercial 0.6 mm $\gamma-Al_2O_3$ spheres (190 m^2/g, Sasol). The impregnated material was dried at 120 °C and then calcined in air at 350 °C for 1 h. Then, Li (5% $_{wt)}$ was added to the Ru/Al_2O_3 catalyst by incipient wetness impregnation with an aqueous solution of $LiNO_3$. The DFM was eventually dried at 120 °C and activated at 450 °C in H_2 (20% in N_2) for 2h.

2.2 Apparatus

The selected DFM was tested in a batch lab-scale apparatus, the Twin Beds system, consisting of two identical bubbling fluidized beds (ID 40 mm), reported in Figure 1, connected to each other by a duct (ID 10 mm) enabling the fast transfer of solid materials (Coppola et al., 2017). The pneumatic transport between the reactors is allowed by generating an overpressure acting on a system of valves located on the top of each electrically heated reactor (1 m high fluidization column). Specifically, the flow can be directed between the two reactors or towards a central vessel to discharge the materials at the end of the test. On the top of each reactor a hopper is also placed to carry out the bed loading. A K-type thermocouple, 40 mm above the distribution plate, connects each bed to a PID controller to handle temperatures, while the output concentrations are measured by a continuous gas analyzer (MRU VARIO LUXX) able to detect CH_4, CO, CO_2 and H_2.
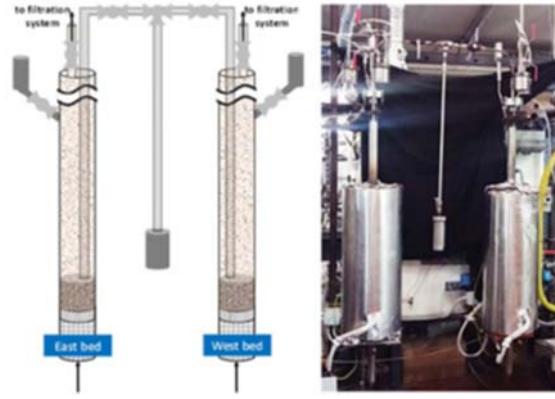
Figure 1. Twin Beds Apparatus.

2.3 Procedure

CO_2 capture and methanation were investigated at the temperatures of 200, 300 and 400 °C and 230, 265 and 300 °C, respectively. At the beginning of the test, the material (20 g) was loaded into the carbonation reactor, where a bed of inert silica in the size 800-900 μm was already fluidized at a fluidization velocity of 0.5 m/s. The presence of silica sand was necessary to keep temperature variations to a minimum and to assure the segregation of DFM particles to the top of the bed (Coppola et al., 2019). Carbonation was carried out in one reactor by feeding 5% CO_2 in N_2 stream for 8 min followed by purging 2 min in pure N_2 before the transfer to the methanation reactor. Here, once the material transfer was completed, the hydrogenation started with a flow of 4% H_2 in N_2 for a total duration of 8 min, followed by 2 min of N_2 purging. Then the DFM was transferred back to the carbonation reactor for another ICCR cycle: five complete cycles of carbonation and hydrogenation were carried out for each test condition. By measuring the concentration in the outlet gases, the molar flows of the species of interest were calculated as follows:

$$F_i^{OUT}(t) = c_i^{OUT}(t) \cdot F_{tot}^{OUT}(t)$$

$$F_{tot}^{OUT}(t) = \frac{F_{N2}}{c_{N2}(t)} \cdot 100$$

where F_i^{OUT} indicates the molar flow of the outlet species (i = H_2, CO_2, CH_4, CO), c_i^{OUT} their concentration in the stream and F_{tot}^{OUT} the total molar flow exiting the reactor. The latter is calculated through the nitrogen balance, being F_{N2} and c_{N2} its molar flow and outgoing concentration, respectively. The total amount of the species could be calculated along a certain time interval (0-t_f) discretizing the following integral and replacing it by the summation:

$$\int_0^{t_f} F_i^{OUT}(t)dt \approx \sum_{j=0}^{t_f} F_i^{OUT}(j) \cdot \Delta j$$

with Δj the sampling time interval of the signal (1s).

3. Results

The typical molar flow of outlet CH_4 as a function of time is reported in Figure 2, which refers to the LiRu/Al_2O_3 test at methanation and carbonation temperatures of 300 °C (similar qualitative trends were obtained at the other operating conditions). In this figure, all the 5 methanation steps of a complete ICCR experiment are depicted: outlet CH_4 shows a rapid increase with a maximum reached after 20-30 s and a following slower decrease due to the progressive depletion of the captured CO_2. The DFM behaviour appears quite stable and reproducible over the cycles from the second cycle onwards. The slight delay in methane production of the first cycle may be due to the residual presence of RuO_x on the DFM, which is reduced simultaneously with methanation step to the catalytically active metal form.
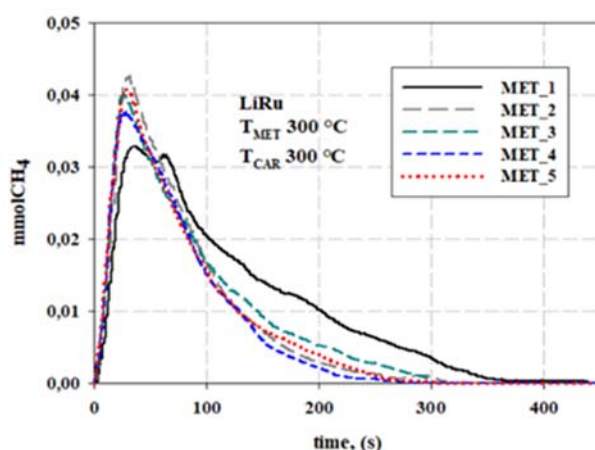
Figure 2. Temporal CH$_4$ outlet molar flow for the Li-Ru/Al$_2$O$_3$ test at methanation and carbonation temperatures of 300 °C. The curves refer to the 5 methanation cycles.

An overview of the results for all the test conditions is obtained by integration of the temporal concentration profiles of the gaseous species of interest to calculate the overall outlet amount. Figure 3 summarizes the average amount of outlet CH$_4$ over the last 4 cycles, in terms of mmol produced per gram of DFM, for all the test conditions.
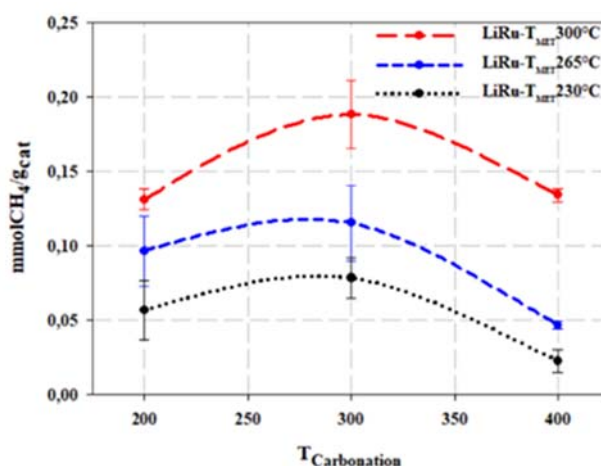
Figure 3. Average methane production under all the ICCR tests conditions with Li-Ru/Al$_2$O$_3$ DFM.

The produced CH$_4$ increases with the methanation temperature from 230 to 300 °C due to kinetic limitations, since the system did not reach chemical equilibrium. When considering the CO$_2$-capture temperature effect, with the increase of carbonation temperature from 300 °C to 400 °C, for all the methanation temperatures, produced CH$_4$ decreases, as expected for an exothermic process such as the CO$_2$ chemisorption. This process is favored at lower temperatures, still proceeding with fast kinetics. At the lowest carbonation temperature investigated of 200 °C, CH$_4$ production, under all methanation conditions, was lower than in the case of the CO$_2$-capture at 300 °C. However, this finding seems to be attributable to the experimental procedure during the test at the carbonation temperature of 200 °C, where the DFM material experimented a rapid temperature increase when transferred to the methanation reactor, which worked at higher temperatures. Under these conditions, during the purge phase before the reduction step was started, a significant CO$_2$ stripping occurred. This finding can be supported by reporting the total amount of the measured carbon-containing species (CH$_4$ + CO$_2$ + CO) at the outlet (Figure 4) for all the experiments: this amount, in terms of mmol of carbon per gram of DFM material, monotonically decreases when increasing the carbonation temperature. The CO$_2$ released during methanation for the tests with carbonation temperatures of 300 and 400 °C was significantly lower than at 200 °C, and practically negligible at 400 °C. Under such conditions, the CH$_4$ yield, expressed as CH$_4$ produced per

CO_2 transferred from the CO_2-capture step, which is the ratio between the values reported in Figures 3 and 4, is almost equal to unity. Table 1 summarizes the yield values for all the operating conditions.
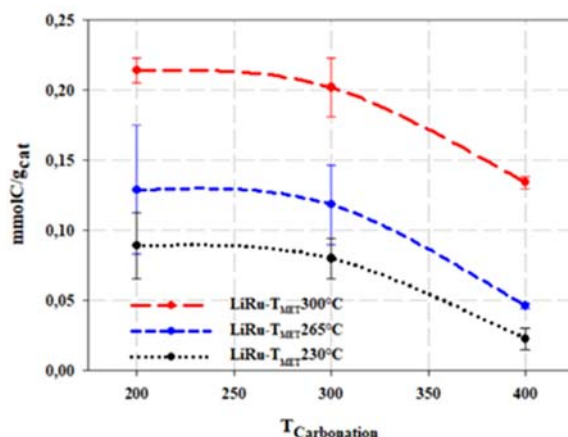
Figure 4. Overall amount of carbon-containing species at the methanation outlet produced under the ICCR tests conditions with Li-Ru/Al_2O_3 DFM.

Table 1. Methane yield under the CCR tests conditions.

$T_{CAR} \rightarrow$ / $T_{MET} \downarrow$	molCH$_{4-out}$/molC$_{out}$		
	200°C	300°C	400°C
230°C	64%	98%	100%
265°C	75%	97%	100%
300°C	61%	93%	100%

4. Conclusion

In this study, integrated CO_2 capture and reduction (ICCR) to capture and convert CO_2 from flue gas into CH_4 was proposed in a chemical looping process based on dual interconnected fluidized beds configuration. A highly performing dual function material was prepared by dispersing low loadings of Ruthenium (1%) and Lithium (5%) over fluidizable γ-Al_2O_3 spheres. The selected DFM was tested in the Twin Beds system, an experimental batch lab-scale apparatus consisting of two bubbling fluidized beds connected to each other by a duct enabling the fast transfer of solid materials under cyclic operation. In this work, after each CO_2 capture step, the DFM was rapidly transferred in the second reactor where the methanation in 4% H_2/N_2 mixture occurred. The process was repeated for a total of 5 complete cycles. Carbonation and methanation steps were carried out in the temperature ranges 200-400 °C and 230-300 °C, respectively. The DFM performance showed good stability over the cycles. The CO_2 uptake decreased with increasing carbonation temperature, as expected for a chemisorption process. However, at the lowest carbonation temperature of 200°C, the CO_2 amount released in the transient phase before methanation was larger due to the DFM transfer to a higher methanation temperature. Thus, higher CO_2 conversions to CH_4 occurred at higher carbonation temperatures. When considering the methanation temperature, the kinetic constraints of the reaction determined the best performance, in terms of methane yield, at the highest methanation temperature (300 °C). The limitation due to the experimental transient phases resulted, as an overall effect, in an optimal condition corresponding to the case in which carbonation and methanation occurred at the same temperature of 300°C. Interestingly, the methane yield approached 100% under the highest tested temperature. It may be worth noting that in a more realistic continuous chemical looping system, the possibility of decoupling the two processes may entail a large potential intensification: by physically separating the phases it would be possible to split the exothermicity of the whole process and to optimize each single step in terms of temperature and other operating parameters.

Acknowledgment

References

Gotz, M., Lefebvre, J., Mors, F., McDaniel Koch, A., Graf, F., Bajohr, S., Reimert, R., Kolb, T. Renewable Power-to-Gas: A technological and economic review. Renew. Energy. 2016. 85, 1371–1390

Bobadillaa, L. F., Riesco-Garcíab, J. M:, Penelás-Pérezb, G., Urakawaa, A. Enabling continuous capture and catalytic conversion of flue gas CO_2 to syngas in one process. Journal of CO_2 Utilization. 2016. 14, 106-111

Duyar, M. S.,Trevino, M.A.A., Farrauto, R. J. Dual function materials for CO_2 capture and conversion using renewable H2. Appl. Catal. B Environ. 2015. 168–169, 370–376

Omodolor, S., Otor, H.O., Andonegui, J.A., Allen, B.J., Alba-Rubio, A.C. Dual function materials for CO2 capture and conversion: a review. Ind. Eng. Chem. Res. 2020. 59 (40)

Cimino, S., Russo, R., Lisi, L. Insights into the cyclic CO_2 capture and catalytic methanation over highly performing Li-Ru/Al_2O_3 dual function materials. Chemical Engineering Journal. 2022. 428, 131275

Li, D.i., Ichikuni, N., Shimazu, S., Uematsu, T. Catalytic properties of sprayed Ru/Al_2O_3 and promoter effects of alkali metals in CO_2 hydrogenation. Appl. Catal. A Gen. 1998. 172 (2), 351–358

Cimino, S., Boccia, F., Lisi, L. Effect of alkali promoters (Li, Na, K) on the performance of Ru/Al_2O_3 catalysts for CO_2 capture and hydrogenation to methane. J. CO_2 Util. 2020. 37, 195–203

Coppola, A., Scala, F., Gargiulo, L., Salatino, P. A twin-bed test reactor for characterization of calcium looping sorbents. Powder Technology. 2017. 316, 585–591

Coppola, A., Massa, F., Salatino, P., Scala, F. Fluidized bed CaO hydration-dehydration cycles for application to sorption-enhanced methanation. Combustion Science and Technology. 2019. 191,1724–1733

THE BEHAVIOR OF DIFFERENT LIMESTONES FOR SORPTION ENHANCED GASIFICATION IN PRESENCE OF STEAM IN A LAB-SCALE TWIN FLUIDIZED BED SYSTEM

Fiorella Massa[1], Antonio Coppola[1], Fabio Montagnaro[2], Fabrizio Scala[1,3]*

[1]*STEMS, Consiglio Nazionale delle Ricerche, P.le Tecchio 80, 80125 Napoli, Italy*

[2]*Dipartimento di Scienze Chimiche, Università di Napoli Federico II,*

Complesso Universitario di Monte Sant'Angelo, 80126 Napoli, Italy

[3]*DICMaPI, Università di Napoli Federico II, P.le Tecchio 80, 80125, Napoli, Italy*

Email: *fabrizio.scala@unina.it*

Abstract

In situ CO_2 capture by Ca-based sorbents during biomass or waste gasification, determines the shift of the chemical equilibrium of the homogeneous water-gas shift reaction ($CO+H_2O=CO_2+H_2$), allowing to enrich the syngas stream in H_2. The above mentioned process is called Sorption-Enhanced Gasification (SEG), which is based on the Calcium Looping concept. In this work the behavior of six limestones, in terms of CO_2 capture capacity and attrition/fragmentation tendency, was analyzed in a lab-scale twin interconnected fluidized bed apparatus under operating conditions simulating those of sorption-enhanced gasification in presence of steam. Each sorbent was processed for ten calcination/carbonation cycles, carrying out carbonation at two temperatures (650°C and 700°C), with inlet CO_2 and H_2O concentration of 10%. CaO carbonation degree over the cycles, particle size distribution at the end of the tests, and impact fragmentation in an ex situ apparatus, were investigated. The results were compared with those of previous tests carried out in the absence of H_2O, to analyze the role of steam on the sorbent behavior: literature in fact reports complex effects of this species on the carbonation reaction. No monotonic effect of increasing temperature in presence of steam was detected in terms of CO_2 capture capacity, due to the combination of kinetics and diffusion enhancement, on the one hand, and sintering and thermodynamic constraints, on the other. At the highest carbonation temperature, steam-induced sintering was enhanced and lower fragmentation indexes were observed, being the particles mechanically more resistant. However, if considering the comparison with tests under dry conditions, at a given carbonation temperature, the presence of steam seems to enhance structural fragilization phenomena.

1. Introduction

Sorption-Enhanced Gasification (SEG) process relies on the CO_2 removal during gasification of a solid fuel to increase the H_2 production by shifting the equilibrium of the water–gas shift reaction towards the products (Zaccariello et al., 2023). This process is based on the Calcium Looping (CaL) concept, a post-combustion technique aimed at removing CO_2 from flue gas, usually carried out in Dual Interconnected Fluidized Beds (DIFB) by using Ca-based sorbents (Coppola et al., 2020). As with the CaL technology, also SEG can rely on the application of inexpensive limestone sorbents cycled between two reactors. Gasification occurs at circa 600–700 °C in the gasifier-carbonator, where the gasifying stream, solid fuel and CaO are fed. In this reactor, the primary syngas is enriched in H_2 by means of the capture of CO_2 via CaO carbonation (CaO + $CO_2 \rightarrow CaCO_3$), and the solid stream, containing carbonated sorbent, unconverted CaO and gasified char, is sent to the combustor-calciner. In this step, at 800–900 °C, the solid is contacted with air and, in case of need, with an extra fuel: specifically, the

sorbent is calcinated (CaCO$_3$→CaO + CO$_2$) to produce a CaO stream ready for a new cycle. In the framework of the sustainable approaches to mitigate global warming effects, the concept can be applied to a biomass as starting fuel, resulting in a process with negative CO$_2$ emissions (Balsamo et al., 2023). The calciner-combustor, where the endothermic calcination occurs, operates at a higher temperature than the carbonator and the regenerated sorbent stream can act as the heat carrier to support the overall endothermic gasification reactions. For the proper development of such processes in DIFB configuration, characterized by continuous cycling operations, sorbent deactivation, due to thermal and chemical sintering, and loss, due to elutriation, with the consequent need of a continuous fresh sorbent make-up, must be taken into account.

2. Experimental

2.1 Lab-Scale Twin Fluidized Bed System tests

The SEG tests were carried out in a DIFB apparatus purposely devised for the study of looping processes, consisting of two identical fluidized beds (ID 40 mm) working in batch mode and interconnected by a duct allowing the pneumatic transport of solid material between the two environments by means of a system of valves. The reactor is described in depth elsewhere (Coppola et al., 2017). The selected sorbents are 6 natural limestones from different zones of Europe: Massicci (MAS) and Sardo (SAR) from Italy, Tarnow Opolski (TAR) and Czatkowice (CZA) from Poland and Schwabian Alb (SCH) and EnBW (EBW) from Germany. The calcination temperature was fixed at 850 °C, simulating the oxidizing conditions in a combustor-calciner by feeding 10% CO$_2$ in air. As for the carbonation, two temperatures were investigated, 650 °C and 700 °C, with CO$_2$ and steam both at 10% by volume and balanced by N$_2$ to reproduce reducing conditions typical of a gasifier-carbonator. Each sorbent (with an initial mass of 10 g and in the size range 400–600 μm) was calcinated and carbonated for ten complete cycles of 10 min (plus an eleventh calcination stage before the discharge of the processed material). Both beds were fluidized at a superficial velocity of 0.5 m/s. By continuously measuring the CO$_2$ concentration at the carbonator outlet, we calculate the degree of carbonation of Ca, for the generic N-th stage of carbonation, as follows:

$$X_{Ca} = \frac{\int_0^t \left[W_{CO_2}^{in} - W_{CO_2}^{out}(t) \right] \mathrm{d}t}{m_0 \, f_{CaCO_3}} \frac{MW_{CaCO_3}}{MW_{CO_2}}$$

where $W_{CO_2}^{in}$ is the inlet CO$_2$ mass flow rate, $W_{CO_2}^{out}(t)$ is the mass flow rate at the carbonation outlet, t is the carbonation time, MW the molecular weight and f$_{CaCO3}$ the mass fraction of CaCO$_3$ in the limestone (in the range 94-100% for the selected sorbents). The X$_{Ca}$(N) trends have been analyzed applying the Initial Activity Decay (IAD) model introduced in Coppola et al. (2023a):

$$X_{Ca}(N) = k_1 N^{-k_2}$$

where k$_2$ is the decay constant that measures the resistance to sintering (the higher k$_2$, the worst the resistance), while k$_1$ = X$_{Ca(N = 1)}$ considers the sorbent initial activity. The Particle Size Distribution (PSD) of the sorbent was characterized by manual sieving of the bed material at the end of the test. Sieving was carried out in 8 size intervals with an average diameter d$_i$ between 56 μm and 500 μm, by stating x(d$_i$) as the mass fraction of particles that fall into the range of average diameter d$_i$. The particles finer than the lower limit of the initial particle size range (400–600 μm) are indicated as "fragments", being the cumulative mass fraction of fragments in the bed:

$$f_{FR}^{in-bed} = \sum_{d_i < 400 \, \mu m} [x(d_i)]$$

2.2 Ex-situ impact fragmentation tests

The impact fragmentation phenomenon was studied in an ex-situ apparatus, since the DIFB reactor did not reproduce realistic impact fragmentation conditions. The system is described in detail in Coppola et al. (2023b). Briefly, a batch of particles is entrained by a gas flow at a controlled velocity and collided with a solid target. The materials subjected to impact fragmentation tests were the preprocessed sorbents at the end of a complete DIFB-SEG test: 1 g mass of these samples was re-sieving in the reference size range 0.4–0.6 mm and impacted at velocities able to reproduce conditions likely established near the gas distributor of large-scale FB systems: 17, 24, 31, 38 and 45 m/s. The PSD data of fragments per impact were obtained as already described.

3. Results

3.1 Degree of Ca conversion

Trends of $X_{Ca}(N)$ for the six limestones are reported, by way of example, for the carbonation temperature of 700 °C, in Figure 1 (a). Data confirm the trends generally observed by other authors (Donat et al., 2012): a decay of X_{Ca} over the cycles due to thermal sintering. Table 2 summarizes the main results, among which, the average value ($X_{Ca,av}$) for each sorbent over the ten carbonation stages. At the carbonation temperature T=650 °C, on average, MAS had the lowest carbonation activity ($X_{Ca,av}$=22.3) while the one behaving better was SCH ($X_{Ca,av}$ =32.0%). Differences in reactivity of the sorbents would appear to rely on their porosimetric characteristics (Fennell et al., 2007), being favored by higher surface areas: in our work, MAS and SCH showed a specific surface area of 4.28 and 9.99 m^2/g, respectively, with CO_2 capture results highlighting, conversely, the lowest and highest carbonation degree value. When carrying out carbonation at 700 °C, $X_{Ca,av}$ became the lowest for the other Italian limestone, SAR, with SCH still being the best performing in terms of $X_{Ca,av}$. As the temperature increased, two main opposing effects occurred, namely increased kinetics and CO_2 solid-state diffusion on one hand, and sintering promoted by steam on the other, which determined a non-monotonic effect of carbonation temperature on $X_{Ca,av}$. Table 2 also reports the IAD model results in terms of decay constant and coefficient of determination. A fitting example is reported in Figure 1 (b) as well, for MAS at 700 °C. Although a good sintering resistance is not directly related to high calcium conversion degrees, at T=650 °C, the most resistant material to the decay in CO_2 capture capacity was SCH, while the most inclined was MAS, which are also the sorbents with highest and lowest $X_{Ca,av}$, respectively. At T=700 °C, the role of the most resistant material to sintering was taken by EBW. The comparison with data previously obtained at the same temperatures but in the absence of water vapour (Coppola et al., 2023a), suggests that the non-monotonic trend in the capture capacity with increasing temperature is due to the fact that the negative influence of sintering promoted at higher temperature counterbalances the positive effect on kinetics and diffusion. In the absence of steam, the positive effect of carbonation temperature, was, instead, clear for all sorbents.

(a)   (b)
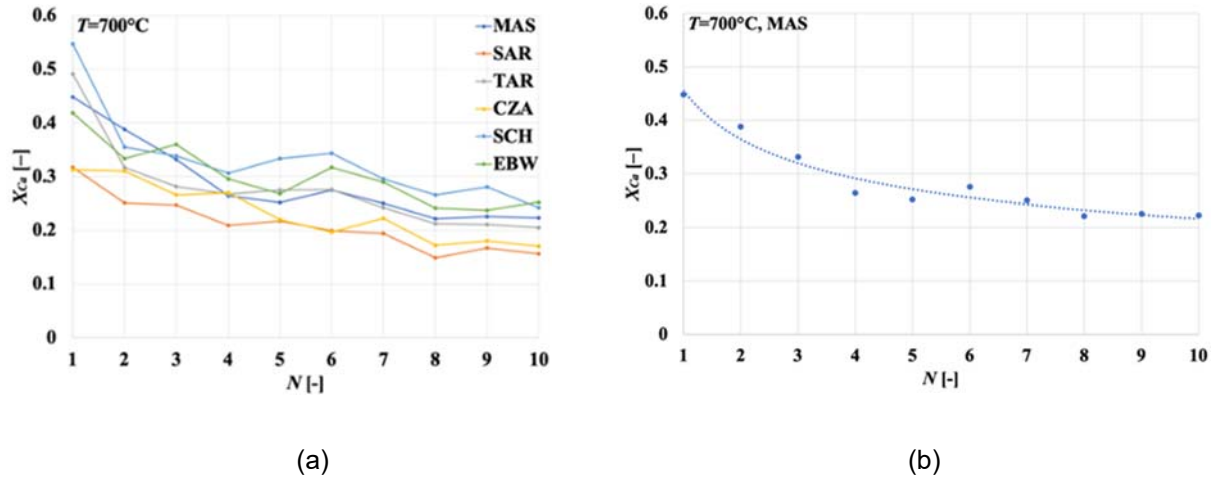
Fig. 1. Degree of Ca conversion as a function of the number of carbonation stages at 700°C (a);
Application of the IAD model at =700°C, MAS sorbent (b).

Table 1. Relevant values for process parameters, for the six investigated sorbents.

	MAS	SAR	TAR	CZA	SCH	EBW
$X_{Ca,av}$ (650°C) [–]	0.223	0.271	0.274	0.274	0.320	0.291
$X_{Ca,av}$ (700°C) [–]	0.288	0.210	0.278	0.232	0.331	0.301
k_2 (650°C) [–], IAD model	0.533	0.549	0.371	0.414	0.263	0.417
R^2 (650°C) [–], IAD model	0.962	0.976	0.909	0.937	0.826	0.928
k_2 (700°C) [–], IAD model	0.324	0.304	0.334	0.295	0.277	0.228
R^2 (700°C) [–], IAD model	0.954	0.931	0.913	0.836	0.846	0.837
f_{FR}^{in-bed} (650°C) [–]	0.336	0.175	0.365	0.396	0.427	0.380
f_{FR}^{in-bed} (700°C) [–]	0.284	0.217	0.303	0.266	0.363	0.258
$f_{FR,av}^{impact}$ (650°C) [–]	0.158	0.089	0.155	0.152	0.204	0.149
$f_{FR,av}^{impact}$ (700°C) [–]	0.091	0.123	0.102	0.113	0.138	0.143

3.2 Sorbent in-bed and impact fragmentation

Data for in-bed fragmentation are reported in Table 2. At T=700 °C, lower fragmentation indexes for all the sorbents but SAR were observed, likely due to the particles hardening promoted by sintering in presence of steam. The main observation may highlight that sorbents characterized by higher amount of in-bed fragments, due to the presence of finer particles generated, were able to better interact with CO_2 during the gas-solid heterogeneous carbonation reaction. When considering the impact fragmentation phenomenon, for all the sorbents pre-processed at 650 °C and 700 °C upon carbonation, the fraction of fragments increased as v increased, as expected. In Table 2 the average value $f_{FR,av}^{impact}$ over the 5 impact velocities investigated is reported: the general effect, for all sorbents but SAR, is that increasing temperature determined materials more resistant to impact fragmentation (in line with in-bed fragmentation results). Figure 2 summarizes the results, by way of example for the

sorbent MAS, at the two investigated temperatures of 650 °C (a) and 700 °C (b). In this figure we report data of $f_{FR}^{impact}(v)$, along with their average values; in addition the data obtained for previous tests under dry conditions are reported for comparison, to analyze the effect of steam. This figure highlights the general trend observed for most of the sorbents (apart from some exceptions): the presence of steam led to a more fragilized structure, with, in turn, samples more prone to impact fragmentation. Another trend involves the slope-increase of these curves for impact velocities around 24–31 m/s, in most cases. On a log-log plot, this reveals an increase in the value of k if one assumes a $f_{FR}^{impact} \propto v^k$ relationship, that indicates a transition from a chipping- to a splitting-based regime, i.e. from the formation of fractures upon surface, producing fine chips, to fractures throughout the particle, determining the "splitting" of the parent particles into fragments of similar size.

(a) (b)
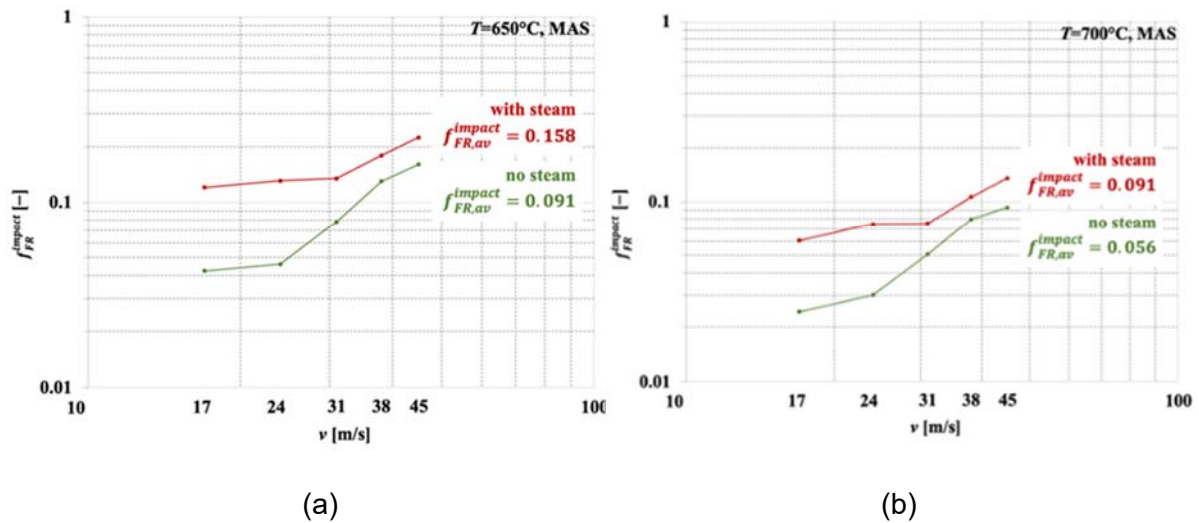
Fig. 1. Cumulative mass fraction of fragments generated upon impact vs. impact velocity (comparison of presence vs absence of steam upon carbonation; MASSICCI sorbent; carbonation at 650 °C (a) and 700 °C (b).

4. Conclusions

A set of six limestones was tested in a lab-scale twin fluidized bed system under simulated sorption-enhanced gasification conditions. Different aspects must be taken into account to design realistic processes, such as the decline of CO_2 capture capacity over cycling and fragmentation phenomena with the consequent need to provide a make-up flow of fresh sorbent. The presence of steam, for example, analyzed in this work, was able to fragilize the sorbent structure, yielding samples which generally give higher amounts of fragments. Two carbonation temperatures were investigated: no monotonic effect of this parameter, in presence of steam, was observed in terms of the CO_2 capture degree. In fact, the increase of temperature had a positive influence on carbonation kinetics and CO_2 solid-state diffusion, but the carbonation reaction is exothermal and steam, at 700 °C, enhanced sintering phenomena. The last effect appears to be significant, as, on the other hand, under dry conditions higher carbonation temperatures led to larger CO_2 capture for all the six sorbents. Although tests were carried out on different limestones to highlight behaviors not necessarily dependent on the characteristics of a specific sorbent, some findings pave the way for future investigation mostly focused on the effect of sorbents morphological characteristics on the observed trends.

Acknowledgment

References

Zaccariello, L., Montagnaro, F. Fluidised bed gasification of biomasses and wastes to produce hydrogen-rich syn-gas – a review. J. Chem. Technol. Biotechnol. 2023. 98, 1878–1887

Coppola, A., Senneca, O., ScalaF., Montagnaro, F., Salatino, P. Looping cycles for low carbon technologies: a survey of recent research activities in Naples. Fuel. 2020. 268, 117371

Balsamo, M., Montagnaro, F., Anthony, E.J. Socio-economic parameters affect CO_2 emissions and energy consumption – an analysis over the United Nations countries. Curr. Opin. Green. Sustain. Chem. 2023. 40, 100740

Coppola,A., Scala, F., Gargiulo, L., Salatino, P. A twin-bed test reactor for characterization of calcium looping sorbents. Powder Technol. 2017. 316, 585–591

Coppola, A., Massa, F., Montagnaro, F., Scala, F. Analysis of the behaviour of limestone sorbents for sorption-enhanced gasification in dual interconnected fluidised bed reactor. Fuel. 2023a. 340, 127594

Coppola, A., Sattari, A., Montagnaro, F., Scala, F., Salatino, P. Performance of limestone-based sorbent for sorption-enhanced gasification in dual interconnected fluidized bed reactors. AICHE J. 2023b. 69, e17588

Donat, F., Florin, N.H., Anthony, E.J., Fennell, P.S. Influence of high-temperature steam on the reactivity of CaO-based sorbent in cyclic carbonation/calcination for CO_2 capture. Environ. Sci. Technol. 2012. 46,1262–1269

Fennell, P.S., Davidson, J.F., Dennis, J.S., Hayhurst, A.N. Regeneration of sintered limestone sorbents for the sequestration of CO_2 from combustion and other systems. J. Energy Inst. 2007. 80, 116–119

Session G:

Fine particle and nano-particle systems

OPTIMIZATION OF DUST HOLDING CAPACITY OF HIGH EFFICIENCY FILTER MEDIA IN HIGH DUST ENVIRONMENT

Wenhan Yu[1], Feng Chen[1]*, Minghua Li[2], Haiyu Cao[2], Xiaolin Wu[1], Zhongli Ji[1]

1. Beijing Key Laboratory of Process Fluid Filtration and Separation, College of Mechanical and Transportation Engineering, China University of Petroleum, Beijing 102249, P. R. China

2. China North Vehicle Research Institute, Fengtai, Beijing 100072, P. R. China

*Email: chenfeng@cup.edu.cn

Abstract

The gas-solid filtration process involves intricate interactions among particles, fluids, and filter media, presenting a multifaceted kinetic challenge across various scales and phases. High-efficiency filter media currently face limitations in dust holding capacity when operating in high dust concentration environments. This study delves into augmenting high-efficiency filter media by incorporating a dust-holding layer on the windward side, serving as a dust carrier to decelerate filter cake formation. We investigate how the structural characteristics of this dust-holding layer influence the dust-holding capacity of the filter media. Additionally, microscopic observation of particle deposition elucidates the process and spatial pattern of dust accumulation within the fibers. Our findings demonstrate that integrating the dust-holding layer effectively enhances the dust holding capacity of high efficiency filter media. Notably, we observe that a higher fiber filling ratio in the layer correlates with reduced dust holding capacity. Furthermore, we observe that once the dust-holding layer reaches its capacity limit, increasing its thickness does not yield further improvements in dust holding capacity.

1. Introduction

High-efficiency filter materials are essential for effectively filtering harmful dust, fumes, and other impurities from gases. These materials are primarily categorized into glass fiber filter media and polytetrafluoroethylene (PTFE) membrane filter media. Glass fiber filter media is characterized by a dense fiber structure, small pore size, and exceptional retention performance for particulate pollutants. PTFE membrane filter media offers advantages such as a narrow pore size distribution, high porosity, and high efficiency with low resistance (Liu et al. 2021; Tang et al. 2017; Leung. 2008; Leung. 2009). These two materials find widespread applications in various industries including automotive, machinery, chemical, and nuclear sectors.

Gas-solid filtration materials are typically evaluated based on filtration efficiency and dust holding performance. High efficiency filtration materials excel at capturing dust particles, making dust holding capacity a crucial factor in assessing filter media performance. Various parameters, including filter material structure, particle characteristics, fluid flow rate, and viscosity, collectively influence dust holding performance. Among these, the structural characteristics of the filter material play a pivotal role in determining dust holding capacity. Recent studies by Liu et al. (2021) involved the composite of PTFE membrane material with polypropylene meltblown material to create a filter material with enhanced dust holding capacity for NaCl particles. Similarly, Long et al. (2018) developed a nanocomposite material through the wet moulding method, improving dust holding capacity for carbon smoke particles. However, industries such as automotive, machinery, and chemicals face high concentrations of dust pollutants, leading to rapid cake formation and increased resistance in high-efficiency filtration materials. This results in a decline in dust-holding performance and reduces the service life of filtration equipment. Consequently, enhancing the dust holding performance of high-efficiency filtration materials in environments with high dust concentrations has emerged as a critical area of current research.

In this study, a novel structural material was formulated by integrating high-efficiency filter media with polyester fiber (PET) filter media. The PET filter media serves as a carrier for the dust, essentially forming the dust-holding layer, which effectively retards cake formation. Meanwhile, the high-efficiency filter media acts as the primary filtering layer, ensuring consistent filtration efficiency. This composite material meets the technical requirements for high dust holding capacity and filtration efficiency. The study also analyzed the impact of the structural properties of PET filter media on the dust holding capacity of the composites. These findings offer a theoretical foundation and data support for designing new filters with high efficiency and dust holding capacity.

2. Methods and materials

The experimental device used in this study was the AFC131 filter media dynamic and static test bench manufactured by TOPAS in Germany. The flow chart of the device can be seen in Fig. 1. The dust used for the experiments was A2 standard dust, and it was generated using the Topas SAG-410 dust generating device. The apparent air velocity during the experimental filtration was maintained at 0.1 m/s, with a dust concentration of 1000 mg/m^3. Throughout the experiment, pressure drop data at both ends of the filter media was continuously recorded in real time by the differential pressure transmitter, while the flow rate was kept constant by the flow controller.
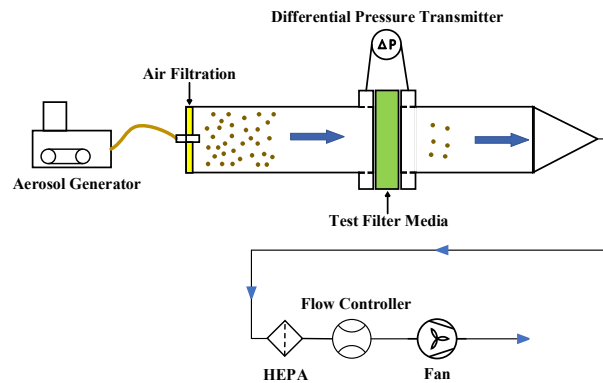
Fig.1. Schematic diagram of experimental device.

The study compared and analyzed two types of glass fiber filter materials (H12 and U15 in descending order of accuracy) and one type of PTFE film filter material (H14 in accuracy) by evaluating their dust capacity. The pressure drop curves of the three filter materials are illustrated in Figure 2, indicating that all three operate on surface filtration with similar pressure drop growth rates. This suggests that the precision and material of the filter do not significantly impact the pressure drop growth rate in high concentration dust environments. Therefore, the study recommends selecting PTFE film material as the filter-layer in the new composite filter material structure.
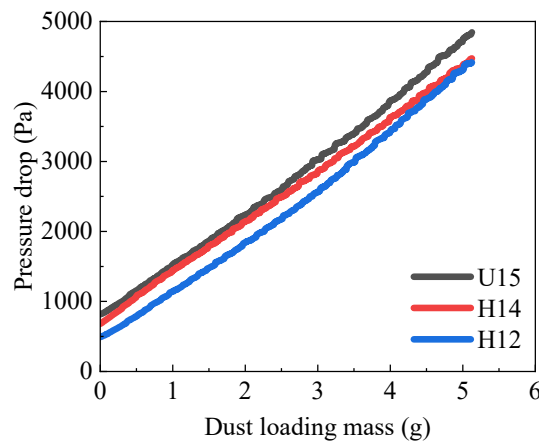
Fig. 2. Pressure drop curve of high efficiency air filter media.

Three PET filter materials with grammage weights of 50 g/m², 100 g/m², and 150 g/m² were chosen for the dust-holding layer in a new composite filter media structure. These materials served as primary filter materials with larger fiber diameters and pore sizes, resulting in lower filtration efficiency. The fiber filling ratio of the PET filter media increased as the gram weight increased. The experimental composite filter media's structure is illustrated in Fig. 3, with PET materials categorized into filter materials A, B, C, D, and E based on different grammage weights and thicknesses. Filter material F was used as a comparative experimental filter material, consisting of a single layer PTFE high efficiency filtration material.
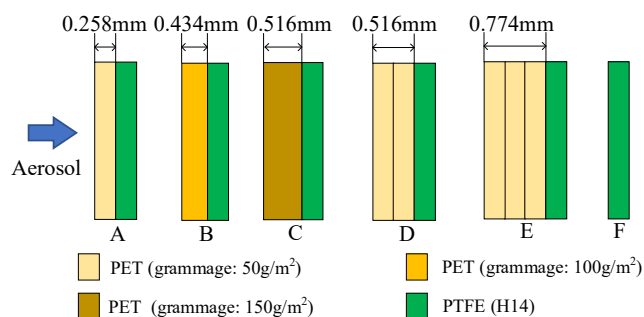
Fig. 3. Schematic diagram of composite filter structure.

3. Results and discussion

3.1 Composite Filter Media Dust Holding Capacity Analysis

In order to compare the dust holding capacity of composite filter media, PTFE (filter media F) was used as the reference filter media. Dust holding experiments were conducted under identical experimental conditions for filter media A, B, C, and F. The results, depicted in Fig. 4, show that the initial points of the dust holding curves for the four filter media almost coincide, with similar resistance levels between composite filter media and PTFE. As dust accumulates within the filter media, pressure drop gradually rises. Notably, when the pressure drop reaches 5000 Pa, the dust holding capacity of composite filter media A, B, and C surpasses that of filter media F.
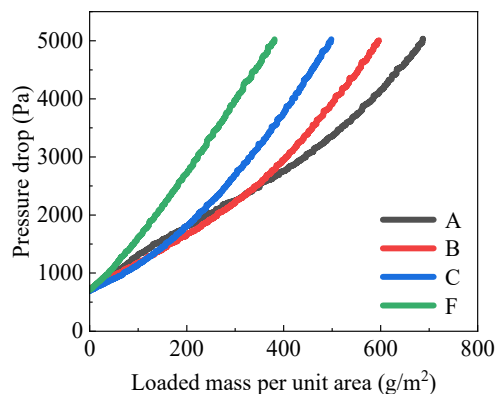
Fig. 4. Dust holding curve of filter media A、B、C、F.

The SEM surface diagrams in Fig. 5 illustrate the differences between PET and PTFE filter media after dust holding. PET filter media exhibits lower filtration precision, with a deep filtration mechanism at the initial stage of dust holding. A2 dust particles are captured by the fibers of the filter media and adsorbed on their surface. As dust particles accumulate, the pores of PET filter media gradually become blocked, resulting in a slow increase in pressure drop. On the other hand, PTFE filter media offers higher filtration precision, primarily engaging in surface filtration during the dust holding process. Dust accumulates on the surface, forming a filter cake and leading to a faster growth in pressure drop. In the dust holding process of composite structure filter media, dust first passes through the dust-holding layer (PET) before entering the filter-layer (PTFE). Large particles are captured by the dust-holding layer, while

small particles are intercepted in the filter-layer. The reduced accumulation of particles on the surface of the filter-layer slows down the rate of cake formation, ultimately increasing the dust holding capacity of the high efficiency filter media.

(a) PET   (b) PTFE
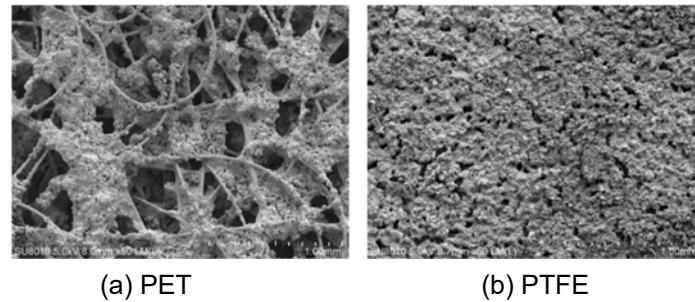
Fig. 5. SEM image of filter surface after dust holding.

In summary, the dust holding capacity of composite filter material is obviously increased compared with HEPA filter material, and the slope of process pressure drop curve is gradually increased. Part of the dust is deposited in the dust-containing layer, and the other part is accumulated on the surface of the high efficiency filter material, thus slowing down the growth rate of the resistance of the filter material and prolonging the service life of the high-efficiency filter material in the high-dust environment. The structure of "initial effect PET filter material + high efficiency filter material" is an ideal filter material model that can achieve high efficiency and high dust holding capacity.

3.2 Effect of fiber filling ratio on dust holding properties

The fiber filling rates of the composite filter media A, B, and C dust-holding layers were calculated to be 14%, 17%, and 21%, respectively, according to the fiber filling rate formula. Figure 6 illustrates the dust deposition mass of composite filter media A, B, C dust-holding layer and filter-layer. The dust holding capacity of the composite filter material decreases as the fiber filling rate of the dust-holding layer increases. Additionally, the dust mass of each material layer decreases with an increase in the fiber filling rate of the dust-holding layer. A higher fiber filling rate leads to higher filtration efficiency of the dust-holding layer and reduces the mass of dust reaching the filter-layer surface. However, a higher fiber filling rate causes more serious pore space blockage by dust, resulting in higher pressure drop and lower dust-holding capacity of the dust-holding layer when the same mass of dust is deposited. Consequently, a higher fiber filling rate corresponds to a lower dust holding capacity of the composite filter media.
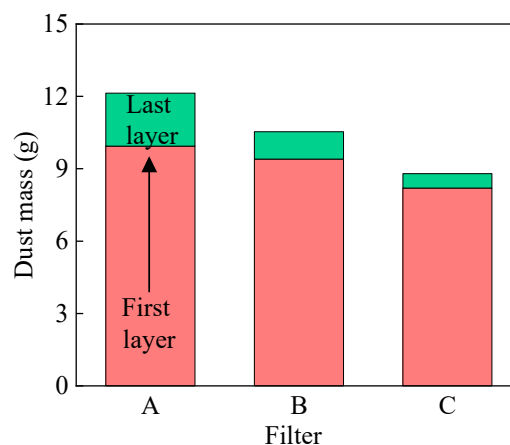
Fig. 6. Dust mass of each layer.

3.3 Effect of thickness on dust holding properties

To investigate the impact of dust-holding layer thickness on the performance of composite filter media, objects A, D, and E were chosen for the experiment. The experiment involved

using 1-layer, 2-layer, and 3-layer PET filter media (50 g/m2) to ensure that thickness was the only variable. Dust holding experiments were carried out under identical conditions for the three filter media, resulting in dust holding curves depicted in Fig. 7(a). The dust holding capacity of the composite filter media increased gradually with thicker dust-holding layers. However, the growth rates of dust holding capacity and pressure drop for filter media D and E were very similar, suggesting that the dust holding capacity would reach a limit with a specific thickness of the dust-holding layer. Beyond this point, increasing the thickness of the filter media would not further enhance its dust holding capacity.

Figure 7(b) shows the dust deposition quality of each layer of the composite filter media after dust holding. The dust deposition mass of the dust-holding layer of filter media A is the smallest and the dust mass of the filter-layer is the largest. The smallest thickness of the dust-holding layer of filter media A also has the lowest filtration efficiency, resulting in more dust being deposited in the filter-layer, causing a higher pressure drop. When the thickness of the dust-holding layer is increased, the filtration efficiency is increased and the space to hold the dust is increased. This reduces the accumulation of dust in the filter-layer and increases the dust holding capacity of the composite filter media.

(a) Dust holding curve   (b) Dust mass of each layer
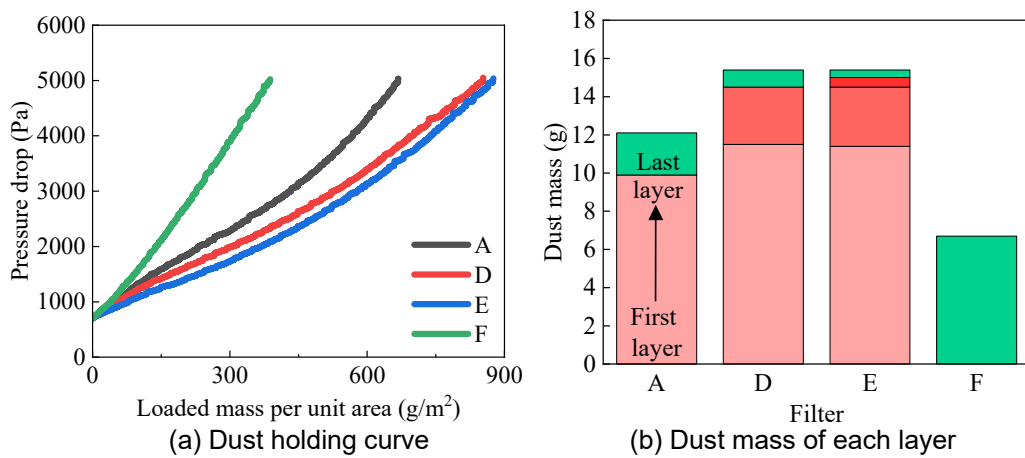
Fig. 7. Dust holding of filter media A、D、E、F.

The dust mass of the first two dust-holding layers of media D and E is the same, and the dust mass of the last two layers of media E is the same as that of the filter-layer of media D. The dust mass of the first two layers of media D and E is the same. When the thickness of the dust-holding layer is increased to 3 layers of PET filter media, the dust holding capacity is not enhanced. During the filtration process, dust particles follow the airflow into the filter media and are captured by the fibers. The particles gradually clog the pores of the media and eventually form a filter cake. The SEM cross-section of the dust-holding layer after holding the dust is shown in Fig. 8, and it can be seen that the position of the filter cake is close to the surface of the dust-holding layer. When the cake is formed, the filtration efficiency increases and the dust particles are captured by the cake layer. Thereafter, the dust particles hardly enter the interior of the filter media but accumulate on the surface of the dust-holding layer. Therefore, although filter media E has the largest thickness of the dust-holding layer and theoretically holds more dust, the formation of the filter cake on the surface of the dust-holding layer prevents the dust particles from entering the interior of the dust-holding layer, resulting in the dust holding capacity of filter media D and E being close to each other.
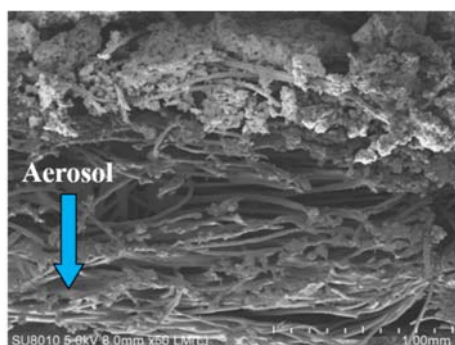
Fig. 8. SEM image of PET filter section after dust holding.

4. Conclusion

This paper addresses the issue of low dust holding capacity in high efficiency filter media when exposed to high concentration dust conditions. By adding a dust-holding layer to the surface of high efficiency filter media, a composite structure was created to enhance dust holding performance. The study also explores the impact of structural parameters of the dust-holding layer on the overall dust-holding performance of the composite filter media. The conclusions are as follows:

(1) In high concentration dust environments, HEPA filter media of varying precision (U15, H14, H12) operate under surface filtration mode with similar dust holding performance. Addition of a dust-holding layer significantly increases dust holding capacity. The 'primary PET filter media + high-efficiency filter media' structure is identified as ideal for achieving both high efficiency and high dust holding capacity.

(2) The study reveals that a higher filling ratio of the dust-holding layer leads to lower dust holding capacity in the composite filter media. Increased fiber filling rate enhances filtration efficiency but may also result in higher pressure drop due to pore blockage by dust, ultimately reducing dust capacity.

(3) Increasing the thickness of the dust-holding layer, when fiber filling rate remains constant, improves dust holding capacity of the composite filter media. However, beyond a certain thickness, the formation of a filter cake on the layer's surface captures dust particles, rendering further thickness increase ineffective in enhancing dust holding performance.

Acknowledgment

References

Liu, H., Lin Z., Zhang W., et al. A clogging capacity study of PTFE HEPA medium structure. Building Energy & Environment. 2021. 35(4), 35-37.

Tang, M., Hu J., Liang, Y., et al. Pressure drop, penetration and quality factor of filter paper containing nanofibers. Textile Research Journal. 2017. 87(4), 498-508.

Leung, W., Hung, C. Investigation on pressure drop evolution of fibrous filter operating in aerodynamic slip regime under continuous loading of sub-micron aerosols. Separation and Purification Technology. 2008. 63(3), 691-700.

Leung, W., Hung, C., Yuen, P. Experimental investigation on continuous filtration of sub-micron aerosol by filter composed of dual-layers including a nanofiber layer. Aerosol Science and Technology. 2009. 43(12), 11741183.

Liu, C., Liu, J., Ding, Y., et al. Preparation and properties of expanded polytetrafluoroethylene membrane composites with high dust holding capacity for high efficiency air filtration. Journal of Textile Research. 2021. 42(5), 31-37.

Long, J., Tang, M., Sun, Z., et al. Dust loading performance of a novel submicro-fiber composite filter medium for engine. Materials. 2018. 11(10), 1-17.

Wang, Q., Lin, X., Chen, D. Effect of dust loading rate on the loading characteristics of high efficiency filter media. Powder Technology. 2016. 287, 20-28.

Xu, H., Bream, B., Bahk, Y., et al. Effects of relative humidity and particle type on the performance and service life of automobile cabin air filters. Aerosol Science and Technology. 2016. 50(6), 542-554.

JET ASISSTED FLUIDIZED BED PRODUCTION OF BATTERY HETERO AGGREGATES WITH STRUCTURAL ANALYSIS

Zhi Cheng Hua*, Robert Kräuter, Stefan Heinrich

Institute of Solids Process Engineering and Particle Technology, Hamburg University of Technology, Germany. Denickestraße 15, 21073 Hamburg.

*zhi.cheng.hua@tuhh.de

Abstract

One of the main challenges of all-solid-state-batteries (ASSBs) is the upscaling of the production process of the cathode composite. In this study, the use of a vibrating fluidized bed is proposed for the mixing, coating and aggregation of the battery materials. Thus, the fluidization and mixing behaviour cathode material consisting of lithium iron phosphate (LFP), carbon black (CB) and sodium chloride (SC) (model system) or lithium-indium chloride (LIC) is investigated. It was shown that all materials could be fluidized using a vibrated fluidized bed. The electronic conductivity as well as the cell capacity using LIC was evaluated. Utilizing an assisting downwards pointed microjet within the vibrated fluidized bed further enhanced the fluidization and enabled the creation of hetero agglomerates. The success of the hetero-agglomerate and aggregate production was confirmed via SEM and FIB-SEM.

The mixing was analyzed via segmentation of the SEM images using Metas' segment anything model (SAM) (Kirillov et al., 2023; Witte et al., 2023). The segmented image was then compared with human segmentation, and it was found that the SAM performs well detecting particles. A classification using a K-means algorithm based on the roundness of the identified particles was used.

1. Introduction

The global demand for high performance batteries has grown immensely, especially for electric vehicles (EVs). One challenge that EVs have yet to overcome is their relative short range in comparison to combustion engine cars. To improve the range of EVs, superior batteries with increased energy densities, both gravimetrically and volumetrically are required. In recent years, a new battery technology, ASSBs, have emerged, promising up to 70% more volumetric and 40% gravimetric energy density compared to conventional lithium ion batteries by using a metallic lithium anode (Janek und Zeier, 2016). ASSBs are potentially more energy dense, but also are inherently safer and environmentally friendly due to the lack of combustible volatile organic compound (Janek und Zeier, 2016; Weiss et al., 2020). In ASSBs, the solid electrolyte that is replacing the liquid electrolyte has to offer the ionic conductivity by making mechanical contact between the particles allowing ions to diffuse through the material. A major challenge is the large-scale production of cathode composite with low interfacial resistance. Utilizing small particles, especially sub-micron and nanosized particles have exhibited an increased performance (Bielefeld et al., 2019). However, processing small particles for this purpose have only been realized on lab scale using ball mills or mortars, which is why in this contribution a vibrated fluidized bed with jet assistance, capable of upscaling, is examined in this contribution.

While the fluidization behavior of fine particles has been explored, the mixing of different nanoparticles in a fluidized bed was determined on different scales (e.g. micro or nanoscale) (van Ommen et al., 2012). This was mainly done by using imaging techniques like SEM or TEM. Additionally, end-use properties can be evaluated to determine the quality of mixing (Wei et al., 2002). This contribution confirms the fluidization of proposed battery materials, and investigates their mixing and aggregation in a vibrated fluidized bed with microjet assistance. The product properties are evaluated through the electrical powder conductivity

and specific capacity of the product. A new method to evaluate of the scale of mixing is proposed. First, the success of the heteroaggregate production and evaluation of the mixing quality is confirmed through SEM and FIB. Second, the obtained images are segmented with SAM. Lastly, the segmented particles (masks) are classified into their respective species using a K-means algorithm.

2. Experimental Section

A vibrated fluidized bed with microjet assistance was used. Vertical vibration was applied through the mechanical movement of a rotating plate, which is connected to a motor. The rotational speed was controlled using a frequency variator. A sketch of the machine including its geometry is shown in Figure 1. The motion of the vibrated fluidized bed is that of a piston crank mechanism, in which the rotation of the motor leads to the vertical movement of the fluidized bed through a linear shaft. Based on the geometry, the resulting acceleration can be approximated as sinusoidal (see Figure 1).
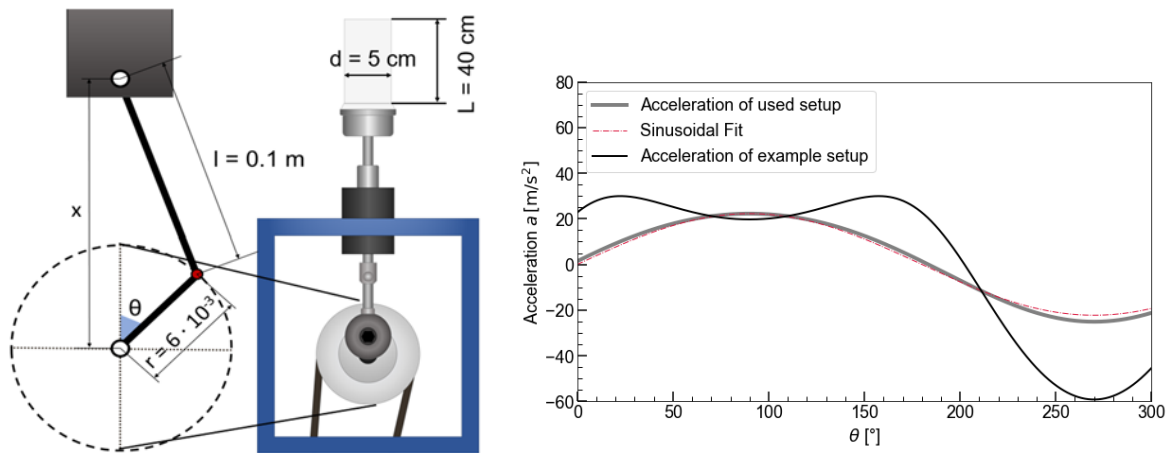
Figure 1: Left: Setup of the vibrated fluidized bed including dimensions and geometry of the piston crank mechanism Right: Acceleration over rotation angle of an example setup with other dimensions, sinusoidal fit and of used setup.

The pressure measurement was done using a USB-DAQ6003 (National Instruments, USA) in conjunction with sensitive differential pressure measurements that is capable of very low differential pressures (PX165 pressure transducers, Omega Engineering GmbH, Germany). Additionally, a downwards pointing microjet can be installed in the fluidized bed, providing high velocity gas flows leading to agitation of particles and aiding the fluidization. Additionally, the nozzle diameter is set to 4 mm and distance to the distributor plate of 1 cm. The vibration induces an alternating change of pressure signal. To capture the bed pressure drop more accurately, the pressure drop is measured with a sampling rate of 2500 Hz and averaged for each second to remove outliers in the bed pressure drop. The flow rate was controlled using two mass flow controllers (EL-FLOW Select, Bronkhorst Germany). Dry Nitrogen (Nitrogen 5.0) was used for the fluidization of the particles. As for the microjet, the pressure line was supplied with 10 bar pressure, resulting in an approximate jet outlet velocity of 320 m/s (Quevedo et al., 2010).
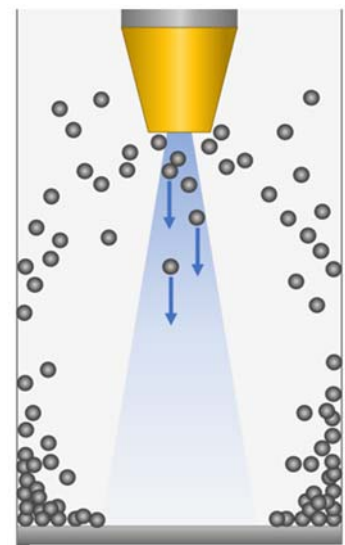
Figure 2: Microjet setup

An overview of used particle species and their material properties for the model system are given in Table 1.

Table 1: Particle size, Raw and bulk density and used weight composition.

	Lithium iron phosphate	Carbon black	Sodium chloride	Lithium indium chloride
Primary particle size $d_{50,3} [\mu m]$	0.5	0.04	9.22	≈ 1.0
Raw density $[\frac{kg}{m^3}]$	3600	2100	2200	2590
Bulk density $[\frac{kg}{m^3}]$	354	82	300	-
Weight composition [%]	58	4	38	38

3. Fluidization and mixing behavior of fine materials

In this chapter the fluidization and mixing behavior is investigated. In literature it is stated that very fine particles fluidize as agglomerates. This is caused by the high ratio of surface forces in comparison to body forces, namely van der Waals, capillary forces or electrostatic forces. During fluidization soft agglomerates are formed, that change their shape and their size over time during fluidization. In this section the bed pressure drop and agglomerate size distribution is investigated by using a Camsizer XT (Retsch GmbH, Germany) to measure the agglomerate size distribution. While the mixing behavior of free-flowing particles are relatively well understood, the mixing of cohesive particles requires percolation of different species throughout the agglomerates. This can only be achieved if the process, in this case a vibrated fluidized bed, provides sufficient forces to break soft agglomerates. For each experiment, a bed height of 10 cm was chosen for the fluidization experiments.
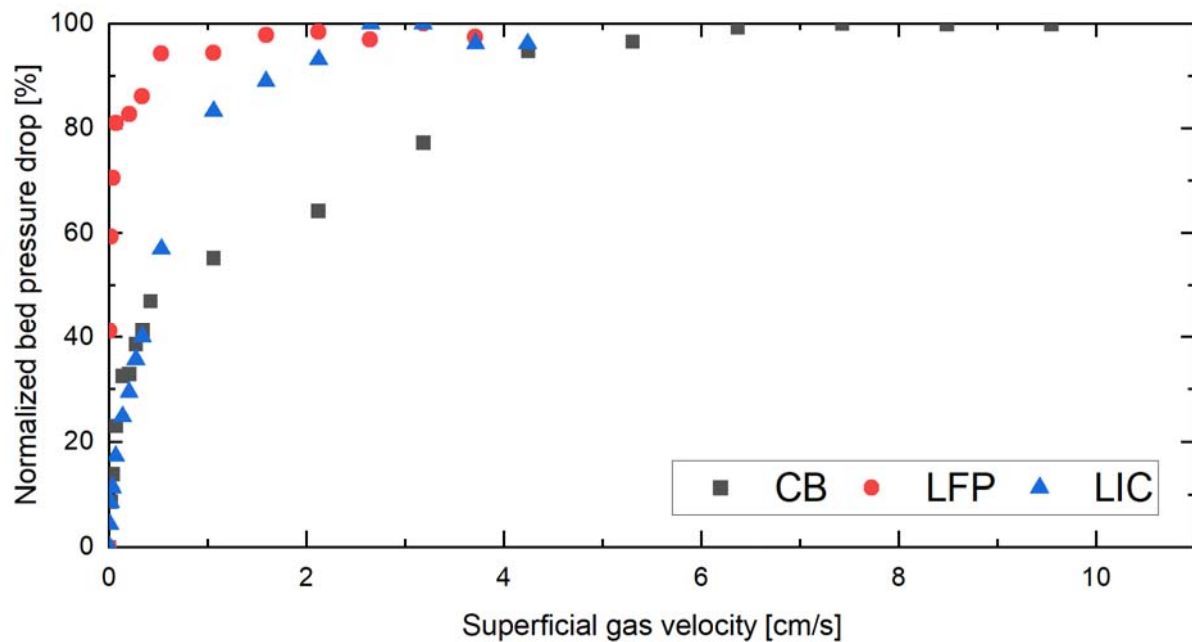
Figure 3: Bed pressure drop for CB, LFP and LIC at 8.8 Hz vibration frequency.

From Figure 3 follows that all particles could be fluidized. The normalized bed pressure drop of 100% indicates that the weight of the particles was fully carried by the fluidization gas. The minimal fluidization velocity was estimated to be the lowest gas flow, where the bed pressure drop becomes independent of the gas velocity. To evaluate the mixing process of the vibrated fluidized bed, the electrical powder conductivity of the model material system using NaCl is investigated using the method Westphal et al. (Westphal et al., 2017). A fixed ratio (see Table 1) for each material and a bed height for 10 cm is chosen. The vibration intensity, the fluidization velocity and processing time are varied. The specific powder conductivity can be an indicator of the percolation of the electronically conductive material through the material.
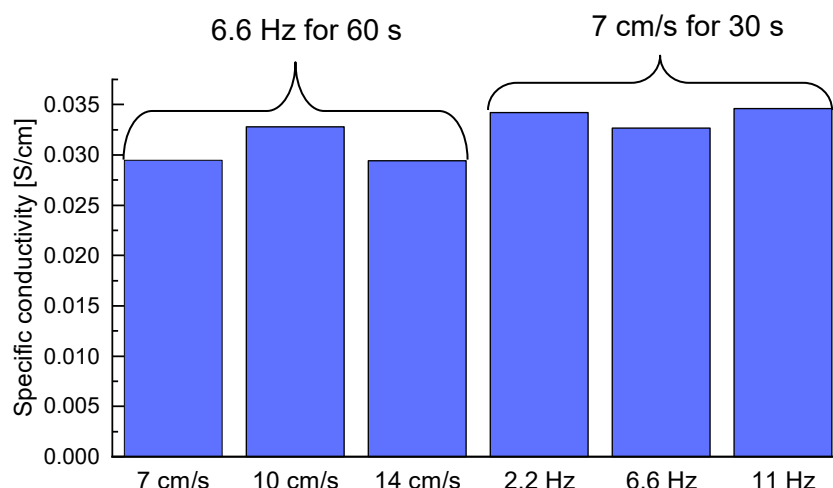
Figure 4: Specific powder conductivity for different fluidization gas velocities with 60 s fluidization time and a vibration frequency of 6.6 Hz and specific powder conductivities for different vibration frequencies with 30 s fluidization time and superficial gas velocity of 7 cm/s.

From Figure 4 can be extracted that increasing the fluidization gas or increasing the vibration frequency does not change the specific resistance significantly. Compared to the results from Witte et al. the specific resistance is between $0.06\frac{S}{cm}$ and $0.09\frac{S}{cm}$ for their process with the same material system and starting composition (Witte et al., 2023). A higher specific conductivity can be attributed more carbon being mechanically connected to each other, enabling flow of electrons through the carbon black. Comparing with the results from Witte et. al. it cannot be deduced whether the carbon black content was different after the processing or if carbon black was elutriated during fluidization. However, it can be concluded, that the vibrated fluidized bed is unable to produce homogenously mixed agglomerates within the given parameter range since the electronic powder conductivity doesn't change significantly in the given parameter range. FIB-SEM imaging was used to confirm that the produced particles were indeed not fully percolated by all materials homogeneously but rather as agglomerates consisting of a single particle species (homoagglomerates) with particles of other species on the surface, making them heteroagglomerates with a homoagglomerate core. Repeating the experiment with LIC instead of SC and a processing time of 60 minutes and a vibration frequency of $11\,Hz$ did not change the morphology or composition of the produced agglomerates, as they were still mostly homoagglomerates with no measurable capacity through cyclovoltammetry.

4. Microjet treatment

In this section the treatment of the agglomerates is considered through a downwards directed micronozzle with high velocity gas flow (see Figure 2). The particles are fluidized with a velocity of 3 cm/s and a vibration frequency of $f = 11\,Hz$ was applied. The distance of the nozzle to the distributor plate was set to 1 cm. In respect to the nozzle diameter, which highly adds to the superficial gas velocity and promotes elutriation with increasing diameter, was set to 1 mm and the processing time limited to 1 minute. The resulting sample consisting of LFP, NaCl and CB was investigated using SEM and FIB-SEM:
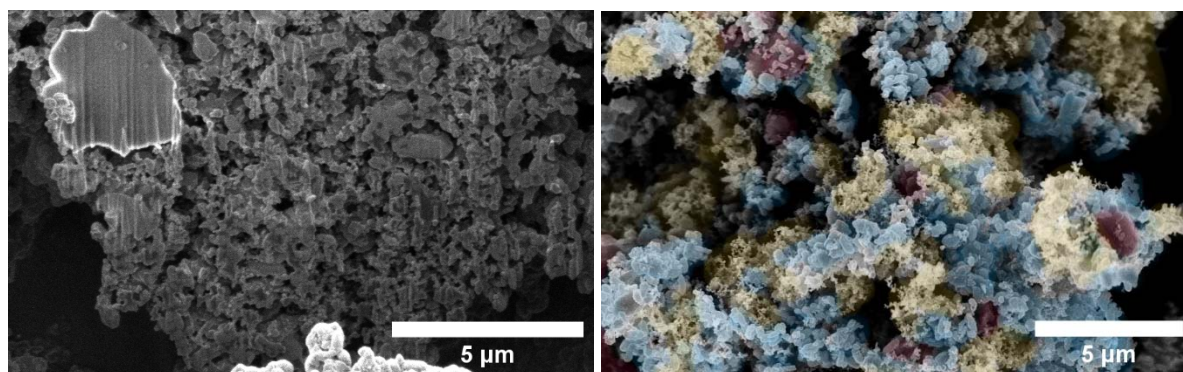
Figure 5: Left: FIB-SEM cross section of composite material that was mixed using a microjet for one minute. Right: False color image of the surface of composite material obtained by SEM with done by manual segmentation.

From Figure 5 can be learned that the SC is mainly within the material and not at the surface. This is most likely attributed to its size (see Table 1), leading to SC acting as a host particle onto which the guest particles, LFP and CB, adhere to. This leads to SC mostly not being visible on the surface of the agglomerates, as the guest particles coat the SCs surface. This was confirmed by more cross sections, showing that almost all of the SC is within the material. In the FIB-SEM cross section (Figure 5) it can be seen that both LFP and carbon black is distributed well. This is also the case when looking at the surface of the composite. As can be seen previously, different particles are mixed and contacted and therefore it can be assumed that heteroagglomerates can be produced. Heteroagglomerates are composites, mainly of particles of small size (submicron and nanoparticles), where particles of different species are contacted (heterocontacts) that can result in new properties of the material. In this case, the heterocontacts facilitate both ionic and electronic flow within the composite, thereby enabling its functionality as a solid-state battery. Additional FIB-SEM images reveal that large chunks of unbroken LIC remain within the composite. Presumably there is no network for the lithium ions to the active material that could enable the diffusion of ions.

5. AI Image Segmentation via SAM

In the previous section there is no objective metric to determine an objective mixing quality by only using imaging techniques. To address this issue, the SAM model is employed to segment the SEM images. Then, a K-means algorithm is used to classify the different particle masks according to their species (LFP, SC or NaCl). Like the false color image Figure 5, that was drawn with subjective judgement based on the differences in size and morphology, the goal is to differentiate or segment each particle and classify them by their species. Flattening the observed surfaced, prepared by the pressing of the sample, resulted in better images and detection of the particles. This is due to the contrast differences that occur when particles are at a different height, due to the obstruction of the signal. While the detection of particles using SAM lead to a meaningful result, the classification using a roundness factor was promising, but still insufficient for a subsequent quantitative analysis of

the segmentation results. To further improve the classification accuracy, other methods like training a convolutional neural network (CNN) to classify each mask identified by the SAM may be able to classify the particles more accurately.
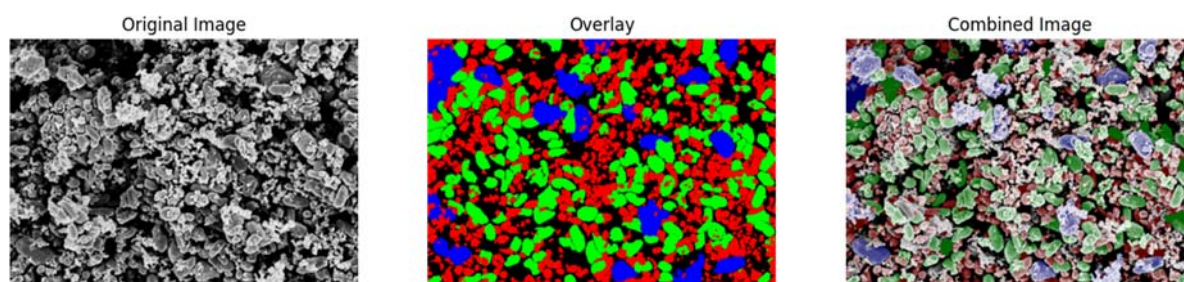
Figure 6: Left: SEM image. Middle: Segmentation and classification (overlay) of obtained SEM image Right: Combined image.

6. Conclusion

In this contribution a vibrated fluidized bed with microjet assistance was introduced with the aim of improving the mixing of nanoagglomerates. Two ASSB material systems were investigated in regards to their electrochemical performance, electronic conductivity and capacity. It was found that a vibrated fluidized bed enables the fluidization of ultra-fine particles as agglomerates, but is most likely unable to break the agglomerates. On the other hand, the introduction of a microjet lead to well-mixed agglomerates, that were analyzed using SEM and FIB-SEM. Further, a new method to analyze the microstructure, employing Meta's SAM, a pre-trained machine learning model capable of zero shot segmentation, of was introduced. Lastly, the segmented particles were classified by a K-means algorithm that led to an insufficient classification of some particles, but overall a good result for most particles.

Literaturverzeichnis

Bielefeld, Anja; Weber, Dominik A.; Janek, Jürgen (2019): Microstructural Modeling of Composite Cathodes for All-Solid-State Batteries. In: *J. Phys. Chem. C* 123 (3), S. 1626–1634. DOI: 10.1021/acs.jpcc.8b11043.

Janek, Jürgen; Zeier, Wolfgang G. (2016): A solid future for battery development. In: *Nat Energy* 1 (9). DOI: 10.1038/nenergy.2016.141.

Kirillov, Alexander; Mintun, Eric; Ravi, Nikhila; Mao, Hanzi; Rolland, Chloe; Gustafson, Laura et al. (2023): Segment Anything. Online verfügbar unter http://arxiv.org/pdf/2304.02643.pdf.

Quevedo, Jose A.; Omosebi, Ayokunle; Pfeffer, Robert (2010): Fluidization enhancement of agglomerates of metal oxide nanopowders by microjets. In: *AIChE J.* 56 (6), S. 1456–1468. DOI: 10.1002/aic.12075.

van Ommen, J. Ruud; Valverde, Jose Manuel; Pfeffer, Robert (2012): Fluidization of nanopowders: a review. In: *J Nanopart Res* 14 (3). DOI: 10.1007/s11051-012-0737-4.

Wei, Dongguang; Dave, Rajesh; Pfeffer, Robert (2002). In: *J Nanopart Res* 4 (1/2), S. 21–41. DOI: 10.1023/A:1020184524538.

Weiss, Manuel; Simon, Fabian J.; Busche, Martin R.; Nakamura, Takashi; Schröder, Daniel; Richter, Felix H.; Janek, Jürgen (2020): From Liquid- to Solid-State Batteries: Ion Transfer Kinetics of Heteroionic Interfaces. In: *Electrochem. Energ. Rev.* 3 (2), S. 221–238. DOI: 10.1007/s41918-020-00062-7.

Westphal, Bastian Georg; Mainusch, Nils; Meyer, Chris; Haselrieder, Wolfgang; Indrikova, Maira; Titscher, Paul et al. (2017): Influence of high intensive dry mixing and calendering on relative electrode resistivity determined via an advanced two point approach. In: *Journal of Energy Storage* 11, S. 76–85. DOI: 10.1016/j.est.2017.02.001.

Witte, Joscha; Hua, Zhi Cheng; Kolck, Victor; Kruggel-Emden, Harald; Heinrich, Stefan; Schmidt, Eberhard (2023): Investigation of a Jet-Based Direct Mixing Process for Improved Structuring of Conductive Battery Hetero-Agglomerates. In: *Processes* 11 (11), S. 3243. DOI: 10.3390/pr11113243.

Atomic layer deposition ultrathin amorphous TiO_2 film in a fluidized bed reactor for improving the weatherability of TiO_2 pigment

Jing Guo[1,2,*], Bingkang Niu[1,2], Huifang Lou[1,2], Zhengyi Chao[1,2]，Youzi Liu[1,2]

1. School of Chemistry and Chemical Engineering, North University of China, Taiyuan 030051, China

2. Shanxi Province Key Laboratory of Chemical Process Intensification, North University of China, Taiyuan 030051, China

* Email: guojing0519@nuc.edu.cn

Abstract

Normally, a transparent inert film is coated on the surface of TiO_2 particles to enhance the weatherability of the pigment. Liquid-phase coating process is mainly used in industry, which difficult to get really uniform films. This work combining nanoparticle fluidization technology with atomic layer deposition (ALD) technology to achieve precise surface modification of a large number of micro-nano particles. First we explored the fluidization characteristics of TiO_2 nanoparticles in a home-made atmospheric fluidized bed ALD reactor to ensure the uniform fluidization of a large number of nanoparticles. Then $TiCl_4$ and H_2O were used as precursors to deposit amorphous TiO_2 films on the surface of TiO_2 nanoparticles. Compared with other traditional coating materials, amorphous TiO_2 has higher light refractive index, and realizes the suppression of the photocatalytic activity of TiO_2 without introducing other substances, demonstrating greater application potential in TiO_2 pigment coating field. The process is a gas-phase coating method, which is efficient, no waste water, and easy to scale up. This work shown the excellent property of interface engineering in improving pigment weatherability and can also provide guidance for the design of nanoparticle surface modification.

1. Introduction

TiO_2 is widely used in painting, plastics, papermaking and other fields due to its excellent brightness, whiteness and stability. However, the inherent photocatalytic activity of TiO_2 will promote the oxidation of organic substances around it, resulting in discoloration and cracking of the coating. Normally, a transparent inert film such as Al_2O_3, SiO_2, or ZrO_2 is coated on the surface of TiO_2 particles to enhance the weatherability of the pigment. The coating not only be thick enough to shield the photocatalytic activity of the TiO_2 but also thin enough to ensure the excellent brightness and whiteness of the TiO_2 pigment. Liquid-phase coating process is mainly used in industry, which difficult to get really uniform films. Wu et al. studied the morphology of the hydrous alumina coating on the surface of TiO_2 particles under different pH values and temperatures by liquid phase deposition method, only at a specific pH value and temperature could obtain the uniform and continuous Al_2O_3 film[1]. Zhang et al. prepared ZrO_2 coated TiO_2 particles, only at a reaction temperature of 80 ºC and pH values ranging from 7 to 9 with a mole ratio of $ZrOCl_2$ to TiO_2 of 1:51 could get the dense and continuous ZrO_2 coating layers[2]. The preparation conditions of liquid methods to get uniform coating film are harsh, and the products need to be washed, dried and other post-processing operations. It is necessary to find a simple method to prepare ultra-thin dense and uniform shielding film.

ALD is a vapor deposition method, which achieves self-limiting growth by alternately introducing two reactants into the reaction chamber to ensure the coating thickness at the atomic scale[3]. The traditional ALD technology is static operation mainly aimed at the flat substrate, using for particle modification is limited by the diffusion of the precursor, and the processing capacity is small[4]. Particle fluidization is widely used in powder treatment due to its good gas-solid contact efficiency and high mass and heat transfer rate. However, nanoparticles are small and easy to agglomerate, which are difficult to fluidize in traditional fluidized beds. Vibration fluidization is considered to be an effective method to improve the fluidization state of nanoparticles. Yang et al. studied the fluidization behavior of SiO_2, TiO_2

and ZnO nanoparticle agglomerate in a vibration fluidized bed (VFB), and proved that the vibration force can reduce the minimum fluidization velocity of cohesive particles and improve their fluidization quality[5]. Guo et al. used fluidized bed ALD reactor to deposit uniform, conformal, sub-nanometer Al_2O_3 and SiO_2 films on the surface of TiO_2 nanoparticles, which could effectively shield the photocatalytic activity of TiO_2 nanoparticles[6,7]. Yu et al. used pulsed CVD method to coat SnO_2, SiO_2 and TiO_2 amorphous layer on the surface of anatase TiO_2 particles. The amorphous TiO_2 film has a higher refractive index than the traditional SiO_2 inert layer, which can maintain the luminescence ability of the TiO_2 pigment. At the same time, the amorphous TiO_2 film can inhibit the photocatalytic activity of TiO_2 and improving its weatherability[8]. However, this pulsed CVD is a static vacuum batch operation, which is limited by the diffusion of the precursor and can only process a small amount of particle. In view of the above problems, we build a homemade vibration fluidized bed ALD reactor to achieve precise modification of a large amount of TiO_2 pigment under ambient pressure.

In order to ensure the uniform coating of TiO_2 nanoparticles, the fluidization characteristics of nanoparticles in a homemade ALD reactor were studied. Under the optimal fluidization conditions, amorphous TiO_2 films were deposited on the surface of TiO_2 pigment. The shielding effect of the coating film on the photocatalytic activity of TiO_2 nanoparticles was verified by the degradation of methylene blue under UV light irradiation.

2. Experimental

2.1 Atomic layer deposition amorphous TiO_2 films on the surface of TiO_2 nanoparticle

Amorphous TiO_2 films were deposited on the surface of anatase TiO_2 nanoparticles using $TiCl_4$ and H_2O as precursors. 2.0 g dried and sieved TiO_2 nanoparticles were put in the fluidized bed reactor. The ALD process is carried out according to the following steps, as show in Fig.1. First introduced $TiCl_4$ precursor and chemically adsorbed on the surface of TiO_2 NPs; second the excess $TiCl_4$ precursor and by-products were blown out of the reaction chamber by N_2; the third step, H_2O as the second precursor was carried into the reactor with N_2, and react with adsorbed $TiCl_4$ on the surface of TiO_2 to form amorphous TiO_2 film; then the excess H_2O and by-products were blown out of the reaction chamber by N_2. The samples obtained after deposition are named as x-cycles TiO_2, where x represents the number of ALD cycles.
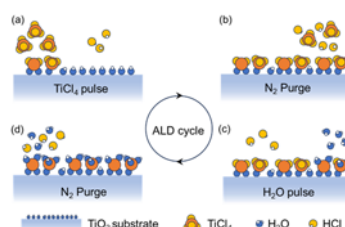
Fig. 1. The ALD process diagram

3. Results and discussion

3.1 Fluidization behavior of TiO_2 NPs in homemade fluidized bed ALD reactor

For the homemade fluidized bed ALD reactor, in order to achieve uniform coating of a large number of TiO_2 nanoparticles, it is necessary to ensure uniform fluidization of the nanoparticles.

Fig. 2. The bed pressure drop curves of TiO_2 nanoparticles under different amplitudes

3.1.1 Effect of amplitude on the fluidization state of TiO_2 nanoparticles

In order to verify the fluidization behavior of nanoparticles in our homemade fluidized bed reactor and determine the optimal fluidization conditions of TiO_2 nanoparticles, the fluidization characteristics of TiO_2 with an initial bed height of 5 mm under different amplitudes were studied. Fig. 2 shows the variation of bed pressure drop of TiO_2 NPs with gas velocity under different amplitudes. Within the range of gas velocity in the current study, when the amplitudes are 0.7 mm and 0.8 mm, the bed pressure drop increases slowly with the increase of gas velocity. With the increase of gas velocity, the phenomenon of channeling and agglomeration occurs in the bed, but no fluidization occurs. When the amplitude reach to 1.2 mm, the bed pressure drop increases slowly with the increase of gas velocity. When reaching the minimum fluidization velocity, the TiO_2 nanoparticles begin to fluidize, and some of the particles occur to elutriate, the bed pressure drop continues to increase with the increase of gas velocity. In theory, during fluidization the pressure drop of the gas velocity bed will remain unchanged[9], while in our work, the pressure drop of the bed continuously increase with the increase of gas velocity. The pore size of the quartz sand core filter above the reactor in this experiment was about 150-178μm, and the size of nanoparticle agglomerates under vibration conditions was generally tens of microns, which would continuous enter into the pores of the filter to increase the pressure drop of the bed. The minimum fluidization velocity is 4.40 cm s^{-1}, 3.14 cm s^{-1} and 2.83 cm s^{-1} when the amplitude is 1.2 mm, 1.3 mm and 1.4 mm, respectively. With the increase of amplitude, the minimum fluidization velocity decreases gradually. When the amplitude increased from 1.3 mm to 1.4 mm, the bed pressure drop curves were very close, and the minimum fluidization velocity didn't change much. It shown that when the amplitude reaches a certain extent, the effect of increasing the amplitude on promoting the quality of nanoparticle fluidization is weakened. In addition, too large amplitude will lead to an increase in energy consumption. Therefore, 1.2 mm was selected as the appropriate amplitude in this experiment.

3.1.2 Effect of initial bed height on the fluidization state of TiO_2 nanoparticles

Fig. 3(a) is a plot of bed pressure drop versus gas velocity at different initial bed heights of TiO_2 nanoparticles. When the initial bed height is 5,10,15,20,25 mm, the minimum fluidization velocity is 4.40, 4.71, 6.28, 8.16, 10.05 cm s^{-1}, respectively. With the increase of the initial bed height, the minimum fluidization velocity increases gradually. Fig. 3(b) is the curve of bed expansion ratio with gas velocity under different initial bed heights of TiO_2 nanoparticles. As shown in Fig. 3(b), after the TiO_2 nanoparticles reached stable fluidization, the bed expansion ratio increased first and then decreased with the increase of the initial bed height. When the initial bed height was 10 mm, the bed expansion ratio was the largest. Under the experimental conditions, TiO_2 NPs with different initial bed heights all could be fluidized, and the initial bed height of 10 mm had better fluidization quality.

3.1.3 The change of the agglomerates during the TiO_2 nanoparticle fluidization

Fig. 4. is a microscopic picture of TiO_2 nanoparticle agglomerates after different fluidization time. As shown in Fig. 4(a) and Fig. 4(b), before fluidization TiO_2 nanoparticle agglomerates were mainly simple agglomerates with a size of less than 20 μm. During the fluidization, under the combined action of internal viscous force and external shear force, simple agglomerates continued to grow to form porous composite agglomerates with a size of 40-50 μm, which was consistent with the literature[10]. By observing the color change of particle agglomerates after different fluidization time, it can be found that with the extension of fluidization time, the color of the agglomerates gradually change from white to pink, and the dyed particles and the pure particles were mixed. This is because during the fluidization process, the collision between particles and particles, particles and pipe wall and the impact of gas make the agglomerates breakup and coalescence continuously. The average porosity of the agglomerates is about 0.91[11], which can ensure that the nanoparticles are in full contact with the precursor to achieve a uniform coating on the surface of the TiO_2 NPs.
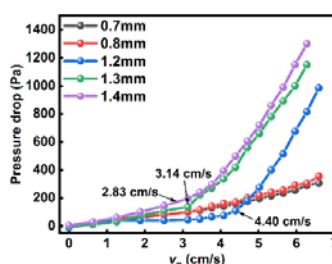
3.2 Fluidization behavior of TiO_2 NPs in homemade fluidized bed ALD reactor

On the basis of uniform fluidization of nanoparticles, in order to improve the weather resistance of TiO_2 pigment, we used ALD technology to deposit amorphous TiO_2 films on the surface of TiO_2 NPs, explored the coating thickness and its photocatalytic inhibition

performance, and verified the performance of the homemade fluidized bed atomic layer deposition system.
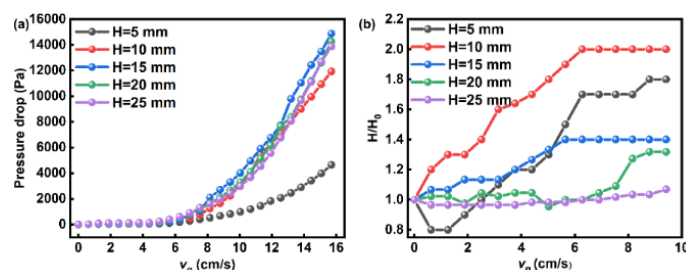
Fig. 3. (a) Bed pressure drop and (b) bed expansion ratio for TiO_2 at different initial bed heights
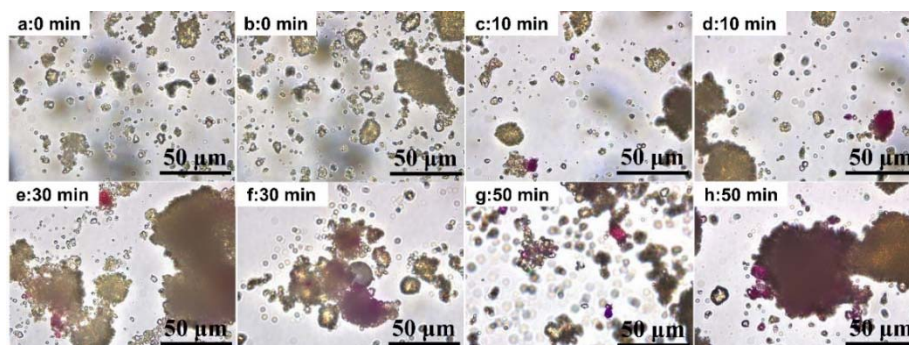
Fig. 4. Microscopic images of TiO_2 nanoparticle agglomerates after different fluidization time

3.2.1 The mechanism of ALD amorphous TiO_2 process

The reaction process of 5-cycles TiO_2 sample was monitored by an on line mass spectrometer, the result is shown in Fig. 5. No $TiCl_4$ signal were detected, the molecular fragment signal peaks detected by the quadrupole mass spectrometer were H^+(m/z=1), H_2O (m/z=18), $H^{35}Cl^+$ (m/z=36), $H^{37}Cl^+$ (m/z=38). The mass fragments of 36 and 38 are the expected mass signals of HCl, and their relative intensity is consistent with the expected chlorine isotope abundance[12] . From Fig. 5(a), the signals of each substance fragment show the same change trend during the five ALD cycles, indicating that the reaction follows the ALD mechanism.
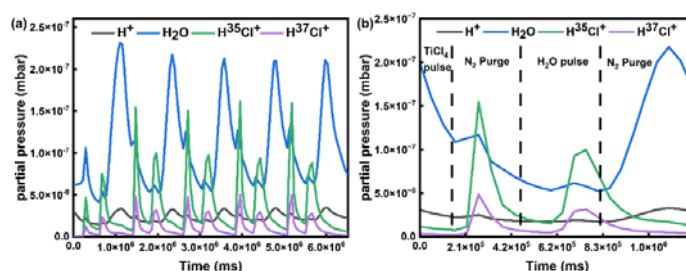
Fig. 5. ALD process mass spectra(a)5 ALD cycles(b)1 ALD cycle

3.2.2 Morphology analysis of amorphous TiO_2 thin films

Fig. 6 shown the TEM images of the pure TiO_2 nanoparticles and the samples coated with amorphous TiO_2 film. Fig. 6 (b-f) shows the TEM images of the samples obtained after 2,5,10 and 30 ALD cycles, respectively. It can be clearly observed that the surface of TiO_2 NPs were coated with a uniform and dense amorphous TiO_2 film. With the increase of ALD cycles, the thickness of the coatings also increases significantly, indicating that the atomic layer deposition has good shape retention and cyclic periodicity. As shown in Fig. 7, the thickness of amorphous TiO_2 film increases linearly with the increase of ALD cycles, and the growth rate is about 1.09 Å / cycle.
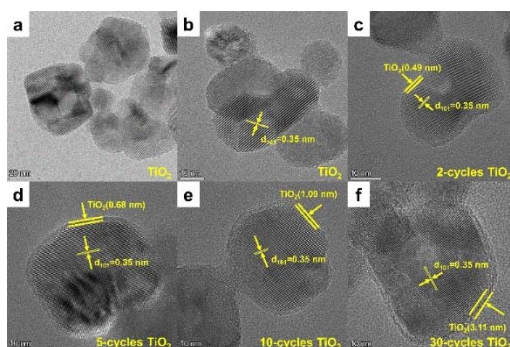
Fig. 6. TEM images of pure TiO$_2$ and x-cycles TiO$_2$ nanoparticles
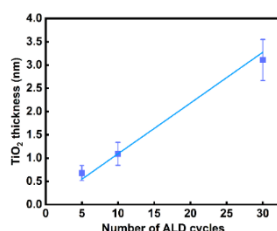
Fig. 7. Growth rate per cycle for the amorphous TiO$_2$ thin film

3.2.3 The photocatalytic activity of coated TiO$_2$ NPs

Fig. 8(a) is the photocatalytic activity diagram of MB degradation by anatase TiO$_2$ and x-cycle TiO$_2$ samples. It can be seen that after the deposition of amorphous TiO$_2$ film, the photocatalytic activity of series x-cycles TiO$_2$ samples was lower than that of pure anatase TiO$_2$, indicating that the amorphous TiO$_2$ film can inhibit the photocatalytic activity of anatase TiO$_2$. Fig. 8(b) is the degradation rate diagram, and Fig. 8(c) is the relationship between the reaction rate constant and the number of ALD cycles. With the increase of the number of ALD cycles, the reaction rate constant gradually decreases, indicating that the photocatalytic activity gradually decreases with the increase of the number of ALD cycles. After 30 ALD cycles, the thickness of amorphous TiO$_2$ film was only about 3.1 nm, and the photocatalytic activity of anatase TiO$_2$ was almost completely shielded. Fig. 9 is the mechanism of amorphous TiO$_2$ film deposited by fluidized bed ALD to shield the photocatalytic activity of TiO$_2$ pigment.
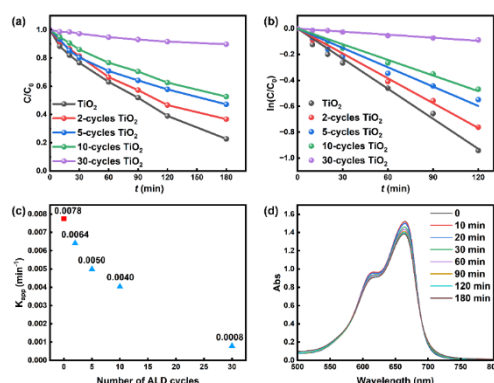
Fig. 8. Photocatalytic degradation of MB diagram of the series TiO$_2$ samples

4. Conclusion

Our homemade fluidized bed ALD reactor can realize the uniform fluidization and surface coating of a large number of nanoparticles. In this work, under the optimal fluidization conditions of TiO$_2$ nanoparticles, using TiCl$_4$ and H$_2$O as precursors, ALD dense and uniform amorphous TiO$_2$ film on the surface of anatase TiO$_2$, the growth per cycle was about 1.09 Å / cycle. After 30 ALD cycles, the film thickness was only 3.1 nm, which could suppress the photocatalytic activity of TiO$_2$ completely. Amorphous TiO$_2$ coating can not only improve the

weatherability of the TiO$_2$ pigment but also can maintain their good optical properties without introducing other foreign substances. This method has a good prospect in the field of precise modification of a large number of nanoparticles.
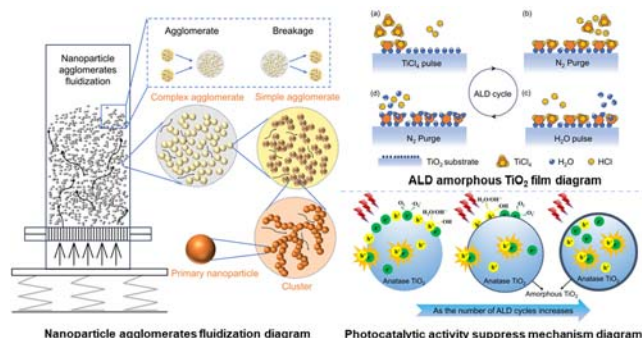
Fig. 9. The mechanism of amorphous TiO$_2$ film deposited by fluidized bed ALD to shield the photocatalytic activity of TiO$_2$ pigment

Acknowledgment

References

[1]   Wu H-X, Wang T-J, Jin Y. Morphology "Phase Diagram" of the Hydrous Alumina Coating on TiO$_2$ Particles during Aqueous Precipitation[J]. Industrial & Engineering Chemistry Research, 2006, 45(15): 5274-5278.

[2]   Zhang Y, Yin H, Wang A, et al. Evolution of zirconia coating layer on rutile TiO$_2$ surface and the pigmentary property[J]. Journal of Physics and Chemistry of Solids, 2010, 71(10): 1458-1466.

[3]   Goulas A, Ruud Van Ommen J. Atomic layer deposition of platinum clusters on titania nanoparticles at atmospheric pressure[J]. Journal of Materials Chemistry A, 2013, 1(15): 4647.

[4]   Longrie D, Deduytsche D, Detavernier C. Reactor concepts for atomic layer deposition on agitated particles: A review[J]. Journal of Vacuum Science & Technology A: Vacuum, Surfaces, and Films, 2014, 32(1): 010802.

[5]   Yang J, Zhou T, Song L. Agglomerating vibro-fluidization behavior of nano-particles[J]. Advanced Powder Technology, 2009, 20(2): 158-163.

[6]   Guo J, Benz D, Doan Nguyen T-T, et al. Tuning the photocatalytic activity of TiO$_2$ nanoparticles by ultrathin SiO$_2$ films grown by low-temperature atmospheric pressure atomic layer deposition[J]. Applied Surface Science, 2020, 530: 147244.

[7]   Guo J, Van Bui H, Valdesueiro D, et al. Suppressing the Photocatalytic Activity of TiO$_2$ Nanoparticles by Extremely Thin Al$_2$O$_3$ Films Grown by Gas-Phase Deposition at Ambient Conditions[J]. Nanomaterials, 2018, 8(2): 61.

[8]   Yu Y, Wu K, Lu S, et al. Engineering an ultrathin amorphous TiO$_2$ layer for boosting the weatherability of TiO$_2$ pigment with high lightening power[J]. Chinese Journal of Chemical Engineering, 2019, 27(11): 2825-2834.

[9]   Longrie D, Deduytsche D, Detavernier C. Reactor concepts for atomic layer deposition on agitated particles: A review[J]. Journal of Vacuum Science & Technology A: Vacuum, Surfaces, and Films, 2014, 32(1): 010802.

[10] Yao W, Guangsheng G, Fei W, et al. Fluidization and agglomerate structure of SiO$_2$ nanoparticles[J]. Powder Technology, 2002, 124(1-2): 152-159.

[11] Bahramian A, Grace J R. Fluidization of titania nanoparticle agglomerates in a bench-scale conical vessel[J]. Powder Technology, 2017, 310: 46-59.

[12] Matero R, Rahtu A, Ritala M. In Situ Quadrupole Mass Spectrometry and Quartz Crystal Microbalance Studies on the Atomic Layer Deposition of Titanium Dioxide from Titanium Tetrachloride and Water[J]. Chemistry of Materials, 2001, 13(12): 4506-4511.

EFFICIENT POWDER REUSE IN SELECTIVE LASER SINTERING PROCESS VIA FLUIDIZED BED SYSTEM.

Daniele Sofia[1]*, Rossella Girimonte[1]

[1]*Department of Computer Engineering, Modeling, Electronics and Systems, University of Calabria, Via P. Bucci cubo 44/a Rende (CS), 87036, ITALY*

*Email: daniele.sofia@unical.it

Abstract

This study introduces an innovative method for the recovery and reuse of unsintered powder in the Selective Laser Sintering (SLS) process, widely used in additive manufacturing for creating complex components with a broad range of powder materials. The main challenge in this process is the effective management of unsintered powder, particularly the separation of aggregates formed during the sintering phase, to avoid compromising the properties of the reused material. The proposed fluidized bed system employs a gas flow to fluidize the powder, effectively separating the aggregates and restoring the powder's granularity to a quality similar to its original state. This process not only improves material efficiency by reducing waste but also maintains the desired properties of the powder for continuous reuse in the SLS process.

Experimental results demonstrate that the powder recovered through this method retains its essential characteristics, such as particle size distribution and flow properties, enabling its direct reuse in the SLS process work chamber. This approach represents a significant step toward sustainability and economic efficiency in additive manufacturing, providing a viable solution for powder reuse and reducing the environmental impact associated with the production of new powder.

1. Introduction

Selective Laser Sintering (SLS) stands as one of the forefront technologies in the field of additive manufacturing, offering the capability to create complex components with a wide array of materials. Despite its undeniable advantages, the SLS process is accompanied by specific technical challenges, including the management of unsintered powder [1]. Effective separation of powders in the SLS process is crucial for maintaining the high quality of finished parts and the efficiency of the production process. Aggregates formed during sintering, if not removed, can compromise the quality of the produced components, causing surface defects, undesired porosity, and, in extreme cases, structural failure of the piece.

Traditionally employed techniques for powder separation in the SLS process include mechanical methods such as sieving and filtration. While these techniques can be effective to a certain extent, they have limitations in terms of efficiency, especially when it comes to separating particles of very similar sizes or removing finely dispersed aggregates [2]. These methods may also require significant manual interventions, increasing downtime in the process and impacting overall productivity.

Fluidized bed separation emerges as a promising technique to address these challenges. This method leverages a gas flow to fluidize the powder, allowing for an effective and automatic separation of aggregates from fine powders [3]. The ability to operate continuously and automatically makes fluidized bed separation an ideal solution to minimize downtime in the SLS process, significantly enhancing production efficiency. Moreover, its effectiveness in

recovering powder of a quality similar to the original supports material reuse, helping to reduce costs associated with producing new powder and the environmental impact of the process.

Adopting a fluidized bed system for powder separation in the SLS process represents a significant advancement towards more sustainable and economically efficient additive manufacturing processes [4]. The capability of this method to ensure a quick and automated recovery of powder not only optimizes resource use but also paves the way for broader adoption of SLS technology in production areas where powder management is a critical bottleneck.

2. Materials and Methods

In this study, we adopted an innovative approach for the recovery and reuse of unsintered powder in the Selective Laser Sintering (SLS) process, leveraging the unique capabilities of the Sintratec Kit SLS apparatus and Sintratec PA12 Powder polymer, combined with the use of a fluidized bed column for effective separation of aggregates from the powder [5]. Below, we provide a detailed description of the materials and methods used.

2.1 Materials

Sintratec PA12 Powder is a high-performance polyamide powder designed for Selective Laser Sintering (SLS) 3D printing, widely used in industrial additive manufacturing. Known for its exceptional mechanical strength, durability, and precision, it's ideal for creating both functional prototypes and end-use parts [6].

PA12 Powder's key advantages include its ability to withstand significant mechanical stress, impact, and fatigue, making it suitable for demanding environments. It also maintains integrity under high temperatures and resists a variety of chemicals, ensuring longevity and reliability. The powder offers excellent dimensional stability and precision, producing parts with tight tolerances.

While SLS parts typically have a rough surface texture, PA12 parts can be post-processed for a smoother finish if needed [7]. The material's versatility makes it suitable for various industries such as automotive, aerospace, consumer goods, and medical devices. It enables the creation of complex designs without support structures, reducing waste and increasing efficiency.

PA12 is used extensively for durable components like hinges and gears in the automotive and aerospace sectors, custom prosthetics and surgical instruments in medical fields, and consumer products like protective cases and sports equipment. Its robustness and versatility make it a valuable material for innovative and reliable 3D printing solutions [8].

Table 1. Characteristics of PA12 Powder.

Materials	Tm ($\circ$C)	ρ_B (kg/m^3)	ρ_P (kg/m^3)	d_{10} (μm)	d_{50} (μm)	d_{90} (μm)	$d_{3,2}$ (μm)	$d_{4,3}$ (μm)
PA12	210	525	1130	15	46	91	20	50

Sintratec PA12 Powder is a cornerstone material in SLS 3D printing, offering a harmonious balance of performance, durability, and versatility. Its widespread adoption not only drives innovation in design and product development but also promotes sustainable manufacturing practices by optimizing material use and minimizing waste [9]. This material is truly at the forefront of advancing the capabilities and applications of additive manufacturing.
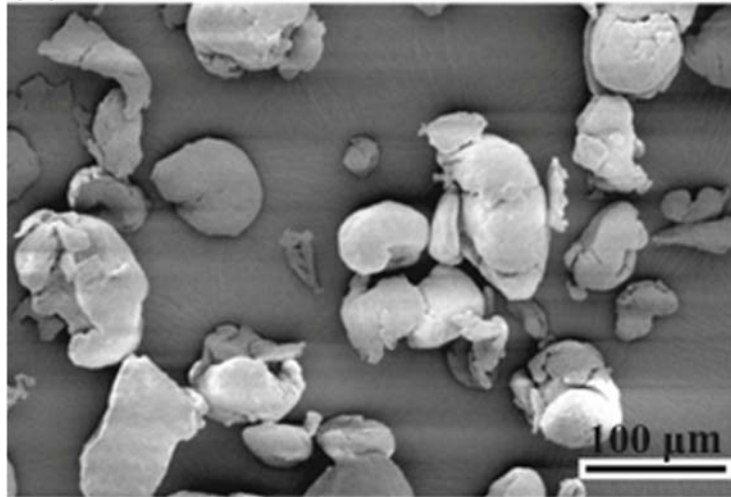
Figure 1. Electron microscopy of PA12 powder.

2.2 SLS apparatus

For this study, we used the Sintratec Kit SLS apparatus, chosen for its innovative design and research-friendly features. This system is particularly advantageous because of its open parameter settings, which allow precise adjustments to key printing parameters such as laser speed and temperature. These adjustments are crucial for tailoring the SLS process to various materials and experimental needs.

The Sintratec Kit offers a maximum print volume of 110 x 110 x 110 mm, providing ample space for diverse experimental designs. However, for optimal results, we recommend a print volume of 90 x 90 x 90 mm. The laser speed is highly adjustable, ranging from 5 to 600 mm/s, enabling fine-tuning to suit different materials and desired print qualities.

Layer height can be set between 100 and 150 µm, which facilitates the creation of detailed and precise layers. The overall dimensions of the apparatus are 520 x 520 x 360 mm, making it compact yet powerful. Weighing 36 kg, the unit is stable during operation, ensuring consistent performance.

Temperature control is another critical feature of the Sintratec Kit. The chamber temperature can be adjusted between 30 and 145 °C, which is essential for maintaining optimal conditions for various materials. Additionally, the surface temperature can be set from 80 to 180 °C, providing further control over the printing process.

These specifications make the Sintratec Kit highly versatile and efficient under a wide range of conditions. The ability to adjust parameters like laser speed and temperature allows for extensive experimentation with different materials, optimizing the printing process to achieve the best possible results. This flexibility is essential for advancing SLS technology and exploring new possibilities in additive manufacturing.

Figure 2. *Sintratec Kit SLS Apparatus*.

2.3 Method

The study embarked on an innovative journey to explore the recovery and reuse of unsintered powder in the Selective Laser Sintering (SLS) process, leveraging the unique capabilities of the Sintratec Kit SLS apparatus and the high-performance Sintratec PA12 Powder, alongside a fluidized bed column for effective aggregate separation [10]. This methodical approach aimed to enhance the sustainability and efficiency of SLS manufacturing processes. Here's how the study was meticulously structured to achieve its objectives:
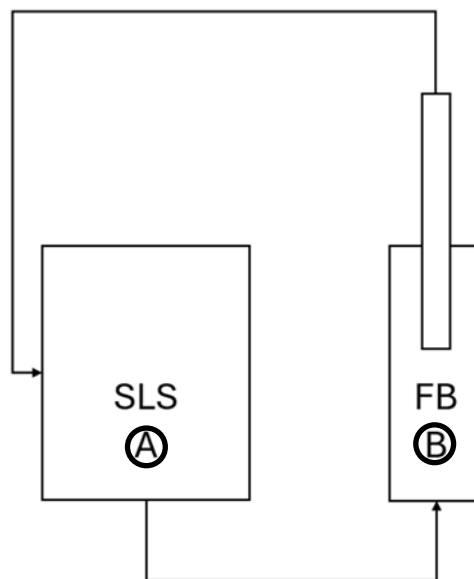
Figure 3. Process scheme.

The study began with the preparation of the Sintratec PA12 Powder, which was carefully loaded into the Sintratec Kit SLS apparatus. Ensuring proper setup and even distribution of the powder was crucial for optimal sintering conditions. The SLS printing process then followed, using specific parameters to fully utilize the potential of the PA12 powder [11].

After the sintering process, attention was focused on recovering the unsintered powder. This phase was essential for collecting the powder that had not been fused by the laser. The recovery process was conducted using an automatic suction system to ensure the transfer of

all residual powder from the sintering process, including the aggregates formed during the process [12].

The recovered powder was then introduced into the fluidized bed column. Using an airflow, the powder was fluidized within the column to effectively separate larger aggregates from finer powder particles. This process aimed to restore the quality of the powder to make it suitable for reuse in the SLS process. The fluidized bed column played a crucial role in attempting to achieve this quality restoration.

The separated powder was then reloaded into the Sintratec Kit SLS apparatus for subsequent printing cycles. Throughout the study, each phase was designed to build upon the previous one, creating a comprehensive approach to exploring the recovery and reuse of powder in SLS printing. By combining the innovative use of the Sintratec Kit, the properties of PA12 powder, and the efficiency of the fluidized bed column, the study aimed to explore new possibilities in additive manufacturing [13].

3. Results and discussion

The study results showed that the upper layers of the fluidized bed column contained less mass, with a higher concentration of finer particles at the top. Consequently, it is necessary to recover the powder from the top of the bed to avoid the formation of aggregates, which tend to accumulate at the bottom of the column.

This observation suggests that the powder recovered from the upper layers, being finer and more homogeneous, can be further processed in the SLS apparatus using automated suction systems. This technique improves the efficiency and quality of the sintering process while ensuring the sustainability of powder reuse. As evident in Fig. 4, the automated recovery of powder from the upper layers of the fluidized bed can be integrated into the workflow to optimize production.
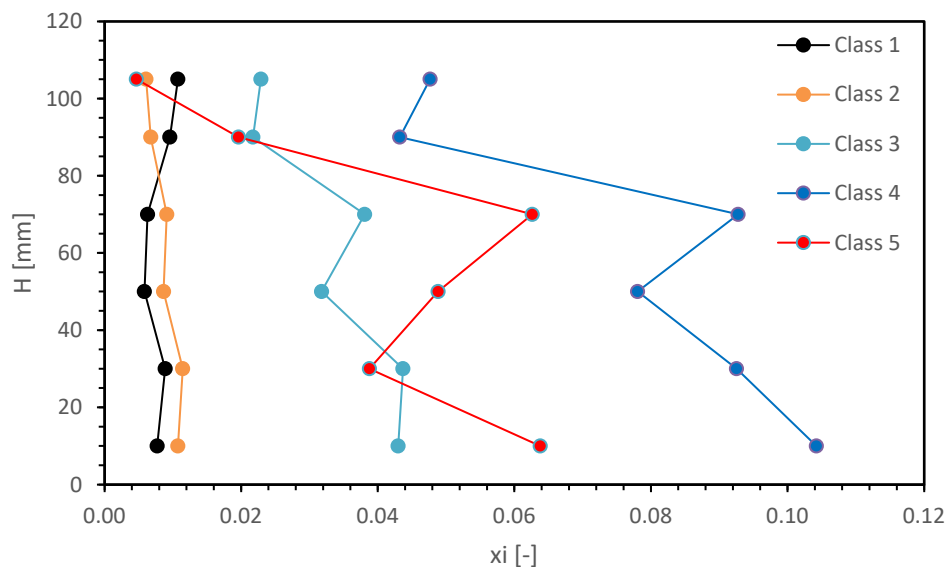
Figure 4. Particle size class profiles versus column height.

4. Conclusion

This study demonstrated the effectiveness of an innovative system for recovering and reusing unsintered powder in the Selective Laser Sintering (SLS) process. Using the Sintratec Kit SLS along with a fluidized bed column significantly improved the management of residual powder and ensured the quality of the reused material.

The results showed that finer powder accumulates in the upper layers of the column, while aggregates concentrate at the bottom. This highlighted the need to recover powder from the upper layers to avoid aggregates that could compromise print quality. The powder recovered from the upper layers was homogeneous and suitable for further sintering cycles.

The use of automated suction systems to recover powder from the upper layers enhanced process efficiency, reducing waste and promoting sustainability. This approach not only optimizes material usage but also offers significant economic and environmental benefits, making additive manufacturing more sustainable.

The study validated an effective method for powder recovery and reuse in the SLS process, opening new avenues for sustainability in additive manufacturing. The combination of innovative technologies represents an important step towards more efficient and environmentally friendly production processes.

References

[1] X. Luo, Y. Liu, C. Gu, Z. Li, Study on the progress of solidification, deformation and densification during semi-solid powder rolling, Powder Technol. 261 (2014) 161–169. doi:10.1016/j.powtec.2014.04.001.

[2] C. Liu, Z. Xia, J.T. Czernuszka, Design and development of three-dimensional scaffolds for tissue engineering, Chem. Eng. Res. Des. 85 (2007) 1051–1064. doi:10.1205/cherd06196.

[3] L.S. Ojala, P. Uusi-Kyyny, V. Alopaeus, Prototyping a calorimeter mixing cell with direct metal laser sintering, Chem. Eng. Res. Des. 108 (2016) 146–151. doi:10.1016/j.cherd.2015.11.015.

[4] D.D. Gu, W. Meiners, K. Wissenbach, R. Poprawe, Laser additive manufacturing of metallic components: materials, processes and mechanisms, Int. Mater. Rev. 57 (2012) 133–164. doi:10.1179/1743280411Y.0000000014.

[5] 3D printing: from dental braces to astronauts' seats, Econ. Sep 7th. (2013).

[6] P. Bertrand, F. Bayle, C. Combe, P. Goeuriot, I. Smurov, Ceramic components manufacturing by selective laser sintering, Appl. Surf. Sci. 254 (2007) 989–992. doi:10.1016/j.apsusc.2007.08.085.

[7] Salehi Kahrizsangi, H., Sofia, D.,Barletta, D., Poletto, M. Dust generation in vibrated cohesive powders Chemical Engineering Transactions doi 10.3303/CET1543129

[8] M. Agarwala, D. Bourell, J. Beaman, H. Marcus, J. Barlow, Direct selective laser sintering of metals, Rapid Prototyp. J. 1 (1995) 26–36. doi:10.1108/13552549510078113.

[9] W.E. Frazier, Metal Additive Manufacturing: A Review, J. Mater. Eng. Perform. 23 (2014) 1917–1928. doi:10.1007/s11665-014-0958-z.

[10] R. Grimm, SLS and SLA, different technologies for different applications., Prototyp. Technol. Int. '97, UK Intern. Press. Dorking, UK. (1997) 130–138. http://ci.nii.ac.jp/naid/10006770200/en/.

[11] K. McAlea, Materials and applications for the SLS selective laser sintering process, Proc. 7th Int. Conf. Rapid Prototyping-1997. (1997) 23–33. http://ci.nii.ac.jp/naid/10011711406/en/.

[12] G.N. Levy, R. Schindel, J.P. Kruth, Rapid Manufacturing and Rapid Tooling With Layer Manufacturing (Lm) Technologies, State of the Art and Future Perspectives, CIRP Ann. - Manuf. Technol. 52 (2003) 589–609. doi:10.1016/S0007-8506(07)60206-6.

[13] M. Schmidt, D. Pohle, T. Rechtenwald, Selective laser sintering of PEEK, CIRP Ann. - Manuf. Technol. 56 (2007) 205–208. doi:10.1016/j.cirp.2007.05.097.

Session H:
Industrial experience and
application

FLASH CALCINATION OF MAGNESITE IN TRANSPORT BED: REACTION CHARACTERIZATION AND INDUSTRIAL APPLICATION

Zhennan Han[a,b], Ping An[a], Xuejing Liu[a], Guangwen Xu[*,a]

[a] *Key Laboratory of Resources Chemicals and Materials (Shenyang University of Chemical Technology), Ministry of Education, Shenyang 110142, China.*

[b] *Laboratory of Engineering Thermochemistry, Guangdong University of Technology, Guangzhou, 510006, People's Republic of China.*

*Email:gwxu @ipe.ac.cn

Abstract

This work presents a comprehensive study on the transport bed flash calcination (TBFC) process applied to powder magnesite (<150 μm). First, a micro fluidized bed reaction analyzer (MFBRA) was used to obtain the kinetics of magnesite calcination. Then, a pilot-scale calciner were used to investigate the reaction characteristics of magnesite calcination in transport bed. And process simulation was conducted to optimize the energy-saving strategy for this novel technology. Results showed that calcination of powder magnesite at 850-1000 °C is a quick reaction that allows 99% of its containing $MgCO_3$ to be decomposed in 1-2 s. The activity of calcined product depends on both its decomposition rate and microstructure. During calcination, the surface structure of product changes from loose and porous to dense and smooth, even in a few seconds. For TBFC, the preferred process arrangement is proved to be four-stage preheating for magnesite and two-stage cooling for MgO. A recently commissioned commercial TBFC plant indeed produced the lightly burned magnesia according to the anticipation of our study, while it also required an energy consumption that is 40% lower than what required for the conventional reverberatory furnace.

Introduction

Magnesite (mainly composed of magnesium carbonate, $MgCO_3$) is rich in resources in China, accounting for about 25% of the world's magnesite reserves. It is a main raw material in magnesium and refractory industry and widely used for production of building materials, chemical, paper, aerospace, automobile, and environmental protection (Zhao, 2007; Demir, 2008). Generally, magnesite calcination for producing magnesium oxide is the initial step for its utilization. Industrial magnesium oxide is typically produced by using reverberatory furnace with block magnesite (30-50 mm) as material, thus leading to a long calcination time (up to 12 hours low product activity, poor material adaptability, high energy consumption and so on.

The reaction equation of magnesite calcination reaction is listed as follow:

$$MgCO_3 \xrightarrow{\Delta} MGO + CO_2$$
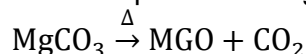
Recently, a novel process named transport bed flash calcination (TBFC) with powder magnesite as material was developed by Shenyang University of Chemical Technology (SYUCT) to solve those problems existed in traditional technology. This work presents a comprehensive study on the novel TBFC process. First, a micro fluidized bed reaction analyzer (MFBRA) was used to analysis the kinetics of magnesite calcination. Then, a pilot-scale transport bed calciner were used to investigate the reaction characteristic of magnesite calcination in transport bed. And process simulation was conducted to optimize the energy-saving strategy for this novel technology. Finally, the obtained results provide the necessary fundamentals and vital information to guide the engineering development of an advanced flash calcination technology using the transport bed reactor, which was recently successful commissioned into industrial production.

Results and discussion

1. Reaction kinetics of magnesite calcination

A schematic diagram of MFBRA is shown in **Figure 1**. This system consists of an electric heating furnace, a quartz reactor having a diameter of 20 mm, a mass spectrometry (Ametek Dycor LC-D 100) used for analyzing the concentration of CO_2 in the released gas product and an online feeding device. As shown in **Figure 2**, we can clearly see that the complete decomposition time of magnesite in TG is over 4 min at a heating rate of 40 °C/min, but the required time is just a few seconds (3-5 s) in MFBRA above 750 °C.
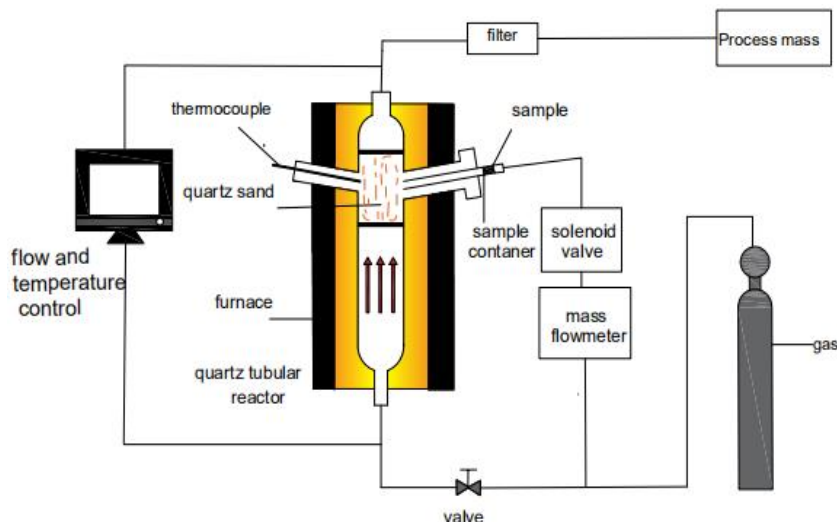
Fig. 1. Schematic diagram of the micro fluidized bed reaction analyzer (MFBRA).
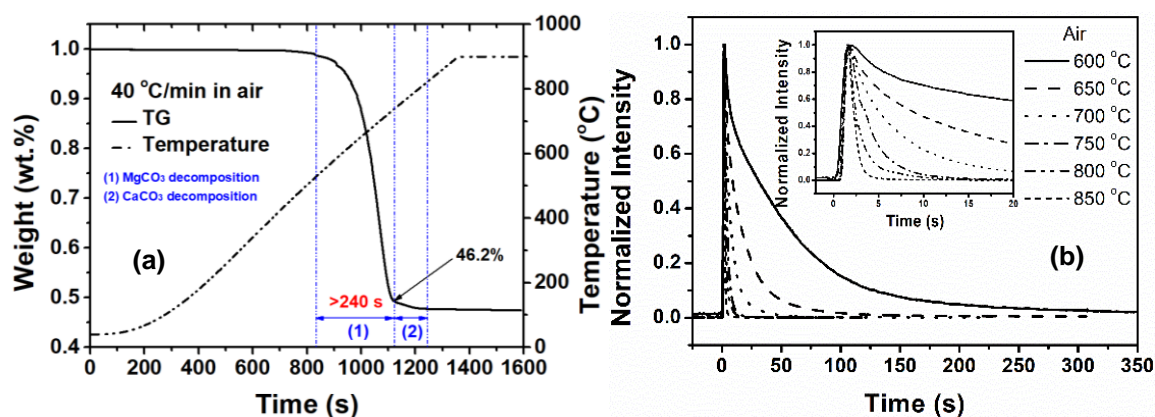
Fig. 2. Magnesite calcination in TG (a) and MFBRA (b).

Flynn-Wall-Ozawa and Coats-redfern methods (Bagchi, 1981) was used to calculate the kinetic data measured by TG, and the kinetic data measured by TG MFBRA is calculated by the isothermal kinetic equation (Yu, 2010). As shown in **Table 1**, the activation energy measured using TG and MFBRA are 236.6 and 124.16 kJ/mol, indicating that MFBRA can enhance mass transfer and effectively reduce the inhibition of external diffusion on reaction.

Table 1. Kinetics parameters of magnesite calcination in air measured using TG and MFBRA

Analyzer	E (kJ/mol)	lg A (s^{-1})	G(x)
TG (Air)	236.60	15.81	-ln(1-x)
MFBRA(Air)	124.16	5.69	-ln(1-x)

2. Magnesite calcination in transport bed

Figure 3(a) shows the flowsheet of the pilot-scale plant with a height of 10 m and a capacity of 1 kg/h magnesite. This plant is consisted of gas combustor, transport bed calcinator, product collector (cyclone), bag filer and induced draft fan. During test, C_3H_8 is adopted as the fuel. The hot-temperature flue gas generated from combustion can heat powder magnesite rapidly and then carry the calcined magnesite sample out of reactor. Every magnesite sample is calcinated 8 times to analysis the dynamic changes in the composition and micro-structure of magnesite particle. The residence time of particle in calcinator is about 0.75 second for each time. **Figure 3(b)** shows the $MgCO_3$ decomposition ratio against calcination times, and the decomposition ratios are calculated by Eq. (1) based on TGA of calcinated magnesite samples. For the magnesite samples with a particle size of 0.05-0.15 mm, the decomposition ratios both reach up to 99.1-99.4% after 3 calcination times, indicating $MgCO_3$ can decompose almost completely as residence time above 2.25 seconds. And this phenomenon is consistent with the MFBRA result.
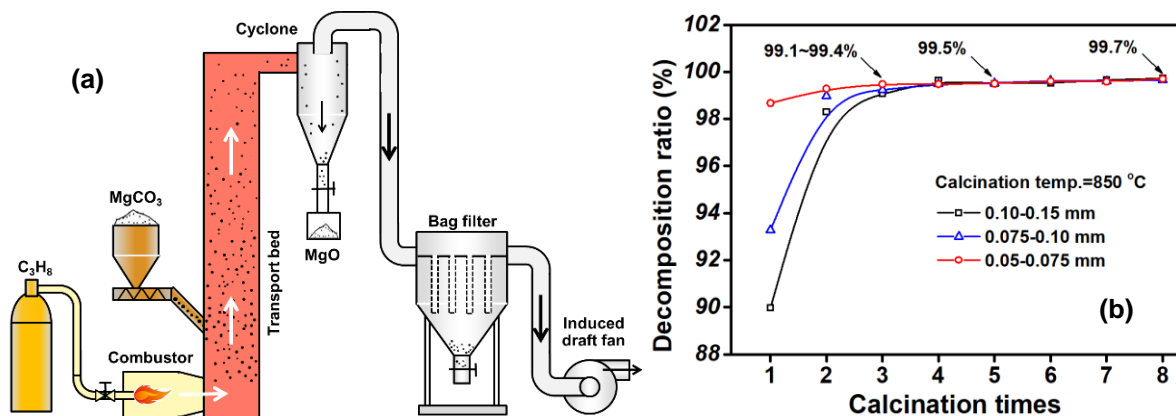
Fig. 3. Flowsheet of the pilot-scale plant (a) and $MgCO_3$ decomposition ratio (b)

As shown in **Figure 4**, the XRD pattern demonstrates that the MgO is the dominant mineral phase in the samples produced from magnesite with particle size of 0.05-0.075 mm. The intensities of MgO diffraction peaks are enhanced with increasing repeated times of calcination, which is consistent with **Figure 3(b)**. The grain size of MgO crystal in those calcined magnesite samples are also calculated by Scherrer formula, shown in Eq. (2), based on the half-peak width of peak at 2θ=42.5°. As shown in **Table 2**, the grain size of MgO crystal continuously increases after multiple calcination due to recrystallization at high temperature.
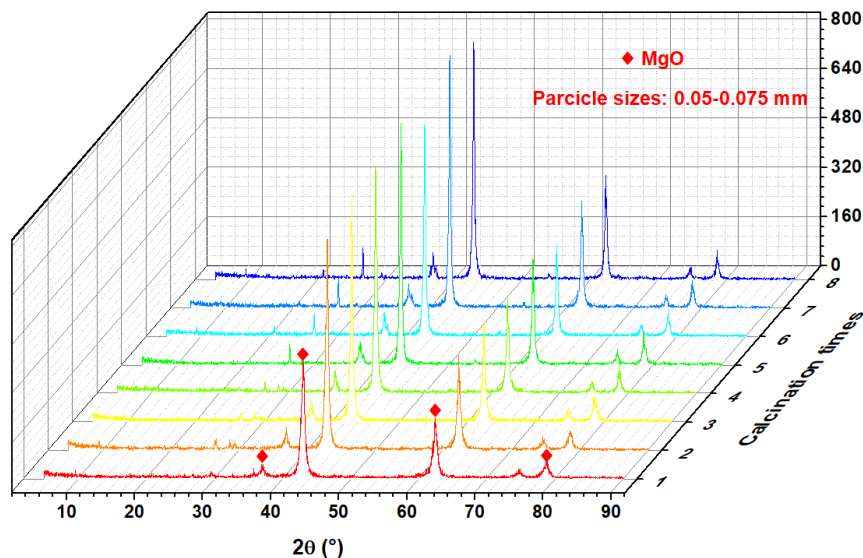
Fig. 4. XRD pattern for calcined magnesite samples with different times of repeated calcination.

Table 2. Half-peak width of peak at 2θ=42.5° in XRD pattern and grain size of MgO crystal.

Parameters	Calcination times							
	1	2	3	4	5	6	7	8
B	0.737	0.517	0.481	0.444	0.427	0.399	0.379	0.379
D (nm)	12.0	17.7	18.3	20.6	21.3	21.4	22.9	24.0

B-Half-peak width of peak at 2θ=42.5°; D-Grain size of MgO crystal.

Morphological characterization of several samples is performed to observe changes in the solid structure after calcination. As shown in **Figure 5**, the surface of the samples with 3-4 calcination times is porous and rough. With calcination times increasing, the granular shape continuously disappears and the surface becomes considerably smoother. A previous study of Eubank (1951) indicated that calcination of magnesite included two distinct steps: (1) loss of gases and (2) recrystallization or sintering. Therefore, the loss of gases leaves a very porous structure with a large internal surface area and a great reactivity for the products with less calcination times or residence time. However, excessive calcination times or residence time will inevitably lead to recrystallization or sintering and a dense particle structure with a smaller surface area and a lower reactivity.
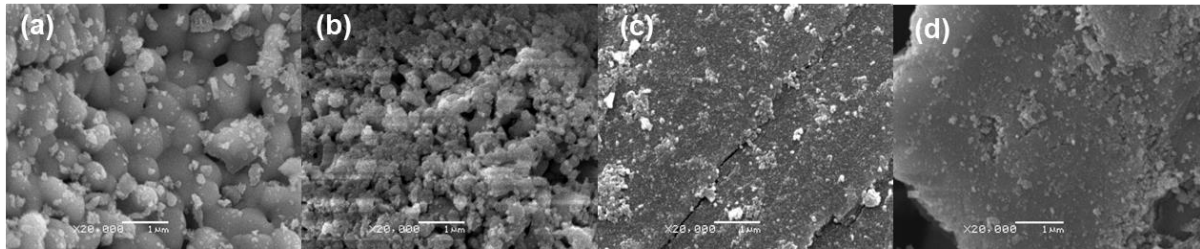
Fig. 5. SEM images of calcined magnesite samples with different calcination times
(a) 3 times, (b) 4 times, (c) 5 times and (d) 7 times

3. Energy-saving strategy for TBFC process

The TBFC process is mainly composed of a calciner implementing the light calcination of magnesite, a magnesite preheating system and a MgO cooling system. In the preheating system, the fed magnesite is heated by flue gas from the high-temperature calciner. While, in the cooling system, the high-temperature MgO is cooled down by air sent to the calciner. A schematic diagram of the TBFC process with two-stage cooling and four-stage preheating is shown in **Figure 6**(a). Based on the kinetic data obtained by measuring magnesite calcination in air using MFBRA, the process simulation was employed to investigate energy-saving strategy for TBFC technology. **Figure 6**(b) illustrates the influences of different stages of cooling and preheating on energy consumption and efficiency of TBFC. The energy consumption decreases with the increase in the number of preheating and cooling stages. Concerning the energy efficiency, the more the heat-exchange stages, the lower the increased energy efficiency. Increasing the magnesite-preheating stages is more dominant in raising the energy efficiency than having more MgO-cooling stages does. For TBFC, the preferred process arrangement is proved to be four-stage preheating for magnesite and two-stage cooling for MgO, and the corresponding energy consumption is about 4100 kJ/kg-MgO and energy efficiency is 66.8%. Comparing with the traditional reverberatory furnace, the energy effciency is almost doubly higher.
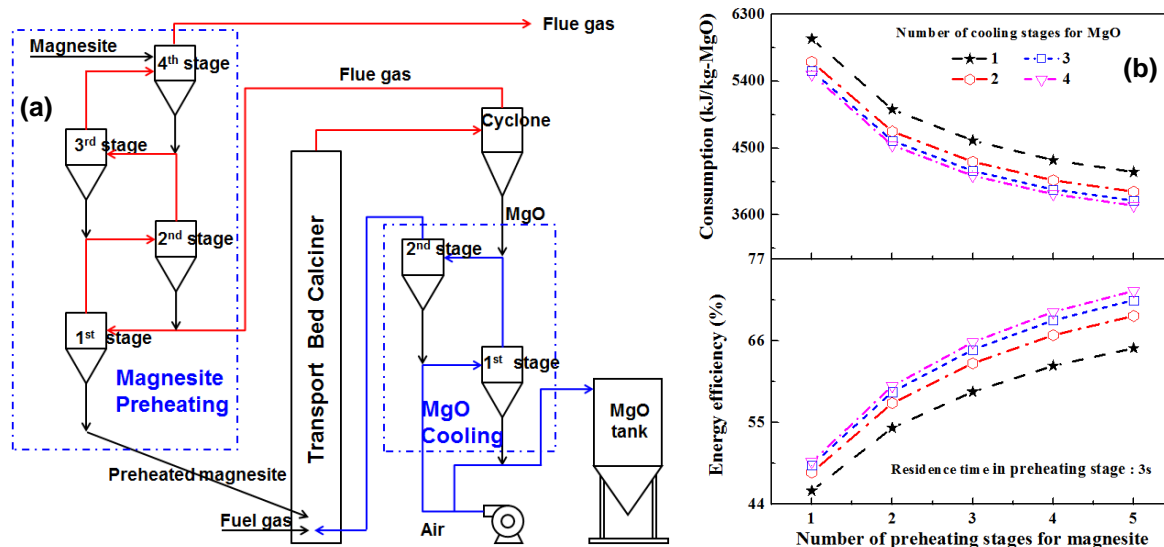
Fig. 6. A schematic diagram of the TBFC process with two-stage cooling and four-stage preheating (a), energy consumption and efficiency varying with number of preheating and cooling and stages (b).

4. Industrial application of TBFC process

A demonstration plant of TBFC (shown in **Figure 7**) with its operation capacity of 580,000 t/a magnesite is successfully commissioned into commercial running in 2023. This capacity is about 30 times that of the conventional reverberatory furnace. As anticipated, the TBFC of magnesite exhibited its remarkably good performance. The coloration time of calcined product was found to be about 50-90 s and this justifies the obviously high activity for the generated product in TBFC. It also complies with the decomposition ratio of fed magnesite, by reaching the expected high value of 98-99%. From the industrial plant we further realized an energy consumption of about 130 kgce for producing one ton light burned magnesia. This is much lower than that, say, about 220 kgce, for the conventional RF as well as suspension kiln. It presents essentially an advanced calcination technology guaranteed by using transport bed to calcine granular magnesite.
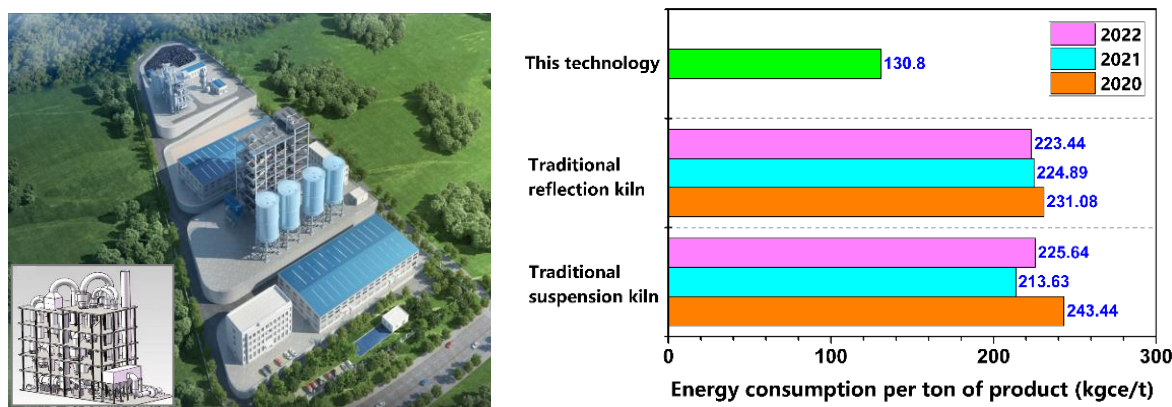
Fig. 7. A demonstration plant for TBFC: (A) three-D design and (B) energy consumption performance.

Conclusion

The complete decomposition time of magnesite in TGA is above 4 min at heating rate of 40 °C /min, but it is just a few seconds (3-5 s) in MFBRA above 750 °C. The activation energy measured in MFBRA and TGA are 125 kJ/mol and 236 kJ/mol respectively, showing a good suitability of MFBRA for rapid reaction in fluidized bed at a specific temperature. For powder magnesite with particle sizes of 0-0.15 mm, it just needs 1.5-2.3 s to complete the calcination reaction as temperature is above 800 °C in pilot-scale reactor. However, with the calcination

times exceeding 4 times or residence time exceeding 3 seconds, the recrystallization or sintering will lead to a large grain size of MgO crystal and a dense particle structure with a smaller surface area and a low reactivity. For TBFC, the preferred process arrangement is proved to be four-stage preheating for magnesite and two-stage cooling for MgO. From the running of its industrial demonstration, TBFC required an energy consumption that is 40% lower than what required for the conventional reverberatory furnace, indicating its superiority to be an advanced calcination technology.

References

Bagchi, TP, KP Sen. Combined differential and integral method for analysis of non-isothermal kinetic data. Thermochimica Acta. 1981. 51, 175-189

Demir, F., B Dönmez. Optimization of the dissolution of magnesite in citric acid solutions. International Journal of Mineral Processing. 2008. 87 (1-2), 60-64

Eubank, WR. Calcination studies of magnesium oxides. Journal of the American Ceramic Society. 1951. 34, 225−229

Yu, J., JR Yue, ZE Liu. (2010). Kinetics and Mechanism of Solid reactions in Micro Fluidized Bed Reactor. AIChE Journal. 2010. 56, 2905-2912

Zhao, Y., G Zhu. Thermal decomposition kinetics and mechanism of magnesium bicarbonate aqueous solution. Hydrometallurgy. 2007. 89 (3), 217-223

BIOCHAR PRODUCTION IN LARGE-SCALE DUAL FLUIDIZED BED – MIXING AND CHAR PROPERTIES

Diana Carolina Guío-Pérez*[1], Anna Köhler[2], Eduardo Arango[3], Julian Keller[2] Kentaro Umeki[3], David Pallarès[1]

[1] Division of Energy Technology, Department of Space, Earth, and Environment, Chalmers University of Technology, Gothenburg, SE-412 96, Sweden
[2] BioShare AB, Karlstad, SE-655 92, Sweden
[3] Division of Energy Science, Department of Engineering Sciences and Mathematics, Luleå University of Techonlogy, Luleå, SE-971 87, Sweden

*carolina.guioperez@chalmers.se

Abstract

This work presents novel information about biochar production in industrial-scale dual fluidized bed (DFB) systems. The system used in theis work is located at Chalmers University and consists of a 12 MW CFB combustor and 4 MW BFB pyrolizer. The BFB unit where the char is produced has a cross section area of 1.44 m² and was operated at 800 °C with steam as fluidization gas. The mixing of the fed batches of biogenic feedstock particles was recorded by means of a camera probe. Digital image analysis of the recordings was used to study the horizontal mixing of the feedstock. Further, the composition and physical properties of the biochar produced were analyzed in relation to the conversion conditions experienced. Results show that for the conditions tested, dispersion is the dominant mechanism for the horizontal mixing of the biochar in front of negligible convection by the solids crossflow. However, increased solids crossflow yields faster dispersive mixing, in line with recent findings. Quality of the obtained biochar lies in the range of equivalent chars reported in literature and obtained under laboratory scale. Indication of an increase in fix carbon content due to increase in the residence time could be observed. Further investigations will be carried out regarding the impact of the cross flow rate and the fluidization velocity in the particle dispersion, as well as the composition of the innorganic fraction of the char.

1. Introduction

The demand for biochar is predicted to grow steadily in the coming decades as new needs arise for different uses, e.g. soil amendment, carbon sequestration, water filtration. Furthermore, biochar is highly attractive to industrial sectors seeking to reduce their carbon footprint by replacing fossil carbonaceous feedstock with one of biogenic origin. This is foreseen to become a main share of the global biochar demand and involves sectors like metallurgy (iron, aluminum, and steel and alloy industries) and production of plastics and rubber. However, the use of biochar as feedstock in industrial processes often sets specific reuirements in the properties of the biochar, specially in terms of content of volatile matter, ash content, or concentration of different elements (e.g. alkali, phosphorus).

The scale-up of biochar production with indirectly heating technologies (e.g. screw furnaces) is limited by the lack of heat transfer surface. Some technologies use direct heating (e.g. rotary kilns) for the production of activated carbon (similar to biochar) and have been scaled up to approximately 60 kton/year. However, these are dedicated/stand-alone units in which the pyrolysis gas (an otherwise highly valuable by-product) is diluted and/or partially burnt, result in a low efficiency (since biochar represents a smaller share of the input biomass in terms of both mass and energy), making high the final cost for biochar production [Yaashikaa et al., 2020], roughly within the range 250-2,000 EUR/ton, i.e. well-above that of fossil carbon sources such as coke or anthracite. Aiming at overcoming the poor efficiency, many investigations focus on developing alternative technologies which can integrate biochar

production in a way that optimizes the use of the input biomass.

One technology designed to efficiently integrate the conversion of biomass to biochar is based on the use of interconnected fluidized bed reactors. Fluidized bed technology has been identified as having the potential to produce biochar on a large scale [Kim et al., 2019] due to its high heating ratio and the possibility of reactor integration through a dual fluidized bed (DFB) configuration. In such a configuration, the biomass is pyrolyzed in a fluidized bed reactor, and the energy required for this conversion is provided by biomass combustion in a coupled fluidized bed combustor. Thus, the bed material circulating between the two reactors acts as heat carrier. This concept can be realized as a new plant or as a retrofit of an existing fluidized bed boiler plant. A retrofit implementation in a reference case of a 100 MW$_{th}$ combustor has the potential to provide flexible biochar production of up to roughly 80 kton/year (corresponding to -290 kt $_{CO2}$/y).

The fate of a biomass particle in the fluidized bed pyrolysis reactor is important since it is linked to the residence time and the mass and heat transfer rates during conversion, and ultimately to the properties of the resulting biochar. By means of both model simulations (e.g.[Farzaneh et al., 2013]) and experiments (e.g. [Liu and Chen, 2011]), previous research has offered indications of how larger and lighter particles (such as converting biomass) will mix in a fluidized bed, both laterally and axially. However, most of the literature on the topic of fuel mixing regards investigations in small-scale beds and often under cold conditions. Regarding the effect of scale, Liu and Chen [Liu and Chen, 2010] showed that the lateral solids dispersion coefficient strongly increases (up to 1 order of magnitude) with cross-sectional bed dimensions. Regarding the effect of temperature, Olsson et al. [Olsson at al., 2012] determined the lateral biomass dispersion coefficient experimentally in a large-scale unit (1.44 m^2 in cross section) under cold conditions, resulting in values around 10^{-3} m^2/s, i.e. 1-2 orders of magnitude lower than those obtained at hot conditions. To overcome the requirement of a hot and large-scale unit to produce result data with quantitative relevance for industrial applications, fluid-dynamical scaling can be used (see e.g. [Köhler et al., 2020]), which allows higher operational flexibility and the use of more advanced measurement techniques.

The scarce information in literature on fuel mixing in large hot fluidized bed units regards the lateral fuel dispersion coefficient: Niklasson et al. [Niklasson et al., 2002] estimated the lateral fuel dispersion coefficient in a combustor (2.2 m^2 in cross section) to be around 10^{-1} m^2/s. Chirone et al. [Chirone et al., 2004] refined this finding by determining the lateral fuel dispersion to 10^{-2} m^2/s inside the bed and 10^{-1} m^2/s on the bed surface in a 0.37m-id hot combustor. Sette et al. [Sette et al., 2016] carried out direct measurements of the fuel mixing by means of a camera probe in a unit with a cross section of 1.44 m^2 and operated at 800 °C in presence of a solids cross-flow. This study concluded that increased solids cross-flow (which induced average lateral solids velocities of up to 5·10^{-2} m/s) enhances axial segregation of the biomass particles, which in turn increased their lateral mixing (in line with the above-cited findings by Chirone et al.). Further, with under fluid-dynamically scaled conditions, Sette et al. [Sette et al., 2015] found indications that the solids cross-flow clearly enhances the lateral velocity of fuel particles immersed in the bed but not as much that of (lighter and/or larger) fuel floating on the bed surface. Thus, the impact of the solids cross-flow on the overall lateral fuel mixing depends strongly on the fluidization velocity, as the latter governs the axial mixing and thus the shares of in-bed and bed-surface fuel.

Given the existing literature, for the large-scale production of biochar in fluidized bed systems, there is a need for further investigation of both the mixing of feedstock in hot large-scale bubbling fluidized beds and the characteristics of the biochar produced. The aim of this work is to acquire first experiences for the large-scale production of biochar in a dual fluidized bed system. For this, experiments were carried out in a hot (700-900 °C) large-scale (1.44 m^2) bubbling fluidized bed in presence of a solids cross-flow forced by a CFB furnace. The mixing of the biochar was measured by means of a camera probe and studied through digital image analysis, while the resulting char particles were extracted for analysis.

2. Methodology

2.1 Experimental setup and test procedure

2.1.1. Biochar production

The experimental unit used in this work is the dual fluidized bed system at Chalmers University (see a schematic in Fig.1) consisting of a retrofit of the original 12 MW CFB combustor with the addition of an interconnected 2-4 MW

Figure 1: Principle for biochar production in a dual fluidized bed system.

BFB reactor (here acting as pyrolizer) which is heated indirectly by the external circulation of hot solids from the CFB furnace, which pass through the cyclone and a particle seal. In order to hinder the raw pyrolysis gas from entering the combustor, another particle seal is located after the outlet of the pyrolizer and before solids inlet to the CFB furnace. Note that since this unit is a retrofit, the combustion reactor is much larger than strictly needed for the intended process. More details of the system can be found elsewhere Sette et al., 2015].

As schematized in Fig.2 (top view of the pyrolizer), the bed material conveyed from the CFB furnace enters the reactor at the rear-right corner and exits through an overflow baffle at the rear-left corner, establishing in this way a solids cross-flow in the pyrolizer. The height of the exit baffle sets the fluidized bed height, which for the present tests was 0.4 m. The feedstock is fed from the front-right corner by gravity, i.e., so-called bed surface feeding. The bed solids in the pyrolizer consisted of silica sand (Baskarp B28 from Sibelco Nordic AB) have a particle density of 2655 kg/m^3 and a mean size of 270 μm. The feedstock used to produce biochar consisted of wood pellets with a diameter of 6 mm and a mean height of 20 mm.

Figure 2: Top view of the pyrolysis chamber at Chalmers Univ. used in the experimental campaign

The experimental procedure for the production of biochar started off from stable operation with in input of wood chips to the CFB combustor corresponding to a thermal input of 2 MW$_{th}$, and a circulation rate of sand of 6.5 kg/s. This yielded a temperature of 840 ºC in the pyrolizer. The procedure for biochar production started by gradually reducing the fuel feeding rate to the combustor and simultaneously increasing the fuel feeding rate to the BFB pyrolizer, until the latter reaches 480 kg/h of biomass pellets. Subsequently, the particle seals located upstream and downstream of the pyrolizer are de-fluidized in order to stop the solids cross-flow in the pyrolizer (thus ensuring that the biochar produced does not leave towards the CFB furnace). The temperature in the pyrolizer bed – which decreased in absence of the inlet of hot solids – was monitored and the feedstock feeding was stop when it reached 550 ºC (after about 20 minutes). During this time, the pyrolizer bed was fluidized with 100 kg/h of steam. By keeping the fluidization gas, the bed continued to cool down, and finally when it reached 300 °C, the fluidization was stopped. Once it reached room temperature, the whole content of the pyrolizer was removed and biochar was separated from the bed material by sieving.

2.1.2. Biochar tracking

The experiments devoted to tracking the biomass mixing were carried out in presence of a solids cross-flow of bed material, set to either 2.65 kg/s or 6.5 kg/s, yielding respectively mean residence times of 290 and 118 s for the bed material and average bed solids horizontal velocities (in the direction of the cross flow, from right to left in Fig. 2a) of roughly 4 and 10 mm/s. With this, small batches of feedstock (about 0.2 l) were fed into the pyrolizer. The surface of the pyrolizer was recorded until no pellets were observed for at least five minutes. The video camera probe with double cooling system (water and nitrogen gas) was inserted in a port at the top (about 1 m above the nozzle level) of the front wall (see Fig.2a) with an
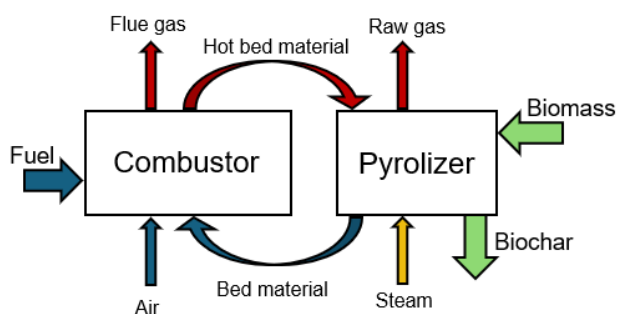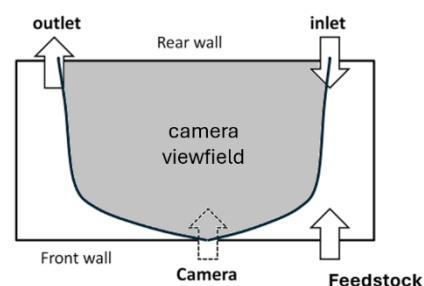
inclination of 45º towards the bed surface. The field of view of the camera was maximized by means of a lens, which allowed monitoring over about the 75% of the bed surface.

2.2 Digital image analysis

The digitalized videoframes (see example in Fig.3) were imported to a software for digital image analysis. Out of the field of vision, the analysis domain is defined corresponding to the bed surface. The so-called inlet and outlet bands (marked in green and red in Fig.3, respectively) are delimited, these correspond to the right and left boundaries of the analysis domain and are placed 1.2 m apart from each other. Each video frame is analyzed to quantify the number of pellet observations in each of these bands. From these data, statistics could be generated about the residence time of the converting pellets within the analysis domain in the bed.
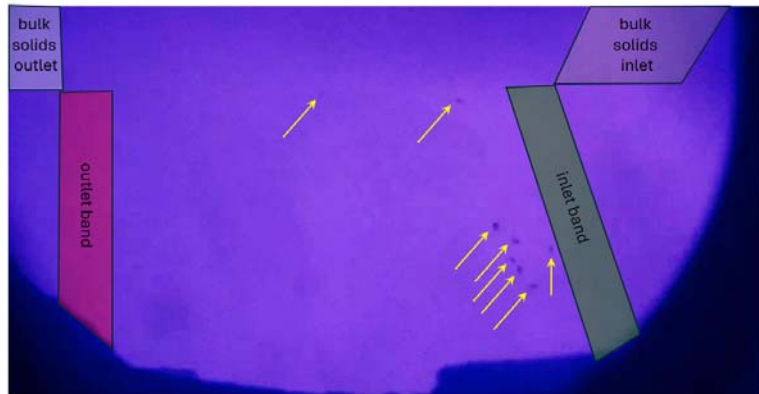
Figure 3: Digital image analysis of the video recordings. The videoframe indicates the detected biochar particles (arrows), the inlet and outlet for the bulk solids cross-flow, and the inlet and outlet bands used in the data processing.

2.3 Biochar characterization

Biochar samples collected from different sections of the experimental unit were characterized by proximate analysis and ultimate analysis (using a CHNS-O elemental analyzer EA3000 from Eurovector Srl) based on standard ISO 16948:2015.

3. Results and discussion

3.1 Horizontal mixing of the biochar

Figure 5 shows the time distribution of the biochar observations captured by the digital image analysis of the video recordings at the inlet and outlet bands (see Fig.3), for a total of 6 repetitions with low solids crossflow ($u_{crossflow}$=4 mm/s). As seen from Fig.5a, the median time of observation at the inlet band is 36 s, while that for the outlet band resulted in 52 s, i.e. 16 s later. The time zero is set to the moment when the biomass is injected into the fuel feeding system. Figure 5b shows that the time distribution of the biochar observations is slightly narrower for the outlet compared to the inlet, which may indicate either the need for more experimental repetitions or a deviation from the ideal convection-dispersion pattern typically

a) cumulative probability   b) probability density
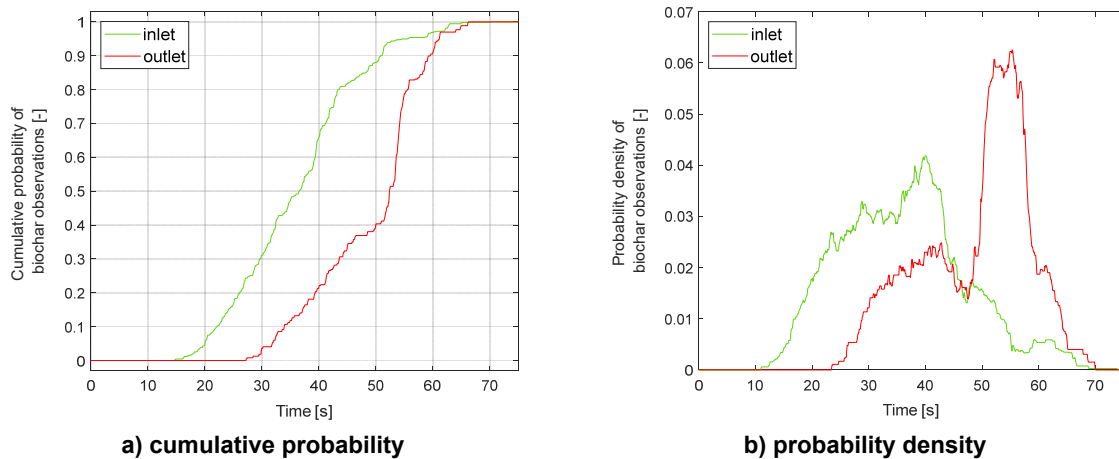
Figure 5: Time distribution of the biochar observations at the inlet and outlet bands (see Fig.3), for the low solids crossflow case ($u_{crossflow}$=4 mm/s)

applied to the horizontal solids mixing. For the two solids crossflow levels studied, the respective median residence times for the biomass (16 and 5 s) are much shorter than the respective mean residence times for the bed material (290 and 118 s). This indicates that biomass dispersion induced by the bubble flow through e.g. splashing is clearly dominant in front of the horizontal conveying drag induced by the crossflow of bed solids.

Neglecting the convection mechanism, the dispersion coefficients for the horizontal mixing of biomass shown in Table 1 are obtained from the Einstein equation. The horizontal dispersion of biochar is clearly enhanced by the increased solids crossflow, in line with recent findings by the authors [Farha et al., 2024].

Table 1: Main parameters of the horizontal solids mixing

Bulk solids crossflow [m/s]	Biochar median residence time [s]	Biochar horizontal dispersion coefficient [m^2/s]
4.1e-3	16	0.045
10.2e-3	5	0.144

3.2 Properties of the produced biochar

Table 2 summarizes the results of the proximate analysis for the biochar collected. The samples with lower particle size found in each location have greater ashes content, this is presumably related to contamination with bed material. The sample WPC3-01 collected in the chamber's front (close to the outlet) presents a higher fixed carbon composition, possibly associated with longer reaction times. However, the sum of samples with different particle sizes collected in this area results in greater total inorganic content.

Table 2. Distribution of biochar in each location and their proximate analysis.

Code	Collection area	Particle size [mm]	Mass fraction*[%]	Moisture [%]	Volatile matter [% DW]	Ash [% DW]	Fixed carbon [% DW]
WPC1-01	Center	> 1 mm	89.7	3.4 ± 0.2	17.1 ± 0.2	2.9 ± 0.1	80.0 ± 0.3
WPC1-02		< 1 mm	10.3	2.8 ± 0.3	13.5 ± 0.7	29.9 ± 0.1	56.5 ± 0.7
WPC2-01	Close to inlet	> 1 mm	94.2	4.8 ± 0.2	16.9 ± 0.3	2.6 ± 0.1	80.5 ± 0.3
WPC2-02		< 1 mm	5.8	3.9 ± 0.7	12.8 ± 0.9	13.3 ± 1.9	73.9 ± 2.1
WPC3-01	Close to outlet	> 2 mm	40.4	3.0 ± 0.3	10.3 ± 0.6	5.0 ± 0.4	84.7 ± 0.7
WPC3-02		1 - 2 mm	25.5	0.6 ± 0.1	3.6 ± 0.3	84.4 ± 1.2	12.0 ± 1.2
WPC3-03		< 2 mm	34.0	0.7 ± 0.1	2.8 ± 0.9	87.0 ± 0.9	10.3 ± 1.2

This mass fraction refer to the distribution of this particle size in each collection area.

Figure 6 shows the Van Krevelen diagram of the biocarbon produced (plotted according to the results of the ultimate analysis). Based on the carbon ratios, biochar with similar quality to coal were obtained during this experiment. Additionally, these results are in the range of the values reported for pyrolysis products from woody biomass reported in the literature [Della Rocca et al., 1999; Şensöz and Can, 2002; Wang et al., 2013; Recari et al., 2014; Chiodo et al., 2016; Li et al., 2016].
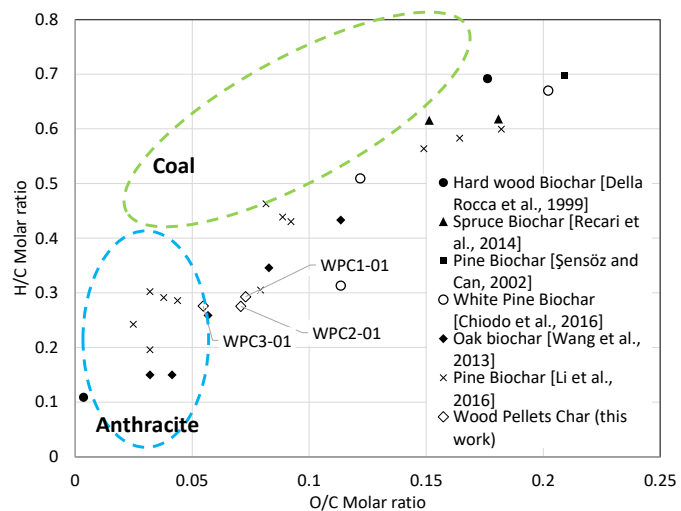
Figure 6. Van Krevelan diagram of pyrolysis products from woody biomass.

4. Conclusion and further work

The horizontal mixing of biochar at the hot large-scale conditions tested showed to be governed by dispersion rather than solids crossflow convection. However, increased solids crossflow enhances the dispersion significantly. The ultimate analysis of the produced biochar

reveals a quality similar to that of biochar reported in literature produced at lab scale, while the proximate analysis indicate possible improvement of the fix carbon content by increase in the residence time.

After these first experiences reported here, the planned future activities will mainly focus on expanding the test matrix to investigate the impact of different feedstocks (varying the biomass type, size and shape) and operational conditions (fluidization velocity and solids cross-flow rate). Further image analysis of the video recordings and use of statistics will be use to calculate an average horizontal velocity and horizontal dispersion coefficient of the feedstock by tuning of MonteCarlo simulations obeying a 1-dimensional convection-dispersion transport scenario.

Acknowledgment

References

Yaashikaa, P.R., Senthil Kumar, P., Sunita Varjani, A. Saravanan, A. 2020. *A critical review on the biochar production techniques, characterization, stability and applications for circular bioeconomy*. Biotechnol.Rep., e00570.

Kim, M., Park, J., Yu, S., Ryu, C., Park, J. 2019. *Clean and energy-efficient mass production of biochar by process integration: Evaluation of process concept*. Chem. Eng. J., 355, 840-849.

Farzaneh, M., Sasic, S., Almstedt, A., Johnsson, F., Pallarès, D. 2013. *A study of fuel particle movement in fluidized beds*. Ind. Eng. Chem. Res., 52, 5791–5805.

Liu, D., Chen, X. 2011. *Experimental profiles of lateral mixing of feed particles in a three-dimensional fluidized bed*. AIChE J., 57(6)

Liu, D., & Chen, X. 2010. *Lateral solids dispersion coefficient in large-scale fluidized beds*. Combust. Flame, 157(11), 2116–2124.

Olsson, J., Pallarès, D., Johnsson, F. 2012. *Lateral fuel dispersion in a large-scale bubbling fluidized bed*. Chem. Eng. Sci., 74, 148–159.

Köhler, A., Pallarès, D., Johnsson, F. 2020. *Modeling axial mixing of fuel particles in the dense region of a fluidized bed*. Energy & Fuels.

Niklasson F, Thunman H, Johnsson F, Leckner B. *Estimation of solids mixing in a fluidized-bed combustor*. Ind. Eng. Chem. Res. 2002;41(18):4663–73

Chirone, R., Miccio, F., & Scala, F. (2004). *On the relevance of axial and transversal fuel segregation during the FB combustion of a biomass*. Energy & Fuels, 18(4), 1108–1117.

Sette, E., Berdugo Vilches, T., Pallarès, D., Johnsson, F. 2016. *Measuring fuel mixing under industrial FB conditions - A camera-probe based fuel tracking system*. Appl. Energy, 163, 304–312.

Sette, E., Pallarès, D., & Johnsson, F. 2015. *Influence of bulk solids cross-flow on lateral mixing of fuel in dual fluidized beds*. Fuel Process. Technol. , 140, 245–251.

Farha, M., Guío-Pérez, D-C., Johnsson, F., Pallarès, D. 2024. *Characterization of the solids crossflow in a bubbling fluidized bed*. Submitted to Powder Technol.

Della Rocca PA, Cerrellla EG, Bonelli PR, Cukierman AL. 1999. *Pyrolysis of hardwoods residues: on kinetics and chars characterization*. Biomass Bioenergy, 16:79–88.

Şensöz S, Can M. 2002. *Pyrolysis of pine (Pinus brutia Ten.) chips: 1. Effect of pyrolysis temperature and heating rate on the product yields*. Energy Sources, 24:347–55.

Wang X, Xu W, Zhang L, Hu Z, Tan H, Xiong Y, et al. 2013. *Char characteristics from the pyrolysis of straw, wood and coal at high temperatures*. J Biobased Mater Bio, 7:675–83.

Recari J, Berrueco C, Abelló S, Montané D, Farriol X. 2014. *Effect of temperature and pressure on characteristics and reactivity of biomass-derived chars*. Bioresour Technol, 170:204–10.

Chiodo V, Zafarana G, Maisano S, Freni S, Urbani F. 2016. *Pyrolysis of different biomass: direct comparison among Posidonia Oceanica, Lacustrine Alga and White-Pine*. Fuel,164:220–7.

Li A, Liu L, Wang H, Xu B, Jin F, Liu L, Hu H. 2016. *Effects of temperature and heating rate on the characteristics of molded bio-char*. Bioresources, 3259–74.

THE PARTICLE SYSTEM CHALLENGES FOR CALCIUM LOOPING PROCESS: REVIEW AND FUTURE RESEARCH DIRECTIONS

Yijun Liua, *, Zhanmin Yanga, Fangjun Wangb, Wenguo Xiangb, *, Yanyan Wanga, Huafang Yanga

a School of Electrical Engineering, Nanjing Vocational University of Industry Technology, Nanjing 210023, China

b Key Laboratory of Energy Thermal Conversion and Control of Ministry of Education, School of Energy and Environment, Southeast University, Nanjing 210096, China

*E-mail: yijun.liu@niit.edu.cn/wgxiang@seu.edu.cn

Tel.: +86-18752017259

ABSTRACT:

Calcium looping technology is a promising carbon capture and heat storage technology to integrate in solid recovery fuel treatment and cement industry. Even though calcium looping process in coupled fluidized bed reactors is already industrially available and the function of itself has been demonstrated at TRL 6. However, there are still several issues about its future market adaptation and commercialization, while further improvement on particle system are desired. Application flexible, scale adaptable and closed-loop automatic control particle system for calcium looping are the ultimate development objective. In this work, based on existing knowledge, principles and foundations, gas-solid contact efficiency and active space time, real-time solid recirculation flux measurement in demonstration-scale, solid-solid separation and synergistic as sorbent and catalyst are discussed in details as future focuses to offer more ideas, to promote interdisciplinary and to provide references for other similar technologies (e.g. other chemical looping processes).

Keywords: calcium looping; particle system; scaling; gas-solid contact efficiency

1.Introduction

1.1 Overview

Global warming is today's environmental challenge primarily caused by greenhouse gas emissions referring to CO2 [1]. CO2 capture, utilization and storage (CCUS) strategy is an essential way in the future short and medium-term blueprint for zero-emission clean energy and industry. Herein, calcium looping (CaL) is one promising technical route to serve in the short and medium-term CCS scenarios [2–4]. CaO appears to be the best metal-based sorption candidate, considering the factors including cost, down-stream application, availability, capacity, and ease of regeneration [5]. CaL is flexible to integrate into all aspects of CCS strategy, i.e. pre-combustion, post-combustion, and oxy-combustion carbon dioxide capture [6]. In recent years, target of "1.5 ℃" from intergovernmental Panel on Climate Change (IPCC) [7] and program of carbon neutral before the mid of 21th century in many regions are proposed, which indicates the domination of non-carbon based and renewable energy in the future vision. Therefore, the role of CCS technology has tendency to deploy in carbon-based industry and carbon-loop market rather than power market. Based on this development expectations, Fig.1 presents a vision of the most promising clean energy production/storage routes with CaL deployment.
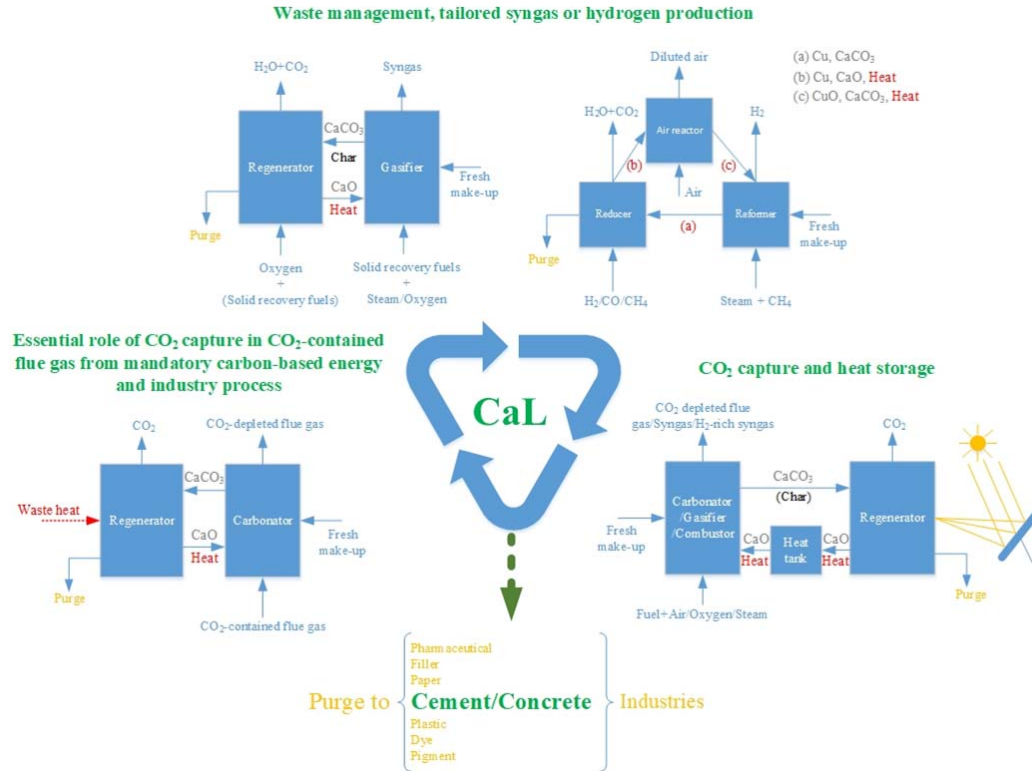
Figure 1 A vision of the promising clean energy production routes with CaL deployment

Although calcium looping technology is industrially available and the function of itself has been demonstrated at technology readiness level 6 (TRL 6), commercialization of calcium looping technology in such vision still has several challenges. Up to date in publications, the facilities with complete entities of carbonator and regenerator are listed in Table.1.

Table 1 The reported facilities of calcium looping technology around the world

Region[*]	Organization	Thermal power	Descriptions		References
			Carbonator/Gasifier	Regenerator	
Austria	TU Wien	100 kW$_{th}$	Lower BFB, Upper riser (bamboo-like internals), CFB	Riser (reducer pipe)	[8–14]
		8 MW$_{th}$	BFB	Riser (reducer pipe)	[15,16]
Canada	CANMET Energy	75 kW$_{th}$	Two stages BFB	BFB/Moving bed	[17]
	Dal	[-]	BFB	Riser (no reducer or internals pipe)	[18]
China	SEU	10 kW$_{th}$	Compact fluidized bed (upper riser and BFB)	Riser (no reducer or internals pipe)	In this work
		1 MW$_{th}$	Design and construction phase		[-]
	ZJU	[-]	Riser (no reducer or internals pipe)	Riser (no reducer or internals pipe)	[19,20]
	THU	[-]	Riser (no reducer or internals pipe)	Riser (no reducer or internals pipe)	[21]
Germany	IFK, Uni-Stuttgart	20 kW$_{th}$	BFB	Riser (no reducer or internals pipe)	[22]
		200 kW$_{th}$	Riser (reducer pipe)	Riser (reducer pipe)	[22]
	TU Darmstadt	1 MW$_{th}$	CFB	CFB	[23–29]
		20 MW$_{th}$	Design phase		[30,31]
Spain	INCAR-CSIC	30 kW$_{th}$	Riser (no reducer or internals pipe)	Riser (no reducer or internals pipe)	[32,33]

		300 kWth	Riser (no reducer or internals pipe)	Riser (no reducer or internals pipe)	[34]
		1.7 MWth	CFB	CFB	[35]
		3 kWth	BFB	Rotary kiln	[36]
Taiwan, China	ITRI	500 kWth	BFB	Rotary kiln	[37]
		1.9 MWth	BFB	Rotary kiln	[36,38]
		10 MWth	Design phase		[37]
USA	OSU	120 kWth	Entrained bed	Rotary kiln	[39]

*According to the "ISO 3166-1" document published by the International Organization for Standardization (ISO). Sorted in initial alphabetical order [40].

In the initial development of calcium looping technology, heat resource for regeneration and sorbent sustainable adsorption performance are two inherent challenges. In the future, the challenges can be faced by integrating with other technology or process. Details are discussed as follow.

1.2 Heat resource and transfer

An inherent challenge along with calcium looping technology is heat resource for regeneration process. Although the carbonation process is exothermic, the heat in carbonating process cannot support the regeneration since the required temperature in regenerator is much higher than carbonator, while extra heat resources are needed. Therefore, heat normally generates in regenerator from several heating resources and transfers through bed materials or heating surface to the carbonator [2]. Several proposals for the regenerator heating resources are 1) combustion of residue char from carbonator; 2) combustion of extra fuels, such as biomass or natural gas, etc. 3) concentrated solar energy heat; 4) combining heat from cement or industry plant; 5) heat from oxidation reaction in chemical looping process; 6) electric heating.

Combustion of residue char from carbonator is primarily applied in pre-combustion carbon dioxide capture strategy, since this is not feasible for post-combustion CO_2 capture application. The char generated in gasification process flows to the regenerator and combusts in air or oxygen-enriched atmosphere. The disadvantages of this strategy are the mixing of nitrogen and carbon dioxide, as if using air directly, or the utilization of energy-intensive and costly air separation unit (ASU) if using oxygen-enriched gas in regenerator. It is notable that the disadvantage of CO_2-N_2 gas mixing would be offset if carbon dioxide is only proposed to store underground for enhancing oil production recovery, or carbon-neutral biomass is used as fuel. Furthermore, extra fuel is normally required when char supply from carbonator is inadequate. Combustion of extra fuel to supply heat has been commonly regarded as cost-effective way in demonstration-scale calcium looping system, but it will be subjected under more or less system efficiency penalty (e.g. 6~8% for post combustion). Renewable biomass waste as fuel has increasingly become an important alternative energy resource to them. Biomass waste is a carbon-neutral energy and a net negative carbon balance can be achieved if combined with appropriate carbon storage and utilization strategy, further probably removing CO_2 from the atmosphere [41,42]. The biomass-based calcium looping process has significant possibilities to offer a sustainable and efficient pathway to utilize biomass [43]. Furthermore, calcium-based materials not only can be used as carbon carrier, but also as catalyst for biomass tar reforming during gasification/pyrolysis process. Combination of this process with solid recovery fuel (SRF) management has a potential to makes the best of both way, as depicted in Fig.1.

Combining calcium and chemical looping (CaL-CLC) concept was firstly proposed by Abanades et al. [44] in 2010, Spain. The regeneration heat can be generated from oxidation reaction in chemical looping process, which is also a particle-derived technology. Two kinds of particle, e.g. carbon carrier and oxygen carrier, are ideally cycled in a mutual system with different duties. Nevertheless, this concept is facing serious engineering challenges since there is no report on it with any lab-scale facility tests closing to real conditions to date. More works are desired in the future. Electric heating strategy is generally employed on bench-scale or lab-scale facility for basic research and development. It has great flexibility to help researching the flow mechanism in a specific reactor under realistic hot conditions. However, it is impossible and uneconomical to utilize this strategy in

full-scale or demonstration-scale facility, while self-heating should be fulfilled under this scale.

Calcium looping is also an emerging and promising thermochemical energy storage technology [45], which is inherently to resolve regeneration heating resource problem [46]. Combination of concentrated solar energy (CSE) or cement plant with calcium looping process are current researching hot-spots for solving the issue of heating resources. Calcium looping combined with CSE can help to storage heat from ever-changing and weather-depend solar energy. However, it has limited report on real testing facility for application basing on this strategy [47–49]. Calcium looping combined with cement plant is complementarity while extra heat from heat-intensive cement plant can be used in regeneration and calcium-based sorbent purge can be used as raw materials without pre-crushing for cement production.

1.3 Sorbent sustainable adsorption performance

The long-term performance of calcium-based sorbent materials is the other inherent challenge. So far, a decline in CO2 capture performance during cyclic operation is inevitable. Fig.2 presents a general equation for deactivation, which has been proven to be valid for many common limestone up to 500 cycles [50]. According to this situation, three common strategies are presented in engineering practical way: 1) design of calcium looping system based on the infinite (minimum) adsorption capability ($X_{Critical}$), and further enhance the infinite sorption capacity of the sorbent material. However, as author known to date, sorbent cost and performance are positive exponential correlation, which has conflict with the goal for industrialization as low cost-effective CO2 capture technology [51]. 2) Improvement of operating conditions in carbonator and regenerator is a practical way to enhance the sorbent cycle performance, such as pre-calcination of sorbent, addition steam in regenerator and carbonator, etc. [52]. However, this strategy may not be good candidates, primarily as a result of their short-term enhancement benefit and an increase in energy-cost. 3) Consensus to date, CaL technology has a significant potential to be a feasible CO2 capture system combined with cement plants [53]. Thus, the sorbent after certain cycle numbers (N_{Purge}) is purged from system and make-up/fresh sorbent is supplied in. Meanwhile, the relative benefit achieved from this strategy will be the lower solid inventory and flux required in the carbonator reactor, which thanks to an increase in the active fraction of bed materials with fresh make-up. This advantage also reduces the difficulty and cost on the reactor design and construction.

$$X_N = \frac{1}{1/(1-X_r) + kN} + X_r$$
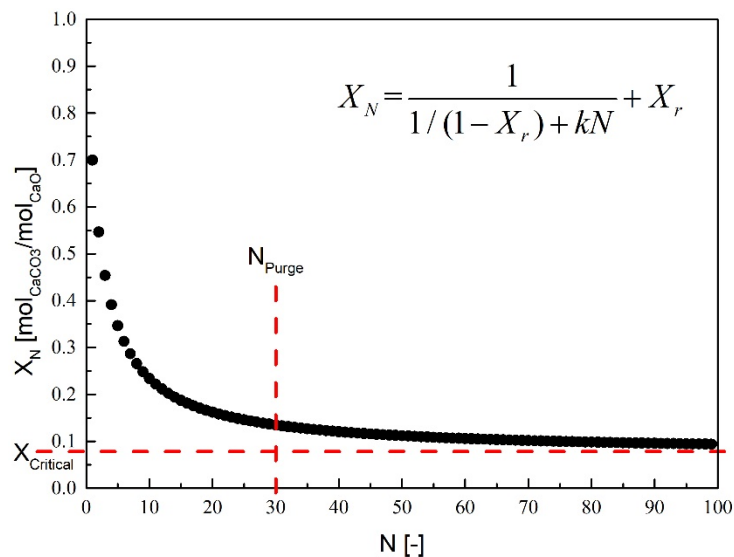
Figure 2 A general equation for calcium looping cycle deactivation [50]

Over the past two decades, many previous studies focused on carbonation/calcination reaction kinetic modeling, the mechanism of deactivation from micro-level evidence and improvement method for calcium-based materials, etc. However, modified materials under mild testing conditions are far

away from the industrial applications. There is a critical difference between mild conditions and engineering practice, also primarily referring to the solid-gas contact efficiency discussed later. Many activation strategies are conducted to enhance the cyclic performance of the sorbents, but pose new challenges such as the cost of the synthesis route, the scale-up pathways of the sorbents, the assessment of cyclic performance under mild conditions, and the ignorance of mechanical strength and attrition resistance [51]. Many attempts have been made to develop powder-like or nanoparticles to enhance sorbent performance and solid-gas contacting, but it still causes difficulties in engineering. In this regard, Raganati and Ammendola [54] recently reviewed sound-assisted fluidization for temperature swing adsorption technology, which is desired to be applied with such powder-like or nanoparticles sorbent.

At present, continuous sorbent purge and make-up of fresh sorbent is a balancing choice for demonstration-scale engineering. Combination with other industries is a prospective way for commercial application of CaL process [52]. For instance, the purged and deactivated limestone or dolomite can be continuously used as feedstock in the cement industry [55]. The deactivated, crushed and powder-like calcium-based sorbent purges have an advantage to be used as pre-treatment raw material in cement industry and heat-intensive cement production process is benefit for providing regeneration heat. Calcium-based waste (e.g. eggshell, seashell, etc.) is another potential and sustainable calcium source alternating to natural minerals [56,57]. Furthermore, the versatility and abundance of calcium-based materials have led to it becoming an essential formulation component within the pharmaceutical, filler, paper, concrete, plastic, dye, and pigment industries [58].

1.4 Work structure

In addition to the two above-mentioned challenges in the initial development stage, in this work, issues are focused on the particle system of calcium looping process. The purpose of these work is to help promote the particle system in a cost-effective, intelligent and scale flexible way to enhance future calcium looping commercial competitiveness. The research data on above kilowatt-scale or megawatt-scale facilities are still limited, which probably due to expensive operating and labor costs, inadequate driving force of economic benefit, or confidentiality of technology. As the carbon market and emission tax are maturing, development of calcium looping technology will be profit-driven in many industries more than just in energy production and its cost will be more effective. The specific issues, such as solid-gas contact efficiency under different operating conditions and reactor design, optimal balance between capture efficiency and active space time, accuracy, non-intrusive and online solid recirculation flux measurement, solid-solid separation and synergistic of catalysis and sorption, in single or multiple particle system are studied and discussed. The structure of this paper is shown as follow.
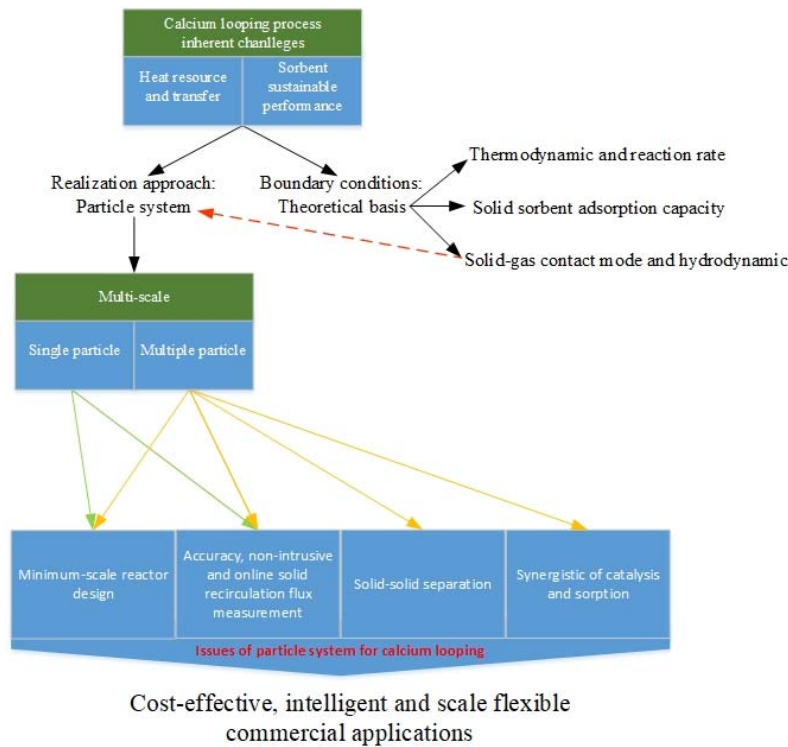
Figure 3 The structure of this work

2. Theoretical basis

2.1 Thermodynamic and reaction rate

The calcium looping process is generally realized with a carbonator and a regenerator. To design a carbonator and a regenerator, it is essential to understand the relationship between chemical equilibrium atmosphere and operating temperature for CO_2 capture by CaO, presented by Baker [59], as shown in Fig.3.
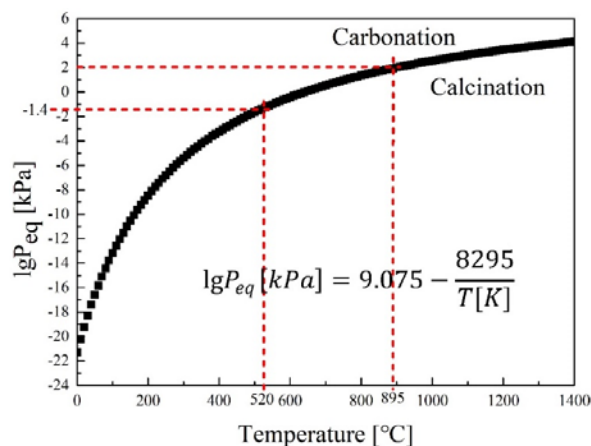
Figure 4 Equilibrium partial pressure of CO2 above CaO as a function of temperature from Baker equation [59]

Baker's equation provides several indications: 1) at atmospheric pressure, 100% CO_2 partial pressure and 0.04% CO_2 partial pressure (CO_2 concentration in atmospheric) versus 895 ℃ and 520 ℃ for balance between carbonation and calcination. 2) At constant CO_2 partial pressure, an increase in temperature is unfavorable to carbonation. 3) At constant temperature, a decrease in pressure is unfavorable to carbonation. Pressure swing under constant temperature has more challenge comparing to temperature swing under constant pressure. Mechanical design constraints,

sophisticated instrumentations requirements, high costs and limited universal applicability preclude the implementation of pressure swing [60,61]. In regard of reaction rate, according to Arrhenius equation or modified Arrhenius equation in Eq.1 [62] and Eq.2 [63], and reaction rate equation in Eq.3 as follow:

$$k = Ae^{\frac{-E_a}{RT}} \tag{1}$$

$$k = BT^n e^{\frac{-E_a}{RT}} \tag{2}$$

$$\frac{d[CaCO_3]}{dt} = k(T)[CaO]^m[CO_2]^n \tag{3}$$

An increase in reaction temperature can enhance reaction rate, while this characteristic favors regeneration process. Thus regenerator can always operate at atmospheric pressure under much higher temperature. However, for the carbonation process, an increase in temperature under constant CO_2 partial pressure is a disadvantage according to the above thermodynamic properties. It indicates that an increase of pressure and temperature in carbonator at the same time can enhance reaction rate and capture efficiency in a balanced manner.

2.2 Solid sorbent adsorption capacity

Adsorption capacity is a key parameter for system performance and the performance was commonly tested under mild condition. The mild condition means that multi-cycle performance is tested on the thermo-gravimetric analyzer (TGA) or small batch (tube) bed, with inlet gas switch and focusing on chemical reaction, and without particle transport and almost no mechanical wear. There are countless testing results of different calcium-based materials and under different temperature and pressure environments from many researchers around the world [51]. The CaO conversion is defined as follow:

$$X_{CaO} = \frac{\Delta m_{car}}{m_{sorbent} y} \cdot \frac{M_{CO_2}}{M_{CaO}} \tag{4}$$

where Δm_{car} is the mass change during the carbonation, $m_{sorbent}$ is the initial sample mass, y is the CaO mass fraction in the sample, M_{CO_2} and M_{CaO} are the mole mass of CO_2 and CaO, respectively. Unfortunately, the decay trend of adsorption capacity appears in the cycle performance for all calcium-based carbon carriers. All of these research results indicate that the CO_2 capture performance decreases with an increase in cycle numbers, especially in several initial cycles. After certain cycles, the CaO conversion mostly stable around 0.1~0.3, while Chou et al. [37] gave a constant value of 0.174 for conversion after infinite cycles.

2.3 Solid-gas contact mode and hydrodynamic

In the traditional chemical or power industry, the body of knowledge for solid-gas reactors has been built up systematically [64]. Typical reactors are continuous stirred-tank reactor (CSTR), plug flow reactor (PFR) or the fixed/fluidized bed (FB) reactor, etc. Herein, in calcium looping process, CO_2 concentration in gas production from carbonator and decomposition of $CaCO_3$ in regenerator are primarily concerned. Originally, regenerator only needs heat for calcination of $CaCO_3$, thus the solid-gas contact mode can be more focused in carbonator. For instance, rotary kiln was used as regenerator [37]. The mode of solid-gas contact in carbonator can be divided into two types: solid-gas countercurrent and co-current contact mode, as shown in Fig.5.
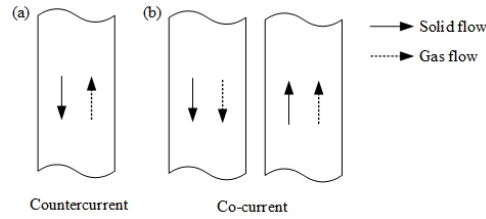
Figure 5 The mode of solid-gas contact

For countercurrent contact mode, solid and gas flowing bodies flow in opposite directions to each other, where typical carbonators are moving bed and bubbling fluidized bed. The throughput of gas is relatively smaller under per unit-area and control of reactor temperature distribution is more difficult. Co-current contact mode has two ways: co-current upstream and co-current downstream. Meanwhile, co-current downstream requires much higher reactor and solid/gas residence time is relatively short. Turrado et al. [65] studied fine CaO-based sorbent performance with a few seconds of gas/solid contact time using a co-current downstream drop tube reactor. Moreover, co-current downstream design is normally as auxiliary part in system, referencing to the facility in the Tsinghua University for chemical looping process [66]. In a narrow sense, co-current contact mode usually refers to fluidized bed riser. Fluidized bed has been widely applied and studying in industries since 1950s [67] and so far typical application are fluid catalytic cracking (FCC) reactor and the circulation fluidized bed combustion (CFBC) reactor, etc. Fluidized bed has several fluidization regimes, or hydrodynamics under different superficial velocities. Fig.6 presents the Grace's fluidization diagram under different particle sizes and superficial velocities and flow regimes description [68].
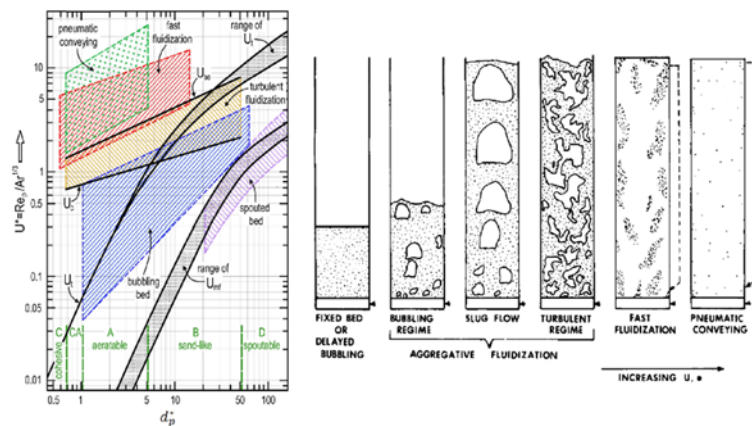
Figure 6 Grace's fluidization diagram and flow regimes description [68]

Interestingly, operation of bubbling fluidized bed (BFB) is under countercurrent and co-current contact mode at the same time. BFB has larger bubble size, which may result in serious gas bypass through the bed. However, interest in the technology of gasification has shown since its first appearance. Fast fluidized bed or high density/flux circulation fluidized bed is a desirable fluidization regime while it has the criterion of solid circulation rate reaching 200 kg/(m²s) and the average solid holdup of 10% as the boundary to demarcate with pneumatic conveying or low density/flux circulation fluidized bed [69]. Fast fluidization regime has advantages of larger solid holdup per area, higher solid-gas contact efficiency and higher solid flux, but its forming conditions are harsh. Three prerequisites are proposed for operation in fast fluidization regime [70]: 1) appropriate superficial velocity; 2) appropriate solid flux under certain superficial velocity; 3) appropriate particle properties. Basically, all prerequisites are depended on gas and particle properties, i.e. Archimedes number (Ar).   In general, the riser pipe without internals and as carbonator or regenerator can provide sufficient height and help forming the fast fluidization regime, e.g. the facilities in ZJU, THU and INCAR-CSIC. Several institutes designed a reducer pipe as the riser. In IFK, a 200 kW$_{th}$ facility consisted with three

reactors was designed, i.e. gasifier, carbonator and regenerator. Thus the system can be operated under different modes for post- and pre-combustion carbon capture CaL process. The gasifier and carbonator are reducer pipes while the pipe as the gasifier has small internal diameter in the lower part and large internal diameter in the upper part, and the pipe as the carbonator is quite the opposite. Larger diameter part with relatively smaller superficial velocity limits the larger or heavier particles, e.g. char, in the specific region. TU Wien designed and constructed a two-stage non-divider reactor, within a lower bubbling fluidized bed as the gasifier and an upper bamboo-like riser as tar reformer and carbonator. It is interesting that the bamboo-like pipe can help to form an almost countercurrent flow conditions for gas phase and solid, which produces no volatiles, avoids insufficient gas phase conversion and reduce tar content and entrainment of coarse particles. Circulating fluidized bed (CFB) has been widely accepted as carbonator or regenerator by TU Wien, TU Darmstadt, INCAR-CSIC and IFK. The circulating fluidized bed has several advantages of sufficient, flexible and controllable solid residence time under specific reactor height. More details of structure can be found from references in Table.1.

Furthermore, a compact fluidized bed reactor, as shown in Fig.7 (b), was firstly proposed by Xiang et al. [71] for chemical looping hydrogen generation process in 2009 and adopted as carbonator/gasifier for CaL by Chen et al. [72] in 2011 in SEU (Fig.7 (c)), and cold flow model was initially designed and constructed in 2017 [73,74] and electrically heated hot rig system at sub-pilot scale was built in 2019, as shown in Fig.7 (a). The compact fluidized bed structure is simple and benefits for retrofit of old facilities, reduction of particle wear, sorption enhancement and tar reforming.
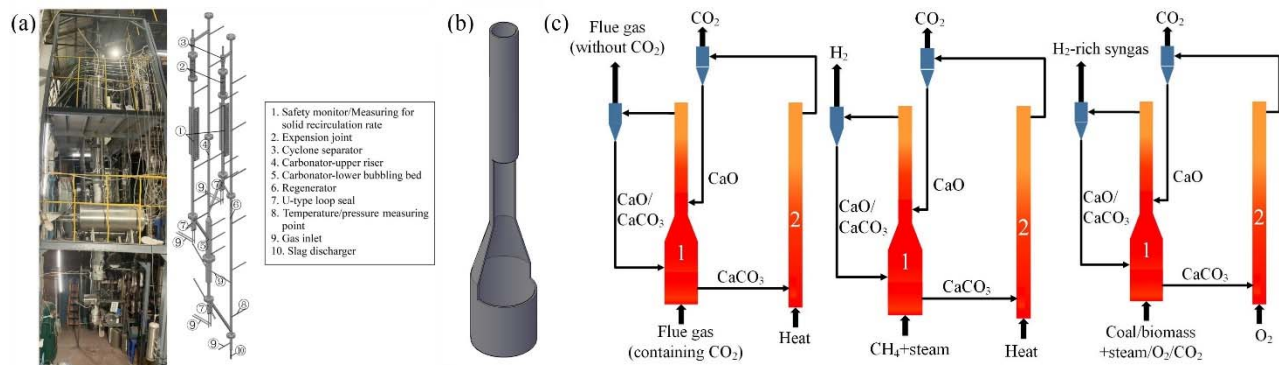
Figure 7 Compact fluidized bed carbonator/gasifier: (a) sub-pilot scale 10 kWth electrically heated system; (b) structural details of compact fluidized bed; (c) schematic of applications for CaL

2.4 Developed model

Carbon dioxide capture efficiency and cycle capability of calcium-based sorbent are two key and basic index to evaluate the system performance using technical-economic analysis (TEA) and life-cycle assessment (LCA), and further helping with the technological development, commercial demonstration and market deployment. In this work, the two index mentioned before are named as "carbon balance" and "calcium tracing" to characterize any calcium looping system performance in general.
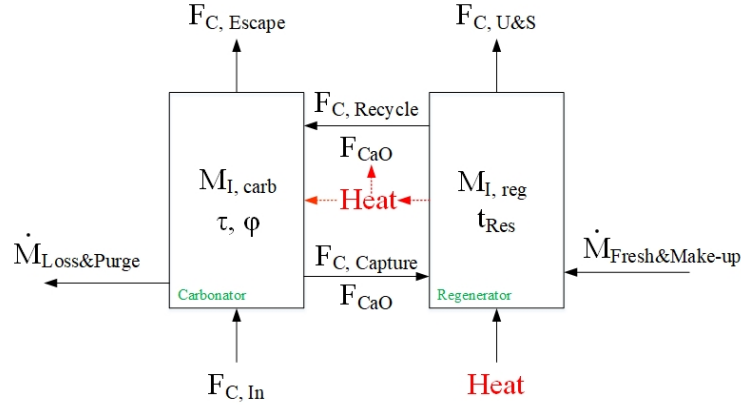
Figure 8 Key indexes for calcium looping in dual fluidized bed. Res: Solid residence time; U&S: utilization & storage; τ: Space time; φ: solid-gas contact efficiency.

Based on illustration of carbon balance in Fig.8, system efficiency, carbonator efficiency and regenerator efficiency can be defined in Eq.5~Eq.7. Further researches can be carried out on specific facility to find the influences of operating parameters on the efficiency indicators.

$$E_{system} = \frac{F_{C,U\&S}}{F_{C,In}} \tag{5}$$

$$E_{carb} = \frac{F_{C,In} - F_{C,Escape}}{F_{C,In}} \tag{6}$$

$$E_{reg} = \frac{F_{C,U\&S}}{F_{C,In} - F_{C,Escape}} \tag{7}$$

Closure of a carbon balance is an essential methodology to character the performance of calcium looping in dual fluidized bed [75]. INCAR-CSIC and IFK previously studied and comprehensively evaluated the methodology to interpret experimental results on three lab-scale hot rigs in 2011 [76]. According to the experiment result, the carbonator efficiency is defined as

$$F_{CO_2} \cdot E_{carb} = F_{Ca} \cdot (X_{carb} - X_{calc}) \overset{X_{calc} \to 0}{=} n_{Ca} \cdot \left(\frac{dX_{carb}}{dt} \right) \tag{8}$$

, while the regenerator efficiency is normally postulated approaching to 100% (full calcination), although the requirement of high temperatures and/or low partial pressures of CO_2 are needed. Thus, the carbonator efficiency can be equal to the system efficiency.

Herein, particular emphasis is put on the behavior of natural limestone and dolomite, which would be the only practical choices for the technology to meet its main goal of reducing CO_2 capture costs. The purged limestone and dolomite are continuously utilized in cement plant as raw resource. During the carbonation-regeneration cycle, the other problems are the reaction kinetics of carbonation with fast and slow reaction region, and the mixing of different states/cycle numbers carbon carriers in the system. IFK and INCAR-CSIC have thoroughly studied the operating parameters determining the CO_2 capture efficiency [75]. Two approaches were proposed with two assumptions: 1) Approach A: all particles in carbonator are able to react and have same average characteristics; 2) Approach B: only a fraction of the particles with sufficiently short residence time are active in the carbonator and can react in the fast reaction regime. Related formulas are listed in Table.2 [77–83].

Table 2 Two approaches for the operating parameters determining the CO2 capture efficiency [77–83]

$$F_{CO_2} E_{carb} = n_{Ca} \left(\frac{dX_{carb}}{dt} \right)_{reactor} \tag{9}$$

Approach A	Approach B

$$E_{carb} = k_{sA} \cdot \varphi\tau \cdot \left(X_{ave} - X_{carb} \right) \cdot \left(\bar{\upsilon}_{CO_2} - \upsilon_{eq} \right) \qquad E_{carb} = k_{sB} \cdot \varphi\tau \cdot f_{active} X_{ave} \cdot \left(\bar{\upsilon}_{CO_2} - \upsilon_{eq} \right) \tag{10}$$

$$\tau_A = \tau \cdot \left(X_{ave} - X_{carb} \right) \qquad\qquad\qquad \tau_B = \tau \cdot f_{active} X_{ave} \tag{11}$$

Solid-gas contacting effectivity factor and carbonator space time:

$$\varphi\tau = \frac{n_{Ca}}{F_{CO_2}} \tag{12}$$

Fraction of carbonator active particles

$$f_{active} = 1 - e^{\left(\frac{-t^*}{n_{Ca}/F_{Ca}} \right)} \tag{13}$$

Time needed for a particle entering the carbonator to increase its carbonate content from X_{calc} to $X_{max,ave}$

$$t^* = \frac{X_{ave} - X_{calc}}{(dX / dt)_{reactor}} = \frac{X_{ave} - X_{calc}}{k_{sB}\varphi X_{ave} \left(\bar{\upsilon}_{CO_2} - \upsilon_{eq} \right)} \tag{14}$$

The carbonation surface kinetic constant (k_s), solid-gas contacting effectivity factor (φ) and average CO_2 carrying capacity (X_{ave}) are generally derived from thermal-gravity (TG) experiments or backward the value from experiments on the specific facility. Moreover, the X_{ave} is determined on molar flow of fresh make-up limestone fed into the system (F_0), molar flow of recycled solids inside the loop (F_R) and number of calcination and full carbonation cycles (N), as shown in Eq.17 [50].

$$X_{ave} = \sum_{N=1}^{N=\infty} r_N X_N = \sum_{N=1}^{N=\infty} \frac{F_0 F_R^{N-1}}{(F_0 + F_R)^N} \cdot \left(\frac{1}{(1 / (1 - X_r)) + kN} + X_r \right) \tag{15}$$

This equation has a limitation that the weights of F_0 is too great on X_{ave}, which also indicates the X_{ave} will be equal to zero if no fresh sorbent supplied ($F_0 = 0$), even though it has sufficient solid recirculation flux and sorbent with a small number of loops. Typically, a necessary condition to conveniently obtain a certain CO_2 capture efficiency value is that the active flow of CaO supplied to the carbonator is greater than the molar flow of CO_2 being captured. However, heat waste from regenerator and mechanical wear of excessive sorbent are inevitable. Therefore, calcium tracing technique is necessary to be developed to help enhancing system performance in the future. Another interesting issue is mass and molar balance inequality. Solid recirculation flux should be equal at inlet and outlet of reactor to maintain bed material inventory, preventing solid empty or fullness. Its equivalence mass flow are not equal if molar flows of CaO at inlet and outlet of carbonator are equal. This indicates that the flow area of reactor inlet and outlet should be different to offset the inequality when design the connected reactor. Calcium looping technology would be gradually assimilated into decentralize energy system in future development. Thus, flexible reactor design according to different market size becomes more and more important for future calcium looping technology.

3. Different scale and scaling law

3.1 Multi-scale analysis

In the study of calcium looping technology, multi-scale analysis is a very useful tool to help understanding different research results between micro-scale and macro-scale [84]. As shown in the Fig.11, multi-scale concept can be divided into three parts, and each part has its own micro-scale and macro-scale levels.
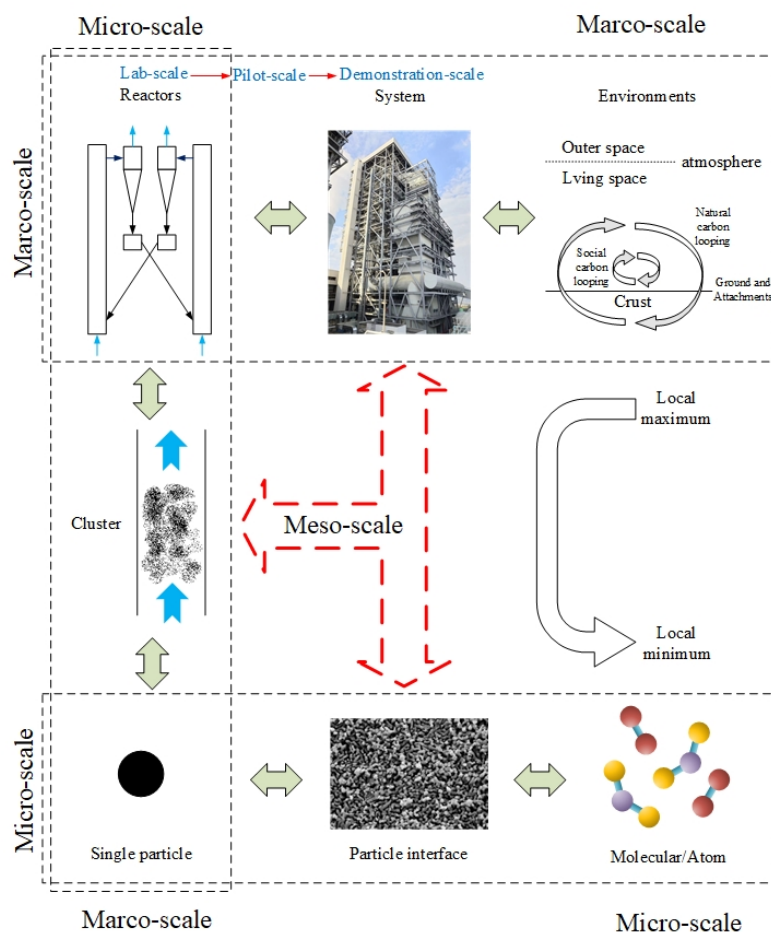
Figure 9 Multi-scale analysis landscape

From different parts, developing suggestions from research results are inconsistent at times. Among micro-scale molecular/atom to macro-scale single particle part, research results concluded that the smaller size of particle has more benefits for chemical reaction. The smaller particle size enables more fully contact and reaction of gas-solid molecules at the molecular/atom level. But among micro-scale single particle to macro-scale reactors part, operation of fine powder in fluidized bed is very difficult because its adhesion between the particles, the agglomeration and the channel flow. According to Geldart particle group classification [85], group A, A-B, B, B-D particles are more applicable in fluidized bed. The relationship between different scales is essential to learn for steady, concrete, cost-effective and safe development of reactors.

3.2 Scaling law for hydrodynamic

For industrial application, development of reactor generally starts from cold and small-scale to hot and large-scale, finally in commercial-scale. It indicates that hydrodynamic feasibility is the first step to realize calcium looping process. The use of reactors with homogeneous flow patterns of solid-gas two-phase flows, e.g. spouted bed reactor or fluidized bed reactor, is the most developed solution to carry out the carbonation and regeneration reactions. In many other commercial applications, e.g. FCC, etc., the fluidized bed has a large diameter and height and operates at elevated temperature and pressure. To properly design a fluidized bed the fluid dynamics must be well understood since it directly influences the bed performance. Full-scale trial reactors full of uncertainties and represent a high cost and risk. Herein, detailed fluid dynamic investigations should be carried out more conveniently and cost-effectively on small beds at ambient conditions. For this proposal, designers particularly concern about the relationship between the performances of large commercial reactors and results obtained from much smaller pilot plants.

Glicksman scale-up [86,87], Horio scale-up [88,89], Chaos scale-up [90–93] and Novel scale-up [94] are previous reported scaling laws for integral fluidized bed hydrodynamic. Glicksman scaling law is the classic scaling law, which was firstly proposed in 1984, USA [86]. This law non-dimensionalized the governing equations for a two-phase flow and proposed a full set of non-dimensional numbers. Nevertheless, the full set is often not useful while a balance cannot be found at different ambient conditions. Therefore, a simplified set as follow with the goal of reducing the number of dimensionless parameters was derived to allow more flexibility.

$$\frac{u_0^2}{gL}, \ \frac{\rho_p}{\rho_g}, \ \frac{G_s}{\rho_p u_0}, \ \frac{L_1}{L_2}, \ \text{bed geometry}, \ \phi_p, \ \text{PSD} \tag{5}$$

where $\frac{u_0^2}{gL}$, the Froude number. The $\frac{\rho_p}{\rho_g}$ is the density ratio between the gas and the particle phase. The $\frac{G_s}{\rho_p u_0}$ is for scaling the solid recirculation flux, G_s. The $\frac{L_1}{L_2}$ is the scaling factor. The bed geometry generally means the equivalent diameter and height of the reactor. The Φ_p is the sphericity of particles. The PSD is the particle size distribution. The dimensionless solid circulation flux G_s is not considered in the design because the investigated system is normally a freely circulating fluidized bed in which the solid circulation flux is not an independent variable. Horio et al. [89] proposed a scaling law in 1986, Japan. They supposed a magnification (m) number that all parameters as follow should be changed according to this number.

$$\begin{cases} u_{mf}, u_0 - u_{mf} \\ D_t, L, l \\ u_0, u_t, v_0, d_p, \rho_p, \rho_f, \mu \\ d_{cl}, u_c, u_a, v_c, v_a, \varepsilon(\zeta, \xi), \alpha \end{cases} \tag{6}$$

where u or u_0 is superficial gas velocity, D_t and L is column diameter and height, l is arbitrary length parameter in CFB design, d_p is mean particle size, ρ is density, μ is viscosity and v is superficial particle velocity. ε is voidage, ζ is z/L, ξ is $2r/D_t$ and α is D_c/D_t. Subscripts of a, c, cl, d, f and p mean annulus, core, cluster, dilute phase, fluid and particles, respectively. However, all scaling laws above generally bases on empirical correlations, which would be not useful to control the relative deviations within certain range (e.g. 20%).

Deterministic chaos theory was firstly proposed for scaling law in 1993, Netherlands [93]. The correlation dimension and Kolmogorov entropy (K) may be used as an unambiguous tool to assess quantitatively the dynamic similarity, while chaotic attractor and information group Kd_p/U_0 should be kept constant in dimensionless scaling. d_p is particle diameter and U_0 is superficial gas velocity. Nonetheless, this methodology is overly dependent on the pressure measurement technics and signal processing accuracy. With the development of the computational fluid dynamics (CFD) and multi-physics coupling technology, a novel scaling strategy based on virtual simulation is emerging and developing [94].

4. Particle system issues

From the above basic content of calcium looping process, the essence of this process is accomplishment of a single/multiple particle(s) system. The single particle system primarily refers to post-combustion carbon dioxide capture calcium looping process (CaL) and the multiple particles system mostly attributes to sorption-enhanced gasification (SEG) process or CaL-CLC process. In the carbonator, sorbent is generally in excess of the existing CO_2 required to ensure the capture efficiency. This will cause a decrease of sorbent utilization efficiency and an increase of purged sorbent due to mechanical wear rather than deactivation. Excessive waste sorbent will put redundant processing pressure on down-stream processing industries. Optimization of operating condition is the key to help facing cost challenge and breaking through TRL-6 to higher level. So far, most of testing facilities are manual or open-loop semi-automatic control. It is obviously that the advantages

of closed-loop automatic control can save labor cost and match requirement more accurate without wasting of process capacity according to market demand, further reducing operation cost. The difficulty to achieve this aim is to accurately identify the operating states of calcium looping system, primarily referring to the topics as follow to date.

4.1 Minimum-volume reactor design

It is necessary to know the demands of processing capacity of carbon dioxide or solid fuel or syngas production according to local market before design of a reactor. Ideal reactor design can help to realize minimum or ideal gas-solid ratio, 100% gas-solid contact efficiency and solid flow in order. 100% gas-solid contact efficiency means that each gas molecule can contact with solid once at least. An ideal operating condition is that solid after reaction in fast chemical region can be transferred immediately to the next reactor. The influences on this condition are gas-solid ratio and solid flow control. Gas-solid ratio is much easier to be controlled through gas flow meter and solid feeder, but solid flow control is much difficult to be dominated in typical bubbling fluidized bed reactor, which has chaos type phenomenon. Fig.10 shows the intrinsic mechanism of minimum-volume reactor design, where the volume-time relationship of solid fuel and calcium-based sorbent are presented in Fig.10 (a). As in Fig.10 (b), ideally, the design size of the reactor should be greater than or equal to the minimum volume of sorbent and fuel.
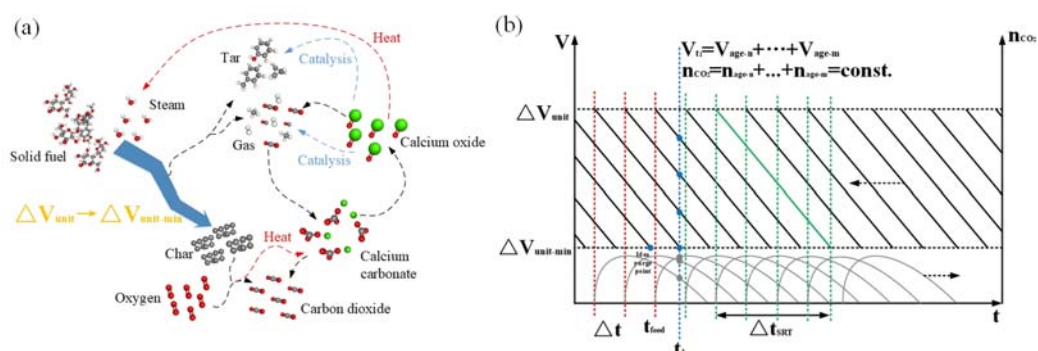
Figure 10 The intrinsic mechanism of minimum-volume reactor design

Gas-solid contact efficiency is an essential factor in gas-solid two-phase system, since calcium looping system is admittedly no exception to pay attention on it. Although the regenerators in ITRI [36] and OSU [95] are rotary kiln, where the solid-gas contact can be ignored. In micro/small-scale and mild condition experiments for studying reaction mechanism, the gas-solid contact efficiency is generally omitted or is defaulted to the idea condition (i.e. 100%). However, the gas-solid contact efficiency cannot be ignored in scaled-up fluidized bed for studying carbonator or system operation.

So far, the gas-solid contact efficiency is not well understood and lacks a rigorous definition [96]. Wang et al. [96] reviewed the development state in the understanding of gas–solid contact efficiency in the circulating fluidized bed riser reactor. Geng et al. [97] have summarized different definition methods of the efficiency only for fluid catalytic cracking (FCC) process, i.e. gas-solid catalytic reaction system (C-RS). However, this system is much different from CaL process, i.e. gas-solid non-catalytic reaction system (NC-RS). In C-RS, the focus is on gas production rather than solid catalyst, thus the feed-gas conversion on solid is the most important index. Adversely, solid conversion efficiency is more focused in fluidized bed combustion (FBC) process. But in NC-RS, the gas and solid are all reactants. It is need to focus on either the gas product or the solid product. For post combustion CaL process, gas conversion is the most important index, while SEG process is more complex, which is both a C-RS and a NC-RS, including: 1) fuel and gasify agent (NC-RS); 2) CO_2 and sorbent (NC-RS); 3) catalyst and tar (C-RS).

Herein, Eq.10 mentioned before have considered the solid-gas contacting factor (φ) in the

carbonator. However, this factor is a custom parameter, which is generally calculated from the experimental data through the inverse formulas of Eq.10 [33]. Predication of the gas-solid contact efficiency in a designed reactor can further help to reduce test cost and to improve the reactor design and operating conditions. The studies of gas-solid contact efficiency in a riser have raised that operating conditions, flow structure, solid holdup and gas profiles, cluster, gas–solid interactions, types of reactors and some other factors can make a contribution to the efficiency [98]. However, there is no common standard research method or definition, and limited studies of gas-solid contact efficiency for calcium looping process to date [96,98–102]. Ozone concentration profile method is widely used in the studies of the efficiency in a riser, since it only can applied under atmosphere and needs correction factor for calibration in each case with no generalized [103].

So far, fast/turbulent fluidized bed in a riser is widely accepted as carbonator for calcium looping in post-combustion CO_2 capture application [2], while bubbling fluidized bed is normally considered as the gasifier/carbonator for sufficient solid residence time and fuel/char conversion [8,104]. IFK and CSIC studied a fast and a turbulent fluidized regime in risers for calcium looping process, and suggested that gas-solid contact efficiency factor can reach approximately 100% in this regimes [4]. It is noteworthy that its minimum active space time is around 50 seconds, which indicates the solid molar flow or inventory in carbonator is still much larger than gas molar flow. Although excessive solid can enhance contact efficiency but also can cause heavy burden in downstream purged solid processing industries (e.g. cement plant).

Optimization of reactor internal structure is an alternative way to enhance solid-gas contact efficiency. Multi-stage or multi-regime fluidized bed was also broadly utilized to help improving the efficiency. For instance, IFK and SEU have utilized the multi-regime (variable inner diameter) riser to enhance the efficiency. Addition of internals in such reactors can further help enhancing the efficiency although it would increase mechanic wear and abrasion of bed materials, e.g. the bamboo-like riser in TU Wien [8]. More detailed hydrodynamic modelling works and improvement are desired for such reactors.

4.2 Real-time solid recirculation flux measurement in demonstration-scale

Solid recirculation flux is a significant factor in dual fluidized bed (DFB) system. Burkell et al. [105] have proposed eight ideal standards for solid recirculation flux measurement: 1) real-time; 2) accuracy; 3) no disturb on system; 4) high temperature resistance; 5) reliable; 6) flexible; 7) scalable; 8) no demarcation. So far, there is no measuring method meets all the standards. The handbook "principle, design and operation of circulated fluidized bed boiler" [106] summarized eight measuring methods while particle descent rate, pressure drop variation in the standpipe and radiative tracing particle are possible real-time no disturb measuring methods. Observation window is needed in particle descent rate method. The flow area in the standpipe and descent rate of particles should not be too large and fast, otherwise the error of measurement will be unacceptable. Pressure drop variation in the standpipe method depends on fluidization rate, solid flow rate and particle characteristics [107]. It has a limitation that each specific facility should be calibrated and measuring range is narrow. Radiative tracing particle method has advantages in measuring accuracy, no disturb and real-time, but cost-in-use performance and tracing particle scarcity impede its development in practical application.

Combination of above measuring methods is a promising way. For calcium looping process, the 200 kW_{th} pilot-scale system in IFK has deployed Electrical Capacitance Tomography (ECT) and Microwave Doppler Radar (MDR) for measuring solid recirculation flux [108]. ECT-MDR method is a potential method to meet the eight standards. More researches on solid recirculation flux measurement are desired in the future to help realizing accurate closed-loop control.

4.3 Solid-solid separation

Solid-solid separation is necessary to conduct in SEG and CaL-CLC process, primarily referring to sorbent and ash separation or sorbent and oxygen carrier (OC) separation. This need differs from the conventional circulating fluidized bed applications (e.g. FCC or FBC). In SEG gasifier, generated

char has porous structure to adsorb tar molecule during the gasification process. The metal component in ash/char has catalytic effects on the tar molecule conversion [109–111] or oxygen transport capacities to help partial oxidation in the gasifier [112]. Therefore, ash/char particles play a positive role in the gasifier, which prefer to longer residence time in the system rather than purging with deactivation sorbent. In CaL-CLC looping process, the binary calcium-based and copper-based particles have different cycling performance and regulation of particle ratio is preferred. Appropriate solid-solid separation technology can help system to get more operation flexibility. The separation principle generally bases on different particle characteristics. Fig.11 depicts three solid-solid separation methods based on different principles.
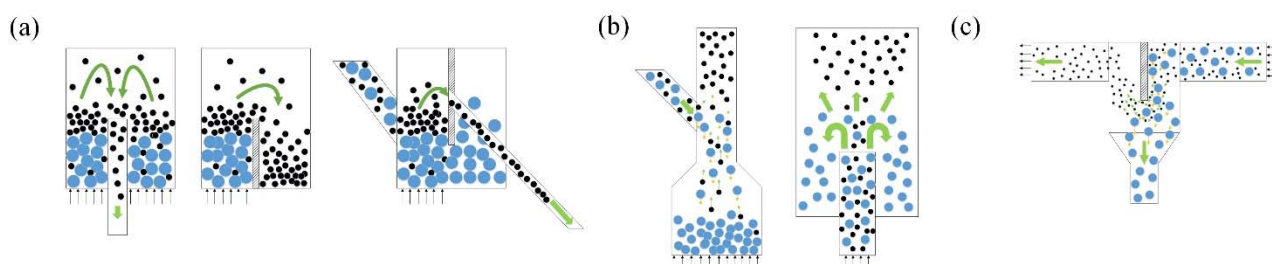
Figure 11 Solid-solid separation methods based on different principles: (a) float in bubbling fluidized bed; (b)

different terminal velocities; (c) inertia effects. Blue cycle: sorbent particles. Black cycle: Char/Ash particles.

Many researchers have found the flotsam and jetsam behavior in the bubbling fluidized bed. Commonly, the larger and lighter particles tend to float on the bed surface and smaller and heavy particles on the other hand tend to move downwards in the bed [16,113–115]. Fig.11 (a) illustrates three different routes to separate particles applying by bubbling fluidized bed. The draft pipe or baffle are set at appropriate bed height to collect particles which have flotsam behavior. In Fig.11 (b), Liu et al. [73] studied the binary particles separation in a compact fluidized bed. The difference between particle terminal velocities can help separation with different internal size pipes. Cheng et al. [66,116] utilized this principle and designed a annular (fountain-like) carbon stripper for CLC. Wang et al. [117,118] designed a solid-solid separator for separated gasification chemical looping combustion basing on inertia effects ,as shown in Fig.11 (c). All applications can be referenced for SEG or CaL-CLC process in the future. Furthermore, there is a challenge in calcium looping process that calcium-based sorbent particle size decreases with an increase of cycling numbers. The changes on sorbent particle size and morphology leads the variation of particle fluidization characteristics and failure in separator operation. Further development of novel separator to solve such problems is desired for calcium looping process.

4.4 Synergistic functions as carrier and catalyst

Regard of calcium looping in SEG process, calcium-based material not only can be used as sorbent, but also as catalyst. Because of this, the quantitative description of SEG process becomes more complicated. Li et al. [119] reviewed applications of calcium-based catalysts in biomass pyrolysis/ gasification. They elucidated the mechanism for quite satisfying adsorption performance of CaO, but also clarified the challenges and difficulties to describe and calculate the catalytic kinetics, which is rarely reported in evident.

As shown in Fig.9, "blue" indicates that CaO under operating conditions in this region only has catalytic effect, while CaO has synergistic effects under operating conditions in the "green" region.

Calcium-based sorbent as catalyst can enhance tar conversion and CO_2 production. Further, the balance point of CO_2 partial pressure would raise to "green" region (as shown in the sub-graph in Fig.9) and adsorption would lead the deactivation of catalytic effect on a part of CaO. A fluctuation of balance point would occur in the "green" region until all CaO sorbents convert to $CaCO_3$.
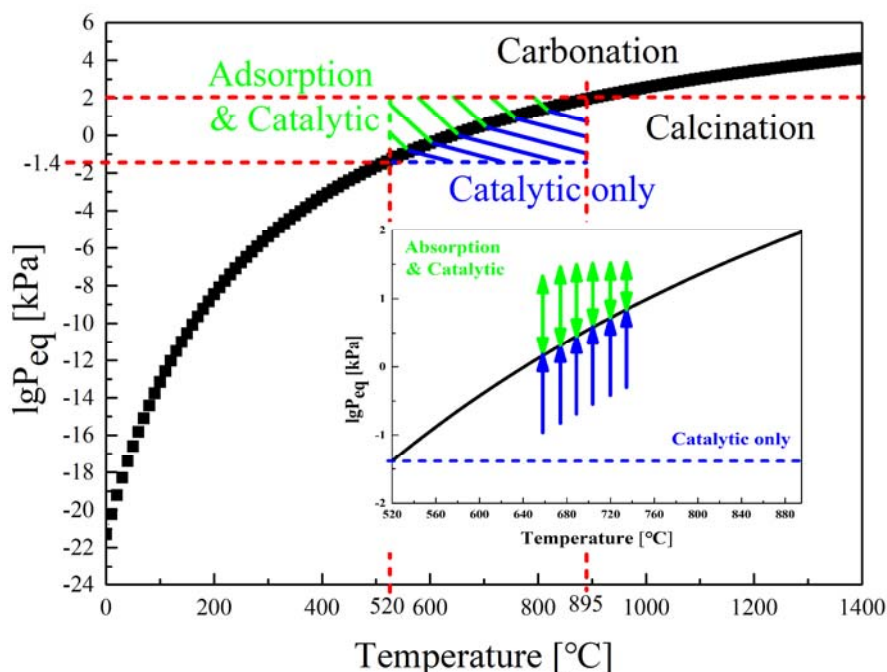
Figure 12 Schematic of synergistic effects on Baker's graph

Whether in biomass or organic solid waste pyrolysis/gasification process, calcium-based material is a good candidate as CO_2 and SO_2 sorbent, and tar cracking/reforming catalyst. It has a strong interest to further explore the synergistic functions of calcium-based material as such sorbent and catalyst.

5. Conclusions and perspective

The use of calcium-based sorbents to absorb CO_2 at high temperatures is critical in both pre-combustion and post-combustion capture to reduce global warming caused by growing CO_2 levels. This work concludes several promising calcium looping application routes and discusses several issues of particle system for further calcium looping technology commercial development. A closed-loop automatic control in calcium looping system is the ideal destination for its flexible adaptability to commercial market. Other issues and suggestions are as follow:

- According to thermodynamic and reaction rate characteristics, an increase of pressure and temperature at the same time takes advantages for calcium looping process.
- The performance decay of calcium-based sorbent is inevitable to date. For practical commercial application, utilization of calcium-based solid waste as fresh sorbent and consumption of purged deactivation sorbent in other industries (e.g. cement industry, etc.) are cost-effective and viable options.
- Researches on sorbent material indicate that nanoparticles has superior performance, but the use of powdered sorbents or nanoparticle aggregates is far away from the industrial applications where particles with well-defined pelletized external morphologies are necessary. Multiple-scale analysis is a possible way to in-depth understand the contradiction in a balance

manner.

- Dual fluidized bed (DFB) is applied based on calcium looping intrinsic fundamental, i.e. two steps. DFB generally consists of two coupled fluidized beds. Fast fluidized bed with internal solid circulating is widely accepted as carbonator and regenerator, while bubbling fluidized bed is benefit for SEG process.

- Gas-solid contact efficiency should be fully considered in pilot-scale facility while it still has no rigorous definition and so far only can be calculated from experiment data on specific reactor. Prediction of the efficiency in a designed reactor is impossible and more works are desired. The effect of active space time should be considered otherwise excessive solid will cause heavy burden in downstream purged solid processing industries.

- Synergistic functions of calcium-based material as CO_2/SO_2 carrier and catalyst are strongly interested in future in-depth researches. Meanwhile, internal structure design of reactor according to synergistic functions can help conversion of tar generated from municipal, agriculture and forestry solid waste in the future.

- Accurate online measurement of solid recirculation flux in DFB can help developing closed-loop automatic control and reducing long-term operation cost. Interestingly, the flow area of inlet and outlet of reactor should be different to offset the inequality when design the system.

- Development of a novel scaling law assisted by computational fluid dynamics is significant not only for reactor design, but also for flexibility under different scale application scenario.

- Solid-solid separation can improve the use ratio of bed material and ease the processing burden in the downstream. Appropriate solid-solid separation technology can help system to get more operation flexibility.

- The research experience here for the calcium looping process system (carbon carrier) may also be valid for other chemical looping systems (e.g. applied with oxygen/nitrogen/hydrogen carrier, etc.), especially using interconnected circulating fluidized beds.

Acknowledgment

References

[1] IPCC. The Intergovernmental Panel on Climate Change (IPCC) Special Report on Global Warming of 1.5°C. 2019

[2] Hanak DP, Anthony EJ, Manovic V. A review of developments in pilot-plant testing and modelling of calcium looping process for CO_2 capture from power generation systems [J]. Energy Environ Sci 2015;8:2199–249

[3] Yu FC, Phalak N, Sun Z, et al. Activation strategies for calcium-based sorbents for CO_2 capture: A perspective [J]. Ind Eng Chem Res 2012;51:2133–42

[4] Dieter H, Bidwe AR, Varela-duelli G, et al. Development of the calcium looping CO_2 capture technology from lab to pilot scale at IFK , University of Stuttgart [J]. Fuel 2014;127:23–37

[5] Salaudeen SA, Acharya B, Dutta A. CaO-based CO_2 sorbents: A review on screening,

enhancement, cyclic stability, regeneration and kinetics modelling [J]. J CO_2 Util 2018;23:179–99

[6] Hanak DP, Michalski S, Manovic V. From post-combustion carbon capture to sorption-enhanced hydrogen production: A state-of-the-art review of carbonate looping process feasibility [J]. Energy Convers Manag 2018;177:428–52

[7] Rogelj J, Shindell D, Jiang K, et al. Mitigation Pathways Compatible with 1.5°C in the Context of Sustainable Development. In: Global Warming of 1.5°C. An IPCC Special Report on the impacts of global warming of 1.5°C above pre-industrial levels and related global greenhouse gas emission pathw. 2018

[8] Fuchs J, Müller S, Schmid JC, et al. A kinetic model of carbonation and calcination of limestone for sorption enhanced reforming of biomass [J]. Int J Greenh Gas Control 2019;90:102787

[9] Aghaalikhani A, Schmid JC, Borello D, et al. Detailed modelling of biomass steam gasification in a dual fluidized bed gasifier with temperature variation [J]. Renew Energy 2019;143:703–18

[10] Priscak J, Fürsatz K, Kuba M, et al. Investigation of the formation of coherent ash residues during fluidized bed gasification of wheat straw lignin [J]. Energies 2020;13

[11] Soukup G, Pfeifer C, Kreuzeder A, et al. In situ CO_2 capture in a dual fluidized bed biomass steam gasifier - Bed material and fuel variation [J]. Chem Eng Technol 2009;32:348–54

[12] Schmid JC, Pfeifer C, Kitzler H, et al. A new dual fluidized bed gasifier design for improved in situ conversion of hydrocarbons. Int. Conf. Polygeneration Strateg., 2011

[13] Mauerhofer AM, Fuchs J, Müller S, et al. CO_2 gasification in a dual fluidized bed reactor system: Impact on the product gas composition [J]. Fuel 2019;253:1605–16

[14] Stollhof M, Penthor S, Mayer K, et al. Influence of the loop seal fluidization on the operation of a fluidized bed reactor system [J]. Powder Technol 2019;352:422–35

[15] Koppatz S, Pfeifer C, Rauch R, et al. . H_2 rich product gas by steam gasification of biomass with in situ CO_2 absorption in a dual fluidized bed system of 8 MW fuel input [J]. Fuel Process Technol 2009;90:914–21

[16] Kraft S, Kuba M, Hofbauer H. The behavior of biomass and char particles in a dual fluidized bed gasification system [J]. Powder Technol 2018; 338: 887–97.

[17] Lu DY, Hughes RW, Anthony EJ. Ca-based sorbent looping combustion for CO_2 capture in pilot-scale dual fluidized beds [J]. Fuel Process Technol 2008; 89: 1386–95.

[18] Udomsirichakorn J, Basu P, Abdul Salam P, et al. CaO-based chemical looping gasification of biomass for hydrogen-enriched gas production with in situ CO_2 capture and tar reduction [J]. Fuel Process Technol 2014; 127: 7–12.

[19] Long H. Mechanism and Experimental Study on Hydrogen Production from Biomass without Oxygen Using CaO as Absorber. [D] 2011.

[20] Nai R. Experiments on the key processes of coal chemical looping gasification based on CaO sorbent. [D] 2015.

[21] Fang F, Li Z shan, Cai N sheng. Continuous CO_2 Capture from Flue Gases Using a Dual Fluidized Bed Reactor with Calcium-Based Sorbent [J]. Ind Eng Chem Res 2009; 48: 11140–11147.

[22] Armbrust N, Duelli G, Dieter H, et al. Calcium looping cycle for hydrogen production from biomass gasification syngas: Experimental investigation at a 20 kW_{th} dual fluidized-bed facility [J]. Ind Eng Chem Res 2015; 54: 5624–34.

[23] Ströhle J, Junk M, Kremer J, et al. Carbonate looping experiments in a 1 MW_{th} pilot plant and model validation [J]. Fuel 2014; 127: 13–22.

[24] Haaf M, Hilz J, Peters J, et al. Operation of a 1 MW_{th} calcium looping pilot plant firing waste-derived fuels in the calciner [J]. Powder Technol 2020; 372: 267–74.

[25] Daikeler A, Ströhle J, Epple B. Experimental flow structure analysis in a 1 MW_{th} circulating fluidized bed pilot plant [J]. Chem Eng Sci 2019; 195: 921–34.

[26] Hilz J, Helbig M, Haaf M, et al. Investigation of the fuel influence on the carbonate looping process in 1 MW_{th} scale [J]. Fuel Process Technol 2018; 169: 170–7.

[27] Ströhle J, Hilz J, Epple B. Performance of the carbonator and calciner during long-term carbonate looping tests in a 1 MW_{th} pilot plant [J]. J Environ Chem Eng 2020; 8: 103578.

[28] Hilz J, Helbig M, Haaf M, et al. Long-term pilot testing of the carbonate looping process in 1 MW_{th} scale [J]. Fuel 2017; 210: 892–9.

[29] Kremer J, Galloy A, Ströhle J, et al. Continuous CO_2 Capture in a 1MW_{th} Carbonate Looping

Pilot Plant [J]. Chem Eng Technol 2013; 36: 1518–24.

[30] Hilz J, Haaf M, Helbig M, et al. Scale-up of the carbonate looping process to a 20 MW$_{th}$ pilot plant based on long-term pilot tests [J]. Int J Greenh Gas Control 2019; 88: 332–41.

[31] Haaf M, Hilz J, Helbig M, et al. Assessment of the operability of a 20 MW$_{th}$ calcium looping demonstration plant by advanced process modelling [J]. Int J Greenh Gas Control 2018; 75: 224–34.

[32] Alonso M, Rodríguez N, González B, et al. Carbon dioxide capture from combustion flue gases with a calcium oxide chemical loop. Experimental results and process development [J]. Int J Greenh Gas Control 2010; 4: 167–73.

[33] Rodrı́guez N, Alonso M, Abanades JC. Experimental Investigation of a Circulating Fluidized-Bed Reactor to Capture CO_2 with CaO [J]. AIChE J 2011; 57: 1356–66.

[34] Diego ME, Alonso M. Operational feasibility of biomass combustion with in situ CO_2 capture by CaO during 360 h in a 300 kW$_{th}$ calcium looping facility [J]. Fuel 2016; 181: 325–9.

[35] Diego ME, Arias B, Méndez A, et al. Experimental testing of a sorbent reactivation process in La Pereda 1.7 MW$_{th}$ calcium looping pilot plant [J]. Int J Greenh Gas Control 2016; 50: 14–22.

[36] Chang MH, Huang CM, Liu WH, et al. Design and Experimental Investigation of Calcium Looping Process for 3-kW$_{th}$ and 1.9-MW$_{th}$ Facilities [J]. Chem Eng Technol 2013; 36: 1525–32.

[37] Breault R. Handbook of Chemical Looping Technology. 2018

[38] Chang MH, Chen WCW, Huang CM, et al. Design and Experimental Testing of a 1.9MW$_{th}$ Calcium Looping Pilot Plant [J]. Energy Procedia 2014; 63: 2100–8.

[39] Wang W, Ramkumar S, Li S, et al. Subpilot demonstration of the carbonation-Calcination reaction (CCR) process: High-temperature CO_2 and sulfur capture from coal-fired power plants [J]. Ind Eng Chem Res 2010; 49: 5094–101.

[40] ISO. ISO 3166-1 alpha-3 codes [S].

[41] Minx JC, Lamb WF, Callaghan MW, et al. Negative emissions - Part 1: Research landscape and synthesis [J]. Environ Res Lett 2018; 13

[42] Mendiara T, García-Labiano F, Abad A, et al. Negative CO_2 emissions through the use of biofuels in chemical looping technology: A review [J]. Appl Energy 2018; 232: 657–84.

[43] Zhao X, Zhou H, Sikarwar VS, et al. Biomass-based chemical looping technologies: The good, the bad and the future [J]. Energy Environ Sci 2017; 10: 1885–910.

[44] Abanades JC, Murillo R, Fernandez JR, et al. New CO_2 capture process for hydrogen production combining Ca and Cu chemical loops [J]. Environ Sci Technol 2010; 44: 6901–4.

[45] Chacartegui R, Alovisio A, Ortiz C, et al. Thermochemical energy storage of concentrated solar power by integration of the calcium looping process and a CO_2 power cycle [J]. Appl Energy 2016; 173: 589–605.

[46] Ortiz C, Valverde JM, Chacartegui R, et al. The Calcium-Looping ($CaCO_3$/CaO) process for thermochemical energy storage in Concentrating Solar Power plants [J]. Renew Sustain Energy Rev 2019; 113: 109252.

[47] Tregambi C, Troiano M, Montagnaro F, et al. Fluidized Beds for Concentrated Solar Thermal Technologies—A Review [J]. Front Energy Res 2021; 9: 1–26.

[48] Gómez-Barea A, Suárez-Almeida M, Ghoniem A. Analysis of fluidized bed gasification of biomass assisted by solar-heated particles [J]. Biomass Convers Biorefinery 2021; 11: 143–58.

[49] Almendros-Ibáñez JA, Fernández-Torrijos M, Díaz-Heras M, et al. A review of solar thermal energy storage in beds of particles: Packed and fluidized beds [J]. Sol Energy 2019; 192: 193–237.

[50] Rodríguez N, Alonso M, Abanades JC. Average activity of CaO particles in a calcium looping system [J]. Chem Eng J 2010; 156: 388–94.

[51] Chen J, Duan L, Sun Z. Review on the Development of Sorbents for Calcium Looping [J]. Energy and Fuels 2020; 34: 7806–36.

[52] Dean CC, Blamey J, Florin NH, et al. The calcium looping cycle for CO_2 capture from power generation, cement manufacture and hydrogen production [J]. Chem Eng Res Des 2011; 89: 836–55.

[53] Perejón A, Romeo LM, Lara Y, et al. The Calcium-Looping technology for CO_2 capture : On the important roles of energy integration and sorbent behavior [J] 2016; 162: 787–807.

[54] Raganati F, Ammendola P. Sound-assisted fluidization for temperature swing adsorption and

calcium looping: A review [J]. Materials (Basel) 2021; 14: 1–24.

[55] Hornberger M, Moreno J, Schmid M, et al. Experimental investigation of the calcination reactor in a tail-end calcium looping configuration for CO_2 capture from cement plants [J]. Fuel 2021; 284.

[56] Salaudeen SA, Acharya B, Heidari M, et al. . Hydrogen-rich gas stream from steam gasification of biomass: Eggshell as a CO_2 sorbent [J]. Energy and Fuels 2020; 34: 4828–36.

[57] Salaudeen SA, Tasnim SH, Heidari M, et al. Eggshell as a potential CO_2 sorbent in the calcium looping gasification of biomass [J]. Waste Manag 2018; 80: 274–84.

[58] Grimes CJ, Hardcastle T, Manga MS, et al. Calcium Carbonate Particle Formation through Precipitation in a Stagnant Bubble and a Bubble Column Reactor [J]. Cryst Growth Des 2020; 20: 5572–82.

[59] Baker EH. . The Calcium Oxide-Carbon Dioxide System in the Pressure Range 1-300 Atmospheres [J]. J Chem Soc 1962: 464–70.

[60] Fennell P, Anthony B. Calcium and Chemical Looping Technology for Power Generation and Carbon Dioxide (CO_2) Capture. 2015.

[61] Yin J, Qin C, Feng B, et al. Calcium Looping for CO_2 Capture at a Constant High Temperature [J] 2014.

[62] Arrhenius equation. [W] 1997.

[63] Modified Arrhenius equation. [W] 1997.

[64] Ii P, Fan L. Principles of Gas-Solid Flows. 1998

[65] Turrado S, Arias B, Fernández JR, et al. Carbonation of Fine CaO Particles in a Drop Tube Reactor [J]. Ind Eng Chem Res 2018; 57: 13372–80.

[66] Cheng M, Li Y, Li Z, et al. An integrated fuel reactor coupled with an annular carbon stripper for coal-fired chemical looping combustion [J]. Powder Technol 2017; 320: 519–29.

[67] Fraser S, Basu P. Circulating Fluidized Bed Technology. 1991.

[68] Grace JR. Contacting modes and behaviour classification of gas—solid and other two‐phase suspensions [J]. Can J Chem Eng 1986; 64: 353–63.

[69] Grace JR, Issangya AS, Bai D, et al. Situating the high-density circulating fluidized bed [J]. AIChE J 1999;45:2108–16

[70] Musun G. Handbook of fluidization. [B] 2008

[71] Wenguo X. Experimental Study on Coal Gasification Oxygen-carrying Combustion Combined Cycle System and Oxygen-carrying Combustion. [D] 2009.

[72] Chen S, Wang D, Xue Z, et al. Calcium looping gasification for high-concentration hydrogen production with CO2 capture in a novel compact fluidized bed: Simulation and operation requirements [J]. Int J Hydrogen Energy 2011;36:4887–99

[73] Liu Y, Sun Z, Toan S, et al. Investigations on fluid dynamics of binary particles in a dual fluidized bed reactor system for enhanced calcium looping gasification process [J]. Powder Technol 2020; 361: 803–11.

[74] Liu Y, Chen S, Zhu M, et al. Investigation of a dual cold-flow fluidized bed for calcium looping gasification process [J]. Powder Technol 2019; 353: 10–9.

[75] Charitos A, Rodríguez N, Hawthorne C, et al. Experimental validation of the calcium looping CO_2 capture process with two circulating fluidized bed carbonator reactors [J]. Ind Eng Chem Res 2011; 50: 9685–95.

[76] Rodriguez N, Alonso M, Abanades JC, et al. Comparison of experimental results from three dual fluidized bed test facilities capturing CO_2 with CaO [J]. Energy Procedia 2011; 4: 393–401.

[77] Abanades JC. . The maximum capture efficiency of CO_2 using a carbonation/calcination cycle of CaO/$CaCO_3$ [J]. Chem Eng J 2002; 90: 303–6.

[78] Abanades JC, Rubin ES, Anthony EJ. Sorbent Cost and Performance in CO_2 Capture Systems [J]. Ind Eng Chem Res 2004: 3462–6.

[79] Zhen-shan L, Ning-sheng C, Croiset E. Process Analysis of CO_2 Capture from Flue Gas Using Carbonation/Calcination Cycles [J]. AIChE J 2008; 54.

[80] Grasa GS, Abanades JC, Alonsob M, et al. . Reactivity of highly cycled particles of CaO in a carbonation/calcination loop [J]. Chem Eng J 2008; 137: 561–7.

[81] Rodriguez N, Alonso M, Grasa G, et al. . Heat requirements in a calciner of $CaCO_3$ integrated in a CO_2 capture system using CaO [J]. Chem Eng J 2008; 138: 148–54.

[82] Romeo LM, Abanades JC, Escosa JM, et al. . Oxyfuel carbonation/calcination cycle for low cost

CO$_2$ capture in existing power plants [J]. Energy Convers Manag 2008; 49: 2809–14.

[83] Weimer T, Berger R, Hawthorne C, et al. Lime enhanced gasification of solid fuels: Examination of a process for simultaneous hydrogen production and CO$_2$ capture [J]. Fuel 2008; 87: 1678–86.

[84] Li J, Zhang J, Ge W, et al. Multi-scale methodology for complex systems [J]. Chem Eng Sci 2004; 59: 1687–700.

[85] Geldart D. Types of Gas Fhidization [J]. Powder Technol 1973; 7: 285–92.

[86] Glicksman LR. Scaling relationships for fluidized beds [J]. Chem Eng Sci 1984; 39: 1373–9.

[87] Glicksman LR, Hyre MR, Farrell PA. Dynamic similarity in fluidization [J]. Int J Multiph Flow 1994; 20: 331–86.

[88] Masayuki H, Hiroyuki I, Yo K, et al. A Scaling law for cirulating fuidized beds [J]. J Chem Engnerring Japan 1989; 22: 587–92.

[89] Horio M, Nonaka A, Sawa Y, et al. A new similarity rule for fluidized bed scale‐up [J]. AIChE J 1986; 32: 1466–82.

[90] Taofeeq H, Al-Dahhan M. Comparison between the new mechanistic and the chaos scale-up methods for gas-solid fluidized beds [J]. Chinese J Chem Eng 2018; 26: 1401–11.

[91] Schouten JC, Vander Stappen MLM, Van Den Bleek CM, et al. Scale-up of chaotic fluidized bed hydrodynamics [J]. Chem Eng Sci 1996; 51: 1991–2000.

[92] Bleek CM, Schouten JC. Deterministic chaos: a new tool in fluidized bed design and operation [J]. Chem Eng J 1993; 53: 75–87.

[93] Bleek CM, Schouten JC.. Can deterministic chaos create order in fluidized-bed scale-up [J]. Chem Eng Sci 1993; 48: 2367–73.

[94] Li C, Teng X, Peng H, et al. Novel scale-up strategy based on three-dimensional shear space for animal cell culture [J]. Chem Eng Sci 2020;212:115329.

[95] Ramkumar S, Iyer M V., Fan LS. Calcium looping process for enhanced catalytic hydrogen production with integrated carbon dioxide and sulfur capture [J]. Ind Eng Chem Res 2011;50:1716–29.

[96] Wang C, Zhu J. Developments in the understanding of gas–solid contact efficiency in the circulating fluidized bed riser reactor: A review [J]. Chinese J Chem Eng 2016; 24: 53–62.

[97] Qiang G. Gas-solids flow behavior and contact efficiency in a high-density conveying fluidized bed. [D] 2014.

[98] Geng Q, Zhu X, Liu YY, et al. . Gas-solid flow behavior and contact efficiency in a circulating-turbulent fluidized bed [J]. Powder Technol 2013; 245: 134–45.

[99] Dry RJ, Christensen IN, White CC. Gas-solids contact efficiency in a high-velocity fluidised bed [J]. Powder Technol 1987; 52: 243–50.

[100] SU L, Liu B, Zhang M, et al. Analysis of research methods on gas-solid contacting efficiency in circulating fluidized bed reactor [J]. Petrochemical Technol & Appl 2017; 35: 492–6.

[101] Valverde JM, Pontiga F, Soria-Hoyo C, et al. Improving the gas-solids contact efficiency in a fluidized bed of CO$_2$ adsorbent fine particles [J]. Phys Chem Chem Phys 2011; 13: 14906–9.

[102] Zhou S, Qiao C, Yang H, et al. Gas solid contact efficiency of pyridine synthesis reactors [J]. Can J Chem Eng 2020: 1–10.

[103] Bolland O, Nicolai R. . Describing mass transfer in circulating fluidized beds by ozone decomposition transfer in circulating fluidized beds by ozone decomposition [J]. Chem Eng Commun 2001; 187: 1–21.

[104] Fuchs J, Schmid JC, Müller S, et al. Dual fluidized bed gasification of biomass with selective carbon dioxide removal and limestone as bed material: A review [J]. Renew Sustain Energy Rev 2019; 107: 212–31.

[105] Burkell JJ, Grace JR, Zhao J, et al. Measurement of Solids Circulation Rates in Circulating Fluidized Beds. Pergamon Press plc; 1988.

[106] Kefa C. Theoretical Design and Operation of Circulating Fluidized Bed Boilers. [B] 1998.

[107] Monazam ER, Panday R, Shadle LJ. Estimate of solid flow rate from pressure measurement in circulating fluidized bed [J]. Powder Technol 2010; 203: 91–7.

[108] Dieter H, Hawthorne C, Zieba M, et al. . Progress in Calcium Looping post combustion CO$_2$ Capture: Successful pilot scale demonstration [J]. Energy Procedia 2013; 37: 48–56.

[109] Chen YH, Schmid M, Chang CC, et al. Lab-scale investigation of palm shell char as tar reforming catalyst [J]. Catalysts 2020; 10.

[110] Chen YH, Schmid M, Kertthong T, et al. Reforming of toluene as a tar model compound over straw char containing fly ash [J]. Biomass and Bioenergy 2020; 141: 105657.

[111] Chen Y, Parvez AM, Schmid M, et al. Reforming of tar model compounds over sustainable and low-cost biochar: Special focus on spontaneous gasification reactivity and tar reforming kinetics for reformer design [J]. Chem Eng J 2021; 408: 127350.

[112] Schweitzer D, Nagel F, Schmid M, et al. Biomass Ash as Oxygen Carrier in Fluidized Bed Processes. 4th Int. Conf. Chem. Looping, 2016, p. 1–17.

[113] Kraft S, Kirnbauer F, Hofbauer H. Investigations using a cold flow model of char mixing in the gasification reactor of a dual fluidized bed gasification plant [J]. Powder Technol 2017; 316: 687–96.

[114] Rowe PN, Nienow AW, Solids P. Particle mixing and segregation in gas fluidised beds. A review [J]. Powder Technol 1976;15:141–7.

[115] Zhang Y, Jin B, Zhong W. Experimental investigation on mixing and segregation behavior of biomass particle in fluidized bed [J]. Chem Eng Process Process Intensif 2009; 48: 745–54.

[116] Cheng M, Sun H, Li Z, et al. Annular Carbon Stripper for Chemical-Looping Combustion of Coal. 4th Int. Conf. Chem. Looping, 2016.

[117] Wang X, Wang X, Shao Y, et al. Coal-fueled separated gasification chemical looping combustion under auto-thermal condition in a two-stage reactor system [J]. Chem Eng J 2020; 390: 124641.

[118] Wang XX, Wang XX, Kong Z, et al. Auto-thermal operation and optimization of coal-fueled separated gasification chemical looping combustion in a pilot-scale unit [J]. Chem Eng J 2020; 383: 123159.

[119] Li H, Wang Y, Zhou N, et al. Applications of calcium oxide–based catalysts in biomass pyrolysis/gasification – A review [J]. J Clean Prod 2021; 291: 125826.

ADDRESSING THERMAL INERTIA AND INCREASING LOAD-BEARING CAPACITY IN CFB BOILERS THROUGH NOVEL ANTI-WEAR DEVICE IMPLEMENTATION

Xiannan Hu[1], Tong Wang[1], Haowen Wu[1], Hairui Yang*, Xin Liu[2], Qiuyu Tang[2]

[1]Key Laboratory of Thermal Science and Power Engineering of Ministry of Education, State Key Laboratory of Power Systems, Department of Energy and Power Engineering, Tsinghua University, Beijing 100084, China
[2] Taiyuan JETLINE Electric Power Technology Co., Taiyuan 030024, China

*Email: *yhr@mail.tsinghua.edu.cn*

Abstract

Improving the flexibility of coal-fired plants in China is becoming increasingly urgent. CFB boiler plants exhibit low load change rates due to the thermal inertia from significant heat accumulation in the refractory material. Although various measures to retrofit the refractory have been implemented, their current effectiveness is limited. For the first time, a new approach involving a honeycomb compound anti-wear device to replace the refractory was implemented in the dense region of a 440 t/h industrial CFB boiler. After two operational retrofits, this technique proved effective in addressing heat release issues from the heating surface and reduced the bed temperature by approximately 50℃. Additionally, the temperature distribution within the furnace became more uniform, with an average difference of 52℃ between the bed and furnace outlet temperatures at nearly full load. Dynamic results of load changes indicated a decrease in the boiler's thermal inertia, thereby accelerating the load change rate. The boiler's equivalent rated evaporation capacity increased by 7.3%, with its maximum output reaching 450t/h. The boiler's load-bearing capacity has seen significant improvement. This provides a valuable reference for enhancing the flexibility of CFB units.

1. Introduction

Circulating Fluidized Bed (CFB) boiler plants are one of the most important ways of clean and efficient utilization of low-quality coal in China due to their good coal adaptability and low-cost pollutant control (Yue et al., 2017). The expanding scale of renewable energy sources has challenged the flexibility of the power grid recently (Heptonstall and Gross, 2021), but the ability of most CFB units to consume new energy is not satisfactory (Zhang et al., 2023). As hundred tons of materials continue to circulate in the furnace, a fixed thickness of refractory material is laid on the heating surface to prevent abrasion (Hu et al., 2023a), and the thermal inertia formed by the accumulation of heat in the refractory during load changes leads to low boiler's ramp (Hu et al., 2024), which is the main reason for limiting the peak shaving of CFB units.

There are many industrial experiments for the refractory retrofits (Chen et al., 2022), and the efficient techniques mainly include two: using high thermal conductivity wear-resistant materials or replacing refractory by metal grilles. Li (Li et al., 2009) calculated a CFB boiler at full load conditions and found that the thermal inertia of the refractory was an order of magnitude greater than that of bed material. Dong (Dong et al., 2023) simulated the variable load process of using high thermal conductivity wear-resistant materials in the whole loop, and the boiler's ramp was increased by about 10%. Sun (Sun et al., 2023) studied the thermal inertia of a 300 MW CFB boiler, and the thermal inertia was reduced by about 30% on average after the addition of both metal grilles in the furnace and high thermal conductivity wear-resistant materials in the dense region.

Even though the application of high thermal conductivity materials can increase the boiler's ramp, the benefit is not remarkable. This is because the gas-solid two-phase flow inertia is the dominant mechanism (Hu et al., 2023b), instead of heat transfer inertia. The metal grilles

enhance the heat transfer coefficient of the water wall and, more importantly, also improve the attached-wall downward moving solids flow behavior, which results in reducing thermal inertia significantly. Thus, the boiler's ramp can be further improved by modifying the zone in the furnace where the refractory is laid with anti-wear metal grilles.

In this work, a 135 MW CFB boiler at Shuangxin Power Plant in Ordos, Inner Mongolia, China, was selected. A honeycomb structure compound anti-wear device was used to replace the refractory in the dense region, which was the first attempt in the industry. The effects before and after its retrofits were compared, and changes in load capacity and bed temperature, etc. were discussed. On this basis, some suggestions to improve the thermal inertia are proposed to provide references for practical operation.

2. Experimental Boiler

Experiments were conducted in a 135 MW super-high pressure CFB boiler designed by Jinan Boiler Company. The furnace is 35.5 m tall, with a cross sectional area of 7.36 m x 15.2 m, the bottom is laid with refractory material and the outlet is connected to two identical cyclones. The water wall tube has an outer diameter of 60 mm, an inner diameter of 46 mm, and a finned tube thickness of 7 mm. A plate superheater and a plate reheater are also arranged in the furnace. The design operation parameters were listed in Table 1.

Table 1. Design parameters of the 135 MW CFB boiler

Item	Unit	Value	Item	Unit	Value
Main steam flow rate	t/h	440	Exhaust gas temperature	℃	140
Main steam pressure	MPa	13.74	Boiler efficiency	%	89
Main steam temperature	℃	540	Reheat steam temperature	℃	318
Reheated steam flow rate	t/h	353	Reheat steam pressure	MPa	2.65
Reheated steam pressure	MPa	2.45	Hot air temperature	℃	200
Reheated steam temperature	℃	540	Feed water temperature	℃	248
Drum pressure	MPa	15.15	Primary air ratio	-	0.6

The main material of the refractory at the bottom of the furnace is silicon carbide wear-resistant coroplast, which has an average thickness of about 100 mm due to the wear-resistant demand in the dense region. This material is reported to have a thermal conductivity (at 900 °C) of approximately 2.5 W/(m·°C), which is negative for heat transfer process.

3. Results and discussion

3.1 Use of the Honeycomb Anti-wear Device

The boiler is regularly operated at high load, and the most obvious problem is tha the bed temperature is too high, resulting in insufficient load capacity. The average bed temperature of the boiler reached nearly 1,000°C, with the maximum value exceeding 1,030°C. The boiler's bed temperature is also very high. Therefore, the researchers used a honeycomb structure compound anti-wear device to replace partial refractory in the dense region. This new technique is inspired by the structure of honeycomb and spacecraft heat sinks, and adopts the "6+1" positive hexagon as the base shape, shown in Fig.1(a).

| (a) | (b) |

Fig.1 The honeycomb compound anti-wear device in the furnace

The retrofit solution was implemented in 2 times in the following locations: (a) 800 mm down from the upper edge of the dense region as the baseline, the removal of the 1300 mm height of the refractory in the rear wall, in which the arrangement of the device height of 1100 mm, the length of the removal of 15 meters, a total of five rows, the release of the heated area of about 17 square meters (the projected area). With 200 mm remaining, an anti- wear beam was constructed with the refractory along the upper edge in this area. (b) The modified area in the front wall was 14 m × 1.25 m, the specific implementation was similar to solution a. The two sides wall corresponded to each other with the area of 6.3 m × 2 m. The total release of the heated surface was 42.7 square meters (projected area), the scene after retrofit as shown in Fig.1(b).

3.2 Steady State Analysis

The steady state data of the boiler before the retrofit, after the first retrofit, and after the second retrofit were selected for comparison. The temperatures in the furnace, including the dense region and the outlet, were adopted from the data recorded in the distributed control system (DCS). The comparison of the CFB boiler stabilized at 92% load (about 125 MW) was shown in Fig.2(a). It is obvious that bed temperature decreased significantly after both retrofit, with the original average bed temperature of about 1000 °C, then decreased by about 50 °C, and the maximum value decreased by nearly 60 °C. For the whole hydrodynamic loop, the heat absorption is reflected the temperature change in the furnace side exactly.

Visible from the vertical axis of the Fig.2(a), due to the low heat transfer coefficient in the bottom, which mainly caused by the low thermal conductivity of the refractory, the heat generated by combustion in the furnace could not be removed by working fluid in time. Thus, the mismatch between the supply and demand of energy led to elevation of bed temperature. While in the dilute region, due to the lack of inert energy transfer properties of the refractory, the working fluid instantly absorbed large heat, the temperature drop in the flue gas increased significantly. This phenomenon was evident that, with the completion of both retrofit, the temperature distribution along height is more homogeneous, and the difference between bed temperature and furnace outlet temperature was 52℃ on average, the maximum deviation was only 63℃. The result was satisfactory when the boiler was close to full load.

(a) At 92% load   (b) At 74% load
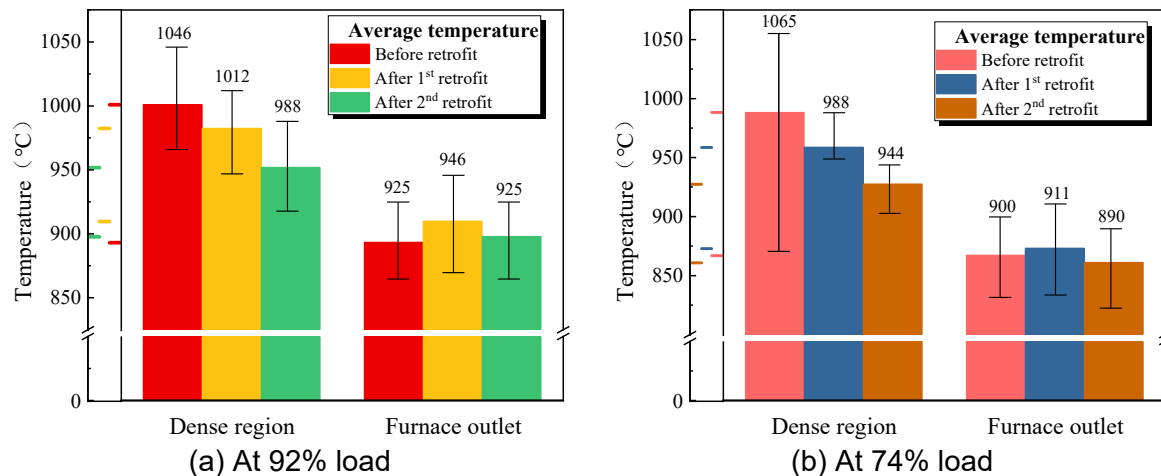
Fig.2 Comparison of furnace temperature before and after retrofit at partial load

We also selected the results at 74% boiler load, approximately 100 MW, shown in Fig.2(b). The comparison of the effect before and after retrofit was similar to that at the unit's 125 MW output, where the average bed temperature decreased by 61°C, while the maximum bed temperature decreased by 121°C. This is because of the increased combustion instability and non-uniformity in the furnace under partial load, and the instability of gas-solid flow led to ununiform distribution of temperature in the furnace, and the same uneven heat absorption on the water side. The difference between the lowest and highest temperature at the bottom was nearly 200°C. After using nearly 60 square meters of honeycomb structure compound anti-wear device instead of refractory, it is obvious that not only the bed temperature is reduced, but also the uniformity of bed temperature is improved. This is the combined result of the

increased heat transfer coefficient in the dense phase zone and the increased primary and secondary air temperatures (compared to the same load).

3.3 Transient Operation Analysis

In three distinct periods, we selected the unit's load variation conditions, including both load increase and decrease. As illustrated in Fig.3, the difference between the average bed temperature and the furnace outlet temperature as load changes is listed. Generally, this temperature difference is inversely proportional to the load variation. For instance, as shown in Fig.3(a), after a rapid drop in load, the substantial thermal inertia of bed materials accumulated at the bottom of the furnace causes the temperature to change slowly. Meanwhile, due to the low concentration of materials in the dilute phase zone and the combined heat absorption by the platen superheater, reheater, and water walls, the furnace exit temperature responds promptly to the load decrease, thereby increasing the temperature difference.

(a) Before retrofit

(b) First retrofit

(c) Second retrofit
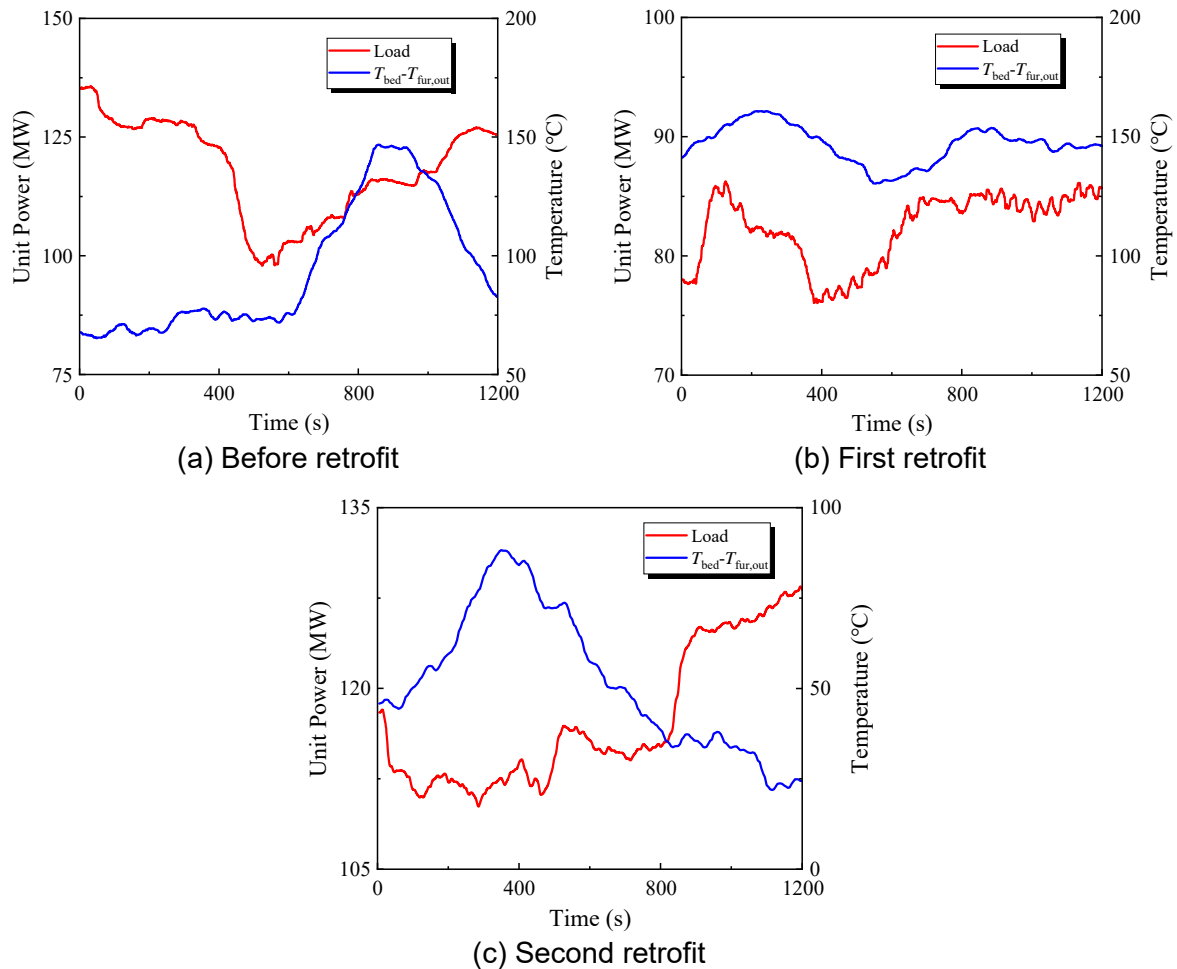
Fig.3 Variable load characteristics of furnace temperature at different periods

However, the mechanism of this physical process does not appear to be consistent in Fig.3 (b), as the boiler is operating at partial load (about 50% ECR). The uneven temperature distribution along the furnace height and the large deviation (120℃ on average) lead to a trend that coincides with the load variation. It is evident that the operational effectiveness, indicated by the uniformity of furnace temperature, improves after each retrofit. In Fig.3(c), as the boiler approaches full load conditions, the difference between bed temperature and furnace outlet temperature has decreased to as low as 50°C. More intriguingly, the thermal inertia of the boiler has also decreased. In Fig.3 (a), there is approximately a 360s spatial-temporal overlap between the "peaks" of temperature difference and the "valleys" of load variation. After two retrofits, the time interval between "peaks" and "valleys" is reduced to about 300 seconds, as

seen in Fig.3(c). Furthermore, the maximum load change rate of the unit has also increased, as evidenced by the steepness of the load variation curve in Fig.3.

The outcomes of the retrofits are reflected in the reduction of bed temperature on the furnace side. On the working fluid side, as this boiler operates as a natural circulation boiler, the pressure of the steam drum, along with the main steam valves, is strictly controlled during actual operation. Additionally, with the presence of spray water desuperheaters, the temperature variation of the working fluid within each heating surface is not significant. Instead, it is the evaporative capacity/main steam flow rate that reflects the effectiveness of the retrofits. Here, this work introduces the equivalent rated boiler evaporation under load changes, as represented by the following equation:

$$\tilde{D}_b = \frac{D_s}{P_e} \times 135MW$$

(1)

Its physical meaning corresponds to the boiler's load-bearing capacity under any conditions (during load change periods). Converting the main steam flow rate under the three aforementioned load change periods into equivalent load-bearing capacities yields the results shown in Fig.4. This boiler has a relatively high operating lifespan and is influenced by coal prices. In practice, the boiler often burns low-priced and low-calorific-value coal, leading to significant differences from the design coal. This results in an inability to meet the design values for feed coal PSD, reduced effective circulating ash content, and inability to exchange heat in the dense region.
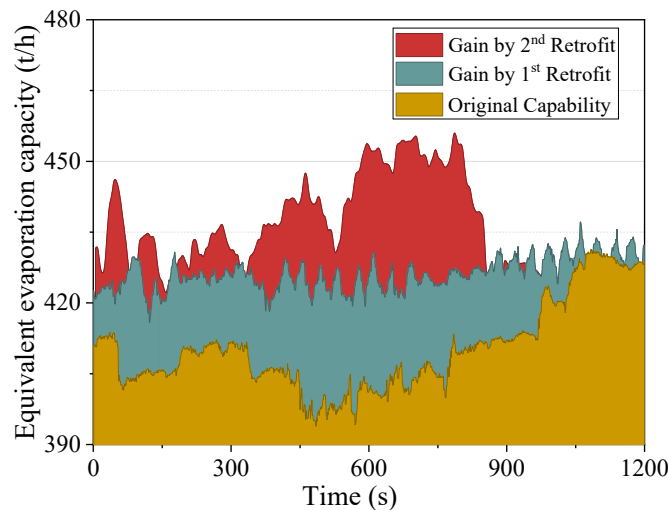
Fig.4 Equivalent boiler evaporation during load changes

Prior to the retrofits, the boiler's output was maintained at around 405 t/h. However, the output gradually increased after the retrofits because during load reduction, the boiler utilized stored energy, including the thermal inertia of the refractory. After the first retrofit, the heat absorption capacity of the water walls was enhanced. The average equivalent output was around 426.1 t/h, an increase of 5.2% compared to before the retrofit (as indicated in the green area of Fig.4), but it still did not reach the boiler's design value. With the second retrofit, the area of the heating surfaces increased, the heat transfer coefficient increased, and the cooling capacity of working fluid improved. This provided additional driving force for natural circulation, allowing more water to be evaporated into the superheating system. As shown in the red area of Fig.5, the average equivalent evaporation was 434.4 t/h after the retrofit, an increase of 7.3% compared to before the retrofit. The short-term maximum output can reach 450 t/h, and the thermal inertia is also reduced.

4. Conclusion

Industrial CFB boilers operating at low parameters and with long service lifespans often face common issues such as high bed temperature and poor load-bearing capacity. This work

introduces a solution: a honeycomb structure composite anti-wear device in the dense phase zone as a substitute for refractory material. This marks the first application in the Chinese industrial sector.

The operational results after the retrofits demonstrate that this technology effectively addresses the issues of heat release from the heating surface and reduces bed temperature. It not only prevents damage to the heating surface caused by accumulated heat but also effectively controls the generation of pollutants inside the furnace. Analyzing the dynamic characteristics of load variation after the unit's retrofit reveals a reduction in the boiler's thermal inertia and a decrease in thermal resistance between the furnace side and the working fluid side. This allows the physical processes inside the furnace to respond more quickly to the operating parameters of working fluid, thereby effectively enhancing the boiler's load-bearing capacity.

This technology can improve the working conditions in the furnace within the normal range, and provide a reference for current hot topics in the transformation of coal-fired power plants to enhance flexibility.

Notation

T_{bed}	Bed temperature, ℃	$T_{fur,out}$	Temperature of furnace outlet, ℃
$\tilde{D}_b$	Boiler equivalent evaporation, t/h	D_s	Main steam flow rate, t/h
P_e	Unit power, MW		

Ackonwledgement

References

Yue G. X., Cai R. X., Lu J. F., et al., 2017. From a CFB reactor to a CFB boiler–The review of R&D progress of CFB coal combustion technology in China[J]. Powder Technology. 316: 18-28.

Heptonstall P. J., Gross R. J. K., 2021. A systematic review of the costs and impacts of integrating variable renewables into power grids[J]. nature energy. 6(1): 72-83.

Zhang H., Lyu J. F., Yue G. X., 2023. A review on research and development of CFB combustion technology in China[J]. Powder Technology. 414: 118090.

Hu X. N., Deng B. Y., Liu H. P., et al., 2023a. Status and development trend of rapid load regulation technology for circulating fluidized bed boiler[J]. Clean Coal Technology, 29(6): 11-23.

Hu X. N., Zhou T., Li C. R., et al., 2024. Investigation on Dynamic Characteristics under load regulation in CFB boiler with whole loop model[J]. Chemical Engineering Science. 287: 119784.

Chen H., Yao Y. G., Zhang G. Q., et al., 2022. Recent research and application on anti-wear technology of furnace water-wall in circulating fluidized bed boiler[J]. Clean Coal Technology. 28(12): 18-29.

Li J. J., Li Y., Lu J. F., et al., 2009. An analysis of Thermal inertia of a CFB (Circulating Fluidized Bed) boiler. Journal of Engineering for Thermal Energy and Power. 24(05): 609-613+681.

Dong Z. H., Lu X. F., Shi L. C., et al., 2023. Influence of Thermal Inertia of Refractory Material in Furnace on the Peak Regulating Rate of Circulating Fluidized Bed Boiler. Power Generation Technology. 44(4): 514-524.

Sun G. R., Wu H. W., Liu S. Z., et al., 2023. Thermal Inertia of 330 MW Circulating Fluidized Bed Boiler during Load Change. Journal of Thermal Science. 32(5): 1771-1783.

Hu X. N., Li C. R., Zhang S. H., et al., 2023b. Unraveling the Mystery of Inertia Generation in CFB Boilers: A Whole-loop Dynamic Modeling Methodology. Journal of Electrical Power. 38(6): 451-459.

TECHNICAL SCHEME OF ULTRA-SUPERCRITICAL CFB BOILER WITH DEEP PEAKING CHARACTERISTICS

Junfeng Wang[1,2,3,4], Xiwei Ke[3,4*],Gang Wang[2], Xin Guo[2], Wang Yu[2], Xiaoguo Jiang[2], Junfu Lyu[1,3,4]

(1,Department of Energy and Power Engineering, Tsinghua University, Beijing, 100084, China; 2.Harbin Boiler Company Limited, Harbin 150046, China; 3.Beijing Huairou Laboratory, Beijing, 101400, China; 4.Shanxi Research Institute of Huairou Laboratory, Taiyuan, 030000, China)

Email: Xiwei Ke @sxri.hrl,ac,cn

Abstract

Under the background of carbon neutrality, the new power system based on new energy puts forward the demand for deep peaking of coal power units. The ultra-supercritical circulating fluidized bed generator set with low carbon and clean characteristics is the future development direction. This paper analyzes and studies the key technology of deep peak regulation in the design of 660MW ultra-supercritical CFB boiler. The uniformity of flow field in large furnace is analyzed. The influence of external heat exchanger on low load combustion temperature is discussed. The low load stability of vertical water wall power system under ultra-supercritical parameters is studied. The results show that the flow field uniformity of M-type single furnace and the external heat exchanger can improve the combustion temperature at low load, and the hydrodynamic system with secondary rise has better stability at low load. This paper provides technical support for the development of 660MW ultra-supercritical CFB boiler with deep peaking capacity.

Keywords

Ultra-supercritical; CFB boiler; deep peaking regulation, external heat exchanger, hydrodynamic system

1. Introduction

Under the "dual-carbon" strategic goal, the installed capacity of new energy generating units such as wind power, photovoltaic power and hydroelectric power in China continues to increase[1]. These power sources are generally intermittent and unstable, and can not guarantee stable output of electrical energy. Various energy storage technologies can not become the main means of deep peak regulation in the short term. Therefore, it is required that coal power should be changed from a quantity storage power source to a regulation power source, and coal power should have the ability of deep peak regulation.

Compared with various coal combustion methods, CFB boilers have the characteristics of strong coal adaptability, low stable combustion load, and low pollutant control cost[2][3], which is very suitable for China's current coal power policy requirements of deep peak load regulation and ultra-low emission[4]. However, the development of CFB boiler technology is relatively late, and currently it is mainly subcritical and supercritical parameter boilers. Compared with pulverized coal boilers that have reached ultra-supercritical parameters, CFB boiler parameters are still relatively low, so the power generation efficiency of CFB boiler units is also relatively low. In the world, the first supercritical parameter CFB boiler was put into operation in Poland in 2009[5] and the first ultra-supercritical parameter CFB boiler was put into operation in South Korea in 2019[6]. China's first supercritical parameter CFB boiler was put into operation in 2013[7], and then more than 50 supercritical CFB boilers were put into operation successively, but no ultra-supercritical CFB boiler has been put into operation yet.

The current research on deep peak regulation of CFB units mainly focuses on the low load and fast variable load operation control strategy[8][9], variable load characteristics[10], pollutant

control[11][12], and the economy of deep peak regulation[13]. There are relatively few researches on the boiler design scheme of CFB boiler under deep peaking. In this paper, 660 MW ultra-supercritical CFB boiler is taken as the research object. Harbin Boiler Works Co., LTD. (HBC) improves the capacity of depth peak regulation and flexible operation of boiler through reasonable design of boiler scheme.

2. Boiler design scheme

For the depth peaking of CFB boiler, it is required that the boiler has good low-load stable combustion characteristics, operation regulation characteristics and low-load hydrodynamic stability. These are related to the furnace type, separator layout, coal feeding mode, external bed setting, hydraulic power and so on. Therefore, reasonable boiler design scheme can improve the depth of the boiler peak load and the ability of flexible operation adjustment.

The 660MW ultra-supercritical CFB boiler scheme adopted in this paper is developed on the basis of the successful experience of the first 600MW ultra-supercritical CFB boiler which was developed more than 10 years ago[7]. The boiler scheme can not meet the requirement of depth peaking due to the technical mastery and historical environment at that time. It is mainly reflected in the following problems: the lack of uniformity of flow field in the furnace causes large deviation of combustion bed temperature, low temperature of low-load bed, slow response speed and bad regulation of secondary coal feed, and insufficient stability of low-load hydrodynamic system. It is necessary to improve the boiler design scheme to study the ultra-supercritical CFB boiler suitable for deep peaking.

Based on the analysis and research on the depth peak-loading characteristics of CFB boilers, HBC innovatively proposed a simplified M-type 660MW ultra-supercritical CFB furnace structure[14], as shown in Fig .1. The boiler scheme adopts M-type arrangement, 4 cyclone separators which are uniformly arranged behind the furnace. Fuel is uniformly fed into 12 feed entrances from the front wall of the furnace, 4 medium temperature superheaters are installed in the 4 External Heat Exchangers(EHE). The hydrodynamic system adopts the Double ascent mode.
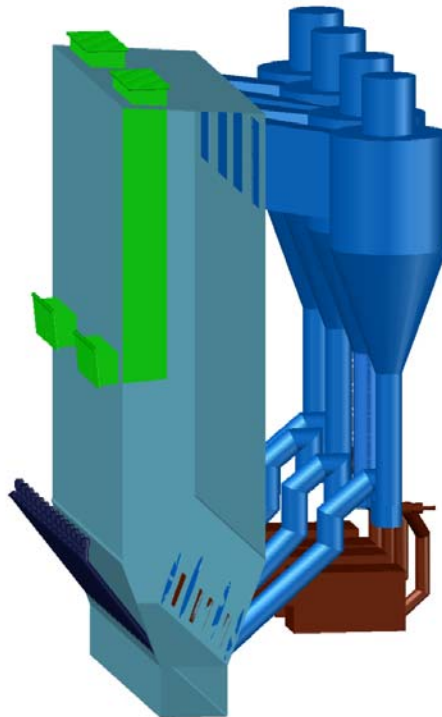

Fig. 1. Simple M-type arrangement 660 ultra-supercritical CFB boiler scheme.

3. Analysis of the characteristics of depth peak regulation

In order to meet the requirements of low load operation and adjustment flexibility, this paper focuses on the design of HBC M-type 660MW ultra-supercritical CFB boiler in the furnace in

terms of low load combustion stability, operation regulation characteristics, and hydrodynamic force stability under wide load conditions.

3.1 Design scheme to improve combustion stability in furnace under low load

The main factors affecting the combustion stability are the uniformity of the flow field and the combustion temperature. With the development of large-scale CFB boilers, the fluidization and combustion control in the furnace have become more difficult, and the uniformity of the flow field in the furnace has become more difficult[15][16]. In the design of boiler scheme, it is necessary to consider the mixing uniformity of materials in the furnace and the uniformity of temperature field in the furnace, and to improve the combustion temperature at low load.

(1) The flow field in the furnace adopts the uniform design concept

With the continuous increase of CFB boiler capacity, it is increasingly difficult to ensure the uniformity of flow field in the furnace[17][18]. The poor uniformity of the flow field in the furnace will affect the combustion stability in the furnace[19][20], which is not conducive to stable combustion at low load. In order to improve the uniformity of the flow field in the furnace, the boiler design adopts the uniformity design concept. The boiler adopts M-type single furnace structure with single air grid. 12 points of uniform coal feed are set on the front wall of the furnace(see Fig. 2(a)), and the fluidized air at the bottom of the furnace is uniformly fed into the water cooled air chamber at 6 points(see Fig. 2(a)). The return legs of 4 loop seals and 4 EHE are uniformly arranged(see Fig. 2(b)). The 4 outlet ducts entering the cyclone separator are uniformly arranged on the back wall of the furnace(see Fig. 2(c)).

(a) Feed coal and furnace fluidized air arrangement

(b) Return legs arrangement   (c) Furnace outlet ducts arrangement
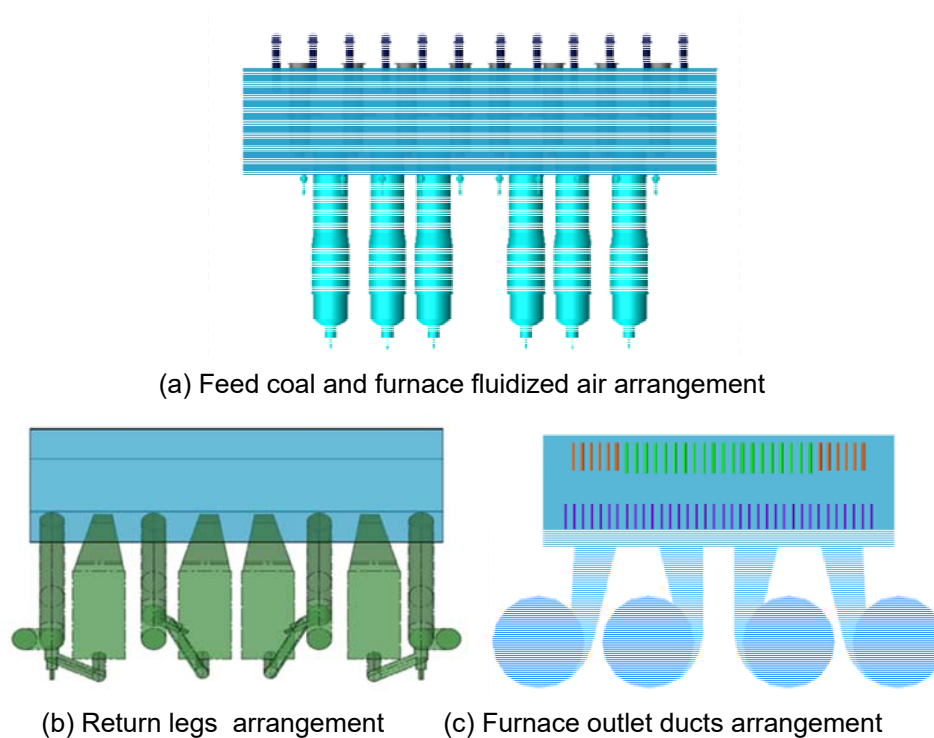
Fig. 2. Uniform layout scheme

Numerical simulation is used to calculate the flow field distribution characteristics of the furnace scheme. Flow deviation of cyclone separator is an important parameter to measure the uniformity of circulation system[17]. Fig .3. shows the flow field cross section diagram of the upper furnace, cyclone separator and its inlet flue. The calculation results show that the flow deviation of the furnace with 4 separators is less than 5%. That means the flow field is relatively uniform, and the layout structure adopted in this scheme is reasonable.
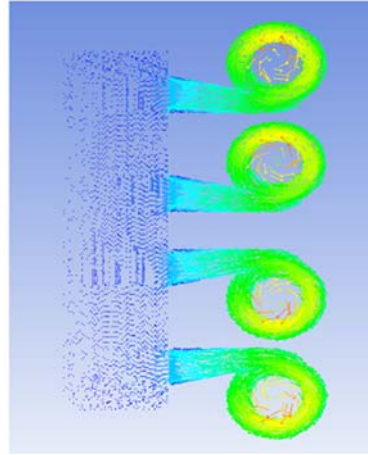
Fig. 3. Numerical simulation of the furnace flow field

(2) Use four superheaters EHE to increase low-load combustion temperature

EHE is a very effective measure to increase low-load combustion temperature[21]. Under low-load operation, the heat transfer of the internal heating surface can be reduced by reducing the ash flow into EHE, thus reducing the heat absorption in the furnace and increasing the combustion temperature in the furnace[22][23].

EHE is usually equipped with a superheater or reheater heating surface. The reheater heating surface arranged in EHE is mainly used to adjust the temperature of reheated steam, and can not be used to adjust the combustion temperature in the furnace. Through reasonable matching of heating surface, this boiler scheme adopts 4 EHEs all arranged medium temperature superheaters, and the reheated steam temperature is adjusted by the mature double flue duct at the back pass. Thus, all 4 EHEs can be used to adjust the combustion temperature in the furnace, which can significantly increase the low-load combustion temperature. FIG. 4 shows the comparison of combustion temperature changes in the furnace with and without EHE. It can be seen that at 20% load, the combustion temperature at the bottom of the furnace with EHE can reach 780℃, which is about 80℃ higher than that at the bottom of the furnace without EHE. It is indicated that the use of 4 superheaters EHEs have a better low-load stable combustion characteristics.
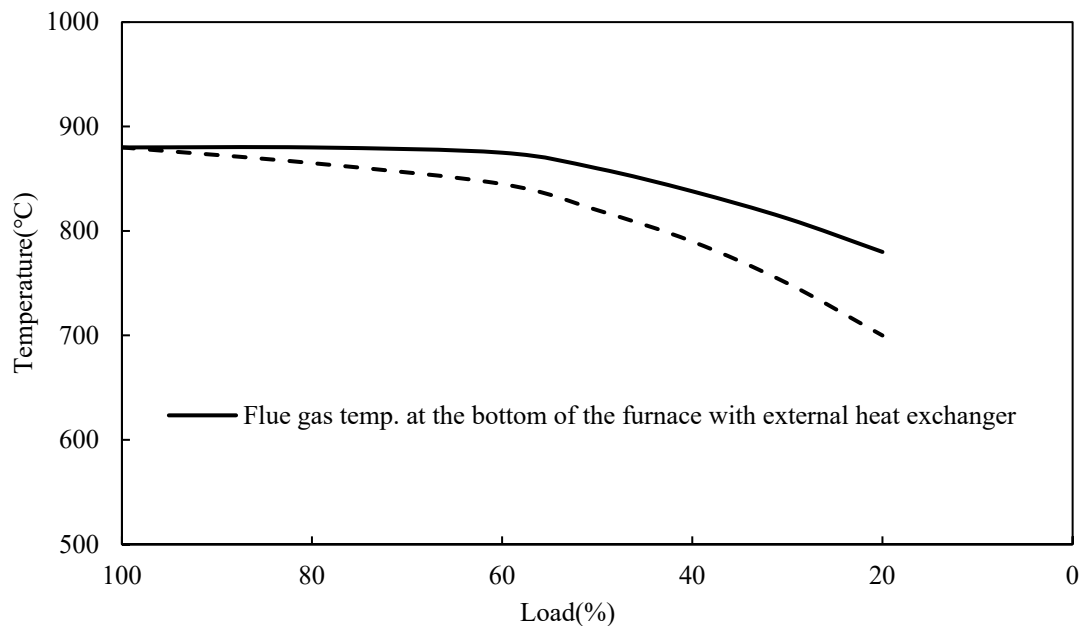
Fig. 4. Comparison of combustion temperature in furnace with or without setting EHE

To sum up, the furnace scheme of M-type 4 cyclone separators and 4 superheater EHEs has a small deviation of combustion temperature in the furnace, and the combustion temperature in the furnace is about 780℃ at 20% load. It meets the requirement that the minimum stable combustion temperature without oil is greater than 750℃, and can be stable combustion in the furnace at 20% load.

3.2 Design scheme to improve operation regulation characteristics

The depth peaking requires the boiler to have flexible operating regulation characteristics. This paper analyzes the coal regulation and the heat transfer regulation characteristics in the furnace.

(1) The coal feeding system scheme can be quickly and flexibly adjusted

In order to achieve rapid load change in CFB boiler, the coal is required to have the ability of rapid response and flexible adjustment to quickly change the combustion state in the furnace. Especially for supercritical direct current boilers, the superheated steam temperature is regulated by coal-water ratio, and the regulating capacity of coal directly affects the change of parameters on the water and water side. Therefore, the design of coal feeding system needs to be focused on.


(a) Two-stage coal feeding scheme of H-type   (b) One-stage coal feeding scheme of M-type
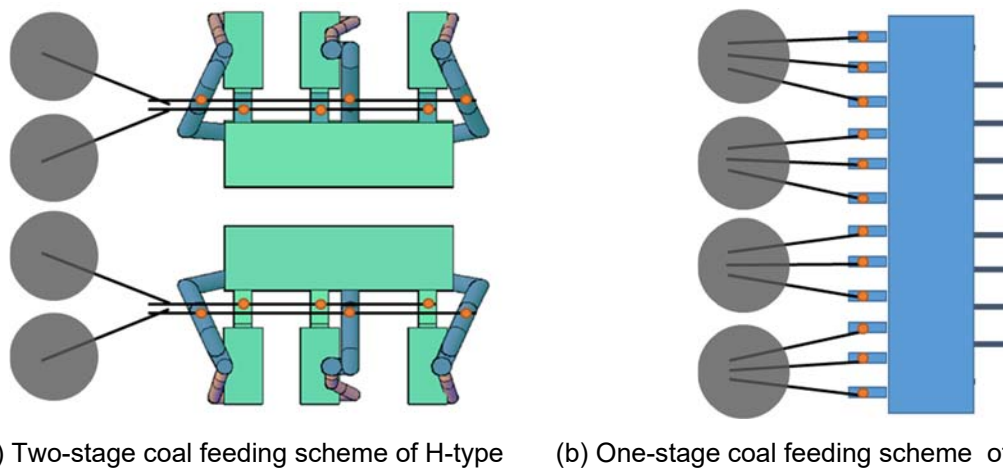
Fig. 5. Schematic diagram of two coal feeding schemes

For boilers with H-type arrangement, a two-stage coal feed scheme is adopted, as shown in Fig. 5(a). There are 4 feed lines in series. For each feed line,the coal passes through the primary feed line and then enters the secondary feed line. The response speed of the two-stage feeding scheme is slow. At the same time, each coal feeding line is set up 3 coal dropping points, and the coal feeding amount between the 3 coal dropping points can not be adjusted during operation. Therefore, the coal feeding scheme of H-type furnace layout has slow response speed and poor regulation, which is not conducive to the operation regulation of the boiler.

The M-type furnace adopts a one-stage coal feed scheme, as shown in Fig. 5(b). 12 independent coal feed lines are set, and each coal feed line corresponds to only one coal drop point. The coal feeding response speed is fast, and the coal feeding amount of each coal feeding line can be independently adjusted, and the coal feeding regulation is good.

Compared with the two-stage coal feed scheme of the H-type boiler, the one-stage coal feed scheme of this furnace type has a fast response speed, about 1/3 response time of the two-stage coal feed, and each coal feed line can adjust the coal feed amount independently, with strong adjustment ability, which is conducive to the flexible adjustment of the operation of the boiler when the load changes.

(2) Furnace material adjust

Relevant studies show that during the variable load of CFB boiler, the concentration of fine ash involved in external circulation is the main factor affecting the variable load rate[9]. The EHE of this furnace type scheme can be used as a buffer bin for ash storage, and the ash

flow into or out of EHE can be controlled by the EHE inlet cone valve and the EHE fluidization risk when the load changes, so as to realize the adjustment of fine ash particles in the furnace. Through this adjustment, the ash concentration in the furnace can be adjusted when the load changes, thus affecting the heat exchange in the furnace and improving the operation adjustment characteristics.

3.2 Series double ascent hydrodynamic system for wide load operation

Compared with pulverized coal boilers, a large amount of circulating materials in CFB furnace scour the heating surface inside the furnace, and the water cooling wall of the furnace can only adopt the vertical tube structure. Meanwhile, the temperature and heat load of the CFB furnace are lower, and the overall heat load in the furnace is more uniform[24]. According to the characteristics of CFB boiler, the water system of supercritical or ultra-supercritical CFB boiler can only adopt the hydrodynamic scheme of medium and low mass flow rate[25][26]. The cooling capacity of this hydrodynamic system is relatively low, and the hydrodynamic stability is poor, especially under low load conditions.

Due to the limitation of furnace height of CFB boiler, the area of water wall around the furnace of supercritical and ultra-supercritical CFB boiler is not enough to meet the need of evaporative heating surface layout, and additional evaporative heating surface needs to be arranged[28]. The hydraulic power system of the first 600MW supercritical CFB boiler, which has been put into operation, adopts a one-rise hydraulic power system scheme in which the furnace water cooling wall is connected to the water partition wall[29](see Fig. 6(a)). The hydrodynamic system of this scheme is simple, but the mass flow rate of the water cooling wall is low, and there are parallel heating surfaces of one side and two sides, which is not conducive to the stability of the low-load hydrodynamic force.

The boiler scheme studied in this paper adopts a double ascent hydrodynamic system with a higher mass flow rate of water wall in series with water panel (see Fig. 6(b)). After rising the water wall of the furnace, the feedwater is led out through the connecting pipe into the water panel, and then leads out into the steam separator. Compared with the parallel single ascent system, the Series double ascent system has higher mass flow rate of furnace water wall, better cooling capacity at low load, and relatively small temperature deviation of water wall.

(a) Parallel single ascent   (b)Series double ascent
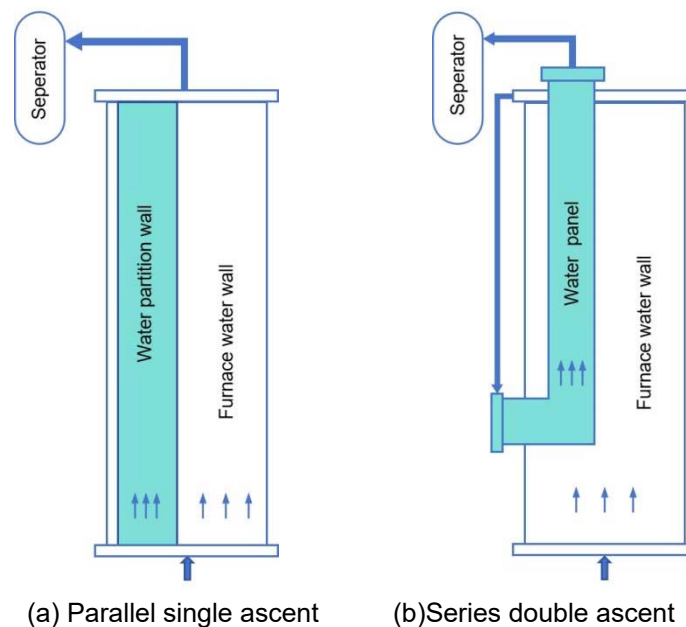
Fig. 6. Schematic diagram of two hydrodynamic systems

Through the modeling and calculation of the Series double ascent hydrodynamic system, the calculation results of the 100% load and 20% load are shown in Table 1. It can be seen that: at 100% load and 20% load, the Maximum wall temp. deviation of water wall water panel are all lower than the 50℃ deviation requirement recognized in the industry. The results show that the boiler's hydraulic power is safe and reliable under 20% load condition.

Table 1. Summary of hydrodynamic calculation results.

Location	100%load	20%load
Average medium temp. at outlet of water wall	410	325
Max medium temp. at outlet of water wall	424	327
Average wall temp. at outlet of water wall	429	353
Max wall temp. at outlet of water wall	460	359
Maximum wall temp. deviation of water wall	31	6
Average medium temp. at outlet of water panel	436	365
Max medium temp. at outlet of water panel	452	360
Average wall temp. at outlet of water panel	465	396
Max wall temp. at outlet of water panel	13	36
Maximum wall temp. deviation of water panel	425	337

4. Conclusion

In the scheme design of the 660MW ultra-supercritical CFB boiler, a number of measures are taken to improve the depth peak load capacity of the boiler, and the following conclusions are drawn: 1) The boiler layout scheme with 4 M-type cyclone separators has a small deviation of the combustion temperature field in the furnace, and the scheme with full superheater EHE has a better low-load combustion temperature; 2) The variable load regulation characteristic of the boiler is improved by using the independently adjustable one-stage coal feeding scheme and the EHE which can adjust the ash concentration in the furnace; 3) The series double ascent hydrodynamic system with higher mass flow rate has the characteristics of safety and reliability of the 20% load. The simplified M-type 660MW ultra-supercritical CFB boiler furnace type scheme adopted by HBC has good deep peak regulation characteristics. The boiler technical scheme has advantages in the furnace combustion stability, operation regulation characteristics and hydrodynamic stability at low load.

References

[1] State Council Information Office. China's energy development in the new era[EB/OL]. Beijing,(2021-10-20),http://www.scio.gov.cn/zfbps/32832/Document/1695117. htm.
[2] Leckner B.Fluidized bed combustion： Mixing and pollutant limitation[J].Progress in Energy and Combustion Science,1998,24(1)： 31-61.
[3] Johnsson J E.Formation and reduction of nitrogen oxides in fluidized-bed combustion[J].Fuel,1994,73(9)： 1398-1415.
[4] Lyu Junfu1, Jiang Ling1, Ke Xiwei1,et,al.Future of circulating fluidized bed combustion technology in China for carbon neutralization[J].Coal Science and Technology, 2023,51(01)： 514-522.
[5] Jantti T,Rasanen K.Circulating fluidized bed technology towards 800 MWe scale-lagisza 460 MWe supercritieal CFB operation experience[C]//Power Gen Europe.Milan,Italy,2011.
[6] Jantti T,Nuortimo K,Ruuskanen M,et al.Samcheok green power 4×550MWe super-critical circulating fluidized bed steam generation in South Korea [C]//Power Gen Europe.Colon,Germany,2012.
[7] Yue G X,Ling W,Lyu J F,et al.Development and demonstration of the 600MW supercritical CFB boiler in Baima power plant[C]//Proceedings of the 22nd Fluidized Bed Conversion.Turku,Finland,2015.
[8] JIANG Chunlei, NIU Ruixue. Research on operation method of deep peak-shaving of 330 MW CFB unit[J]. Journal of Shenyang Institute of Engineering (Natural Science), 2017, 13(4): 326–330.
[9] LIU Jizhen, HONG Feng, GAO Mingming, et al. Research on the control strategy for quick load change of circulating fluidized bed boiler units[J]. Proceedings of the CSEE, 2017, 37(14): 4130–4137,S20.

[10] CAI Jin, SHAN Lu, WANG Zhining, et al. Variable load characteristics of a 350 MW supercritical circulating fluidized bed boiler[J]. Thermal Power Generation, 2020, 49(9): 98–103, 108.

[11] ZHANG Chongchong, MA Suxia, ZHANG Jianchun, et al. Pollutant emission from 350 MW CFB boiler under varying load condition[J].Thermal Power Gene ration, 2020, 49(1): 41–47.

[12] ZHANG Chongchong. Study on dynamic characteristics of pollutant emission from CFB boiler under variable load[D]. Taiyuan: Taiyuan University of Technology, 2019.

[13] YU Ruihong, WANG Taotao. Economic analysis of deep peak load regulation of 350 MW supercritical CFB Unit[J]. Coal Science &Technology Magaz ine, 2020, 41(5): 12–13, 27.

[14] Jiang Xiaoguo,Wang Junfeng,Gao Xinyu.Plan of HBC's 600MW ultra supercritical CFB boller[J].Power System Engineering,2017,33(04)：47-48+51.

[15] Guo Qiang,Wang Quanhai,Lu Xiaofeng,et al.Numerical study on gas flow characteristic in three parallel separators of a large-scale CFB boiler[J].Proceedings of the CSEE,2019,39(13)：3851-3859.

[16] Cheng Leming,Xu Linjie,Xia Yunfei,et al.Key issues and solutions in development of the 600 MW CFB boiler[J].Proceedings of the CSEE,2015,35(21)：5520-5532.

[17] Xu Linjie,Cheng Leming,Ji Jieqiang,et al.Integrated numerical model for ultra/supercritical CFB boilers[J].Proceedings of the CSEE,2018,38(02)：348-355+664.

[18] Mo Xin,Cai Runxia,Huang Xiaodan,et al.The effects of wall friction and solid acceleration on the mal-distribution of gas-solid flow in double identical parallel cyclones[J].Powder Technology,2015,286：471-477

[19] Xu Linjie.Numerical model development of an ultra/supercritical Circulating Fluidized Bed boiler[D].Zhejiang University,2017.

[20] Zheng Yue,Lu Xiaofeng,Yang Wenqi,et al.Simulation of particle concentration distribution in a large-scale Circulating Fluidized Bed Boiler at different material-returning deviations[J].Proceedings of the CSEE,2020,40(03)：848-859.

[21] Xin Shengwei,Zhang Man,Wang Junfeng,et al. R esearch on key technology of external heat exchanger in the large-scale circulating fluidized bed boiler[J].Clean Coal Technology,2020,26(03)：120-125.

[22] Cai Runxia,Zhang Man,Mo Xin,et al.Operation characteristics of external heat exchangers in the 600MW supercritical CFB boiler[J].Fuel Processing Technology,2018,172：65-71.

[23] Wang H,Xin S,Zhang P,et al.Study on the actual operation characteristics of fluidized bed heat exchanger in a supercritical CFB boiler[C]//IOP Conference Series：Earth and Environmental Science.Xiamen,China,2020.

[24] Yerushalmi J,Turner D H,Squires A M.The fast fluidized bed[J].Industrial & Engineering Chemistry Process Design and Development,1976,15(1)：47-53.

[25] Wu Yuxin,Lu J,Zhang J,et al.Heat flux and hydrodynamics of the membrane wall of supercritical pressure circulating fluidized bed boiler[C]//Proceedings of the 5th International Symposium on Multiphase Flow,Heat Mass Transfer and Energy Conversion.Xi'an：Xi'an Jiaotong University Press,2006.

[26] Wang Wenyu,Li Yaode,Zhao Yunjie,et al.The experimental investigation on flow and heat transfer characteristics of the rifled water wall tube of an ultra-supercritical CFB Boiler[J].Proceedings of the CSEE,2018,38(02)：373-382+667.

[27] Pan Jie,Yang Dong,Chen Gongming ,et al.Thermal-hydraulic analysis of a 600MW supercritical CFB boiler with low mass flux[J].Applied Thermal Engineering,2012,32：41-48.

[28] Shen Zhi,Yang Dong,Wang Siyang,et al.Experimental and numerical analysis of heat transfer to water at supercritical pressures[J].International Journal of Heat and Mass Transfer,2017,108：1676-1688.

[29] Zhou Xinglong,Cheng Leming,Xia Yunfei,et al.Heat transfer characteristic of water wall and partition wall in a 600 MW CFB boiler[J].Proceedings of the CSEE,2014,34(02)：225-230.

INVESTIGATION OF COMBUSTION CHARACTERISTICS OF LIGNITE IN CIRCULATING FLUIDIZED BED

Liu Xinglei*, Wei Geng, Li Weicheng, Lin Shanhu, Guo Qiang, Zhou Qi, Nie Li

Dongfang Bioler Co., Ltd., 611731, Chengdu, China

*Email: *liuxinglei2a@163.com*

Abstract

Circulating Fluidized Bed(CFB) technology was used with low heat content coals, while achieving lower emission of pollutants. Dongfang conducted experiments on the 3MWth CFB experimental platform for lignite from different regions, obtaining experimental data on the combustion characteristics and pollutant emission characteristics of lignite. Dongfang had designed and manufactured lignite CFB units, achieving good combustion and low emissions of pollutants for different regions lignite fuel, further verifying that lignite fuel was very suitable for using CFB technology in practical engineering.

Key words: Circulating Fluidized Bed(CFB), Lignite, Combustion characteristic

1. Introduction

The circulating fluidized bed (CFB) was a type of fluidized bed combustion, while achieving lower emission of pollutants. In 1923, Winkler's coal gasifier represented the first significant large-scale industrial application of fluidized bed. In 1939, Warren Lewis and Edwin Gilliland developed a new gas–solid process, while they were trying to find an appropriate gas–solid contacting process for fluid catalytic cracking. Though CFB process was used extensively in the petrochemical industries, but it did not have a direct entry into the field of coal combustion for steam generation. In 1982, the first CFB boiler was designed exclusively for the supply of steam and heat in Vereinigte Aluminum Werke at Luenen, which generated 84 MW total(9 MW electricity, 31 MW process steam, 44 MW molten salt melt) by burning low-grade coal washing residues[1]. In 1986, the Bubble fluidized bed (BFB) boiler with an evaporation capacity of 35t/h, designed and manufactured by Dongfang Boiler Factory at the Yongrong Mining Bureau Power Plant in Sichuan[2]. In 1996, the 250 MWe CFB boiler was designed and manufactured by Alstom at the Gandanne power plant in France. In 2009, the 460 MWe supercritical direct current CFB boiler was designed and manufactured by Foster Wheeler at the Łagisza Power Plant in Poland[3]. In 2013, the 600 MWe supercritical CFB boiler was designed and manufactured by Dongfang Boiler Co., Ltd. at the Baima Power Plant in Sichuan of China[4]. Power plants that use CFB technology could burn low grade fuels at high efficiency and without the need for expensive fuel preparation. Circulating fluidized bed power generation were developed rapidly in China and even globally, becoming the preferred technology route for clean coal combustion.

Lignite was one of the most abundant types of coal, and its total proven reserves in the world was 195 billion tons, accounting for 22.6 % of the total coal reserves. Lignite had a low degree of coalification under the influence of coal formation age, with the characteristics of high moisture content (30–60 %), high ash content (15–30 %), high volatile content (>37 %), and low calorific value (12.56–14.56 MJ/Kg)[5]. Lignite constituted a major energy source and had been used for energy production as a fossil fuel.

This article combines characteristics of lignite and CFB technology, to explore efficient combustion and clean utilization of lignite in different regions, providing important support for combustion characteristic, pollutant emission characteristic, as well as the operation characteristic.

2. Experimental

2.1 Lignite Characteristics

Lignite was the lowest grade coal with the least concentration of carbon. Lignite had a brown or dark brown appearance and undergoes dehydration after peat deposition, which had a relatively short formation time in coal resources, generally characterized by high moisture content, high volatile matter, low ash melting point, and easy slagging.

Table 1. Summary of lignite analysis data from different regions

Parameter	Symbol	Unit	Bosnia-Herzegovina	Romania	Turkey	Indonesia	Brazil	China
Moisture	Mad	%	27.54	12.83	12.11	12.31	9.42	24.69
Moisture	Mar	%	37.02	39.07	43.26	30.65	15.17	29.19
Ash	Aar	%	11.32	19.49	15.35	4.18	44.21	33.52
Volatiles	Vdaf	%	82.62	60.53	59.52	52.89	43.03	50.45
Fixed Carbon	FCar	%	8.97	16.36	16.75	30.71	23.14	18.48
Low calorific value	$Q_{net,ar}$	MJ/kg	12.00	9.30	9.60	16.86	10.75	9.65
Carbon	Car	%	35.66	28.3	28.17	46.21	28.37	27.55
Hydrogen	Har	%	2.49	2.16	2.34	3.24	2.29	1.47
Nitrogen	Nar	%	1.15	0.59	0.72	0.63	0.07	1.24
Sulfur	St,ar	%	0.17	1.03	1.96	0.13	1.76	1.80
Oxygen	Oar	%	12.19	9.38	8.20	14.96	8.13	5.23
Deformation temperature	DT	$^{\circ}C$	1145	1209	1175	1130	1314	1250
Softening temperature	ST	$^{\circ}C$	1237	1227	1181	1150	1407	1400
Hemisphere temperature	HT	$^{\circ}C$	1244	1237	1184	1170	1432	1400
Flow temperature	FT	$^{\circ}C$	1251	1257	1203	1190	1450	1450
Ignition temperature	To	$^{\circ}C$	325	295	306	353	387	326

Table 1 shows the summary of lignite analysis data from different regions. The volatile content of fuel was relatively high, and the ignition temperature range of thermal gravimetric analysis (TGA) was 295 $^{\circ}C$ ~ 397 $^{\circ}C$, which could be beneficial for saving the oil or natural gas amount during start process and reducing the start-up cost. Lignite had a low softening temperature with a serious tendency to slagging. However, due to operating temperature was 850 $^{\circ}C$ ~ 950 $^{\circ}C$, there was no coking phenomenon during the lignite combustion. CFB technology was very suitable for lignite fuels.

2.2 Experimental platform

This article conducted experimental research on Dongfang 3MWth CFB combustion test bench(Figure 2.1). The test bench mainly consisted of ignition device, air distribution device, the main circulation circuit, tail flue, water cooling system, flue and air system, feeding system, slag discharge device, as well as steel structure. The combustion chamber height reached 24.5m, ensuring the combustion reaction time. The ABB flue gas composition online analyzer was used to test the flue gas components such as O_2, NO_X, SO_2, and CO_2. The effects of operating temperature, oxygen concentration at CFB furnace outlet, staged combustion, limestone characteristics, as well as the pollutant emission characteristics were investigated.

1. CFB combustion chamber
2. Cyclone separator
3. Return feeder
4. Tail shaft
5. Limestone addition system
6. Fuel addition system
7. Fluidized air chamber
8. Cooling water system
9. Air preheater
10. Ignition air duct
11. Slag discharge system
12. Water supply pump
13. High pressure fluidization fan
14. Primary fan
15. Secondary fan
16. Induced draft fan
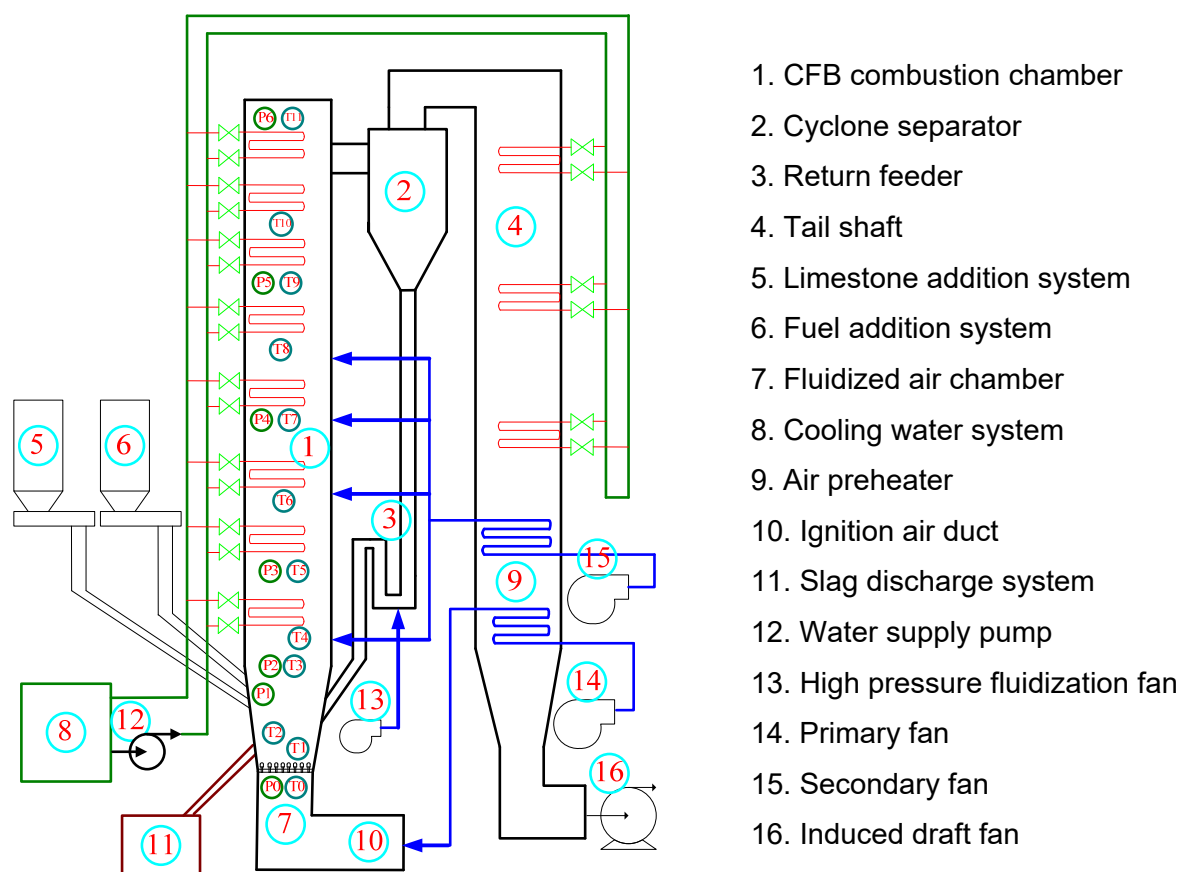
Fig. 2.1. Layout diagram of Dongfang 3MWth CFB test bench

3. Results and discussion

3.1 Combustion Characteristic

Experimental research on combustion characteristics of lignite from typical regions of Bosnia and Herzegovina, Romania, Brazil, and China were conducted on Dongfang 3MWth CFB experimental platform, and combustion and emission characteristics of lignite were obtained, which were showed in table 2.

Table 2. Summary of lignite Combustion Characteristic from different regions

Item	Unit	Bosnia-Herzegovina	Romania	Brazil	China
Operating temperature	℃	850~880	~860	850~900	~900
Carbon content of fly ash	%	2.00	1.18	0.55	1.75
Carbon content of slag	%	1.64	1.13	1.14	1.40
Fuel combustion efficiency	%	99.4	99.2	98.7	97.6
Nitrogen	%	1.15	0.59	0.07	1.24
Original NOₓ emissions	mg/Nm³	40~180	65~134	110~215	72~202
Sulfur	%	0.17	1.03	1.76	1.80
Ca/S molar ratio of ash	1	2.84	0.80	0.21	0.22
Original SO₂ emissions	mg/Nm³	140~314	3500~4000	6800~7288	7970~8200
Self desulfurization efficiency	%	48~77	14~25	7~13	0.3~3.1

Lignite from Bosnia-Herzegovina and Romania had characteristics such as low ignition temperature, low flammability, and low pollutant emissions, stable operation could be achieved at operating temperature of 850 $^{\circ}$C ~880 $^{\circ}$C, without any coking phenomenon, combustion efficiency were above 99%. Lignite from Brazil, and China ash content were significantly higher, so combustion efficiency were slightly lower, fuel combustion efficiency were 98.7% and 97.6% respectively.

3.2 Pollutant Emission Characteristic

Lignite from typical regions of Romania, Brazil, and China had higher sulfur content, and lower Ca/S molar ratio (KS, self = 0.13~0.80), desulfurization efficiency was low, which were necessary to reduce the SO_2 emissions by adding desulfurization agents. Figure 3.1 shows Brazilian lignite desulfurization efficiency by adding limestone. When calcium sulfur molar ratio of limestone increased to 1.6, the desulfurization efficiency reached 95%, indicating the limestone had a significant effect on desulfurization.

The Bosnia and Herzegovina lignite Ca/S molar ratio was KS, self=2.84, CFB combustion could achieve desulfurization efficiency 48%~77%. The original emission SO_2 was 140 mg/Nm^3 ~ 314 mg/Nm^3. Figure 3.2 showed relationship between nitrogen oxide emissions from Bosnian lignite and operating oxygen level (operating temperature was about 850 $^{\circ}$C). The concentration of nitrogen oxides increased with the increase of oxygen content at the CFB furnace outlet. Figure 3.3 shows the relationship between nitrogen oxide emissions from Bosnian lignite and operating temperature (oxygen concentration was about 3.3%). The concentration of nitrogen oxides increases with the increase of operating temperature.

Fig. 3.1. Effect of desulfurizer on desulfurization efficiency	Fig. 3.2. Effect of oxygen on nitrogen oxides Emission Fig.	3.3. Effect of temperature on nitrogen oxides Emission
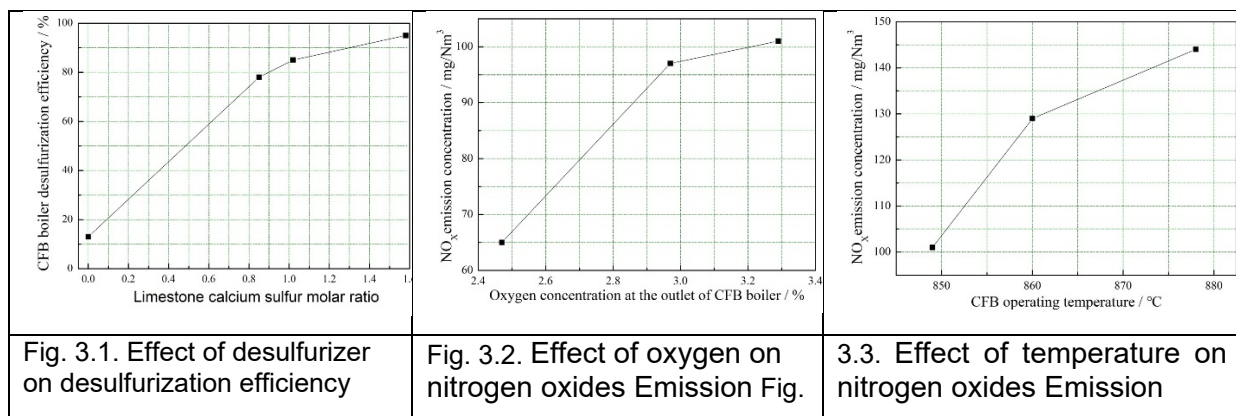
3.3 Operating characteristics

Dongfang Boiler independently designed and manufactured the 300MWe CFB boiler for Bosnian lignite, and conducted systematic performance tests on engineering equipment. The Bosnian lignite ash content was 7.5%~12%, the total moisture content was 39%~49%, and the received base low calorific value was 9.0 MJ/kg ~12MJ/kg in the engineering project. Under lignite particle size D99<20mm and D50=2mm, stable combustion and bed material storage in the furnace were achieved, without the need to add inert materials. By adjusting feed of limestone, sulfur dioxide emission concentration was controlled below 174mg/Nm^3. By adjusting operating temperature and furnace outlet oxygen concentration, nitrogen oxide emission concentration was controlled below 167mg/Nm^3. According to ASME PTC4 standard, fuel combustion efficiency reached 99.6%, and CFB boiler low calorific value thermal efficiency reached 93.1% (the heat loss caused by fuel moisture QpLWF>1%).

Based on low ash content and high moisture content of Indonesian lignite, as well as specific needs of users, Dongfang Boiler had designed and developed different capacities CFB units. Using appropriate particle size river sand as the starting bed material could maintain stable long-term operation. By adding appropriate particle size limestone, desulfurization effect could be achieved, which could be used as a circulating material to stay for a long time. By adjusting operating temperature and furnace outlet oxygen concentration, nitrogen oxide

emission concentration was controlled below 200mg/Nm^3. According to ASME PTC4 standard, boiler low calorific value thermal efficiency reached 94.3%.

4. Conclusion

By using CFB technology, self desulfurization could be achieved during combustion process for lignite, and by adding desulfurizers, sulfur dioxide emissions could be significantly reduced. the original emission concentration of nitrogen oxides could be controlled below 200 mg/Nm^3 generally, and by adjusting operating temperature and furnace outlet oxygen content, the nitrogen oxide concentration could be controlled below 100 mg/Nm^3. Experiments on Dongfang 3MWth CFB test bench and engineering CFB units had shown that lignite had good combustion characteristics, low pollutant emissions, and there was no slagging problem. Lignite fuel was very suitable for using CFB technology.

References

[1] Basu Prabir. Circulating Fluidized Bed Boilers: Design, Operation and Maintenance. 2015. 10. 1007 /978-3-319-06173-3.

[2] LIU Xinglei, GUO Qiang, et al. Experimental Platform Design of 3MWth Circulating Fluidized Bed and Experimental Research [J]. Dongfang Electric Review. 2019. 131. 31-36.

[3] Hotta, A. Foster wheeler's solutions for large scale CFB boiler technology: features and operational performance of Łagisza 460 MWe CFB Boiler. In Proceedings of the 20th International Conference on Fluidized Bed Combustion. 2010. 59–70.

[4] Jie Pan, Dong Yang, et al. Thermal-hydraulic analysis of a 600 MW supercritical CFB boiler with low mass flux, Applied Thermal Engineering, Volume 32, 2012, 41-48.

[5] Han R, Zhou A, Zhang N, et al. A review of kinetic studies on evaporative dehydration of lignite[J]. Fuel, 2022, 329: 125445.

DESIGN OF A NEW TYPE OF CFB BOILER BURNING THE HIGH ALKALI AND HIGH CHLORINE COAL

Yuping Li[1,2]， Qigang Deng[1,2]*， Meng Dong[1,2]， Min Huang[1,2]， Lixiao Wei[1,2]，

Binbin Qiu[1,2]， Hu Su[1,2]， Jiayi Lu[1,2]

Dongfang Boiler CO,. LTD, West Gaoxin District, Cheng Du 611731, P. R. China；

Clean Combustion and Flue Gas Purification Key Laboratory of Sichuan Province

dengqg@dbc.com.cn

Abstract

The Sha'er Lake area in Xinjiang is mainly composed of high alkali and high chlorine coal, which has extremely strong fouling and corrosion characteristics. It poses a serious risk of fouling and corrosion on the heating surface of power plant boilers, affecting their normal operation. This article analyzes the design scheme of a pure combustion Shale Lake coal circulating fluidized bed boiler for a certain project, and takes corresponding measures to prevent contamination and corrosion of Shale Lake coal during combustion, providing technical reference for the utilization of high alkali and high chlorine coal.

Key words: Shal Lake coal; CFB boiler; Contamination and Corrosion

1　Introduction

Xinjiang coal reserves account for approximately 40% of China's total coal reserves[1]. Therefore, it is of great importance to ensure the clean and efficient use of this resource in order to guarantee China's energy security and to achieve the "dual-carbon goal". Shal Lake coal is a typical coal type in Xinjiang, with a reserve of nearly 100 billion tonnes [2]. It is characterised by high reactivity and high-quality chemical and power coal properties. However, the content of sodium oxide (in terms of ash) in Shal Lake coal is more than 4%, and the content of chlorine is more than 0.3%[3], which is a typical high-alkali and high-chlorine coal.The problems of coking, fouling, corrosion and emission of chlorine-containing pollutants in the process of utilisation of this coal are extremely serious, which restricts the safe, efficient and clean utilisation of Shal Lake coal.

This article presents a new type of circulating fluidised bed boiler designed to burn high-alkali and high-chlorine coal at high temperatures and pressures. The boiler is intended to address the issue of boiler fouling and corrosion by utilising Xinjiang Shal Lake coal exclusively.

2　Basic information of the project

2.1　Boiler parameters

The principal design parameters of the boiler are presented in Table 1.

Table 1 Boiler Parameters

Item	Unit	BMCR
SH steam：		
Flow	t/h	480
Pressure	MPa.g	9.8
Temp.	°C	540
Feed water：		

Temp.		°C		158	

2.2 Fuel characteristics

The composition of the boiler fuel and ash is presented in Tables 2 and 3.

Table 2 Fuel composition analysis

Item	Symbol	Unit	Design Coal	Check Coal 1	Check Coal 2
Total Moisture	Mt	%	26.87	24.00	22.6
Ash	Aar	%	8.11	9.46	10.01
V.M.	Var	%	22.88	37.55	24.11
Carbon	Car	%	47.94	48.39	50.77
Hydrogen	Har	%	2.25	2.24	2.47
Oxygen	Oar	%	13.29	15.33	13.40
Nitrogen	Nar	%	0.54	0.49	0.62
Chlorine	Clar	%	0.5	0.58	0.85
Sulfur	St,ar	%	0.5	0.09	0.13
Heat value,ar	Qnet,ar	kJ/kg	16299	16880	17670

Table 3 Ash composition analysis

No.	Item	Unit	Design Coal	Check Coal 1	Check Coal 2
1	SiO_2	%	8.52	36.69	10.28
2	Al_2O_3	%	13.09	11.39	5.36
3	Fe_2O_3	%	7.21	6.54	6.67
4	CaO	%	32.72	32.63	37.31
5	MgO	%	3.47	1.55	7.53
6	K_2O	%	0.24	1.07	0.31
7	Na_2O	%	2.78	0.93	18.95
8	TiO_2	%	0.04	0.47	0.36
9	SO_3	%	16.26	2.66	4.51
10	CL	mg/kg		<100	

2.3 General arrangement of boiler

The boiler employs a single drum, single furnace, natural circulation, full suspension structure, and a fully closed arrangement structure. Fig.1 illustrates the boiler's general arrangement.
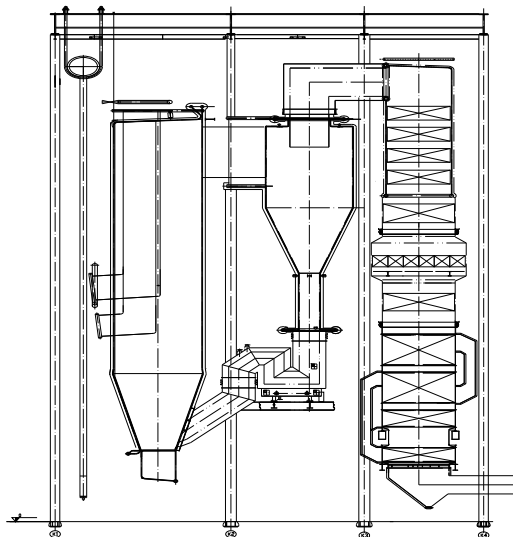

Fig.1. General arrangement of boiler

The furnace chamber is constructed with a full membrane wall structure, which is followed by two high-efficiency worm shell cyclone separators. The U-type return feeder, situated beneath the cyclone, directs the solid particles that have been separated by the cyclone separator to the furnace chamber.

The flue gas passes through the separator exit flue and then into the rear flue.

When the boiler burns high-alkali and high-chlorine coal, the conventional coal-fired design can no longer adapt to the staining and corrosion characteristics of the fuel, so the boiler design process can take the following measures to improve the operational reliability of the boiler.

3 Boiler Design Essentials

Table 2 illustrates that the chlorine content of the designed fuel for the boiler is 0.5%, with the highest chlorine content observed in the verified fuel at 0.85%. This is considerably higher than that of conventional power coal. This article proposes anti-fouling and corrosion measures for boiler combustion of Shal Lake coal, which is distinguished by its high alkali and high chlorine characteristics.

3.1 Anti-fouling measures

3.1.1 Bed temperature design

The furnace chamber is a fully water-cooled membrane wall structure, and a water-cooled screen is arranged in the furnace chamber to control the bed temperature. This effectively reduces the release of alkali metals from the coal in the combustion process, prevents coking in the furnace, and facilitates the desulphurisation of the furnace and the suppression of NOx generation.

3.1.2 Flue gas temperature design

It is posited by the field of literature [4] that when the flue gas temperature exceeds 650 ℃, there is a high probability of contamination occurring; conversely, when the flue gas temperature is lower than 650 ℃, contamination is essentially non-existent. The flue gas temperature at the exit of the furnace is much higher than 650 ℃, and the heating surface in the rear flue is situated within the critical temperature range for contamination.

In order to reduce the flue gas temperature at the entrance of the heating surface in the rear flue, a cooled flue is arranged after the cyclone, which cools the flue gas temperature quickly. The cooled flue is equipped with a hydrodynamic soot-cleaning device, which can regularly clean the fouled layer on the cooled flue and clean it up in time by the spiral soot conveyor arranged under the empty flue. The cooled flue is equipped with a hydrodynamic soot-cleaning device, which is designed to remove contamination layer from the flue. This is achieved by the spiral soot conveyor, which is situated beneath the empty flue and is activated when necessary.

It is challenging to regulate the flue gas temperature solely through the cooled flue. Consequently, a water-cooled tube bundle is positioned subsequent to the cooled flue, with the objective of controlling the inlet flue temperature of the heating surface in the rear pass (650℃) and preventing the occurrence of contamination within the specified temperature range. The water-cooled tube bundle employs a design of large intercept, which serves to prevent contamination bridging and effectively addresses the issue of contamination.

3.2 Anti-corrosion measures

3.2.1 Anti-corrosion at high temperatures

One of the key causes of chloride corrosion is the boiler heating surface wall temperature, as highlighted in literature[5],This literature demonstrates a clear relationship between the heating surface wall temperature and metal corrosion curve (see Fig.2). When the wall temperature is lower than 150 ℃, chloride corrosion is mainly dominated by electrochemical corrosion. This electrochemical corrosion occurs at a temperature of 130 ℃, which is the most serious. When the wall temperature is higher than 480 ℃, it is classified as a high-temperature corrosion. This is characterised by the decomposition of $FeCl_3$ and $Fe_2(SO_4)_3$. Between 150 ℃ and 480 ℃, the wall temperature interval is classified as a low corrosion rate interval. This is characterised by the generation of $FeCl_3$ and $Fe_2(SO_4)_3$. Decomposition occurs between 150 and 480 degrees Celsius, which is the low corrosion rate interval. The main products of this decomposition are $FeCl_3$ and $Fe_2(SO_4)_3$. In order to prevent corrosion, it is necessary to control the wall temperature of the heating surface between 150 and 480 degrees Celsius.
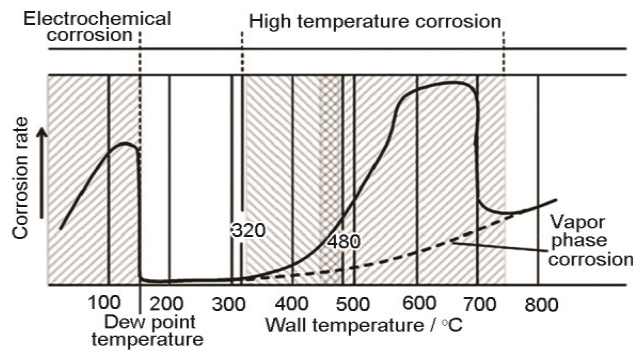
Fig. 2. Relationship between tube wall temperature and corrosion rate at the heating surface

The main steam outlet temperature of the boiler is 540°C, while the tube wall temperature is within the high corrosion rate interval depicted in Fig. 2, indicating a high risk of high-temperature corrosion.

Table 3 illustrates that the chlorine content of coal ash is below 100 mg/kg. The majority of the chlorine present in the combustion process is stored in the flue gas, and the risk of chlorine corrosion caused by the ash on the heating surface is considerably lower than that of the flue gas. Consequently, the high-temperature superheater is isolated from the high-chlorine flue gas, the high-temperature superheater is positioned in the external bed, or the high-temperature grade heating surface of the furnace can be sprayed to avoid direct contact with the flue gas, thus resolving the issue of high-temperature corrosion in the presence of high-chlorine flue gas.

Furthermore, the medium-temperature superheater and low-temperature superheater are situated after the water-cooled tube bundle, with their outlet wall temperatures being regulated to a maximum of 480℃. The boiler is equipped with a cooled flue and a water-cooled tube bundle, which has enabled the inlet flue gas temperature of the superheater to be controlled within 650℃. This has resulted in a more conducive environment for the control of the wall temperature of the heating surface at the rear pass, and has reduced the risk of high-temperature corrosion.

3.2.2 Anti-corrosion at low temperatures

The rear pass of the boiler is equipped wjth an economiser and the tube air preheater. The temperature of the economiser tube wall has remained within the 150 to 480°C range, indicating a low corrosion rate, can't do special consideration. The temperature of the air preheater outlet flue gas and tube wall is relatively low, necessitating the evaluation of corrosion caused by acid gas condensation in the flue gas. The boiler design control air preheater outlet flue gas temperature(not too low). In order to avoid winter or cold environments, the air preheater inlet air temperature is low, which increases the risk of condensation on the tube wall. Therefore, a warm air heater has been installed to improve the air. The preheater inlet temperature should be set such that the air preheater wall temperature is higher than the acid dew-point temperature . Furthermore, the last stage of the air preheater should utilise corrosion-resistant steel in order to minimise the risk of corrosion in low temperatures.

3.2.3 Other anti-corrosion measures

The boiler employs spraying technology in the high-temperature smoke area of the cooled flue from the furnace to the inlet of the water-cooled tube bundle. This is done to prevent direct contact between the water-cooled wall and the cooled flue and high-chlorine flue gas.A corrosion-resistant nickel-chromium alloy coating, comprising a homogeneous mixture of Cr_2O_3 and nickel oxide, has been demonstrated to effectively reduce the corrosion rate of the underlying metal substrate [6].

In terms of soot blowing, in addition to the cooled flue, the use of hydraulic soot removal and the rest of the heated surface soot blowing are employed in the long retractable soot blower. When the soot blowing ceases, the soot blower exits the flue wall, thus reducing the residence time of the flue gas.

The boiler entry coal exhibits a low ash content and, during operation, the addition of bedding material, such as limestone or kaolin, can be employed to further reduce the risk of corrosion.

3.3 Selection of materials for heated surfaces

It has been observed that carbon and low-alloy steels tend to exhibit high corrosion rates in the presence of chloride ions. A significant number of researchers have indicated that Ai-containing nickel-based alloys exhibit enhanced corrosion resistance in chlorinated environments [7].

In the literature on the waste incineration boiler commonly used, a comparison of steel high temperature corrosion resistance is presented in order of increasing resistance from good to bad. The 12 kinds of steel are as follows: The order of corrosion resistance of the steel high-temperature alloys is as follows: TP347H > TP316L > TP321 > TP310S > TP304 > 12Cr1MoVG > 15Mo3 > 20G > SA-210 ≥ T11 ≥ T91 > T22[8]. It can be seen that TP347H has better corrosion resistance.

Therefore, in the selection of materials for the heated surfaces, in order to further reduce the risk of corrosion, materials with better corrosion resistance can be used.

4 Conclusion

This article considers the technical difficulties of combustion of Shal Lake coal, which affect the safe and stable operation of the boiler for a long period of time. It proposes a new type of circulating fluidised bed boiler for combustion of high alkali and high chlorine coal, which can provide a reference for the comprehensive utilisation of the Shal Lake coal. The main conclusions are as follows:

1）The boiler employs a temperature control mechanism to suppress the precipitation of alkali metals. This is achieved through the use of a cooled flue and a water-cooled tube bundle, which collectively serve to reduce the contamination of alkali metals on the heating surface of the rear pass.

2）During the combustion process, the majority of the chlorine present in the coal is released into the flue gas, with the chlorine content in the ash being relatively low. The main steam outlet temperature of the boiler is 540°C, according to the corrosion curve, which indicates that the high-temperature superheater is in a high corrosion rate interval. The high-temperature superheater can be arranged in an external bed or sprayed to avoid high-temperature corrosion caused by direct contact with highly chlorinated flue gas.

3）The medium-temperature superheater, low-temperature superheater and economizer control the wall temperature in the low corrosion temperature range of 150~480℃. To reduce the risk of corrosion, the heated surfaces can be made of materials with better corrosion resistance.

4）The boiler furnace and cooled flue employ spraying technology, the heating surface of the cooled wall employs hydraulic ash cleaning, and the other heating surfaces employ a long telescopic ash blowing device. Additionally, a certain quantity of bed material, limestone or kaolin, can be incorporated during operation to further diminish the risk of corrosion.

References

[1] Xinhua News Agency．Xinjiang has newly confirmed coal resource reserves of 250 billion tons, ranking third in the country [EB/OL]．(2011-03-08).

[2] L.Y. Li, H.Z. Tan, X.B. Wang et al., Research Progress and Applied Technical Status of High Chlorine Coal Utilization, 2022,42(11):4040-4060.

[3] J.B. Zi, X.B. Wang, P.L. Shao, S.M. Liao, Design and Operation Analysis of CFB Boiler Burning High Sodium and Chlorine Coal, 2021,36(04):98-104.

[4] L. Nie, W.G. Bai, S.M. Ran et al., Experimental Study on ash Deposition characteristics of High Sodium Coals from Xinjiang, 2015,35(02):108-112.

[5] X.G. Jiang, X.B. Liu, Research Progress and Direction Thinking on Corrosion of Key Heat Transfer Components in Waste Incineration Boilers, 2020,40(03):205-214.

[6] B. Yang, Z.Q. Zhong, Q.X. Huang et al., Research Development of High Temperature Chlorine Corrosion in Waste Incineration Boilers, 2016,29(06):5-11+17.

[7] Y.S. Li, Y.Niu, W.T. Wu, Chlorination of Metallic Materials at High Temperature, 2000,(01):41-44.

[8] L.K. Huang, Z. Fang, R. Liu, High Temperature Corrosion Resistance Contrast Test of Common-Used Steels in Waste Incineration Boiler, 2020,3(04):24-27+4